UNDERSTANDING THE SELF-ASSEMBLY PROCESS AND BEHAVIOR OF METAL-SEAMED PYROGALLOL[4]ARENE NANOCAPSULES

A Dissertation

Presented to

The Faculty of the Graduate School

University of Missouri-Columbia

In Partial Fulfillment

Of the Requirements for the Degree

Doctor of Philosophy

By

ANDREW V. MOSSINE

Dr. Jerry L. Atwood, Dissertation Supervisor

MAY 2014

The undersigned, appointed by the dean of the Graduate School, have examined the dissertation entitled

UNDERSTANDING THE SELF-ASSEMBLY PROCESS AND BEHAVIOR OF METAL-SEAMED PYROGALLOL[4]ARENE NANOCAPSULES

Presented by **Andrew V. Mossine**

A candidate for the degree of doctor of philosophy of **Chemistry**,

And hereby certify that, in their opinion, it is worthy of acceptance

Professor Jerry L. Atwood (CHAIR)

_____

Professor Stephen Lombardo (OUTSIDE MEMBER)

_____

Professor Carol A. Deakyne (MEMBER)

_____

Professor Silvia Jurisson (MEMBER)

_____

Professor Timothy Glass (MEMBER)

_____

ACKNOWLEDGMENTS

First of all, I would like to thank Dr. Jerry Atwood for giving me the opportunity to be a part of his group, not only as a graduate student, but also as a fresh and untested undergraduate more than five years ago. This early research experience certainly solidified my resolve to attend graduate school, but it also showed me what a joy research can be. Dr. Atwood's valuable advice, faith in my abilities, and his encouragement to think independently has allowed me to not only grow as a researcher but also as a person.

I am also extremely grateful to Dr. Silvia Jurisson, both for the opportunity to collaborate with her group, but also for giving me the chance to take part in the NIBIB training grant program, which allowed me to broaden my research experience by traveling to Washington D.C. for an internship at the NIH.

I would also like to express my gratitude to Dr. Carol Deakyne for all of the collaborative projects that we have worked on together, as well as the invaluable discussions pertaining to my projects and a genuine interest in our group's work as a whole.

I also want to express particular thanks to Dr. Charles Barnes for trusting me enough to use (and not break) the scXRD instrument, for helping me refine the painfully problematic structures that I'd bring him, and all the while for trying to teach me a thing or two about X-ray crystallography. I can honestly say that very little of this work would have been possible without his assistance. On a related note, a big thank you also goes to Dr. Lesa Beamer, both for the inter-group collaboration as well as for teaching me the basics of protein crystallography.

I'd also like to thank both past and present members of the Atwood lab, specifically Dr. Harshita Kumari, Dr. Drew Fowler, and Dr. Nick Power. You've all been there to encourage me, collaborate with me, but also check me when I went astray or started yet-another pet project without finishing the previous one. Thanks also to my other committee members, Drs. Timothy Glass and Stephen Lombardo, as well as to all of the staff at the Department of Chemistry at MU.

And finally, a very special thank you goes to my immediate family; my parents Val and Olga Mossine, and my brothers Paul and Michael, and to my wonderful and loving wife Kelli. You've all been there for me, through thick and thin, and your love, support and patience is what gets me through the toughest of days. Thank you all!

TABLE OF CONTENTS

LIST OF FIGURES

LIST OF GRAPHS

LIST OF TABLES

LIST OF ABBREVIATIONS AND DEFINITIONS

4,4'-bpy (or, alternately just bpy): 4,4'-bipyridine

Ace: Acetone

Cold: "non-radioactive" or consisting fully of naturally-occurring nuclides

Dimer: a dimeric PgC nanocapsule that consists of 2 PgCs and 8 M^{2+} cations as well as several additional ligands

DMF: dimethyl formamide

DMSO: dimethyl sulfoxide

***Endo*-ligand**: A guest molecule on the inside of a MONC that also functions as a ligand for M^{2+} centers.

***Exo*-ligand**: ligand for M^{2+} centers found on the outside of the MONC.

Hexamer: hexameric PgC nanocapsule: consists of 6 PgCs and 24 M2+ cations

Hot: "radioactive" or consisting partly of radionuclides

***In situ* crystallization**: Synthesis of the material and its crystallization in the same container

In situ: In the reaction mixture

MALDI-TOF: matrix assisted laser desorption/ionization- time of flight mass spectrometry

MeCN: acetonitrile

MeOH: methanol

MOF: metal-organic framework (as in literature, it is used synonymously with "coordination polymer")

MONC: metal-organic nanocapsules

OAc: acetate

Peripheral ligand: used synonymously with exo-ligand

PgCx: *C*-alkylpyrogallol[4]arene (x, if present, denotes length of C-alkyl group)

Py: pyridine

Radionuclide: a nuclide (nuclear species) that is unstable and therefore exhibits radioactivity

RsCx: C-alkylresorcin[4]arene (x, if present, denotes length of C-alkyl group)

RT: room temperature

scXRD: single crystal X-ray diffraction

W.R.T: with respect to

ABSTRACT

C-alkylpyrogallol[4]arenes (PgCs) are bowl-shaped compounds that are commonly used as supramolecular building blocks in the construction of larger entities such as capsules, nanotubes, and layered networks. Many of these assemblies are constructed using non-covalent means and, as such, are inherently unstable in polar media. Although metal coordination with the hydroxyl-rich PgC upper rim can be exploited to synthesize assemblies with enhanced stability, few reports of this can be found in the literature. Thus, a thorough investigation of these metal-seamed assemblies and their manipulation is of importance.

Prior work in the Atwood lab has produced three examples of metal-organic nanocapsules (MONCs) based on PgCs. These include two hexameric MONCs (based on Cu^{2+} and Ga^{3+}) as well as a single example of a dimeric MONC (based on Zn^{2+}). As it was unknown whether other metal cations could lead to the formation of similar entities, PgC complexation experiments were conducted with other first series transition metal cations, notably Ni^{2+}, Co^{2+} and Mn^{2+}. All of these led to nanocapsular materials, which were identified and studied using single crystal X-ray diffraction (scXRD). Once the foundational studies were complete, syntheses were also performed under varied conditions, specifically with Ni^{2+} and Cu^{2+}. This led to the characterization of both dimeric and hexameric MONCs with these two metals, as well as the characterization of many other capsular materials. The information collected from these experiments also led to an intriguing question: which specific conditions lead to the formation of dimeric vs. hexameric MONCs?

To answer this question, solid-state analysis using scXRD was coupled to *in situ* analysis utilizing small angle neutron scattering (SANS). This work showed that the formation of the dimer is typically favored at higher temperatures while the formation of the hexamer is favored

at lower temperatures for both of the metals tested. Studies that varied time of measurement as well as the solvent system during synthesis were also performed. Furthermore, SANS was also used to study Fe^{3+}-PgC complexes. These complexes are difficult if not impossible to crystallize, and therefore cannot be studied using scXRD. SANS was used in conjunction with elemental analysis to deduce a structure for these materials.

In addition to understanding the synthesis of MONCs, another goal was to also use them for other (possibly practical) purposes. To this end, PgC-based MONCs were used as building blocks in metal-organic frameworks (MOFs). This involved the use of divergent ligands to "link" capsular monomers together, resulting in one and two dimensional frameworks. This work not only produced functional materials that may be useful in future research efforts, but also showed that exo-ligand exchange can be used to derivatize MONCs into potentially useful and functional materials.

The introduction of radioisotopes into the nanocapsule was another method by which functionality could theoretically be imparted into MONCs. It was envisioned that MONCs could potentially be used as carrier systems for radioisotopes, and thereby function as agents for therapy or medical imaging. Copper hexamers constructed from $^{64}Cu^{2+}$ were therefore prepared and studied in a living system. However, these studies were unsuccessful at showing that the copper-seamed MONCs differed in behavior from ^{64}Cu *in vivo*, either due to poor labeling efficiency or metabolism. Nevertheless, radiolabeling of hexameric nanocapsules was helpful in broadening our understanding of these materials. Some of the studies that were conducted include those that gauge the solubility and stability of nanocapsules, as well as others that explore the conditions required for cationic uptake and exchange

Chapter 1: Pyrogallol[4]arenes in the context of supramolecular chemistry

1.1 Supramolecular chemistry

Supramolecular chemistry, literally "chemistry beyond the molecule," is the field of chemistry that deals with the creation of chemical assemblies out of individual molecular precursors.[1] Unlike other fields of chemistry, where covalent bonding is the primary driving force of chemical transformation, supramolecular chemistry instead relies on the rational implementation of non-covalent inter- and intra-molecular forces in the design of a wide variety of complex molecular systems. These systems are often made up of multiple molecular building blocks and are commonly referred to as super- or supramolecules. The building blocks that make up supramolecules and other supramolecular frameworks can vary tremendously, and range from simple organic molecules[2] to large macrocycles[3], metal-organic complexes[4], and peptide fragments[5,6].

The beginnings of supramolecular chemistry are rooted in the mimicry of biological systems, where weak forces often dictate structure and function of biomolecules, such as in the cooperative hydrogen bonding in DNA or the "lock and key" protein/ligand interaction.[7] As such, a good portion of research in supramolecular chemistry was and still is dedicated to finding synthetic versions of biosubstrates for various ligand molecules. This has since evolved into the subfield of host-guest chemistry, which is a generalized, synthetic version of biosubstrate mimicry. Here, the interactions between a typically larger molecule, the host, and a typically smaller molecule, the guest, are studied. Another focus of supramolecular chemistry is that of self-assembly. In analogy to viral capsids, where several protein segments assemble to form a

whole capsular entity, supramolecular self-assembly deals with the formation of larger complex species from smaller synthetic building blocks. This subfield goes hand in hand with host-guest chemistry, as these large self-assembled structures are frequently hosts for smaller molecular guests.

Supramolecular chemistry is really not one cohesive field, nor does it have one purpose, direction, topic or overarching methodology. It is instead a synthetic paradigm that is used by researchers in a wide range of disciplines to propel their own distinct objectives. These objectives are often very practical, cutting-edge solutions to 21st century problems, some of which include chemical sensing, gas adsorption, energy production, and drug delivery. As such, it is no wonder that, broadly speaking, supramolecular research continues to be one of the fastest growing directions in chemical research.

1.2 Non-covalent forces relevant to supramolecular chemistry

The principle of molecular self-assembly and host-guest chemistry relies on cooperative interactions of molecules. This requires that an attractive interaction between the different components takes place. In supramolecular chemistry, these interactions are typically electrostatic (non-covalent) bonds where electrons are not shared between atoms. This differs from other branches of chemistry, where the end goal is the formation of covalent bonds (where electrons are formally shared) resulting in a more or less permanent connection between the constituents. The formation of supra-molecules, however, is reversible due to the much weaker non-covalent bonds that hold the assemblies together. This section will describe the forces that typically contribute to supramolecules. In addition, coordinative bonds will also be briefly discussed. While coordinative bonding can be and has been considered to be covalent in nature,

it is often used as a driving force in supramolecular self-assembly and is of some importance to the contents of this thesis.

1.2.1 Ionic and Ion-dipole interactions:

Ionic bonds are bonds between oppositely charged ions. It is a relatively strong force (40-4000 kJ/mol)[8], and is responsible for the organization of ions within salt or mineral crystals but can also persist in solution, given the right conditions. Although it is not a covalent bond *per se*, electrons are shared to a certain extent between the constituents, which results in electrical conductivity in the molten state.

A much more important variant of the ionic bond to supramolecular chemistry is the ion-dipole interaction. In this type of interaction, an ionic species is attracted to the oppositely charged end of a polar (but non-ionic) molecule. As the polar molecule does not have a fully positive or negative charge, this force is necessarily weaker (50-500 kJ/mol)[8] than in ion-ion interactions, where both species carry permanent charges. Nevertheless, it is conceptually much easier to capitalize on this interaction, as polar molecular species are relatively common as functional groups in organic molecules. This concept is also important to the field of ion sensing, where molecular receptors are used to attract and measure ionic analytes.

In addition to typical ion-dipole interactions, an ion can also interact with quadrupoles, such as aryl rings. This leads to interactions such as the cation-π bonding between the alkali cations and benzene, as well as the much rarer anion- π bonding between halide anions and aromatic systems outfitted with electron withdrawing groups.[8,9] On account of their high charge density, ions can also be used to induce dipoles in normally non-polar species, leading to weak ion-induced dipole interactions.

1.2.2 Dipole-dipole interactions:

Dipole-dipole interactions occur when two oppositely charged sides of dipolar molecules electrostatically interact. The electrostatic interaction can occur between individual poles, but in small enough molecules, both positive and negative poles from one molecule will interact with both poles of an adjacent molecule. The strength of this interaction (5-25 kJ/mol, when one does not consider hydrogen bonding)[8] is weak in comparison to interactions involving ions due to the complete absence of permanently charged species. However, this force is responsible for much of the assembly processes in supramolecular chemistry, as it allows for the interaction of large molecules with an overall neutral charge by virtue of smaller functional groups found on these molecules. As with ion-induced dipole interactions, polar species can also induce dipoles in non-polar molecules, although this is again a fairly weak interaction.

1.2.3 Hydrogen bonding:

A subset of dipole-dipole interactions is hydrogen bonding. This interaction is perhaps the biggest driving force in supramolecular self-assembly due to the near ubiquity of its constituents and its relatively high strength (10-200 kJ/mol)[8]. Hydrogen bonds occur between two molecular moieties, a hydrogen donor and a hydrogen acceptor. The hydrogen donor is a dipolar group of the H-A type, where H is a hydrogen atom with a partial positive charge and A is an electron-withdrawing atom to which the hydrogen is covalently bound. The second group, a hydrogen acceptor, contains a lone pair of electrons and, like A, is usually an electron-rich

atom such as N, O, or one of the early halogens. The hydrogen of the donor is attracted to the hydrogen acceptor *via* an electrostatic charge, thereby forming what is essentially the prototypical dipole-dipole interaction. The best example of hydrogen bonding occurs in water, where the oxygen atom functions both as A and B. This shared donor-acceptor role is prevalent in many molecular species that are capable of hydrogen bonding, particularly in larger molecules where hydroxyl (-OH) and amine ($:NR_xH_{3-x}$) groups are present. This includes many molecular species of biogenic origin, where hydrogen bonding is responsible for three-dimensional structure.

In addition to hydrogen bonding that involves protons that are significantly polarized by electron withdrawing groups (i.e., hydrogens involved in N-H···O or O-H···O bonding), there is another class of hydrogen bonding that occurs over longer distances and is also significantly weaker.[10] This type of hydrogen bonding takes place between the classic acceptor atoms such as oxygen or nitrogen, but with a C-H hydrogen as the donor. Therefore, this type of hydrogen bonding is often referred to as C-H···O or C-H···N bonding. Because of the different chemical environments the carbon can be part of, the polarity of the C-H bond is highly variable, and therefore the hydrogen bond between the C-H donor and hydrogen acceptor is also highly variable in both distance and strength. For example, if the carbon is part of an aromatic ring system, or is adjacent to other electron withdrawing groups, the C-H···Acceptor hydrogen bond can be quite strong. Hydrogen bonding in un-activated environments (such as branched aliphatic systems) is also possible if an appropriate acceptor is present, although it is also a much weaker bond and is more similar to a dipole-induced dipole bond than to a true hydrogen bond.

1.2.4 Other non-covalent forces:

Another ubiquitous, but weaker set of forces that contributes to inter-molecular interaction is known collectively as the Van der Waals (or V.D.W) forces. These include some of the stronger forces already mentioned (non-hydrogen dipole-dipole and dipole-induced dipole attractions) but also some that have not. These include London dispersion forces (induced dipole-induced dipole between similar molecules; 0.05-40 kJ/mol)[8] CH-π type interactions[11] and π- π stacking interactions (50-500 kJ/mol)[8]. These occur over much longer distances, and with the exception of π- π stacking are generally weaker than the other forces described in this section, but are still valuable towards the construction of supramolecular assemblies.

1.2.5 Coordinative bonding:

As the name suggests, coordinative bonding does involve the formation of a dative bond, wherein two electrons are shared between two atoms. These electrons typically come from a ligand (Lewis base), which are shared with empty orbitals in a metal cation (Lewis acid). Due to the involvement of the d and f orbitals as well as the larger size of the metal cations that are typically found in coordination complexes, the "coordination number", or the number of constituents bound to the metal center can vary tremendously, from two up to twelve for some of the lanthanides and actinides. The strength of coordinative bonds can be quite large, but generally varies depending on the nature of the ligands and the central cation. The role of coordinative bonding in supramolecular chemistry comes from its role in arranging ligands

around a central locus. This is because metal ions can, in a sense, act as docking stations for electron-donating moieties on supramolecular building blocks that are not proximally located to one another. Therefore, this can cause a change in the geometric configuration of an otherwise linear molecule, create a yet-bigger supramolecular building block out of smaller entities, or cause several molecules, such as macrocycles to self-assemble into other, more interesting entities. The latter case is significant, as it is way by which nanocapsules are synthesized in later parts of this thesis.

1.3 Macrocyclic building blocks

Although there is a diverse range of molecules that can be used as supramolecular building blocks (indeed, most, if not all molecules can be used to form supramolecular assemblies), one particular molecular class stands out among all the others in both its uniqueness and frequency of use in supramolecular research. This molecular class is the macrocycle. At the most basic level, macrocycles are cyclic oligomers of what would otherwise be an unexciting polymeric fragment. While they inherently share the parent oligomers' chemical functionality, the main purpose of such oligomeric cyclization is in the formation of a cavity at the molecules' center. This, in turn, creates a distinct chemical microenvironment for guest species, which is why macrocycles are so universally used for host-guest research. The nature of the cavity thus formed is highly variable and depends largely on the materials (monomers) used to fabricate the macrocycle. It can vary in size, shape, and in the number of openings to the surrounding environment. These factors, along with the chemical environment within and outside the cavity, dictate the types of molecules which will be recognized as guests. By controlling the processes that govern their formation, macrocycles can be specifically synthesized to accommodate

specific guest species and to fulfill specific roles. Structural tuning also allows macrocycles to act as building blocks, particularly in cases where the end result is a capsular or tubular entity. Their use for this purpose is particularly important in the context of this thesis, as the chemistry described herein specifically deals with this kind of implementation of macrocyclic molecules. This section will therefore briefly describe several different types of macrocycles and some examples of their uses. Additional classes of supramolecular assemblies include mechanically interlocked structures/rotaxanes,[12-14] catemers,[15-17] foldamers,[18-21] and various molecular (and metal-organic) frameworks,[22,23] but as stated before, these will not be covered here.

1.3.1 Crown ethers and similar molecules:

Macrocycles that at least partially consist of repeating ethyleneoxy $(-CH_2-CH_2-O-)_n$ units are collectively known as the crown ethers due to their resemblance to a king's crown (the non-cyclic variants of crown ethers are known as podands).[8] The main utility of crown ethers is derived from the position of the oxygen atoms, which point towards the interior of the "crown." This makes the inner cavity electron-rich and perfect for the uptake of positively charged guest species, specifically cations, *via* ion-dipole interactions. An improvement of their synthesis and their use as ionophores was accidentally discovered by Pedersen, one of the founding fathers of host-guest chemistry, as a byproduct from the synthesis of yet another ionophore he was working on for cations of the alkali metals.[24] Their electron-rich cavity coupled with a hydrophobic exterior (particularly when groups such as various catechols are used as structural units) allows the crown ethers to be used to solubilize highly polar cationic species in non-polar/hydrophobic media.

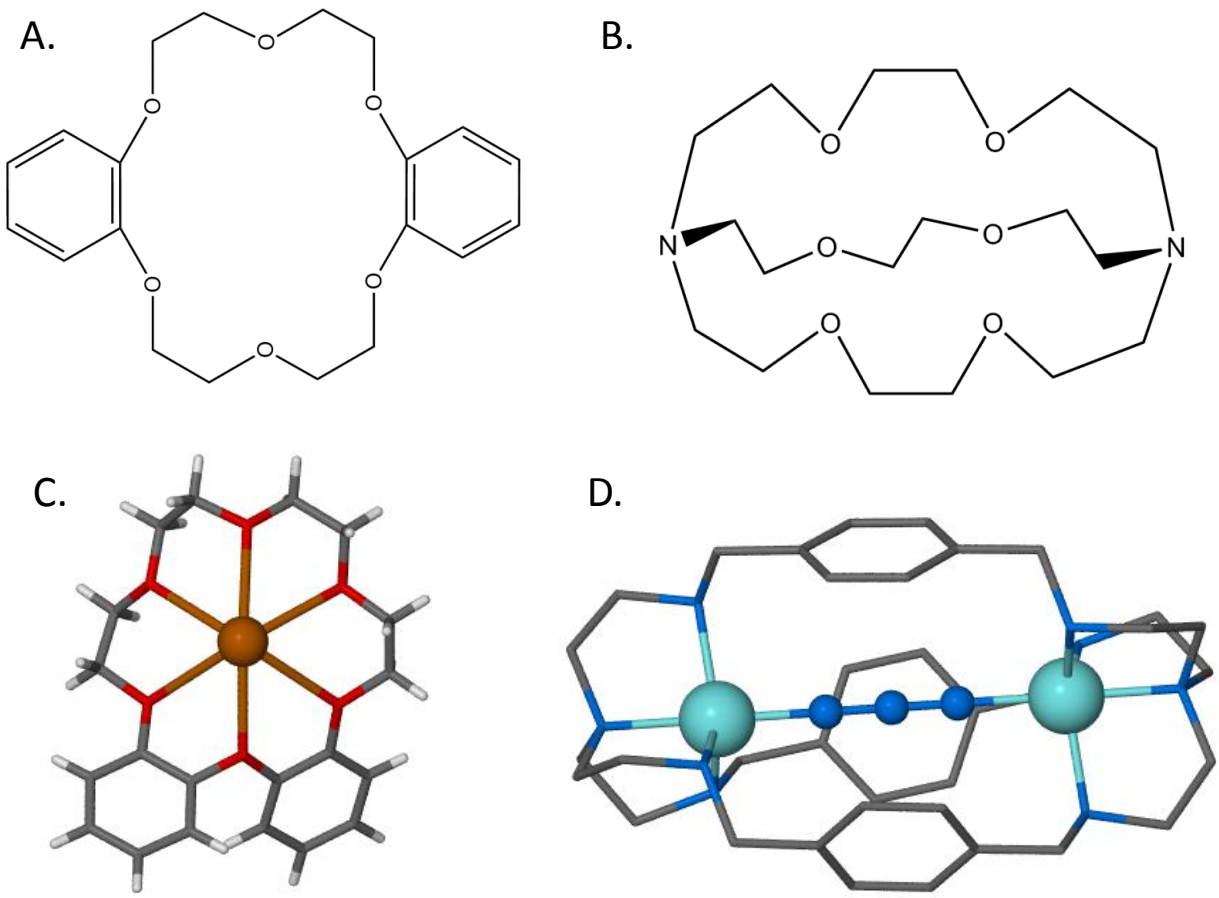

Figure 1.1: Examples of crown ethers and cryptands. Chemical structures of dibenzo-18-crown-6 (A) and [2.2.2]-cryptand (B) are shown. Crystal structure of a dibenzo-crown K^+ complex[25] (C) and a "cascade complex" (D) where an N_3^- anion is incarcerated between two copper centers.[26]

The size of crown ethers can easily be changed by using appropriate reagents to create a bigger or smaller ring, with a varied number of electron-donating oxygen atoms. To quickly demarcate specific crown ethers from others, a nomenclature system has been established: any non-ethyleneoxy substituent is listed first, followed by the number of atoms in the ring, the family name (crown), and finally the number of oxygen donors. For example, dibenzo-18-crown-6 (Fig 1.1a) has two benzo groups, an eighteen-membered ring, and six oxygen donor

atoms. One can gain selectivity for specific cations by correctly selecting the ring size of the crown ether, and although almost any crown ether will bind to any cation, a difference in cavity/ion size leads to much weaker binding between the two. In addition to ring size, other modifications can also be made to the basic polyether crown skeleton. Structural units, such as aryl groups or alkyl chains can change the solubility when attached to the backbone of the crown, but to change the chemical function, the skeleton itself must be changed. For example, the addition of nitrogen centers as a complementary to/replacing the oxygens leads to the formation of so-called aza-crowns or cyclens, which are also useful as ionophores, but have different complexation capacity than the regular crowns. Crown-cation complexes, specifically Cu^{2+} complexes, have been used as (indirect) ionophores for anions, and are known as "cascade complexes." While the cation is incarcerated within the crown through coordinative bonds that are parallel to the axis of the macrocycle, additional exposed coordinative sites bind to the anion as additional ligands.[27] (Fig.1.1d) Likewise, immobilized Zn^{2+} crown complexes have been used as sensors for the amino acid histidine.[28] In both of these cases, the fluorescence of the complex changes when the guest species is bound to the metal center, and therefore the guest can be detected. In addition to their affinity towards cations, crown ethers have also been used to stabilize some unusual molecular species. One example is the alkalides, which are the rare and unstable singly anionic salts of the alkali metals.[29] Stabilization of these species occurs through the stabilization of their cationic counterpart. In the case of the sodium analog (from a sodium melt), the crown ether incarcerates a sodium as a Na^+ cation, which passes its valence-shell electron onto another sodium, creating a Na^- species in the process.

Cryptands are macrocycles that are similar to crowns, but can be thought of as an improvement on the basic two-dimensional crown ether skeleton. Two amine nitrogen atoms on

diametrically opposite sides of the macrocycle act as bridgeheads that allow for three molecular chain attachments, versus the maximum of two that is possible with ethyleneoxy linkages. This produces a "crypt-like" three-dimensional enclosure, which has a significantly higher affinity towards cations (particularly alkaline earths) but is also much more selective for *specific* cations due to increased geometric constraints.[30] The most prototypical of these is known as the [2.2.2] cryptand, which is displayed in figure 1.1b (the numerical "2" represents the number of oxygens per chain). Cryptand-like hosts that contain a large number of (protonated) amine nitrogen moieties can be used to bind anionic species. These are known as aza-cryptands, and two similar compounds are the catapinands and sepulchrates. Anion binding occurs in much the same way as cation binding in regular crowns or crypts, except that the negatively-charged anionic guest is attracted to positively charged N-H groups of the host.

1.3.2 Cyclodextrins

Cyclodextrins are essentially cyclic oligomers of starch, which is normally a linear polymer of repeating glucose monomers. Unlike most macrocycles, which are produced using standard synthetic chemical means, cyclodextrins are produced enzymatically.[8] The most common cyclodextrins produced in this way are the α, ß, and γ cyclodextrins, which are 6, 7, and 8-membered macrocycles, respectively, although others with much larger ring sizes can also be produced (see Fig 1.2a for the structure of γ-cyclodextrin). The structural features of a cyclodextrin are essentially inverted from that of crown ether, namely that the interior is hydrophobic while the exterior is hydrophilic. This makes cyclodextrins great at solubilizing molecular species that are normally only poorly soluble in aqueous media. This includes many different pharmaceutical agents, and several patents have been awarded for cyclodextrin-

pharmaceutical compositions.[31-37] One specific benefit of cyclodextrins for this purpose is that they are not only water-soluble but also biocompatible, as they are a naturally occurring product. Nevertheless, cyclodextrins can also be covalently modified by virtue of the large number of reactive hydroxyl groups at their exterior. Therefore, they can be tailored to encapsulate specific guests based on structural unit homology or act as better catalysts due to these modifications.[38]

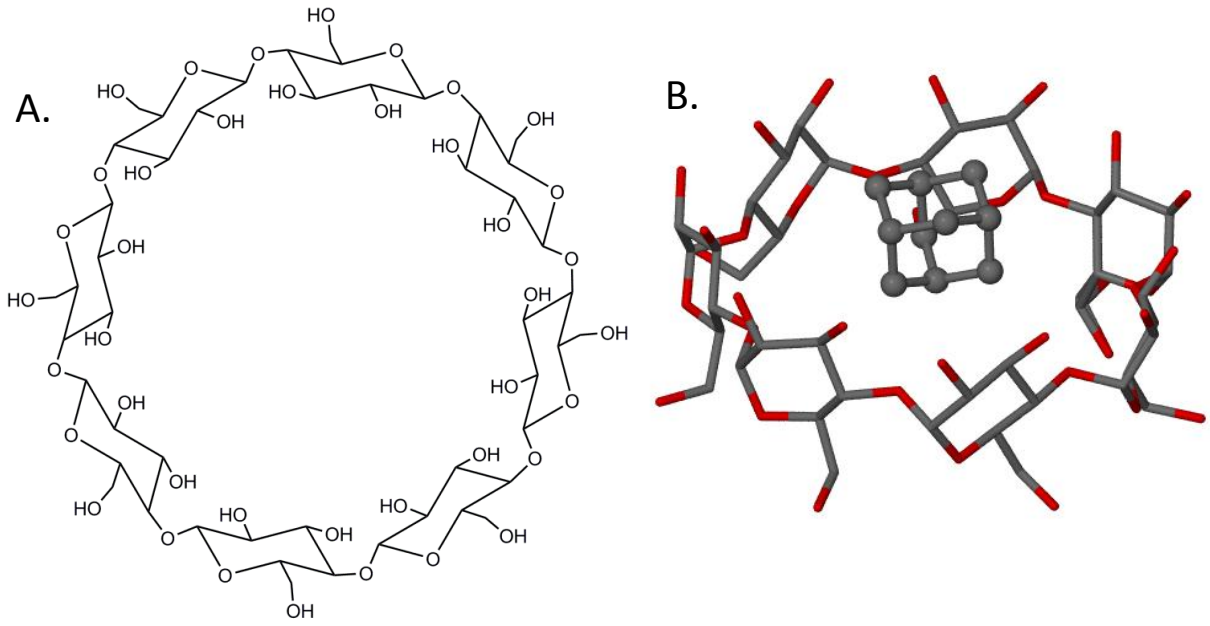

Figure 1.2: Examples of cyclodextrins. Molecular structure of γ-cyclodextrin (A) and a crystal structure of the same macrocycle with an adamantane guest[39] (B).

Aside from the encapsulation of lipophilic pharmaceutical agents, cyclodextrins have also been used for many other purposes. One particularly useful discovery was that cyclodextrins are capable of acting as enzyme-like entities, something that has always been touted as a specific goal for macrocycles of all sorts. In enzymes, guests are immobilized within a binding pocket or cavity. This greatly increases the rate of any given reaction between the enzyme and the guest as compared to the same reaction in solution, as it puts reactive groups in proximity to the guest.

Analogously, the reaction rate of the incarcerated guest with the cyclodextrin hydroxyl groups or other moieties on the surface is also increased. This is particularly the case with acetyl hydrolysis from aromatic systems, where the acetyl passes to the cyclodextrin hydroxyls, as well as a whole series of halogenation reactions where the cyclodextrin acts as a relay and transfers the halogen from solution to the guest in a selective manner.[40]

1.3.3 Cucurbiturils

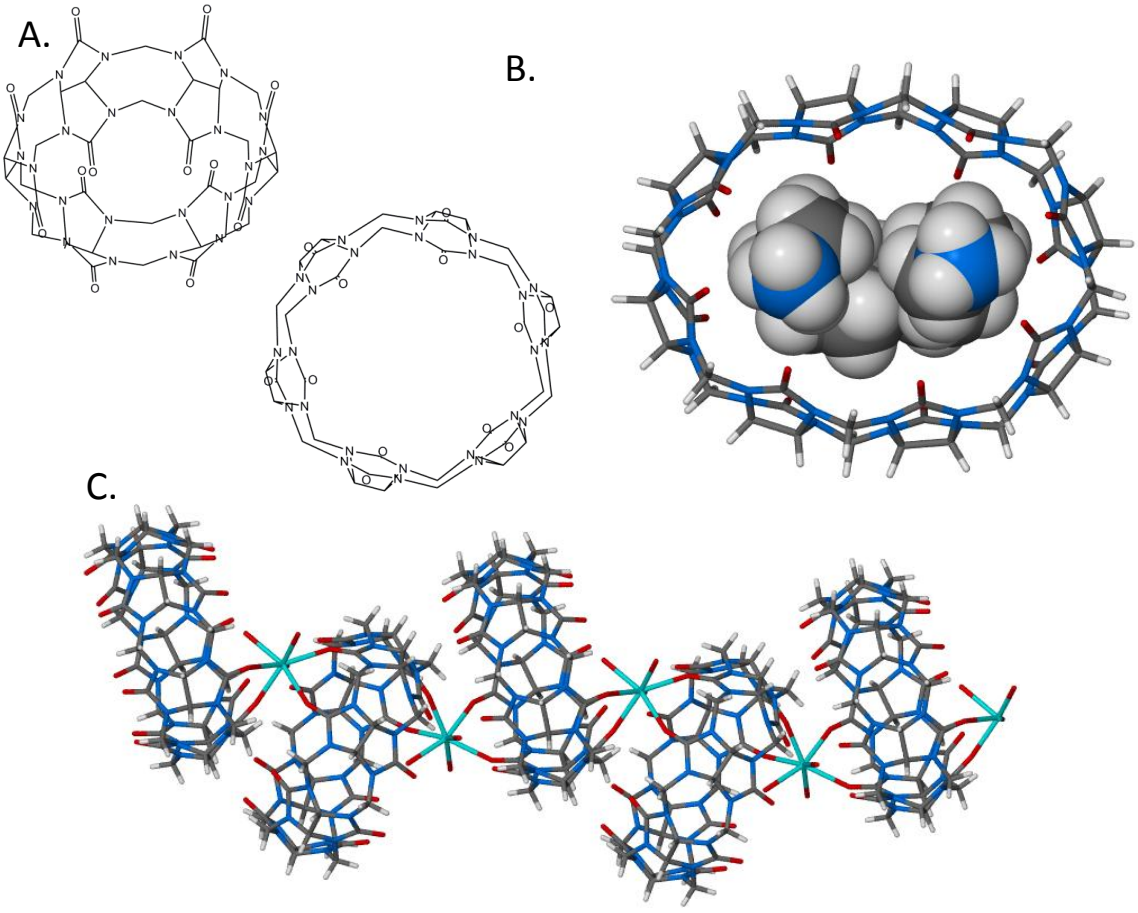

Figure 1.3: Examples of cucurbiturils (CBs). Two views of the molecular structure of CB6 (A); diamine guest inclusion complex of CB8 (B)[41] and a nanotubular coordination polymer of CB6 with Cd^{2+} (C)[42]

Cucurbiturils (CBs) are macrocyclic compounds that are conjugates of formaldehyde and glycouril monomers. Their name, like the crown ethers has a direct link to their appearance, which is similar to the pumpkins and gourds of the cucurbitaceae family.[43] As such, they are round in shape and tapered at both ends. Like many other macrocycles, the cucurbiturils come in many different ring sizes, the formation of which depends on specific conditions during synthesis. The most common of these is the 6-membered macrocycle (Fig. 1.3a,c), but the reaction product is usually a mixture and many others are also synthesized.[44] Interestingly, the 10-membered macrocycle is solely found as a host-guest complex with the 5-membered macrocycle following synthesis, and removal of the 5-membered species is important in taking advantage of the 10-membered species' large internal volume. The interior of these macrocycles favors cationic guests due to cation-dipole interactions with carbonyl groups, along with more hydrophobic guests that interact with the hydrophobic inner-ring structure. For this reason, cucurbiturils can also encapsulate whole metal complexes, particularly those composed of smaller hydrophobic ligands.[45] The outer rim of cucurbiturils is much narrower than the internal cavity, so a barrier exists to larger guests entering and leaving the cavity, and this must be considered when deciding on potential guest molecules.[43] Unlike the cyclodextrins, they are only sparingly soluble in water, unless an acidic/basic solution is used. This limits their use in biologically-relevant settings, but more recent analogs that feature water-solublizing groups have also been synthesized.

As with cyclodextrins, cucurbiturils have been used for a range of different purposes, most of which involve the encapsulation of a guest within the inner cavities. Some of these include their use as catalytic centers, molecular switches, rotaxanes and textile waste stream remediation.[43,44]

1.3.4 Calixarenes

Over the past several decades, these four, five, six, or eight-membered macrocycles of the calixarene superfamily have carved out a place for themselves within experimental and theoretical chemistry, and for several very good reasons. Most simple calixarenes are synthesized *via* a one-pot condensation reaction involving inexpensive reagents and catalysts, and are purified with common solvents, often without the use of column chromatography.[46] Many different phenols and electrophilic bridging substrates can be combined to create calixarenes in this way, and the use of other aromatics such as pyrrole and hydroquinone lead to similar analogs such as calix[n]pyrroles and pillar[n]arenes, respectively. After formation, they are far from immutable entities, as they act as rigid templates for a wide degree of post-synthetic functionalization.[46] Indeed, the final product in some research involving these macrocycles often bears little resemblance to the starting material. For these reasons, the calixarenes have been used in a broad scope of research and this family now encompasses hundreds of different compounds and more than ten thousand research papers (scifinder search: "calixarene") have been published regarding these macrocycles

1.3.4.1 Brief history of the calixarenes

The propensity for phenols to react with aldehydes, notably formaldehyde, to form polymeric resins has been known since at least the 1870s from the works of von Baeyer.[47] It was later realized that by "curing" these resins with heat, a hard solid would form. This solid became economically important in the early 20th century as Bakelite; the world's first commercially produced plastic. This led to a boom in research efforts on phenol condensation reactions,

notably within the forthcoming plastics industry. Up to this point, however, only linear polymers were known to be produced from phenol/aldehyde condensation reactions. The first hints of cyclooligomerization (i.e. the formation of a finite cyclic product) came in the 1940s from the work of Zinke and Ziegler. Aiming to study a new version of Bakelite formed from p-alkylphenols, they stumbled upon a colorless solid after heating the resinous product in oil. Based on the results of another researcher studying resorcinol/aldehyde condensations at the same time, who proposed that the resultant products were tetrameric, Zinke and Ziegler also reported this compound as having a tetrameric structure. A refinement in the synthesis of this material came several years later by the Petrolite Oil Company while addressing customer complaints into one of their phenol-based oil demulsifiers.[47] Their procedure, which involves a base-catalyzed condensation of formaldehyde with a phenol, followed by high temperature cracking of the resinous polymer in an aromatic solvent is still often used to form calixarenes to this day. It was later determined that these solids actually contained a myriad of stereoisomers and several cyclic products. Work with these cyclic tetramers, now coined calixarenes, greatly expanded following the advent of NMR and XRD instrumentation and by the seminal research efforts of Boehmer, Ungaro, Gutsche, among others.[46-48] Today, hundreds of research groups around the world work with calixarenes and calixarene-like compounds to fulfill a wide variety of research interests in a broad range of disciplines.

1.3.4.2 Synthesis of calixarenes

The formation of calixarenes typically follows the condensation of two building blocks to yield a cyclic product. The two main reactants that give rise to calixarenes are almost always an aromatic component, usually a phenol of some sort, as well as an electrophile, which is usually an aldehyde or an acetal, most commonly formaldehyde. As such, the reaction is an electrophilic aromatic substitution, where the aldehyde or other bridge building moiety is the electrophile. Refluxing the reactants in the presence of an acidic (or basic) catalyst results in the condensation of these reagents into a wide array of polymeric, oligomeric, and cyclic products, all having an alternating phenol-bridge-phenol topology. Sometimes, a large portion of the product is polymeric, and must be cracked into smaller oligomers by reheating the material at high temperatures. The linear oligomers condense onto themselves and onto other oligomers to form the cyclic end product referred to as the calix[n]arenes, with the n signifying the number of phenols and bridges present in the molecule. The most common bridge is a single carbon atom, which results from the use of an aldehyde during the initial reaction. However, many different bridging molecules can be used to generate oxa-, aza- and thia-calixarene derivatives that have bridges made up of the corresponding atoms (O, N, and S, respectively). Likewise, a huge range of phenols and phenol-like molecules can be used for the aromatic component. By using resorcinol and pyrogallol, resorcinarenes and pyrogallolarenes can be generated, and these will be discussed in more depth in later parts of this chapter. The way in which these cyclic oligomers form is of some debate, and much work has been dedicated to identifying the conditions required to form oligomers of specific cyclic topology.[47] Often the dictating factor is the temperature at which the polymer is cracked, as well the solvent system that is used to carry out the cracking reaction. Mixtures of cyclic oligomers are quite common, but are often easily

separated by fractional crystallization or selected for by modifying the conditions during synthesis.

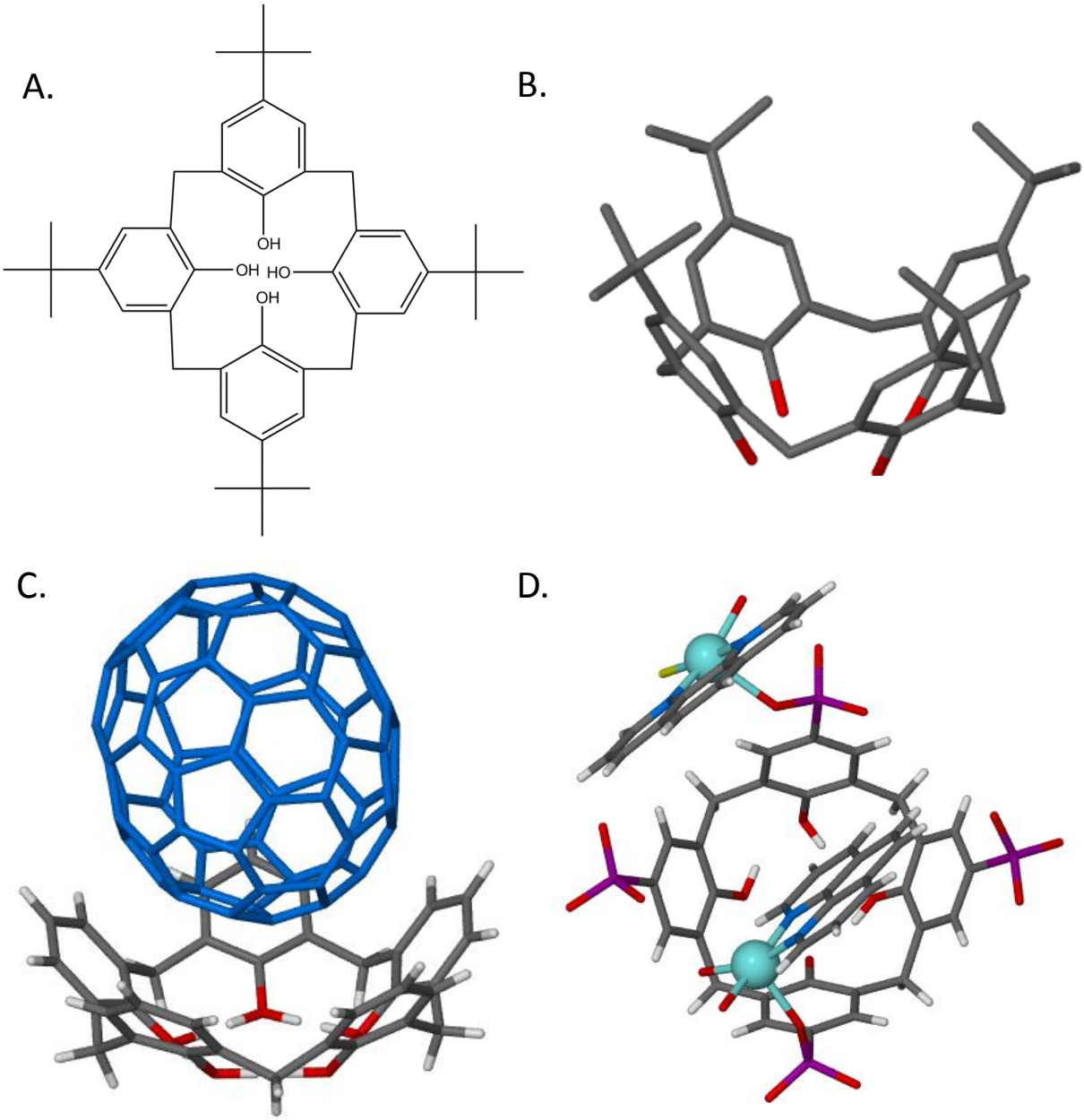

Figure 1.4: Examples of calixarenes. Molecular structure of t-butylcalix[4]arene (A) and its geometric "cone" conformation (B), an inclusion complex of calix[6]arene with C_{70} (C),[49] and a metal complex of sulfonatocalix[4]arene with Cu^{2+} (D).[50]

In addition to various ring sizes, calixarenes also come as different conformers. For example, a calix[4]arene (a four-membered macrocycle) can occur in four unique conformations: the cone (rccc), chair (or 1,2-alternate; rctt), partial cone (rcct) and 1,3-alternate (rctc). The most common and the most useful, however, is indeed the cone, due to the partially enclosed internal cavity.

1.3.4.3 Uses of calixarenes

As with other macrocycles, the use of the calixarenes is vast, but is often based on the bowl as the distinguishing structural element. In fact, the resemblance of the bowl to a chalice, or calyx, was what gave the calixarenes their unique name in the first place.[51] The interior of the bowl is notable as it functions as an artificial receptor in host-guest complexes (Fig. 1.4c).[52-56]. Other conformers that do not possess a bowl are also available, but these tend to find a much more limited use. In addition, the structural rigidity of calixarenes allows one to use them as rigid scaffolds on which to build useful features. It was their promise in this regard that led Gutsche to pursue calixarenes as a rigid template on which to house all of the components of an artificial aldolase mimic.[8] This concept has been expanded to a wide array of research, and calixarenes have since been used as enzyme mimics/components in enzymatic systems, [57-59] structural templates for the design of new pharmaceutical agents,[60] metal complexes and catalysts (Fig. 1.4c).[61-64] In addition to these types of studies, the self-assembly of calixarenes into functional materials has also been extensively investigated, as has its potential for gas adsorption.[65-67]

1.3.5 Resorcinarenes

A subtype of the calixarene family of molecules is the resorcin[4]arene (RsC). As its name suggests, resorcinol (instead of other phenols) is used as the main structural component of this macrocycle. Cyclocondensation with an aldehyde (formaldehyde cannot be used) leads to the formation of a macrocyclic molecule that is surprisingly different from most calixarenes. The main difference between the two is the chemistry of the upper and lower rims. Unlike the calixarenes, where the compressed lower rim houses the aryl hydroxyls while the divergent upper rim contains various R-groups, resorcinarenes have a "flipped" arrangement of rims, with a hydroxyl-rich (and hydrophilic) upper rim and a typically hydrophobic lower rim (Fig. 1.5b). In addition, calixarenes with R-groups at the bridgehead carbons are rare, while in resorcin[4]arenes a bridgehead R-group is always present. Therefore, the RsC macrocycle can be considered to be an ampiphilic species.

As the positions of the hydroxyls on the upper rim allows for the formation of an extensive inter-molecular hydrogen bonding network, one of the more important directions for RsC research is self-assembly. Self assembly of RsCs can involve other structural components, but often the distinguishing feature is the inter-molecular interactions between the macrocycles themselves. In this respect, one of the most important motifs is the hydrogen-bonded hexamer (Fig. 1.5c).[68] The hexamer consists of six RsC macrocycles that undergo hydrogen bonding with one another as well as with several structural water molecules. The end result of these interactions is a nearly spherical entity that is stable in non-polar solvents and possesses a large internal volume. This large internal cavity is the structural feature that is of interest to scientists, as it possesses sufficient internal space for guest encapsulation,[69,70] and catalysis as a nano-

reactor.[71-73] Other important motifs that are based on the self-assembly of the resorcin[4]arene macrocycle are dimers,[74,75] nanotubes,[76,77] and various framework solids.[78-81]

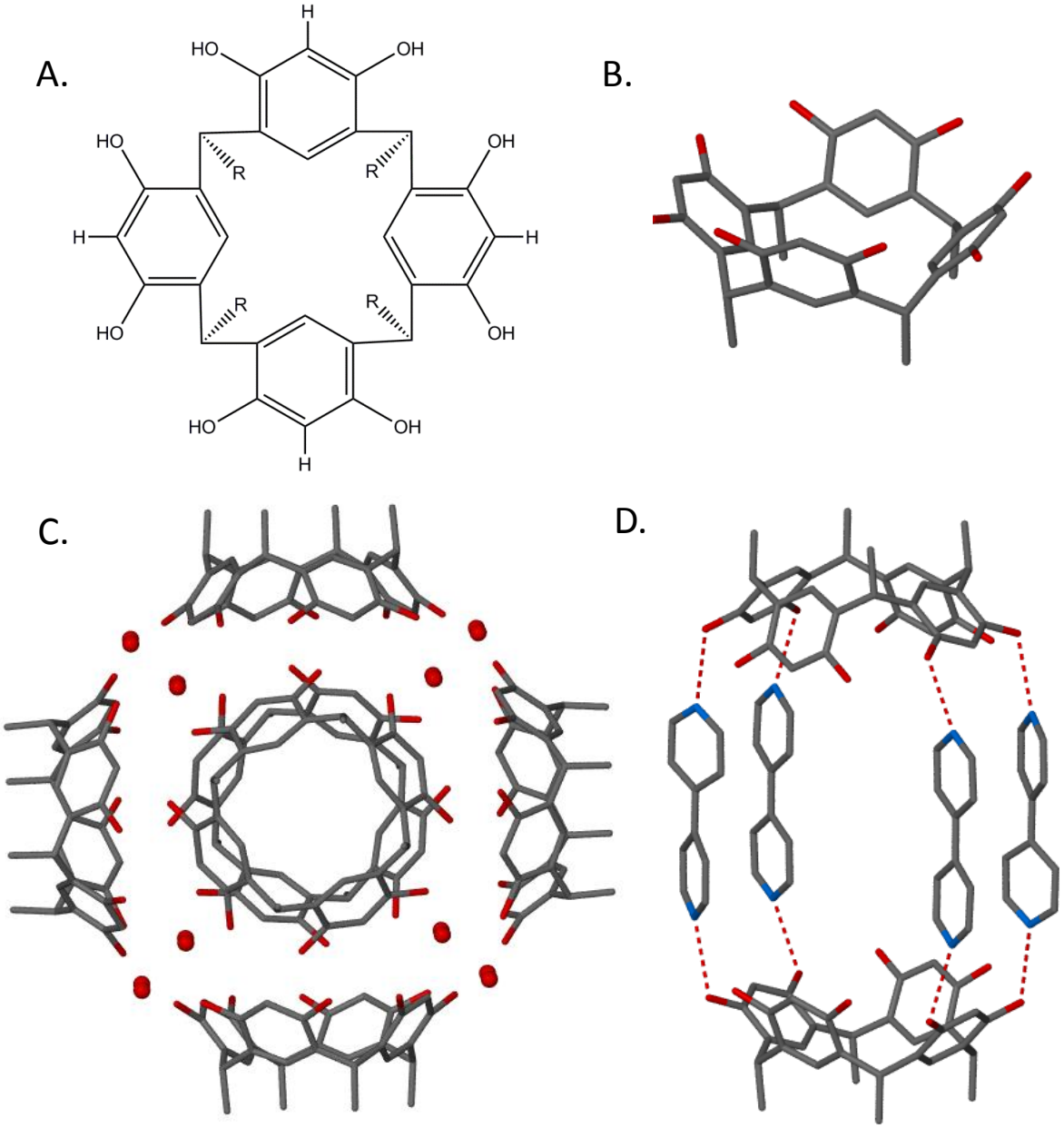

Figure 1.5: Examples of resorcinarenes: Chemical structure of resorcin[4]arene (A) as well as the structure of the "cone" conformer (B). Two important self-assembled structures: the RsC hexamer (C)[68] and extended cavity resorcinarene/bipyridine complex (D).[82]

The positions of the hydroxyl groups on the resorcinol ring also lead to another valuable use for these macrocycles: post-synthetic covalent modification. Resorcinol, also called 1,3-dihydroxybenzene, has a vacant site between the two hydroxyl groups (at the "2" position) that is highly activated for electrophilic aromatic substitution. As such, covalent modification of the macrocycle is quite simple. This has led to a variety of different research efforts, including the expansion of the RsC cavity to accommodate larger guests, functionalization of the upper rim for catalytic/molecular recognition purposes (as with the calixarenes), or to completely incarcerate guest species. The latter concept gives rise to compounds called carcerands and hemi-carcerands, which are a wholly different type of container molecule.

1.4 Pyrogallol[4]arenes

Pyrogallol[4]arenes (PgCs) are the macrocyclic products that are formed from the acid-catalyzed cyclo-condensation of pyrogallol (1,2,3-trihydroxybenzene) with various aldehydes. Aside from a few notable caveats, they are similar to the resorcin[4]arenes in both structure and function. The pyrogallol rings act as the primary structural component, while the aldehydes form carbon bridges that connect adjacent pyrogallols and act as attachment points for the R-groups. As with calix[4]arenes and resorcin[4]arenes, the most commonly used isomer is the cone, which features an upper and lower rim (Fig 1.6 for comparison of the three). The upper rim is hydrophilic, as it consists of the hydroxyl-rich "tops" of the pyrogallol rings. The lower rim is typically hydrophobic in character, as it contains the pendant R-groups of the macrocycle, which are also typically hydrophobic. Because the use of PgCs as supramolecular building blocks is the overarching theme of this thesis, this macrocycle will now be discussed in detail.

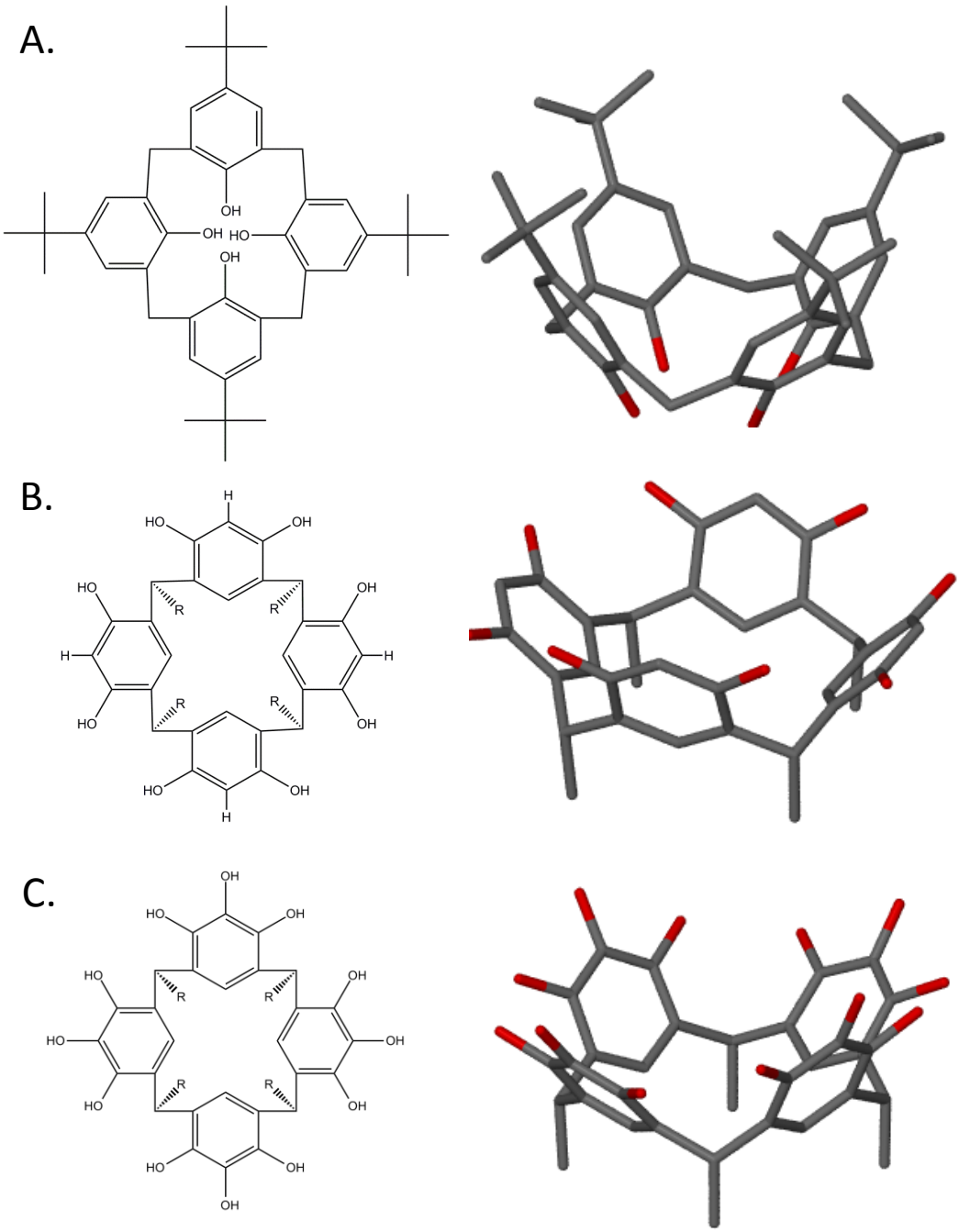

Figure 1.6: Comparison of a calix[4]arene (A), resorcin[4]arene (B) and pyrogallol[4]arene (C).

1.4.1 Pyrogallol[4]arenes: synthesis and structural discussion

The cyclo-condensation process between pyrogallol and an aldehyde can lead to both macrocycles and non-cyclic oligomers/polymers, but unlike the calixarenes, pyrogallol[4]arenes do not require a multistep polymer cracking stage, and can be formed rather simply *via* a one-pot synthesis. The conditions that are required for synthesis are typically quite mild, and a 1:1 mixture of pyrogallol:almost any aldehyde will form the tetrameric product in a wide range of solvent systems (Fig. 1.7). Due to the commercial availability of many simple aldehydes, many simple functional R-groups can be incorporated into the PgC lower rim. These include naphthyl[83], *C*-bromoalkyl,[84] *C*-chloroalkyl,[84] and ferrocenyl,[85] among others. More complex groups can probably be introduced to the PgC ring system by utilizing pre- or post-synthetic modification of the aldehyde/R-group, but this concept has not been thoroughly explored. One research group, however, did use microwave-assisted methods to post-synthetically functionalize both the upper and lower rims of 4-hydroxyphenylpyrogallol[4]arene with alkyl or aryl halides in the presence of K_2CO_3,[86] and postsynthetic haloalkylation was also used by another group to turn PgCs into dendrimeric "star polymers.[87]

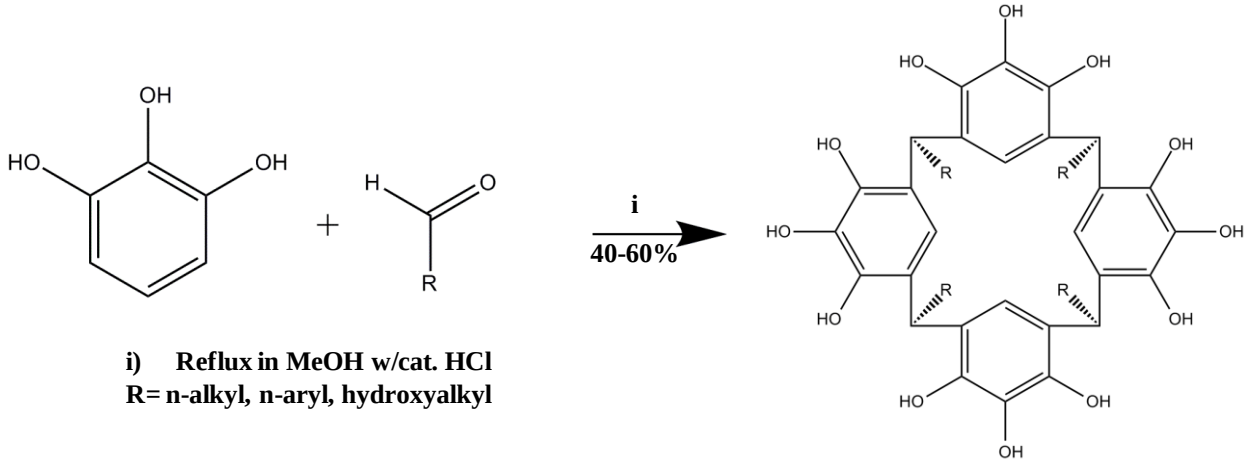

i) Reflux in MeOH w/cat. HCl
R= n-alkyl, n-aryl, hydroxyalkyl

Figure 1.7: Typical reaction scheme for the synthesis of pyrogallol[4]arenes

Although formaldehyde cannot be used to form a PgC without bridgehead R-groups (i.e. with hydrogen atoms in place of aliphatic/aromatic groups) as in calixarenes, such macrocycles can nevertheless be generated under certain conditions. One example utilized a trimethoxypyrogallol-Sn^{4+} complex as a starting reagent and trioxane as the source of formaldehyde.[88] "Mixed macrocycles" can also be formed from the reaction of aldehydes with a mixture of resorcinol and pyrogallol. [89] As expected from the similarity of pyrogallol and resorcinol, this results in a mixture of macrocyclic products.

Like calix[4]arenes and resorcin[4]arenes, PgCs can come in various isomeric forms (Fig. 1.8). However, unlike calixarenes, where all four of the theoretically possible isomers can be isolated quite readily, only the rccc "cone" and rctt "chair" conformers are typically formed in reactions involving pyrogallol. Typically, the use of aliphatic aldehydes leads strictly to the cone conformer, while the use of α-aromatic aldehydes leads to the chair conformer. The exception is acetaldehyde and 4-hydroxybenzaldehyde, as both conformers are generated in most cases. The two conformers can be separated from the bulk mixture due to the low solubility of the chair conformer in most solvents. Although pyrogallolarenes are typically found as cyclic tetramers, a cyclic hexameric product (pyrogallol[6]arene) can also be isolated under certain conditions (Fig. 1.8). This product (unfortunately) is not found as the theoretical rccccc "cone" conformer, but rather in an rtctct conformation, which limits its use in host-guest complexes.[90]

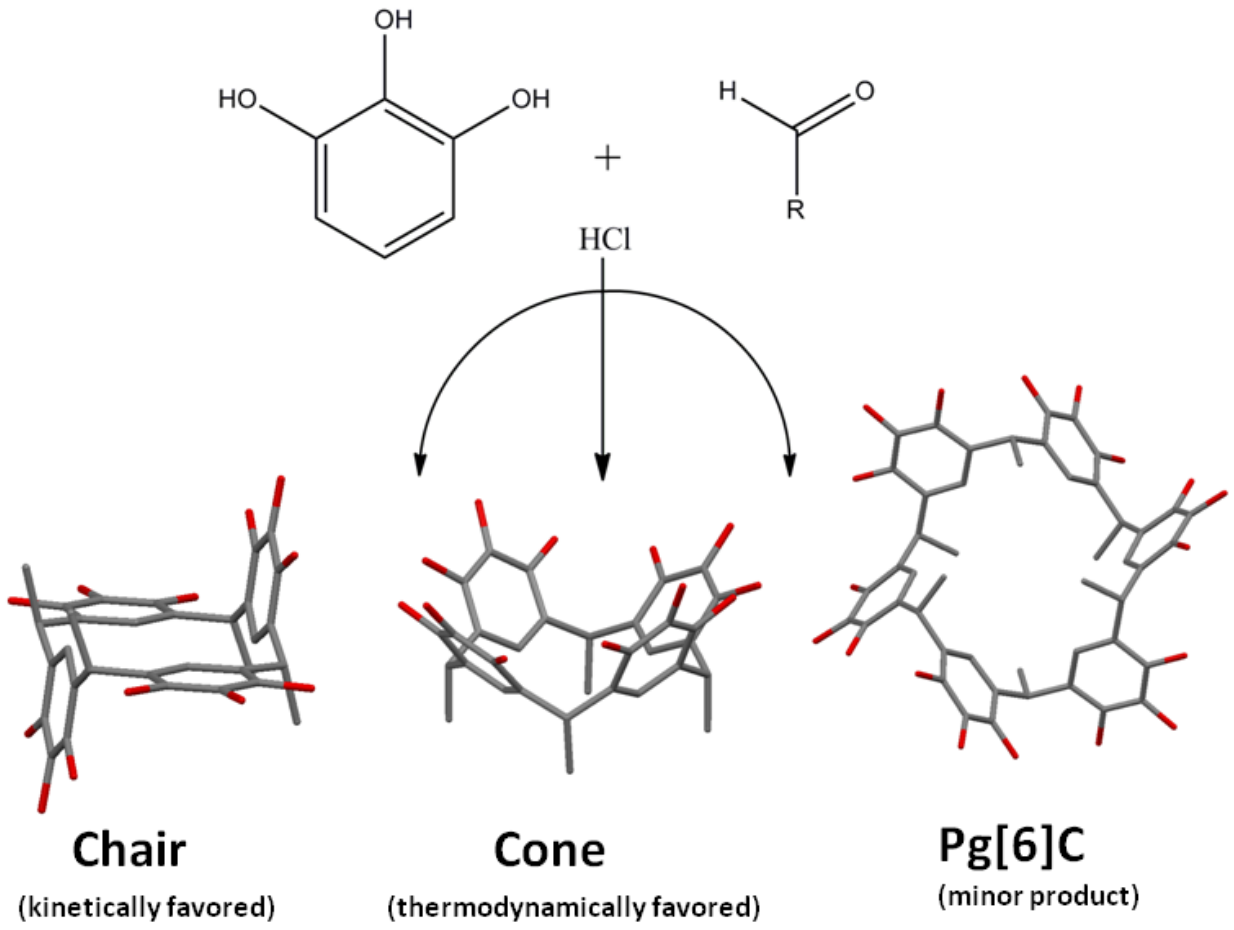

Figure 1.8: Typical products that are formed during the PgC-forming cyclocondensation reaction. For C-alkyl pyrogallol[4]arenes, the cone is the thermodynamically favored product while the chair is the kinetic product. The chair conformer is the kinetically and thermodynamically favored product with aryl-tailed PgCs

Purification of the macrocycle after synthesis is typically quite simple, as most of the time the product precipitates from the mother liquor as a white or pink powder that can be removed by vacuum filtration. Additional cyclic product can be removed from the mother liquor by cooling, or alternately by successive cycles of rotary evaporation and re-dissolution in acetonitrile. Net yields typically average approximately 50%, depending on the aldehyde that is

used. While the other 50% (oligomeric product) can usually be recovered and recycled (cracked) to form more cyclic product, it is usually discarded.

Yields of PgC can sometimes be improved by using the appropriate solvent system, which leads to increased precipitation from the mother liquor. For long-chain aldehydes, methanol leads to the highest yields, while shorter-chain aldehydes fare better with ethanol or ethyl acetate. The latter solvent is particularly useful in the synthesis of C-methylpyrogallol[4]arene, which is difficult to synthesize in high yields in any other solvent. Pyrogallol[4]arenes can also be synthesized in the complete absence of solvent, simply by grinding together pyrogallol and an aldehyde for a short period of time in the presence of small amounts of *p*ara-toluenesulfonic acid.[91] Microwave-assisted synthesis is another green approach toward the production of PgCs. This technique was used to great effect in reducing the time of synthesis (to 5-10 minutes) and improving yield substantially with a variety of PgCs.[92,93] An additional benefit of using this method was that some phenylpyrogallol[4]arenes, which are typically formed as the rctt "chair" conformer under standard synthetic conditions, were found to form exclusively the rccc "cone" conformer when microwave irradiation was used. As the cone conformer is significantly more useful for host-guest and self-assembly research, this synthetic method could prove indispensable in providing phenylpyrogallol[4]arenes for these purposes in the future.

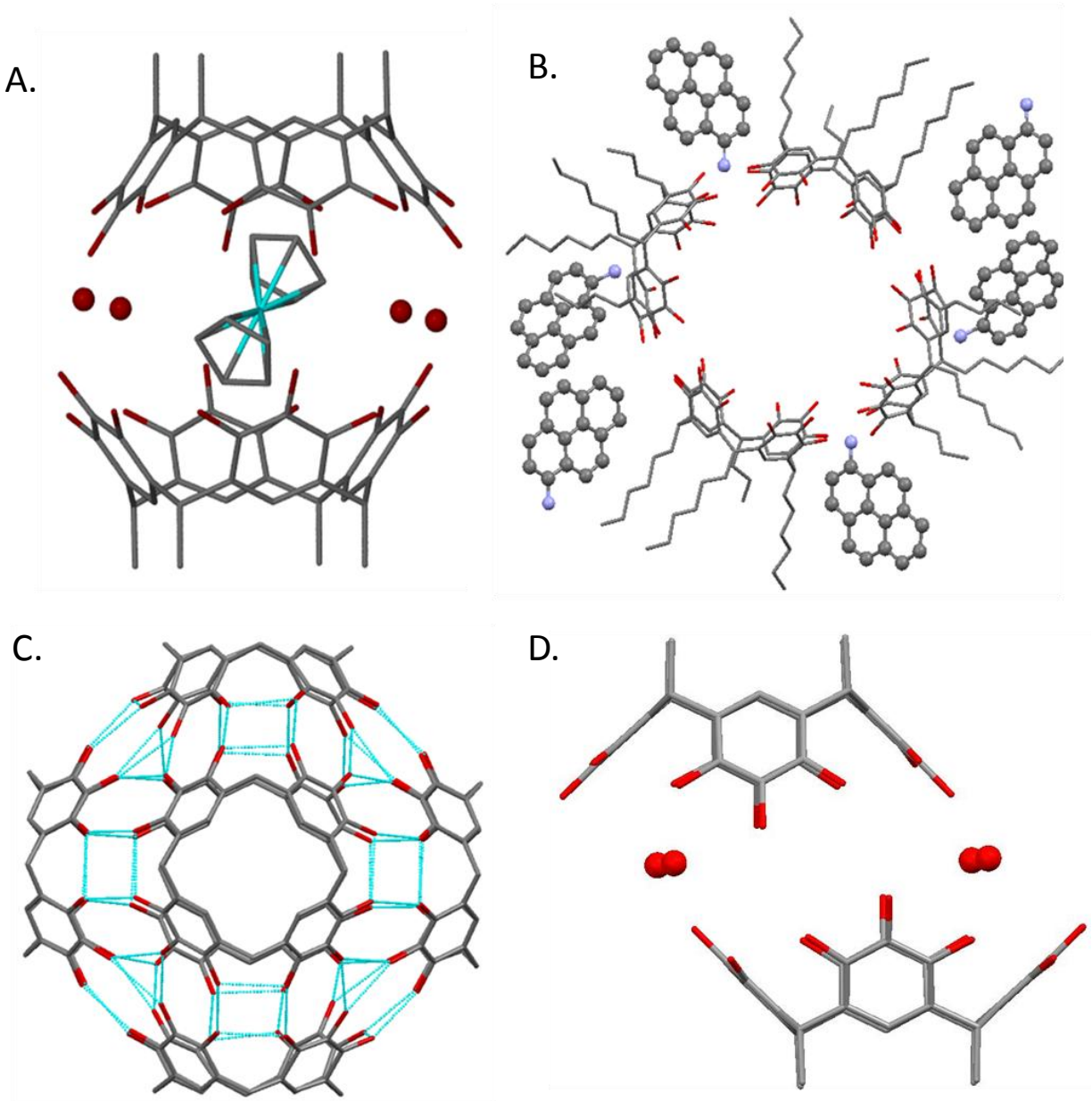

Figure 1.9: Several important (non-covalent) assemblies of PgC: Dimer (A), portion of a nanotube (B), hexamer (C) and portion of a bilayer (D).

1.4.2 Pyrogallol[4]arene self-assembly and solid-state structures

Pyrogallol[4]arenes can co-crystallize with a wide variety of solvent/non-solvent guests to yield an even greater variety of different solid-state structures. Research efforts into their interaction with various guest species, and the analysis of these interactions via scXRD and NMR currently makes up the bulk of PgC research. Although explored on and off for various purposes since the late eighties, the first report of a pyrogallol[4]arene crystal structure came in 1999.[94]
This seminal report helped to establish that, like resorcin[4]arenes, pyrogallol[4]arenes can self-assemble into a number of different solid-state motifs, largely dictated by the conditions of crystallization. In this report, two different solid-state packing arrangements were observed with ethanol and acetonitrile as the solvents. The first was a "wave-like" layered motif (which is now referred to as a "bilayer"), which features a hydrophilic region that encompassed the upper rims and most of the solvent molecules, and a hydrophobic region that largely encompassed the *C*-alkyl tails of the lower rim (Fig. 1.9d).

A second crystal form, a hexameric capsular motif, was also found to occur *via* low temperature dissolution in acetonitrile, followed by solvent evaporation (Fig. 1.9c).[94] While similar to the corresponding resorcin[4]arene hexamer, the PgC version lacked the structural water molecules of its RsC counterpart and was reported to be much less stable and more difficult to crystallize. Later work with *C*-propylpyrogallol[4]arene, however, showed that the hexameric motif could indeed be reproducibly crystallized by the addition of small amounts of either nitrobenzene or dichlorobenzene to a solution of the PgC, followed by solvent evaporation.[95] The stability of the solid-state crystalline solid was also evaluated, and it was found to be stable in an aqueous medium following sonication. Later work showed that hexamers could be formed from many different *C*-alkylpyrogallol[4]arenes, and that varying the

chain length of the lower-rim R-groups could lead to distinct changes in the crystal packing of PgC hexamers, and interestingly to changes in the behavior of the solvent encapsulated within the hexamer.[96]

Studies comparing the interior of the resorcin[4]arene and pyrogallol[4]arene hexameric capsules showed that, while similar in structure and internal volume, their propensity to encapsulate guest species was actually quite different.[97] Furthermore, despite the structural similarity of the two macrocycles, attempts to synthesize hexamers consisting of both RsC and PgC macrocycles proved to be futile in both the solid-state and in solution.[98]

Several studies were performed with the PgC hexamer that aimed to take advantage of this difference in chemistry. Because water was not required as a building block in the PgC hexameric assembly, the internal organization of the guests could be studied in highly non-polar (and water-free) solvents. To this end, Rebek et al. looked at the packing efficiency of long chain hydrocarbons within the PgC hexamer,[99] while several other studies sought to encapsulate larger non-polar guests. Previously, it was shown that PgCs can incarcerate fluorescent guests such as 4-[3-(9-anthryl)propyl]-N,N dimethylaniline (ADMA), pyrenebutanol (PBOH), and pyrenebutyric acid (PBA). However, synthesizing a capsule that contains these guests is a tedious process and often leads to crystals of "empty" hexamers, so a better method was desired. As most simple polyaromatic fluorophores melt at a temperature that is below the decomposition point of PgC (approx. 300°C), molten fluorophores can be used as a "solvent" for PgC macrocycles.[100] As such, this "solvent" is trapped within the PgC hexamer, therefore leading to the encapsulation of fluorophores. This process is not possible with the RsC-based hexamers due to the requirement of structural water, which would have quickly evaporated at the temperatures required to create this "solution."

It should be noted that like the RsC analog, the presence or absence of water during crystallization plays a major part in the identity of solid-state PgC assemblies. The absence of water typically leads to the formation of hexameric assemblies with most long-chain *C*-alkylpyrogallol[4]arenes in non-protic solvent systems. However, on addition of water or other protic solvents, bilayer, dimeric, or nanotubular assemblies are often observed instead.[101] This is best demonstrated with fluorophores, which can also be used to create other non-hexameric host-guest complexes with PgCs. For example, acenapthene was encapsulated within a dimer of *C*-propan-3-olpyrogallol[4]arene in hydrophilic conditions that would not have led to the formation of the hexamer (see Fig. 1.10a for a similar dimer with ferrocene).[102] Likewise, co-crystallization of PgC6 with the fluorophores pyrene or 1-bromopyrene in wet acetonitrile did not lead to encapsulation of the pyrene molecule, but instead led to the formation of a nanotubular motif (Fig. 1.9b).[103] Two other nanotubular motifs were also found to form with "branched tail" PgCs in a partially protic solution of 1:1 EtOH:EtOAc.[104,105]

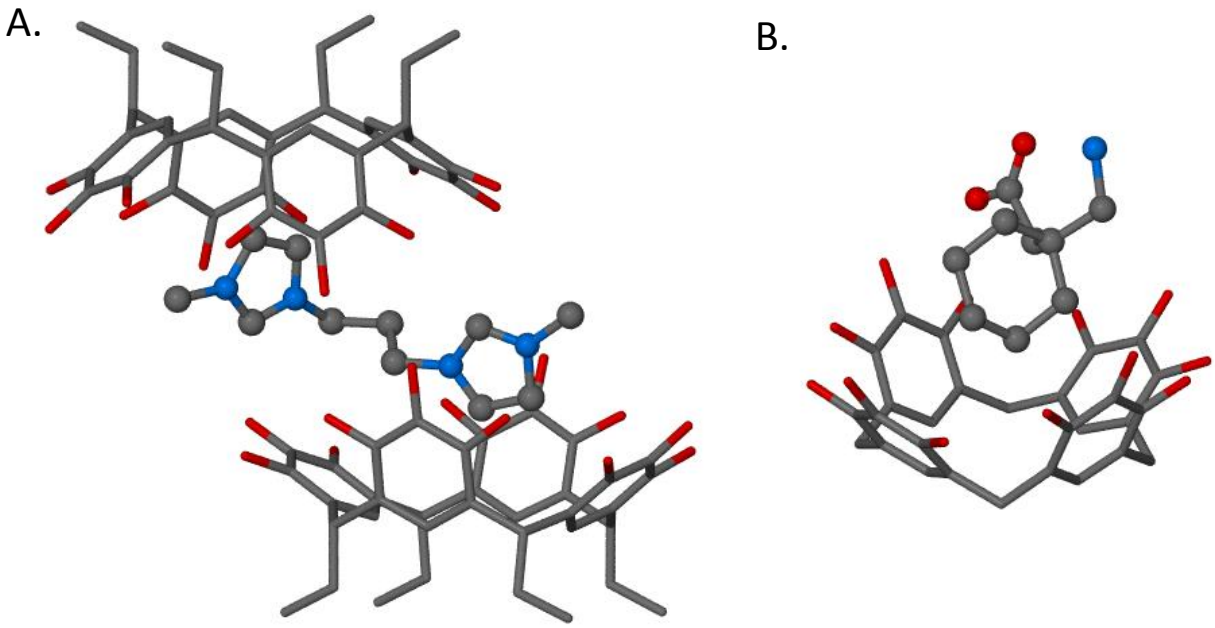

Figure 1.10: The crystal structure of a di-cationic guest with PgC (A), and the structure of a PgC/gabapentin host-guest complex (B)

In addition to the study of topologically-interesting assemblies such as the hexamer, dimer and nanotube, PgCs are also used to study the chemistry of host-guest complexation of important guest species. In particular, the electron-rich pyrogallol[4]arene cavity can be used as a valuable receptor for positively charged species. This selectivity arises mainly from cation-pi interactions between the positive charge and the aromatic bowl of the PgC. This is particularly the case with quaternary ammonium derivatives, a trait that PgC shares with resorcinarenes.[106] As such, they have been used as complexation agents for trimethylammonium-based natural compounds, such as betaine, choline, phosphocholine and carnitine.[107-109] This trait has also been used to form several examples of PgC co-crystals with ionic liquids, where the cationic

portion of the ionic liquid lies within the bowl of the PgC while the anionic counterion plays a stabilizing role on the exterior of the host-guest complex (Fig. 1.10a).[110,111]

Gabapentin, a commonly prescribed pharmaceutical, and one which bears positively charged ammonium groups, was also co-crystallized with PgCs.[112] Two examples of co-crystals of the bilayer-type were formed with gabapentin, which was stabilized within the PgC bowl *via* CH-O and CH-pi interactions. Interestingly, in both cases the positively charged ammonium functional group on gabapentin was not found within the PgC bowl, which was instead occupied by the cyclohexyl ring moiety of the drug, suggesting a difference in selectivity for ammonium vs. alkylammonium groups (Fig. 1.10b).

1.4.2 Other uses for pyrogallol[4]arenes

Due to a hydrophilic upper rim and, typically, a hydrophobic lower rim, PgCs are the prototypical image of an amphiphile. As such, they have been used to assemble monolayers on the surface of water, as seen by Brewster Angle Microscopy.[113] As an extension of this work, significant research efforts by the Gokel group have also shown that pyrogallol[4]arenes can be used to induce porosity in phospholipid membranes.[114] This was achieved by using long-chain PgCs, such as those formed from dodecanal. Their work showed that the pores formed in this way showed open-closed activity over a range of voltages, and were calculated to possess a diameter of approximately 11 Å. The conductance for these pores was significantly greater than that for resorcin[4]arenes , which have been hypothesized to form smaller pores across membranes.

Taking advantage of the phenolic subunits has also been used in research regarding PgCs. In one study, PgCs were shown to display chemiluminescence in the presence of base and hydrogen peroxide.[115] In another, the PgC macrocycle was used as an effective antioxidant agent in preventing temperature-dependent auto-oxidation of high density polyethylene.[116]

1.5 Metal-seamed pyrogallol[4]arene nanocapsules

Due to the many diverse examples of macrocycles exhibiting various types of metal coordination, it is of no surprise that research efforts were eventually undertaken to use PgCs as structural components in metal-seamed entities.[24,117] The most basic approach in creating such a material is to use the native (unmodified) PgC as a ligand for metal ions. Compared to alkyl hydroxyls, which have relatively high pKa values, the aryl hydroxyls found on the upper rim of PgCs are considerably more acidic and therefore more amenable to losing a proton and acting as a good negatively charged oxo-ligand for metal coordination purposes. A single PgC macrocycle provides (at least theoretically) up to twelve deprotonated hydroxyl sites, and can therefore be expected to form poly-metallic arrays featuring multiple PgC subunits. While native RsCs likewise possess many aryl hydroxyl groups on their upper rim, it is nevertheless understandable why PgCs were a suitable candidate for this endeavor while RsCs currently remain largely unexplored as ligands for metals in their native state.

In contrast to RsCs, which contain hydroxyls at the 1- and 3- positions of each aryl ring, PgCs also contain an additional hydroxyl at the 2- position. This leads to a much closer spacing between hydroxyls, and even a quick visual inspection of the macrocycle clearly suggests that PgC should have a greater propensity for bidentate coordination to metals. This is not the case in RsCs where the hydroxyls are more distantly spaced. As polydentate coordination imparts

increased stability over monodentate coordination, this makes PgCs much more likely to bind to metal ions in some coherent fashion. Indeed, one early source of inspiration for trying anything at all with PgCs was the arrangement of hydroxyls within the PgC hydrogen-bonded hexamer. While the hexamer is held together solely through hydrogen bonds, there are twenty four sites present within the hydrogen-bonding network that could clearly accommodate metal centers in a square planar geometry (Fig. 1.11a). These sites consist of four hydroxyls, two each from a pair of adjacent PgCs, thereby forming a planar tetra-dentate unit into which a metal could be incorporated.

It was perhaps this observation that led researchers to use Cu^{2+} (which commonly exists in a square planar coordination geometry) to "seam-up" the hydrogen bonded capsule, and in doing so, create an analogous capsule bound by coordinative bonds rather than hydrogen bonds. This result (it worked!) led to several other notable examples of PgC-based nanocapsules that are held together *via* metal coordination. The investigation of these entities, which include hexameric, dimeric, and nanotubular entities serves as the basis of my work during graduate school. As such, the description and chemistry of these complexes will currently be explored.

1.5.1 Copper hexamer: initial discovery and structural discussion

The first example of a supramolecular cage complex based on PgCs was the copper-seamed hexameric nanocapsule.[118] As previously noted, the authors observed that the hydrogen bonded hexameric sphere contained several sites that could accommodate a transition metal cation. It was initially theorized that the hydrogen-bonded hexamer could be used as a template for the formation of a coordinative-seamed hexamer. Interestingly, pre-templation was not actually necessary, as it was found that simple mixing of PgC solution with Cu^{2+} was all that was

required to construct a hexameric capsule. When $Cu(NO_3)_2$ was added to a methanolic solution of *C*-propan-3-olpyrogallol[4]arene (PgC3OH), scXRD analysis of the resultant crystalline material yielded a $Cu_{24}PgC_6$ nanocapsule of a hexameric topology. As predicted, the 24 Cu^{2+} are located in eight planar tri-copper clusters on the capsule's surface, thereby occupying all of the theoretical binding sites (Fig. 1.11b, c). Of the 72 phenolic hydroxyls originally present

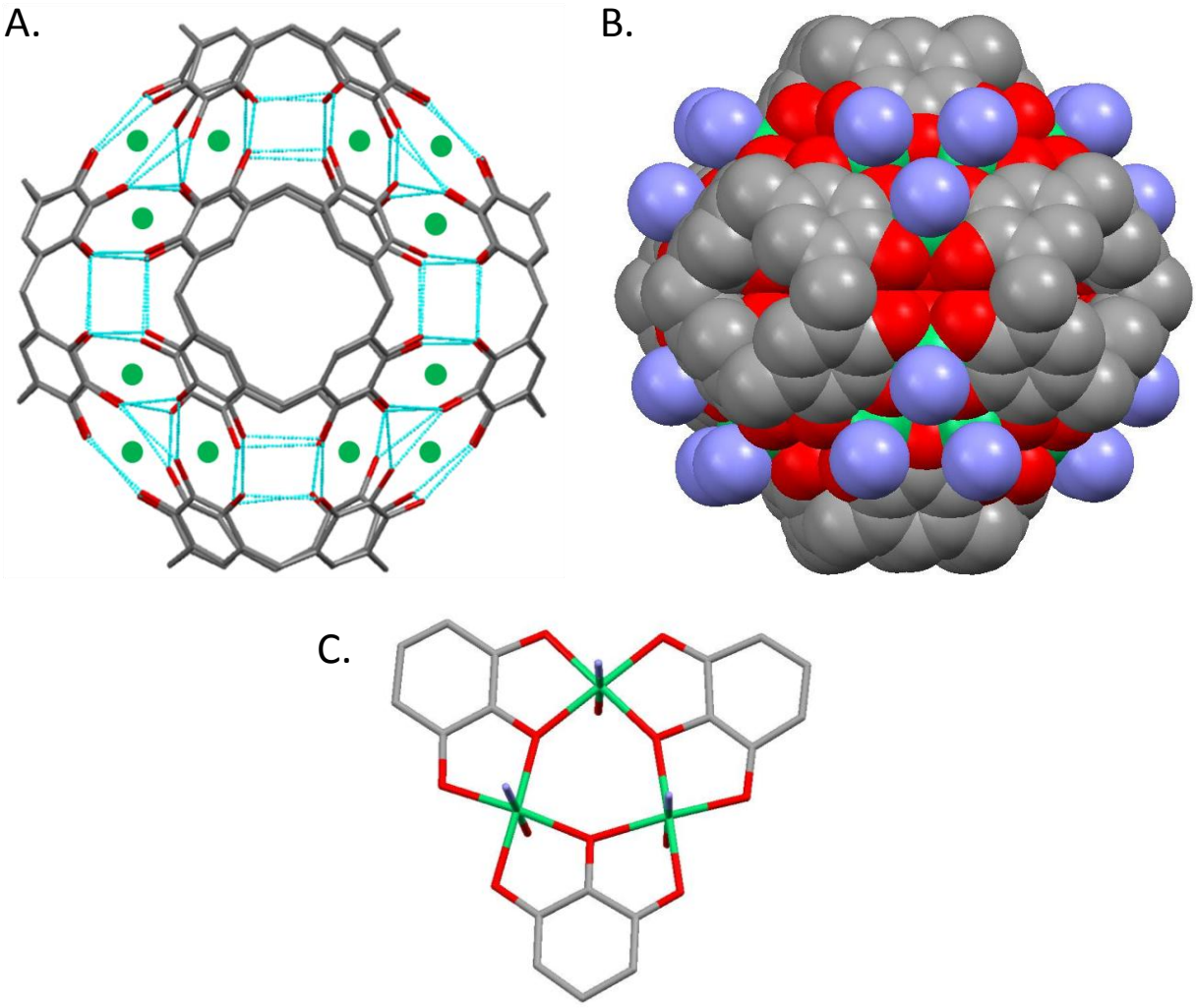

Figure 1.11: Hydrogen-bonded hexamer with green dots at locations of potential metal coordination sites (A) Space-filled representation of the metal-seamed hexamer (B) and a tri-metal cluster that is responsible for holding the assembly together (C)

within the capsule, 48 are used in copper coordination (eight of every twelve hydroxyls per PgC macrocycle). Thus, the capsule is charge-neutral, as the deprotonation of these phenols is concomitantly balanced by the +2 charges of the copper centers. The remaining 24 (protonated) hydroxyl groups participate in hydrogen bonding interactions with one another, thereby leading to an entity that is primarily stabilized by metal coordination but also features non-covalent bonding. The copper centers were not found to be of a consistent square planar coordination geometry, but were on some occasions octahedral. This was due to variable equatorial coordination, with the *endo* sites (from inside the capsule) and the *exo* sites housing additional ligands.

Due to the poor crystallizability but high stability and solubility of the copper-seamed nanocapsule, these entities were, in a later study, investigated using MALDI-TOF mass spectrometry.[119] This was done to elucidate the conditions that would lead to their synthesis and also to determine if any other species were present in the bulk material. Regardless of reactant ratios, synthesis in methanol led to spectra featuring two prominent peaks, one corresponding to an empty "barebones" capsule and another corresponding to a full capsule, as well as a number of smaller peaks in between. A mass difference of 633-635 Daltons, corresponding to approximately 35 water molecules, was observed regardless of the PgC used or any variations in synthetic conditions. Although it was not possible to explain these results, it was postulated that the formation of the hexamer occurs so quickly that variable amounts of solvent are encapsulated upon closure, although this peculiar finding could have also been the result of solvent ejection due to the mass spectrometric method employed. Overall, this study showed that the copper hexamer would form irrespective of PgC:Cu^{2+} ratio in methanol.

Later, these nanocapsules found additional uses in rather unlikely research; as artificial ion channels in phospholipid membranes.[120] Although seemingly nonporous on structural investigation, they nevertheless showed voltage-dependant conduction in the presence of Na^+ and K^+, but were much less effective in the presence of Cs^+. This suggests that molecular species can pass through the metal-seamed capsule, assuming that they are of an appropriate size (Cs^+ was postulated to be too big to fit).

Due to the TEM observations of aggregative behavior in PgC and RsC hydrogen bonded capsules, it was interesting to see if copper-seamed PgC hexamers would likewise form aggregates. Although analogous TEM studies were never conducted, small angle neutron scattering (SANS) was instead used to probe both the stability and aggregative behavior in long-chain copper hexamers.[121] All three of the pendant tail lengths studied (C11, C13, and C17) fit well as core-shell spheres (inner core, along with a shell consisting of the *C*-alkyl tail and solvent) of appropriate diameter under most solvent conditions, suggesting that the nanocapsules are stable. Interestingly, while neither C11 nor C13 showed any aggregative behavior in any of the solvent systems that were examined, C17 in o-xylene fit as an ellipsoid with a length of 115Å along the major axis, and a length of 24Å along the minor axis. These parameters suggest that PgC17Cu hexamers assemble into ellipsoidal chains consisting of five individual nanocapsules, most likely connected *via* inter-digitation of the C17 arms.

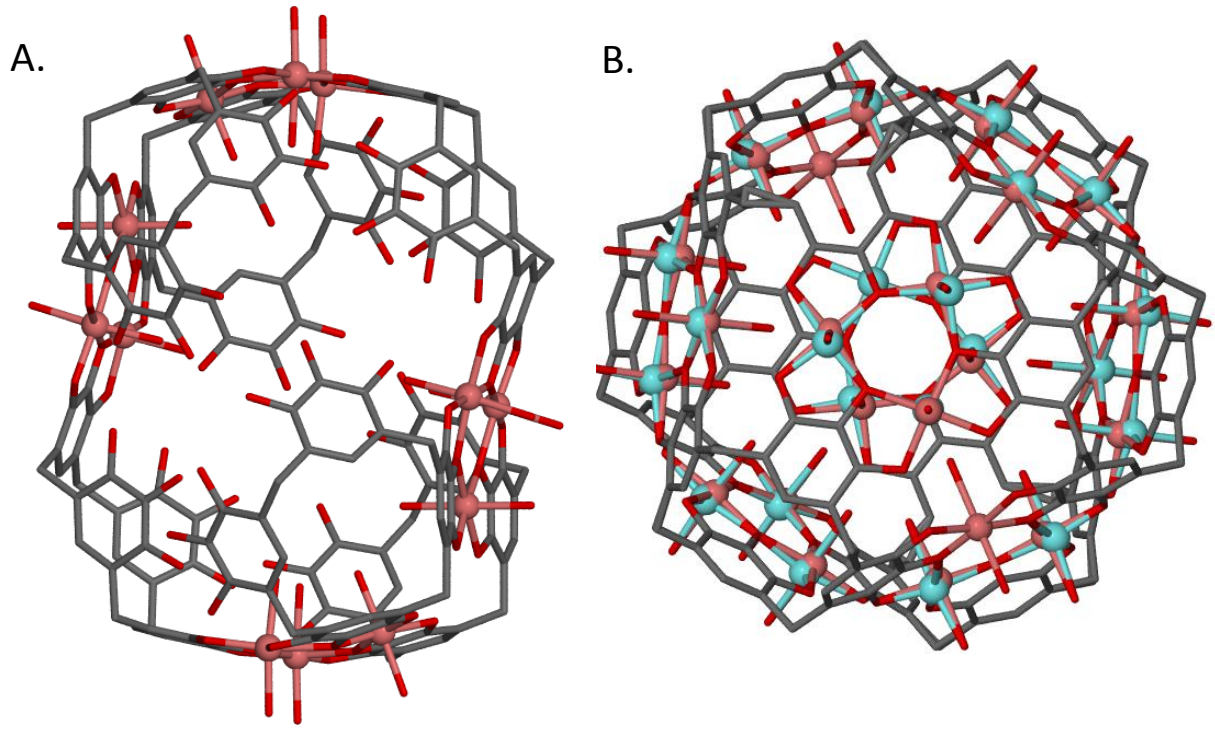

Figure 1.12: Structures of the Ga-seamed "rugby ball" (A) and a mixed Ga^{3+}/Cu^{2+} nanocapsule (B).

1.5.2 Gallium Hexamer: The rugby ball

Soon after the discovery of the copper-seamed hexamer, it was found that Ga^{3+} could also be used to form molecular capsules based on PgCs.[122] Although this capsule featured tri-metal clusters much like the copper-seamed analog, the overall geometry of the capsule was starkly different. Instead of conforming to a spherical shape like the $Cu_{24}PgC_6$ nanocapsule, the $Ga_{12}PgC_6$ featured a "rugby ball" topology with only four metal triads seaming the capsule together (Fig. 1.12). The remaining (open) sites on the capsular periphery are involved in hydrogen bonding interactions. Therefore, this capsule can almost be thought of as a hybrid between the hydrogen-bonded hexamer and a metal-seamed entity. This alternative geometry can be partially explained by a change in the charge of the metal center; from +2 with copper, to +3

with gallium. In copper, six of the nine hydroxyls that hold each triad together are deprotonated leaving three to participate in hydrogen bonding interactions with adjacent triads. In the gallium analog, however, charge balancing dictates that all nine are deprotonated, thus eliminating any intra-capsular hydrogen bonding opportunities between protonated hydroxyls in adjacent clusters. This loss of hydrogen bonding between metal clusters is thought to reduce the rigidity of the PgC bowl, thereby distorting the framework from a sphere to the observed rugby ball in the solid state. This distortion is (perhaps) an adaptive mechanism that helps the capsule to maximize hydrogen bonding between the remaining phenol hydroxyls. This, in turn, disfavors the insertion of additional Ga^{3+}, as the distance between phenol hydroxyls increases to allow for hydrogen bonding.

Due to the partially seamed nature of the gallium hexamer, it was envisioned that the non-gallium containing regions could be used as portals to access the interior of the capsule. To determine if this were the case, Cs^{+} and Ag^{+} were added to a solution of pre-made gallium hexamer in acetone.[123] Structural elucidation of the resulting crystalline material showed that, while not at full occupancy, both Ag^{+} and Cs^{+} could now be found within the cavity of the gallium hexamer. This suggested that the framework of the gallium-seamed hexamer was indeed porous, as dissociation and reformation of the assembly would require the scission of too many Ga-O bonds to be practically feasible.

The unfilled sites in the framework of the gallium hexamer were also obvious targets for attempts to "seam up" these capsules with additional metal ions. It was theoretically postulated that by using other transition metal ions, a capsule containing both gallium and the heterometal could be synthesized, leading to a unique "mixed-metal" entity. As such, premade gallium hexamer was used as a starting reagent for mixed species containing Cu^{2+} and Zn^{2+}.[119,124]

Addition of $Cu(NO_3)_2$ or $Zn(NO_3)_2$ to a solution of gallium hexamer led to the formation of materials with the same topology as the copper-seamed hexamer (Fig. 1.12b). Although it would stand to reason that the added copper or zinc had simply displaced all of the gallium centers in the capsule, inductively-coupled plasma (ICP) analysis showed that this was not the case; the hybrid capsules thus formed contained a 16:8 mixture of Cu^{2+}:Ga^{3+}, or 10:14 mixture of Zn^{2+}:Ga^{3+} respectively. Addition of Cu^{2+} to the mixed Ga/Zn capsule led to the ejection of all of the Zn^{2+} ions and an additional Ga^{3+}, leaving a 13:11 Ga^{3+}:Cu^{2+} ratio. This is a different Ga: Cu ratio than the one that formed from direct addition of Cu^{2+} to premade gallium-seamed hexamers. As such, this result suggests that mixed-metal hexamers with a variety of metal-to-metal ratios can be prepared using non-direct methods.

One thing to note about the mixed metal work was that the metal content of these species was solely found using ICP. This is because the metals found in mixed metal systems such as Cu^{2+}, Zn^{2+}, and Ga^{3+} are proximal to one another on the periodic table and, due to their similar electron counts, cannot be individually differentiated using X-ray crystallography. Because of this, Cd^{2+} was investigated as an alternate to Zn^{2+} to stitch up gallium nanocapsules.[125] The resultant nanocapsule was slightly distorted as compared to all previous examples of mixed-metal capsules, with two different environments for the new Cd^{2+} centers. ICP analysis showed that the 17:3 Ga:Cd ratio, as in the case of Zn^{2+} incorporation, required that some of the original gallium-seamed hexamers have to decompose in order to produce the additional Ga^{3+} needed for the formation of the capsule. NMR experiments also showed that unlike Ga/Zn mixed species, the NMR spectrum of the Ga/Cd capsule did not display any peaks below 0, indicating that the capsule is not in fact closed, but rather open to solvent exchange with the rest of the solution. This suggests that, although not entirely structurally analogous to their lighter counterparts,

mixed Ga/M species bearing heavier elements can be used not only in the crystallographic differentiation of metal centers, but also as channel-like entities that behave non-analogously to the results seen with the copper hexamer.

1.5.3 The Zinc Dimer and the octametal belt

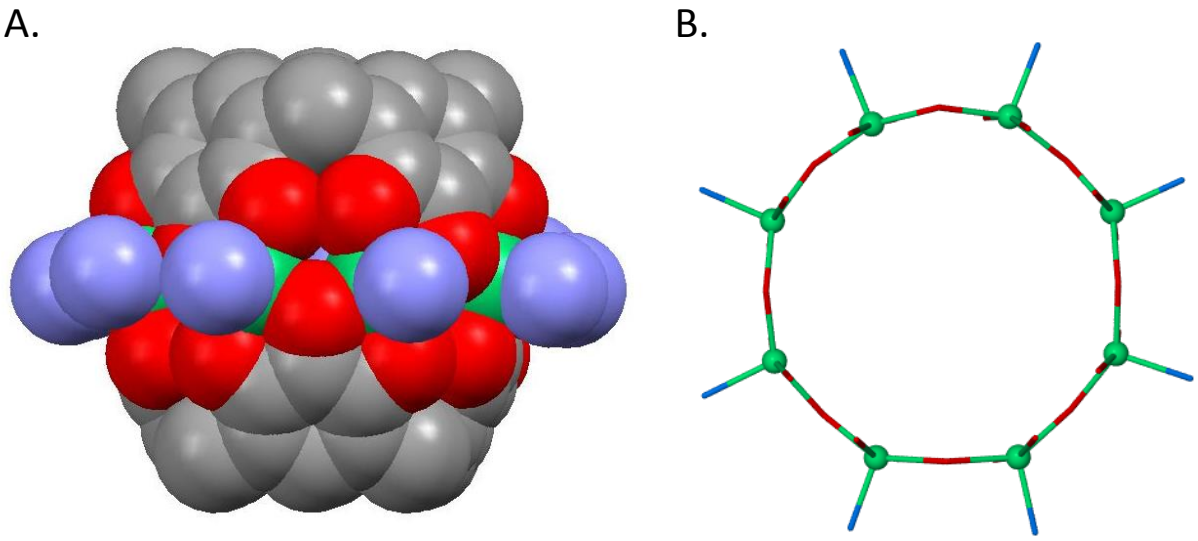

Figure 1.13: Space-filled representation of the metal-seamed dimeric nanocapsule (A) and the "octametal belt" that is responsible for its structural rigidity (B). Metal centers are green, while *exo* ligands are blue.

As hydrogen-bonded hexamers are not the only capsular topology of PgCs, later research looked at other hydrogen-bonded assemblies for inspiration toward the synthesis of metallated species. The hydrogen-bonded dimer, in particular, seemed amenable for retro-insertion of metals into its framework. As predicted, such a metallated dimer formed when PgC was treated with Zn^{2+} in the presence of pyridine (Fig. 1.13).[126] The main structural feature of this assembly is an "octametallic belt" composed of eight equally spaced Zn^{2+} cations that spans the equator of the dimer (Fig. 1.13b). Each metal center is also bound to a single peripheral (*exo*) pyridine

ligand, with the interior of the capsule incarcerating a single guest pyridine molecule. Like the hexameric copper capsule, deprotonation of eight out of twelve hydroxyls per PgC macrocycle leads to a fully neutral capsular species. Unlike the hexamer, however, where the geometry of the metal centers was either octahedral or square planar (tetra- or hexa-coordinate), the dimer instead possesses penta-coordinate metal centers, with four sites taken up by coordination to PgC hydroxyls and the fifth to the *exo* pyridine ligand. MALDI-TOF mass spectrometry was also used to show that both empty and full dimers were present as a mixture in solution, although the nature of why this occurred was unknown. It was also found that the *exo* ligands were stripped off during analysis, leading to a mass signature of a barebones dimer.

Like Ga^{3+}, Zn^{2+} is diamagnetic, and can be readily studied using NMR spectroscopy. This proved to be a benefit in several studies where crystallographic data was either inconclusive or lacking entirely. One study of particular importance that used NMR to great effect showed that the ligands on the periphery of the dimer could be exchangeable for other ligands without rupturing the capsule.[127] In this study, 3-methylpyridine was replaced by dimethyl sulfoxide (DMSO) ligands by azeotropic distillation of a zinc dimer solution in DMSO until the pyridine was removed. 3-methylpyridine ligands were then used to replace DMSO by titrating this ligand back into to the solution, with concomitant monitoring using NMR. The internal guest, a 3-methylpyridine that was incarcerated during initial synthesis was retained throughout the entirety of the experiment. This finding suggests that the dimer can be post-synthetically modified to impart it with specialized functionality, while retaining the overall framework intact. The guest peaks were also shown to experience either upfield or downfield shifting with different ligands, suggesting that the functionality on the exterior of the capsule can electronically affect the interior.

Another study implementing NMR spectroscopy focused instead on the synthesis of zinc dimers from unusual PgCs, namely those bearing phenyl pendant R-groups. Although the predominant conformation in these PgCs is typically the rctt "chair" conformer, it was shown that PgCs of this conformer can nevertheless lead to the formation of dimeric capsules.[128] Analogous synthetic techniques to those used to produce the zinc dimer from rccc "cone" PgCs, performed instead with the rctt conformer led to yellow powders, which are characteristic of zinc-seamed dimers. Although it was not possible to grow diffraction-quality crystals of these materials, it was shown *via* NMR and MALDI-TOF mass spectrometry that dimeric capsules nevertheless did form. This suggests that the formation of capsules from PgCs is energetically favorable and will occur even when a chair-to-cone conformational change is required.

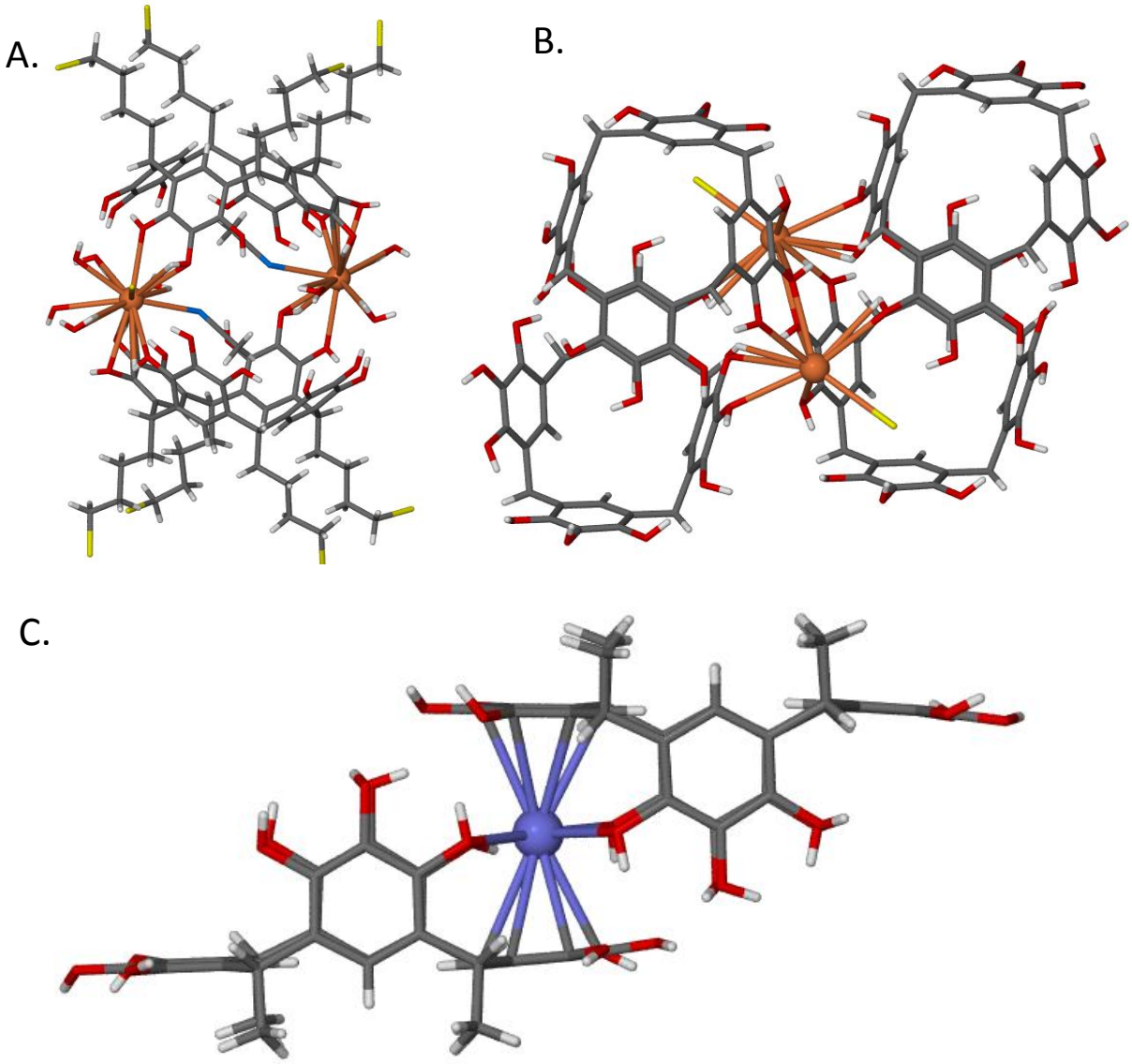

Figure 1.14: Cs^+/PgC complexes based on PgC4Cl (A) and PgC6 (B) and a K^+/PgC complex (C)

1.5.4 PgC frameworks based on alkali salts

Two distinctly different frameworks arise from the interaction of alkali salts with PgC. In the first of such studies, it was shown that PgC1 can form infinite coordinative chains in the presence of several alkali halide salts, notably RbCl, CsBr, and KBr (Fig. 1.14c).[129] The alkali

cations interacted with PgCs via both dipolar cation-O and cation-pi bonding, leading to an unusual framework where the PgC is in the rccc "boat" conformation. The size of the cation played a large part in dictating what type of assembly would result, with Rb^+ and Cs^+ forming 3:2 PgC:cation complexes and K^+ leading to a 1:1 complex.

In a second and distinctly different example of alkali ion coordination with PgCs, Cs^+ was used to form dimers with PgC4Cl and PgC6 exhibiting a 1:1 Cs:macrocycle ratio (Fig. 1.14a, b).[130] It is important to note that unlike PgC1, the longer-chain PgCs like the ones used in this study do not readily crystallize in the "boat" conformation, perhaps due to steric factors introduced by the use of longer lower rim R-groups. As such, the cation-pi bonding seen in the previous example cannot contribute to stabilization of the dimer. Instead, coordination occurs solely with the upper rim hydroxyls of the two PgCs. This leads to an entity that is of greater resemblance to the previously reported zinc dimer, and, likewise, encapsulates two guest acetonitrile molecules in both cases.

1.6 Preface to my graduate work: My undergraduate lab experience at the Atwood Lab

My research with metal-seamed pyrogallol[4]arene macrocycles began as required undergraduate research hours during the summer prior to my senior year at MU. Dr. Atwood had been our lecturer in Advanced Inorganic Chemistry the previous semester, and as the semester went on, he presented various bits and snippets of his research as it pertained to the subject that was being discussed in class. I became interested in the nature of his group's research, and supramolecular chemistry in general. Thus, at the end of the semester I talked to him about working for his group as an undergraduate research assistant for the summer, which he gladly allowed me to do.

The original scope of my project was quite simple; I was to investigate the bimodal mass distribution that was seen in the MALDI-TOF spectra of copper-seamed hexamers. As previously described, these metal-seamed nanocapsules are quite voluminous, containing up to 1250$Å^3$ of free space within their interiors. Since their synthesis is typically conducted in wet methanol, it would be of no surprise to see this void space occupied by the small methanol and/or water molecules, or whatever else was present in solution. The identity and quantity of what was encapsulated by these nanocapsules was initially studied by Dalgarno et al. using MALDI-TOF mass spectrometry.[119] Rather surprisingly, they found that while the MALDI-TOF spectra of this material showed the expected solvent-enriched (or "full") nanocapsules, a rather strong peak corresponding to "empty" nanocapsules was also present. The synthesis of a complex possessing 1250 $Å^3$ of free space is quite amazing, as nature typically "abhors a vacuum," so the purification of such a material would undoubtedly be important to various fields of research and was certainly worthy of at least cursory research.

As such, my project was to first make this mixture of "empty" and "full" nanocapsules using the same approach as in the Dalgarno report. I would then need to devise a method to separate the two species (empty and full) and, if possible, confirm their separation using MALDI-TOF mass spec. We reasoned that since the "empty" capsule enclosed a vacuum, it would be significantly lighter than its "full" counterpart and could thus be separated *via* their different densities in an appropriate medium. Unfortunately, after countless attempts, it became clear that separation could not readily be achieved. MALDI-TOF analysis displayed a bimodal distribution regardless of what was done to the raw hexameric material. The reason for this is still unclear, but it is likely that the MALDI-TOF method itself is responsible for (partially) emptying the capsule. This conclusion is actually in-line with results seen in previous zinc dimer research, where, in addition to the loss of all peripheral pyridine ligands, distinct peaks corresponding to empty and full dimers are evident on MALDI-TOF analysis.[126] While this null result was rather disappointing, I nevertheless continued with studies that employed MALDI-TOF mass spectrometry.

Still naïve to the notion that separation would not be possible, I started to stray from the reported syntheses of these nanocapsules and began to find new ways to make these materials. My rationale in doing this was the following: if it was not possible to separate the two species using reported methods, maybe (through trial and error) I would instead eventually stumble upon a synthetic method that would lead exclusively to one or the other (empty or full). Luckily, the synthesis of PgC-based copper hexamers is actually quite amenable to this "shotgun" approach, as the addition of Cu^{2+} to PgC under almost any condition leads to the formation of the characteristically brown precipitate indicative of nanocapsules. Once again, most attempts resulted in the same bimodal mass distribution. However, one case was distinctly different.

Synthesis of copper-seamed nanocapsules in hot ethylene glycol, followed by MALDI-TOF analysis led to a mass signature that was indicative of a dimer, rather than a hexamer (Fig.1.15a). Prior to this result, only dimers ***or*** hexamers could be formed from individual metals. This, however, showed that both a hexamer and a dimer could be formed from a single metal, depending on the conditions during synthesis.

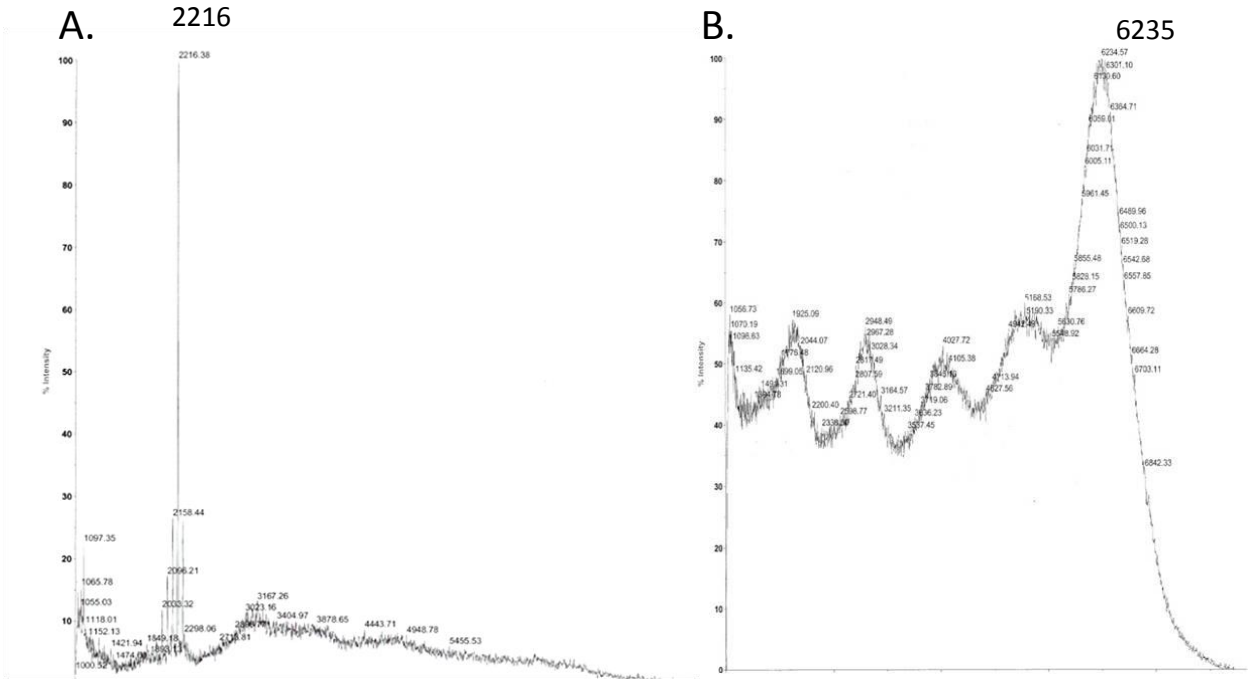

Figure 1.15: MALDI-TOF spectra of a copper-seamed dimer (A) and a nickel-seamed hexamer (B)

Spurred by this result, I decided to investigate if this finding was an isolated incident, or if other metals could likewise be used to form multiple capsular moieties with PgCs. Conveniently around the same time, Dr. Nick Power, then a postdoctoral fellow, asked for my assistance in crystallizing two novel materials that were, judging from their respective mass spectra, presumably nickel- and cobalt-seamed dimers. As these materials were prepared using the same methods previously designated for the synthesis of the zinc-seamed dimer, the result of

yet another dimer was unsurprising. Thus, in conjunction with these crystallization efforts, I decided to see if a broader synthetic approach would likewise lead to the identification of another (non-dimeric) capsular moiety for either nickel or cobalt. It did not take long until a nickel hexamer was identified *via* MALDI-TOF, formed by simple heating of an acetonic solution of PgC5 and nickel nitrate (Fig. 1.15b). Simultaneously, our crystallization efforts resulted in the first reported structures of nickel and cobalt dimers. This showed that copper was not an isolated case where both species were distinct possibilities, as this was also the case with Ni^{2+}. Rather, it was more likely that many metals could be used to form (at least) both dimers and hexamers, if not other unique and unexplored entities. All that was missing was a broad and systematic approach towards their synthesis and characterization, and a person to do it. As such, I decided to stay in graduate school at MU and continue this research as my graduate project.

1.7 Thesis Outline/Objectives:

Research efforts into metal-seamed pyrogallol[4]arene nanocapsules are still arguably in their infancy today and these entities were even less investigated at the beginning of my graduate career. While several publications that focused on characterization had been published prior to the start of my graduate work, there were still many unanswered questions and loose ends in our knowledge of these entities. Of these, perhaps the most important and/or obvious questions regarding PgC-metal complexes are listed below.

1. Can multiple nanomaterials be formed from a single metal cation?
2. What factors control their formation and structure?
3. Can they be modified either pre- or post-synthetically?
4. What other nanomaterials can be formed?
5. Can they be used as building blocks towards the formation of other materials?
6. Can they be used for practical purposes?

As suggested in the preface, the first question had already been partially answered prior to the start of my graduate career; there was indeed proof from MALDI-TOF mass spectrometry that multiple species could form from a single metal. However, crystallographic proof would be needed to both verify that these species were capsular and to be able to structurally examine the resultant material. There are relatively few published structures of PgC-based nanocapsular entities, so a second goal of using crystallography was to expand on our structural knowledge of these compounds. Thus, the second chapter discusses the various techniques used to selectively crystallize dimeric and/or hexameric capsular entities, particularly those built from Cu^{2+}, Ni^{2+}, Co^{2+} and Mn^{2+}. These nanocapsules can be formed in a variety of different conditions, which

leads not only to different crystalline forms of these compounds, but also to the formation of compounds that are altogether different from one another.

Through this initial work, which sought to characterize different nanocapsular materials with scXRD, specific trends were observed. These trends seemed to suggest that the identity of the species (dimeric or hexameric) could be selected for by using the appropriate synthetic methodology. Of particular importance was the effect that time, temperature, and solvent system seemed to have on the formation of these species. Thus, the third chapter focuses on the factors that affect the formation of one species versus another. While the basis of this work lies in results gleaned from scXRD, solid state results only give us a snapshot of what is really going on in any particular system. To remedy this problem, *in situ* studies were conducted using small angle neutron scattering (SANS), in collaboration with Harshita Kumari. Unlike scXRD and MALDI-TOF, which may help to identify the presence of a species but cannot give any information as to its quantity, SANS allowed us to monitor the relative ratio of dimeric and hexameric nanocapsules in a sample over time and using a variety of differing conditions, thus giving us information pertinent to controlling the system. SANS studies also led to the discovery of a third metal-seamed pyrogallol[4]arene moiety, notably the iron-seamed nanotube, a discovery that would likely not had been possible without the use of this method.

In the fourth chapter, the concept of pre- and post-synthetic modification is explored. Specifically, metal-seamed pyrogallol[4]arene nanocapsules are post-synthetically bound to linking ligands used as supramolecular building blocks (SBBs) in metal-organic frameworks (MOFs). MOFs are materials that contain metal centers linked together through divergent ligands. The end result is a molecular lattice that is interlaced by molecular-scale pores and voids. Such materials can be useful in studies where adsorption or separation of small molecular

species is desired, such as, for example, the adsorption of gases for fuel storage purposes or the separation of chemical feedstock. As pyrogallol[4]arene-based nanocapsules contain many coordination sites for ligands at their peripheries, they were obvious candidates in the construction of such assemblies. Both dimeric and hexameric nanocapsules were used in this effort, producing several novel MOF-like materials. Of these, several two-dimensional assemblies possessing a distinct network of large channels were formed. These materials may be useful for future studies, particularly those with a focus on gas/molecular adsorption.

The fifth chapter focuses on the use of radiochemical methods to explore copper-seamed hexameric nanocapsules. The original aim of this work was to introduce a radioisotope, notably ^{64}Cu, into the framework of the nanocapsules, and use this material for imaging and/or therapy in a living subject. While ^{64}Cu labeling was not successful with these materials at the low concentrations required for *in vivo* work , a great wealth of information was nonetheless gathered in regard to the nanocapsules that were made at higher reagent concentrations. Data regarding the yield, solubility, and stability of these materials under conditions that simulate an *in vivo* environment were all collected using radiochemical methods. In addition, a happenstance observation during cationic exchange studies showed for the first time that copper seamed hexamers can sequester additional Cu^{2+} cations, most likely through binding to the interior of the capsule. The variables that control this novel form of Cu^{2+} binding are further explored in this chapter. In addition, while heterogeneous cation exchange has previously been observed with the gallium-seamed hexamer, it was unknown whether other metal cations could likewise displace Cu^{2+} from the copper-seamed hexamer. Conversely, it was also unknown whether Cu^{2+} could displace other cations, such as Zn or Ni, from their respective nanocapsules. As such, ^{64}Cu

was used as a method to determine if such exchange occurred, and the results of these studies are also presented.

In addition to containing supplementary information that pertains to various thesis chapters, the appendix also contains several studies that do not directly pertain to the investigation of the metal-seamed PgC nanocapsules discussed in chapters 2-5. These are listed as appendix chapters; A1 through A6. The first of these chapters discusses the zinc-seamed dimer, which was used to study both ligand exchange and guest encapsulation. Another two chapters involve non-covalent PgC-based host-guest complexes where ferrocene is encapsulated within a PgC dimer. The fourth chapter describes several PgC/glycol complexes of a nanotubular geometry, while the last chapter focuses on the use of the closely-related tetracyanoresorcin[4]arene macrocycle as a unique divergent ligand for Ag^{+}. This work, performed in collaboration with Dr. Praput Thavornyutikarn led to the isolation of a unique one-dimensional MOF as well as the identification of a non-covalent structural motif that was remarkably present in both the structure of the MOF as well as that of the native macrocycle. Chapter A6 contains supplementary data for chapters 1-5, primarily in the form of tables.

Chapter 2: Synthesis and structure of novel PgC-metal seamed MONCs

2.1 Introduction

This chapter describes a number of novel PgC-based metal-organic nanocapsules (MONCs). Specifically, it describes the synthetic and crystal growth techniques that are used to prepare and characterize the MONCs based on copper, nickel, cobalt, and manganese divalent cations. Mass spectrometric and elemental analysis techniques were not used in these studies, so their identification and characterization was almost solely a result of single-crystal X-ray crystallography (scXRD). This method led to the confirmation that MONCs were indeed being formed from the M^{2+} cations and at the same time provided valuable structural information that would be difficult to obtain in any other way. Notably, this includes information on the bond lengths/angles at the metal centers that "seam" the MONCs together, but also information on the identity and geometry of encapsulated guests and *exo*-ligand molecules on the surface of the capsule. This data is used to compare/contrast the MONCs from one another.

The chapter is divided into sections based on the M^{2+} cation that was used for synthesis, starting with a section on Cu^{2+}, then continuing to Ni^{2+}, Co^{2+}, and Mn^{2+}. It is also important to note that a section dedicated to the zinc-seamed dimer is also included in this text, although it is located in the appendix. These sections include information on both the dimeric and hexameric MONCs, and are organized in a logical progression in regard to their structural and synthetic peculiarities. Structural comparisons are made both internally (with other MONCs in this section) as well as externally (with previously published materials). Additional structural data (bond lengths and angles not found in this section) can be found in the appendix.

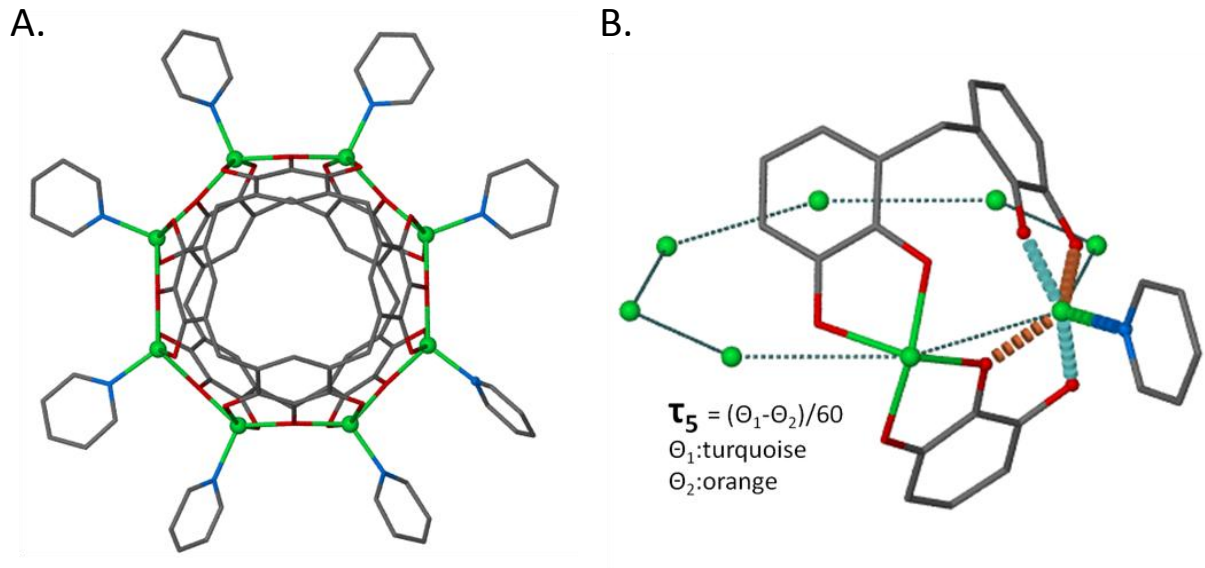

Figure 2.1: Image of a typical dimeric MONC (A) and its corresponding octametal belt (B). Equations and angles used in τ5 calculations are also included in B.

It is important to note that one method of comparison will universally be used in regard to the dimeric MONCs. Although the hexameric MONCs are (geometrically) very similar to one another, the dimeric MONCs are often structurally dissimilar, a fact that can be tied to the coordinate geometry at the metal centers of the "octametal belt". The metal centers at these sites are penta-coordinate and fall somewhere between square pyramidal and trigonal bipyramidal; the extremes of geometry in a penta-coordinate center. The tendency of these metal sites towards one extreme or the other leads to visible changes in the geometry of the overall dimer. Sites where the geometry tends towards trigonal bipyramidal appear as "pinches" in the normally circular octametal belt, while sites that are more square pyramidal appear as depressions in the octametal belt. Both are visually apparent as in-homogeneities in the "circularity" of the dimer, and even dimers that have identical coordination geometries at all eight metal sites are different than analogous dimers constructed from a different metal ion. The tendency of the geometry to

approach square pyramidal or trigonal bipyramidal can be enumerated by using a simple equation that compares the two largest bond angles at a metal center, and which results in single numerical parameter known as the $\tau5$ value (Fig. 2.1b).[131] This parameter, introduced by Addison et al. evaluates the trigonality of distorted five-coordinate systems, with a $\tau5$ value of 1 indicating a perfect trigonal bipyramidal site and a value of 0 indicating a perfect square pyramidal site. The $\tau5$ value can therefore be used to numerically compare the metal geometries in different dimers by the degree to which they approach one extreme in geometry versus the other, without the tedium associated with using multiple bond angle/bond length values to perform a comparison. The value is calculated by the following equation: $\tau5 = (\theta_1 - \theta_2)/60$, where θ_1 and θ_2 are the two largest ligand-cation-ligand angles in the system. The angles involved in this calculation for the penta-coordinate system found in dimers can be found in figure 2.1b. Although the $\tau5$ index is intended to be used solely for penta-coordinate sites, there are instances in this chapter where it is also used to describe hexa-coordinate or tetra-coordinate sites as well. In these cases, the two angles that are used are the same as those for the penta-coordinate analogs, namely those that include the oxo-metal bonds, but not the bond(s) to the *exo*-ligand. While this use is seemingly inappropriate, it reflects our interest in this parameter, namely that it allows us to determine the effect that individual sites have on the "circularity" of the dimer, which is determined by the angles at these particular bonds. The $\tau5$ parameter and its use in hexa-coordinate systems is also used in Ch. 4, where it describes the effect that different coordination geometries have on the structure of a metal-organic framework (MOF).

A few other notes must also be made as to the specifics of the crystallography experiments that were conducted as well as to data workup. The vast majority of the crystallographic data in this section was collected in-house, primarily by the author but also in-

part by Dr. Charles Barnes. A small portion was also collected at the Advanced Light Source (ALS) in Berkeley, California by Dr. Drew Fowler under the supervision of Dr. Simon Teat. The location of collection can be determined by looking at the radiation source in the crystallographic information included for each crystal structure. Data collected at the ALS was collected using synchrotron radiation, while data collected in-house used MoKα radiation produced *via* the photoelectric effect in an X-ray tube. All data was solved/refined using the Shelx-97 software package with x-seed as the interface.[132,133] X-Seed was also used as the interface for molecular image generation with the Persistence of Vision Raytracer (POV-Ray) program. The void volumes inside the hexameric MONCs were determined using the program MS-Roll, which is used more extensively in the fourth chapter and will be described there in more detail.[134] Bond length and bond angle data was obtained when possible from the crystallographic information file (.cif) associated with each structure.

2.2 Synthesis and characterization of copper-seamed MONCs

The interest in PgC-metal assemblies can in no small way be attributed to the discovery of the copper-seamed hexameric MONC.[118] This complex is essentially a large metal-organic "cage", which consists of thirty components: twenty-four Cu^{2+} cations and six PgC macrocycles. In addition, it also contains a large number of guest species that are incarcerated within the capsule during synthesis. A comparison can be drawn with the non-covalently seamed hexamers seen with PgCs and RsCs, which are all spatially and geometrically very similar. However, the MONC is significantly more stable as it is held together through the much stronger coordinativebonding (covalent) rather than hydrogen-bonding (non-covalent). As such, it can be dissolved in a wide range of solvents without the risk of decomposition.

Considering its large size and relative complexity, it is rather surprising that the synthesis of the copper-seamed hexamer is also incredibly simple. In a typical procedure, a PgC is dissolved in methanol and mixed with an excess quantity of methanolic $Cu(NO_3)_2$ at room temperature and at ambient conditions. This leads to the immediate precipitation of the pure hexameric MONC as an air-stable brown solid, which can be removed by filtration. PgC solutions are usually light pink in color, and most copper salts are either blue or green, so it was likely quite obvious to the first person to synthesize this MONC that they had synthesized something novel. It is important to note that unlike the other transition metal cations, copper will coordinate to PgCs without the need of a sacrificial and/or coordinating base. The absence of this extra step is perhaps another reason why this MONC was discovered first, instead of other simple-to-make MONCs like the zinc dimer, which does require a base such as pyridine during synthesis.

While the hexameric MONC has and still is characterized by using scXRD, it is often difficult to grow well-diffracting crystals of this material. As such, MALDI-TOF has also been used in the past to aid in its characterization. This method of analysis is particularly useful as it only requires that the analyte is soluble in solvents that quickly evaporate. Almost any MONC produced using the protocol described earlier can be solubilized in either acetone or methanol, and thus is compatible for this method of analysis. Indeed, it was this method that allowed researchers to show that only the hexameric product was produced using the standard methanolic protocol.[119]

The benefit of producing copper-seamed MONCs in this way is that it is very simple and leads to good, reproducible results. However, it is not the only method of producing copper-seamed MONCs from PgCs. Indeed, the copper-seamed dimeric MONC was discovered

primarily due to a purposeful deviation from this standard synthetic method. As such, this section will explore the synthesis and characterization (*via* scXRD) of both hexameric and dimeric copper-seamed MONCs using methods that differ from those that have already been published in the original few reports. This will perhaps encourage future research efforts involving copper-seamed MONCs to implement diverse synthetic methods, rather than just the methanolic dump-and-filter method.

2.2.1 PgC1CuDMSO dimer

0.608 g PgC_1 was dissolved in 100 mL of DMSO. In a separate flask, 0.799 g of $Cu(OAc)_2 \cdot H_2O$ was dissolved in 100 mL of DMSO. Both solutions were heated to 150 °C and the solutions were mixed, leading to changes in color from colorless and turquoise to dark violet-brown. The solution was taken off heat and allowed to recrystallize at RT. Crystallization occurred over the course of several days

Crystal data for $PgC_1CuDMSO$ dimer (2.1): $C_{80}H_{96}Cu_8O_{32}S_8$, M = 2334.37, Bronze Plate, 0.40 × 0.30 × 0.05 mm^3, triclinic, space group P-1 (No. 2), a = 15.458(2), b = 15.849(2), c = 26.379(4) Å, α = 102.989(2), β = 93.986(2), γ = 100.137(2)°, V = 6158.9(16) $Å^3$, Z = 2, D_c = 1.259 g/cm^3, F_{000} = 2384, Bruker APEX-II CCD, MoKα radiation, λ = 0.71073 Å, T = 100(2)K, $2\theta_{max}$ = 52.8º, 66321 reflections collected, 25055 unique (R_{int} = 0.0352). Final *GooF* = 1.197, *R1* = 0.0652, *wR2* = 0.1880, *R* indices based on 15251 reflections with I >2sigma(I) (refinement on F^2), 1283 parameters, 334 restraints. Lp and absorption corrections applied, μ = 1.549 mm^{-1}.

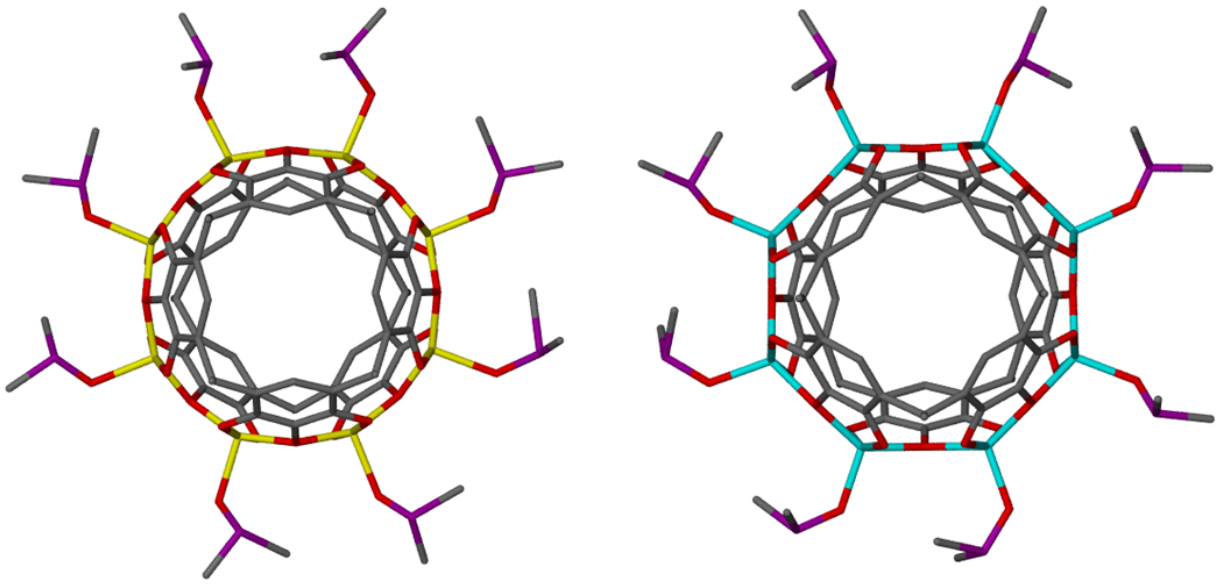

PgC1CuDMSO dimer (cmpd. 2.1)

Metal #	Ligand	θ_1	θ_2	$\tau 5$
Cu1	DMSO	171.75	151.76	0.333
Cu2	DMSO	173.05	154.59	0.308
Cu3	DMSO	173.16	152.79	0.340
Cu4	DMSO	171.81	152.23	0.326
Cu5	DMSO	171.09	151.05	0.334
Cu6	DMSO	171.08	151.37	0.329
Cu7	DMSO	172.25	151.66	0.343
Cu8	DMSO	171.53	151.3	0.337
Average				**0.33**
StD				**0.01**

C3ZnDMSO dimer (published)

Metal #	Ligand	θ_1	θ_2	$\tau 5$
Zn1	DMSO	163.88	137.51	0.440
Zn2	DMSO	162.29	137.75	0.409
Zn3	DMSO	162	137.75	0.404
Zn4	DMSO	163.19	136.25	0.449
Zn5	DMSO	161.99	139.72	0.371
Zn6	DMSO	162.41	135.15	0.454
Zn7	DMSO	162.03	136.87	0.419
Zn8	DMSO	162.2	138.86	0.389
Average				**0.42**
StD				**0.03**

Figure 2.2: Comparison of the structure and coordination geometry in PgC1CuDMSO dimer (2.1) and the published PgC3ZnDMSO dimer.[127]

As synthesis in hot ethylene glycol led to the identification of the first copper-seamed dimer, it was envisioned that synthesis in hot DMSO would likewise lead to a dimeric species. Unlike ethylene glycol, cooling of the solution did not lead to a formation of powder, but rather to the formation of well-diffracting crystals. Structural analysis using scXRD led to a structure of this material, which did, in fact, consist of dimers (Fig 2.2). The structure is generally similar to that of dimers composed of PgCs and Zn^{2+} wherein an octametal belt "seams" two PgC hemispheres together. Each metal along this belt also accommodates a single peripheral ligand; in this case, all of the ligands are DMSO molecules. The interior of the dimer also incarcerates a single guest DMSO molecule, which is disordered over eight positions, each undergoing partial coordination to each of the eight Cu^{2+} centers. While this guest is highly disordered, its identity can be confirmed to be a DMSO (as opposed to an acetate, nitrate, or disordered water) based on the positions of the atoms and the respective bond lengths between them, particularly the 1.7 Å length between the sulfur and carbon atoms. This is consistent with the bond lengths in a non-coordinated/non-encapsulated DMSO. Since the electron density of the oxygen donor atom is divided among eight parts and is therefore very weak, an exact coordinative bond length between the Cu^{2+} centers and the encapsulated DMSO guest/ligand cannot be accurately determined. However, the distance between the electron density peaks that correspond to oxygen atoms and Cu^{2+} have an approximate value of 2.6-2.8 Å, which is significantly larger (and therefore weaker) than the Cu^{2+} - ligand bond length with the *exo* DMSO ligands (2.18±0.01 Å). As such, this (partially) coordinated DMSO does not significantly affect the coordinative geometry of the Cu^{2+} centers.

Although the overall structures of the copper and zinc dimers are similar, the substitution of Cu^{2+} for Zn^{2+} leads to minor, although not insignificant, changes in coordination geometry.

For example, while all of the metal centers in both structures are of distorted penta-coordinate geometry, it is clear from a cursory analysis that the bond angles and lengths are somewhat different. This difference is visually apparent, as the zinc dimer "looks" more polygonal than the copper dimer when viewed perpendicular to the octametal belt (Fig. 2.2). In an effort to quantify this difference, τ5 values were calculated for each structure. Average τ5 values of 0.417 and 0.331 were determined for the zinc dimer and copper dimer (**2.1**), respectively. The tendency toward greater square pyramidal geometry in **2.1** has an overall contractive effect on the octametallic belt, resulting in an adjacent Cu-Cu distance of 3.645 Å in **2.1**, as compared to 3.786 Å for Zn-Zn in the zinc dimer. This contraction could also be due to the shorter mean oxo-metal bond length in **2.1** versus that in the zinc dimer (1.97 ± 0.01 Å vs. 2.05 ± 0.02 Å). Interestingly, the bond to the *exo* DMSO ligands contrasts with this finding, and is actually significantly longer in the copper dimer (2.18±0.01Å in **2.1** vs. 2.00±0.02Å in the zinc dimer). This result is of direct relevance toward future studies concerning host-guest interactions in dimeric metal-seamed capsules, as the implementation of Cu^{2+} over Zn^{2+} allows specific tuning of interior volume and geometry, as well as the behavior of the *exo* ligand.

2.2.2 PgC3CuDMSO dimer

0.720 g of PgC_3 was dissolved in 10 mL of hot dimethyl sulfoxide (DMSO). In a separate vial, 1.15 g of $Cu(NO_3)_2 \cdot 2\ ½\ H_20$ was dissolved in 10 mL of hot DMSO, to which 1 mL of pyridine was added after dissolution. The PgC_3 and copper solutions were mixed in a scintillation vial, resulting in the immediate formation of a dark reddish-brown solution, which was set aside to cool. Crystallization occurred over a period of several weeks. It should be noted that the concentrations can probably be changed to affect the crystallizability of this complex

(i.e. the ratio of PgC:Cu^{2+}:pyridine should be kept at 1:4:12, but the relative concentrations can be increased or decreased to produce the desired effect, namely crystallization)

Crystal data for $PgC_3CuDMSO$ dimer (**2.2**): $C_{109}H_{159}Cu_8O_{38.50}S_{14.50}$, M = 3058.55, red plate , 0.35 × 0.35 × 0.15 mm^3, triclinic, space group P-1 (No. 2), a = 15.554(3), b = 15.674(3), c = 29.508(5) Å, α = 78.853(2), β = 81.590(2), γ = 82.114(2)°, V = 6938(2) $Å^3$, Z = 2, D_c = 1.464 g/cm^3, F_{000} = 3170, Bruker APEXII CCD area detector, MoKα radiation, λ = 0.71073 Å, T = 173(2)K, $2\theta_{max}$ = 46.5º, 58920 reflections collected, 19906 unique (R_{int} = 0.0239). Final *GooF* = 1.086, *R1* = 0.0620, *wR2* = 0.1866, *R* indices based on 15456 reflections with I >2sigma(I) (refinement on F^2), 1341 parameters, 12 restraints. Lp and absorption corrections applied, μ = 1.492 mm^{-1}.

A PgC3 copper-seamed dimer (**2.2**) was prepared to function as a comparative analog to the reported PgC3 zinc dimers. The synthesis was essentially analogous to that of the PgC1 copper-seamed dimer (**2.1**), with very minor alterations. As expected with this synthetic methodology, the ligands and internal guest in this material are all DMSO molecules. In addition, the guest DMSO molecule behaves like that in **2.1** and is disordered over eight positions (Fig. 2.3). As in **2.1**, the coordinative bonds between the guest DMSO and the Cu^{2+} centers are weak and range from 2.6-2.8 Å. It was also of value to compare the τ5 values in the two structures, which were found to be very close to one another (0.34 in **2.2** vs. 0.33 in **2.1**). This suggests that the tail length has little, if any, influence on the geometry of the metal centers in a dimer, something that has always been suspected but never confirmed.

2.2.3 An alternate method of producing PgC3-Cu dimers using metal exchange.

1.395 g of PgC3 was dissolved in 50 mL of acetonitrile. In another container, 6.42 g of the $Zn(NO_3)_2(pyridine)_4 \cdot 2pyridine$ complex was dissolved in 4:1 acetonitrile:water. The two solutions were mixed together, and a yellow precipitate (PgC3Zn dimer) formed immediately and was filtered and dried. It should be noted that alternately, a 1:6 ratio of $Zn(NO_3)_2$:pyridine could likely be used instead of the complex in the synthesis of the zinc dimer, as could almost any ratio of pyridine:Zn^{2+} that exceeds 2:1.

1.33 g of this yellow powder was mixed with 10 mL of hot DMSO, and stirring the material on a heating mantle set to 225°C caused the majority of the powder to dissolve. 2.5 mL of this solution was then added to a clean scintillation vial and 1 mL of 1M $Cu(NO_3)_2$ in DMSO was added. The vial was capped and crystallization occurred after several days of standing at RT.

Crystal data for PgC_3Cu/Zn-DMSO dimer (2.3) : $C_{38.33}H_{51.33}Cu_{2.67}N_{0.33}O_{12.74}S_{5.33}$, M = 1061.14, red plate, .1 × .25 × .25 mm^3, triclinic, space group P-1 (No. 2), a = 15.485(4), b = 15.595(4), c = 29.601(7) Å, α = 78.887(3), β = 81.926(3), γ = 82.098(3)°, V = 6900(3) $Å^3$, Z = 6, D_c = 1.532 g/cm^3, F_{000} = 3290, Bruker SMART CCD area detector, MoKα radiation, λ = 0.71073 Å, T = 173(2)K, $2\theta_{max}$ = 54.7º, 79285 reflections collected, 30447 unique (R_{int} = 0.0424). Final *GooF* = 1.017, *R1* = 0.0713, *wR2* = 0.2070, *R* indices based on 17999 reflections with I >2sigma(I) (refinement on F^2), 1798 parameters, 18 restraints. Lp and absorption corrections applied, μ = 1.526 mm^{-1}.

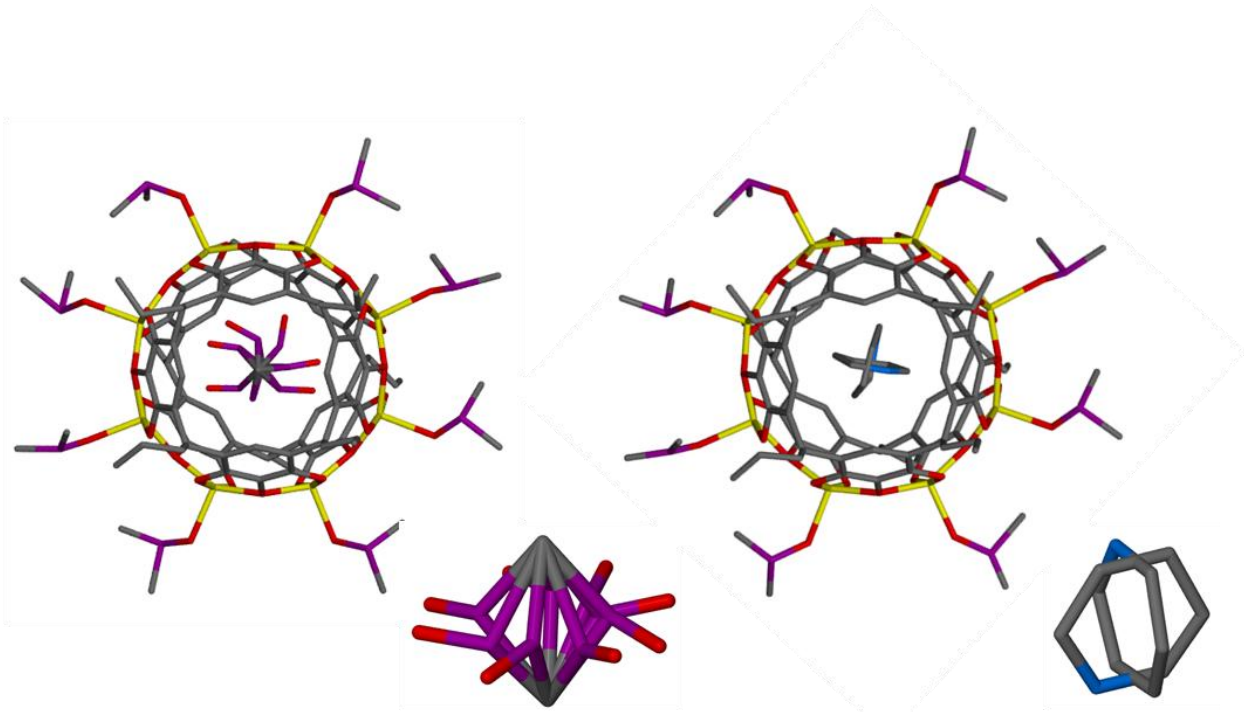

PgC3CuDMSO (cmpd 2.2)					PgC3Zn/CuDMSO (cmpd. 2.3)				
Metal #	Ligand	Angle 1	Angle 2	τ5	Metal #	Ligand	Angle 1	Angle 2	τ5
Cu1	DMSO	173.19	153.38	0.330	Cu1	DMSO	172.08	151.92	0.336
Cu2	DMSO	171.46	151.82	0.327	Cu2	DMSO	169.74	150.1	0.327
Cu3	DMSO	171.53	150.53	0.350	Cu3	DMSO	170.16	148.52	0.361
Cu4	DMSO	172.96	152.55	0.340	Cu4	DMSO	171.28	150.21	0.351
Cu5	DMSO	172.87	153.35	0.325	Cu5	DMSO	171.92	151.45	0.341
Cu6	DMSO	172.12	151.63	0.342	Cu6	DMSO	170.56	149.34	0.354
Cu7	DMSO	171.67	151.33	0.339	Cu7	DMSO	169.89	148.73	0.353
Cu8	DMSO	173.45	153.64	0.330	Cu8	DMSO	172.27	151.53	0.346
Average				0.34	**Average**				0.35
StD				0.01	**StD**				0.01

Figure 2.3: Comparison of the two PgC3Cu dimers **2.2** and **2.3** and their respective internal guest molecules. The difference in incarcerated guests indicates a difference in the origin of the dimers.

The PgC3-Cu dimer was also found to be generated by starting with the PgC3-Zn dimer and exchanging the zincs for coppers. This was done by first synthesizing the PgC3-ZnPy dimeric nanocapsules and then dissolving this material in hot DMSO and adding Cu^{2+}, which replaces the Zn^{2+} cations from the octametal belt. Evidence for the replacement of all of the zinc centers by coppers is the nearly identical unit cell parameters in **2.3** to that in **2.2**, as well as the τ5 values of the metal centers (average value: 0.346), which are all significantly closer to the copper-seamed dimers **2.1** and **2.2** than to the zinc-seamed dimer (Fig. 3.3). This value still is slightly higher than the average τ5 in **2.1** and **2.2**, which can partially be explained by the fact that a different guest species, a pyridine molecule, occupies the interior of the dimer (Fig 2.3). A pyridine guest is geometrically incapable of coordination to the metal centers that surround it, while a DMSO guest molecule is capable of at least a weak bond with Cu^{2+} centers, as demonstrated by the bond distances in compounds **2.1** and **2.2**. The presence of a guest pyridine is, in and of itself, an interesting finding, as it suggests that the internal guest (which is a pyridine in the original PgC3-ZnPy dimer) does not leave the capsule while all of the metal cations are replaced. This may suggest that cation exchange in this system occurs one metal center at a time, and that this process is not a decomposition/reformation event. If complete decomposition and reformation of the capsule *had* occurred during cation exchange, it would be expected that the capsule would contain a DMSO guest, instead of a pyridine. This is because DMSO was used as the solvent and would have grossly out-competed any pyridines for incarceration within the capsule. The conclusion that cation exchange occurs one metal at a time is consistent with the idea that breaking 32 oxo-metal bonds without a stimulus is highly

disfavored (such a stimulus would be the addition of concentrated acid to protonate the PgC hydroxyls, or a strong binding ligand that out-competes PgC for M^{2+} binding). However, the displacement of zinc by copper while the capsule remains intact must occur *via* some chemical mechanism that results in the release of zinc and concomitant binding of copper. This process has yet to be investigated, and its elucidation would likely contribute to a more thorough understanding of cation exchange in other PgC-based MONCs.

2.2.4 Synthesis of a copper dimer bearing acetone ligands and an acetone guest

5 mL of a hot acetonic 10^{-2} M PgC1 solution was mixed with 2 mL of a hot acetonic 10^{-1} M $Cu(NO_3)_2$ solution in a 20 mL scintillation vial, causing a change in color of the solutions from pink and blue to reddish-brown. 500 μL of 10^{-1} M 4,4'-bipyridine was then added to this solution. The vial was then capped and crystallization occurred over the course of several days.

Crystal data for PgC_1Cu-acetone dimer (2.4): $C_{31.83}H_{32.33}Cu_{2.67}O_{11.67}$, M = 771.02, red plate, 0.25 × 0.15 × 0.10 mm^3, triclinic, space group P-1 (No. 2), a = 15.681(5), b = 15.721(5), c = 24.749(7) Å, α = 94.961(4), β = 107.108(3), γ = 98.952(3)°, V = 5703(3) $Å^3$, Z = 6, D_c = 1.347 g/cm^3, F_{000} = 2364, Bruker SMART CCD area detector, MoKα radiation, λ = 0.71073 Å, T = 173(2)K, $2\theta_{max}$ = 55.0º, 63530 reflections collected, 25301 unique (R_{int} = 0.0926). Final *GooF* = 1.115, *R1* = 0.1452, *wR2* = 0.3575, *R* indices based on 12814 reflections with I >2sigma(I) (refinement on F^2), 1102 parameters, 0 restraints. Lp and absorption corrections applied, μ = 1.534 mm^{-1}.

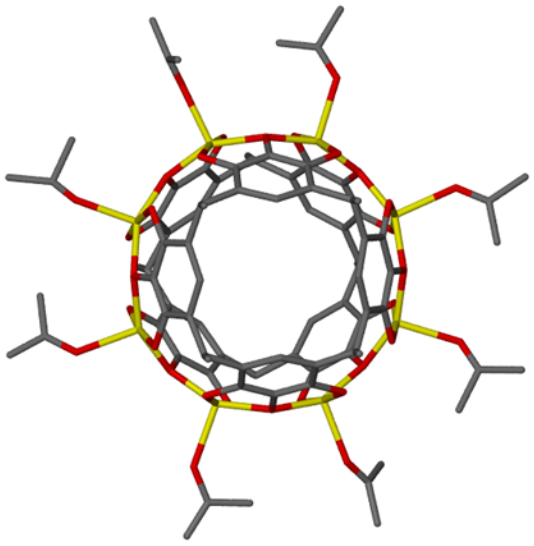

PgC1Cu-acetone dimer (cmpd. 2.4)

Metal #	Ligand	Angle 1	Angle 2	τ5
Cu1	Acetone	173.51	153.07	0.341
Cu2	Acetone	173.02	152.15	0.348
Cu3	Acetone	172.44	151.85	0.343
Cu4	Acetone	172.93	152.06	0.348
Cu5	Acetone	173.19	152.19	0.350
Cu6	Acetone	172.06	151.59	0.341
Cu7	Acetone	172.74	151.43	0.355
Cu8	Acetone	173.39	152.95	0.341
Average				0.35
StD				0.01

Figure 2.4: PgC1Cu-acetone dimer (2.4) and its bond angles/τ5 values

All of the dimeric copper structures thus far have been synthesized in DMSO. However, while DMSO is the one solvent from which well-diffracting crystals of dimeric MONCs can be reliably grown, other solvents can likewise be used to generate crystalline MONCs. The structure presented in this subsection is the only copper-seamed dimeric MONC that has so far been synthesized and crystallized in another solvent, and that diffracted well enough to be suitable for scXRD. The synthesis of this material was somewhat accidental, as it was not intended to produce "standalone" dimers, but rather dimers linked *via* 4,4'-bipyridine. However, a standalone dimer bearing acetone ligands and encapsulating an acetone guest was nevertheless produced (**2.4**). This is likely due to the small amount of linker used (one equivalent of linker for every equivalent of PgC1), which was likely to have been completely protonated by the acid formed during dimer synthesis. Thus, the dimer that formed did not have any 4,4'bpy ligands,

nor did it participate in linking. However, the addition of this ligand/base may have possibly contributed to the crystallization of the MONC by removing the acid formed during the coordination of copper to the PgC and thereby driving the reaction towards the nanocapsular product. It is likely that this result can be recreated using pyridine or some other base, rather than 4,4'-bipyridine, but this has not as of yet been attempted.

With the exception of its ligands, this dimer is structurally analogous to all of the other copper-seamed dimers in this subsection. The average $\tau 5$ value for the copper centers is 0.35, which demonstrates this fact quite nicely (Fig. 2.4). As in the case of the MONCs that encapsulate DMSO, the encapsulated acetone molecule is rotationally disordered over multiple positions, likely due to partial coordination to the eight metal centers. The acetone ligands behave essentially the same as DMSO ligands, although the oxo-metal bond length from copper centers to the acetone oxygen is slightly greater than that for the DMSO analogs (an average of 2.25Å for acetone vs. 2.17-2.20Å for DMSO).

2.2.5 Synthesis of a copper-seamed hexamer from DMSO

0.608 g (1 mmol) of PgC_1 was dissolved in 100 mL of DMSO. In a separate flask, 0.799 g of $Cu(OAc)_2 \cdot H_2O$ (4mmol) was dissolved in 100 mL MeCN. Both solutions were heated to dissolve the solids and were then cooled to room temperature. 5 mL of each solution was then added to a scintillation vial and mixed. This led to a change in color from pink and green to brown. The contents were then allowed to crystallize with a slightly open vial top. Two different types of crystals formed within several days, those with the same unit cell as in **2.2.1** and ones with the unit cell below.

Crystal data for $PgC_1CuDMSO$ hexamer (2.5) : $C_{30.07}H_{14.12}Cu_{2.82}O_{14.16}S_{3.74}$, M = 901.36, rod red, 0.60 × 0.05 × 0.05 mm^3, orthorhombic, space group *Fddd* (No. 70), a = 26.762(5), b = 37.422(7), c = 70.688(13) Å, V = 70792(22) $Å^3$, Z = 68, D_c = 1.438 g/cm^3, F_{000} = 30573, Bruker SMART CCD area detector, MoKα radiation, λ = 0.71073 Å, T = 173(2)K, $2\theta_{max}$ = 55.3º, 201344 reflections collected, 20462 unique (R_{int} = 0.1415). Final *GooF* = 1.569, *R1* = 0.1326, *wR2* = 0.3864, *R* indices based on 10767 reflections with I >2sigma(I) (refinement on F^2), 886 parameters, 81 restraints. Lp and absorption corrections applied, μ = 1.674 mm^{-1}.

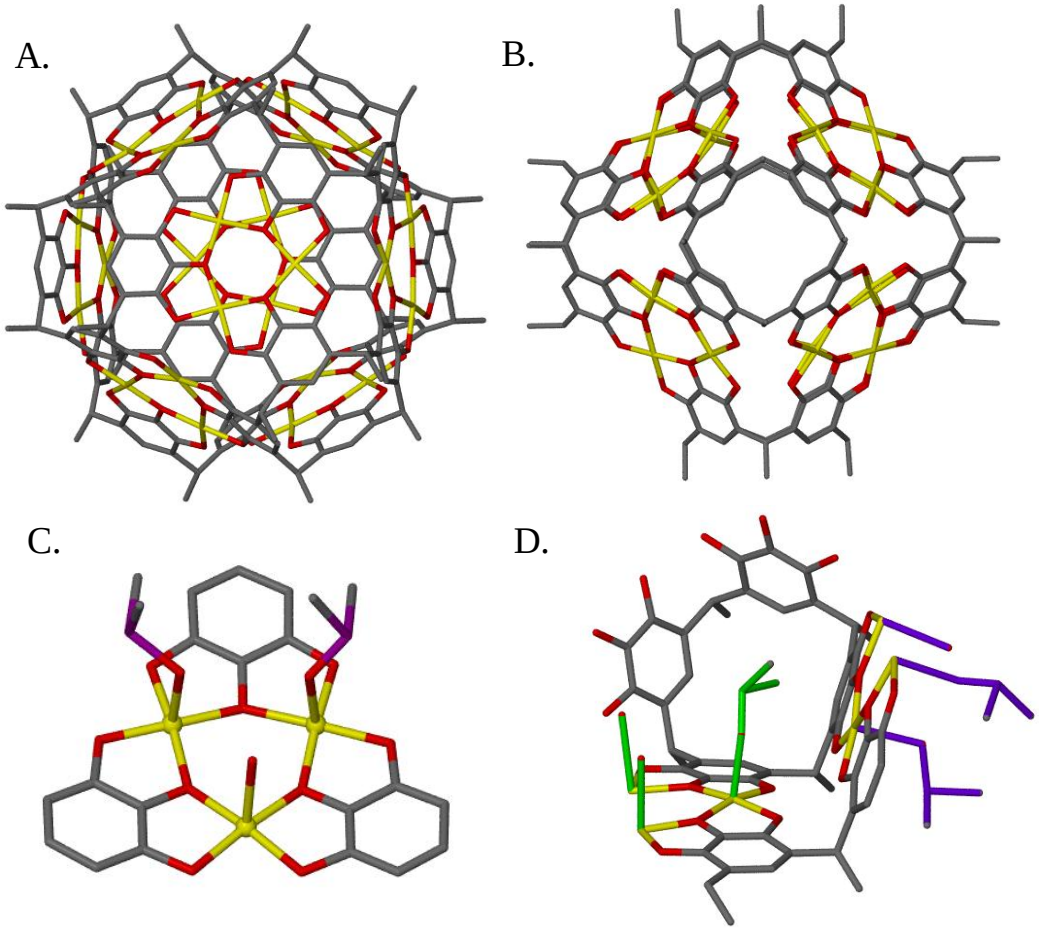

Figure 2.5: PgC1Cu-DMSO hexamer (**2.5**) viewed from two different angles (A,B). C shows one of the eight trimetal clusters in this material as well as three of the *exo*-ligands. D shows that both *endo*-ligands (green) and *exo*-ligands (violet) coordinate to the copper centers in this compound.

Based on the results seen in compounds **2.1** and **2.2**, it was expected that the method used to make this material would result in crystals of a dimer. While this was indeed the case, as crystals of the dimer did form in the scintillation vial used for recrystallization of this compound, a second and morphologically distinct type of crystal also formed alongside the dark rhombic crystals typical of the dimer. Structural determination *via* scXRD showed that the structure of this material was also different; instead of the dimeric motif seen in **2.2**, this new crystalline material was composed of copper-seamed hexamers (Fig. 2.5). The overall structure of these hexamers is essentially analogous to that seen in previous publications, although the interior of the capsule is much better resolved due to the presence of large and well-defined DMSO guests (Fig 2.5, see Table 2.1 in the next subsection for a bonding comparison). As such, these larger (and heavier) guest molecules were found to be much easier to appropriately model than other guest species. DMSO molecules also function as ligands for several of the copper centers, both on the inside and outside of the capsule (Fig. 2.5). Interestingly, the bond length between the copper center and the oxygen donor atoms on DMSO (avg 2.4 Å) is significantly shorter than the analogous bonds in previously published copper hexamers, where water and/or methanol molecules weakly interact with copper centers over very long distances that are more suggestive of non-covalent bonding rather than coordinative bonding (avg. 2.9 Å bond length).[119] These shorter *exo* ligand bonds, however, do not seem to affect the rest of the framework, as both the geometry and length (avg. 1.95 Å) of the PgC-Cu^{2+} oxo-metal bonds is the same as in the previously published structures.

Perhaps the most interesting feature of this material is not so much its structure, but rather its formation alongside crystals of the dimeric MONC. This occurrence is something that has not previously been observed in the study of PgC-based MONCs, and strongly suggests that both of

these MONCs are formed alongside one another during the reaction, although the timing of their formation remains unknown. The growth of two different types of crystals, however, was not seen when the reaction was carried out at higher temperatures. In that case, only crystals of the dimer were observed. While it is difficult (and likely inappropriate) to make a quantitative comparison between the identity of the crystalline materials and the relative amounts of these materials in solution, the disparity between these two experiments may indicate that the temperature of the reaction nevertheless plays an important role in the resultant products. As hexamers are only formed at the lower temperature, this may indicate that the concentration of hexamer at this temperature is greater than at higher temperatures, where only crystals of the dimer form. The desire to quantify the amount of dimer and hexamer in solution led to the studies conducted in Ch. 3, which use small angle neutron scattering to study these MONCs.

2.2.6 Copper-seamed hexamer from acetone and pyridine

320 µL of 1M pyridine in acetone was added to 2 mL of 10^{-2}M PgC1 in 8:1 acetone:water. 80 µL of aqueous 1M $Cu(NO_3)_2$ was then added to this mixed solution, changing the color from pink to brown. The vial was then capped and crystallization occurred over the course of several days. Interestingly, instead of crystallizing in a typical polygonal shape, this material formed "flower"-shaped crystals.

Crystal data for PgC$_1$Cu-Acetone hexamer (2.6): $C_{28.50}H_{24}Cu_3O_{13.38}$, M = 771.10, red prism, 0.15 × 0.15 × 0.10 mm^3, trigonal, space group R-3 (No. 148), a = b = 21.463(9), c = 57.26(2) Å, V = 22843(16) Å^3, Z = 24, D_c = 1.345 g/cm^3, F_{000} = 9336, Bruker SMART CCD area detector, MoKα radiation, λ = 0.71073 Å, T = 173(2)K, $2\theta_{max}$ = 46.5°, 63934 reflections collected, 7289 unique (R_{int} = 0.0938). Final *GooF* = 1.279, *R1* = 0.1044, *wR2* = 0.3104, *R* indices based on 3643 reflections with I >2sigma(I) (refinement on F^2), 575 parameters, 42 restraints. Lp and absorption corrections applied, μ = 1.714 mm^{-1}

Compound	M-O bond length (Å)	M-water/ligand bond length (Å)
PgC3Cu-MeOH (pub'd)	1.95 ± 0.03	2.9 ± 0.2
PgC1Cu-DMSO (2.5)	1.95 ± 0.01	2.4 ± 0.1
PgC1Cu-Acetone (2.6)	1.94 ± 0.01	2.46 ± 0.06

Table 2.1: Comparison of the oxo-metal and ligand-metal coordinative bond lengths in three copper-seamed hexameric nanocapsules. Data for the PgC3Cu-MeOH hexamer was obtained from the report by Dalgarno et al.[119]

As the *in situ* crystallization technique worked in DMSO to produce a hexamer, it was thought that this technique could also be used analogously in another solvent. The most commonly used solvents for MONC synthesis and recrystallization are methanol, acetone and acetonitrile. However, the synthesis of copper-seamed MONCs in methanol and acetonitrile is known to cause instant precipitation at most concentrations. Therefore, these two solvents could not be used for *in situ* synthesis/recrystallization of copper-seamed MONCs. Synthesis in acetone, however, typically does not lead to precipitation and can therefore be used for this purpose. Previous efforts have produced crystals of dimeric copper-seamed MONCs in acetone (**2.4**), so it was not unreasonable to expect a hexameric MONC to crystallize by following a

similar, but slightly modified procedure. Following the results in DMSO (**2.5**), which suggested that temperature plays a role in the formation of hexamers versus dimers, the synthesis of this material was carried out at room temperature, and produced the desired effect, namely that crystals of hexameric MONCs were produced in acetone (**2.6**). As with DMSO, the resultant hexamer is analogous in structure to those that have been published, albeit with a different R-group and internal guests. Interestingly, pyridine molecules were not found within the structure, even though this normally coordinating base was used in the synthesis of this MONC. Although solvent acetone molecules could be found (and modeled) on the exterior of the capsule, the interior of the capsule was significantly more disordered than the DMSO analog, with the only ordered molecules being the waters that coordinate to the copper centers. In general, the oxo-metal bond lengths between the Cu^{2+} and PgC hydroxyls are identical in length to all of the other examples of copper-seamed hexamers (Table 2.1). The bond lengths between the water/acetone ligands and copper centers are similar to the lengths seen with DMSO rather than to the longer lengths seen with the published examples that were synthesized in methanol. This may indicate that acetone is a better (stronger binding) ligand than alcohols, but is nevertheless essentially equivalent to water and DMSO.

2.2.7 Copper-seamed MONCs: summary

This subsection presented several novel examples of both hexameric and dimeric copper-seamed MONCs. All of the structures and synthetic methods used in this section are wholly novel, and introduce an alternative to the traditional techniques used in the preparation of these compounds. One notable commonality in the syntheses that were developed in this subsection is

that the majority of these MONCs were formed or recrystallized in DMSO, which clearly displays the versatility of this compound as a crystallization solvent.

While the copper-seamed dimers are generally similar in structure to the zinc dimers, there are several notable distinctions between the two analogs. The most obvious of these is the coordination geometry at the M^{2+} centers, which tends toward square pyramidal with Cu^{2+} and more towards trigonal bipyramidal with Zn^{2+}. In addition, when compared to the zinc dimer, the oxo-metal bond length between Cu^{2+} and the PgC hydroxyls is consistently shorter (and therefore stronger) in all of the copper dimers described in this section. This may explain why Cu^{2+} can be used to fully displace Zn^{2+} from a pre-made zinc dimer. Interestingly, the trend is reversed with the peripheral ligands, as the Zn^{2+} centers have significantly shorter bonds with *exo* DMSO ligands than in the Cu^{2+} analog. The hexamers described in this subsection are also generally similar to previously reported copper-seamed hexamers, although the bond distances between the Cu^{2+} centers and peripheral ligands are significantly shorter than in published examples. Perhaps the most interesting find regarding the hexamers is that crystals of the hexamer were found in the same vial as crystals of the dimer following *in situ* crystallization. This indicates that the solution used to make this material contained both of the MONCs. A mixture of crystals was not found when the same synthesis was conducted at higher temperatures (only dimers formed), suggesting that temperature plays a part in the identity of the MONC that is formed.

2.3 Nickel-seamed MONCs

The investigation of Ni^{2+} as a metal center in PgC-based MONCs was a turning point in research efforts involving all metal-seamed entities based on PgC. For one, the synthesis and characterization of the nickel-seamed dimeric MONC, together with the cobalt-seamed analog, were the first examples of new PgC-based MONCs to be discovered in more than four years. Their discovery suggested that dimeric capsules can be formed from a wide variety of transition metal cations. Furthermore, the discovery of a nickel-seamed hexamer showed that, like with copper, both dimeric and hexameric MONCs can be formed from a single transition metal cation, and that appropriate synthetic conditions could be used to effectively select for the crystallization of one versus the other. This has led to investigative efforts into the identity of PgC-based MONCs in solution, rather than in the solid state, so that the factors that influence the formation these MONCs can be better understood. This work is described in the next chapter. This section will describe the synthesis and structural characterization of several Ni^{2+} seamed MONCs, which include the dimer, the hexamer, and an odd species (the "pseudodimer") that is structurally unique among all PgC-based complexes.

2.3.1 PgC2Ni dimer bearing asymmetric pyridine ligands.

0.5 g of PgC2 (0.75 mmol) was dissolved in 10 mL of MeCN. In a separate container, 1.5 g of $Ni(NO_3)_2(pyridine)_4$ complex (3 mmol) was also dissolved in 10mL MeCN. The solutions were mildly heated while stirring to dissolve the solids. Once fully dissolved, the two solutions were mixed, which led to the immediate formation of a dark, slightly green precipitate. This precipitate was removed by vacuum filtration, washed with MeCN, then dried in a

dessicator (net yield: 0.46 g). A small amount of the now-yellow precipitate was then dissolved in minimal hot pyridine and allowed to stand uncapped to crystallize.

Note: The $Ni(NO_3)_2(pyridine)_4$ complex was synthesized by dissolving $Ni(NO_3)_2 \cdot 6H_2O$ in hot pyridine and heating the resultant solution under vacuum in a rotary evaporator to drive off the excess pyridine. It is likely, however, that the pre-synthesis of this complex is unnecessary, as it can be generated *in situ* by mixing the appropriate ratio of $Ni(NO_3)_2$ to pyridine in MeCN and then directly mixing this solution with the PgC solution.

Crystal data for PgC_2Ni-pyridine dimer (2.6): $C_{161}H_{155}N_{19}Ni_8O_{24}$, M = 3209.72, Yellow Block, 0.20 × 0.10 × 0.10 mm^3, orthorhombic, space group *Fddd* (No. 70), a = 19.7468(9), b = 27.6774(13), c = 53.647(3) Å, V = 29320(2) $Å^3$, Z = 8, D_c = 1.454 g/cm^3, F_{000} = 13360, Bruker APEX II CCD diffractometer, synchrotron radiation, λ = 0.77490 Å, T = 100(2)K, $2\theta_{max}$ = 58.0º, 39692 reflections collected, 7504 unique (R_{int} = 0.0766). Final *GooF* = 1.040, *R1* = 0.0630, *wR2* = 0.1806, *R* indices based on 5462 reflections with I >2sigma(I) (refinement on F^2), 534 parameters, 131 restraints. Lp and absorption corrections applied, μ = 1.346 mm^{-1}.

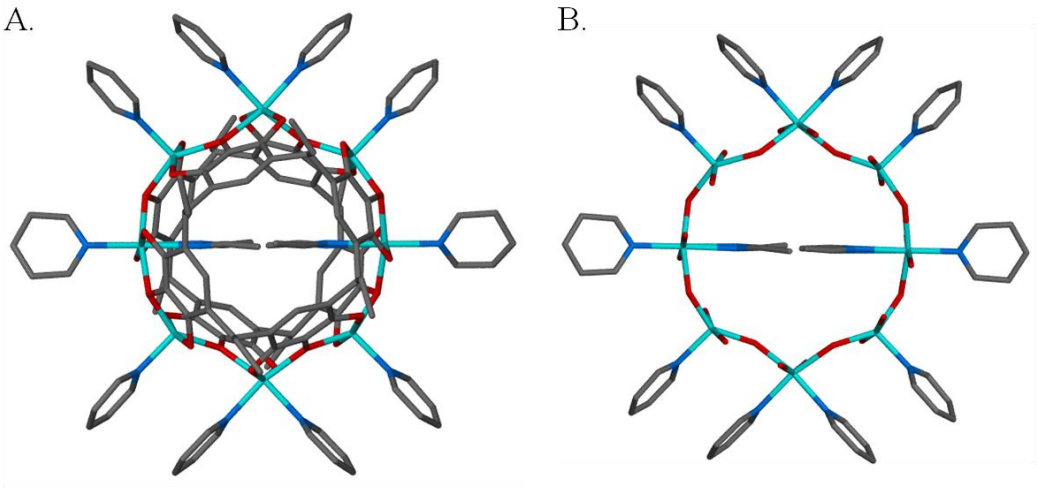

PgC2Ni-pyridine dimer (cmpd. 2.7)

Metal #	Ligand	θ_1	θ_2	$\tau 5$
Ni1	2x pyridine	159.27	110.45	0.814
Ni2	pyridine	170.34	144.59	0.429
Ni3	pyridine	178.55	167.55	0.183
Average				**0.5**
StD				**0.3**

Figure 2.6: PgC2Ni-pyridine dimer (**2.6**). Full structure is shown in A, and the octametal belt (including all ligand donor atoms) is shown in B. A table that shows the bond angles and τ5 values associated with the three unique metal centers is also included.

The procedure above detailed the synthesis and characterization of the first nickel-seamed dimer (**2.7**), and the first new dimeric capsule since the discovery of the zinc-seamed dimers. The asymmetric unit contains three unique metal centers, each of which contains pyridine ligands as well as several coordinative connections to PgC hydroxyls. Symmetry expansion reveals a complete dimeric MONC, which consists of eight metal centers arranged in an octametal belt (Fig. 2.6). Structurally, this dimer resembles the previously described zinc-and copper-seamed dimers, although there are several differences. The most notable of these is the coordination number at the metal centers. While the asymmetric unit only showed a single pyridine ligand per metal center, symmetry expansion shows that several of the Ni^{2+} centers

actually coordinate to two ligands in addition to the four coordinative bonds to the PgC hydroxyls. Two of the Ni^{2+} centers coordinate to two peripheral pyridine ligands and are therefore hexa-coordinate. In addition, this dimer incarcerates a pair of acetonitrile (MeCN) guest molecules, which coordinate to an additional two Ni^{2+} centers, albeit from the inside rather than the outside of the capsule. These *endo* bonds are much shorter (2.23 Å) than the partial *endo* DMSO-Cu^{2+} coordinative bonds seen earlier, suggesting that they are also significantly stronger and that the metal centers at those positions are formally hexa-coordinate. Therefore, the dimer contains a total of four hexa-coordinate and four penta-coordinate Ni^{2+} centers, which are arranged in a 6·5·6·5·6·5·6·5 pattern. This is a unique finding, as both the copper- and zinc-seamed dimeric MONCs only accommodate a single pyridine or DMSO ligand per metal center, thereby making all of the metal centers penta-coordinate. The effect of this is that the geometries in the metal sites of the nickel-seamed dimer are much less uniform than that in the zinc-seamed dimer. This can be enumerated in terms of the τ5 values of the metal centers; while the metal centers in the zinc-seamed dimers average approximately 0.42 with very little standard deviation (0.03), the τ5 values in this nickel seamed dimer are very different from one another, ranging from 0.81 to 0.18 among the three crystallographically-unique metal sites. This is visually evident from the significantly "warped" octametal belt. It is unknown whether the variance in coordination geometry was due to the chemistry of the Ni^{2+} centers or rather due to other factors, such as the synthetic or recrystallization method, so further experiments were conducted to determine if the 6·5·6·5·6·5·6·5 coordination pattern was consistent among all nickel-seamed dimers or not.

2.3.2 PgC3Ni dimer with solely penta-coordinate nickel centers

0.72 g of PgC3 (1.0 mmol) was dissolved in 20mL of MeCN. In a separate container, 2.0 g of $Ni(NO_3)_2(pyridine)_4$ complex (4.0 mmol) was also dissolved in 20 mL of MeCN. The solutions were mildly heated while stirring to dissolve the solids. Once fully dissolved, the two solutions were mixed, which led to the immediate formation of dark, slightly green precipitate. Alternately, the same result could be achieved by co-dissolving 0.72 g of PgC3 (1 mmol) and 1.16 g of $Ni(NO_3)_2 \cdot 6H_2O$ (4 mmol) in 40 mL of MeCN and then adding 1.16 mL of pyridine (16 mmol) once the two solids were dissolved. The amount of pyridine can be changed with minimal change in results, although a greater proportion of pyridine will typically increase yield. This precipitate was then removed by vacuum filtration, washed with MeCN, then dried in a dessicator. A small amount of the now-yellow precipitate was then dissolved in minimal hot DMSO, removed from heat and left to crystallize at room temperature.

Crystal data for $PgC_3NiPy/DMSO$ dimer (2.8): $C_{45.54}H_{38.43}N_{3.02}Ni_{2.78}O_{10.09}S_{1.74}$, M = 1008.57, prism yellow , 0.25 × 0.25 × 0.10 mm^3, monoclinic, space group $P2_1/c$ (No. 14), a = 30.060(3), b = 31.943(3), c = 30.290(3) Å, β = 111.1920(10)°, V = 27118(5) $Å^3$, Z = 23, D_c = 1.420 g/cm^3, F_{000} = 11943, Bruker SMART CCD area detector, MoKα radiation, λ = 0.71073 Å, T = 173(2)K, $2\theta_{max}$ = 42.1°, 180212 reflections collected, 29109 unique (R_{int} = 0.1317). Final *GooF* = 1.303, *R1* = 0.1137, *wR2* = 0.3115, *R* indices based on 13717 reflections with I >2sigma(I) (refinement on F^2), 2935 parameters, 266 restraints. Lp and absorption corrections applied, μ = 1.236 mm^{-1}.

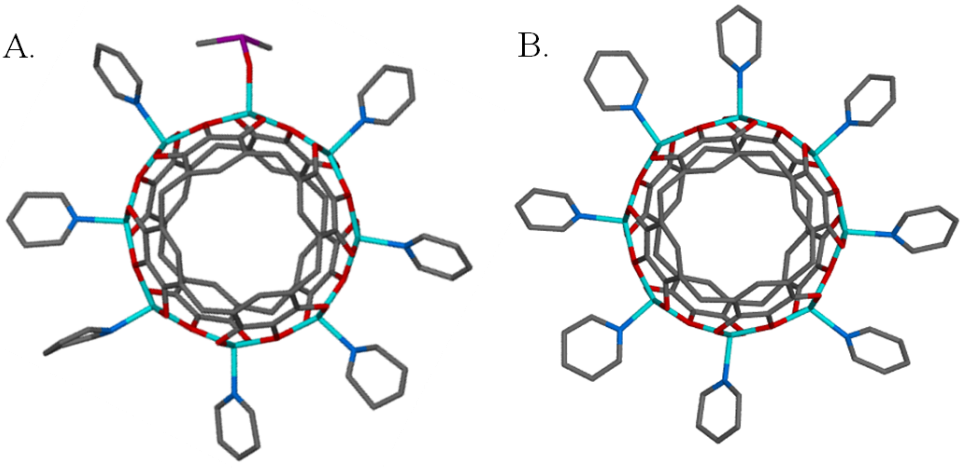

PgC3Ni-pyridine dimer #2 (2.8)				
Metal #	**Ligand**	**θ_1**	**θ_2**	**τ5**
Ni1	pyridine	169.75	146.86	0.382
Ni2	pyridine	169.32	151.24	0.301
Ni3	pyridine	174.11	154.11	0.333
Ni4	pyridine	170.78	151.95	0.314
Ni5	pyridine	170.76	151	0.329
Ni6	DMSO	167.39	147.57	0.330
Ni7	pyridine	171.82	155.27	0.276
Ni8	pyridine	172.39	153.8	0.310
Average				0.32
StD				0.03

PgC3Ni-pyridine dimer #1 (2.8)				
Metal #	**Ligand**	**θ_1**	**θ_2**	**τ5**
Ni1	pyridine	168.49	145.6	0.382
Ni2	pyridine	172.57	153.35	0.320
Ni3	pyridine	171.66	152.66	0.317
Ni4	pyridine	170.3	150.65	0.328
Ni5	pyridine	168.21	145.71	0.375
Ni6	pyridine	170.22	151.07	0.319
Ni7	pyridine	174.38	161.31	0.218
Ni8	pyridine	170.22	149.66	0.343
Average				0.33
StD				0.05

Figure 2.7: Image displaying the two nickel-seamed dimers that make up structure **2.8**, along with their respective bond angles/τ5 values. A single DMSO ligand replaces one pyridine on the periphery of dimer A

Recrystallization of nickel-seamed dimers in DMSO led to solely penta-coordinate Ni^{2+} sites in the dimers that make up this structure (**2.8**). The structure includes two dimeric nanocapsules, each one bearing eight peripheral ligands (Fig. 2.7). The guest species in the dimers are difficult to determine due to their disorder, but the pattern of electron density peaks suggests that both dimers enclose acetonitrile molecules. This is consistent with the previous structure, which was synthesized analogously and also had an encapsulated pair of acetonitriles. The ligands on the exterior of the dimers are slightly different, which is why there may be two dimers as part of the asymmetric unit instead of just one. One of the dimers has eight pyridine

ligands, while the other has seven pyridines and a single DMSO. As in the examples seen with zinc, the single DMSO molecule likely comes about as a result of ligand exchange following synthesis, with the DMSO molecule replacing a pyridine as the material was heated and the pyridine evaporated.[127] The single metal site that harbors this DMSO does not significantly differ in its coordination geometry when compared with the other metal centers ($\tau 5$ at this site equals to 0.32, while the average for the dimer is 0.33 with a standard deviation of 0.03). Perhaps the most important thing about the characterization of this material, though, is that it allows for a comparison to be made in two directions; in terms of how coordination number affects dimeric geometry (a comparison with **2.7**), and in terms of how changing the metal cation that is used affects dimeric geometry (a comparison with previously published zinc-seamed and previously described copper-seamed dimers)

The PgC2-Ni seamed dimer (**2.7**) is visibly different from the dimers reported here. As suggested in that section, the structure of **2.7** is "warped" away from structural circularity due to the presence of both penta- and hexa-coordinate Ni^{2+} sites. The geometry of this structure suggests that this was a correct assessment to make, as the absence of hexa-coordinate sites here produce a geometry that is visibly much more uniformly circular. The reason why the coordination numbers in the two structures differ is uncertain, but may indicate that the recrystallization solvent (DMSO vs. pyridine) dictates the coordination number of a dimer. The cause of this is unknown, but it may be simply incidental. Possibly, both species (those that both have and do not have hexa-coordinate sites) are present in the initial mixture, but the solvent of crystallization, as well as other factors such as the pendant R-group determine which dimeric variant crystallizes first. If this is the case, selective crystallization in various solvents could potentially have some utility as a separation method. This has not, however, been pursued.

Another advantage of isolating and characterizing the nickel-seamed dimer that was described in this section is that the coordinative geometry of these dimers may be directly compared to the geometry in the zinc-seamed dimers, as both species bear solely penta-coordinate metal centers. This allows us to determine the effect that using nickel versus zinc has on the framework. Visually, it is quite clear that there is an effect; although both appear to be reasonably symmetrical, the zinc-seamed dimer looks much more "polygonal" than the nickel seamed analog. However, it was also of value to quantitatively describe this difference. This was done by comparing the $\tau 5$ values of the two dimers. The average $\tau 5$ in the zinc-seamed dimers is 0.42 ± 0.03, while the two dimers in **2.8** have $\tau 5$ values that average 0.32 ± 0.03 and 0.33 ± 0.05, which is a clear difference. Much more similarity exists between these dimers and the copper-seamed dimers seen in the last section, which have typical $\tau 5$ values that average at approximately 0.34. The oxo-metal bond lengths between Ni^{2+} and the PgC hydroxyl are much closer to those in the zinc dimer, averaging at around 2.02 Å versus 2.05 Å with zinc and 1.95 Å with copper.

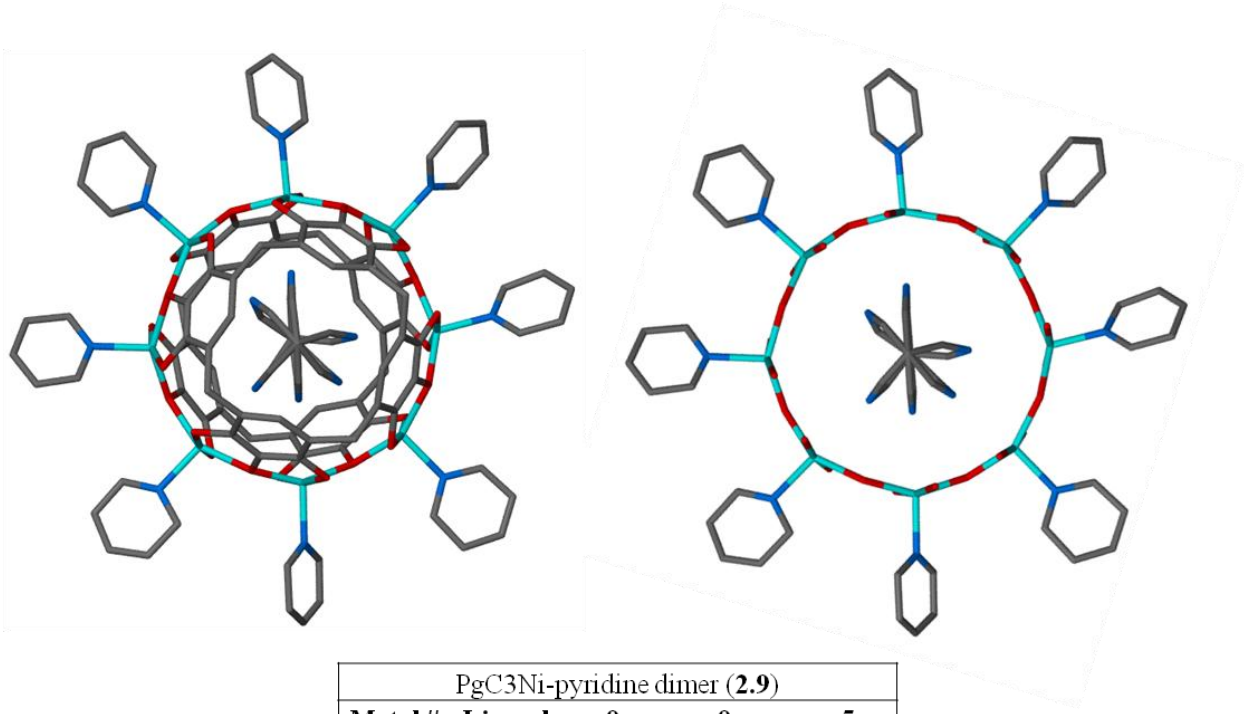

PgC3Ni-pyridine dimer (**2.9**)				
Metal#	**Ligand**	**θ_1**	**θ_2**	**$\tau5$**
Ni1	pyridine	169.1	147.66	0.357
Ni2	pyridine	169.91	151.7	0.304
Ni3	pyridine	175.66	157.89	0.296
Ni4	pyridine	170.15	148.78	0.356
Ni5	pyridine	173.01	148.74	0.405
Ni6	pyridine	173.34	150.74	0.377
Ni7	pyridine	171.41	149.93	0.358
Ni8	pyridine	172.22	150.22	0.367
Average				**0.35**
StD				**0.04**

Figure 2.8: Full structure of **2.9** is shown in A, and the octametal belt (including all ligand donor atoms) is shown in B. A table that shows the bond angles and $\tau5$ values associated with the metal centers is also included.

2.3.3 PgC3Ni dimer recrystallized in pyridine

PgC3-Ni-pyridine dimer solid was prepared analogously to that in 2.3.2. A small amount of the solid was then dissolved in minimal hot pyridine, removed from heat and was capped. Crystallization occurred over a period of several days.

Crystal data for PgC_3NiPy dimers Py solvate (2.9): $C_{141.50}H_{122}N_{14}Ni_8O_{24}$, M = 2872.21, yellow prism, monoclinic, space group $P2_1/n$ (No. 14), a = 18.7651(17), b = 26.349(3), c = 32.554(3) Å, β = 103.288(2)°, V = 15665(3) Å^3, Z = 4, D_c = 1.218 g/cm^3, F_{000} = 5940, Bruker SMART CCD area detector, MoKα radiation, λ = 0.77490 Å, T = 100(2)K, $2\theta_{max}$ = 43.4º, 45620 reflections collected, 14082 unique (R_{int} = 0.0430). Final *GooF* = 1.915, *R1* = 0.1604, *wR2* = 0.4337, *R* indices based on 8373 reflections with I >2sigma(I) (refinement on F^2), 1152 parameters, 330 restraints. Lp and absorption corrections applied, μ = 1.004 mm^{-1}.

This experiment was performed in order to determine if a PgC3 analog of the structure found in 2.3.1 could be synthesized. In contrast to the PgC2-Ni dimer (**2.7**), the PgC3 analog contains only penta-coordinate Ni^{2+} sites. This may be due to the shorter recrystallization time; whereas crystals of **2.7** were produced after several weeks on RT evaporation in excess pyridine, this material formed from cooling a supersaturated solution and crystallization occurred within days. Alternately, as suggested in section 2.3.2, multiple dimeric variants may be present in the crude powder following synthesis. It may simply be that the variant seen here is the one that crystallizes first with PgC3.

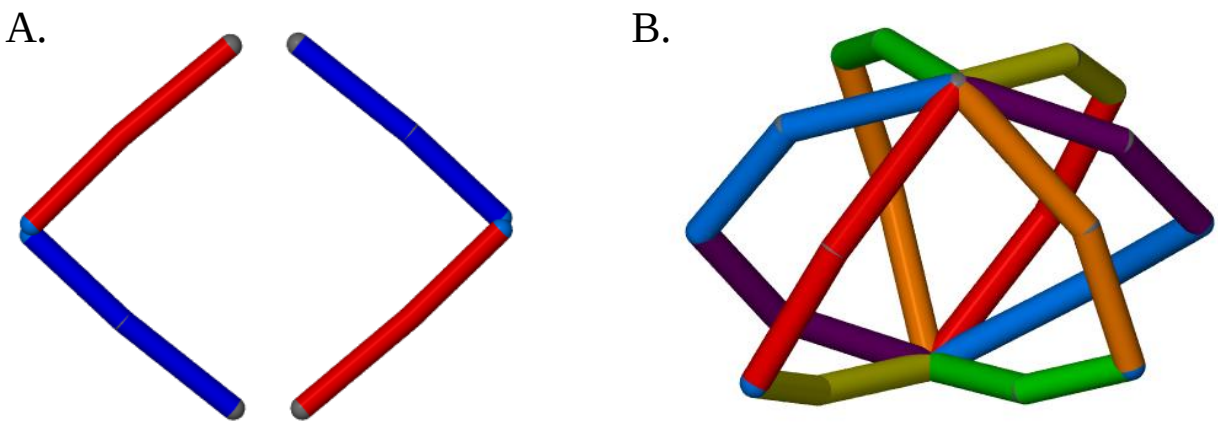

Figure 2.9: Differing spatial arrangements of encapsulated acetonitrile guests in **2.7** (A) and **2.9** (B). Encapsulated acetonitriles come in pairs, so the possible pair arrangements are color coded. A slight bend in the acetonitriles in B is due to disorder in the α-carbons

One unintended benefit from the characterization of this structure is that it further demonstrates the behavior of encapsulated acetonitrile. In **2.7**, the acetonitrile molecules were oriented away from the hexa-coordinate metal sites, which limited their disorder. However, the behavior of encapsulated acetonitrile in a fully penta-coordinate system could not be determined from the structure in **2.8**. The structure of **2.9**, however, was significantly more ordered and the behavior of the internal guest was much clearer. As in cases of DMSO encapsulation in penta-coordinate dimers, the acetonitrile guests (two are assumed to occupy the cavity) can partially coordinate to all of the metal centers. As such, the acetonitrile nitrogens are disordered over eight positions, although there is significant electron density only at six. Furthermore, because the ß-carbons of both acetonitrile guests are fixed in place above and below the plane of the coordination belt, there are also necessarily two positions for α-carbons for each nitrogen. Therefore, the (two) encapsulated acetonitrile guests are actually disordered over sixteen different possible positions, and were modeled accordingly. The arrangement of the pair of

acetonitrile guests is similar to that in **2.7** (parallel relative to one another), except that it repeats an additional three times to account for binding to the other metal centers. The dichotomy between the two structures presents one of the several examples in this text where the coordination number of the metal centers dictates the spatial arrangement of the encapsulated ligand.

2.3.4 Synthesis of PgC3Ni dimer in methanol

0.72 g of PgC3 (1.0 mmol) was dissolved in 20 mL of MeOH. In a separate container, 2.0 g of $Ni(NO_3)_2(pyridine)_4$ complex (4.0 mmol) was also dissolved in 20 mL of MeOH. The solutions were heated while stirring to dissolve the solids. Once fully dissolved, the two solutions were mixed, which led to the immediate formation of yellow precipitate. Alternately, the same result could be achieved by co-dissolving 0.72 g of PgC3 (1 mmol) and 1.16 g of $Ni(NO_3)_2{\cdot}6H_2O$ (4 mmol) in 40 mL of MeOH and then adding 1.16 mL of pyridine (16 mmol) once the two solids were dissolved. The amount of pyridine can be changed with minimal change in results, although a greater proportion of pyridine will typically increase yield. This precipitate was then removed by vacuum filtration, washed with MeCN, then dried in a dessicator. A small amount of the precipitate was then dissolved in minimal hot DMSO, removed from heat and left to crystallize at room temperature.

Crystal data for C_3NiPy/pyridine dimer DMSO solvate (2.10):

$C_{46.60}H_{46.67}N_{2.67}Ni_{2.67}O_{11.17}S_{3.30}$, M = 1085.09, yellow plate, 0.25 × 0.10 × 0.05 mm^3, monoclinic, space group $P2_1/n$ (No. 14), a = 17.006(7), b = 30.032(12), c = 31.522(12) Å, β = 102.322(5)°, V = 15728(11) $Å^3$, Z = 12, D_c = 1.375 g/cm^3, F_{000} = 6741, Bruker SMART CCD area detector,

MoKα radiation, λ = 0.71073 Å, T = 173(2)K, $2\theta_{max}$ = 55.1°, 184258 reflections collected, 35969 unique (R_{int} = 0.1228). Final *GooF* = 1.029, *R1* = 0.0913, *wR2* = 0.2554, *R* indices based on 17795 reflections with I >2sigma(I) (refinement on F^2), 1767 parameters, 24 restraints. Lp and absorption corrections applied, μ = 1.139 mm^{-1}.

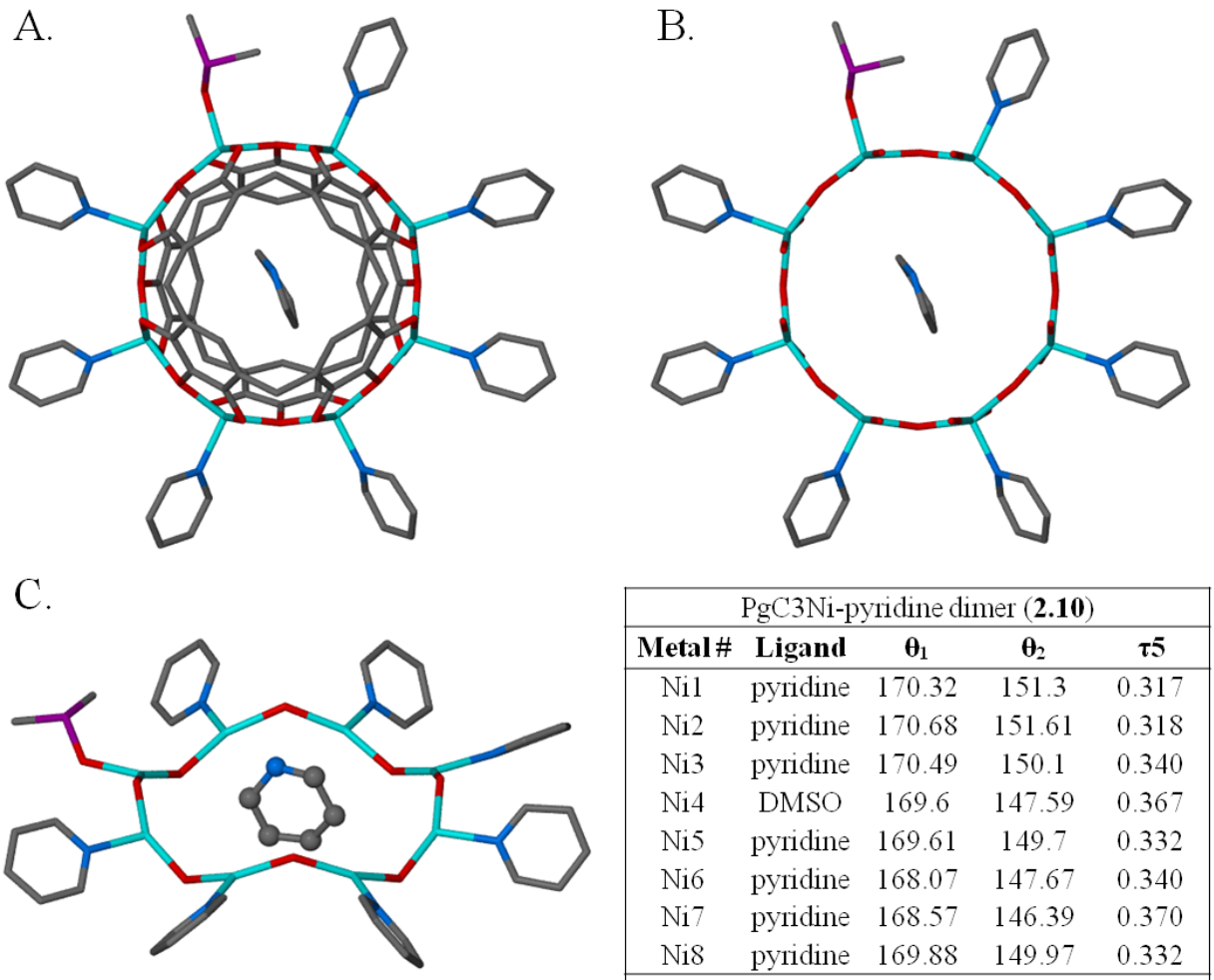

PgC3Ni-pyridine dimer (**2.10**)				
Metal #	**Ligand**	**θ₁**	**θ₂**	**τ5**
Ni1	pyridine	170.32	151.3	0.317
Ni2	pyridine	170.68	151.61	0.318
Ni3	pyridine	170.49	150.1	0.340
Ni4	DMSO	169.6	147.59	0.367
Ni5	pyridine	169.61	149.7	0.332
Ni6	pyridine	168.07	147.67	0.340
Ni7	pyridine	168.57	146.39	0.370
Ni8	pyridine	169.88	149.97	0.332
Average				**0.34**
StD				**0.02**

Figure 2.10: Full structure of **2.10** is shown in A, and the octametal belt (including all ligand donor atoms) is shown in B. C shows the octametal belt and the endo pyridine guest. A table that shows the bond angles and τ5 values associated with the metal centers is also included

While the nickel-seamed dimers in the previous subsections were all slightly different, these differences were a function of the crystallization methods that were employed. Their synthesis, however, was the same, involving the precipitation of the dimer from acetonitrile. This experiment was conducted to determine if the resultant dimer could be changed by changing the solvent during synthesis, so methanol was used instead of acetonitrile while keeping the rest of the conditions the same. Crystallization was then performed in DMSO. The resultant structure shows few major differences from the other nickel dimers; it has all penta-coordinate Ni^{2+} sites at the metal centers and has a ligand composition of seven pyridines and one DMSO. The $\tau 5$ values at the metal centers are also similar to those in **2.8** (0.34±0.02 vs. 0.33-0.34 ±0.03 in **2.8**). One somewhat expected difference, however, is the encapsulated guest, which is a pyridine instead of an acetonitrile. The reason for an alternate guest is, obviously, that acetonitrile was not present during its synthesis. It is unknown why pyridine is encapsulated instead of methanol, but this synthetic methodology may present a facile way of controlling the identity of the guest species. One beneficial outcome of this synthesis is that unlike all previous nickel-seamed examples, the guest (and the rest of the structure) is reasonably well-ordered. It is unknown whether this was merely incidental, but this finding may suggest that using methanol as a solvent for the synthesis of nickel-seamed dimers presents an advantage over acetonitrile if subsequent crystallization is desired.

2.3.5 Synthesis/*in situ* crystallization of the PgC3Ni dimer in DMSO

Although several protocols led to the formation of crystals with the unit cell presented here, a typical synthesis will be listed. Both the concentrations and the relative ratios of the

reagents can be varied to achieve crystallization. In a 20 mL scintillation vial, 0.72 g of PgC3 (1.0 mmol) was co-dissolved with 1.16 g of $Ni(NO_3)_2$ (4.0 mmol) in 10 mL of DMSO. The solution was heated to near-boiling, then 580 µL of pyridine (8 mmol) was added, changing the color of the solution from light green to yellow. The vial was then removed from heat, capped and allowed to stand at room temperature. Crystallization occurred over the course of several days.

Crystal data for PgC_3Py dimer (2.11): $C_{249.77}H_{180.01}N_{16}Ni_{16}O_{55.05}S_{8.68}$, M = 5503.63, yellow block, monoclinic, space group $P2_1/c$ (No. 14), a = 29.8657(11), b = 30.9228(11), c = 32.2546(13) Å, β = 90.403(2)°, V = 29787.4(19) $Å^3$, Z = 4, D_c = 1.227 g/cm^3, F_{000} = 11271, Bruker SMART CCD area detector, MoKα radiation, λ = 0.77490 Å, T = 173(2)K, $2\theta_{max}$ = 45.8º, 210720 reflections collected, 31445 unique (R_{int} = 0.0613). Final *GooF* = 1.721, *R1* = 0.1218, *wR2* = 0.3690, *R* indices based on 22645 reflections with I >2sigma(I) (refinement on F^2), 3147 parameters, 9 restraints. Lp and absorption corrections applied, μ = 1.112 mm^{-1}.

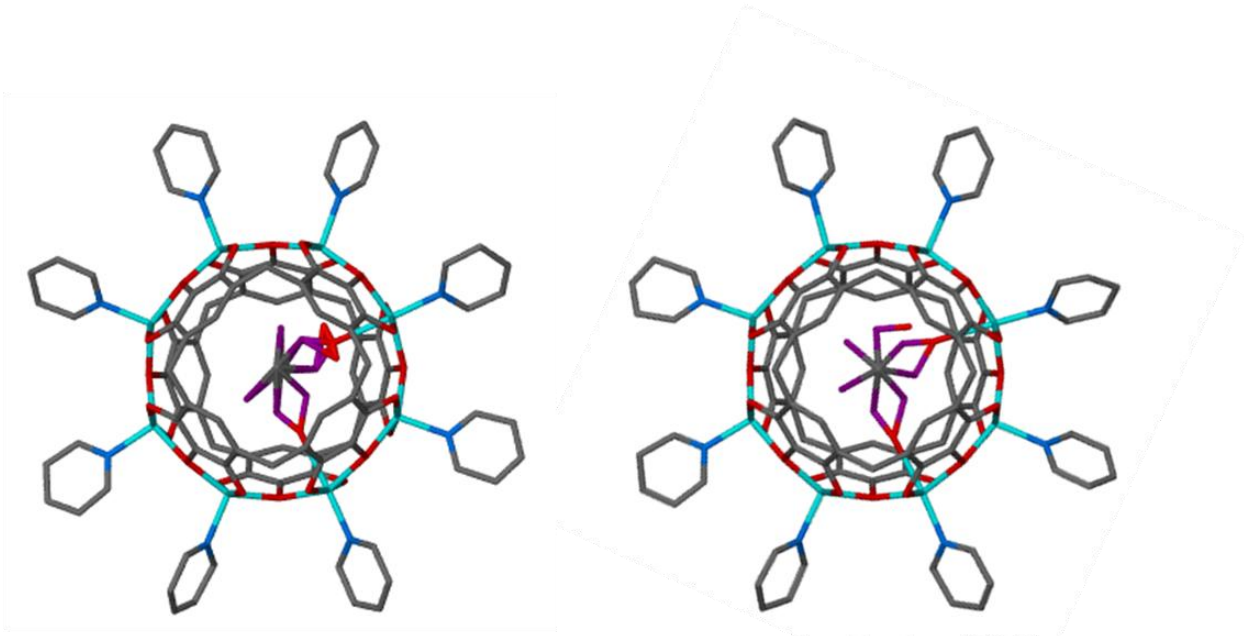

PgC3Ni-pyridine dimer #1 (**2.11**)

Metal #	Ligand	θ_1	θ_2	$\tau 5$
Ni1	pyridine	148.05	168.17	0.335
Ni2	pyridine	150.53	170.66	0.336
Ni3	pyridine	148.97	169.72	0.346
Ni4	pyridine	156.71	175.15	0.307
Ni5	pyridine	154.1	172.28	0.303
Ni6	pyridine	148.01	167.99	0.333
Ni7	pyridine	144.63	168.04	0.390
Ni8	pyridine	143.74	167.11	0.390
Average				**0.34**
StD				**0.03**

PgC3Ni-pyridine dimer #2 (**2.11**)

Metal #	Ligand	θ_1	θ_2	$\tau 5$
Ni1	pyridine	151.26	170.26	0.317
Ni2	pyridine	146.5	168.56	0.368
Ni3	pyridine	146.38	168.49	0.369
Ni4	pyridine	146.09	167.22	0.352
Ni5	pyridine	148.87	168.4	0.326
Ni6	pyridine	150.06	171.01	0.349
Ni7	pyridine	151.49	170.22	0.312
Ni8	pyridine	159.04	175.17	0.269
Average				**0.33**
StD				**0.03**

Figure 2.11: Image displaying the two nickel-seamed dimers that make up structure **2.8**, along with their respective bond angles/$\tau 5$ values

This experiment was yet another attempt to determine if altering the solvent during synthesis could lead to a nickel dimer that differed from those that had been previously made. To this end, the nickel dimer was synthesized (and subsequently recrystallized) using *in situ* crystallization. The resultant crystal structure was, once again, closely analogous to the other penta-coordinate dimers. As expected, the internal guests in both of the dimers that make up the asymmetric unit were the solvent that was used during synthesis; DMSO. The DMSO in one of

the dimers was disordered over several crystallographic positions, but in the other one seemed to be directed towards one of the metal centers, with only minor occupancy in other positions. The DMSO molecule's affinity to this particular metal center does not seem to have a reason, as this metal center does not stand out in any way (τ5 at this center is essentially equivalent to all of the others). Interestingly, both dimers had pyridine *exo* ligands on all eight metal centers, which contrasts with the dimers seen in **2.8**, where recrystallization in DMSO led to the replacement of one of the pyridines with a DMSO. This may have been due to the fact that the scintillation vial was quickly sealed after the addition of pyridine, and therefore much less pyridine escaped from the vial as a vapor.

2.3.6 *In situ* synthesis/crystallization of two examples of PgC3NiPy dimers in methanol

Two crystalline samples were collected from a broad assay that aimed to determine if *in situ* crystallizations of dimers could be performed in methanol.

Compound #1: 0.72 g of PgC3 was dissolved in 100 mL of 9:1 MeOH: H_2O, making a 0.01M solution. $Ni(NO_3)2{\cdot}6H_2O$ was also co-dissolved with pyridine in MeOH to make two solutions, one that was 0.04M w.r.t $Ni(NO_3)_2$ and 0.1M w.r.t pyridine and the other that was 0.12M w.r.t pyridine. 2 mL aliquots of the two solutions were mixed in two separate scintillation vials with 2 mL of each of the nickel/pyridine solutions. The vials were then capped and left to crystallize at room temperature. The solutions were dark at first but turned yellow after the course of several days. Yellow crystals formed after several days.

Crystal data for PgC_3NiPy dimer methanol solvate (2.12) from 1:4:10 PgC3: Ni^{2+}: pyridine: $C_{39.43}H_{37.43}N_{3.14}Ni_{2.29}O_{7.71}$, M = 812.92, yellow plate, 0.35 × 0.35 × 0.05 mm^3, orthorhombic, space group $Pna2_1$ (No. 33), a = 32.791(6), b = 24.367(5), c = 19.468(4) Å, V = 15555(5) $Å^3$, Z = 14, D_c = 1.215 g/cm^3, F_{000} = 5904, Bruker SMART CCD area detector, MoKα radiation, λ = 0.71073 Å, T = 173(2)K, $2\theta_{max}$ = 46.8°, 128039 reflections collected, 22635 unique (R_{int} = 0.1736). Final *GooF* = 1.110, *R1* = 0.1138, *wR2* = 0.2930, *R* indices based on 11289 reflections with I >2sigma(I) (refinement on F^2), 1267 parameters, 62 restraints. Lp and absorption corrections applied, μ = 1.011 mm^{-1}. Absolute structure parameter = 0.51(3) (Flack, H. D. *Acta Cryst*. **1983**, *A39*, 876-881).

Compound #2: 0.72 g of PgC3 was dissolved in 100 mL of 9:1 MeOH:H_2O, making a 0.01M solution. $Ni(NO_3)2{\cdot}6H_2O$ was also co-dissolved with pyridine in MeOH to make a solution that was 0.04M w.r.t $Ni(NO_3)_2$ and 0.12M w.r.t pyridine. 2 mL aliquots of the two solutions were mixed in a two separate scintillation vials with 2 mL of each of the nickel/pyridine solutions. The vials were then capped and left to crystallize at room temperature. The solutions were dark at first but turned yellow after the course of several days. Yellow crystals formed after several days.

Crystal data for PgC_3NiPy dimer methanol solvate (2.13) from 1:4:12 PgC3:Ni^{2+}:pyridine: $C_{32.50}H_{23.75}N_{2.75}Ni_2O_6$, M = 666.21, yellow plate, 0.50 × 0.10 × 0.10 mm^3, monoclinic, space group $C2/c$ (No. 15), a = 27.118(5), b = 30.423(5), c = 17.258(3) Å, β = 91.275(2)°, V = 14234(4) $Å^3$, Z = 16, D_c = 1.244 g/cm^3, F_{000} = 5472, Bruker SMART CCD area detector, MoKα radiation, λ = 0.71073 Å, T = 173(2)K, $2\theta_{max}$ = 55.3°, 82007 reflections collected, 16415 unique

(R_{int} = 0.0885). Final *GooF* = 1.356, *R1* = 0.1245, *wR2* = 0.3662, *R* indices based on 6983 reflections with I >2sigma(I) (refinement on F^2), 721 parameters, 22 restraints. Lp and absorption corrections applied, μ = 1.099 mm^{-1}.

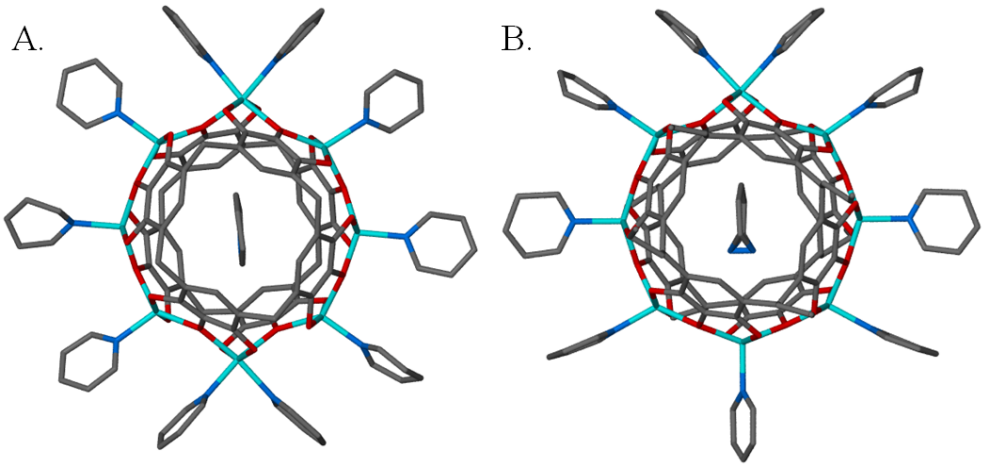

PgC3Ni-pyridine dimer (**2.12**)				
Metal #	**Ligand**	**θ_1**	**θ_2**	**τ5**
Ni1	2x pyridine	156.12	107.85	0.805
Ni2	pyridine	170.05	138.28	0.530
Ni3	pyridine	170.68	144.64	0.434
Ni4	pyridine	171.21	141.02	0.503
Ni5	2x pyridine	156.57	110.57	0.767
Ni6	pyridine	166.64	140.93	0.429
Ni7	pyridine	165.25	144.21	0.351
Ni8	pyridine	169.84	133.54	0.605
Average				0.6
StD				0.2

PgC3Ni-pyridine dimer (**2.13**)				
Metal #	**Ligand**	**θ_1**	**θ_2**	**τ5**
Ni1	2x pyridine	156.95	107.2	0.829
Ni2	pyridine	167.03	134.61	0.540
Ni3	pyridine	167.62	146.35	0.355
Ni4	pyridine	165.98	141.83	0.403
Ni5	pyridine	165.02	141.21	0.397
Average				0.5
StD				0.2

Figure 2.12: Structures of 2.12 (A) and 2.13 (B) along with the τ5 values of the metal centers. Due to the hexa-coordinate sites in both structures, there is significant variance in the τ5 values .

Syntheses in methanol at low enough concentrations (sub 10^{-2}M w.r.t PgC3) did not lead to the formation of a precipitate as in **2.10**, but instead led to the formation of a black solution that eventually lightened to yellow and produced crystals on further standing. Two well-diffracting crystal types were found after an extensive crystallization assay, which were clearly different judging from their differing unit cell parameters. Structural determination showed that

both of the crystals consisted of nickel-seamed dimers (**2.12, 2.13**). As with the methanolic precipitate in **2.10**, the internal guest in both of these is a single well-resolved pyridine molecule. All of the *exo* ligands are also pyridine molecules, and both of the dimers have hexa-coordinate sites. Interestingly, the material that crystallized at a higher pyridine titer only had a single hexa-coordinate site, while the one that crystallized at a lower titer had two sites. This is counterintuitive, as it is expected that a higher titer of pyridine would result in more, not less, pyridine ligands. It is unknown why this occurred, but it is likely connected to the earlier-stated hypothesis that a mixture of dimers exists in solution, and that the crystallization of any particular variant can be due to a number of factors. One factor could be the conversion of the hexameric to the dimeric MONC over time, and a subsequent change in the ligands of a dimer as a result. The coexistence of the nickel-seamed dimer and hexamer in solution is a concept that will be covered in some detail in later parts of this chapter. The main purpose of this experiment, however, was to determine if synthesis in methanol could lead to the formation of some other type of dimer from that seen in earlier sections. To that end, this experiment was a success in showing that it can.

2.3.7 A nickel-seamed hexameric MONC

0.14 g of PgC3 (0.2 mmol) was co-dissolved with 0.23 g of $Ni(NO_3)_2$ (0.8 mmol) in 20 mL of 9:1 MeOH:H_2O. This solution was chilled briefly in the refrigerator to slightly below room temperature. 280 µL of 1M 4-methylpyridine (4-picoline) in MeOH was then added to this solution, immediately changing the color of the PgC/Ni^{2+} solution from green to black. Unlike synthesis in MeCN, however, no immediate precipitation of a yellow solid was observed. The

scintillation vial was sealed and left to crystallize at room temperature. Crystallization proceeded rather quickly, as crystals were readily apparent after approximately 1hr.

Crystal data for PgC_3Ni-4MePy hexamer (2.14): $C_{313.72}H_{298.76}N_{12.14}Ni_{24}O_{112.74}$, M = 7451.73, black rod, 0.60 × 0.25 × 0.25 mm^3, monoclinic, space group $P2_1/n$ (No. 0), V = 21700(6) $Å^3$, Z = 2, D_c = 1.140 g/cm^3, F_{000} = 7680, Bruker APEXII CCD area detector, MoKα radiation, λ = 0.71073 Å, T = 173(2)K, $2\theta_{max}$ = 46.5º, 181887 reflections collected, 31150 unique (R_{int} = 0.0724). Final *GooF* = 1.569, *R1* = 0.1256, *wR2* = 0.3686, *R* indices based on 16741 reflections with I >2sigma(I) (refinement on F^2), 1817 parameters, 219 restraints. Lp and absorption corrections applied, μ = 1.082 mm^{-1}.

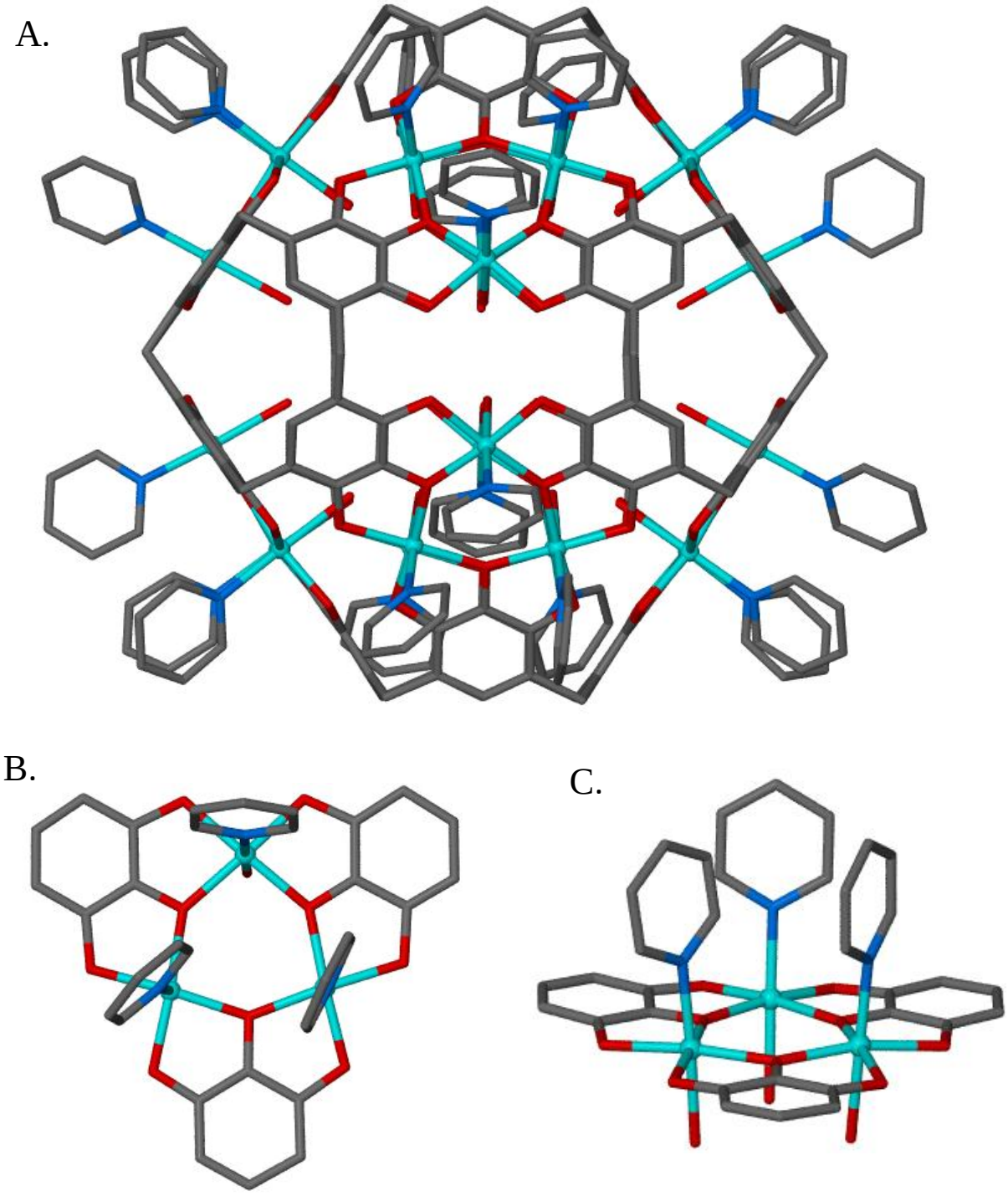

Figure 2.13: Full structure of the PgC3Ni hexamer **2.14** (A) as well as two images of the tri-metal cluster (B, C) that are responsible for the construction of the assembly.

Although proof for the existence of a nickel-seamed hexamer had been obtained using MADLI-TOF mass spectrometry, this MONC had never been crystallized. Several attempts were made to crystallize the hexameric MONC produced by the same techniques as the material used for MALDI-TOF analysis, but this did not lead to positive results. Instead, the crystallization of the nickel-seamed hexamer was somewhat accidental. The synthetic setup described above was actually a part of a larger assay that aimed to compare the behavior of the 4-methylpyridine ligand to that of pyridine following synthesis and *in situ* crystallization in methanol. In short, the crystallization assay was meant to be an analog of the study in 2.3.6. As in 2.3.6, the solution turned dark when all of the reagents were mixed. However, unlike that experiment, dark green crystals formed quickly following mixing. Although dark green crystals formed at almost all of the 4-methylpyridine titers used, the best crystals (i.e., biggest and well-diffracting) formed at the lowest 4-methylpyridine titers. These samples also took longer to form than the others. Structural determination of this crystalline material *via* scXRD showed that the material was not dimeric as assumed, but rather that nickel-seamed hexamers had been synthesized and crystallized (Fig 2.13).

The overall size, shape, and constitution of the nickel-seamed hexamer is largely similar to that of the copper-seamed hexamer (Fig. 2.13). Like the copper analog, six PgC ligands coordinate to 24 Ni^{2+} centers, which are positioned around the spherical hexamer as tri-metal clusters. The internal volumes and surface areas of the nickel- and copper-seamed hexamers are also very similar, although the nickel analog is slightly larger, likely due to longer M-O bonds (Table 2.2). This is also the case for the diameters of the two hexamers, with nickel being slightly longer, although some of this difference is minimized due to a smaller pinch angle of the PgC macrocycle in the copper-seamed analog. The only major difference between the two

hexameric analogs is the additional (non-PgC) ligands that bind to the M^{2+} centers. While there are a few ligands coordinated to the metal centers of the copper-seamed hexamer, all of which are weakly bound (long bond length), several of the copper centers are also of a square planar (tetra-coordinate) geometry. In contrast to this, each of the Ni^{2+} centers in the nickel-seamed analog is always found to coordinate to both an *exo* 4-methylpyridine and an *endo* water molecule. All of the ligands that coordinate to the Ni^{2+} centers (judging from the shorter bond lengths) are strongly bound, and the ligand donor sites are crystallographically better-ordered than the waters in the copper-seamed analog. This may suggest that the ligand occupancy in the nickel-seamed hexamer is greater than that in the copper-seamed hexamer (i.e., the ligands are there all of the time vs. some of the time).

Metal	Core Diameter	Surface area	Volume
Ni (2.14)	18.2	683	1375
Cu (pub'd)	17.9	654	1249

Metal	M-O bond length	M-water/ligand	M-pyridine
Ni (2.14)	2.02 ± 0.02	2.27 ± 0.04	2.09 ± 0.03
Cu (pub'd)	1.95 ± 0.03	2.9 ± 0.2	n/a
Cu (2.5)	1.95 ± 0.01	2.4 ± 0.1	n/a
Cu (2.6)	1.94 ± 0.01	2.46 ± 0.06	n/a

Table 2.2: Comparison of the nickel- and copper- seamed hexameric capsules in terms of their spatial parameters and bond lengths. As before, data for the published PgC3Cu hexamer was used as a basis for comparison.[119]

The finding that the color of the hexameric crystals (dark green) corresponds to the color of the solution that bore them (also dark green) is of special significance. This is also seen with the nickel-seamed dimeric crystals, which are yellow and only begin to form when the solution also starts to turn from dark to yellow. It is therefore easy to draw a connection between the

color of the solution and its composition. As such, the change in color over time as seen when pyridine is used was thought to be indicative of a corresponding change in composition from mainly hexamers to mainly dimers. This was the basis for later work in the next chapter that seeks to enumerate the proportions of the two species in solution using small angle neutron scattering (SANS).

2.3.8 PgC3Ni hexamer from acetonitrile

0.844 g of PgC5 was dissolved in 20 mL of MeCN. In a separate container, 9.0 g of $Ni(NO_3)_2Py_4$ in 13mL MeCN were added to 5mL of H_2O. 6 mL of the nickel complex solution was then added to the PgC solution. This resulted in the instantaneous formation of a yellow solid suspended in a black solution. The solid was removed by filtration, and the black filtrate was placed in a separate container to crystallize. Black crystals formed after approximately one day.

Crystal data for PgC_3Ni hexamer (2.15): $C_{40.50}H_{35.40}N_{2.90}Ni_{2.40}O_{10.40}$, M = 870.02, triclinic, space group P-1 (No. 2), a = 23.731(7), b = 25.076(7), c = 41.508(12) Å, α = 83.358(4), β = 78.399(4), γ = 68.045(4)°, V = 22419(11) Å^3, Z = 20, D_c = 1.289 g/cm^3, F_{000} = 8982, Bruker SMART CCD area detector, MoKα radiation, λ = 0.71073 Å, T = 173(2)K, $2\theta_{max}$ = 55.1°, 258677 reflections collected, 100528 unique (R_{int} = 0.1050). Final *GooF* = 1.153, *R1* = 0.1194, *wR2* = 0.3319, *R* indices based on 37515 reflections with I >2sigma(I) (refinement on F^2), 2972 parameters, 0 restraints. Lp and absorption corrections applied, μ = 1.057 mm^{-1}.

An important observation made in 2.3.7 was that a dark solution may correspond to the presence of hexameric MONCs. This led us to suspect that the dark green filtrate that is produced (and typically discarded) when powdered nickel-seamed dimers are made in acetonitrile may likewise contain hexameric MONCs. To investigate this notion, nickel-seamed MONCs were synthesized in acetonitrile using several different PgCs. The results in all of these were the same, namely that a yellow precipitate suspended in a black solution was formed. The yellow solid was removed from each of these by vacuum filtration, and the filtrate was saved (decanted into a scintillation vial and capped). The filtrate from the synthesis where PgC5 was used led to the formation of black crystals, which were found to consist of hexameric MONCs using scXRD.

With the exception of the ligands (pyridine vs. 4-methylpyridine) the hexamers are essentially analogous with **2.14**. However, the purpose of this experiment was not to find a "new" hexamer, but rather to see if the observations from one set of conditions (i.e., methanolic synthesis) could be extended to another (acetonitrile synthesis). This result shows that this is indeed the case. It also suggests that even though the observation of a color change is usually viewed as anecdotal evidence, such observations may help with the identification of PgC-based MONCs in solution and may aid with their crystallization.

2.3.9 A different PgC-based metal complex: the pseudodimer

Unexpectedly, *in situ* crystallization attempts on Ni^{2+}-based systems in methanol and acetone also produced crystals of a third species, which will be referred to as the "pseudodimer." Black crystals of this species formed at room temperature in cases where higher-than-typical

reagent concentrations were employed (i.e. greater than 10^{-2} M w.r.t PgC, following a 1:4:14 ratio of PgC:Ni$(NO_3)_2$: pyridine). Unlike hexamers and dimers, which typically crystallize within several hours to days when *in situ* crystallization is employed, crystals of a new material were found to form within minutes to an hour of mixing for both PgC3 and PgC4 macrocycles. Incidentally, this was the only species that could be obtained in *in situ* crystallizations of PgC4. Thus, for this reason along with others this macrocycle was rarely used in Ni^{2+} complexation studies.

Crystal data for PgC_3Ni pseudodimer (2.16): $C_{40}H_{48}N_{2.80}NiO_{8.50}$, M = 762.72, black prism, 0.15 × 0.10 × 0.05 mm^3, triclinic, space group P-1 (No. 2), a = 13.251(3), b = 16.057(3), c = 19.501(4) Å, α = 74.410(2), β = 73.841(2), γ = 76.758(3)°, V = 3785.1(12) $Å^3$, Z = 4, D_c = 1.338 g/cm^3, F_{000} = 1614, Bruker SMART CCD area detector, MoKα radiation, λ = 0.71073 Å, T = 173(2)K, $2\theta_{max}$ = 46.6º, 10909 reflections collected, 10909 unique (R_{int} = 0.0000). Final *GooF* = 0.943, *R1* = 0.0808, *wR2* = 0.2087, *R* indices based on 6206 reflections with I >2sigma(I) (refinement on F^2), 954 parameters, 6 restraints. Lp and absorption corrections applied, μ = 0.570 mm^{-1}.

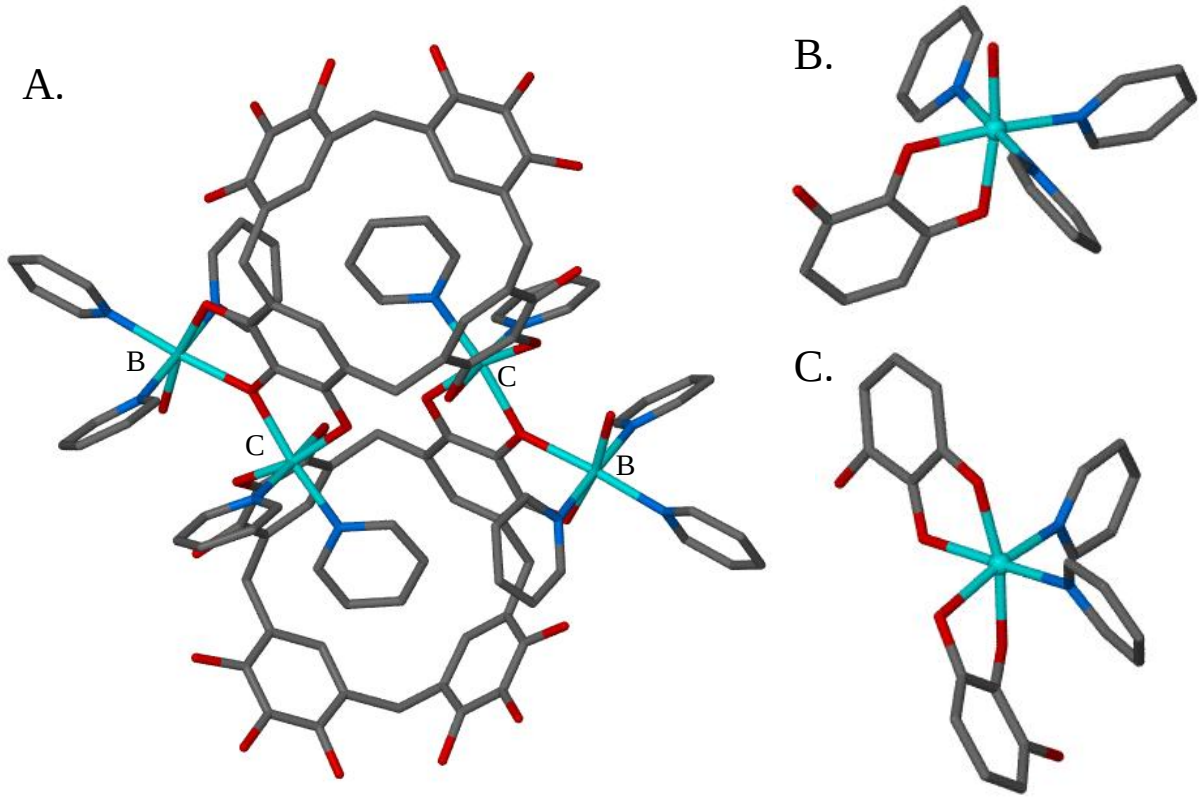

Figure 2.14: Structure of the "pseudodimer" (A) and depictions of the two alternate metal environments within the structure (B and C). Locations of these sites are marked in A by their respective letters

The molecular structure of this material was obtained from scXRD studies on two crystalline samples, although this material was, in fact, isolated multiple times in similar experiments. Structural analysis revealed that this third species was a dimer, where two pyrogallol[4]arene macrocycles jointly coordinate to four Ni^{2+} centers along a shortened coordination "belt" (Fig 2.14). Unlike other PgC dimers, however, the PgC hemispheres do not form a concerted sphere, but rather an ellipsoidal/disc-like, fully open, and divergent framework. As such, the structure of this material is significantly different from other metal-seamed pyrogallol[4]arene frameworks based on transition metal cations, and differs even when

compared to the open frameworks formed by alkali metal salts. The coordination environments for the nickel centers, which are all formally hexa-coordinate, are also quite different than in other examples of PgC/Ni^{2+} coordination. In hexameric, and even "typical" dimeric nanocapsules, there is usually only one distinct coordination environment, or, at most several that are very closely related. In addition, the PgC ligands typically coordinate to the M^{2+} cations along the same plane. Neither of these, however, is true with the pseudodimer. In this compound, there are two very distinct coordination environments for the nickel centers. Two of these, which are located on the outside of the "tetra-metallic" belt, coordinate to only two hydroxyls from a single PgC macrocycle, while the rest of the sites are filled by two pyridines and one water molecule (Formula: $Ni(PgC)_2Py_3(H_2O)_1$; Fig 2.14b). The other two metal centers, located on the inside of the belt and adjacent to one another, each coordinate to four hydroxyls, two from each of the PgC macrocycles. The bidentate coordination from the PgCs is not planar, but instead features two hydroxyl pairs orthogonal to one another (Fig 2.14c). The remaining two coordination sites in this center are occupied by two pyridine molecules, giving the metal center a moiety formula of $Ni(PgC)_4Py_2$. One of these coordinated pyridine molecules is, interestingly enough, located within the "bowl" of the two PgC macrocycles.

While it is difficult to draw any conclusions from the structure alone, the pyridine-in-the-bowl structural feature was particularly exciting, as it seemed to suggest a possible route towards the inclusion of pyridine or other guest species into the interior of "typical" dimers. If (hypothetically) the pseudodimer or a similar compound acted as a molecular precursor to typical dimers, it could be envisioned that the reaction of two pseudodimers would both produce a complete octametal belt and lead to the incarceration of a pyridine within the capsule. Any unneeded species, such as additional PgCs and pyridines would be handily expulsed from the

system. However, it is fully uncertain what role, if any, the pseudodimer plays in the formation of dimers and/or hexamers. This is because, aside from the obvious lack of evidence supporting any real conclusions, incidental evidence can actually point in two separate and distinct directions. For example, the fast rate of crystallization at higher, but not lower, reagent concentrations can suggest one of two things. Either A) this species is a transient precursor for the dimer and/or hexamer, which typically disappears quickly after synthesis but is kinetically trapped at high enough concentrations, or B) that it is simply another molecular species that incidentally requires higher concentrations of reagents to form. Furthermore, any conclusions drawn from its molecular structure can point in both of these directions, as there are both similarities and differences from the structures of the dimeric and hexameric nanocapsules. The distinct Ni^{2+} centers, in particular, seem to point away from this species as a precursor complex. Complicating the issue is that no evidence of ellipsoidal or disc-like species was ever detected using solution-state methods (SANS, next chapter). Thus, the role that this compound plays in the overall scheme of things is not yet known.

2.3.10 Nickel-seamed MONCs: summary

This subsection presented several novel findings regarding nickel-seamed MONCS. The majority of it was dedicated to dimeric MONCs, which were synthesized in several different ways. This led to the finding that the encapsulated guest molecule could be changed depending on the synthetic conditions. Furthermore, several examples of nickel-seamed dimers that had both hexa-coordinate and penta-coordinate metal sites were described. The dimers that show this type of mixed coordination typically appear “warped” due to varying coordinative bond angles amongst the metal centers, and can feature interesting guest geometries. Nickel dimers that have

solely penta-coordinate sites, however, largely resemble those made from copper and zinc. The average $\tau 5$ values at the Ni^{2+} sites in the "homogenous" dimers (0.32-0.34) is much more similar to what is seen with copper (0.33-0.35) rather than to what is seen with zinc (0.42). The oxo-metal bond lengths between the Ni^{2+} and PgC hydroxyls, however, closely approximate those in zinc rather than in copper.

This section also introduced the nickel-seamed hexamer. As with the dimers, the nickel hexamer is structurally similar to the copper hexamer, although it is slightly larger on account of the longer Ni-O bonds. In contrast to the copper hexamer, which can feature tetra-coordinate sites, each of the metal centers is hexa-coordinate and bears an identical arrangement of ligands; a pyridine on the outside and a water molecule on the inside. As with copper, nickel hexamers were found in the same solution with the nickel dimers under certain circumstances. However, certain conditions seemed to favor the eventual formation of dimers, notably that a dark solution (hexamer) would fade over time to yellow (dimer). This may suggest that in addition to temperature, which was found to be a dictating factor with copper, time may also play a part in determining whether crystals of the dimer or hexamer will form from a given synthesis.

2.4 Cobalt-seamed dimers

The possibility that cobalt- and nickel- seamed dimers could be synthesized was investigated simultaneously, and because of this the first cobalt-seamed dimer was discovered at roughly the same time as the first nickel-seamed dimer.[135] Both were synthesized and crystallized using the same technique and their general properties were therefore expected to be similar. However, cobalt-seamed dimers differ from any of the other dimers discovered to-date, specifically from a geometric point of view. Furthermore, a cobalt-seamed hexamer has not been

synthesized despite numerous attempts to do so, suggesting that PgC-Co^{2+} chemistry differs from that of copper and nickel. This section aims to describe the structures of cobalt-seamed dimers that have been discovered so far. Two of these were crystallized in the standard method, namely that a solid sample of the dimer was first synthesized, then dissolved in hot solvent and allowed to cool. Another two examples were synthesized by using the *in situ* crystallization approach introduced earlier.

2.4.1 Discovery of the cobalt dimer- PgC2Co-pyridine

0.5 g of PgC2 (0.75 mmol) was dissolved in 10 mL of MeCN. In a separate container, 1.5 g of $Co(NO_3)_2(pyridine)_4$ complex (3 mmol) was also dissolved in 10 mL of MeCN. The solutions were mildly heated while stirring to dissolve the solids. Once fully dissolved, the two solutions were mixed, which led to the immediate formation of orange-brown precipitate. This precipitate was removed by vacuum filtration, washed with MeCN, then dried in a dessicator (net yield: 0.79 g). A small amount was then dissolved in minimal hot pyridine and allowed to stand uncapped to crystallize. Note: The $Co(NO_3)_2(pyridine)_4$ complex was synthesized by dissolving $Co(NO_3)_2 \cdot 6H_2O$ in hot pyridine and heating the resultant solution under vacuum in a rotary evaporator to drive off the excess pyridine. It is likely, however, that the pre-synthesis of this complex is unnecessary, as it can be generated *in situ* by mixing the appropriate ratio of $Co(NO_3)_2$ to pyridine in MeCN and then directly mixing this solution with the PgC solution.

Crystal data for PgC_2CoPy dimer (2.17): $C_{162}H_{154}Co_8N_{18}O_{24}$, M = 3208.47, Yellow Block, 0.13 × 0.12 × 0.05 mm^3, orthorhombic, space group *Fddd* (No. 70), a = 18.6001(8), b = 28.4944(11), c = 54.266(2) Å, V = 28761(2) $Å^3$, Z = 8, D_c = 1.482 g/cm^3, F_{000} = 13280, Bruker APEX II CCD diffractometer, synchrotron radiation, λ = 0.77490 Å, T = 100(2)K, $2\theta_{max}$ = 42.9º, 26582 reflections collected, 3163 unique (R_{int} = 0.0644). Final *GooF* = 1.051, *R1* = 0.0531, *wR2* = 0.1341, *R* indices based on 2163 reflections with I >2sigma(I) (refinement on F^2), 482 parameters, 64 restraints. Lp and absorption corrections applied, μ = 1.229 mm^{-1}.

A.

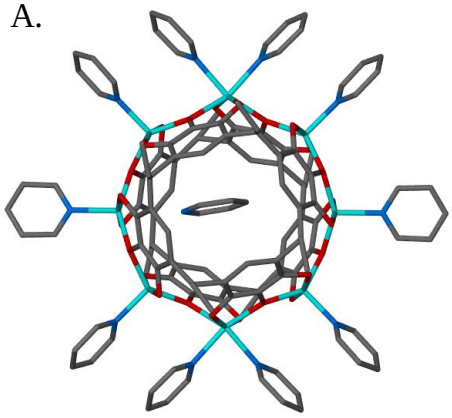

B.

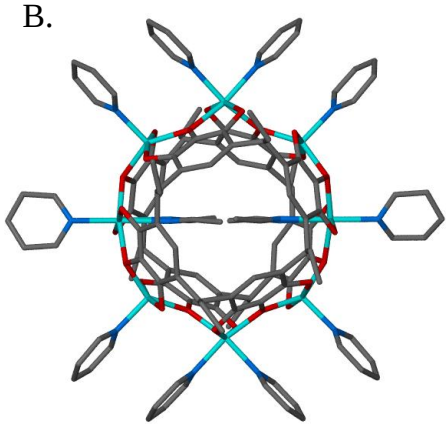

PgC2Co-pyridine dimer (2.17)				
Metal #	**Ligand**	**θ_1**	**θ_2**	**τ5**
Co1	2x pyridine	156.69	120.33	0.606
Co2	pyridine	169.37	138.66	0.512
Co3	pyridine	173.2	149.24	0.399
Average				**0.5**
StD				**0.1**

PgC2Ni-pyridine dimer (2.7)				
Metal #	**Ligand**	**θ_1**	**θ_2**	**τ5**
Ni1	2x pyridine	159.27	110.45	0.814
Ni2	pyridine	170.34	144.59	0.429
Ni3	pyridine	178.55	167.55	0.183
Average				**0.5**
StD				**0.3**

Figure 2.15: Side-by-side comparison of the PgC2Co-pyridine dimer (**2.17**, A) and the PgC2Ni-pyridine dimer (**2.7**, B), along with their respective τ5 tables. The presence of hexa-coordinate sites in **2.17** has a lesser effect on the distribution of τ5 values than in 2.7, although this may be explained by a different guest species.

This was the first example of a cobalt dimer, and is the only example that is currently published.[135] As the methods used to crystallize and synthesize this dimer were identical to those used to synthesize the first nickel-seamed dimer, it is of no surprise that the two structures are of remarkable similarity. Both structures crystallized in the same space group (Fddd) and the asymmetric units of the two are nearly identical. The ligands on the capsular periphery are also the same in both structures: two cobalt centers are hexa-coordinate, bearing two pyridine molecules each, and the rest are all penta-coordinate and bear a single pyridine ligand. The internal guest does differ, as it is a disordered pyridine molecule instead of a pair of acetonitriles. Based on its position, which is proximal to two of the metal centers, this pyridine guest interacts with these metal centers *via* a long coordinative bond (2.86 Å N-Co distance). It is interesting to note that while this pyridine ligand is, in fact, disordered, it is significantly less disordered than the encapsulated pyridines that are often seen in solely penta-coordinate centered dimers, as *endo* pyridines often resemble a "ball of electron density" rather than a well-defined ring system. This may partly be due to the two hexa-coordinate sites, which cannot accommodate any additional ligands from the interior. This, in turn, forces the guest pyridine away from these sites and towards the two penta-coordinate sites that lie on an orthogonal plane. Therefore, disorder is reduced by limiting both spatial and coordinative possibilities from eight to just two. This was also seen in the nickel dimer **2.7** and will also be seen in Ch. 4.

As in the nickel-seamed analog **2.7**, the presence of hexa-coordinate metal sites in this structure leads to an inconsistent coordination geometry in the metal centers. This is perhaps due to some degree of auto-compensation, as the $\tau 5$ values at the metal centers average to a value that is similar to that in the other cobalt-seamed dimers in this section, even though the values themselves are far apart from one another (Fig. 2.15). The inconsistency in the $\tau 5$ values,

however, is less than that in **2.7**, perhaps due to the different chemistry of cobalt and nickel or due to a different encapsulated guest.

2.4.2 A PgC3Co-pyridine/DMSO dimeric analog to PgC3Ni-pyridine/DMSO dimers

0.36 g of PgC3 (0.5 mmol) and 0.725 g of $Co(NO_3)_2 \cdot 6H_2O$ (2.5 mmol) were co-dissolved in 20 mL of 9:1 MeCN:H_2O by stirring/heating on a mantle set to 150°C. Once fully dissolved, 635 µL of pyridine (8 mmol) was added to this mixture, which led to the immediate formation of orange-brown precipitate. This precipitate was removed by vacuum filtration, washed with MeCN, then dried in a dessicator (net yield was unfortunately not recorded). 0.08g of this material was then used for recrystallization in hot DMSO, which was carried out as follows: The material was transferred into a clean scintillation vial along with a stirbar. It was then placed on a heating mantle set at 200°C and hot DMSO was added dropwise using a Pasteur pipette until the solid had fully dissolved. Approximately 500 µL of DMSO was added after this point, so that crystallization would not occur too quickly. The vial was then removed from heat, capped and allowed to stand at RT. Crystallization occurred after several days.

Crystal data for $PgC_3CoDMSO$ dimer (2.18): $C_{55.88}H_{54.50}Co_4N_{1.25}O_{16.75}S_{4.75}$, M = 1399.51, red prism, 0.25 × 0.5 × 0.9 mm^3, triclinic, space group P-1 (No. 2), a = 15.8059(15), b = 29.936(3), c = 32.057(3) Å, α = 72.3350(10), β = 75.7980(10), γ = 80.2580(10)°, V = 13937(2) $Å^3$, Z = 8, D_c = 1.334 g/cm^3, F_{000} = 5732, Bruker SMART CCD area detector, MoKα radiation, λ = 0.71073 Å, T = 173(2)K, $2\theta_{max}$ = 55.0°, 163651 reflections collected, 63060 unique (R_{int} = 0.0562). Final *GooF* = 1.544, *R1* = 0.1661, *wR2* = 0.4230, *R* indices based on 26187 reflections with I

>2sigma(I) (refinement on F^2), 2932 parameters, 60 restraints. Lp and absorption corrections applied, μ = 1.137 mm^{-1}.

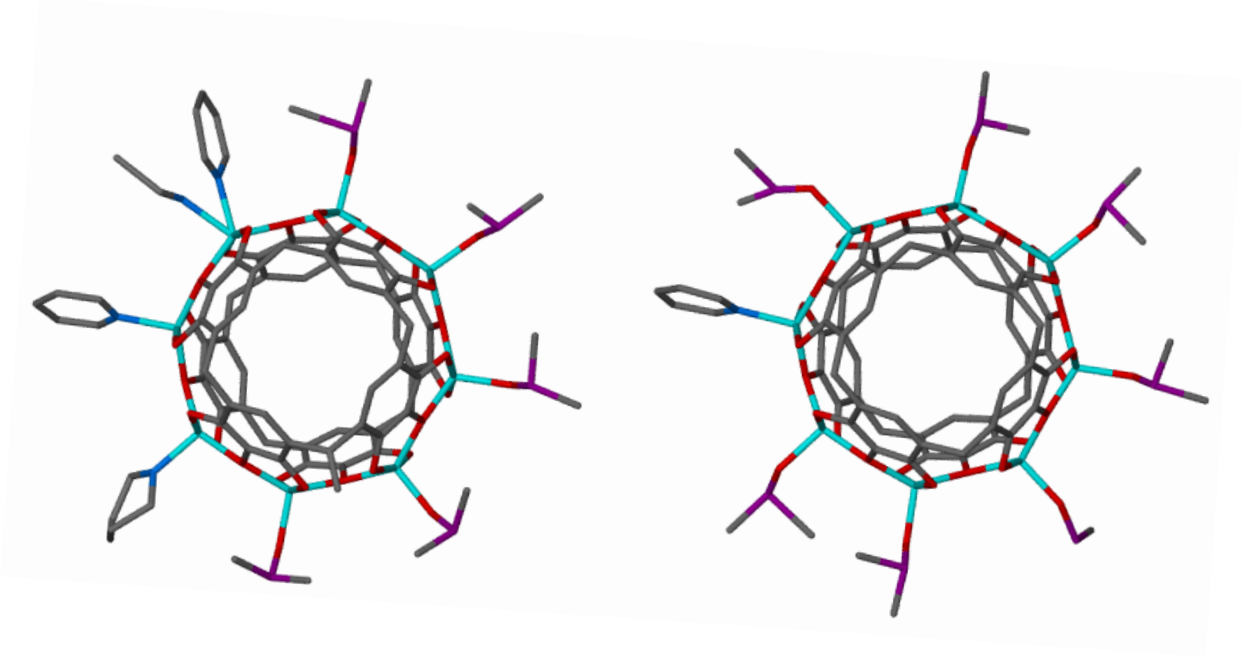

PgC3Co-DMSO/Py dimer #1 **(2.18)**

Metal #	Ligand	θ_1	θ_2	τ5
Co1	DMSO	169.46	139.83	0.494
Co2	DMSO	168.56	139.93	0.477
Co3	DMSO	166.47	136.12	0.506
Co4	DMSO	167.53	137.59	0.499
Co5	DMSO	168.14	142.1	0.434
Co6	pyridine	168.52	144.26	0.404
Co7	pyridine	172.13	147.15	0.416
Co8	pyridine	167.75	141.44	0.439
Average				**0.46**
StD				**0.04**

PgC3Co-DMSO/Py dimer #2 **(2.18)**

Metal #	Ligand	θ_1	θ_2	τ5
Co1	DMSO	169.48	141.19	0.472
Co2	DMSO	167.35	135.77	0.526
Co3	DMSO	167.72	137.12	0.510
Co4	DMSO	168.51	140.45	0.468
Co5	DMSO	169.41	140.54	0.481
Co6	DMSO	170.09	142.56	0.459
Co7	pyridine	169.07	143.04	0.434
Co8	DMSO	170.67	145.33	0.422
Average				**0.47**
StD				**0.04**

Figure 2.16: Image of the two dimers that make up **2.18** and their τ5 tables. Both dimers exhibit a much greater degree of DMSO displacement than the respective nickel dimers, such as 2.8.

The synthesis of this material was essentially analogous to that in the first example of a cobalt-seamed dimer, except that recrystallization was conducted in DMSO rather than in pyridine. The result of this seemingly minor change is that the dimers in this structure only contain penta-coordinate metal sites. This is analogous to the results seen in nickel, where recrystallization in DMSO rather than pyridine led to the same outcome. The asymmetric unit features two dimeric MONCs, each containing a mixture of pyridine and DMSO ligands (Fig. 2.16). One of the MONCs contains five DMSO molecules and three pyridines while the other contains seven DMSO molecules and a single pyridine. Because the original ligand arrangement (prior to recrystallization in DMSO) likely had all pyridine ligands, the majority of the original ligands have been displaced with DMSO. This was not seen with nickel, where DMSO only replaces (at most) one pyridine ligand per dimer. This may suggest that Co^{2+} has different affinities for ligands when compared to Ni^{2+}, which is corroborated by the differences in the M-pyridine and M-DMSO coordinative bond lengths in nickel and cobalt; whereas the bond lengths to pyridine and DMSO are approximately equivalent in Ni^{2+}, the pyridine length is longer than that for DMSO with Co^{2+}, suggesting a weaker bond. The $\tau 5$ values at the metal sites are surprisingly varied, ranging from 0.40 to 0.52, and seem to range higher in cases where DMSO is the ligand and lower when pyridine is the ligand. However, regardless of discrepancy between ligands in the two structures, the average $\tau 5$ values in both of the dimers are approximately equal (0.46 ± 0.04 and 0.47 ± 0.04) These are very high $\tau 5$ values when compared to those in the other dimers, and the tendency of the Co^{2+} centers towards a trigonal bipyramidal geometry can also be seen visually, as the cobalt-seamed dimers also appear more “polygonal” than any other dimer, including those made of zinc. The internal guest in both dimers is (ostensibly) a highly disordered pyridine molecule, although this cannot be verified.

2.4.3 *In situ* synthesis/crystallization of PgC3Co-pyridine in DMSO

0.608 g of PgC3 (1 mmol) and 1.16 g of $Co(NO_3)_2 \cdot 6H_2O$ (4 mmols) were co-dissolved in 10 mL DMSO by stirring and heating on a mantle set at 200°C. 1.2 mL (14 mmol) of 4-picoline was then added, changing the color of the solution from light pink to orange, along with the precipitation of a small amount of orange solid. The solution was heated and stirred until dissolution was complete. The solution was then taken off of the mantle, capped and left to sit at room temperature. Crystallization occurred over the course of several days.

Crystal data for PgC_3CoPy dimer (2.19): $C_{42.22}H_{41.67}Co_{2.67}N_{4.44}O_{10}$, M = 928.50, black prism, .3 × .35 × .35 mm^3, monoclinic, space group $P2_1/n$ (No. 14), a = 28.385(8), b = 16.800(5), c = 28.550(8) Å, β = 112.662(3)°, V = 12564(6) $Å^3$, Z = 12, D_c = 1.473 g/cm^3, F_{000} = 5737, Bruker SMART CCD area detector, MoKα radiation, λ = 0.71073 Å, T = 173(2)K, $2\theta_{max}$ = 55.0°, 144659 reflections collected, 28608 unique (R_{int} = 0.0829). Final *GooF* = 1.107, *R1* = 0.0773, *wR2* = 0.2024, *R* indices based on 15476 reflections with I >2sigma(I) (refinement on F^2), 1420 parameters, 24 restraints. Lp and absorption corrections applied, μ = 1.110 mm^{-1}.

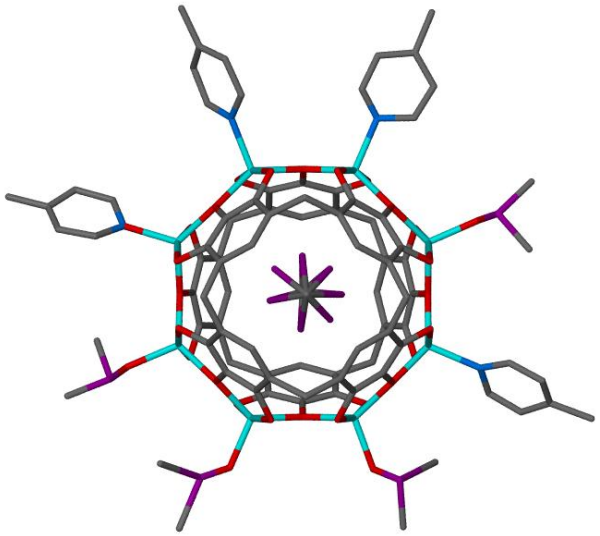

PgC3Co-DMSO/Pico dimer #1 **(2.19)**

Metal #	Ligand	θ_1	θ_2	τ5
Co1	4-picoline	166.13	134.36	0.530
Co2	4-picoline	168.18	135.9	0.538
Co3	4-picoline	166.64	136	0.511
Co4	DMSO	167.46	138.92	0.476
Co5	4-picoline	168.1	138	0.502
Co6	DMSO	167.43	137.72	0.495
Co7	DMSO	168.34	140.65	0.462
Co8	DMSO	168.18	140.21	0.466
Average				0.50
StD				0.03
DMSO Avg.				0.47
4-Picoline Avg.				0.52

Figure 2.17: A PgC3Co dimer (**2.19**) generated from synthesis/in situ crystallization in DMSO. As in other such syntheses, the guest species is a disordered DMSO molecule.

The synthetic procedure detailed above led to the growth of cobalt-seamed dimers (**2.19**). As in **2.18**, treatment with DMSO led to solely penta-coordinate metal sites in **2.19**. The peripheral ligands on these sites include four DMSO molecules, three 4-methylpyridine molecules and a metal center that (partially) contains both of these ligands. The interior of the MONC contains a guest DMSO molecule that is rotationally disordered over multiple positions, an occurrence that has been seen in almost all previous DMSO syntheses.

Because all of the metal centers in this structure are penta-coordinate, the τ5 values at the metal sites do not differ as much from one another as compared to dimers containing hexa-coordinate sites. Nevertheless, the metal centers containing DMSO ligands have lower τ5 values on average than the centers that bear 4-methylpyridine ligands (0.47 vs. 0.52, respectively). As in 2.17, the bond lengths from Co^{2+} to the DMSO ligands are also shorter than those to 4-methylpyridine (1.99 Å vs. 2.04 Å). These significant differences in both the geometry and

length between two different ligands seem to be a property that is unique only to Co^{2+}, as such large differences are not seen with any of the other dimers.

2.4.4 Synthesis and *in situ* crystallization of PgC3CoPy in acetonitrile

This sample came from an assay that aimed to determine the best conditions for growing cobalt dimer crystals, as a function of pyridine equivalents. Crystals grew in almost all of the vials, but the best and biggest crystals grew over an extended course of time in the vials bearing the lowest pyridine titers. This sample had a 1:4:1 ratio of PgC3:Co^{2+}:pyridine, and was therefore the lowest pyridine titer tested. The synthesis is as follows: 2 mL of 10^{-2}M PgC3 solution in MeCN was mixed with 80 µL of 1M $Co(NO_3)_2$, followed by 200 µL of 0.1M pyridine. The solution changed color from light red to black within several seconds. The scintillation vial was then capped and left to crystallize. Crystals grew over an unknown period of time, but were harvested after approximately 6 months following synthesis.

Crystal data for PgC_3CoPy dimer (2.20): $C_{42.22}H_{41.67}Co_{2.67}N_{4.44}O_{10}$, M = 928.50, black prism, .3 × .35 × .35 mm^3, monoclinic, space group $P2_1/n$ (No. 14), a = 28.385(8), b = 16.800(5), c = 28.550(8) Å, β = 112.662(3)°, V = 12564(6) Å^3, Z = 12, D_c = 1.473 g/cm^3, F_{000} = 5737, Bruker SMART CCD area detector, MoKα radiation, λ = 0.71073 Å, T = 173(2)K, $2\theta_{max}$ = 55.0º, 144659 reflections collected, 28608 unique (R_{int} = 0.0829). Final *GooF* = 1.107, *R1* = 0.0773, *wR2* = 0.2024, *R* indices based on 15476 reflections with I >2sigma(I) (refinement on F^2), 1420 parameters, 24 restraints. Lp and absorption corrections applied, μ = 1.110 mm^{-1}.

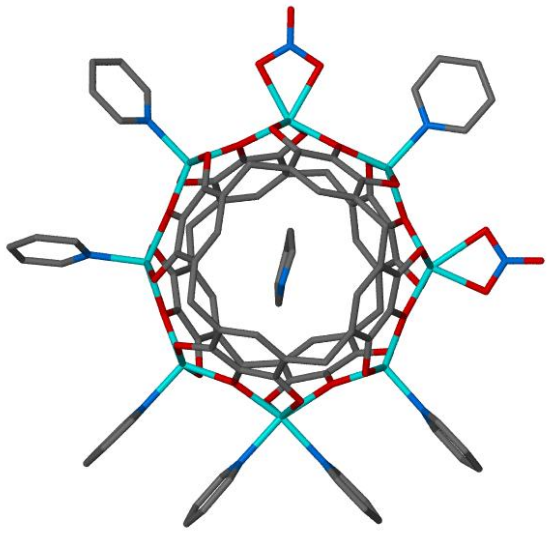

PgC3Co-pyridine/nitrate dimer **(2.20)**				
Metal #	**Ligand**	**θ_1**	**θ_2**	**τ5**
Co1	nitrate	161.52	126.95	0.576
Co2	pyridine	166.98	136.04	0.516
Co3	nitrate	161.48	130.26	0.520
Co4	pyridine	165.52	135.69	0.497
Co5	pyridine	166.72	140.2	0.442
Co6	pyridine	166.68	133.82	0.548
Co7	pyridine x2	150.66	115.65	0.584
Co8	pyridine	164.79	132.44	0.539
Average				0.53
StD				0.05

Figure 2.18: PgC3Co dimer (**2.20**) formed from synthesis in acetonitrile. This dimer has two NO_3^- ligands and it is unknown how the negative charge of these is balanced.

The structure of this cobalt-seamed dimer (**2.20**) differs markedly from all of the dimers in this section, and to an extent from any other dimer seen previously. Its most notable feature is the presence of two nitrate ligands (Fig. 2.18). While nitrate ligands are sometimes seen in zinc-seamed dimers, there is never more than a single nitrate bound to the capsule. The reason for this is that the MONC is charge-neutral and therefore a counterion is required to balance the negative charge of the nitrate anion. This counterion for a single nitrate often comes in the form of a pyridine guest, which can be assumed to be protonated and is therefore a positively-charged pyridinium cation. The cobalt dimer presented here also contains a pyridine guest, which is also likely protonated. However, a singly charged pyridinium it is not enough to balance the negative charge of the two nitrate ligands. Therefore, it is uncertain what balances the charge of this extra nitrate. Although it is easy to say that another pyridinium counterion is located *exo* to the capsule and is lost as a disordered solvent molecule, there is no evidence for this as this structure

is generally well-ordered and most of the extraneous electron density peaks can be modeled as partial occupancy acetonitrile molecules. Alternately, one of the Co^{2+} centers could have somehow been oxidized to Co^{3+}. However, this would be accompanied with a shortening in bond lengths at one of the metal centers, which is not seen. A third explanation is that the MONC itself bears the extra positive charge. Interestingly, there is a very close oxygen to aromatic centroid distance of 3.11 Å between one of the nitrate anions and one of the pyrogallol rings (Fig. 2.19). This close contact between a negatively charged ligand and an aromatic moiety could be the manifestation of charge balancing in the structure, as the pyrogallol ring itself could

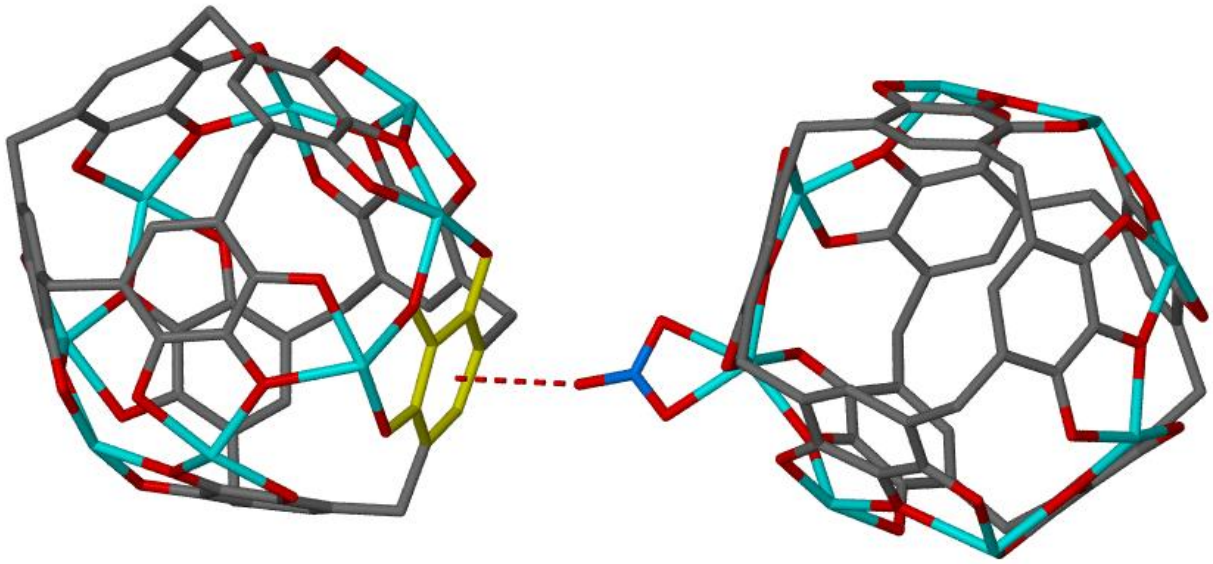

Figure 2.19: A close contact between a nitrate ligand on one dimer (2.20) with a pyrogallol ring on another dimer suggests that the PgC framework itself carries the positive charge that offsets the negative charges of the nitrate ligands.

Bond distance (Å) between the pyrogallol ring atoms in 2.20					
Ring	1···2	2···3	3···4	4···5	5···6
C1-C6A	1.41	1.40	1.38	1.40	1.41
C8-C13A	1.39	1.39	1.40	1.40	1.39
C15-C20A	1.38	1.39	1.41	1.38	1.41
C22-C27A	1.42	1.39	1.41	1.44	1.40
Avg	1.40	1.39	1.40	1.40	1.40
StD	0.02	0.01	0.01	0.02	0.01
Ring	6···1	3···O1	4···O2	5···O3	
C1-C6A	1.38	1.39	1.36	1.35	
C8-C13A	1.40	1.38	1.36	1.38	
C15-C20A	1.40	1.37	1.37	1.39	
C22-C27A	1.39	1.34	1.32	1.32	
Avg	1.39	1.37	1.35	1.36	
StD	0.01	0.02	0.02	0.03	

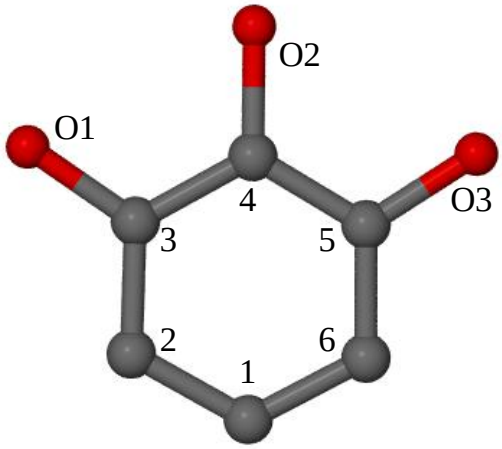

Table 2.3: Bond distances in the pyrogallol rings that make up one of the macrocycles in 2.19. The numbers in orange fall significantly outside of the typical range for bond lengths. All of these are found in a single pyrogallol ring (yellow).

potentially be a positive charge-bearing locus. Consistent with this fact, the pyrogallol ring differs from the others in terms of the bond lengths between its atoms. In particular, when compared to the average, all of the carbon-oxygen bonds are shortened and one of the carbon-carbon bonds is lengthened (Table 2.3). Significant differences in bond length from the average only occur for a single pyrogallol ring, notably, the one that takes part in this close-contact bond. These differences may signify the presence of a positive charge, although this is a matter of speculation.

Aside from the two nitrates, the rest of the ligands on this dimer are pyridines, as is the internal guest. One of the remaining six sites is hexa-coordinate, as it bears two pyridine molecules. As such, this is the only example of a dimer with three octahedral metal sites. These three sites, if treated as penta-coordinate, are the reason why this dimer has by far the largest

average τ5 of any dimer (0.54). This remains true, however, even if just the penta-coordinate sites are averaged (τ5 = 0.51).

2.4.5: Cobalt-seamed dimers: summary

This section described several examples of cobalt-seamed dimers. Most of these were synthesized *via* methods that largely mirror those used for nickel, and as such, were expected to be generally analogous. Although there were several similarities (pyridine and DMSO recrystallizations led to similar coordinative arrangements in both cases), there were actually many notable differences between these two dimers. Of these, the most notable were the significantly larger τ5 values at cobalt centers, which made the resultant cobalt-seamed dimers appear significantly more polygonal than the nickel-seamed dimers. Furthermore, DMSO was found to be a much more common ligand on cobalt dimers, which was partially explained by a shorter coordinative bond length between DMSO and Co^{2+} when compared to the same bond involving pyridine (this could indicate a stronger bond between the two). The encapsulated guests tended to differ as well. Synthesis in acetonitrile, followed by recrystallization in another solvent led to the encapsulation of pyridine with cobalt, while an encapsulated pair of acetonitrile molecules was seen in all cases where this synthetic methodology was used with nickel. The last structure in this subsection was a structural outlier from any of the dimers seen thus far, as it featured two negatively charged nitrate *exo* ligands on the exterior of the capsule as well as several close contacts between these nitrates and adjacent capsules. The presence of two nitrates is significant, as there is nothing in the structure to fully balance their negative charge. However, the close contact seen in this structure may indicate the presence of a positive-negative attraction, and may suggest that the negative charge of the nitrates is counterbalanced by a partially positive charge in the rest of the dimer.

2.5 Manganese-seamed dimeric nanocapsules

Manganese (in the form of Mn^{2+}) reacts with PgCs in an essentially analogous manner to that of Ni^{2+}, Co^{2+} and Zn^{2+}. When PgC and Mn^{2+} are mixed, there is no reaction. However, when a base is added, or a basic counterion to the Mn^{2+} is used, some sort of coordination complex clearly forms. The confirmation of this is the formation of a green precipitate (with acetonitrile) or a change in the color of the solution from pink to green (dilute solutions in methanol or acetone). This is analogous to what is seen with all of the other M^{2+} cations, which all change colors with the addition of PgC and base. If these green Mn^{2+} complexes also behaved analogously in terms of their propensity to crystallize, crystallization would be a simple matter of dissolving the precipitate in hot DMSO, and/or providing enough time for crystals to form from a solution. However, unlike the other transition metal complexes, Mn^{2+} complexes are (unfortunately) very unstable in air. Unless the reaction is performed in an oxygen-free environment, a change in the color of the precipitate/solution from green to red quickly follows the reaction. The resultant material does not crystallize into corresponding red crystals, but colorless crystals of a Mn^{2+} oxalate salt do form eventually, indicating that the decomposition of PgC likely occurred. The role of oxygen is unknown but was confirmed to play a part in decomposition by performing the Mn^{2+}/PgC reactions in a nitrogen atmosphere, which did not cause the precipitate/solution to turn red. Introduction of O_2 to a sample prepared in this way, however, did cause this color change to occur. To combat this effect, it was found that by mixing solutions of the required reagents (PgC, Mn^{2+}, and base) in a scintillation vial, and then quickly sealing the vial, the decomposition can be slowed. In several instances, this approach actually led to the formation of crystals, and data collection *via* scXRD was attempted. However, with most solvents the crystals quickly turned red on exposure to air, and were found

to no longer be suitable for data collection. The only exception to this was when synthesis and crystallization was simultaneously conducted in hot DMSO. By using this solvent, the crystals formed on cooling did not seem to decompose and led to successful data collection in two cases. The resultant complexes were found to be dimeric MONCs and are detailed below.

2.5.1 PgC1Mn dimer with DMSO and 4-picoline ligands

0.608 g of PgC_1 (1 mmol) and 1.00 g of $Mn(NO_3)_2 \cdot 4H_2O$ (4 mmols) were co-dissolved in 15 mL of 4:1 DMSO:ethylene glycol by stirring and heating on a mantle set at 200°C. Once dissolution had occurred, 1.2 mL (14 mmol) of 4-picoline was added. This resulted in a color change from pink to yellow, with the formation of a small amount of precipitate. The solution continued to be stirred and heated until fully dissolved, then taken off of the mantle, capped and left to sit at room temperature. Crystallization occurred over the course of several days.

Crystal data for PgC_1MnDMSO,4-picoline dimer (**2.21**): $C_{48}H_{59.50}Mn_4N_{0.50}O_{18.50}S_{6.50}$, M = 1367.61, yellow plate, 0.25 × 0.25 × 0.10 mm^3, monoclinic, space group $C2/c$ (No. 15), a = 15.330(2), b = 28.012(4), c = 25.687(4) Å, β = 93.380(2)°, V = 11011(3) $Å^3$, Z = 8, D_c = 1.650 g/cm^3, F_{000} = 5624, Bruker SMART CCD area detector, MoKα radiation, λ = 0.71073 Å, T = 173(2)K, $2\theta_{max}$ = 55.0º, 63891 reflections collected, 12589 unique (R_{int} = 0.0370). Final *GooF* = 1.037, *R1* = 0.0952, *wR2* = 0.2796, *R* indices based on 9059 reflections with I >2sigma(I) (refinement on F^2), 704 parameters, 45 restraints. Lp and absorption corrections applied, μ = 1.216 mm^{-1}.

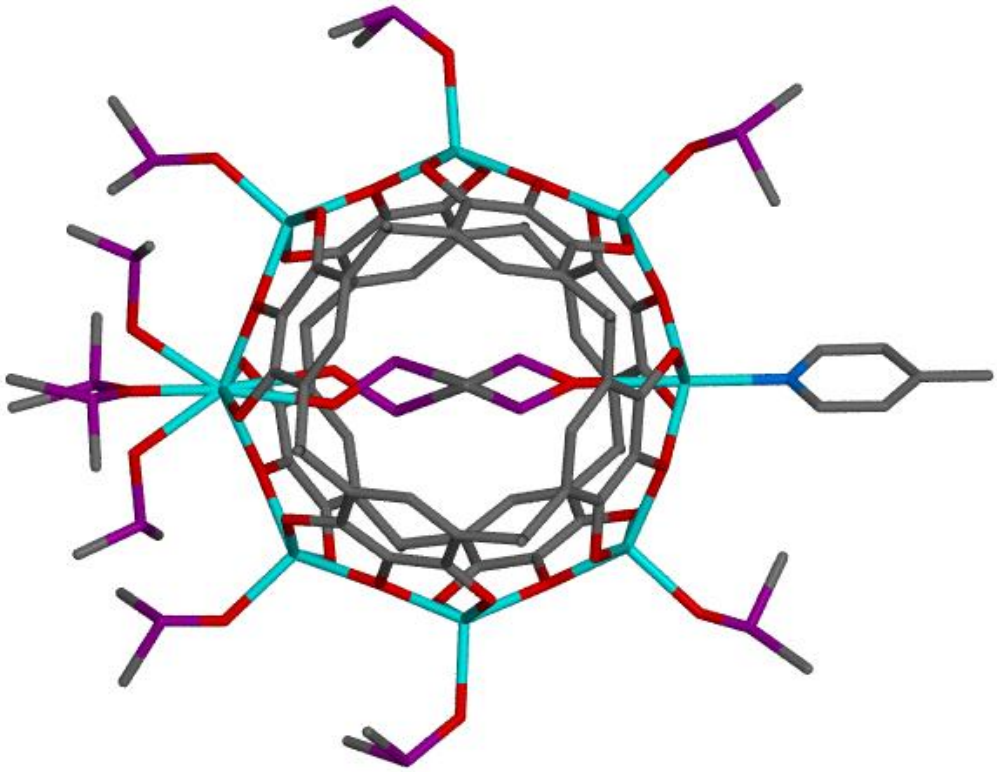

PgC1Mn-DMSO/pico dimer (2.21)				
Metal #	**Ligand**	**θ_1**	**θ_2**	**τ5**
Mn1	4-picoline,DMSO	169.94	152.85	0.285
Mn2	DMSO	162.1	143.46	0.311
Mn3	DMSO	159.25	137.92	0.356
Mn4	DMSO/H2O	157.92	136.14	0.363
Mn5	2xDMSO	159.65	136.89	0.379
Average				0.34
StD				0.04

Figure 2.20: A PgC1Mn dimer (**2.21**) synthesized in DMSO. The resultant ligand arrangement is unique, as it contains two metal sites that are partially hexa-coordinate.

This first example of a manganese-seamed dimer was synthesized/crystallized in DMSO, with 4-methypyridine (4-picoline) as the base. Interestingly, the structure only features a 4-picoline molecule on one of the metal centers (Mn1) as a peripheral ligand, with the rest of the metal centers coordinating to DMSO molecules. Seven of the metal sites accommodate a single peripheral ligand, and the remaining center features an interesting coordination geometry that differs from any seen thus far. On visual inspection, this metal center (Mn5) contains an unprecedented three DMSO ligands. However, closer inspection indicates that in reality, these ligands are too proximal to one another for this result to make sense. Therefore, it is more likely that this site either features a single DMSO ligand or two DMSO ligands, and dimers with both coordination schemes are simultaneously present in the crystal. Interestingly, the internal guest DMSO is actually oriented towards Mn5 and/or towards the 4-picoline molecule on the diametrically opposite side rather than being oriented orthogonally to this site as with most examples of hexa-coordinate metal sites in dimers. The alternate coordination numbers at this site can help to explain this effect and a scenario for how this site works can therefore be envisioned. When two *exo* DMSO ligands coordinate to Mn5, the *endo* DMSO is directed away from Mn5 and towards Mn1, making it also hexa-coordinate. However, when only one DMSO molecule is located at Mn5, the endo DMSO is now directed toward Mn5 as well. This leads to two scenarios, one where there are two hexa-coordinate sites on this dimer, and another where there is only one. Although this mode of coordination cannot be easily corroborated due to the disorder in this structure, what can be said is that this site is clearly different from the others from a geometric point of view. If treated as a penta-coordinate center, Mn5 has the highest $\tau 5$ value of any others in the structure whereas Mn1 has the lowest.

2.5.2 PgC1Mn dimer bearing DMSO and benzoate ligands

0.608 g of PgC_1 (1 mmol) and 0.57 g of sodium benzoate (4 mmols) were co-dissolved in 10 mL of DMSO by stirring and heating on a mantle set at 200°C. 0.98 g of $Mn(OAc)_2 \cdot 4H_2O$ (4 mmols) was separately dissolved in 5 mL of DMSO. Once dissolution had occurred in both solutions, they were mixed, and the color changed from pink to yellow. The solution was then taken off of the mantle, capped and left to sit at room temperature. Crystallization occurred over the course of several days.

Crystal data for PgC_1MnDMSO/Bz dimer (2.22): $C_{23.50}H_{23}Mn_2O_{9.19}S_2$, M = 626.42, bronze plate, .1 × .25 × .5 mm^3, triclinic, space group P-1 (No. 2), a = 15.875(7), b = 15.900(7), c = 29.327(14) Å, α = 104.830(6), β = 96.464(6), γ = 103.483(5)°, V = 6841(5) $Å^3$, Z = 8, D_c = 1.216 g/cm^3, F_{000} = 2556, Bruker SMART CCD area detector, MoKα radiation, λ = 0.71073 Å, T = 173(2)K, $2\theta_{max}$ = 50.0°, 63080 reflections collected, 23454 unique (R_{int} = 0.0948). Final *GooF* = 2.003, *R1* = 0.2251, *wR2* = 0.5434, *R* indices based on 11513 reflections with I >2sigma(I) (refinement on F^2), 1417 parameters, 56 restraints. Lp and absorption corrections applied, μ = 0.899 mm^{-1}.

The second example of a manganese-seamed dimer came from an attempt to form a dimer where all of the *exo* ligands were DMSO molecules. Such a structure would allow for the comparison of manganese-seamed dimers by virtue of their τ5 values to dimers seamed by other metals and bearing solely DMSO ligands. The presence of even a single hexa-coordinate center (such as in **2.21**) skews τ5 values in all of the metal centers, thus making comparison relatively difficult. As such, a structure bearing only penta-coordinate sites was highly desired.

To accomplish this, pyridine or any of its structural analogs were not used as a base. Instead, it was decided that a basic carboxylate counterion would be used instead. There have

been no cases where a carboxylate functioned as a ligand in PgC-based assemblies, so this seemed like a reasonable idea. Thus, manganese acetate was used instead of manganese chloride or nitrate, and additional sodium benzoate was added to increase the amount of base present. This had the intended effect of leading to crystal growth, but it did not lead to the expected crystal structure.

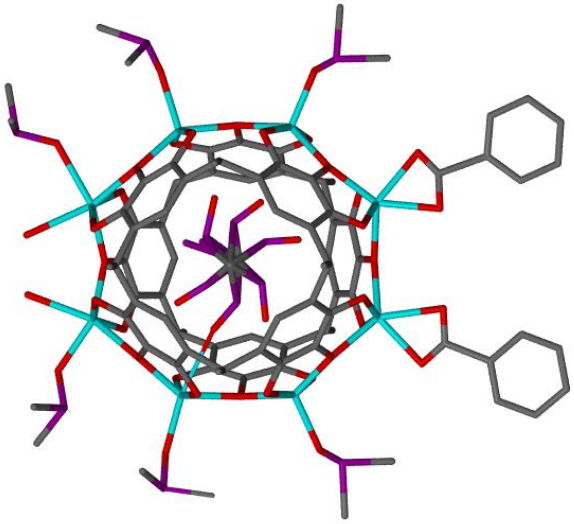

PgC1Mn-DMSO/Bz dimer (2.22)

Metal #	Ligand	θ_1	θ_2	$\tau 5$
Mn1	DMSO	160.88	140.76	0.335
Mn2	DMSO	161.54	142.01	0.326
Mn3	Benzoate	151.1	129.1	0.367
Mn4	Benzoate	151.29	128.22	0.385
Mn5	DMSO	160.62	140.21	0.340
Mn6	DMSO	163.42	145.78	0.294
Mn7	DMSO/H2O	150.74	122.57	0.470
Mn8	DMSO/H2O	149.48	122.82	0.444
Average				**0.32**
StD				**0.02**

Figure 2.21: PgC1Mn dimer that has two benzoate ligands on the exterior. The internal DMSO guest appears unaffected by the hexa-coordinate sites present on this dimer

In particular, it was found that the benzoate anion *likely* acts as a ligand for two of the metal centers (Fig. 2.21). Benzoate's presence cannot be fully confirmed due to the disorder in the structure. However, the larger-than-average τ5 values at these sites suggest that the metal centers are of hexa-coordinate geometry, and the presence of bidentate fragments bound to these two centers suggests that a carboxylate ligand is present at those sites. These fragments coordinate similarly to what is seen with the nitrate anion in zinc and cobalt, but since the nitrate ion was not present in the synthesis, it was ruled out as a possible ligand. Thus, it was clear that the fragment corresponded to either acetate or a benzoate. Usually, such a distinction can be made crystallographically, but this was made difficult due to the disorder in the structure. However, as a partial ring structure was found amid the disorder, it was decided that the ligands are (at least partially) benzoates, and were modeled accordingly. Further structural expansion can partially explain some of the disorder, as there are several close-contacts of c.a. 3.2-3.6 Å between the benzoate phenyl rings and disordered DMSO ligands on adjacent dimers. As the overall framework of the dimer is charge-neutral, one problem with a benzoate ligand is the necessary counterion. This must either be a Na^{+} or a non-coordinated Mn^{2+} in this case, as these are the only cationic species that could be present in this structure. It is difficult to pinpoint the exact location of the cation due to the disorder in the structure, but a prominent (unassigned) peak can be found between the two benzoates at a distance of 2.5-2.6 Å from the coordinating oxygens. It is unknown whether this peak is simply a disordered water molecule or a coordinating cation.

Interestingly, the metal centers that coordinate to the two "benzoates" are not the only hexa-coordinate sites in this structure. Two other sites, which are diametrically opposite of those that coordinate to benzoates, are also hexa-coordinate. Each of these has two ligands, a DMSO

and what is likely a water molecule. The rest of the metal centers each coordinate to a single DMSO molecule. Unfortunately, due to the hexa-coordinate sites on this dimer, the τ5 values at the rest of the metal centers are skewed, which is exactly what this experiment was trying to avoid. Nevertheless, this experiment showed several important things, namely that the benzoate anion can be used as a ligand in manganese-seamed dimers, and that non-pyridine bases can be likewise used to synthesize these dimers, akin to what has been done with copper.

2.5.3: Manganese-seamed dimers: conclusion

The primary purpose for this subsection was to present the two examples of manganese-seamed dimers that have been discovered so far. Both of the structures are structurally odd, and their oddity is difficult to explain due to the rather straightforward methods used to synthesize and crystallize them. Nevertheless, these two examples demonstrate that a PgC-based MONC can be constructed from Mn^{2+}, and this subsection shows that there are a few interesting particularities that arise due to the use of this cation. In particular, the presence of benzoate ligands in **2.22** is a completely novel finding, and although both acetate and benzoate have been used previously (with other metals) in the synthesis of PgC-based MONCs, there has never been an instance of their presence as a ligand in any other structure. Due to the presence of hexa-coordinate metal centers in both of the dimers in this section, direct comparison of their geometry with that of the other dimers was not performed. However, the τ5 values in both of the dimers seem to fall in the 0.3-0.4 range that is typical of copper and nickel, and so it can be expected that a fully penta-coordinate manganese-seamed dimer would likely be more similar to these two metals rather than to zinc and cobalt.

2.6 The structure of various metal-seamed MONCs: summary and conclusions

This chapter described the crystal structures of PgC MONCs based on Cu^{2+}, Ni^{2+}, Co^{2+}, and Mn^{2+}, as well as the methods that were used to synthesize and crystallize them. All of these metal cations were found to be capable of forming dimeric nanocapsules with PgCs, and two (copper and nickel) were also found to form hexamers. Although all of the dimers and hexamers found in this section are structurally similar, in that the arrangement of the PgCs and metal cations is relatively consistent, a closer inspection reveals that there are small but not insignificant differences among them. These differences are the result of the various synthesis and/or crystallization techniques that were used prior to structural elucidation *via* scXRD.

One of the biggest differences between the MONCs is the coordinative geometry of the metal centers. Although the dimers were, in all cases, made up of two PgC macrocycles seamed together by an "octametal belt," the geometry of the belt is visibly different depending on the metal that is used and the number of *exo* ligands that are present on each of the centers (i.e. the coordination number). This difference was quantified by the $\tau 5$ parameter. Typical $\tau 5$ values ranged from 0.32-0.33 with nickel, 0.33-0.35 with copper, 0.41-0.42 with zinc (obtained from published data[126,127]), and 0.46-0.50 with cobalt.

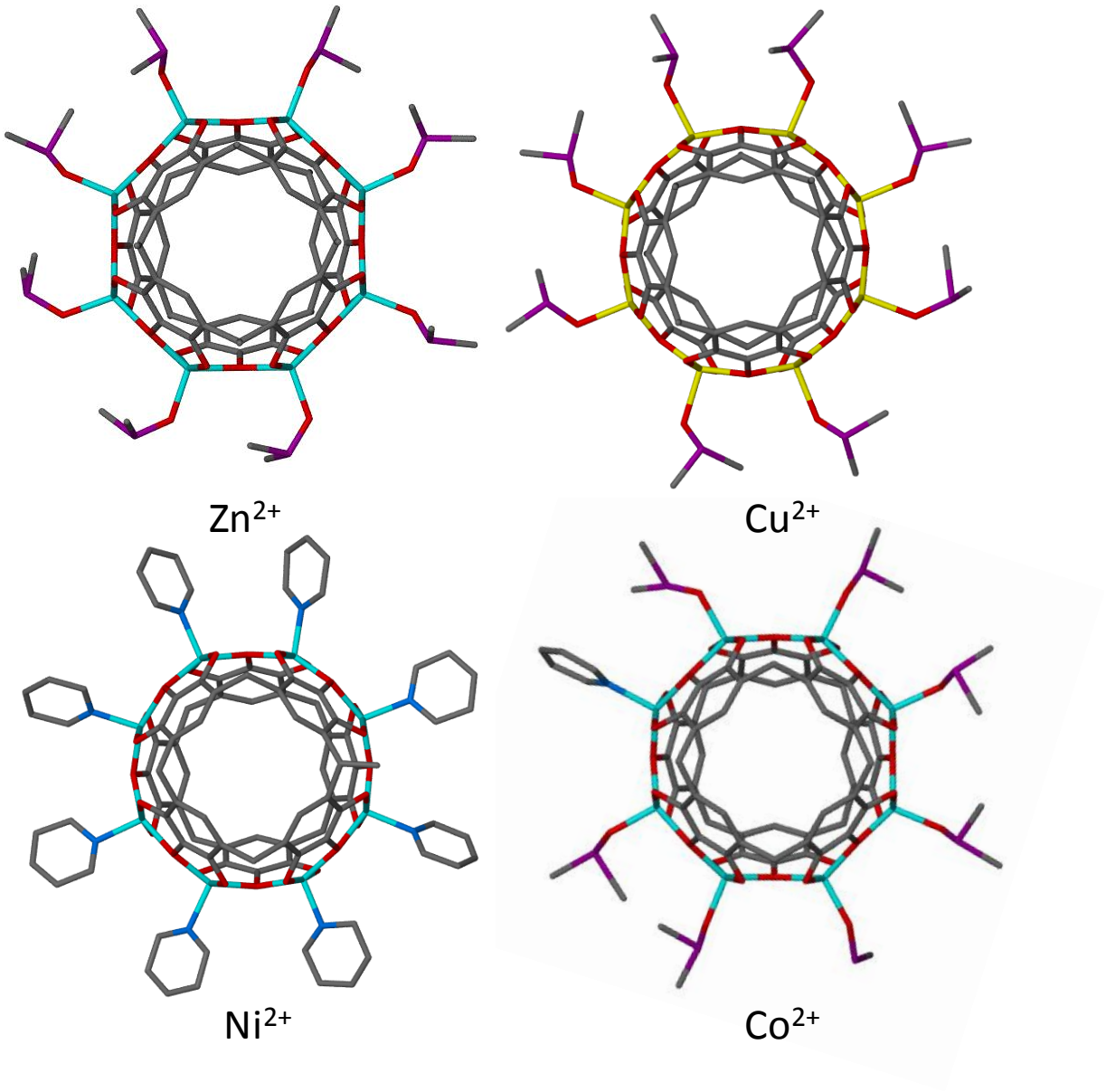

Figure 2.22: Comparison of dimeric MONCs bearing solely penta-coordinate sites.

In addition, the differences in coordination geometry are visually apparent when looking at the structures of the dimers (Fig. 2.22). Although the coordination geometry was affected by the metal identity, the identity of the *exo* ligands and *endo* guest had a very small (but not negligible) effect on the geometry. The only metal where the identity of the *exo* ligand seemed to affect τ5 was with cobalt, where large differences could be seen between Co^{2+} centers bearing

DMSO and 4-methylpyridine ligands. Unfortunately, as both of the manganese dimers featured hexa-coordinate sites, they could not be directly compared with the other dimers. This is because it was also found that the introduction of an extra ligand to normally penta-coordinate sites (thereby making these centers hexa-coordinate) led to a "warping" of the octametal belt. Even a single hexa-coordinate site dramatically changes the geometry of all of the other sites, perhaps as a compensatory measure. This leads to difficulty in directly comparing the geometries of dimers bearing hexa-coordinate sites with those bearing only penta-coordinate sites.

Another difference between the dimers was the identity of the *endo* guest molecule. In most cases, the *endo* guest reflects the synthetic method that was used. For example, it was found that a DMSO guest was incarcerated within the dimer any time DMSO was used as the solvent for the MONC-forming reaction (this was the case for all of the metals). This was also the case with other solvents, such as acetonitrile with nickel dimers and acetone with copper dimers. In other cases, such as with Co^{2+} or Zn^{2+}, the internal guest is not a solvent molecule, but is instead a molecule of pyridine. This difference (solvent versus something else) may reflect a difference in the coordination chemistry of the metal centers, and can potentially be used to selectively incarcerate guest species. The *endo* guest was also found to stay within the interior of the dimer regardless of what happened on the outside, such as recrystallization in another solvent or ligand exchange. Amazingly, this was also the case with metal exchange. In one case, exchange of Zn^{2+} centers for Cu^{2+} centers apparently did not lead to decomposition of the dimer, as the internal guest pyridine was retained throughout the process.

Differences in the identity of *exo* ligands were also seen among the different conditions employed. The vast majority of *exo* ligands were either DMSO molecules or members of the

pyridine family of molecules. This was due to the use of pyridine as a coordinating/sacrificial base in many of the syntheses, and the use of DMSO as a solvent for recrystallization. Copper dimers were also synthesized in acetone and therefore had acetone ligands. In several cases with pyridine, it was also found that two pyridine molecules could bind to a single metal center, thereby forming a hexa-coordinate site(s). It is unknown how and why this dimeric variant forms, but it does so only under certain conditions, namely synthesis/recrystallization in methanol or recrystallization in pyridine with PgC2 as the macrocycle. In addition to standard ligands (solvents), there were also several cases where unusual ligands were present. The nitrate anion was found to be coordinated to Co^{2+} centers, and benzoate anions were found to coordinate to Mn^{2+}. Both were bound in a bidentate fashion and therefore also led to the presence of hexa-coordinate metal sites, with their associated differences in geometry. The reason for their presence is also unknown, but may be due to an absence of other suitable ligands, or to the affinity of these ligands for these particular metal centers. It should be noted that counterion ligands were not found with Cu^{2+} and Ni^{2+} centers, but were also present in several examples of zinc dimers (appendix). Interestingly this trend follows the differences seen in $\tau 5$, with the larger $\tau 5$ values accommodating these strange ligands. This, though, is likely incidental.

Although hexamers could be formed using only two metals, copper and nickel, there were nevertheless clear differences when one was used rather than the other. Perhaps the biggest difference was in the characteristics of the exo and endo ligands. With copper, the Cu^{2+}-ligand bond is quite long and the ligand electron density is often low, meaning that a ligand is there only part of the time. Oftentimes, Cu^{2+} centers do not have ligands at all, which leads to square planar (tetra-coordinate) metal sites. This is never the case with nickel, however, where both *endo* and *exo* ligands are well-ordered, permanently there (full occupancy), and connected *via*

short (strong) bonds to the metal centers. The synthesis of the nickel-seamed hexamers also leads to a different ligand set, which features water molecules as the sole *endo* ligands and pyridine molecules as the sole *exo* ligands. Another difference between the two are the oxo-metal bond lengths between the PgC hydroxyls and the M^{2+} centers, which are shorter for copper than for nickel (this is also the case in the dimer). The result is that the nickel hexamer is metrically larger than the copper hexamer and therefore encloses more internal space.

The nickel pseudodimer is an additional species that was introduced in this chapter. Although it appears to have characteristics of both the dimeric and hexameric MONC, it is not capsular and therefore does not possess *endo* guest molecules. It is likely that this species is simply a byproduct of the MONC forming reaction, although it is also possible that it is an intermediate in the formation of MONCs that is kinetically trapped by crystallization under certain conditions. Regardless of its role in the greater scheme of things, it is the only transition-metal based PgC complex that has been discovered thus far aside from the dimer and hexamer.

2.7 Future Studies regarding the synthesis of PgC-based MONCs

This chapter showed that PgC-based MONCs are not limited to those formed from copper, zinc and gallium salts, but instead can be formed from a variety of metal centers, each with their own peculiarities. As such, the primary future directions for the work outlined in this chapter involve further investigation of PgC's diverse complexation chemistry. The most obvious direction is the investigation of other metal cations, which is not necessarily limited to transition metal cations. Cursory evidence (color changes and precipitation) suggests that a wide range of complexes can be formed simply by mixing PgC with different metal salts and a sacrificial base, such as pyridine, although crystallization of these materials has not been

successful so far. It is important to study these other complexes as it may reveal that other yet unknown morphologies of PgC complexes exist.

It is also essential that the complexes that are already known are investigated more fully. Although broader in scope than what came before this work, the syntheses/structures presented in this text are only the tip of the iceberg of what is possible, even if limited to just the metals seen here and a handful of PgCs. This is particularly evident with the cobalt- and manganese-seamed complexes, where only a few crystal structures are known. The synthetic methodologies used in producing almost all of the complexes for these two metals are analogous to what was used to produce dimers elsewhere, so it is no surprise that only dimers were discovered. Therefore, it is important to investigate other synthetic methodologies, such as those used to form the hexamer with nickel. Some solvents, such as DMF, ethanol, and THF, were also completely unused in these studies, which may also affect the resultant identity of the MONC. In addition, only the nitrate salt of the M^{2+} cations was used in most cases, as well as pyridine ligands. The metal counterion as well as the identity of the coordinating/sacrificial base should therefore also be investigated. All of these may provide a fuller picture of the factors that affect (or do not affect) the synthesis of these MONCs.

There are also several loose ends to tie up with this work as it is. In particular, the question of what causes hexa-coordinate metal sites to form remains unanswered. The hypothesis presented in this chapter was that a mixture of different dimers (and, possibly other MONCs) initially forms, each with its own combination of ligands and coordinative geometry, and that one simply crystallizes prior to all of the others. It is likely, however, that one species predominates, and this notion can be easily investigated using elemental analysis methods on precipitated/powdered samples of dimer. By determining the nitrogen to metal ratio, one can

quickly figure out what proportion of the entire dimeric population does not bear solely penta-coordinate sites, and therefore it can be determined if a mixture or a homogeneous product is formed. Certain conditions will likely lead to a larger or smaller proportion of the partially hexa-coordinate species, and over multiple experiments, the controlling factor can be determined.

In addition, the basis for the pseudodimer's existence is also unknown. A simple experiment that would likely be quite useful in determining its role in the grand scheme of things would be to dissolve the crystalline material in a solvent and track the MALDI-TOF mass spectrum over time. Changes corresponding to its transmutation into the dimer and/or hexamer should be fairly evident as shifts in the dominant mass peak. As there is only half of the metal content needed for a typical MONC in a pseudodimer, it may require additional metal and/or pyridine to form the corresponding MONCs.

Other concepts, such as the instability of the manganese dimer and the exchange of one metal cation for another (as was done in **2.3**) are also topics for investigation and could likewise lead to a better understanding of PgC coordination chemistry.

Chapter 3: Using Small Angle Neutron Scattering to understand PgC-metal complexes

3.1 Introduction and basis for investigation

This chapter seeks to answer an underlying question about MONCs that went relatively unanswered in the last chapter: what factors lead to the formation of dimeric and/or hexameric MONCs? The basis of this question comes from the discovery that both dimeric and hexameric MONCs can form under certain conditions when Ni^{2+} and Cu^{2+} are used as metal centers. In particular, it was noted during the development of the compounds seen in the last chapter that there were several variables that seemed to favor the formation of one MONC versus the other.

The discovery of the first of these variables, temperature, was noted in the introduction to this text as one of the foundations to this project. As a recap, it was discovered that when copper-seamed MONCs were synthesized in hot ethylene glycol, rather than methanol at room temperature, the resultant material consisted of dimers rather than hexamers. In fact, it consisted *exclusively* of dimeric nanocapsules, as seen by MALDI-TOF mass spectrometry. If both MONC species had formed, there would have been characteristic peaks for both species in the spectrum. However, only peaks for the dimer were seen. This gave the impression that either temperature or solvent system was responsible for the formation of one capsular species over the other. More evidence for the notion that temperature was the responsible factor came from the discovery that crystals of copper-seamed dimers would form in hot DMSO, but that a crystalline mixture of both dimers and hexamers would form from a room temperature synthesis. This was also found to be the case in acetone, but with an added note of exclusivity; only hexamers were found at room temperature, and only dimers were found at an elevated temperature. These three findings suggested that the formation of dimers was favored at high temperatures, whereas the formation of hexamers was favored at, or even required, a low temperature synthesis.

Another set of observations came from the discovery of nickel-seamed MONCs. Unlike copper, the first nickel-seamed MONC to be discovered was the dimer. However, it was soon evident that both dimeric and hexameric MONCs could be formed with this metal as well. It is important to note the colors of the two MONC species: nickel-seamed hexamer crystals are dark green (almost black), as is the color of a solution containing hexamers. Crystals of the dimeric MONC, however, are yellow, as is the color of the solution used to produce them. This observation led to the separation of dimeric and hexameric MONCs from synthesis in acetonitrile, where a yellow precipitate (dimeric) was removed from a dark green solution. This solution, when isolated, later formed crystals of the hexamer on standing. As with copper in DMSO, this experiment showed that both species would form following a room temperature synthesis. However, it was also noted that if synthesis/*in situ* crystallization was performed in methanol, crystals of the hexamer could only be obtained within a few hours after synthesis, and at an appropriately high concentration. Low concentrations, however would not lead to crystallization of the hexamer, but instead would lead to an interesting observation regarding color. Although the color of the solution starts off as dark green, it fades to a bright yellow over the course of several days. When this was done most of the time, crystals did not form. However, on several occasions (**2.12, 2.13**) crystals of the dimer formed after several days that, like the new color of the solution, were also yellow. This indicated that in addition to temperature, time may also be a factor in the ratio of the dimer versus the hexamer in solution, with the hexamer somehow transforming into the dimer over a prolonged course of time.

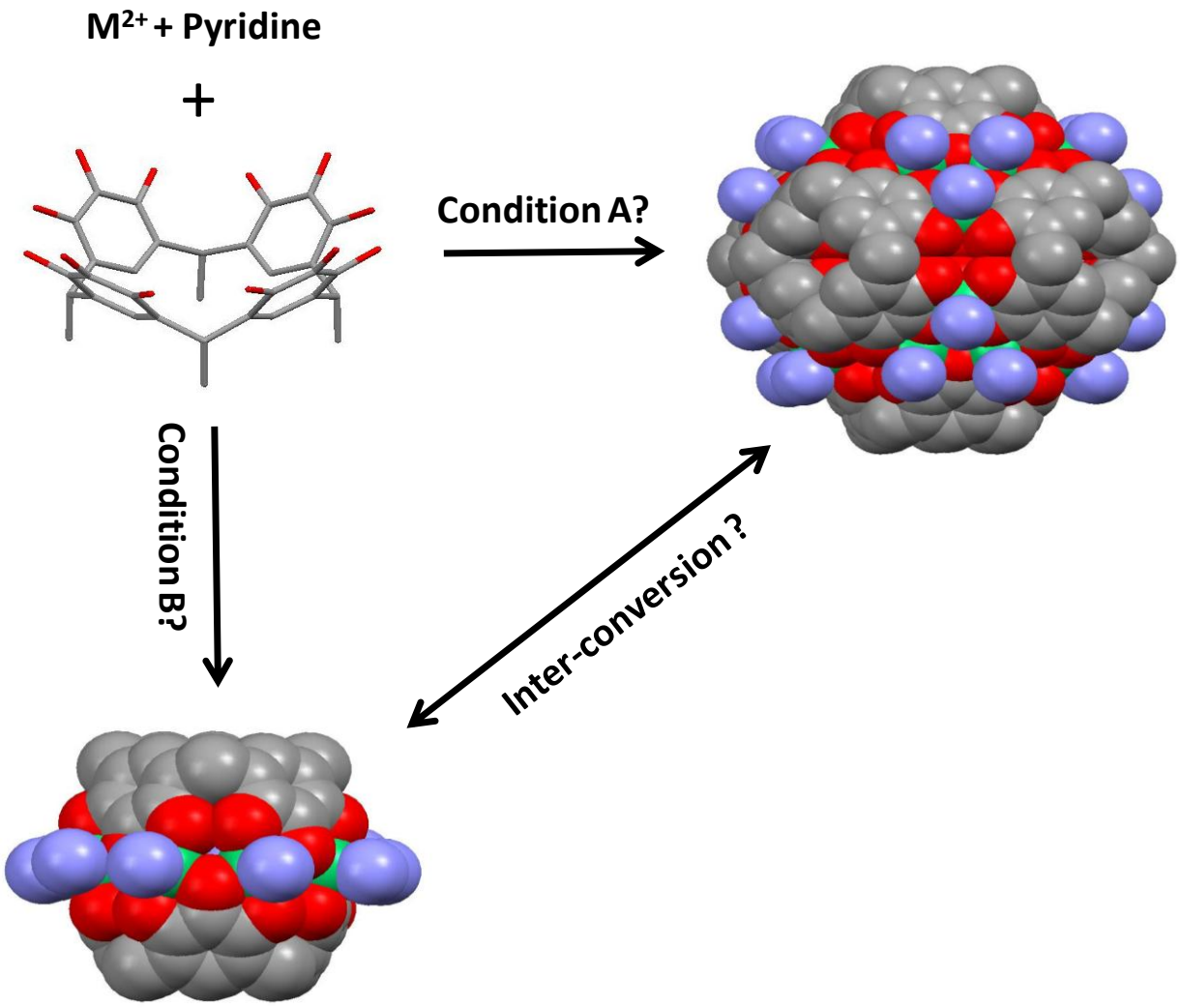

Figure 3.1: Results from scXRD show that different conditions may lead to the selective formation of the dimer or the hexamer, and that inter-conversion between the two may also be occurring.

While important as preliminary data, broad conclusions cannot be derived from these observations. This is because, in addition to the concentration of constituents in solution, crystallization is dependent on many other factors (i.e., solubilities of the constituents, super-saturation, etc). Therefore, crystallization may not be an accurate account of what is actually in solution, and it certainly cannot be used for quantitative analysis. As such, it was imperative that a method be devised that would allow for the quantitative study of these systems in solution,

rather than the nondescript solid-state. This would give a much more accurate account as to the chemistry of these species, as it could potentially give us data regarding the ratio of the two under a wide range of conditions. The method that was selected to carry out this analysis was small angle neutron scattering (SANS). These studies were performed in collaboration with Dr. Harshita Kumari at MU and Dr. Steven Kline at the National Institute of Standards and Technology (NIST). SANS data was not collected, reduced, or largely interpreted by the author (some data interpretation/normalization was done), whose role was to provide materials and to design the experiments. This work can be found elsewhere in its published form and additional data tables can be found in the appendix.[136]

3.2 The basics of Small Angle Neutron Scattering (SANS)

Small angle neutron scattering is a powerful method of analysis that allows one to determine the size, shape and concentration (relative to a standard) of an analyte in solution. The basic idea behind SANS and other small angle scattering methods is that when a beam of radiation is directed towards an analyte that is metrically larger in diameter than the wavelength of the radiation, rather than diffracting the analyte causes the radiation to scatter over a small angle relative to the direction of the beam. In SANS, neutrons are scattered by the nuclei of the analyte's atoms, whereas in techniques such as small angle X-ray scattering, the radiation is scattered by the electron cloud surrounding the nuclei.[137] Different nuclei interact to a different extent with the neutron beam, and therefore the angle at which neutrons are deflected by a nucleus varies depending on the constituents. As such, the theoretical scattering contributions from all of the atoms must be determined prior to measurement. Therefore, the only thing that must be known in advance about the analyte is its chemical makeup. The rest (size, shape,

concentration, etc) comes from the collection and interpretation of scattering data, which will not be covered as it is beyond the scope of this text. SANS is also useful when there are multiple species in solution, which is why it was used in our attempts to understand the relationship of dimers and hexamers in solution.

3.3 Investigating copper and nickel MONCs using SANS

It is known that Cu^{2+} and Ni^{2+} can be used to form both the dimeric and hexameric MONCs from PgCs, so these two cations were the obvious choice to head off our investigations with SANS. Crystalline samples of the dimeric and hexameric MONCs for both of these metals were dissolved in the appropriate deuterated solvents and used as controls two hours after dissolution. It is important to note that the PgC3 macrocycle was used in the synthesis of the control MONC samples; the appropriate synthetic methodologies for these materials can be found in chapter 2 and elsewhere.[119,136] Control data showed that SANS could be used to reasonably differentiate between the two MONCs, as the radii that were obtained following data workup were approximately the same as the radii obtained from scXRD studies (approx. 7 Å and 10 Å for the dimer and hexamer, respectively).

Variables	Constants
Cation used	Reagent concentration
Temperature	Reagent ratio
Time	PgC/base identity
Solvent	

Table 3.1: Variables and constants in experiment 3.3

3.3.1 Investigating copper and nickel MONCs using SANS: experimental variables

Several variables were selected to be tested in regard to their effect on MONC formation (see table 3.1 for summary). These were some of the same variables that seemed to exhibit effects on the identity of MONCs in preliminary studies, notably time and temperature. Measurements were performed two hours following reagent mixing (referred to as "day 0" in later parts of this chapter), as well as three days after synthesis. Synthesis was performed at three different temperatures: -40°C, 23°C and 50°C. The temperature was then maintained at 23°C during a "rest period" following synthesis until the third day, when the samples were placed back into the neutron beam for further analysis. This provided an initial "shock" during synthesis, followed by a prolonged period at RT, a process which resembles the typical conditions seen in MONC crystallizations. In an additional experiment with Ni^{2+} in methanol, the same temperature (-40°C, 23°C or 50°C) was maintained throughout the course of the entire three day experiment. In another experiment, the temperature during synthesis and the rest period was 23 °C, while the temperature during measurement, three days later, was varied. In a sense, this was a reverse of the shock-and-wait methodology described earlier.

In addition to temperature, solvent choice was also investigated as a variable in this experiment. Acetone and methanol were used as solvents for the nickel portion of this experiment, as both dimeric and hexameric nickel MONCs dissolve quite well in these solvents. Methanol, however could not be used with copper, as synthesis in methanol leads to precipitation of the hexameric MONC, even at low reagent concentrations. Therefore, only acetone was used as a solvent for the copper portion of this experiment.

Several potential variables were also kept constant. One of these was the ratio of the reagents used to form MONCs: 1:4:14 PgC:M^{2+}:pyridine. Pyridine is required to synthesize both of the nickel-seamed MONCs under most circumstances, and although this is not necessarily the case with Cu^{2+}, it was also used with copper for the sake of brevity. The pyrogallol[4]arene that was used for all parts of this experiment was PgC3, at a concentration of 10^{-3}M. This is because the control materials that were used were also PgC3-based MONCs.

3.3.2 Investigating copper and nickel MONCs using SANS: experiment and data workup

The SANS experiment was conducted by Dr. Harshita Kumari using the NG7 30m SANS instrument at the NIST center for Neutron Research (NCNR) in Gaithersburg, MD. It is important to note that because neutron beamtime is limited, all of the experiments were performed only once. The SANS data was reduced and modeled by Dr. Harshita Kumari using the IgorPro software package.[138] The data was fitted to spherical, ellipsoidal, and cylindrical models for each data set, although the best fit in all cases was found to be either a unimodal or bimodal Schulz sphere model with the appropriate radii for the MONCs.[139] This resulted in a table of raw volume fractions for the experiments that was provided to the author by Dr. Harshita Kumari (appendix table A6.2.1). To numerically compare the volume fractions of the PgCs that

made up the dimers and hexamers, the following manipulations were then performed on the raw volume fractions (by the author): The volume fractions were first divided by the corresponding volumes of the MONCs ($4/3\pi R^3$ where R is 6.8 Å and 9.8 Å for the dimer and hexamer, respectively), to get the number of dimers and hexamers relative to one another, and then multiplied by either 2 for the dimer or 6 for the hexamer, as these are the numbers of PgC macrocycles per MONC. This gives a relative value of PgCs "bound" within a dimer or hexamer, so that comparison can be made (appendix tables A6.2.2). This treatment does not, however, give an absolute value for anything; these numbers are only appropriate for comparative purposes and to establish trends. To scale these values, the value for the corrected volume fraction for the Ni^{2+} dimer in methanol, at room temperature, and on day 0 was arbitrarily assigned to be the "standard" and was given a value of one. To scale the rest of the data, the corrected volume fractions were divided by the volume fraction of the Ni^{2+} dimer under these conditions. This gave a ratio of "bound" PgCs under specific conditions to the "bound" PgCs under the "standard" conditions (i.e. that of the nickel dimer in methanol on day 0). Therefore, the proportion of "bound" PgCs in a sample under one set of conditions can be compared to all of the others. All volume fractions, including those for the hexamers were scaled in this way (appendix table A6.2.3). Standard deviations are not tabulated with this data due to the low standard deviations (several orders of magnitude less) in the original raw data.

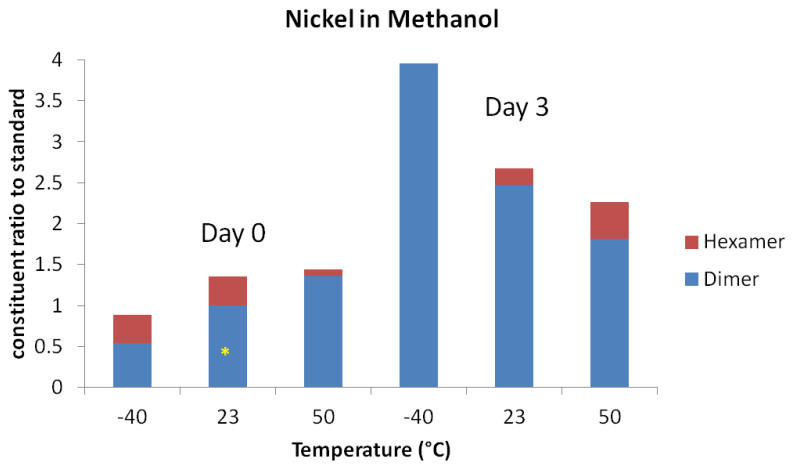

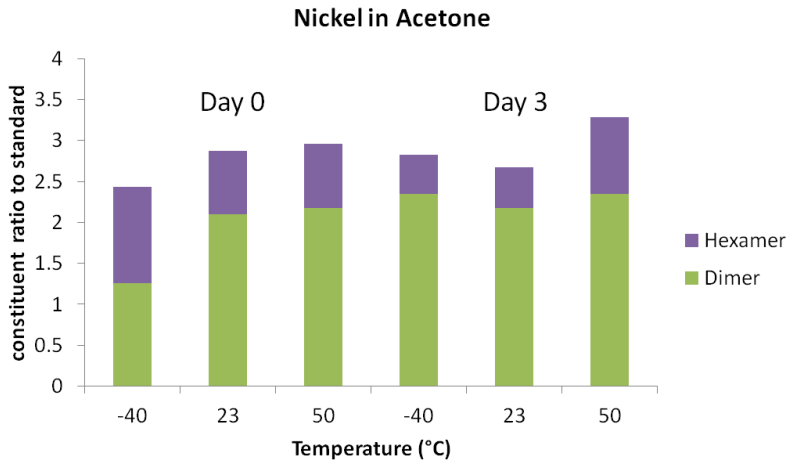

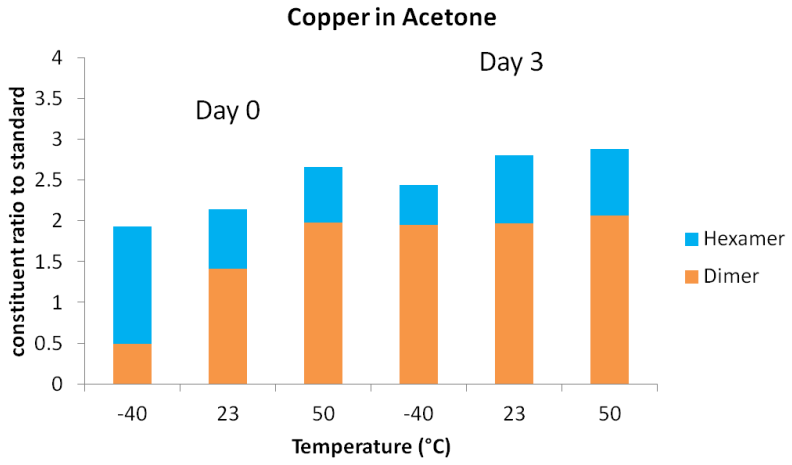

Graph 3.1: The relative ratios of the nickel/copper hexamer and dimer. The "standard" value by which all others are measured is marked with a yellow asterisk.

3.3.3 Investigating copper and nickel MONCs using SANS: results and discussion

The SANS data showed that all of the variables that were selected for this experiment had an effect on MONC formation. Interestingly, the first observation that can be made from the cumulative data is that the net yields (total PgC bound by both MONCs) are not equal among the different portions of the experiment. Furthermore, the net yield increases over the course of three days in most cases, indicating that the MONC-forming reaction does not proceed immediately, but rather occurs over time. This goes against the notion that the formation of MONCs is immediate and their yield is near-stoichiometric, at least in this experiment where precipitation cannot drive the reaction forward. In addition to this broad finding, it was also discovered that the proportion of PgC that was "bound" within dimers exceeded that of hexamer-bound PgC in all but one instance: PgC3Cu on day 0 in acetone, at -40 °C. This finding is congruent with the scXRD findings, as it has been much easier to form crystals of the dimer rather than crystals of the hexamer with all metals. This may, however, be simply incidental.

The first segment of this experiment, where the initial temperature is variable, but is afterwards kept at 23°C, shows several valuable features that help to corroborate our previous findings (Graph 3.1). On day 0 (two hours post-mixing), an increase in temperature led to a concomitant increase in the proportion of the dimer and a decrease in the proportion of hexamer, regardless of the metal or solvent. This is consistent with earlier observations from scXRD, which suggested that increased temperatures favor the dimer, while decreased temperatures favor the hexamer. By following this reaction over the course of three days, additional insight was gained into the nature of the MONC-forming process. As previously stated, the overall yields increased over the course of three days, regardless of temperature, metal or solvent, suggesting that the reaction was not complete after two hours (day 0). This being the

case, one would expect that the proportion of both dimer and hexamer would increase, or at least stay the same, as the reaction continued to completion. This would only be the case, however, if the dimer and hexamer were also fully stable entities that did not decompose. Instead, it was observed that while the proportion of dimer either increased or stayed the same over the course of three days, the proportion of hexamer actually decreased on several occasions, particularly in the low temperature samples. This indicates that a process exists by which hexamers decompose, and that (possibly) an equilibrium exists between the dimeric, hexameric, and possibly monomeric (unbound PgC) species. The equilibrium hypothesis, however, better explains this finding. If the hexamer is truly a kinetic product, the conversion of the dimer into the hexamer would not be favorable at lower temperatures, as there would not be sufficient energy for the process to occur. Inter-conversion of the hexamer into the dimer, however, would require less energy and would therefore be more favorable (**Fig. 3.2**).

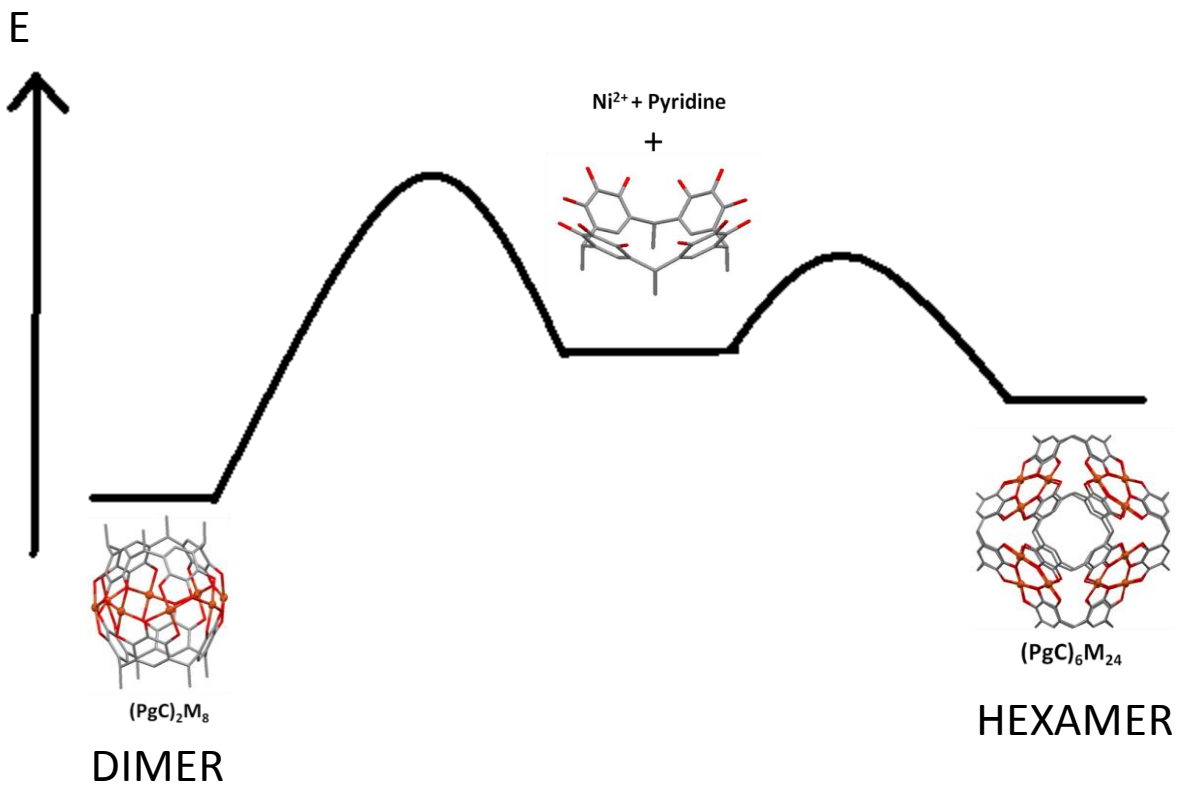

Figure 3.2: A simple energy diagram that may explain the results seen in this experiment. The dimer (thermodynamic product) and hexamer (kinetic product) exist in equilibrium with each other and unbound PgC/ other intermediates.

Another observation that was made in this segment of the experiment is that the behavior of the two solvents differs. In acetone, the proportion of dimer is nearly the same in all three samples for both metals. This may indicate that a maximal concentration of dimer had been reached, after which decomposition (or crystallization) would occur. In methanol, however, the proportion of dimer paradoxically decreases with increasing temperature. Although it cannot be substantiated, this may also be due to an equilibrium between the free PgC macrocycle and the dimer, with the thermodynamic product (dimer) being favored at lower temperatures after synthesis. The initial yields in methanol are also significantly lower than in acetone. This may

suggest that the reaction proceeds at different rates in the two solvents, slower in methanol and faster in acetone. Although these are mere conjectures, the differences between the two solvents nevertheless support our hypothesis that solvent identity plays a role in the outcome of this reaction.

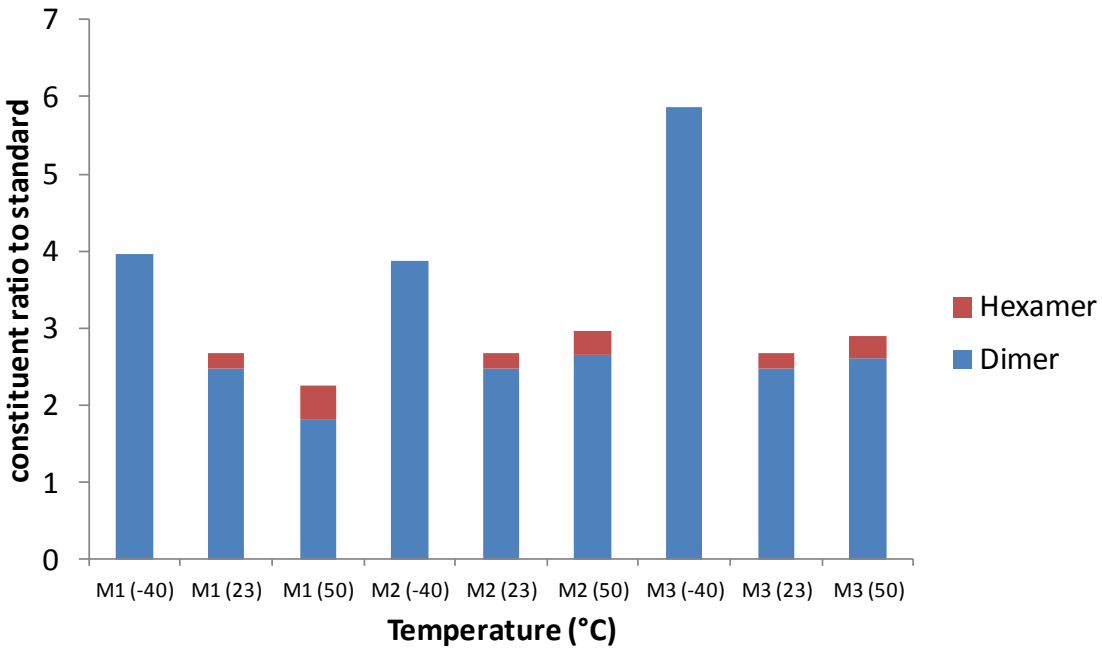

	Initial synthesis	Wait period	Day 3 measurement
Method 1	**variable T**	**RT**	**RT**
Method 2	**RT**	**RT**	**variable T**
Method 3	**variable T**	**variable T**	**variable T**

Graph 3.2: Comparison of data following three different time/temperature methods

A second segment of this experiment was also conducted, where the temperature schedule was changed in the nickel/methanol system. To reiterate, the previous data was all based on a single temperature schedule, wherein the temperature was kept at -40°C, 23°C, or 50°C until measurement on day 0, and afterwards was allowed to heat/cool back to room temperature (23°C). Two other temperature schedules were also investigated, where the temperature was either kept constant throughout the three days or was left at RT, and then changed prior to measurement (graph 3.2). The results of this experiment were rather confusing and little information can be gleaned from this data. However, these results did lead to a rather practical finding: cooling the solution to -40°C during any part of the experiment led to the exclusive formation of dimer in all cases. This may suggest that in addition to initial heating, long-term cooling can also be used as a method to produce pure specimens of the dimer, at least the nickel dimer in methanol. This foregoes the necessity of crystallization, which is the method that is usually used to purify this MONC.

3.3.4 Investigating copper and nickel MONCs using SANS: conclusion

In general, SANS was useful in investigating several different variables that were observed to affect the formation of the nickel and copper MONCs. The SANS data generally confirmed our hypotheses, notably that the amount of dimer generally increased with increasing temperature and over time in solution. The proportion of hexamer decreased with increasing temperature initially, but after three days, only the high temperature syntheses contained more hexamer than before, with many of the low temperature cases exhibiting complete loss of all hexameric product. This seems to follow the hypothesis that the dimer is the thermodynamic product, while the hexamer is the kinetic product. It should be noted that inter-conversion was

not observed when purified MONC samples were used, suggesting that other factors, such as pyridine, or, more likely acidic byproducts of the reaction, likely help to facilitate the inter-conversion of dimer into hexamer and *vice versa*. Some of the data that was obtained, however, was rather confusing, such as the nonsensical decreases in the quantity of dimer in methanol with increasing temperatures and the temperature schedule trials. Therefore, more studies are needed to explain the aberrant behavior in methanol. In addition, studies in other solvents, such as DMSO, DMF, or even ethanol could be of use for both copper and nickel, as well as for other metals, as they may yield more information about this reaction and could yield more practical methods of producing these MONCs either with or without crystallization.

3.4 Investigation of PgC-Fe complexes using SANS

Like all of the other first row transition metals described in this text, iron salts can also be used to form colored complexes with PgCs. Like copper, iron does not require the presence of a base to form a complex, although the addition of a small amount of pyridine will lead to the precipitation of a characteristically deep blue powder. In solution, this complex strongly resembles ink, and for good reason: the blue "gall" inks used to write ancient manuscripts were coordination complexes of iron and various pyrogallol-like species, such as gallic acid. The structure of these complexes, however, remains unknown. Likewise, the structure of the iron-PgC complex has not as of yet been determined, or even a single crystal obtained, despite countless efforts by the author over the past five years. XRD, however, is not the only method that can be used to determine a structure. While the two MONCs in the previous section were both spherical, SANS can be used to study a wide variety of structural morphologies, and can likewise help determine the structure of a material. As such, SANS was also seen as a viable

method to investigate the structure of iron-PgC complexes. This study was done in conjunction with prompt gamma neutron activation analysis (PGAA) as a method to determine the metal to PgC ratio in the resultant structure. This work can also be found in published form elsewhere.[140]

3.4.1 Investigation of PgC-Fe complexes using SANS: experiment setup

PgC1Fe and PgC3Fe complexes were formed analogously to the other MONCs in this chapter; a 1:4 ratio of PgCx:$Fe(NO_3)_3$ in methanol was mixed with 14 equivalents of pyridine, which led to the formation of a blue powder that was removed by vacuum filtration, dried and used in a dry form for PGAA studies. For SANS studies, these materials were re-dissolved in deuterated DMSO at a 3% mass fraction. The studies were conducted at the same facility as in the previous section.

3.4.2 Investigation of PgC-Fe complexes using SANS: PGAA results

As the structure and elemental composition of pyridine and PgC is known, PGAA was used to deduce the Fe:PgC and Fe:pyridine ratios. This was done by determining the C:Fe and C:N ratios and working backwards. The PGAA results for PgC1Fe and PgC3Fe show that the materials have C:Fe ratios of 27.8:1 and 28.5:1 and C:N ratios of 28.1:1 and 29.2:1, respectively. This suggests that Fe and pyridine (the only source of nitrogen aside from the NO_3^- anion, which would behave similarly to pyridine as a ligand anyway) are present in a 1:1 ratio, which is consistent with what is seen in many PgC-based MONCs with pyridine ligands. However, in contrast to the 4:1 metal:PgC ratio typically seen in MONCs, the ratio in this complex was unexpectedly deduced to be 1.3:1, suggesting that this was a structurally novel complex.

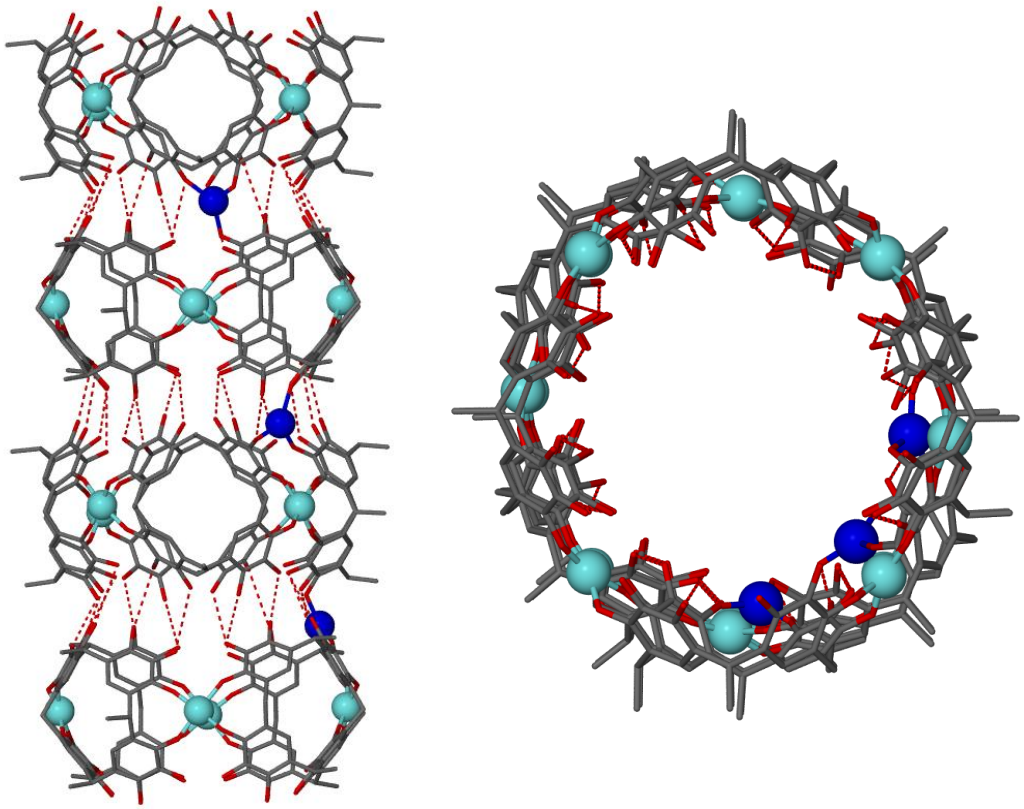

Figure 3.3: A proposed model for the PgC1-Fe coordination complex.

3.4.3: Investigation of PgC-Fe complexes using SANS: SANS results

As with PGAA, data analysis revealed distinct differences between the PgC1-Fe complex and the previously investigated MONCs. Unlike the MONCs, which are spherical, this complex fitted best to a cylindrical model, with a radius of approximately 7Å and a length of approximately 124Å. This indicates that the PgC-Fe complex is likely nanotubular in its morphology. This spatial information was used in conjunction with the PGAA results to construct a possible model for this complex (Fig. 3.3). This model is based on the PgC6-pyrene (non-covalent) nanotube due to a slightly larger, but generally similar diameter. Due to the low

metal:PgC ratio in this material, the coordination environment is significantly different than what is normally seen in other PgC complexes and features only four Fe^{3+} centers coordinating to a "disc" of four PgCs. Adjacent "discs" are connected through both coordinative and hydrogen bonds. While the radius of this complex is more or less consistent with a PgC-based coordination complex, the large length was somewhat intriguing. Interestingly, when the sample was centrifuged, the length of the nanotubular complex decreased as a function of centrifugation time, with a one minute centrifugation time decreasing the length to 45 Å and a two minute duration decreasing it further to 27 Å (the radius of this complex stayed constant at 7 Å). This may indicate that segments of the tube are not strongly bound to one another and can dissociate from one another with an appropriate stimulus (forces during centrifugation). Interestingly, an improvement in modeling statistics concomitantly occurred with centrifugation. This suggests that the original (non-centrifuged) solution likely contains a mixture of different nanotube lengths, which become uniformly shorter with centrifugation, thereby improving the statistics. Such discrepancy in length may therefore explain the difficulty in crystallizing this complex. Similar results were also seen when the complex was dissolved in deuterated methanol, suggesting that solvent identity did not play a factor in the structure of this complex, at least in this case.

3.4.4: Investigation of PgC-Fe complexes using SANS: variable acidity study

In the previous section, it was discovered that although pre-made MONCs were relatively stable and did not inter-convert into other species, MONCs that were produced *in situ* were not necessarily stable and equilibrium between the hexamer and dimer likely formed. This was hypothesized to be due to the presence of acidic reaction byproducts, such as nitric acid (HNO_3) and its pyridinium salt, which could potentially lead to the reversal of the MONC forming reaction. This

concept was therefore also investigated with the PgC1-Fe complex, albeit with an added layer of complexity. Instead of just mixing PgC, Fe^{3+}, and pyridine, additional samples were also prepared where extra nitric acid was added to the mix. The ratio of PgC1:Fe^{3+} was held at a constant 1:4 at a concentration of 10^{-3}M w.r.t. PgC1, while the molar ratio of pyridine to nitric acid was incrementally varied: 1:1, 1:0.8, 1:0.6, 1:0.4, 1:0.2, and 1:0 pyridine: nitric acid ratios were used for this study, with "1" indicating 14 equivalents W.R.T. PgC1. Methanol was used as the solvent in this study.

The samples with the lowest titer of nitric acid (1:0 and 1:0.2) led to similar results as before. The data fitted best to a cylindrical model with a radius of 6.5-7.0Å and a length to 24-25Å. The 1: 0.4-0.8 ratios, however, were found to fit better to a spherical model with a radius of 9.8 Å. As this is nearly identical to the radius seen with copper- and nickel-seamed hexameric MONCs, it stands to reason that increased levels of nitric acid therefore lead to the formation of an iron-seamed hexamer. The 1:1 ratio of pyridine:nitric acid, however, best fit to a spherical model with a diameter of 8 Å, which is closer in diameter to a dimer, rather than a hexamer. This is still slightly large for the typical metal-seamed dimer, and it can be envisioned that the dimers formed under these high-acidity conditions are non-covalent entities, rather than coordination complexes.

3.4.5: Investigation of PgC-Fe complexes using SANS: conclusion

This section presents our investigation of an ostensibly un-crystallizable coordination complex consisting of PgC and Fe^{3+}, and our efforts to determine its structure. The combined use of SANS and PGAA, which provided the dimensions and elemental makeup of the complex, respectively, were required to create a reasonable model for this complex. The model that was created was essentially nanotubular in shape, but with a distinct coordination environment due to a significantly lower metal-to-PgC ratio in this material. As such, this complex is novel in both

its geometry and in its coordination chemistry. Another finding was this complex's inter-conversion into the hexamer under slightly acidic conditions and its further inter-conversion into the dimer in an environment of higher acidity. In addition to its novelty, this finding may lead to efforts in crystallizing an iron-seamed MONC, as one can potentially follow the same synthetic methodology that was used to produce the hexamer here and reproduce it in the lab. Another result that may aid in the crystallization of this complex is the finding that the nanotube is fragmented into smaller lengths *via* centrifugation. This is helpful, as it produces a homogenous mixture of smaller nanotubes that are more likely to crystallize than a heterogeneous mixture of larger nanotubes. However, the most important impact of this work is that it shows that the structure of PgC assemblies does not necessarily have to come from scXRD studies, but can rather be deduced from techniques such as SANS and PGAA, among others.

3.5 Conclusion and Future Studies using SANS

This chapter presented a collaborative study that used small angle neutron scattering (SANS) as a method to investigate the metal-seamed entities based on PgCs in solution. In the first part of this chapter, the relationship between two species, the dimeric and hexameric metal-seamed MONC was explored under varying conditions, whereas in the latter part of this chapter, SANS was used to deduce the structure of a novel Fe^{3+}-based complex. The difference of its implementation in these two projects shows that SANS is a versatile method that is useful for a variety of studies. Indeed, it is one of the few ways in which metal-seamed PgC complexes can be studied in solution. As such, it can be a useful method by which PgC metal complexes can be screened both in terms of their structure and their properties in solution.

Both broad and narrow future studies can be envisioned as coming about from the work in this chapter. For starters, acidity was not used as a variable with the copper and nickel-seamed MONCs, so a repeat of these experiments with nitric acid as a variable (like in 3.4) would be of interest. Likewise, it is not known what happens to the iron nanotube/hexamer/dimer over time and at various temperatures, so studying this material while changing these variables would also result in a fuller understanding of this system. There are also several metal cations that have been used to form MONCs but that have not been fully investigated using SANS, such as zinc, cobalt, and manganese. A similar set of experiments for these metal cations would help to determine if metal identity plays a role in the ratio of dimer to hexamer at certain conditions, and if any trends can be observed. There are also many other variables that can be tested, so the possibility for SANS studies is almost infinite, even with what we already have. Furthermore, there are many other coordinating metal ions on the periodic table that can potentially be used to form MONCs, and that can be quickly screened to see if the complexes that they form are of interest. Perhaps the most interesting of these are potentially the lanthanide/actinide metal ions, as these cations are not limited to a hexa-coordinate ligand field. As such, they may produce truly unique coordination complexes with PgCs, but like iron, they have not been crystallized as of yet.

Chapter 4: Ligand-assisted linking of PgC-based MONCs

4.1: Modification of basic MONCs: introduction and rationale

So far in this text, all research efforts have focused on the synthesis and characterization of PgC-based MONCs, whether in the solid state or in solution. Indeed, the primary emphasis of past research with PgCs has also traditionally been placed on the discovery and characterization of new capsular entities. Tailoring of a MONC's properties to yield functional materials, however, has received much less attention. This is unfortunate, as synthetic control over the properties of a MONC is of incredible importance to the eventual goals of this research, as it is the only way of generating useful materials that serve a practical purpose.

Efforts to control a MONC's properties can be undertaken either pre- or post-synthetically. Pre-synthetic control comes about from choosing the appropriate PgC:metal cation:ligand:solvent system that will spontaneously lead to a MONC of the desired functionality (i.e. synthesis/*in situ* crystallization). While this seems relatively straightforward, the results from the previous chapter suggest otherwise; the dimer vs. hexamer problem is almost always encountered. Thus, although this is a simple method of generating the desired material, it can also be unpredictable. Alternately, MONCs can also be altered post-synthetically. Here, a (simple) MONC is generated, purified, and then used as a template for further chemistry. This approach potentially allows us to forego the dimer/hexamer uncertainty, and instead go directly to performing chemistry on purified samples of either the dimeric or hexameric material, whichever is preferred.

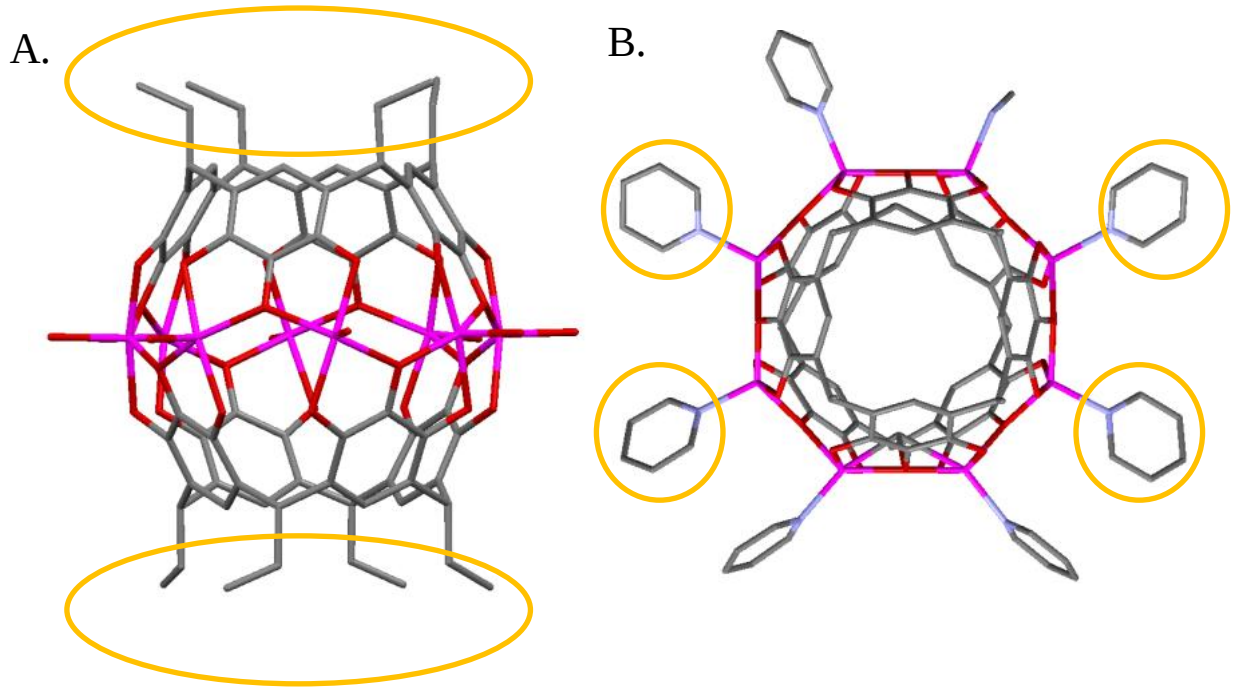

Figure 4.1: The properties of a MONC can be tailored for specific purposes via the pendant R-groups (A) or by the appropriate choice of peripheral ligands (B)

Aside from changing a MONCs identity (i.e. selecting specifically for a dimer or a hexamer) through the choice of metal cation or solvent system, there are theoretically two distinct methods of tailoring the properties of a MONC for a specific function. The first relies on using the pendant R-groups on the PgC lower rim as the functional unit or as a locus for additional chemistry (Fig. 4.1a). While this seems like a reasonable choice, it is limited by inadequate research performed on the subject. Only PgCs with simple R-groups, such as those of the n-alkyl and aryl category have been synthesized to date, and in general this paradigm (i.e. producing modifiable groups on the lower rim) has not been thoroughly explored. There is, however, a second method of modification that is significantly simpler; ligand exchange (Fig. 4.1b). Both dimeric and hexameric MONCs are, in essence, large coordination cages and because of this, the metal ions that seam the cage together are located on the outside, rather than

the inside, of the assembly. Each metal center is primarily bound to the PgC macrocycle, typically through four coordinative bonds. However, each metal center also coordinates to external (or peripheral) ligands. Previous research efforts and those discussed in the first chapter show that the identity of these ligands is not immutable, but can change due to varying synthetic conditions. As such, changing the ligands present on the outside of the nanocapsules is yet another way of changing the chemistry of the MONC. As a proof of principle, and as a way to generate new and useful materials, this paradigm was explored as a method of generating metal-organic frameworks (MOFs).

4.1.1 MOFs: a brief background

Metal-organic frameworks, or MOFs, are crystalline framework solids that are composed of both metal and organic components. The methodologies used in the construction of MOFs are intricately tied to the field of coordination chemistry, as at their most basic, MOFs are just another class of coordination complexes. For this reason, the name "coordination polymer" is often used interchangeably with "MOF" to describe these materials. The immense research efforts that have gone into the synthesis and use of MOFs can largely be attributed to the successes of zeolites, another class of (inorganic) framework compounds. Zeolites have been used extensively for at least the last five decades for a wide range of uses, such as catalysis, ion exchange and guest incarceration.[141] However, as they are solely inorganic entities, and are composed largely of tetrahedral oxo-silicon and oxo-metal bonds, there are limitations to the degree to which they can be "tailored" to fit specific purposes.[1,142,143] The structural limitations imposed on solely *inorganic* framework solids gave rise to research efforts that sought to develop hybrid inorganic-organic materials, which have the rigidity of an inorganic framework

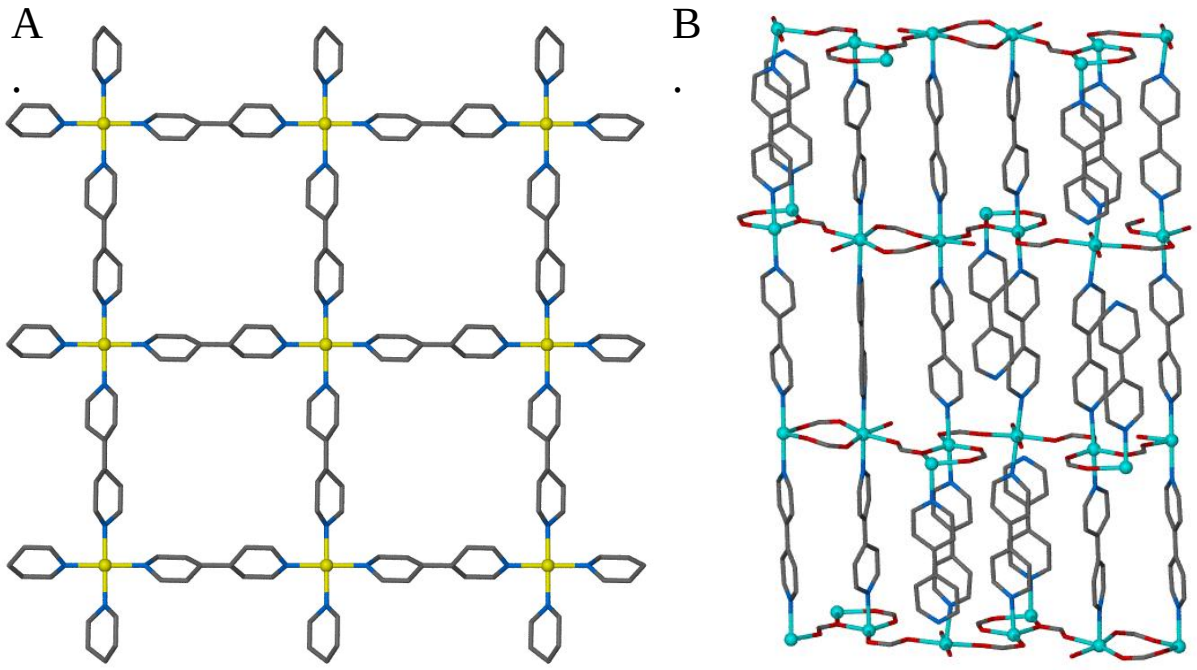

Figure 4.2: A simple two-dimensional MOF constructed from 4,4'-bipyridine linkers and copper(II) nitrate (A) and a three-dimensional zinc(II) MOF used for cyanosilylations consisting of Zn-formate layers bridged with bipyridine ligands (B)[144]

but also the flexibility to accept various organic components. One of the strategies employed was the "coordinative framework", which is, again, the basic premise of a MOF.

As implied by their name, MOFs are composed of two parts: a "metal" and an "organic" component. The "metal" component is typically either a metal or metalloid cation (electron pair acceptor), whose role is to coordinatively bond to ligands (electron pair donors). The ligands, then, are the "organic" component in a MOF, and can vary tremendously in number, shape, and functionality. However, one trait that distinguishes the ligands in a MOF from those in a standard coordination complex is that at least one must be a divergent ligand. A divergent ligand possesses multiple donor sites, but in contrast to a typical polydentate ligand such as EDTA, where the donor sites typically bind simultaneously to the same metal, all of the donor sites on a

divergent ligand do not simultaneously coordinate to one acceptor cation. Instead, their function is to simultaneously coordinate to multiple cations, thereby bridging (or linking) them together. Commonly used divergent ligands are those of the 4,4'-bipyridyl and polycarboxylate families of molecules, as they are both easy to synthesize and have proven to be versatile linking agents.[1,145] As most metal cations have multiple coordinative sites, they can act as acceptors for multiple ligands. Thus, divergent ligands and metal cations can interact in such a way that they are linked in one, two, or three dimensions *ad infinitum*. The end result of linking is the formation of a framework, where the metal cations act as the vertices connected by a rigid and repeating network of ligands (see Fig. 4.2 for examples).[1] Another commonly used analogy is the "node and net", where the metal ions are nodes that connect to one another (*via* ligands) to form a net.[146]

A consequence of the framework's rigidity is the formation of yet another structural component: structural voids. Voids occur in the areas of the framework that are not occupied by ligands or the metal cation, and are perhaps the most functional of the three structural components. Indeed, the formation of nano-scale voids is where the practical utility of MOFs primarily lies. The size and shape of the voids is largely determined by the structure of the framework, which is usually at least somewhat channel-like. This means that molecular guests can, at least theoretically, travel throughout the entirety of the crystalline framework and interact with the components of the MOF in bulk, rather than just with the external crystalline surface. Because the voids are on the order of Ångstroms in diameter, MOFs have an extraordinarily large surface area with which guest species can interact. The interaction of guests with either the ligands or the metal centers is, then, what leads to the chemical utility of MOFs.

Most of the time, however, the voids in a framework are actually occupied by solvent molecules, which enter the MOF during its synthesis. These take up valuable space, thereby prohibiting guest migration, and largely rendering the MOF useless. This problem is often remedied by a process termed "activation," which entails either the partial or complete removal of solvent from the framework.[1] Oftentimes, the removal can simply be done by heating the material in a vacuum, in order to eliminate the solvent by evaporation. In other cases, however, heating can lead to collapse of the framework, so softer methods must be used. These methods include replacement of the (initial) solvent with one that will evaporate at a lower temperature (i.e. replacing DMSO with DCM etc.), thereby requiring milder heating, or by treating the MOF with supercritical carbon dioxide, which effectively pushes the solvent out and replaces it with an easily removable gas.[147] Regardless of the method used, activation leads to the evacuation of the channels throughout the MOF and therefore allows guest accessibility to the interior of the crystal.

Guest binding in MOFs is actually quite poorly understood, but the capacity for MOFs to adsorb guests can be divided into macroscopic and microscopic factors. The macroscopic factors are physical properties, such as the surface area of a MOF as well as the size of its pores.[148] The microscopic factors are the properties that allow sorption to take place in the first place, namely the chemistry of the ligands and metal centers. Thus, by controlling the nature of its components, one can theoretically control the guest binding properties of a MOF. Interaction with the MOF on a microscopic scale occurs either through absorptive absorption, where the guest binds through non-covalent forces, such as VDW, π-interactions, or hydrogen bonding, or through reactive adsorption, where the guest forms chemical bonds with specific functional groups located within the MOF, such as a reactive center on a ligand or an open coordination site

on the metal.[149] In adsorptive adsorption, changes in pressure and temperature are often enough to release the guest from the interior of the MOF, but with reactive adsorption, further chemical manipulation of the material is necessary to release the guest. This more permanent mode of adsorption is important in applications such as the removal of hazardous materials from a waste stream, whereas less permanent adsorption is useful in applications such as hydrogen storage or in chromatography.[148-150]

As mentioned previously, the appeal of working with MOFs is their large internal surface area. One of the most basic uses for these materials is in the sorption of gaseous species.[141] This includes gases such as hydrogen and methane, which are valuable for their potential use as fuels, as well as other gases such as SO_2 and NO_2, which are industrial pollutants. In addition, MOFs can harbor catalytically active sites if functionalized appropriately, particularly if they contain coordinatively unsaturated metal sites.[144,151] Thus, one of the promising applications of MOFs is in an industrial setting, where they replace traditional catalysts. Lastly, because of the variability in the size and shape of MOF voids, they can be used in chemical separations, particularly as stationary phases in GC and HPLC.[150-152]

4.1.2: MOFs and MONCs: some perspective

One recent trend in the development of MOFs has been the replacement of standalone metal cations with metal clusters. The use of clusters is often advantageous as they largely disallow framework interpenetration (catenation) due to their larger size, a problem often encountered in MOFs constructed from standard monometallic building blocks. This is advantageous as it theoretically allows for a greater degree of guest penetration into the framework. In addition, the specific geometries of metal clusters can help impart some degree of predictability to the synthesis of MOFs. This predictability is enhanced by the fact that the

clusters can be pre-prepared prior to linking, imparting a degree of control with respect to the components of the final structure. Finally, the use of metallic clusters can impart a greater degree of catalytic activity to the MOF, particularly if some of the metal centers are coordinatively unsaturated.

One of the first and most widely used metal clusters for MOFs was the Zn_4O cluster.[153,154] When linked with different polycarboxylates, it can be used to create a wide array of different MOFs that are both thermally and vacuum-stable. This discovery spurred the investigation of other similar (and different) compounds for MOF nodes, including large polymetallic cluster compounds such as the polyoxometallates.[155-157] The diversity of the materials currently used for such efforts spurred us to use our own metallic cluster compounds, namely metal-seamed PgC nanocapsules as building blocks for MOFs.

While the purposeful construction of MOFs out of PgC-based nanocapsules would seem to be a wholly novel idea, much of the inspiration for such efforts can be found in both the aforementioned works on metallic clusters as well as in previous studies conducted with PgC-based MONCs. For example, the first reported PgC-based MONC did, in fact, crystallize as a MOF-like assembly.[118] This MONC was a hexameric copper-seamed nanocapsule that (importantly) was constructed from the PgC_3OH macrocycle. Refinement of the crystal structure revealed that some of the terminal hydroxyl groups from the hydroxylpropyl "tails" of each hexameric MONC coordinate to Cu^{2+} centers on neighboring hexamers, thus forming a one-dimensional coordination polymer (Fig. 4.3a).

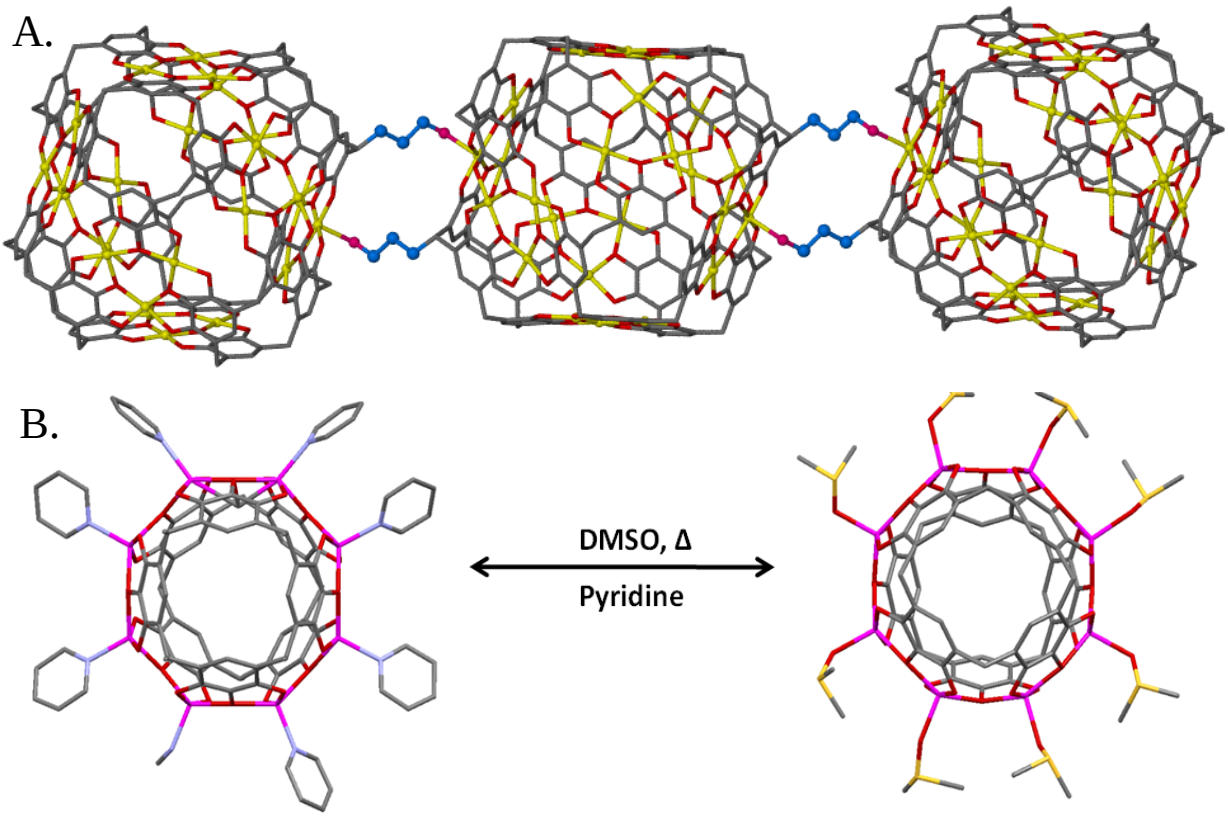

Figure 4.3: Linking seen in previously reported PgC3OHCu hexameric assembly (A) and results from the work of Power et al. on ligand exchange in dimers (B)

Another source of inspiration came with the discovery of the zinc-seamed dimer and its subsequent exploration. Power et al. showed that by heating zinc dimers with peripheral pyridine ligands in DMSO, the pyridine ligands could be distilled off and, on account of its higher boiling point, replaced with DMSO ligands.[127] This process could then be carried out in reverse by cooling the mother liquor and titrating pyridine back into the solution (Fig. 4.3b). One important finding from this was that the process occurred without rupturing the capsule; NMR evidence showed that the unique guest species stayed encapsulated within the capsule. These two pieces of published work concomitantly produced the motivation for this project, as they not only

showed that capsules would, in fact, link together given the proper functionality, but that this could potentially be done both pre- and post-synthetically. 4,4'-bipyridine (bpy) was a logical choice of a linking ligand for these studies, due to its application as a unidirectional charge transfer ligand in MOF's, and its similarity to pyridine, a ligand which is known for its high affinity for PgC-based MONCs. Although other ligands, such as 1,4-pyrazine, 1,3,5-triazine and dicarboxylic acid salts were also (unsuccessfully) pursued as linking ligands, the use of bpy led to several examples of linked nanocapsules, which are discussed here in detail.

4.2 Linking dimeric nanocapsules using 4,4' bipyridine

Our first attempt at post-synthetically linking nanocapsules was performed with the copper- and zinc-seamed dimeric MONCs based on *C*-methylpyrogallol[4]arene (PgC1) as the macrocyclic precursor. Dimeric MONCs bearing the *C*-methyl functionality were thought to be ideal linking candidates for several reasons. For one, their synthesis and purification is rather simple and straightforward, which has been detailed previously (chapter 2). Second, the ligand exchange studies performed by Power et al. were conducted on dimeric nanocapsules, rather than hexameric, so the groundwork for ligand exchange with this particular class of nanocapsules had already been laid. Third, it was inferred that by starting with a macrocycle outfitted with *C*-methyl R-groups, dimeric packing within the crystal would be simplified, which could potentially help with crystallization. This inference comes from past experience in crystallizing dimeric nanocapsules, which shows that PgC-based MONCs with C-alkyl R-groups longer than approximately 3 carbons long do not pack particularly well within a crystal. This is likely due to the many possible positions that the longer alkyl chains can occupy in the crystal, which leads to crystalline disorder and can even limit crystallization altogether. Indeed, reported or not, there

are few crystal structures of MONCs with pendant arms longer than six carbons. Thus, to avoid these problems it is advantageous to use as short a pendant R-group as possible, with *C*-methyl being the simplest option. Although one example of a MOF constructed from MONCs bearing a non-*C*-methyl R-group will be discussed, all other efforts to synthesize MOFs from anything other than *C*-methyl-tailed PgC1 resulted in failure. Thus, the initial choice of *C*-methylpyrogallol[4]arene as the macrocycle was perhaps the most important decision in the success of this study.

4.2.1: Linking copper dimers with 4,4'bpy

Attempts at linking copper dimers were, for no specific reason, performed first. This led to two unique crystal structures, a one-dimensionally linked assembly[158], and a second two-dimensionally linked assembly. The first structure relied on the crystalline dimer formed from DMSO as a starting reagent. However, crystals of the second material were produced *in situ*, where the dimer was simultaneously synthesized and linked.

4.2.1.1 Synthesis and characterization of one-dimensional chains of copper dimers: synthesis and crystallization

PgC_1 (0.608g, 1 mmol) was dissolved in 10 mL of a 1:1 DMSO:MeCN solution. The solution was heated to 80°C and $Cu(OAc)_2$ (0.727 g, 4 mmol) was added, immediately changing the color from a light pink to dark reddish brown. The solution was stirred for an additional 10 minutes to dissolve all $Cu(OAc)_2$ and allowed to cool. Large reddish brown crystals of the native copper-seamed dimer formed after approximately 24 hours. These crystals were then collected and re-dissolved in DMSO. 4,4'-bipyridine (0.313 g, 2 mmol) was added following 10 minutes of

stirring, changing the color of the solution from reddish brown to brown. Small brown crystals found to be the one-dimensional MOF were formed on slow cooling over several days. scXRD structural analysis was performed using synchrotron radiation at Berkeley National Laboratory.

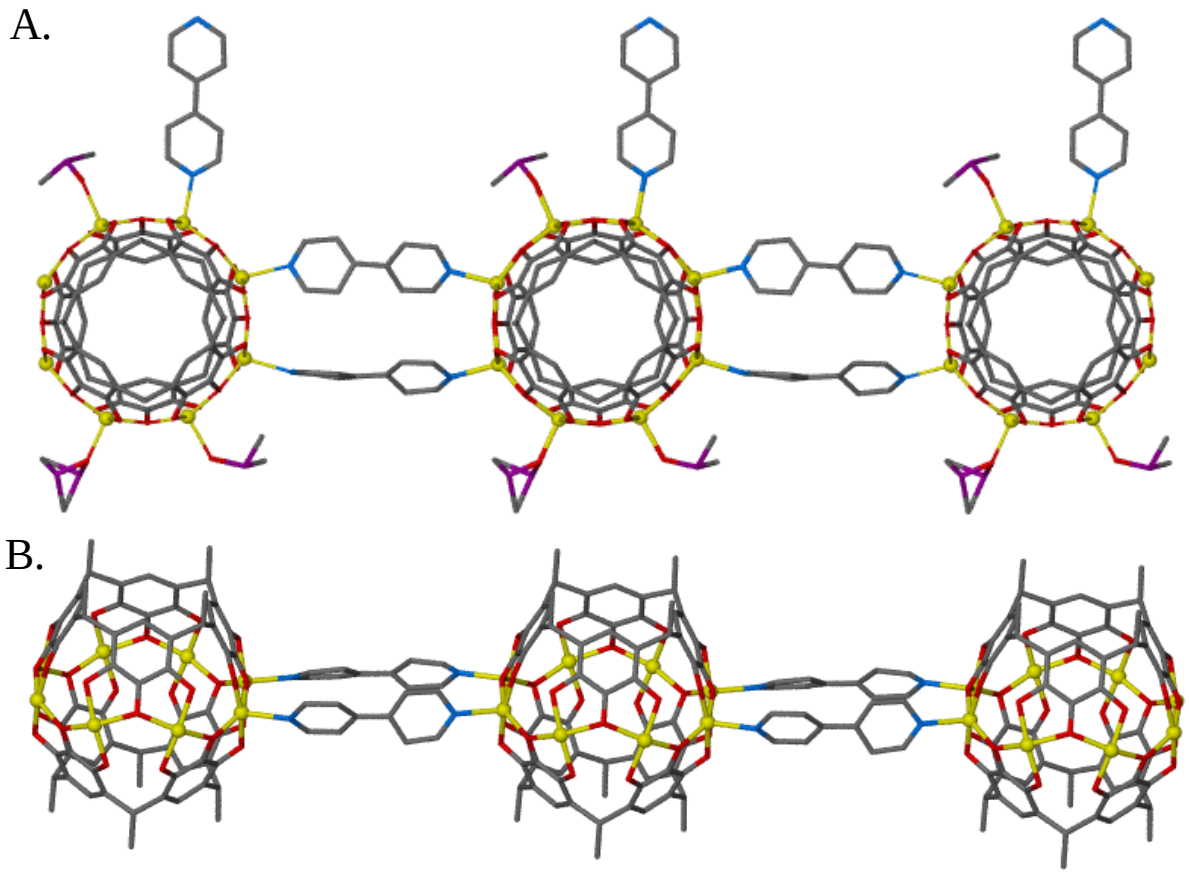

Figure 4.4: A single strand of the 1D-linked copper dimer (**4.1**) when viewed along the 011 (A) and 1 -1 0 (B) lines

Crystal data (4.1): $C_{102}H_{96}Cu_8N_6O_{28}S_4$, M = 2490.41, Brown Plate, 0.05 × 0.03 × 0.01 mm^3, triclinic, space group P-1 (No. 2), a = 15.268(4), b = 15.399(4), c = 26.583(6) Å, α = 103.563(3), β = 96.004(3), γ = 97.402(3)°, V = 5966(2) Å^3, Z = 2, D_c = 1.386 g/cm^3, F_{000} = 2540, Bruker APEX II CCD Diffractometer, synchrotron radiation, λ = 0.77490 Å, T = 100(2)K, $2\theta_{max}$ = 41.4º, 29193 reflections collected, 9307 unique (R_{int} = 0.0908). Final *GooF* = 1.290, *R1* =

0.0928, *wR2* = 0.2289, *R* indices based on 5524 reflections with I >2sigma(I) (refinement on F^2), 638 parameters, 44 restraints. Lp and absorption corrections applied, μ = 1.536 mm^{-1}.

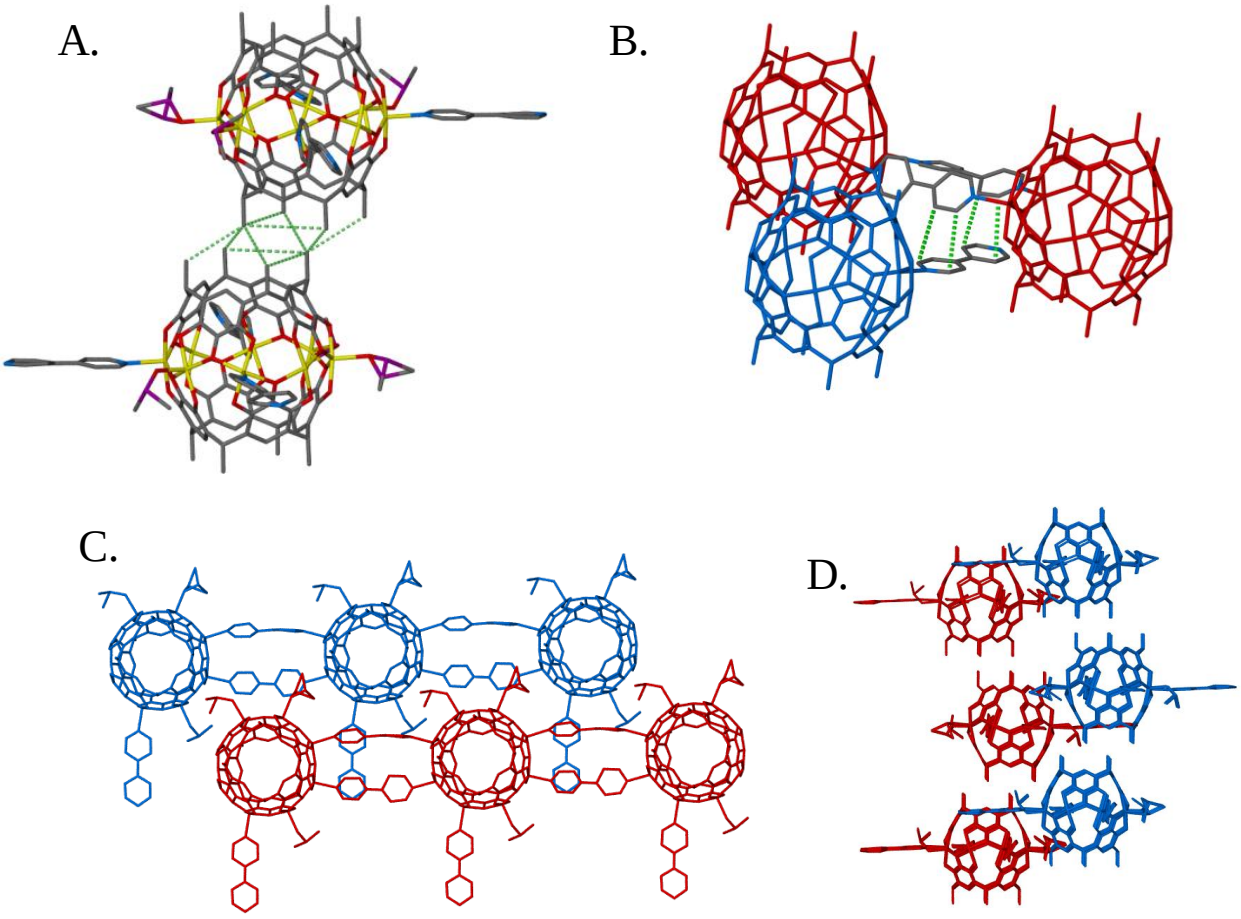

Figure 4.5: Non-covalent interactions in 3.1: interactions between the C-methyl tails (A) and the bpy ligands (B) both contribute to the overall structure (C, D)

4.2.1.2 One-dimensional chains of copper dimers: discussion

Our first attempt at capsular linking led to a unique one-dimensional MOF (**4.1**) that consists of a central dimer linked to adjacent dimers *via* bpy ligands. In this material, N-donor atoms from bpy ligands displace DMSO ligands on five of the eight Cu^{2+} centers. Of these five

bpy ligands, four act as linkers on opposite sides of a given capsule to form the 1-D coordination polymer (Fig. 4.4). The remaining coordinated bpy molecule, which lies perpendicular to the other four bpy ligands does not participate in linking. This bpy does seemingly take part in π-stacking interactions (closest C-C contacts: 3.34 Å and 3.60 Å) with linking bpy ligands from adjacent strands (Fig. 4.5b). Another non-covalent interaction that can be seen on symmetry expansion of the structure is the contacts between the *C*-methyl groups of the "main strand" and another unique adjacent strand (C-C distances 3.98, 4.08, 4.09 Å; Fig. 4.5a). The combination of these two interactions leads to an offset pattern of dimeric stacking, which gives the layers that are formed a "corrugated" appearance (Fig. 4.5c, d). These layers are connected to adjacent layers *via* the π-stacking interactions that were previously discussed. Other non-covalent interactions, involving both coordinated and non-coordinated DMSO molecules are also surely present, but are difficult to describe and enumerate.

PgC1CuDMSO dimer					1D linked PgC1Cu dimer				
Metal #	**Ligand**	**θ_1**	**θ_2**	**τ5**	**Metal #**	**Ligand**	**θ_1**	**θ_2**	**τ5**
Cu1	DMSO	171.75	151.76	0.333	Cu1	4,4'-bpy (l)[a]	169.93	148.94	0.350
Cu2	DMSO	173.05	154.59	0.308	Cu2	DMSO	170.18	151.12	0.318
Cu3	DMSO	173.16	152.79	0.340	Cu3	DMSO	171.42	152.14	0.321
Cu4	DMSO	171.81	152.23	0.326	Cu4	4,4'-bpy (l)[a]	169.04	147.84	0.353
Cu5	DMSO	171.09	151.05	0.334	Cu5	4,4'-bpy (l)[a]	169.24	149.48	0.329
Cu6	DMSO	171.08	151.37	0.329	Cu6	DMSO	172.55	153.32	0.321
Cu7	DMSO	172.25	151.66	0.343	Cu7	4,4'-bpy (u)[a]	172.82	152.53	0.338
Cu8	DMSO	171.53	151.3	0.337	Cu8	4,4'-bpy (l)[a]	171.19	151.45	0.329
Average				**0.331**	**Average**				**0.332**
StD				**0.011**	**StD**				**0.014**

Table 4.1: Comparison of the τ5 values of a PgC1Cu dimer and 1-D linked assembly (4.1)

To determine if linking had any influence on the coordination geometry within the capsule, an average τ_5 value was calculated for the Cu^{2+} centers in this structure. An average value of 0.33 for the copper centers shows that the displacement of DMSO ligands by bpy does not have a significant effect on overall Cu^{2+} coordination geometry, as this number is quite similar to our previous results with the standalone copper dimer. Indeed, individual τ_5 values for specific Cu centers did not show any logical trend that would indicate a difference between DMSO and bpy ligands. This consistency supports the notion that, at least in this case, ligand exchange does not alter the overall dimeric Cu^{2+}-PgC capsule framework, allowing for the use of these moieties as flexible building blocks in the potential formation of larger and more complex assemblies.

4.2.2 Two-dimensional assemblies consisting of copper dimers

As it was clear from the synthesis of **4.1** that linking dimers through peripheral ligands was indeed possible, we began to seek a method that would allow for the construction of MOFs with a higher dimensionality (i.e., two-dimensional arrays). The most obvious method to create such a material was to increase the amount of bpy that was added to the pre-made MONC solution. When this was attempted, however, either precipitate or microcrystalline material formed. Because of this failure, *in situ* crystallization methods in DMSO were employed. Through these studies, it was quickly realized that the order of addition and the overall concentration of the reagents was of utmost importance to the successful generation of this material; adding the bpy to Cu^{2+} prior to the addition of PgC1, or working at concentrations exceeding 10^{-2}M w.r.t. PgC1 would lead to the formation of various non-nanocapsular (simple) MOFs. However, proper order of addition and work at low concentrations produced mixtures of

various dark brown block-like crystals, a color and morphology that is representative of copper dimers. Although the crystals that formed in this way were weakly diffracting, crystallographic data on some of the larger crystals was nevertheless collected on two separate occasions. Both samples had very similar unit cell parameters and formed under similar conditions, so it would stand to reason that the material was the same in both cases. Unfortunately, it was discovered that in addition to being weakly diffracting, these crystalline materials were also polycrystalline. Due to a combination of these factors, it was not possible to work up the crystallographic data to the point of publication. However, a partial structure was nevertheless produced, which showed that a two-dimensional framework of dimers had indeed been created.

4.2.2.1 Synthesis and characterization of two-dimensional chains of copper dimers: synthesis and characterization

All solutions in the following protocol were made in DMSO. 0.08 mL of a 1M $Cu(NO_3)_2$ solution was added to 2 mL of 0.01M PgC1 solution in a scintillation vial. The solutions were briefly stirred, resulting in a change in color from pink and blue to dark red. 0.08 mL of 1M pyridine solution, followed by 0.16 mL of 4,4'-bipyridine solution were then added, resulting in a change of color from dark red to dark brown. The scintillation vial was capped and crystallization occurred after several days.

Crystal data (4.2): $C_{19.33}H_0Cu_{1.33}N_{1.33}O_5S_{1.33}$, M = 458.34, brown plate, 0.35 × 0.15 × 0.05 mm^3, orthorhombic, space group $Pmn2_1$ (No. 31), a = 31.338(6), b = 14.418(3), c = 25.028(5) Å, V = 11309(4) $Å^3$, Z = 12, D_c = 0.808 g/cm^3, F_{000} = 2704, Bruker SMART CCD area detector, MoKα radiation, λ = 0.71073 Å, T = 173(2)K, $2\theta_{max}$ = 46.3°, 7235 reflections collected, 7235 unique (R_{int} = 0.0000). Final *GooF* = 2.174, *R1* = 0.2234, *wR2* = 0.5369, *R* indices based on 4519

reflections with I >2sigma(I) (refinement on F^2), 356 parameters, 49 restraints. Lp and absorption corrections applied, μ = 0.852 mm^{-1}. Absolute structure parameter = 0.9(2) (Flack, H. D. *Acta Cryst*. **1983**, *A39*, 876-881).

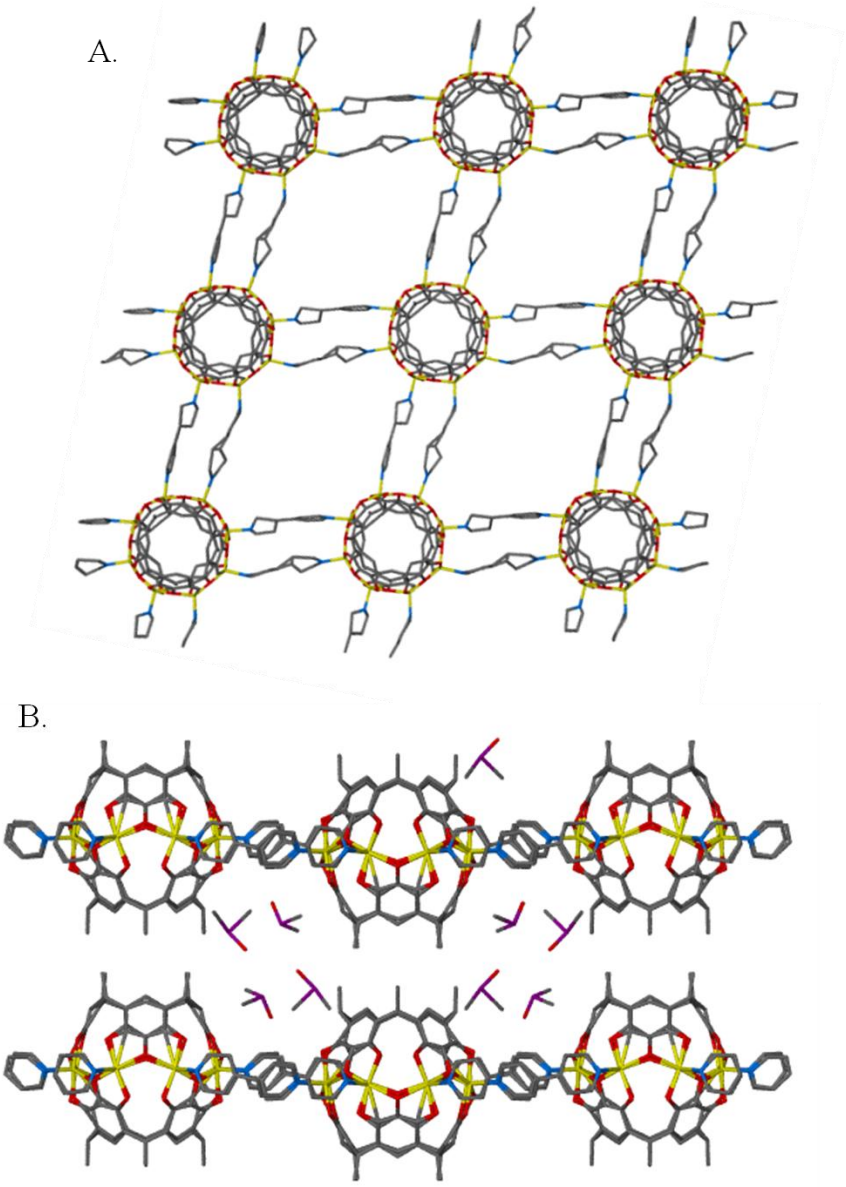

Figure 4.6: Illustration of 2-D linked copper dimer (4.2) when viewed along the b (A) and c (B) crystallographic axes.

4.2.2.2 Two-dimensionally linked copper dimers: discussion

As predicted, a higher concentration of bpy ligand led to the formation of a two-dimensional MOF based on PgC1-Cu^{2+} dimers (**4.2)**. In this structure, all DMSO ligands have been replaced by bpy ligands, which are all used to link adjacent dimers (Fig. 4.6). In this motif, there are formally four bpy ligands per dimer due to ligand sharing. The linking behavior in this structure is similar to that seen in the one-dimensional analog **4.1**, where pairs of bpy ligands are used in coordinative binding to a total of four neighboring dimers. However, the bpy ligands do not bind to coppers in a straight-on fashion, but rather over a slight diagonal. This coordinative peculiarity leads to the formation of a distorted rhombus-shaped lattice, rather than a square-shaped lattice as would be predicted (Fig. 4.6a). The rhombus thus formed is composed of dimers at the vertices and linkers forming the sides. The area inside these rhombuses is composed of "void" space, or, more realistically, disordered solvent molecules whose occupancy cannot be easily resolved using crystallographic means.

As the MOF itself is two-dimensional, it was of interest to determine how layers of this material stacked together, or more specifically, whether any channel-like motifs could be found on symmetry expansion of the structure to multiple layers. Symmetry expansion along the crystallographic b-axis showed that the packing pattern of the two-dimensional sheets differs greatly from the one-dimensional analog. Instead of an offset packing arrangement, the individual rhombuses that make up the framework are positioned directly on top of one another (Fig. 4.6b). As such, the only non-covalent interaction between layers is the interaction of *C*-methyl groups on the lower rim of the PgC macrocycle (C-C distances: 3.6-4.0 Å). As the π-stacking interactions between coordinating and non-coordinating bpy molecules that were seen in the one-dimensional analog **4.1** are absent, it can be argued that this type of packing

maximizes the intra-molecular interactions between adjacent layers, and is perhaps the only efficient way of packing two-dimensional sheets composed of dimeric nanocapsules. This packing arrangement may also help explain the high degree of crystal twinning in this material, as the layers are liable to slip relative to one another.

One important result of this packing motif is that the voids at the center of the rhombuses line up and create channels throughout the structure. These channels propagate unimpeded along the b-crystallographic axis, but are also connected to one another between structural pairs of bpy molecules in adjacent layers, creating a three dimensional network of channels. Much of the space between bpy molecules, and therefore between rhombuses, however, is occupied by "well"-ordered DMSO molecules as well as some higher electron density peaks that may correspond to a higher occupancy of solvent molecules. Indeed, the vast majority of the electron density "q" peaks that could not be assigned to any specific solvent were located within this area, rather than the much greater area found within the center of the rhombus. Thus, it can be argued that the channels effectively encounter barriers at these junctions, and thus are essentially finite along two of the three dimensions, but infinite along the third (although proving this would likely be impossible due to the disorder of the structure).

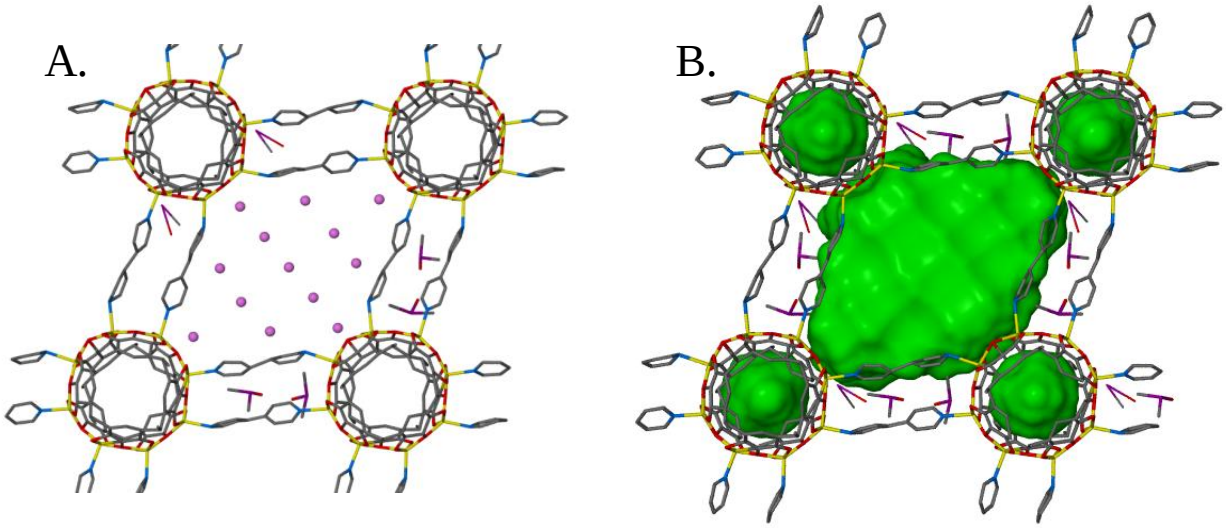

Figure 4.7: A segment of the channel in **4.2** was blocked with dummy atoms (A). Subsequent analysis using MsRoll shows the location of void spaces within the structure (B) corresponding to the interior of the dimers and the blocked-off cavity (Accessible volume: 757 $Å^3$)

Although a molecular channel does not occupy a discrete volume, molecular channels within a crystalline lattice are necessarily constructed of finite repeating units, and as such, the void volume within a repeating unit can be calculated. In this particular MOF, the repeating unit for the channel was the space occupied from one two-dimensional layer to the next. Determining the void volume of this space could potentially help with future studies that would seek to use **4.2** for gas sorption or separation. Although there are several programs that can be used to determine volumes from crystallographic data files, the program MsRoll, which interfaces directly with X-seed, was used for this purpose.[134] This program is used to quantify the volume enclosed by various molecular species, such as nanocapsules, host-guest complexes, and MOFs. It does so by rolling an imaginary ball, or probe, with a user-designated radius within the cavity, and records surface area of the molecular space that it encounters. The surface area is then used

by the program to compute a volume for the cavity. As previously noted, MOFs contain open channels and do not possess discrete cavities. However, the volumes of these channels can still be quantified by appropriately blocking off the ends with imaginary scaffolds of atoms, thereby keeping the probe contained within this imaginary cavity (Fig. 4.7a). In this case, a scaffold of imaginary atoms with a radius of 3 Å was used as a wall to prevent the probe from leaving the test volume. With a probe radius of 1.25 Å, this treatment led to a contact volume of 1061 $Å^3$ and an accessible volume (i.e., minus a 1.25 Å internal "shell") of 757 $Å^3$ per structural unit (Fig. 4.7b). This volume will be useful as a basis of comparison to the structure in the next section, which also features two-dimensionally linked sheets of dimers.

4.2.3 Using zinc-seamed dimers as building blocks in MOFs

Due to our success at generating one- and two-dimensional linked arrays of copper-seamed dimers with 4,4'-bipyridine, it was envisioned that zinc-seamed dimers could likewise be used as unique structural building blocks in MOFs. Of particular interest was whether or not the morphology of the resultant assembly would be similar to that seen with Cu^{2+} or altogether different. Analysis of the octametal belt coordination geometry among various dimeric species shows that dimers generated from different transition metals display clear differences in their coordination environments. In particular, analysis of $\tau 5$ for various metal-seamed dimers shows that there is a significant change in the coordination geometry when one goes from the copper-seamed to the zinc-seamed dimeric MONC. It was therefore hypothesized that if a MOF could be generated from zinc-seamed dimers, it would likewise be geometrically different from the previously synthesized copper-based analogs.

4.2.3.1 Two-dimensionally linked zinc dimers: synthesis and characterization

The rccc "cone" conformer of the *C*-methylpyrogallol[4]arene (PgC1) macrocycle was used for this endeavor. The primary reasoning for this was that it worked on multiple occasions with copper and was thus expected to likewise work for zinc. Furthermore, it would be rational to use it again for the sake of brevity, so that any resultant MOF could be quickly compared to the previous results with copper. A purified sample of dimeric zinc-seamed capsule was used as a precursor for these studies. This material was synthesized in a manner that was similar to, but slightly different from published methods. A solution of PgC1 was added to an acetonitrile solution of $Zn(NO_3)_2$ and pyridine, leading to the precipitation of a yellow solid, which is indicative of dimer formation (typical ratio: 1:4:14 respectively at a $1\text{-}2.5*10^{-2}$ M solution concentration w.r.t. PgC1). The yellow precipitate was removed *via* vacuum filtration, dried in a dessicator overnight and used without further purification. This material was then dissolved in hot dimethyl sulfoxide (DMSO) at a 10^{-2} M concentration, and mixed with a DMSO solution of bpy, in a ratio of 2.5 bpy per zinc dimer. On cooling, small yellow block-like crystals grew over a period of several hours to several days, depending on the concentrations of the reagents. Several other attempts at growing crystals with either higher or lower ratios of dimer to bpy were also attempted, and some of these also led to crystal growth. However, crystals grown using all ratios were in all likelihood isostructural, as they did not differ in their unit cell parameters. Alternately, the same material (i.e. with identical unit cell parameters) could be formed using *in situ* crystallization, wherein PgC_1, $Zn(NO_3)_2$, and bpy were mixed in a hot DMSO solution, with crystal formation apparent after several hours of cooling. This, in fact, led to a change in the guest occupancy from pyridine to DMSO, which was significantly more interesting due to the guest's coordinative behavior. This behavior is discussed in more detail below.

Crystal data (4.3): $C_{29.50}H_{21.50}N_{2.50}O_{7.50}S_{0.50}Zn_2$, M = 677.76, yellow prism, 0.10 × 0.05 × 0.05 mm^3, orthorhombic, space group *Pban* (No. 50), a = 20.780(2), b = 34.908(4), c = 14.4254(15) Å, V = 10464.3(19) $Å^3$, Z = 8, D_c = 0.860 g/cm^3, F_{000} = 2752, Bruker Apex II CCD diffractometer, synchrotron radiation, λ = 0.77490 Å, T = 100(2)K, $2\theta_{max}$ = 45.7°, 49286 reflections collected, 5514 unique (R_{int} = 0.0759). Final *GooF* = 1.514, *R1* = 0.1053, *wR2* = 0.3531, *R* indices based on 3603 reflections with I >2sigma(I) (refinement on F^2), 497 parameters, 134 restraints. Lp and absorption corrections applied, μ = 1.213 mm^{-1}.

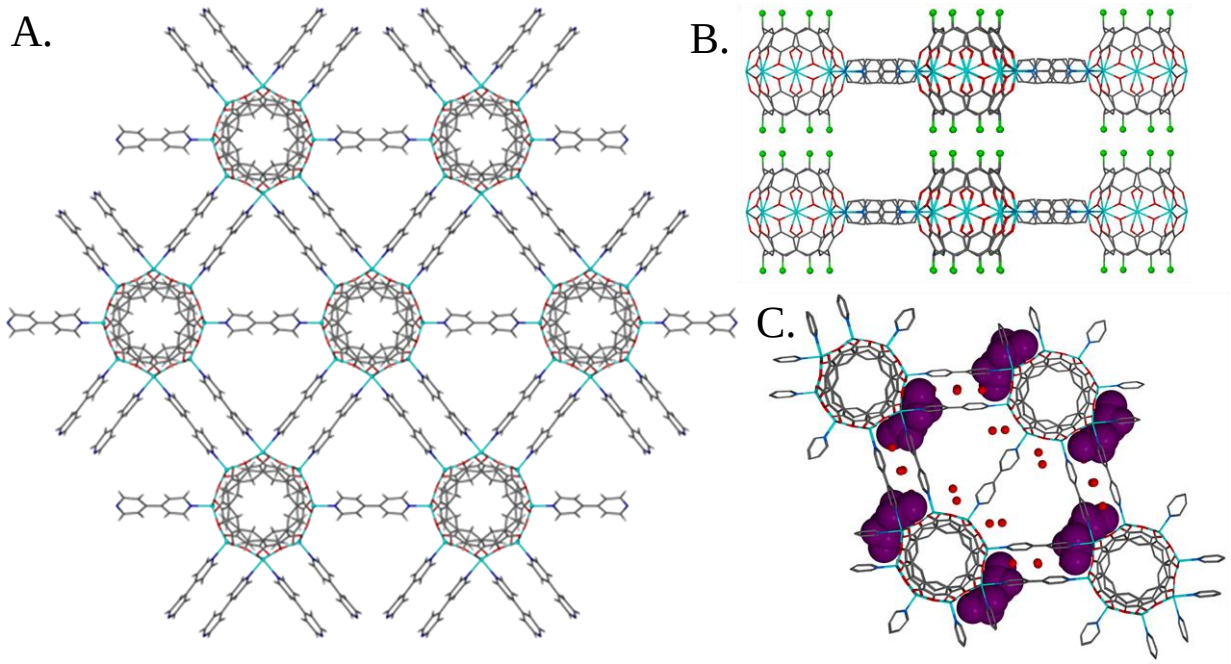

Figure 4.8: View of 2-D Zn MOF (**4.3**) along the crystallographic c axis and a axis, respectively (A, B). C-methyl groups of the pyrogallol[4]arene macrocycle shown in green. C shows arrangement of solvent within the superstructure: ordered DMSO molecules are shown in violet and disordered solvent is shown in red

4.2.3.2 Two-dimensionally linked zinc dimers: discussion

Structural refinement of the single crystal X-ray diffraction data reveals that the result of both synthetic procedures is a novel two-dimensional MOF (**4.3;** Fig. 4.8). This MOF is distinctly different from the two dimensional copper-seamed analog in several ways, most notably in the coordination geometry of the metal centers, number of linking ligands, and the geometry of voids within the structure.

The asymmetric unit of **4.3** contains one half of a PgC1 macrocycle along with three metal centers, one at full occupancy and two at half occupancy, each bearing one half of a bpy ligand. Structural expansion shows a complete dimeric capsule coordinatively linked to six adjacent dimers *via* 10 bpy ligands. Each dimer is connected to two of its neighbors *via* a single bpy unit, and to the other four by two bpy units. Unit cell expansion along the a and b crystallographic axes shows that the long-range order of the structure exhibits a centered hexagonal lattice with the interstitial space between dimers and bpy linkers partially occupied by solvent molecules (Fig. 4.8a). Of these, a crystallographically unique and ordered DMSO molecule lies on the periphery above and below pairs of bpy molecules (Fig. 4.8c). The position of this DMSO molecule is quite similar to the placement of a unique DMSO present in the copper-seamed analog, which may suggest that there are favorable non-covalent interactions between structural DMSO and bpy molecules. Additional solvent molecules, modeled as disordered water molecules, occupy the space within two adjacent triangular portals between dimers, as well as among linker molecules.

As with the copper-seamed analog **4.2**, unit cell expansion along the c axis shows that parallel layers of the MOF stack in a perfect AA layer arrangement (Fig. 4.8b). Again, this is

perhaps due to favorable (VDW) interactions between *C*-methyl groups on adjacent dimers (C-C distances: 3.73 and 3.76 Å). The direct consequence of this stacking pattern is, as before, that a network of channels runs through the structure, notably along the c crystallographic axis. This is due to the stacking of the aforementioned triangular portals, which are largely devoid of both structural and solvent molecules. In addition to being connected to one another along the c-axis, these triangular channels also appear to be interconnected along the a- and b-axes, at junctions between individual MOF layers. However, as with the 2-D linked copper dimers, these regions are heavily populated by solvent molecules and electron density "q" peaks, so it is uncertain whether these regions are truly connected to one another in a solvated crystal.

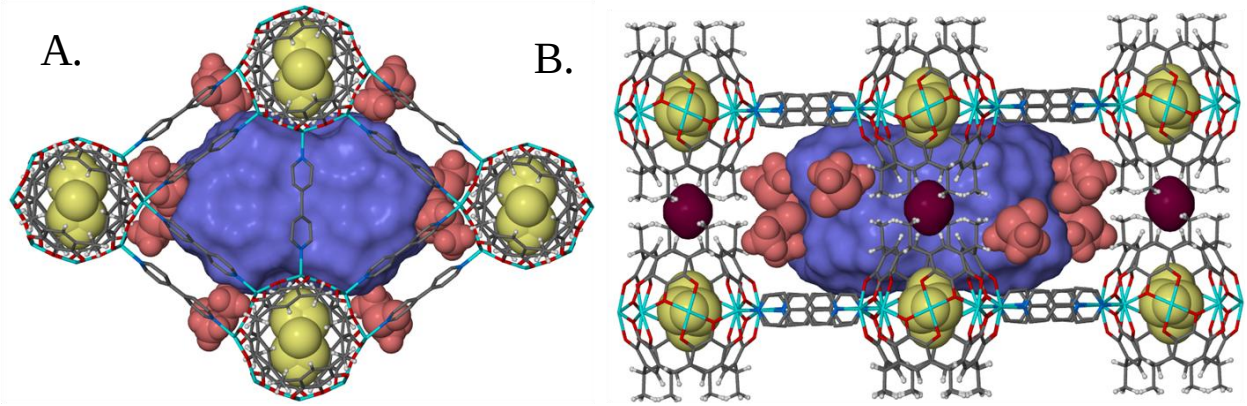

Figure 4.9: Image of the volume contained within a pair of triangular portals (violet) in **4.3** when viewed along the c axis and a axis (A, B). Smaller voids (maroon) are present between pendant c-methyl chains of the dimers. Incarcerated (yellow) and structural (red) DMSO molecules are also shown.

In the interest of using this assembly for molecular sorption/separation studies, and to compare it to the two-dimensional copper dimer-based MOF **4.2**, it was important to determine the void volumes contained within the structure. Of specific interest were the triangular portals, as, with an area of 143.5 $Å^2$ per layer, these are the largest and most easily defined free space-containing motifs found in the structure. In essence, pairs of triangular portals are one concise void that is only superficially split by a bpy molecule. As such, it was advantageous (and much easier) to calculate the volume of a pair, rather than of individual voids. This volume was again calculated by blocking the voids off at their borders with dummy atoms prior to volume analysis using MsRoll. This treatment gave an accessible volume of 705 $Å^3$ per triangular pair with a probe radius of 1.25 Å (Fig 4.9). This can be compared to the 757 $Å^3$ voids present in the copper-seamed analog, which, aside from the lack of a bpy unit that spans the cavity, is metrically similar.

Unexpectedly, MsRoll also revealed the presence of additional voids within the structure, located between the pendant *C*-methyl arms of adjacent nanocapsules (colored maroon in Fig. 4.9). These voids are significantly smaller, with a molecular volume of 42 $Å^3$ and an accessible volume of only 4 $Å^3$ once methyl hydrogens are included in the molecular structure. As such, these voids are unlikely to be useful in the storage of any but the smallest of guest species.

To enable formation of this unique MOF, the coordination geometry of the zinc centers is drastically altered as compared to that in the native dimer or when compared to the two-dimensional copper analog**.** As each dimer accommodates a total of ten peripheral ligands, two more than seen prior to linking, a change in the coordination number of two Zn centers from 5 to 6 is necessary. The geometry of the other six zinc centers is altered to compensate for this distortion, as is the framework's normally spherical shape. One particular outcome of this is an

increase in the capsule's molecular volume, from previously published values of 141 $Å^3$ and 143 $Å^3$ in the native dimer to 147 $Å^3$ in the MOF.[126,127]

Interestingly, this change in coordination geometry also affects the internal DMSO guest. In other examples of guest encapsulation within a dimer where each metal center is penta-coordinate, the guest tends to be badly disordered over multiple possible positions. This is partially due to the fact that coordinating guests, such as pyridine and DMSO can loosely coordinate to all eight of the metal centers in a dimer, as each penta-coordinate metal center is equally likely to accommodate an additional ligand. This mode of internal coordination, however, is not possible with the dimers that make up this MOF. As two of the zinc centers are formally hexa-coordinate, they cannot accommodate additional ligand binding from the interior. This causes the internal guest DMSO to instead be directed toward the remaining penta-coordinate centers, reducing guest disorder and allowing the DMSO molecule to be modeled over four discrete positions. This suggests that control over the coordination number of the metal centers in PgC-based dimers, if possible, can be used to control the behavior of the internal guest, an idea that has yet to be thoroughly explored, but that has previously been seen with nickel- and cobalt-seamed dimers in chapter 2.

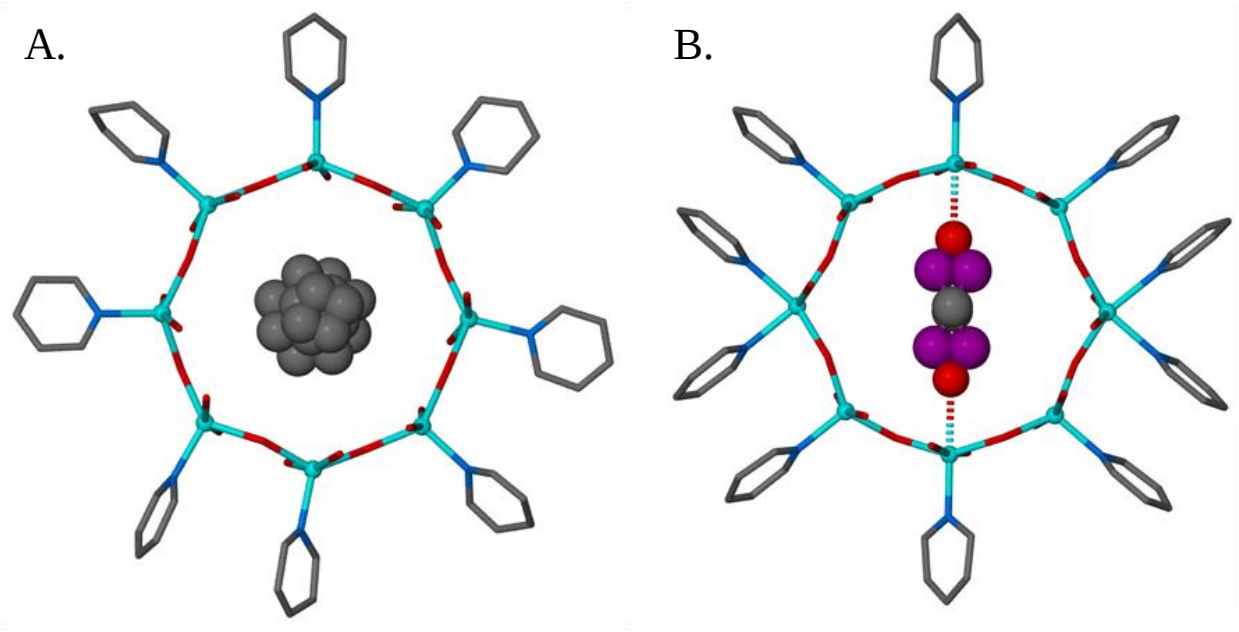

Figure 4.10: Comparison of guest behavior and geometry of a standard penta-coordinate zinc dimer (A.) and 2-D Linked dimer **4.3** (B.). Pyridine guest in **A** is fully disordered (grey) while DMSO guest in **4.3 (B)** is directed away from existing hexa-coordinate zinc sites, leading to decreased guest disorder.

Assembly	C3ZnDMSO (1)	C3CuDMSO	C1Cu4,4'bp	C1Zn4,4'bp (2)			C2CoPy			C2NiPy		
Metal Centre	Zn (average)	Cu (average)	Cu (average)	Zn1	Zn2	Zn3	Co1	Co2	Co3	Ni1	Ni2	Ni3
Angle 1 (°)	162 ± 1	172 ± 1	171 ± 1	170	166	156	173	169	157	179	170	159
Angle 2 (°)	137 ± 1	152 ± 1	151 ± 2	148	139	121	149	139	120	168	145	110
τ5	0.42 ± 0.03	0.33 ± 0.01	0.33 ± 0.01	0.37	0.45	n/a	0.40	0.51	n/a	0.18	0.43	n/a
coordination #	5	5	5	5	5	6	5	5	6	5	5	6

Table 4.2: Comparison of the τ5 values of several dimeric MONCs, including structure 4.3 (labeled as "2"). Published zinc dimer (solely penta-coordinate) is labeled as "1".[126,127,135,136,158]

To quantify the distortion that is introduced by this aberrant coordination geometry, $\tau 5$ values were calculated for the two crystallographically unique penta-coordinate zinc centers in **4.3**. At 0.37 and 0.45, these values differ significantly from one another, as well as from that of previously reported zinc dimers, where the metal centers average at 0.42 with minimal deviation. The octahedral sites in the MOF likely place strain on the spherical framework, thereby forcing geometric compensation by the other metal centers. This coordinative discrepancy, however, may not be due to the use of bpy ligands per se, but instead due directly to the structural constraints enforced by the hexa-coordinate centers. Proof for this conclusion can be found with the previously reported copper-seamed bpy linked dimers, where replacing DMSO ligands for bpy ligands did not lead to a significant change in $\tau 5$ or a change in coordination number. In addition, this conclusion is also supported by our previous work with Co and Ni seamed dimers (chapter 2), and an analogous (but non-linking) zinc dimer with 2,4'-bpy ligands (appendix). Although on most occasions these dimers were found to bear solely penta-coordinate geometries at metal centers, they were nevertheless found to harbor octahedral sites on several occasions, usually two pyridine ligands. The distortion created by these ligands led to a similar effect to the one seen with this MOF (Table 4.2). This further suggests that coordination geometry, rather than ligand identity, is responsible for structural distortion.

4.2.4 Using PgCs with alternate pendant R-groups in the construction of linked assemblies

Up to this point, several examples of MOFs constructed from PgC-based MONCs have been described. However, all of the examples so far have used PgC1 as the macrocyclic building block. These macrocycles have the shortest possible pendant R-group on the lower rim, and as such were expected to pack more efficiently than MONCs constructed from macrocycles bearing

larger groups. This was indeed the case, as MOFs constructed from PgC1-based MONCs both pack closely together and show a predictable mode of interaction between layers. This knowledge is important for the creation of other related materials, as it allows us to make predictions about the resultant structure prior to the material's synthesis. Nevertheless, it was also of interest to see whether structural analogs could be generated, namely those bearing non-*C*-methyl pendant R-groups. This would help to determine if other factors (aside from the metal used) could be employed to alter the structure of the MOF, and to determine to what degree this would occur. Theoretically, the coordination geometry of the metal centers is independent of the pendant R-group used, and thus would not be expected to change. Thus, it can be predicted that the R-group would influence the packing of layers, rather than the geometry of the framework, which would have a direct influence on the shape of the resultant channels.

Several attempts have been made in the past to link MONCs constructed from other C-alkylpyrogallol[4]arenes, such as PgC3, PgC6 and PgC3OH. With the latter example, it was expected that inter-layer hydrogen bonding would help to stabilize the structure. However, crystalline materials unfortunately never formed. Aside from PgC3OH, there are no other easily available PgCs that have R-groups on the lower rim that are capable of hydrogen bonding interactions, so hydrogen bonding was given up in favor of other layer-stabilizing non-covalent forces. One of the easiest to explore was π-π stacking, as many examples of PgCs that bear R-groups with aryl functionality have been synthesized.[85,93] Unfortunately, most of these can only be synthesized in the rctt "chair" macrocyclic conformation, which results in inherent asymmetry of the resultant dimer, and thus less of a chance of appropriate layer packing.[128] In addition, macrocycles in an rctt conformation cannot be crystallized using *in situ* methods due to the additional steps that must be taken to synthesize the corresponding zinc dimers from these

materials. There are, however, two exceptions to these general rules. PgC1Ph and PgC2Ph are macrocycles that bear the appropriate functionality for π-π stacking, but due to a short alkyl bridge between the macrocycle and the phenyl ring, the macrocycle is typically found in the rccc "cone" geometry. This not only allows for a greater degree of symmetry in the resultant dimer, which (hopefully) has a positive effect on layer packing, but the short alkyl bridges also impart flexibility to the phenyl groups so that they can interact in the most efficient manner possible. With this in mind, these two macrocycles were used as starting reagents for zinc dimers used in further linking attempts.

4.2.4.1: Two-dimensionally linked zinc dimers bearing *C*-methylphenyl R-groups: synthesis and characterization

As both *in situ* and post-synthetic linking methodologies were successful in producing linked materials with PgC1Zn dimers, both of these methods were also (simultaneously) attempted to create linked materials with PgC1Ph and PgC2Ph. Both of the macrocycles were synthesized in the conventional manner, using the appropriate aldehydes (phenylacetaldehyde and phenylpropionaldehyde) in a 1:1 pyrogallol:aldehyde ratio (24hr. reflux in methanol w/ catalytic HCl). The macrocycles were then used towards the formation of zinc-seamed MONCs.

For post-synthetic efforts, wherein pyridine ligands would be replaced by bpy ligands on a pre-existing dimer, the respective dimer was first synthesized by mixing a 10^{-2}M acetonitrile solution of the macrocycle with 1M aqueous solutions of $Zn(NO_3)_2$ and pyridine, in a 1:4:14 PgC:Zn^{2+}:pyridine ratio. This led to the formation of yellow precipitate (indicative of dimer formation), which was filtered off, dried, and re-dissolved in DMSO to make a $5 * 10^{-3}$M solution of the dimer (10^{-2}M w.r.t PgC). 4,4'-bipyridine (as a 1M solution in DMSO) was then

added to aliquots of this solution, ranging in ratios from 1:2 to 1:10 dimer:bpy. *In situ* crystallizations were prepared similarly: DMSO solutions of all of the reagents (typically 1M solutions, except for PgC, which was at 10^{-2} M) were mixed in scintillation vials so that the final ratio was 1:4:8:x (PgC:Zn^{2+}:pyridine:bpy), where x ranged from 1-5. All vials were initially capped, but then opened if crystallization had not yet occurred. This was done to allow the DMSO-rich solution to adsorb atmospheric water (DMSO is hygroscopic), which would eventually lower the solubility threshold of the material and thus lead to its crystallization. As with PgC1, crystallization occurred within several weeks in many of the vials that received the higher titers of bpy. Most of this material, however, was either weakly diffracting, badly twinned, or both. Crystals also formed at the lower titers (1:1-2 PgC:bpy) for both macrocycles following several months of crystallization. The crystalline material thus formed was both larger and better diffracting than the previously crystallized material. Although both PgC2Ph and PgC1Ph formed crystals in this way (both *in situ* and post-synthetic approaches worked), and data was collected several times for both permutations, only a 1:4:8:2 ratio of PgC1Ph:Zn^{2+}:pyridine:bpy led to crystalline material sufficient for structural analysis. Details and discussion on the structure produced in this way follows.

Crystal data for PgC_1PhZn dimer 4,4'-bpy linking (4.4): $C_{43.25}H_{28.25}N_3O_{9.88}S_{0.38}Zn_2$, M = 890.70, yellow hexagonal plate, 0.30 × 0.25 × 0.02 mm^3, monoclinic, space group $C2/c$ (No. 15), a = 35.085(8), b = 20.994(5), c = 33.674(7) Å, β = 105.708(3)°, V = 23877(9) $Å^3$, Z = 16, D_c = 0.991 g/cm^3, F_{000} = 7260, Bruker SMART CCD area detector, MoKα radiation, λ = 0.71073 Å, T = 173(2)K, $2\theta_{max}$ = 55.1°, 137261 reflections collected, 27163 unique (R_{int} = 0.2222). Final *GooF* = 1.254, *R1* = 0.1466, *wR2* = 0.3912, *R* indices based on 10049 reflections with I

>2sigma(I) (refinement on F^2), 951 parameters, 122 restraints. Lp and absorption corrections applied, μ = 0.859 mm^{-1}.

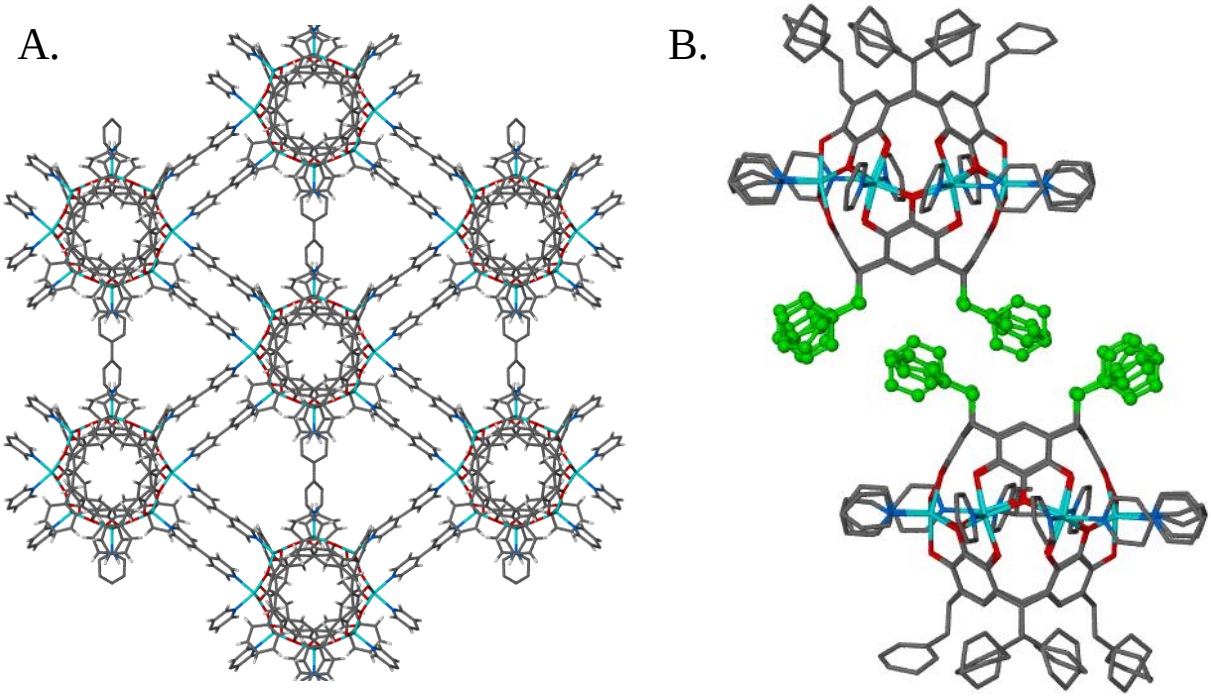

Figure 4.11: Image of a C-methylphenyl-footed 2-D Zn MOF (**4.4**) along the crystallographic a-b and b-c planes, respectively (A, B). R-groups are shown in green (B), and are staggered with respect to one another on adjacent nanocapsules.

4.2.4.2: Two-dimensionally linked zinc dimers bearing *C*-methylphenyl R-groups: discussion

As predicted, the change in the pendant R-group from C-methyl to C-methylphenyl did not have a significant impact on the coordination geometry of the zinc centers, or on the linking network. Indeed, when viewed as a single 2-D layer, the MOF that formed (**4.4**) is essentially isostructural with **4.3** (Fig. 4.11a) While the τ5 values do differ, particularly when the hexa-

coordinate site is excluded from calculations, the overall connectivity is the same, as is the arrangement of the ligands. However, when the interaction of multiple layers is examined, the picture changes entirely. Rather than packing in the AA pattern seen in both previous examples of 2-D MOFs (**4.2** and **4.3**), individual layers of **4.4** pack in an offset ABAB pattern when viewed along the crystallographic c axis (Fig. 4.12). This is attributable to the bulkier R-groups on the PgC macrocycle, which themselves are arranged in an offset, staggered pattern (Fig. 4.11b).

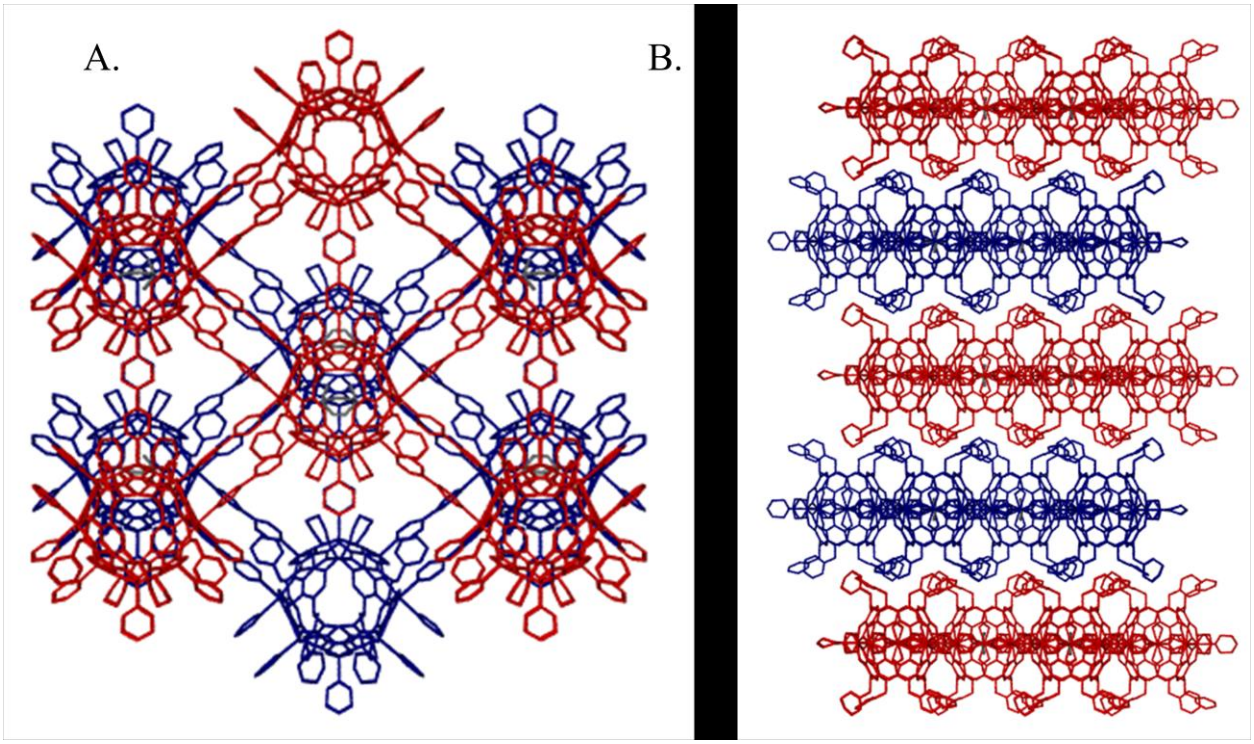

Figure 4.12: Packing of layers in **4.4** as viewed along the c and a crystallographic axes. Adjacent layers are colored blue or red for contrast

It is interesting to note, however, that most of the phenyl rings on the R-groups do not seem to participate in π-stacking interactions as predicted, but instead are positioned in such a way as to take up as much space as possible between the MOF layers. Several phenyl-phenyl distances in the 3-4Å range can be found, which is possibly indicative of an interaction, but as most of the shorter contacts are located between phenyls on the same macrocycle, most of these are intra- rather than inter-molecular interactions. However, because all of the phenyl rings on the R-groups are disordered over two or more positions, it is not possible to verify this or any other claim regarding interaction distances, as it is uncertain what disordered component is interacting with what else. What can be said is that the deviation in the packing pattern of this MOF from that of **4.3** is definitely mediated by the alternate R-groups that are used, which behave quite differently from the *C*-methyl groups used in **4.3**.

The staggered arrangement of the R-groups shifts the 2-dimensional layers relative to one another (**Fig. 4.12**). This, in turn, shifts the triangular voids found within the structure relative to one another as well. This has a profound effect on the shape of the channels that are seen on symmetry expansion; rather than propagating directly through the framework in a clear and concise manner, the channels zigzag between layers (**Fig. 4.13**). While the exact solvent occupancy of the channels cannot be determined, the space within the channels is at least partially occupied by the (disordered) phenyl rings from the R-group. This occupancy likely has a reductive effect on the volume per structural unit. However, another effect of the larger R-groups is an increase in the spacing between layers, which is increased from approx. 14.5Å in **4.3** to 17.3Å in **4.4**. Thus, it was not certain whether the channels in this structure were reduced or increased in overall volume when compared to the channels found in **4.3**.

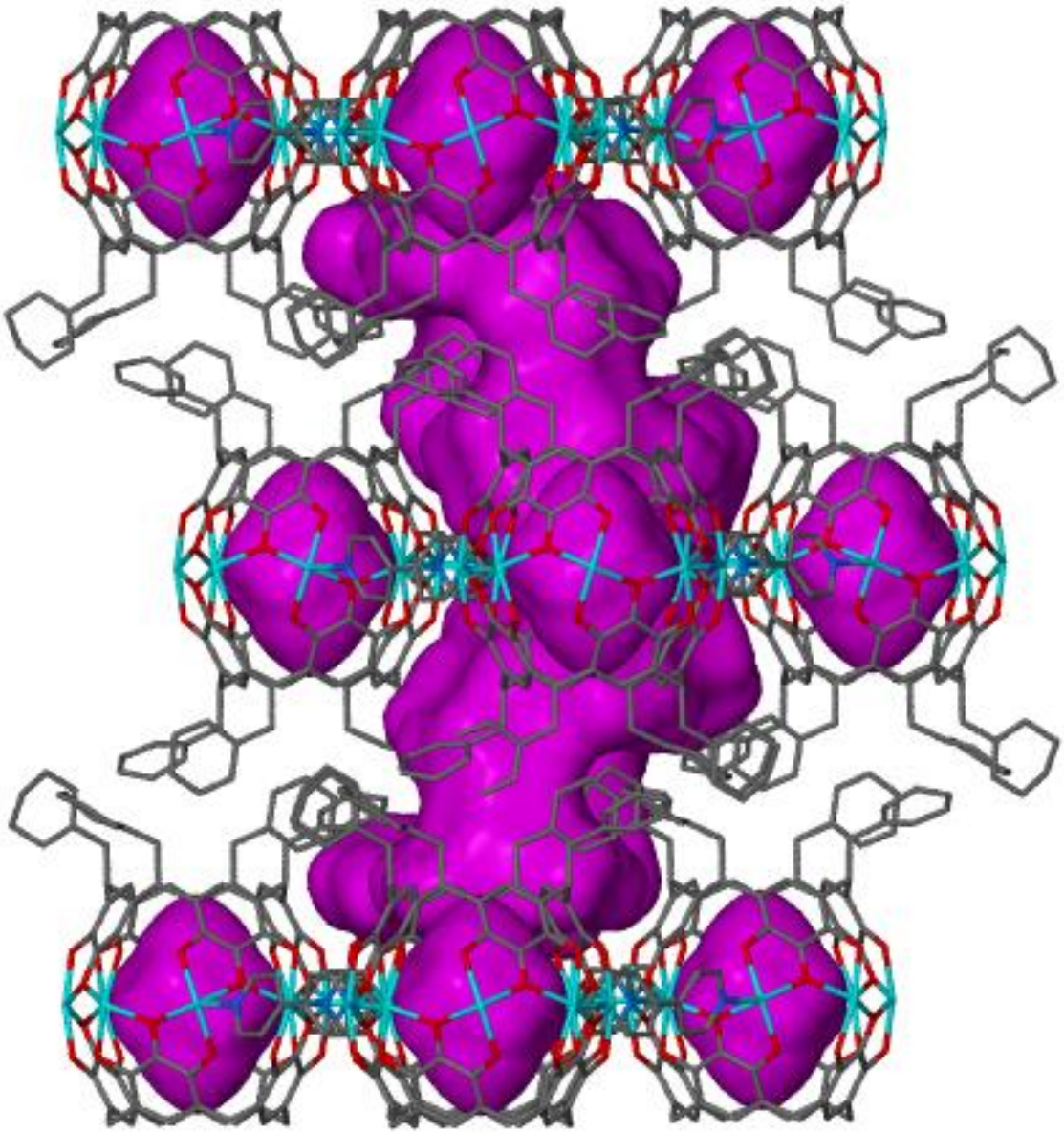

Figure 4.13: Image of the void volume within three layers of 4.4. Voids located within dimeric MONCs are also included in this image

To answer this question, MsRoll was once again used to determine the void volume per structural unit. A pair of units, bound by three MOF layers was actually analyzed together due to the odd shape of the channels. A larger probe with a 1.5 Å diameter was used because it was not possible to correctly block off the model complex without having the 1.25 Å probe either leave the complex or get stuck (which makes the program crash). Using the 1.5 Å probe, the complex was found to have a total contact volume of 1957 $Å^3$ and an accessible volume of 1329 $Å^3$. This then gives a contact volume of approximately 979 $Å^3$ and an accessible volume of 664 $Å^3$ per structural unit, which is the space between a pair of layers. This value is approximately equal to the volume per structural unit in **4.3** under the same conditions, a rather unexpected result due to the different channel shape (**4.3** has contact and accessible volumes of 1021 $Å^3$ and 658 $Å^3$, respectively, when a 1.5 Å probe is used).

4.2.5: Linking dimeric MONCs with 4,4'-bipyridine: conclusion

This section describes several examples of MOF-like coordination polymers based on dimeric MONCs as a building block and 4,4'-bipyridine as a linker. Variable synthetic techniques can lead to either one- or two-dimensional linked architectures with copper, while only two-dimensional arrays were seen with zinc. Distinct differences were seen between the two metals in the two-dimensional frameworks. These differences are largely due to the coordination geometries of the metal centers. In particular, while copper dimers bear solely penta-coordinate metal sites, zinc dimers also have two hexa-coordinate sites, each of which accommodate two linking ligands. As a result, this changes the overall linking framework. Several non-covalent structural motifs were observed to play a part in the packing of MOF layers in all of the structures. Most notable of these were non-covalent contacts between the *C*-methyl R-groups from dimers in adjacent layers. Changing the R-group led to a change in the packing

of layers, but did not change the linking arrangement or the coordinative bonding at the metal centers. These results suggest that while the framework connectivity can be modulated by changing the identity of the metal that seams the MONC, modulation of the voids present in the MOF can be done by changing the R-group at the lower rim of the PgC macrocycle.

4.3 Linking hexamers using 4,4'bpy

Following our successes at linking dimeric MONCs, it was envisioned that hexameric MONCs could likewise be linked into poly-dimensional arrays with divergent ligands. Apart from sheer curiosity, there are several other reasons for pursuing such an effort. One benefit of working with hexameric, rather than dimeric MONCs as starting materials for MOFs is the increase in size when going from a dimer to a hexamer, with the latter being more than twice the volume of the former. A larger volume of the primary structural unit could lead to larger voids, channels, or other free space-containing motifs in a linked framework. Another closely related benefit is that the metal centers in a hexamer do not fall on a single plane. Thus, hexamers are not limited to one- and two-dimensional MOFs like dimers, but can potentially lead to linking in all three dimensions. Three dimensional scaffolds can potentially lead to channels that are structurally unique when compared to those found in one- and two-dimensional arrays, and could perhaps themselves propagate in three-dimensions.

While several attempts were made at linking *pre-made* hexameric MONCs (i.e. dissolve purified hexamer in a solvent, then add bpy linker), these attempts normally resulted in the formation of precipitates or in crystals that were too fine for data collection. Because of this, synthesis/*in situ* crystallizations were attempted instead. DMSO was used as the solvent of choice for these attempts, partially due to earlier successes at using this solvent for the same

purpose with copper- and zinc-seamed dimeric nanocapsules, and because it is known that copper-seamed hexameric capsules do form in DMSO at low enough temperatures (i.e. RT). While there was a definite risk that a coordination polymer of dimeric capsules would form instead, this outcome was seen to be a benefit rather than a detriment. Very few examples of linked assemblies have been synthesized, so any new structure would bring benefit to these studies. Nevertheless, efforts were still undertaken to maximize the proportion of hexamer that would form by properly cooling the stock solutions to room temperature prior to use. PgC1 was again chosen as the macrocycle for these efforts, for reasons described earlier. Multiple attempts over several years resulted in two structures, displaying one- and two-dimensionally linked arrays based on hexameric MONCs. A three-dimensional analog is still elusive.

4.3.1 One-dimensionally linked hexameric copper nanocapsules

4.3.1.1 One-dimensionally linked hexameric copper nanocapsules: synthesis and characterization

All solutions in the following protocol were made in DMSO. 0.08 mL of a 1M $Cu(NO_3)_2$ solution was added to 2 mL of 0.01M PgC1 solution in a scintillation vial. The solutions were briefly stirred, resulting in a change in color from pink and blue to dark red. 0.04 mL of 1M 4,4'-bipyridine solution was then added, resulting in a change of color from dark red to dark brown. The scintillation vial was capped and crystallization occurred after several days.

Crystal data (4.5): $C_{33.72}H_{17}Cu_3N_{0.50}O_{12.62}S_{3.45}$, M = 932.25, brown plate, 0.30 × 0.10 × 0.05 mm^3, triclinic, space group P-1 (No. 2), a = 21.037(4), b = 23.386(5), c = 23.704(8) Å, α = 105.406(4), β = 106.525(4), γ = 105.991(3)°, V = 9971(5) $Å^3$, Z = 8, D_c = 1.242 g/cm^3, F_{000} =

3728, Bruker SMART CCD area detector, MoKα radiation, λ = 0.71073 Å, T = 173(2)K, $2\theta_{max}$ = 55.2º, 117293 reflections collected, 45297 unique (R_{int} = 0.0944). Final *GooF* = 1.201, *R1* = 0.1290, *wR2* = 0.3665, *R* indices based on 18547 reflections with I >2sigma(I) (refinement on F^2), 1898 parameters, 0 restraints. Lp and absorption corrections applied, μ = 1.460 mm^{-1}.

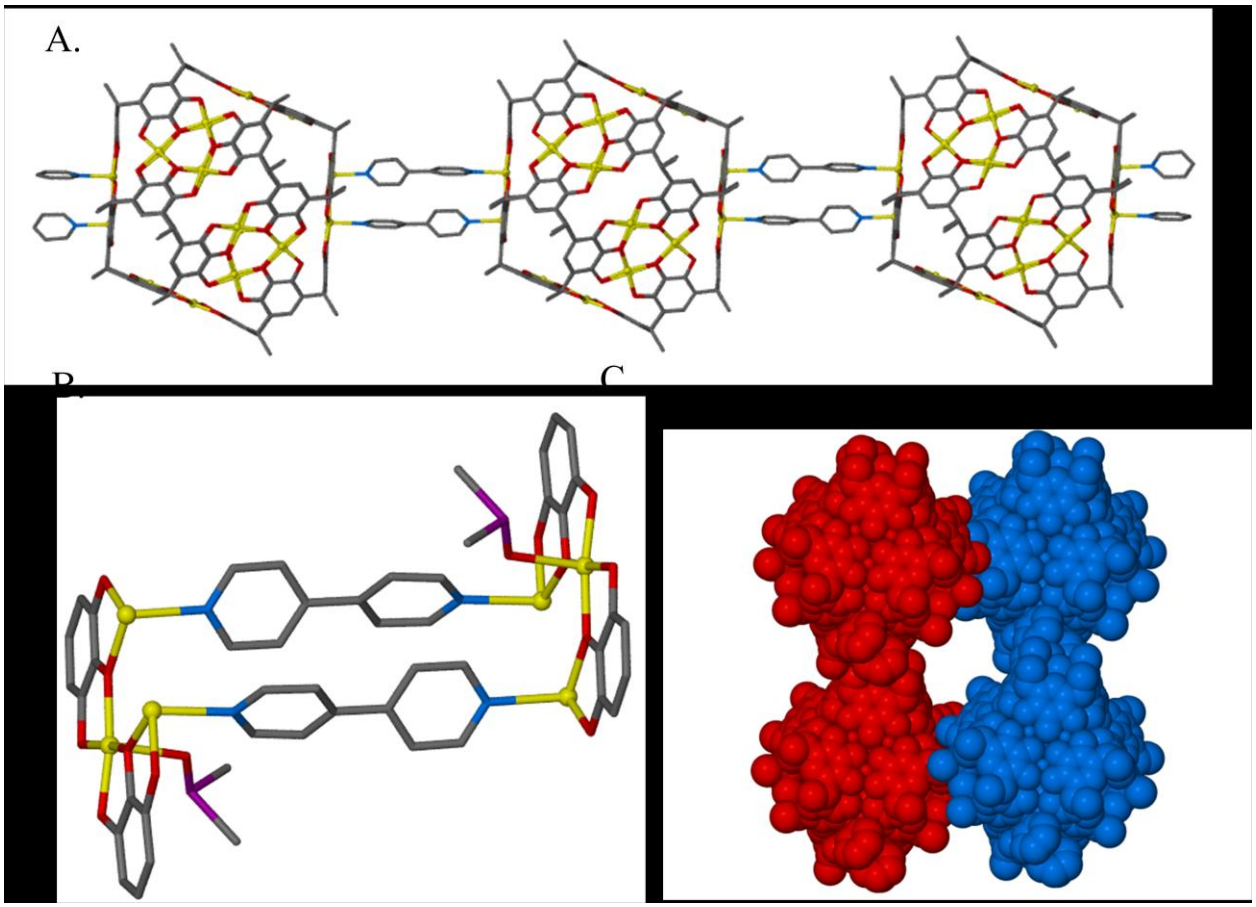

Figure 4.14: A single chain of **4.5**, a 1-D coordination polymer of copper hexamers (A). B shows the structural unit that links capsules together, where pairs of bpy link copper clusters on adjacent capsules. C shows the voids that are present between adjacent chains (blue and red).

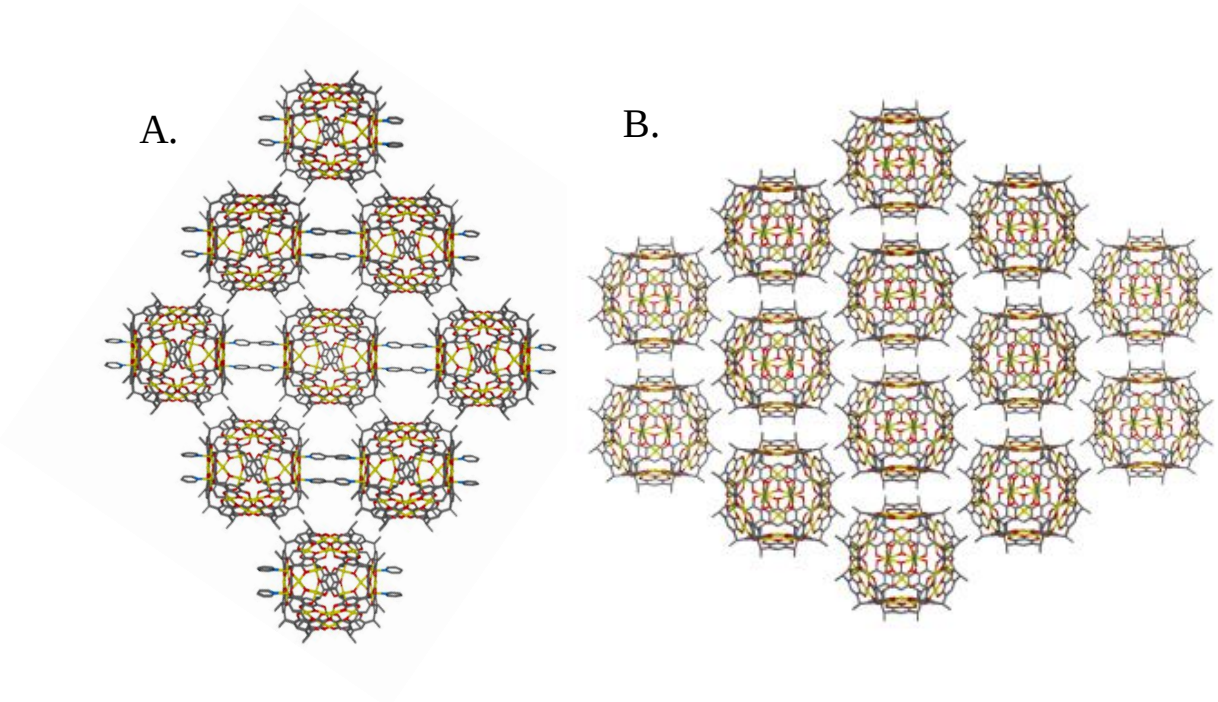

Figure 4.15: Symmetry expansion of 3.5 when viewed along the A axis (A) and 1 1 1 line (B)

4.3.1.2 One-dimensionally linked hexameric copper nanocapsules: discussion

As a first example of hexameric linking, the synthetic methodology described above led to crystals of a one-dimensional coordination polymer of hexameric MONCs (**4.5;** Fig. 4.14). The asymmetric unit features one-half of a hexameric MONC, one unique bpy molecule, as well as many structural DMSO molecules. The DMSO molecules are either coordinated to structural coppers as ligands or are located inside or outside of the capsule, with the latter two types of DMSO being particularly disordered. Symmetry expansion along all three crystallographic axes shows that the hexamers are linked in discrete chains, with each hexamer connected to adjacent hexamers *via* two bpy linker molecules (Fig. 4.14b, 4.15a). These chains pack as centered

hexagons when the expanded structure is viewed parallel to the chains along the lines represented by the 0 1 1 and 111 miller indices (Fig. 4.15). As in the other linked examples, the *C*-methyl chains on adjacent hexamers undergo non-covalent interactions with one another, albeit at longer distances than in dimeric linking (shortest C-C distances: 3.87 Å and 3.94 Å). These are the only discrete interactions that are observed between chains, although a complex VDW network that encompasses the solvent DMSO molecules also likely exists. This may, however, be secondary to the inter-capsular VDW interactions, which are seen in other examples of MONC linking.

When viewed along the 1 0 1 line, voids can be seen between adjacent MONC chains (Fig. 4.14c). On further symmetry expansion, these voids overlap to form discrete channels. Much of the space within these channels is occupied by the solvent DMSO molecules that are neither coordinated to nor encapsulated by the MONCs. Efforts to establish a volume for these channels in an analogous manner to what was done with the dimers (i.e. using MsRoll), was unfortunately hindered by the large number of atoms present within this structure, thus causing the program to freeze unpredictably when an appropriate model is built for volume analysis. The square area of the channels, however, can be estimated, as the channels metrically approximate a parallelogram. By using this geometric comparison and measuring the closest contacts between parallel MONCs that make up the walls of the channels, an area of approximately 130 $Å^2$ is obtained, slightly smaller than what is seen with the two-dimensional zinc MOF.

Linking in **4.5** occurs through two structural coppers located in parallel tri-metal clusters, which are inverted relative to one another (Fig. 4.14b). The remaining copper in each of these clusters coordinates to a single DMSO molecule, which is relatively well ordered when compared to other DMSO molecules in the structure. Thus, each of the clusters involved in

linking accommodates three independent ligands, although only two of these are linking ligands. While each tri-metal cluster could theoretically accommodate three linking ligands, it is clearly evident why this would be disfavored with bpy as a linker (disregarding the impossibility of this due to metal cluster inversion). As bpy ligands are "planar" ligands, they must be arranged parallel to one another when MONCs are used as a structural unit, as the proximity of the metal centers would cause them to bump into one another otherwise. If the third (unlinking) copper site in this MOF were to accommodate a third bpy ligand, it would simply bump into the other two, regardless of its orientation. Indeed, the DMSO ligand that is seen in this cluster is angled away from the bpy ligands to avoid such a collision. A potential counterexample to this theory can be seen with the nickel-seamed hexamers, which always have three aromatic pyridine ligands per tri-metal cluster. However, pyridines lack the rigidity of a doubly bound bpy molecule and can freely rotate to take up the most sterically favorable positions relative to one another. Nevertheless, in many cases these pyridines are still "rotationally" disordered, detailing the problem of having three aromatic ligands constrained within a small area.

It is interesting to note that although (stoichiometrically) a 1:2 ratio of bpy:Cu^{2+} was used in its synthesis, the 1:12 bpy:Cu^{2+} ratio found in this MOF indicates that many of the bpy molecules were not used for linking. This may suggest that other, bpy-rich entities had formed, but did not crystallize. Alternately, and more probably, a significant portion of the bpy molecules may have been protonated, and thus could not function as ligands, as a sacrificial base was not added to neutralize the acid that was released on the formation of the MONC. Based on this observation and our goal of MOFs with a higher dimensionality, a sacrificial base (usually pyridine) was used in all subsequent attempts to link hexameric MONCs, including in the synthesis of the two-dimensionally linked hexameric MONC described below.

4.3.2 Two-dimensionally linked hexameric copper nanocapsules

4.3.2.1 Two-dimensionally linked hexameric copper nanocapsules: synthesis and discussion

All solutions in the following protocol were made in DMSO. 0.08 mL of a 1M $Cu(NO_3)_2$ solution was added to 2 mL of 0.01M PgC1 solution in a scintillation vial. The solutions were briefly stirred, resulting in a change in color from pink and blue to dark red. 0.08 mL of 1M pyridine solution, followed by 0.08 mL of 4,4'-bipyridine solution were then added, resulting in a change of color from dark red to dark brown. The scintillation vial was capped and crystallization occurred after several days.

Crystal data for PgC_1Cu 4,4'bp 2D hexamer: $C_{23}H_{12.36}Cu_{2.18}N_{0.73}O_{8.18}S_{1.18}$, M = 606.31, plate brown , × × mm^3, monoclinic, space group $C2/m$ (No. 12), a = 39.652(7), b = 33.594(10), c = 37.00(2) Å, β = 90.33(4)°, V = 49281(33) $Å^3$, Z = 44, D_c = 0.899 g/cm^3, F_{000} = 13336, Bruker SMART CCD area detector, MoKα radiation, λ = 0.71073 Å, T = 100(2)K, $2\theta_{max}$ = 38.9º, 136122 reflections collected, 21549 unique (R_{int} = 0.1192). Final *GooF* = 1.956, *R1* = 0.2022, *wR2* = 0.5007, *R* indices based on 11286 reflections with I >2sigma(I) (refinement on F^2), 882 parameters, 0 restraints. Lp and absorption corrections applied, μ = 1.115 mm^{-1}.

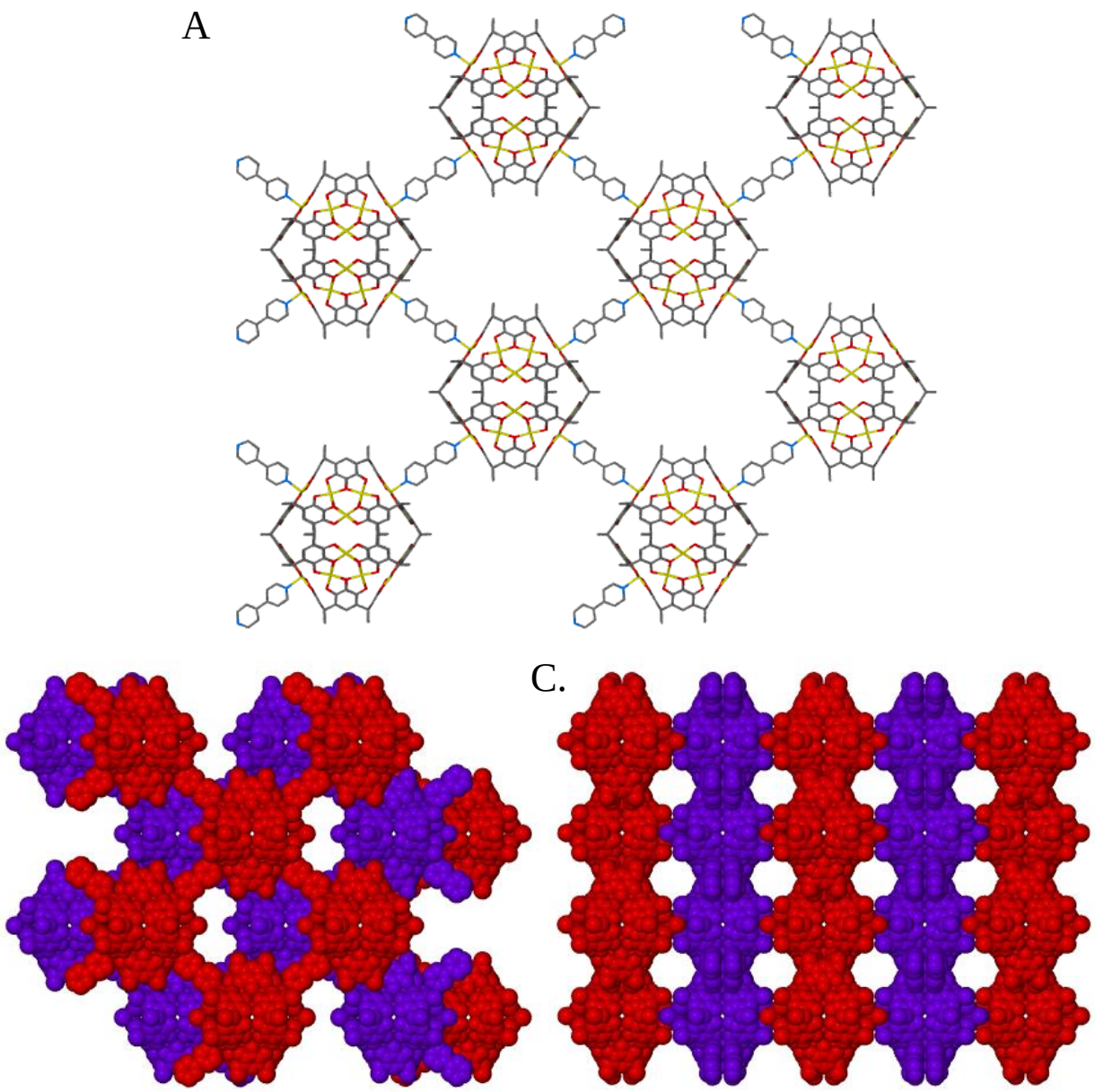

Figure 4.16: A single layer of 2-D linked hexamers **4.6** (A) Multiple layers stack offset relative to one another. B and C show perspective views of the stacking arrangement, as well as of the channels that run through the structure along the a-b and b-c crystallographic planes, respectively.

4.3.2.2 Two-dimensionally linked hexameric copper nanocapsules: discussion

Following the results from the previous experiment, another crystallization study was performed that sought to isolate either a two- or three-dimensionally linked MOF. This led to the isolation of a 2-dimensional MOF based on hexameric MONCs (**4.6**). The synthesis was conducted based on lessons and inferences learned in the first experiment, namely that the addition of a sacrificial base was likely of value and that a higher proportion of bpy ligand:PgC should be added. This was done to provide the greater number of un-protonated bpy molecules that would be needed for multidimensional linking. This approach turned out to have the desired effect, namely that the asymmetric unit of this assembly contains *two* unique bpy molecules per one-half of a MONC, as compared to the single bpy in **4.5 (**Fig. 4.16**)**. The asymmetric unit also contains several structural DMSO molecules, which again play one of three roles, either coordinating to Cu^{2+} metal centers, acting as encapsulated guests, or acting as external solvent molecules that fill in any gaps within the structure.

As in the one-dimensional analog, inter-capsular linking occurs *via* pairs of bpy linker molecules, which are doubly coordinated to adjacent tri-metal clusters that are inverted relative to one another. This second case of pairwise coordination is supportive of the previous claim that π-stacking interactions allow two, but not three bpy molecules to coordinate per tri-metal cluster. All bpy coordination occurs along one distinct plane, namely the ab crystallographic plane. As such, the geometry of the MOF as a two-dimensional layer is readily observed by viewing the assembly along the c crystallographic axis (Fig 4.16a). This perspective view also shows that, like in all of the other MOFs described so far, voids are present in the framework, which develop into channels on symmetry expansion. One type of void is a result of bpy linking, in that a large amount of space is left over between MONCs (Fig. 4.16b). A second set of voids

is also apparent by viewing the structure along the a crystallographic axis (Fig. 4.16c). These voids occur as a result of uneven packing of MOF layers, and are likely connected to the first type of void, thereby leading to a three-dimensional grid of channels. However, as with the one-dimensional hexameric analog **4.5**, it is difficult to find and block off a repeating unit of the channel that these voids produce, and the sheer number of atoms in the structure would more than likely cause problems when building a suitable model to do so. Therefore, MsRoll cannot be used to determine the void volume per structural unit. It is also difficult to determine where these voids begin and end, as layers of this MOF do not neatly stack in the AA arrangement seen in the other assemblies. Rather, the layers are offset, which allows for VDW contacts between C-methyl groups on the exterior of the capsules (shortest C-C distances: 3.94 Å and 3.81 Å), a motif seen in all other examples of capsular linking in this chapter (Fig. 4.16b). Interestingly, unlike in the other assemblies, where *C*-methyls from multiple PgCs take role in VDW interactions, only one of the six total PgCs in this assembly takes part in VDW interactions with adjacent nanocapsules. This may be partly due to structural incompatibilities of extensive VDW contacts and a 2-D grid of hexamers.

4.3.3 Linking hexameric nanocapsules: conclusion

Herein, it has been shown that hexameric MONCs can be used as building blocks towards the construction of MOFs. Although significantly different from their dimeric counterparts, and arguably much more difficult to work with, appropriate synthetic techniques can nevertheless produce both one- and two-dimensional linked analogs of what is seen with the dimers. The MOFs constructed from hexamers are also distinctly different from the dimers in how they pack within a crystalline lattice and in the voids that are produced, although similarities in the structure-dictating non-covalent interactions are clearly observed (i.e. VDW contacts

between *C*-methyl groups). As both of the examples of linked hexameric MOFs show the presence of channels within their respective structures, gas/guest sorption studies should eventually be performed. However, it is important to note that it is still difficult to produce these materials in bulk, and so the efficiency of the synthesis of these materials may need to be improved first.

4.4 "Directly linking" copper-seamed dimeric nanocapsules

The last part of this chapter will cover a rather unusual form of linking, which, for lack of a better term, was named "direct" linking on its discovery. While this form of linking is ligand-based, and does result in the formation of a coordination polymer, it is radically different from the bpy-based linking modality seen in the rest of the chapter. This is because the ligands that link the assembly together are, surprisingly, the dimers themselves. The coordinative bonding that is responsible for this type of linking enforces steric and geometric constraints on the rest of the system, leading to a fully unique coordination geometry that is seen nowhere else. Thus, direct linking is interesting not only from a MOF-building perspective, but also as a case study on unique dimer geometries.

4.4.1 First example of directly linked dimers

4.4.1.1 Synthesis (accidental) and characterization of directly linked dimers

Contrary to the strategic approach used to construct the 4,4'-bpy arrays, the discovery of direct linking was by complete accident. The original synthetic details were not appropriately recorded, as the first crystals of this material came from an abandoned copper dimer crystallization attempt. What follows is the best recollection of the original synthesis, which is at least partially taken from laboratory notes recorded at the time: PgC_1 was first heated at reflux in

2-bromopyridine. The objective of this is no longer certain, but was likely done as an attempt to synthetically add a pyridine moiety to the PgC macrocycle. This solution was cooled and added directly into H_2O, leading to the formation of a tan precipitate. This was likely done to isolate the resultant product, as PgCs are only sparingly soluble in water. The solid was filtered off, leaving a red aqueous solution. I am not entirely certain as to what happened to the solid, but the solution, which was by the color assumed to have some amount of the material still dissolved in it, was not discarded but rather used toward a copper chelation attempt. Methanolic $Cu(NO_3)_2$ was added to this solution, giving a light brown emulsion. Emulsions typically do not lead to crystallizations with PgC-based MONCs, so HCl was added to this solution, in hopes that this would help solubilize the solid material. However, it was feared that too much acid had been used to accomplish dissolution, so pyridine and $NaHCO_3$ were titrated back to the solution to raise the pH to neutral. This (again) led to slight precipitation of a brownish solid, so acetone was added to dissolve the material. After this observation, the material was left to crystallize for several days, during which time the acetone evaporated, leaving a brown precipitate. As a precipitate had formed, rather than crystals, the crystallization attempt was deemed a failure. However, when the material was about to be disposed of, several small plate-like crystals were noticed among the brown precipitate, which were removed and analyzed using scXRD. Although the crystals gave weak diffraction spots, diffraction was nonetheless observed close to the limit of resolution (0.77 Å), indicating a highly ordered material. It was because of this observation that data was collected.

Crystal data for PgC_1Cu directly linked dimer #1 (4.7): $C_{41}H_{28}Cu_4NO_{14}$, M = 1012.80, brown plate, .01 × .10 × .15 mm^3, monoclinic, space group $C2/c$ (No. 15), a = 28.049(7), b = 14.459(3), c = 23.001(5) Å, β = 114.931(5)°, V = 8459(3) $Å^3$, Z = 8, D_c = 1.591 g/cm^3, F_{000} = 4072, Bruker SMART CCD area detector, MoKα radiation, λ = 0.71073 Å, T = 173(2)K, $2\theta_{max}$ = 55.3º, 48682 reflections collected, 9789 unique (R_{int} = 0.0894). Final *GooF* = 1.111, *R1* = 0.1173, *wR2* = 0.3282, *R* indices based on 5863 reflections with I >2sigma(I) (refinement on F^2), 498 parameters, 12 restraints. Lp and absorption corrections applied, μ = 2.051 mm^{-1}.

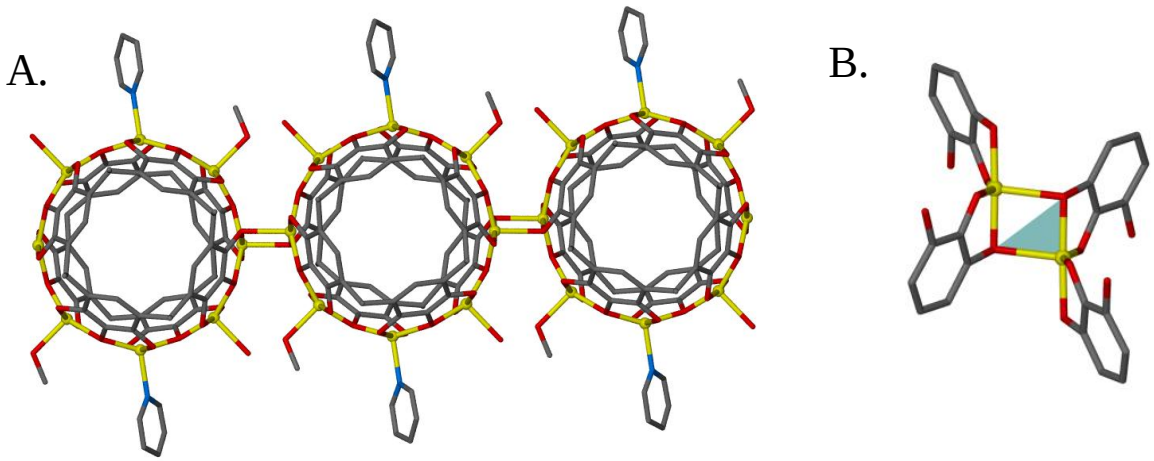

Figure 4.17: A chain of "directly linked" dimers 4.7 (A). B shows the coordinative connectivity at the site of linking.

4.4.1.2 A first example of directly linked dimers: discussion

Initial inspection of the dimeric MONC produced by this method (**4.7**) revealed what was otherwise a normal dimeric capsule, albeit with unusual peripheral ligands. The asymmetric unit contains one half of a dimeric MONC, as well as three ligands: one methanol, one water, and one pyridine. An additional pyridine is incarcerated within the capsule and is disordered over two

discrete positions. Ordered non-coordinating solvent molecules seem to be entirely absent. Although there are several prominent peaks that could be modeled as water and/or methanol molecules, the distances between these peaks and structural components of the MONC are too short (i.e. well below 3 Å) to be reasonable.

One particularly unusual trait about this dimer, however, is that solvent molecules are found to be coordinated to several of the metal centers. Solvent molecules from the synthesis of dimeric MONCs such as water, methanol, acetone, or acetonitrile, are not typically found as peripheral ligands, so the presence of four of such ligands coordinated to a dimer is quite novel. Furthermore, two of the metal centers initially appeared to be tetra-coordinate as they did not seem to have any ligands at all. This is something that has never been previously seen to occur with dimeric MONCs, as the curvature of the octametal belt necessitates penta- or hexa-coordinate geometry. It was expected that if tetra-coordinate sites were present, the coordination geometry at these sites would be dramatically different from the other metal centers. However, the coordinative geometry at these sites appeared to be quite similar to the other metal centers, with $\tau 5$ values that were only slightly different from the mean (Fig 4.20). This observation was explained on symmetry expansion of the crystal structure, which showed that these sites did indeed accommodate ligands, which were surprisingly the hydroxyls from the upper rims of adjacent dimers. This unusual mode of coordinative bonding was initially suspected to be a result of problems during data work-up, so the crystal data was reinvestigated to eliminate both crystal twinning and/or a false solution as the cause of this finding. No problems were found, suggesting that this result was, in fact, real.

The linking motif in this structure is a pair of coordinative Cu-O bonds, arranged in a rectangle (Fig 4.17b). This rectangle is orthogonal to the plane of the octametal belt. This

differs from bpy linking where Cu-Ligand-Cu pairs are instead parallel to this plane. The lengths of the coordinative bonds that link adjacent dimers are slightly longer than typical copper-phenoxy bonds that seam a dimer (2.25 Å vs. an average of 2 Å per oxygen-copper bond along the octametal belt), but this bond length is perfectly reasonable for a peripheral ligand-Cu^{2+} bond. Coordination occurs at two sites on any given MONC, and at metal centers that are diametrically opposite of each other. This leads to the formation of linear one-dimensional chains on symmetry expansion (Fig. 4.17a). While it can be envisioned that almost any of the metal sites that are not immediately adjacent to the site of linkage can also be used for linking, the reason for the linearity of the assembly is sterics. Although linking in other locations would leave enough space to accommodate the main framework of the dimer, this would leave no space for the other ligands. Thus, in being arranged linearly, the dimer maintains all of the ligands necessary for penta-coordinate, rather than tetra-coordinate metal centers.

Due to the rather haphazard methods that led to this assembly's synthesis, it was uncertain as to what particular factors led to its formation. Indeed, the fact that a linked assembly formed using this method in the first place was almost as surprising as its features. One hypothesis for its formation is that the addition of HCl in sub-stoichiometric quantities to copper-seamed dimers did not lead to the decomposition of the dimers, but rather led to the removal of pyridine ligands *via* protonation. This leaves vacant coordinative sites on metal centers, which are filled by whatever ligands are present at the time, in this case, solvent molecules and other dimers. However, as solvent molecules vastly outnumber the number of dimeric MONCs in solution, and so would drastically outcompete dimers for coordination, the presence of dimers as ligands is difficult to explain. One likely explanation for this is that coordination to a phenoxy group is preferable to coordination to a solvent molecule. This is self-consistent, as the dimer

itself is held together by such bonds already. Assuming that this is the case, solvent ligands could effectively be displaced by coordination to a dimer, regardless of the excess of these molecules. This type of displacement, where a ligand of higher affinity displaces one of a lower affinity has previously been demonstrated in many other examples (i.e. pyridine or DMSO for 4,4'-bpy), and is the primary reason why post-synthetic ligand exchange works in the first place.

In any case, it is clear that at least some reorganization of ligands took place, either before or after the linking event. Evidence for this is found in the distance between the methanolic oxygen and water molecule on adjacent dimers (2.75 Å), which is indicative of a hydrogen bond. Although it cannot be definitively proven that this bonding was not merely an accident, it is highly unlikely that some reorganization would not have occurred to yield such a favorable interaction. Interestingly, another favorable interaction that is consistent with something seen in the bpy linked structures is VDW connections between dimers. Here, such contacts are apparent between the C-methyl groups of every other dimer (shortest C-C distances of 3.80Å and 3.86Å), as the individual chains pack in an ABAB layered arrangement.

4.4.2 Second Example of directly linked dimers

4.4.2.1 Characterization and structural discussion of a second example of directly linked dimers

As only a small portion of the crystals were used for data collection, a second batch of crystals was also sent to the ALS to obtain better data and to ameliorate any remaining doubts that this structure was a false solution. This led to an entirely different crystal structure.[158]

Crystal data for PgC_1Cu directly linked dimer #2 (4.8): $C_{80}H_{72}Cu_8N_3O_{27.50}$, M = 2023.73, Red Block, 0.06 × 0.04 × 0.02 mm^3, triclinic, space group P-1 (No. 2), a = 14.4861(5), b = 14.5856(5), c = 22.0546(7) Å, α = 75.001(2), β = 75.107(2), γ = 67.849(2)°, V = 4102.2(2) $Å^3$, Z = 2, D_c = 1.638 g/cm^3, F_{000} = 2050, Bruker APEX II CCD Diffractometer, synchrotron radiation, λ = 0.77490 Å, T = 100(2)K, $2\theta_{max}$ = 76.0°, 78795 reflections collected, 33539 unique (R_{int} = 0.0364). Final *GooF* = 1.032, *R1* = 0.0451, *wR2* = 0.1122, *R* indices based on 23721 reflections with I >2sigma(I) (refinement on F^2), 1094 parameters, 10 restraints. Lp and absorption corrections applied, μ = 2.114 mm^{-1}.

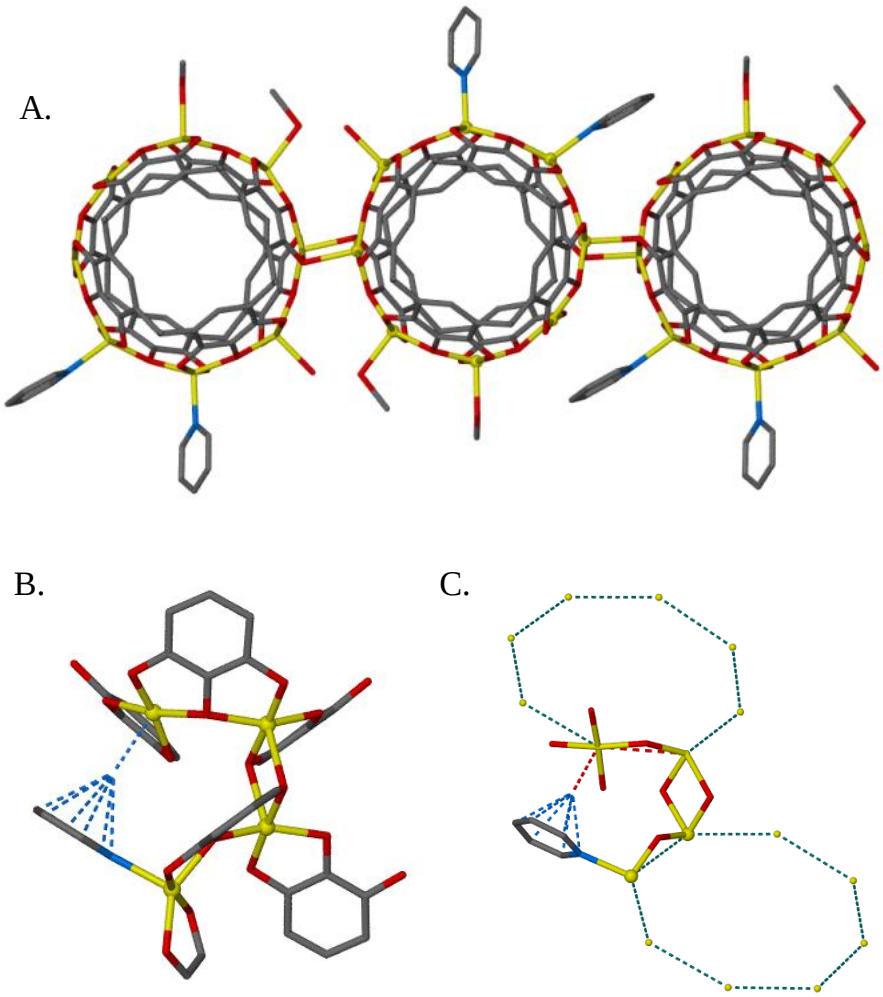

Figure 4.18: A chain of directly linked dimers **4.8** (A). A pyridine ligand adjacent to the site of linking enforces a tetracoordinate geometry at one of the copper sites. B and C are two perspective views of this tetracoordinate site, which also show the pyridine molecule.

The unit cell of another crystal from this batch was different from the one collected at MU, signifying a different material (**4.8**). Structural examination following data workup confirmed this fact, although the resultant material also displayed direct linking (Fig. 4.18a). However, there were nevertheless several notable differences. The asymmetric unit, for one,

includes a complete dimer, rather than a half of one. The reason for this is that the ligands around the periphery are different in number and are organized in a significantly different manner than in **4.7**. Overall, there are two pyridines, two methanols, and a water molecule that are coordinatively bound to different metal centers on the dimer's periphery. Two diametrically opposite sites are again used in linking by the same motif as what was seen before, and by bonds of the same length (2.25 Å).

It is clear, however, that the coordinative geometry of the dimers that encompass this structure is significantly different, judging by the clearly "warped" appearance of the octametal belt. This is due to the eighth copper center, which surprisingly does not possess a ligand, and is truly tetra-coordinate. This unique feature is due to steric crowding, as one of the pyridine molecules on an adjacent capsule approaches too close to this metal center for it to accommodate a ligand (Fig. 4.18b, c). Consequently, the geometry at this metal center is very nearly square planar, with both coordinative angles equal to approximately 170°. Cu-O bond angles typically average significantly lower than 170° for at least one of the angles, so this site appears visually different when compared to the bonding at the other sites. There is likely to be some sort of interaction between the pyridine and this unsaturated copper center, judging by the short centroid-copper distance (3.7 Å) as well as an even shorter bond to one of the carbons on the pyridine ring (3.17 Å).

To enumerate this difference and to determine if it had any effect on the rest of the metal centers, τ_5 values were calculated for the coordinative copper centers in this structure. Mean τ_5 values were computed both including (wherein this center was treated as if penta-coordinate) and excluding this center, giving mean values of 0.322 and 0.367, respectively. With this treatment, the tetra-coordinate center has a τ_5 value of 0.008, indicating near-perfect square pyramidal

geometry (actually square-planar since the site was actually tetra-coordinate). Thus, it is understandable why the difference between the two former τ_5 values is so large; the low value at this site significantly brings the average downward. The increased tendency towards trigonality by a concomitant increase in τ_5 in all other metal centers, however, is an interesting finding and may be due to some degree of auto-compensation to minimize the change in Cu-O bond distances and angles caused by the flattening around this metal center (Fig. 4.20). This compensation is unlikely to have been caused by linking, per se, but rather by steric factors alone. This is substantiated by the results from **4.7**, which did not have a square planar site and consequently did not show the same increase in trigonality.

Another recurring motif in this structure is the role played by hydrogen bonding. This structure has a particularly interesting hydrogen-bonding network that will now be discussed (Fig. 4.19). The interaction between a coordinated water molecule and a coordinated methanol on adjacent dimers within a single chain is again present in this structure. Crystallographically well-ordered non-coordinating solvent molecules are also present, and one of these, a pyridine molecule, takes part in this ligand-based hydrogen-bonding network by binding to the coordinated methanol molecule *via* a very short 2.55 Å hydrogen bond. The coordinated water molecule also participates in additional hydrogen bonding interactions by bonding to a hydroxyl group on an adjacent strand of dimers that is located "above" the water molecule. Hydrogen bonding to another strand of dimers ("below") is also apparent, and is mediated by a solvent methanol and a solvent water molecule. These act as a bridge for an interaction between one of the coordinated methanols and one of the hydroxyls at the tetra-coordinate site. Other non-coordinating solvent molecules also interact *via* hydrogen-bonding with the hydroxyls on the capsular periphery, but these have a less apparent effect on structure. Overall, this leads to a

rather complex hydrogen-bonding network, which non-covalently connects adjacent strands of dimers. Another interaction that is present is, once again, VDW contacts between *C*-methyl groups on dimers, as this assembly also packs in the ABAB packing arrangement seen earlier.

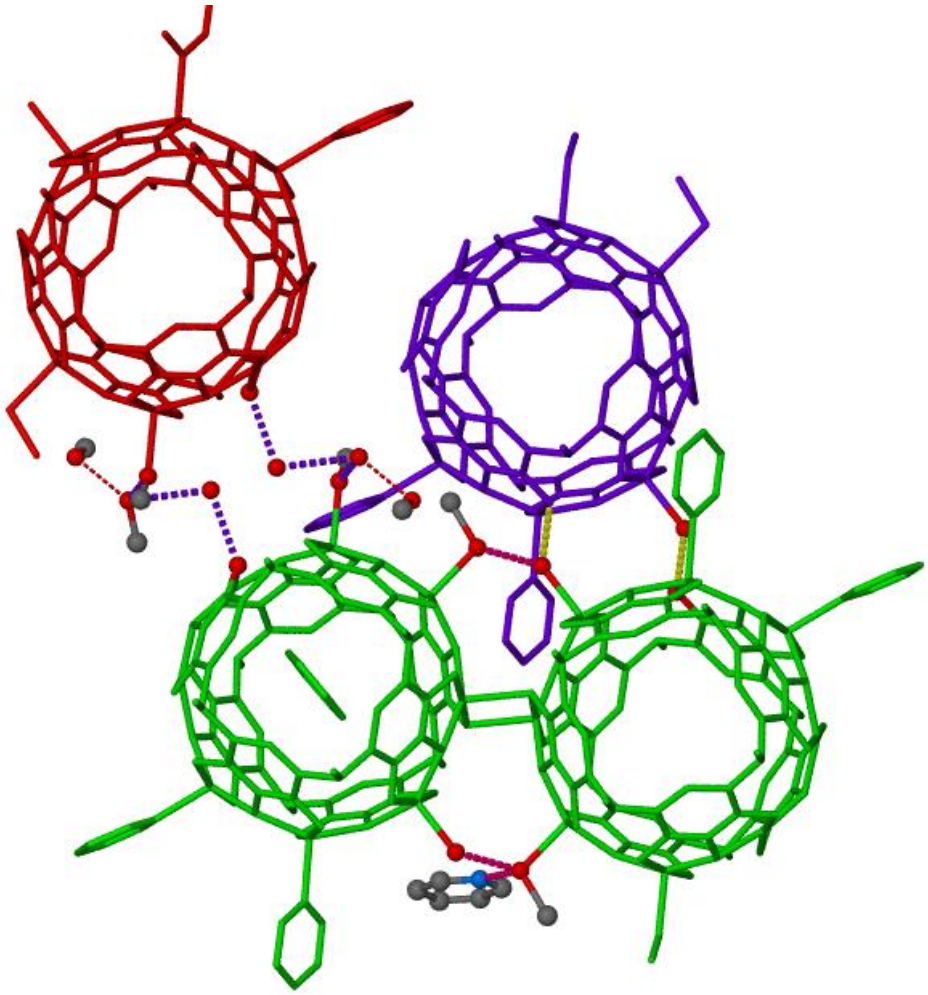

Figure 4.19: Hydrogen-bonding connectivity in **4.8** between three adjacent chains. Main chain (green) forms hydrogen bonds with a chain "below" (violet, bonds are yellow) and a chain "above" (red, bonds are violet). Hydrogen bonds between adjacent dimers on the same chain are also shown (pink bonds).

4.4.3 Development of a synthetic methodology to intentionally produce directly linked dimers

As this material was discovered accidentally, it was of interest to retroactively develop a more cohesive synthetic methodology that could a) be used to synthetically reproduce this material and b) to publish this work in good conscience. This development required a logical backtracking and an analysis as to what was important and what was not. For one, refluxing PgC1 in 2-bromopyridine was likely unimportant, as the substituted pyridine did not appear in the structure. However, the pretreatment of PgC1 with some sort of base seemed to be of value, as it was likely that this led to the deprotonation of some or all of the hydroxyl moieties in the upper rim, thereby priming the macrocycle to form a MONC. The addition of a base also reduces the amount of acid that is generated from synthesis, as at this stage the acid (HNO_3) likely does not lead to linking, but instead merely leads to reduced yields. Thus, PgC1 was pretreated with $NaHCO_3$. Pyridine was also likely necessary for at least the initial synthetic step (dimer creation), so it too would be used in this synthesis. Adding an acid *after* synthesis, however, is necessary to remove some of the coordinated pyridine molecules and produce open coordinative sites to which dimers can bind. Thus, following synthesis, HNO_3 was added to accomplish this task. The synthesis was also carried out in water, as a matter of consistency, followed by the addition of acetone to dissolve any precipitated material. These concepts were used to develop the synthesis below.

4.4.3.1 Synthesis (intentional) and characterization of directly linked dimers

A 10^{-3} M aqueous solution of PgC1 was prepared by boiling PgC1 in water until most of it had dissolved (solution was actually an emulsion). 80 µL of 1 M $NaHCO_3$ was added to 5 mL of this solution. In a separate vial, 200 µL of aqueous 10^{-1} M $Cu(NO_3)_2$ was added to 80 µL of aqueous 1M pyridine. After the resultant solution was mixed, 80 µL of aqueous HNO_3 was added, followed by 5 mL acetone to dissolve the resultant brown emulsion. The material was then allowed to crystallize *via* evaporation, leading to the formation of small plate-like crystals.

Crystal data for PgC_1Cu directly linked dimer #3 (4.9): $C_{44.75}H_{33}Cu_4N_2O_{14.50}$, M = 1084.89, plate brown , 0.20 × 0.05 × 0.01 mm^3, monoclinic, space group $P2_1/c$ (No. 14), a = 14.583(10), b = 26.828(19), c = 23.484(17) Å, β = 99.341(9)°, V = 9066(11) $Å^3$, Z = 8, D_c = 1.590 g/cm^3, F_{000} = 4380, Bruker SMART CCD area detector, MoKα radiation, λ = 0.71073 Å, T = 173(2)K, $2\theta_{max}$ = 46.6º, 74919 reflections collected, 12920 unique (R_{int} = 0.2982). Final *GooF* = 1.021, *R1* = 0.0872, *wR2* = 0.2117, *R* indices based on 5183 reflections with I >2sigma(I) (refinement on F^2), 1145 parameters, 16 restraints. Lp and absorption corrections applied, μ = 1.921 mm^{-1}.

4.4.3.2 Intentionally synthesized directly linked dimers: discussion

A rational synthetic effort was used to intentionally produce a third example of "direct" linking with copper-seamed dimers (**4.9,** Fig. 4.20c). Its synthesis is perhaps the most significant

thing about this assembly, as it shows that direct linking can be produced intentionally. The dimeric chain produced in this way differs from both of the previous examples (**4.7** and **4.8**), primarily in the identity and order of the peripheral ligands. However, several notable structural features, such as the ABAB chain packing arrangement and inter-dimer hydrogen bonding are preserved. In addition, the sterically-induced square planar site seen in **4.8** is also present, along with the causative close-contact pyridine ligand. Interestingly, the average τ5 value is only slightly higher than that in **4.7**, which does not possess any square planar sites (Fig. 4.20). The standard deviation among the τ5 values in the structure, however, more closely resembles that in **4.8**, suggesting that some sort of geometric perturbance does take place.

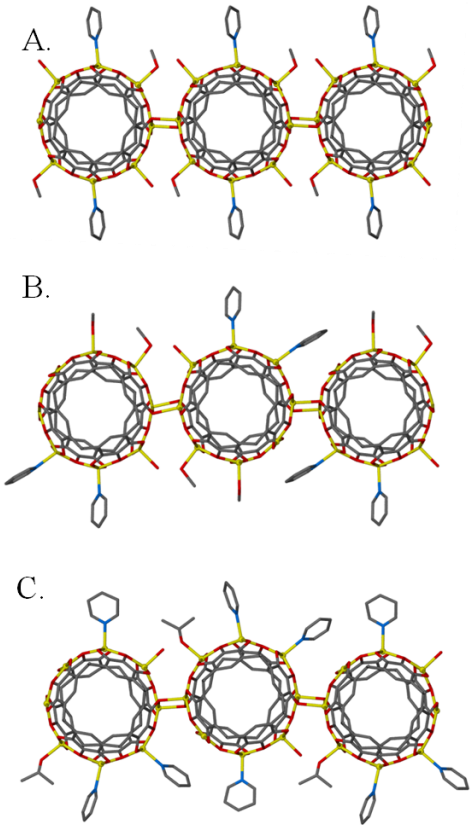

4.7

Metal #	Ligand	Angle 1	Angle 2	τ5
Cu1	adj dimer	177.89	156.93	0.35
Cu2	water	173.91	153.81	0.34
Cu3	pyridine	170.96	150.26	0.35
Cu4	methanol	173.49	151.73	0.36
Cu5				
Cu6				
Cu7				
Cu8				
Average				0.35
StD				0.01

4.8

Metal #	Ligand	Angle 1	Angle 2	τ5
Cu1	pyridine	168.81	147.1	0.36
Cu2	pyridine	168.48	147.13	0.36
Cu3	adj dimer	177.61	156.64	0.35
Cu4	n/a	169.88	169.38	0.01
Cu5	methanol	174.41	152.47	0.37
Cu6	methanol	172.45	151.07	0.36
Cu7	adj dimer	177.1	154.73	0.37
Cu8	water	169.3	145.02	0.40
Average	(excludes Cu4)			0.37
StD				0.02
Average	(includes Cu4)			0.32
StD				0.13

4.9

Metal #	Ligand	Angle 1	Angle 2	τ5
Cu1	n/a	171.88	168	0.06
Cu2	pyridine	171.55	151.72	0.33
Cu3	water	170.7	149.17	0.36
Cu4	adj dimer	176.03	155.94	0.33
Cu5	pyridine	167.65	145.26	0.37
Cu6	pyridine	166.87	144.25	0.38
Cu7	acetone	175.35	155.37	0.33
Cu8	adj dimer	176.91	156.27	0.34
Average	(excludes Cu1)			0.35
StD				0.02
Average	(includes Cu1)			0.31
StD				0.10

Figure 4.20: Comparison of the structures and τ5 values in directly-linked dimers **4.7** (A) **4.8** (B) and **4.9** (C).

The ligands in this structure include three pyridines, one acetone, and one water molecule. Analogously to the other two examples of dimeric linking, the acetone and water ligands from adjacent linked dimers interact *via* hydrogen bonding. The extensive hydrogen bonding network seen in **4.8**, however, is not seen in this structure. Many of the non-coordinating solvent molecules are either disordered or of a completely unknown identity. The cause for the lack of this hydrogen-bonding network and unknown identity of the solvents in both **4.9** and **4.7** is uncertain, but may have to do with a favorable ligand arrangement (or a larger number of hydrogen-bonding ligands) in **4.8** that make this possible. Alternately, because the data for **4.8** was collected at the ALS, and is therefore significantly stronger, it could be that what is lacking in **4.7** and **4.9** is simply data resolution, which allows one to see this extended hydrogen-bonding network.

4.4.4 Directly Linked dimers: conclusion

This section presented a novel method of linking PgC-based MONCs that did not rely on the use of divergent ligands. Instead, linking occurs directly between copper centers and phenoxy groups on adjacent dimers. This results in very closely spaced dimers along a linked chain, which, due to steric factors, leads to some interesting structural peculiarities. The most notable of these is perhaps the enforcement of a tetra-coordinate copper site due to ligand crowding, something that has never been seen with dimeric MONCs. Although the first two structures in this section were synthesized by accident, hints were gathered from the series of events that led to the materials' formation, allowing for the construction of a proper synthetic protocol for the generation of this material. Although the exact method by which direct linking occurs can only be guessed at, the basis of the synthetic methodology that was developed centers

on the concept of using of an acid to remove (protonate) some of the pyridine ligands around a dimer, thereby forcing the dimer to look for alternative ligands, namely solvent molecules and other dimers. As a proof of principle, this protocol was used to generate another directly linked analog, which shared many of the same structural characteristics of the first two structures, thus showing that direct linking can be controlled. The synthetic method that was developed may potentially be useful in the linking of other MONCs, including dimers seamed by other metals or maybe even hexameric nanocapsules. While it is uncertain if directly linked assemblies have any practical purpose, they may be useful for gas sorption research if functionalized with appropriate R-groups. Furthermore, as the result of the formation of an infinite chain of O-Cu-O bonds, directly linked materials may be interesting for other fields of research that aim to study the electronic/magnetic properties of transition metal complexes.

4.5 Nanocapsular linking: Summary

This chapter presented several novel ideas in regard to PgC-based metal-organic nanocapsules (MONCs). First and foremost, the concept of ligand exchange was presented as a method of modifying the properties of MONCs, thereby leading to functional materials. This concept was tested by using ligand exchange as a method of linking MONCs together to form metal-organic frameworks (MOFs). The divergent ligand 4,4'bipyridine (bpy) was used for these efforts, and was found to successfully displace pyridine and DMSO ligands from the periphery of MONCs. The structural properties of the MOFs formed in this way were then described, as were their similarities and differences. Both dimeric and hexameric MONCs were investigated, and examples of both one- and two-dimensionally linked MOFs were synthesized with both capsular motifs. Furthermore, both zinc- and copper-seamed dimers were investigated

as building blocks in MOFs, and it was found that the identity of the metal played a significant role in the structure of the resultant material. The packing of MOF layers in a crystal was also described, as were the non-covalent forces that played a role in layer packing. As the PgC1 macrocycle was used for most of these studies, one non-covalent motif that was found in all of the structures was a VDW interaction between *C*-methyl groups from dimers in adjacent layers. This interaction seemed to be a major contributor in determining the overall structure of the MOFs that were synthesized. This result differs from crystal packing in other PgC non-covalent assemblies, where the packing of macrocycles is largely solvent-mediated and the role played by the C-alkyl R-group is secondary. This knowledge can potentially be used to predict the geometry of other linked assemblies, and perhaps determine the ligands that would/would not form MOFs based on whether they would allow such contacts. As proof that non-covalent interactions had a large part in dictating the overall structure, an analog of a two-dimensionally linked zinc-seamed MOF was formed that had an alternate R-group on the macrocyclic lower rim. The result was that the MOF layers packed in an entirely different manner, thereby showing that the structure of a MOF can be easily affected by changing the R-groups on the lower rim. This substitution also changed the structure of the voids that run through the structure, a finding that may have later significance if gas/molecular adsorption studies are ever performed. In the last part of this chapter, another linking methodology was presented where divergent ligands were not used to mediate linking. Instead, dimers were linked directly to one another *via* coordination of copper centers to hydroxyl groups on the upper rim of the PgC macrocycle. This "direct linking" methodology led to several interesting structural peculiarities, including tetra-coordinate copper sites and hydrogen bonding between dimers. Most importantly, however, direct linking presented an important alternative to ligand-based linking.

4.6 Nanocapsular linking: future work

This chapter presented several interesting structures that can be considered as a starting point for further research with MONC-based MOFs. One obvious extension of this research is that of gas/guest sorption/separation. As all of the structures presented in this chapter bear voids and channels, they should all theoretically be able to bear molecular guests. This may require the activation of these materials. Activation can potentially be achieved by removing the solvent DMSO found commonly within these channels using heat or other solvents. Alternately, these materials can also be synthesized in solvents that are easily removable from a framework, such as methanol, acetone or acetonitrile.

Further exploration of linking with other ligands may yield materials with voids that are distinctly different from those presented in this section. The ligand used in this chapter (4,4'-bipyridine) is the most basic example in a broad molecular family used to construct MOFs, and many of the other family members may likewise be useful in creating linked entities. Other classes of ligands should also be explored, as they can produce yet other examples of linked assemblies with MONCs. In addition, direct linking may also be used in conjunction with ligand-mediated linking to yield yet other interesting assemblies.

As the main purpose of this chapter was to use ligand-mediated linking as a proof of concept for MONC modification, this broader concept should also be explored in further detail. Ligands that lead to capsular linking are just one of many ligand classes that can impart MONCs with specific function. Complex ligands bearing functionalities such as metal chelates or even other macrocycles may be useful in creating other hybrid entities out of MONCs. Other ligands, such as those that would render MONCs water-soluble or direct the MONC to a target in a living

system could also be useful for therapeutic purposes, particularly when coupled with the material in the next chapter.

All in all, the results of this chapter are just the beginning for research dealing with MONC-ligand exchange. There are many possibilities, both resulting in the formation of other MONCs as well as the formation of other functional MONCs that could be formed as a result of ligand-exchange methodologies.

5. Understanding the chemistry of MONCs using radiochemical methods

5.1 Overview:

This chapter focuses on the incorporation of radioisotopes, specifically ^{64}Cu, into metal-organic nanocapsules (MONCs). The purpose of this is twofold: to use radioisotopes to study the fundamental properties of MONCs, and to also explore the possibility of using MONCs as carriers for radioisotopes in living systems (i.e., as radiopharmaceuticals). Results related to the first goal comprise the majority of this chapter, as efforts to study MONCs *in vivo* were largely unsuccessful. These involve basic studies such as those that gauge the stability, solubility and propensity toward metal exchange, as well as a series of experiments that explore an unprecedented second form of copper binding in copper-seamed hexameric MONCs. In addition, several studies regarding their stability in biologically relevant media were also conducted, which may assist with additional future experiments in living systems. The research in this section was conducted in collaboration with Dr. Silvia Jurisson and the Jurisson group, as well as with Dr. Tim Hoffman at the H. S. Truman V.A. Hospital Biomolecular Imaging Center.

5.1.1 Brief background of radiochemistry and radiochemical methods

Radioisotopes are unstable isotopes of elements that transform (or decay) to yield other isotopes, often of entirely different elements. The decay process can create high energy particles including, but not limited to, alpha particles (helium nuclei), beta particles (electrons or, alternately, positrons), gamma rays (high energy EM waves), as well as neutrons. Radioactive decay of individual radioisotopes is a predictable process, yielding products in a discrete distribution of energies and species, and occurring over a specific timeframe (or half-life). Radioactive decay can be measured by using devices designed for the sole purpose of detecting

the high-energy particles produced during the decay process. This type of analysis gives valuable insight into the composition of a sample, its age, as well as its origin.

Aside from the isotopes of very light elements such as hydrogen, the chemistry of any given isotope differs little from the naturally-occurring element, which itself usually consists of an isotopic mixture. This includes the chemistry of most radioisotopes, a property that is exploited in the field of radiochemistry. By replacing naturally occurring isotopes with their radioactive counterparts, radioisotopes of almost every element on the periodic table have been used as valuable markers to study the chemistry and bioactivity of a vast number of compounds. While the chemistry of the molecule remains the same, the eventual radioactive decay of the "replaced" atom (or rather, its high-energy decay products) can be detected and used to gain information about the molecule, such as its location in a sample, chromatography plate, or living system. This has particularly important implications in medicine. Techniques such as positron emission tomography (PET) play an important diagnostic role in identifying areas of disease or cancer in a patient through this modality. In addition, radionuclides also serve an important use in cancer therapy. As the high-energy particles emitted from radioisotopes are indiscriminately destructive of living tissue, including cancerous tissue, a radioisotope-doped molecule that binds exclusively to cancer cells will, at least in theory, kill the cancer without significantly affecting the surrounding tissue, thereby curing the patient.

5.1.2 Rationale and Goals

While our interest with radioisotopes does include goals related to their use in a clinical setting (i.e., eventual medicinal applications of MONCs), radioisotopes can also be used in a much more simple sense, namely to conduct fundamental research. There are several advantages in specifically using radiochemical methods to study the chemistry of PgC-based MONCs. Perhaps the most important of these is the insensitivity of the radionuclide to the conditions of the system. Specifically, the ability to detect the radionuclide is not affected by the chemical environment that the radionuclide is in, or the properties of the analyte: it is either present or absent. This differs significantly from other methods, where the properties of the MONC can potentially hinder the use of the method or confound the results. This property makes radionuclides useful in studying the fundamental chemistry of MONCs, such as determining solubility, stability, metal exchange, and interaction with other chemical species. As previously mentioned, another positive characteristic of radionuclides is that they chemically behave analogously to the element that they replace. In the case of MONCs, this means somehow appropriately integrating radionuclides into the framework, and then using the resultant material to study the chemistry of MONCs. Likewise, their behavior in a living system can also be studied through this method, with the detection method being imaging instrumentation not unlike that used for studies in human subjects.

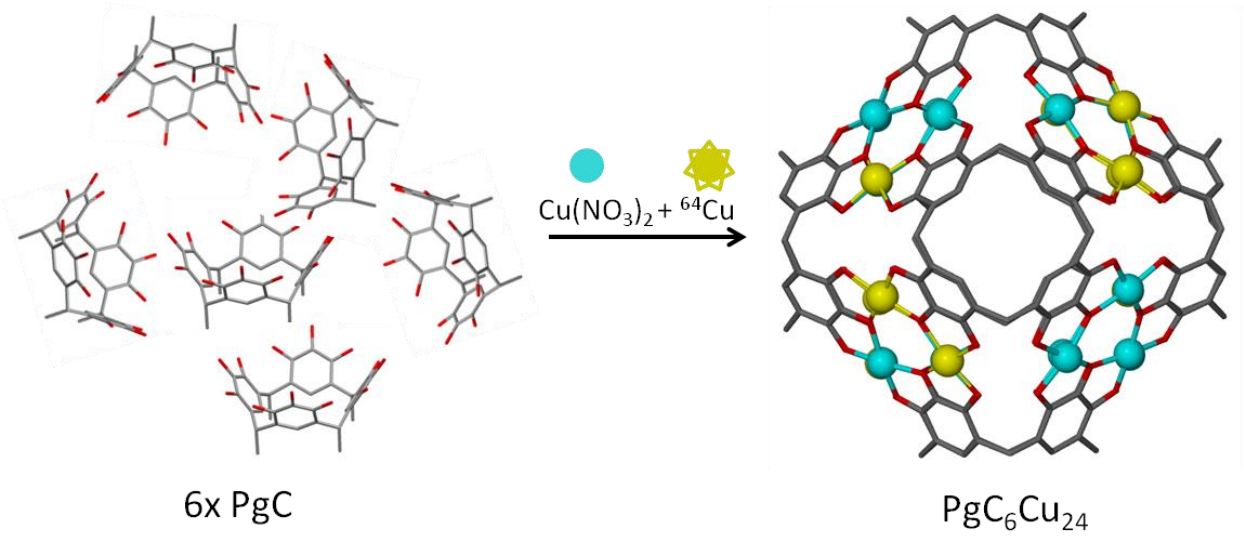

Figure 5.1: Radiolabeled copper-seamed hexamers ($PgCx_6Cu_{24}$) can be generated by adding a mixture of natural and radioactive ^{64}Cu (carrier-added solution) to a solution of PgC macrocycle

While there are several methods that can be used to integrate radioisotopes into PgC-based MONCs, perhaps the simplest is to use transition metal radioisotopes during their synthesis (Fig. 5.1). This serves a dual purpose, allowing one to study the bulk properties of the material, and secondly, allowing one to easily track the cationic component (the metals that seam up the MONC) and how it reacts to changes in environmental conditions.

The availability of ^{64}Cu from MURR as well as the ease of formation/purification of the copper hexamer spurred the use of this radioisotope as a starting point for these studies. ^{64}Cu decays via beta decay (39.6 %), electron capture (41 %) and positron decay (19.3 %), and the 0.5ll MeV photons produced by positron/electron annihilation can be easily detected by a NaI(Tl) well detector.[159] With a half-life of 12.8 hours, this isotope is appropriate for studies that take multiple days, such as those that gauge stability, or for those of a shorter length. One added benefit is that free $^{64}Cu^{2+}$ is soluble in a wide variety of solvents, including water, whereas ^{64}Cu

bound by PgC (i.e., within a MONC) is not. This helps tremendously in the purification of the MONC, as the un-reacted ^{64}Cu can be easily removed with water, dissolving any excess copper, while keeping the MONC as an insoluble solid. So far, our experiments have described the solubility of the copper hexamer in various solvents, as well as its stability in biologically relevant media. In addition, a happenstance finding that additional copper ions can be incorporated into the MONCs *after* their formation has led to an entirely different set of experiments that seeks to enumerate these additional coppers and explain their presence. It is important to note that the empirical formula $PgCx_6Cu_{24}$ will be used from now on to exclusively describe the hexameric copper-seamed MONC, where x defines the length of the pendant R-group on the PgC. Several R-groups were used during these investigations, and this nomenclature allows for a quick determination as to which one in particular was used.

5.2.1 Synthesis and purification of $PgCx_6Cu_{24}$

The formation and purification of $PgCx_6Cu_{24}$ with carrier-added ^{64}Cu solution (where ^{64}Cu is used as a mixture with non-radioactive Cu^{2+}) was a fundamental component of all radiolabeling experiments. Thus, it was necessary to develop a standard synthetic protocol for the formation and purification of $PgCx_6Cu_{24}$. The method that was developed for this purpose was partially based on the method previously detailed by Dalgarno et al., but with several important modifications.[119] Under standard laboratory conditions, where no radioactive components are used, the synthesis of $PgCx_6Cu_{24}$ is typically conducted by mixing solutions of PgC with an excess of a Cu^{2+} salt, typically the nitrate. This leads to immediate precipitation of a brown solid ($PgCx_6Cu_{24}$) that is removed *via* filtration from the mother liquor and dried prior to use in further experiments. However, as filtering/drying can lead to the formation of radioactive

dust, this method of purification was incompatible with work involving ^{64}Cu. Thus, centrifugation was used instead to purify the material. Methanol was used as the solvent for the reaction, as previous studies using MALDI-TOF mass spectrometry showed that synthesis in this solvent leads exclusively to the formation of the hexameric MONC. This avoids any confusion regarding the identity of the solid material, as our previous work demonstrated that certain solvent systems, such as acetone, result in a combination of dimeric and hexameric species.

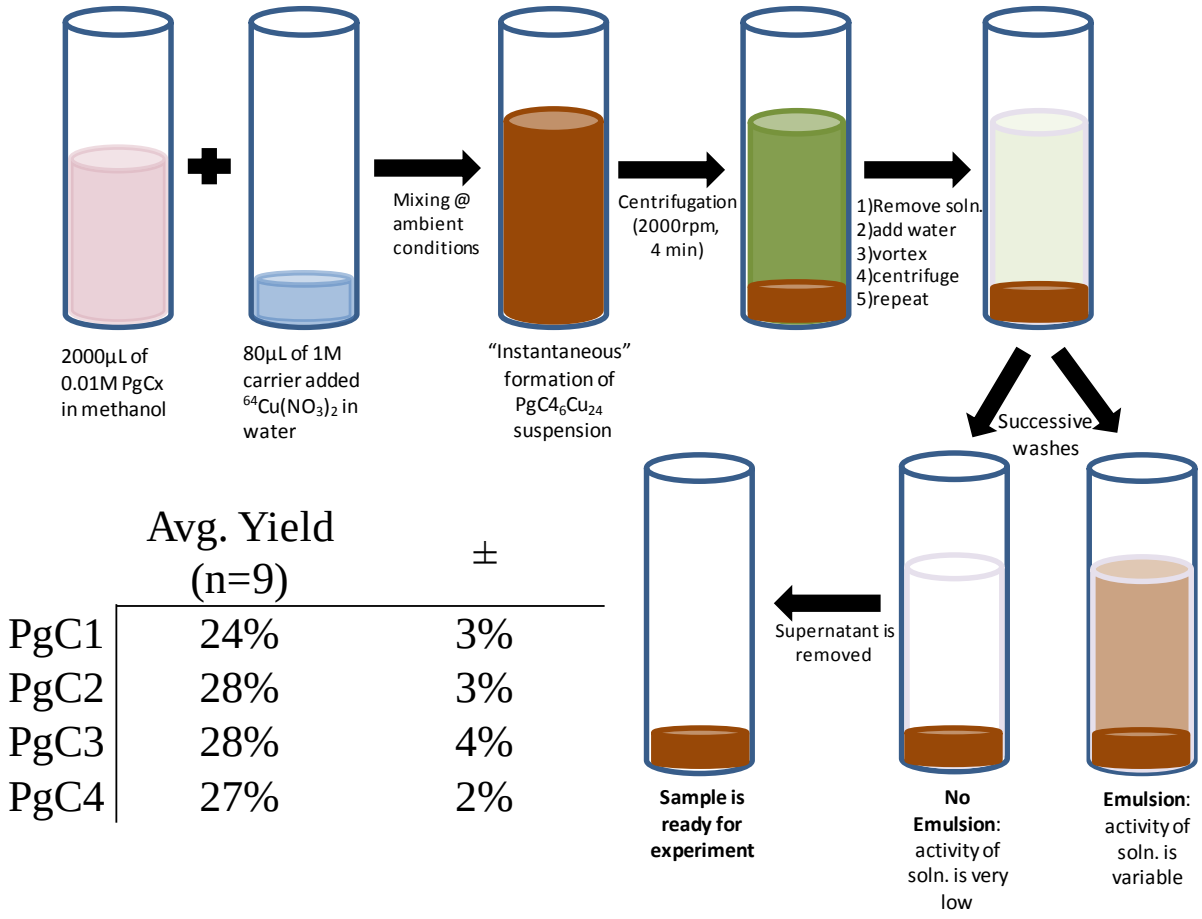

	Avg. Yield (n=9)	±
PgC1	24%	3%
PgC2	28%	3%
PgC3	28%	4%
PgC4	27%	2%

Figure 5.2: Synthesis scheme for the generation of radiolabeled $PgCx_6Cu_{24}$. Table at bottom left shows average yields of $PgCx_6Cu_{24}$ using this method and PgC1-4

Following these criteria, the synthesis was conducted as follows (Fig. 5.2): In a small centrifuge tube, 2 mL of methanolic 0.01 M PgC solution was mixed with 80 µL of carrier-added aqueous 1 M $^{64}Cu(NO_3)_2$. The specific activity of the carrier-added aqueous 1 M $^{64}Cu(NO_3)_2$ stock solution used for synthesis was highly dependent on the length of the experiment to be conducted. Typically, the specific activity ranged from 0.002mCi/mmol (for short experiments with no lag time) to 0.10mCi/mmol (for stock solutions used in multiple long length experiments over the course of several days). This led to the immediate formation of $PgCx_6Cu_{24}$ as a brown emulsion, which was vortexed briefly and centrifuged to form a solid pellet of MONC at the bottom of the tube, with mother liquor on top. The mother liquor (containing unreacted PgC, Cu^{2+}, and any dissolved/partially suspended $PgCx_6Cu_{24}$) was carefully removed with a Pasteur pipette from the centrifuge tube. The solid was then mixed with 2 mL of water, vortexed to promote mixing, and centrifuged again. This was repeated twice, with the aqueous layer being removed both times in order to remove any remaining free Cu^{2+}. This treatment resulted in a sample of pure $PgCx_6Cu_{24}$, absent of any free Cu^{2+}, unreacted PgC, or HNO_3 byproducts, and was then used for further experiments. It should be noted that the specific activity of the carrier-added aqueous 1 M $^{64}Cu(NO_3)_2$ stock solution used for synthesis was highly dependent on the length of the experiment to be conducted. Typically, the specific activity ranged from 0.002mCi/mmol (for short experiments with no lag time) to 0.10mCi/mmol (for stock solutions used in multiple long length experiments over the course of several days).

During the course of treatment/purification, the material was monitored by counting the contents of the tube with a NaI(Tl) well detector. This was partially done to spot any incongruence during synthesis as well as to determine the net yield of the reaction. As a 4:1 copper:PgC ratio was used, which is the actual ratio of copper:PgC in the MONC, a stoichiometric or near-stoichiometric (100%) yield was the expected result. Actual yields, however, typically ranged from 25-30% depending on the PgC that was used (Fig. 5.2), lower than the near-stoichiometric yields using traditional means. However, it is important to note that a significant amount of MONC remained suspended/dissolved in solution after the initial centrifugation step, and could not be recovered regardless of centrifugation time.

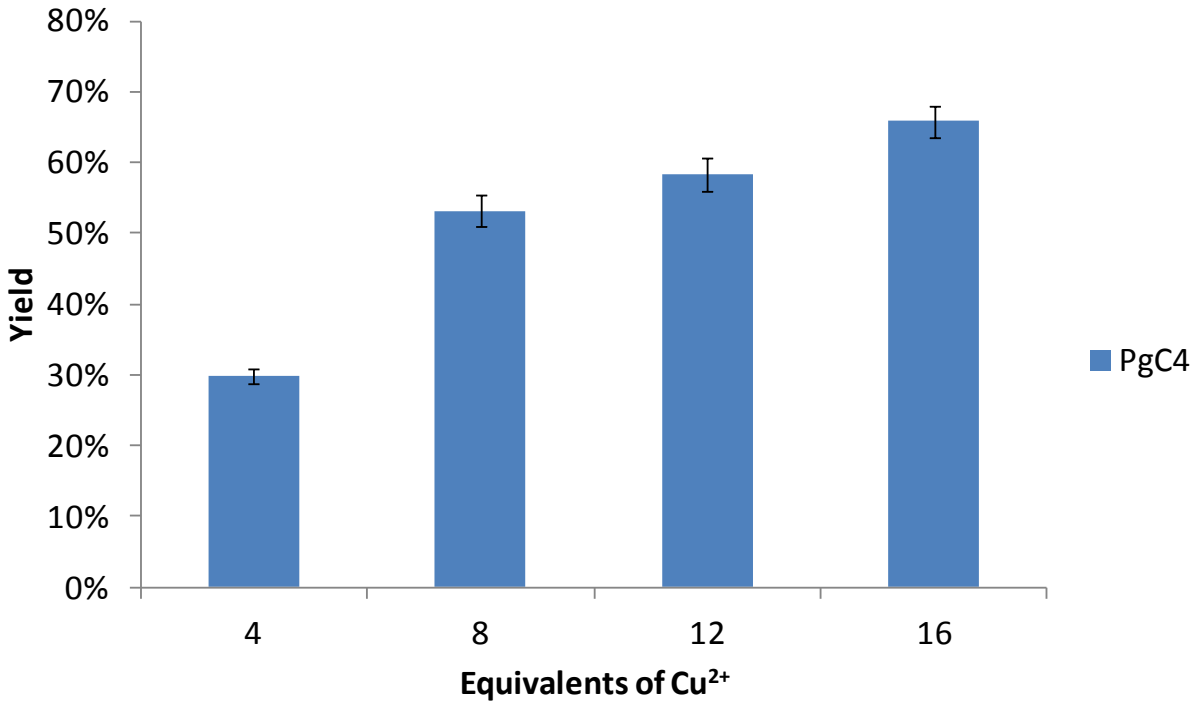

Graph 5.1: The yield of MONC can be increased by increasing the amount of Cu^{2+} that is added relative to the concentration of PgC.

To determine if yields could be improved, a number of different Cu^{2+}:PgC ratios were investigated (Graph 5.1). An increase in the proportion of Cu^{2+} did lead to increased synthetic yields, perhaps due to a "salting-out" effect that excess Cu had on suspended MONC. However, as the effect was not spectacular in improving yields (excess copper never led to stoichiometric yields), a 4:1 copper:PgC ratio was nonetheless used for all other experiments, as there was not enough reason to justify using excess copper.

5.2.2 Synthesis of RsC4-Cu complex

Resorcin[4]arenes (RsCs) are another family of macrocyclic compounds that are structurally similar to the pyrogallol[4]arenes. While pyrogallol[4]arenes have a total of twelve hydroxyl groups lining the upper rim, resorcin[4]arenes only have eight. As such, the two macrocyclic families behave in a chemically similar way when it comes to forming non-covalent assemblies. This is not the case, however, with their ability to chelate metals. While there is a diverse variety of capsular and non-capsular metal complexes that have been reported with PgCs, few have been reported with native (unmodified) RsCs. However, it was unknown if there was a chemical basis for this (four less hydroxyls per macrocycle), or if it was simply from a lack of trying and/or the failure of the resultant complex to crystallize. Assuming that such a complex would behave similarly to PgC-metal complexes (and would therefore be insoluble in water), it was predicted that its presence could quickly be determined with ^{64}Cu.

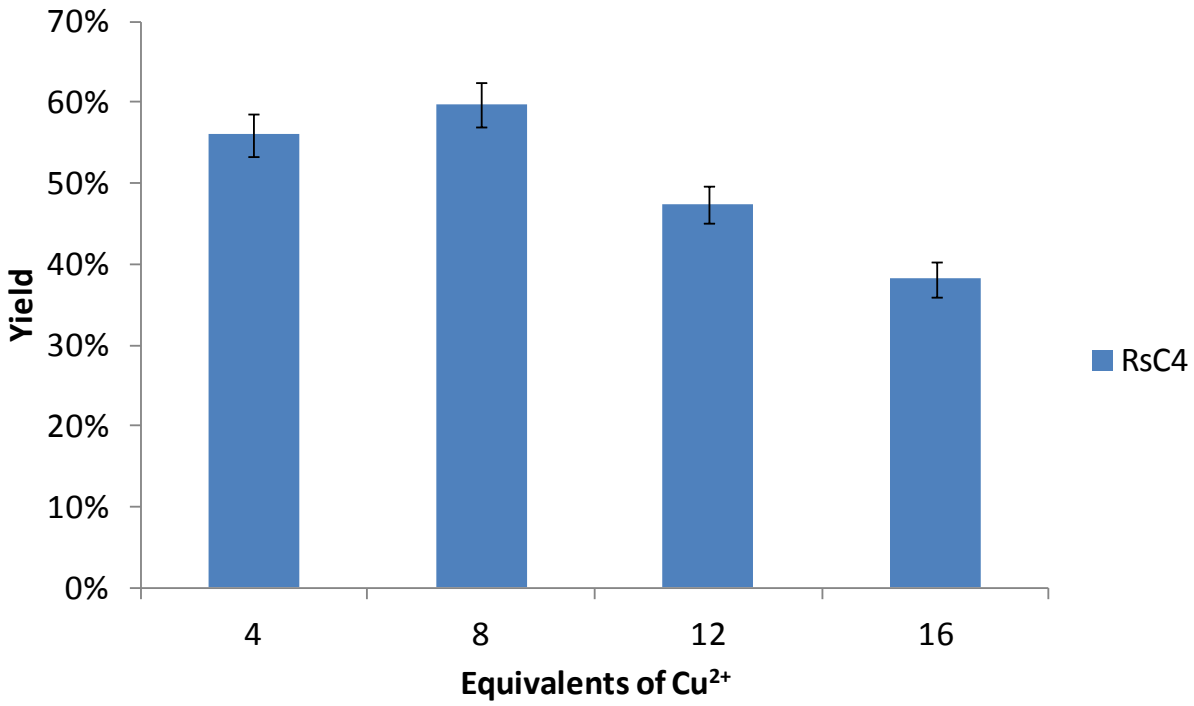

Graph 5.2: Calculated ratios of Cu^{2+}:resorcin[4]arene as a function of the amount of copper added. The complex formed is still currently unidentified.

Initially, treatment of a 10^{-2} M methanolic solution of RsC4 with aqueous 1 M carrier-added $^{64}Cu(NO_3)_2$ did not lead to the formation of a precipitate or any distinguishable color change. While this result was discouraging, a second attempt was nonetheless conducted, this time with the addition of pyridine during synthesis as well. The addition of a coordinating base like pyridine theoretically serves two purposes. It can drive the reaction forward by eliminating any HNO_3 that is formed on the deprotonation of phenolic oxygens. It also has the potential to stabilize copper centers by filling in any open coordinative sites that were not used for coordination with RsC. Accordingly, when the synthesis was repeated with concomitant addition of pyridine, the solution changed from a blue color, indicating free Cu^{2+}, to a black color, indicating that some sort of a reaction had taken place. This material was still soluble in

the mother liquor, so excess water was then added to this solution, causing a dark colored precipitate to form. The material was then purified analogously to $PgCx_6Cu_{24}$ and counted using a NaI(Tl) well detector during all synthetic and purification steps. In stark contrast to PgC, this complex was found to bind significantly less copper, with a calculated ratio of 2 RsC per copper, assuming a theoretical yield of 100% for the reaction (Graph 5.2). However, as such an assembly has never been characterized *via* XRD (or any other method for that matter), the actual yield could not be determined, making this ratio more or less of a conjecture. However, what this result did show was that RsC can indeed bind copper and form an (as of yet) unidentified complex. This suggests that, akin to PgC, RsC is worthy of future research studies that focus on metal coordination of calixarene-like macrocycles.

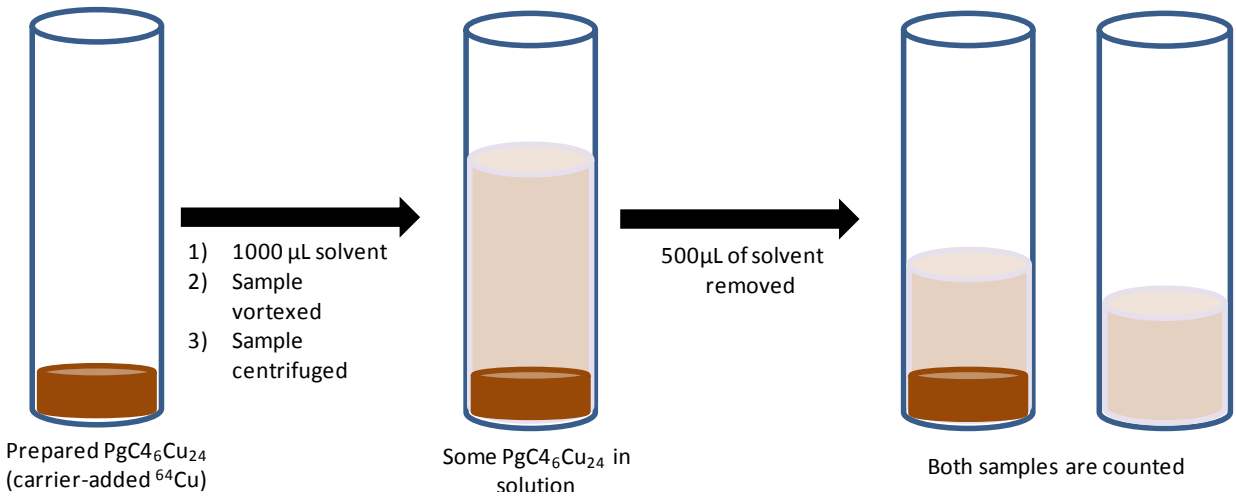

% of counts in 100µL soln

	H2O	MeOH	IsoOH	EtOH	Brine	Hexane	MeCN	EtOAc	Acetone
PgC1	0.11%	0.11%	8.01%	0.20%	**0.75%**	0.38%	2.47%	9.03%	**15.58%**
PgC2	**0.92%**	**0.71%**	**8.81%**	**8.02%**	**0.45%**	**7.59%**	5.09%	8.84%	11.29%
PgC3	**0.29%**	0.20%	**6.09%**	**2.82%**	0.63%	1.49%	7.34%	9.03%	4.20%
PgC4	0.36%	0.17%	**7.76%**	**4.09%**	0.45%	1.92%	4.17%	8.90%	5.61%

Figure 5.3: Diagram of the scheme used for solubility measurements. Table below shows the solubility of PgCx$_6$Cu$_{24}$ complexes in various solvents. **Bold** denotes the formation of an emulsion (untrustworthy data)

5.3 PgCx$_6$Cu$_{24}$ solubility determinations

Due to the simplicity in detecting small amounts of dissolved analyte using radiochemical methods, the solubility of PgCx$_6$Cu$_{24}$ in various solvent systems was evaluated. This was an important step toward, arguably, more interesting studies of these compounds, aiding in appropriate solvent choice as well as accurate solvent corrections. Solubility was evaluated in a rather simple manner (Fig. 5.3): PgCx$_6$Cu$_{24}$ was synthesized and purified as previously described, counted, and then a solvent of choice (usually 1 mL) was added to the

centrifuge tube, which was then vortexed for at least one minute, and centrifuged. A 500 µL aliquot of the solution was removed and counted using a NaI(Tl) well detector. The solution-plus-solid that remained in the centrifuge tube was also counted. The solubility of $PgCx_6Cu_{24}$ could then be determined by dividing the counts in the solvent aliquot by the counts of the material at the beginning of the analysis. Since the net yield for this reaction was known, it was possible to roughly express the solubility in mol/liter (appendix). However, because it was unknown how much volume the MONC solid took up in the bottom of the centrifuge tube, which itself requires a correction factor, solubilities were also calculated as a percent of total counts in 100 µL solvent (Fig. 5.3). These values could then be used to easily correct data in other experiments that followed a similar procedure or determine how much solvent was required to dissolve $PgCx_6Cu_{24}$ that was prepared in the standard way delineated in previous sections of this chapter. One additional consequence of this experiment was a more accurate tabulation of net yields for $PgCx_6Cu_{24}$. As solubility was evaluated for nine different solvents, this experiment necessitated that the compound was synthesized and purified nine separate times. Data was recorded for all steps during synthesis/purification, and this conveniently produced an average yield from each of the nine trials (Fig. 5.2).

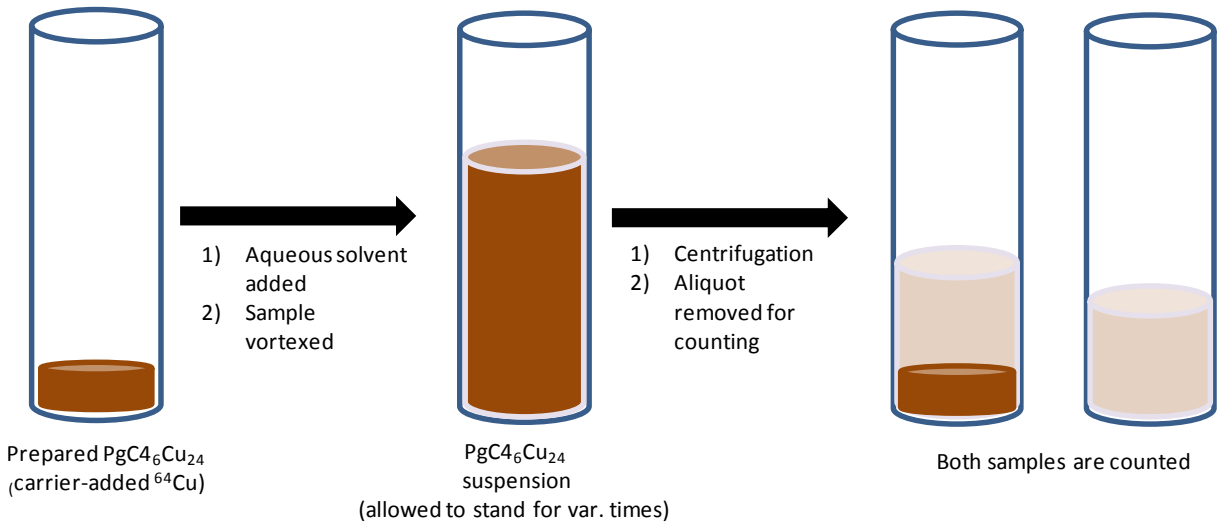

Figure 5.4: Scheme for the rudimentary analysis of stability in aqueous solvent

5.4.1 Stability Determination in aqueous media

One long-term goal in our studies with MONCs is to use these entities as a delivery system of radionuclides into a living system, and potentially as a radiopharmaceutical. Thus, it was imperative to study copper-seamed MONCs in a biologically relevant environment. The closest estimate to such an environment in a chemistry lab is, obviously, an appropriate aqueous medium. Lack of stability in such an environment would hamper any future *in vivo* studies, so this study was of great significance as it would tell us whether or not to proceed in this direction.

Stability was first evaluated in water, as this is the most basic aqueous medium. An experiment that was essentially analogous to the solubility determinations was carried out to determine stability, albeit over a longer timeframe (Fig. 5.4). Water was added to a centrifuge tube containing purified (and counted) $PgCx_6Cu_{24}$, which was vortexed until the solid was suspended in solution. The suspension was then left undisturbed over a prolonged course of time (up to 42 hours). The material was then centrifuged and an aliquot of the supernatant was removed for counting. As in the solubility determinations, the count rate of this aliquot was

compared to the count rate of the bulk material. $PgCx_6Cu_{24}$ is poorly soluble in water, while free Cu^{2+} is very soluble. Thus, it was expected that if the compound was water-unstable, a time-dependant increase in count rate of the supernatant would result as free Cu^{2+} entered the solution upon its dissociation into ligand and metal ion. However, it was instead observed that little, if any, counts could be detected in the water aliquot, regardless of treatment duration. This suggested that, at least in water, the $PgCx_6Cu_{24}$ suspension was stable to dissociation. The stability of $PgCx_6Cu_{24}$ in phosphate-buffered saline (PBS) was then analyzed. This experiment would determine if any additional cations or potentially chelating anions (phosphate, in particular, has affinity towards copper) would lead to $PgCx_6Cu_{24}$ degradation. However, PBS treatment likewise was shown to have no effect on the material. As a final test for stability prior to *in vivo* work, stability was gauged in mouse serum. This would as closely as possible emulate the effect of a true living environment on $PgCx_6Cu_{24}$. An extended course of treatment once again led to no increase of counts in solution. This indicates that copper-seamed MONCs are stable in biologically relevant media, at least under the conditions of this study.

While these trials certainly showed that $PgCx_6Cu_{24}$ was stable as a suspension, it was uncertain whether this was truly the result of inherent stability of the material, or, rather, kinetic inertness due to its low solubility in water. To determine if this was the case, a competition experiment was performed with Na_4EDTA, a high affinity chelator for a wide variety of metal ions. Due to its chelating strength, Na_4EDTA should be capable of breaking $PgCx_6Cu_{24}$ apart as long as some sort of interaction was occurring between the solution and the suspended solid.

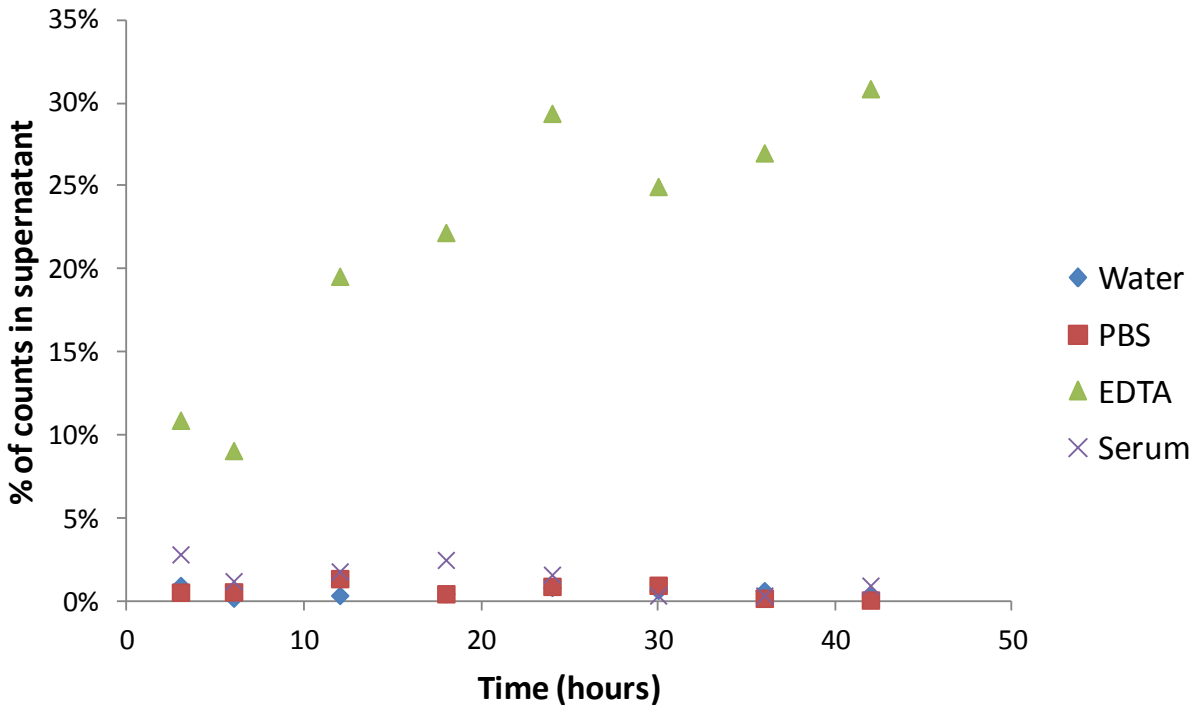

Graph 5.3: Results from the stability determination experiment: MONCs are stable in biologically relevant solution, time-dependent decomposition of $PgC4_6Cu_{24}$ in 1 M aqueous Na_4EDTA solution shows that MONCs do interact with the solution to a certain extent even as an emulsion.

To determine if this was the case, a proof of concept experiment was conducted without radioactivity by fully dissolving MONC in ethyl acetate and adding an aqueous solution of Na_4EDTA, which layered at the bottom. Over a course of time, the aqueous layer began to turn green, indicating that copper was transferring to the aqueous layer, and thus was being lost from $PgCx_6Cu_{24}$. This indicated that $PgCx_6Cu_{24}$ could indeed be degraded by this ligand. To determine if a suspension of the material would likewise be degraded by Na_4EDTA, an analogous stability experiment was carried out, with aqueous 1 M Na_4EDTA as the solvent. This was done as before, with carrier-added ^{64}Cu used to form $PgCx_6Cu_{24}$ so that the loss of copper to

the aqueous layer could be quantified (Graph 5.3). As expected, this caused a time dependent increase of copper in the aqueous solution, suggesting that even as a suspension, MONC is not immune to factors that would lead to its degradation. This gives credence to the stability experiments performed in aqueous media, as it shows that any degradation caused by those systems would be readily apparent.

5.4.2 Animal Studies

One of the primary goals laid out in the beginning of this chapter was to investigate the behavior and distribution of MONCs in a living system. Such research is important, as it allows us to determine if MONCs can be used in a living system as pharmaceutical agents. To this end, studies that involved the injection of ^{64}Cu-labeled MONCs into mice were arranged in collaboration with Dr. Tim Hoffman at the H.S. Truman V.A. Hospital Biomedical Imaging Center.

In contrast to the synthetic methods in the rest of the chapter, where bulk quantities of material are generated, MONCs were generated at very low concentrations (tracer levels) so as not to cause toxicity in the animal. In addition, PgC3OH was used instead of other PgCs, as it is significantly more water-soluble. A 10^{-2} M solution of PgC3OH was prepared by first dissolving approximately 0.08g PgC3OH in 1 mL of ethanol and adding 9 mL of water. This solution was then diluted to make a 10^{-4} M solution, by adding 100 µL of this solution to 10 mL water. This was then mixed with $^{64}Cu(NO_3)_2$ (carrier added, but undiluted) from Essential Isotopes to give an injection activity of approximately 300 µCi. This mixture was then injected into a mouse, as were approximately 300 µCi of $^{64}Cu(NO_3)_2$ (into a different mouse), which functioned as a control. Imaging was performed on a Philips Medical Systems MOSAIC Small Animal PET system.

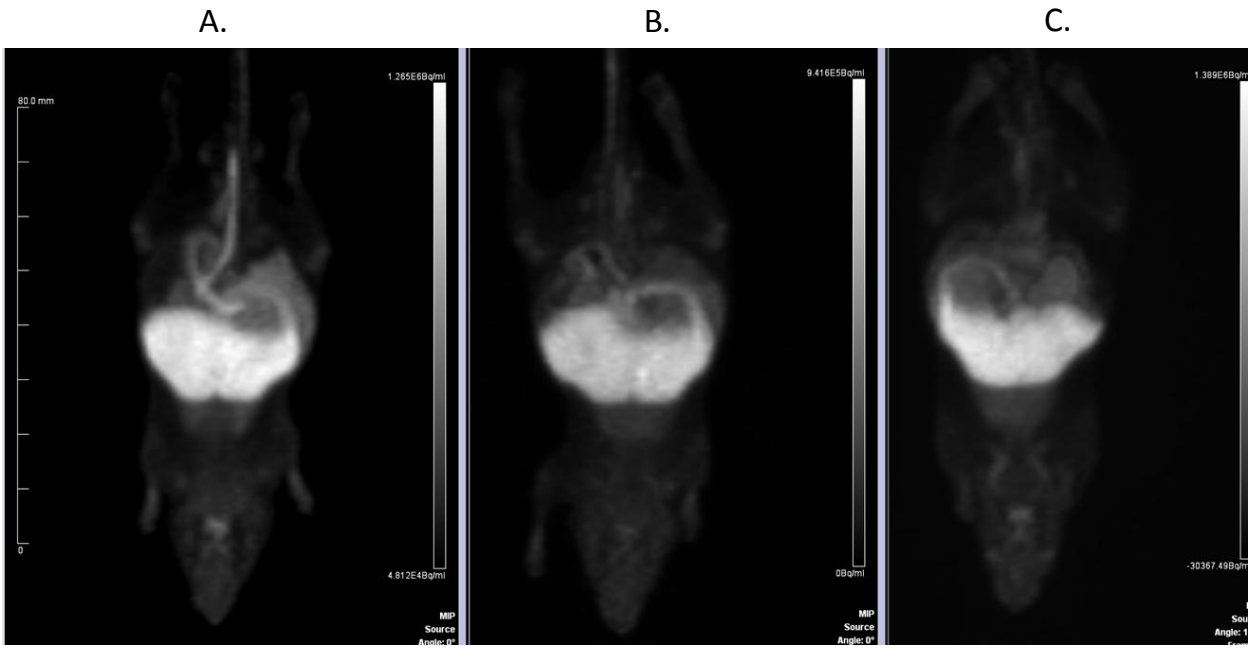

Figure 5.5: PET images of a mouse injected with free ^{64}Cu as a control (A) as well as mice injected with ^{64}Cu-labeled MONC solution (B,C). The ^{64}Cu uptake profile is the same in all three cases, suggesting that MONCs are either metabolized quickly or the synthesis did not work.

The resultant images from this study are shown in Figure 5.5a and 5.5b, where a is the control and b is the MONC solution. As is clearly visible, the ^{64}Cu uptake is nearly identical in both images. This suggests one of three things; the labeling did not work, MONC is metabolized quickly and produces free $^{64}Cu^{2+}$, or the profile of the labeled MONC and free ^{64}Cu is exactly the same (unlikely). Another experiment was conducted, where in addition to ^{64}Cu and PgC3OH, a 10^{-3}M $NaHCO_3$ solution was also added to help drive the MONC-generating reaction forward. However, this too had the same profile (Fig 5.5c) as the control, suggesting that the labeling procedure likely did not work. More research is required to determine the reason for labeling not working and/or a method of synthesis at low concentrations. Alternately, it could be that a PgC with a different functionality may be required to direct the MONC to a specific location in the

organism. This would clear up any ambiguity about the possibility of the MONC simply having a similar bio-distribution profile to free $^{64}Cu^{2+}$.

5.5 Metal exchange studies: An Overview

As previously mentioned, a notable problem with PgC-based MONCs is their resistance to study with most analytical techniques, often even with scXRD, which is (ironically) the standard method by which these entities are studied. Thus, in addition to *in vivo* studies, another important goal of this project was to use radiochemistry as a technique to study the chemistry of MONCs. Specifically, radiochemical methods allow us to study the metal content of MONCs without having to consider interfering factors, such as variable solvent encapsulation, ligands, etc., that hinder or confound the use of other techniques. This is specifically important in the study of metal exchange. Previous studies showed that gallium-seamed MONCs can undergo cation exchange, with Ga^{3+} cations being replaced by other cations, such as Cu^{2+} and Zn^{2+}.[119,124,125] In addition, it was also shown that additional cation binding can occur within the *interior* of the nanocapsule, something that was never considered or studied with the copper-seamed MONC.[123] However, even with gallium, these studies were labor intensive in working out the conditions of crystallization and often gave ambiguous results regarding the metal composition of the now-mixed metal MONCs. Further studies to investigate metal exchange in non-gallium seamed MONCs are strongly hindered by these factors, where crystallization and subsequent study with XRD is even more difficult, if not impossible.

With these limitations in mind, it was clearly evident that using radiochemical techniques would A) simplify previous studies of metal exchange, and B) could easily be extended to the study of transition metal exchange with a wide variety of non-gallium-seamed MONCs. As my studies in this project focus on copper-seamed MONCs, they were, for a lack of a better term, a

guinea pig to test the plausibility of similar studies. Furthermore, this was another method of studying the stability of copper-seamed MONCs, this time by gauging the effect that other transition metal cations have on the stability of the copper-seamed MONC.

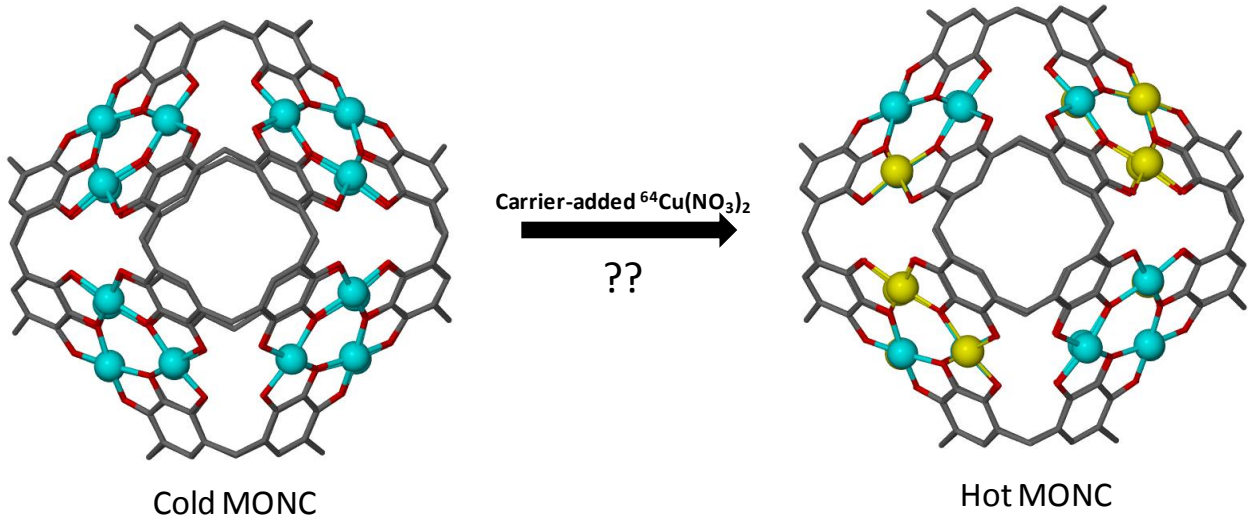

Figure 5.6: Can "cold" framework coppers in the $PgCx_6Cu_{24}$ MONC be replaced with ^{64}Cu?

5.5.1 Initial exchange studies

The first of these studies aimed to determine whether free Cu^{2+} would exchange with framework copper ions in $PgCx_6Cu_{24}$ (Fig. 5.6). Aside from being an object of pure interest, this study qualitatively tested the strength of the oxo-copper bonds that hold the assembly together, and therefore, its stability. The setup of this experiment was rather simple (Fig. 5.7): "Cold" (nonradioactive) $PgCx_6Cu_{24}$ would be co-dissolved with carrier-added $^{64}Cu(NO_3)_2$. As both $PgCx_6Cu_{24}$ and most copper salts are soluble in acetone, this solvent was used for the study. After a period of time, the solution would first be counted, then $PgCx_6Cu_{24}$ would be precipitated with excess water, washed several times to remove any remaining free copper, and counted again using a NaI(Tl) well-detector. An increase in the count rate of the precipitate

above background would, at least theoretically, indicate that "cold" framework copper ions had exchanged for ^{64}Cu.

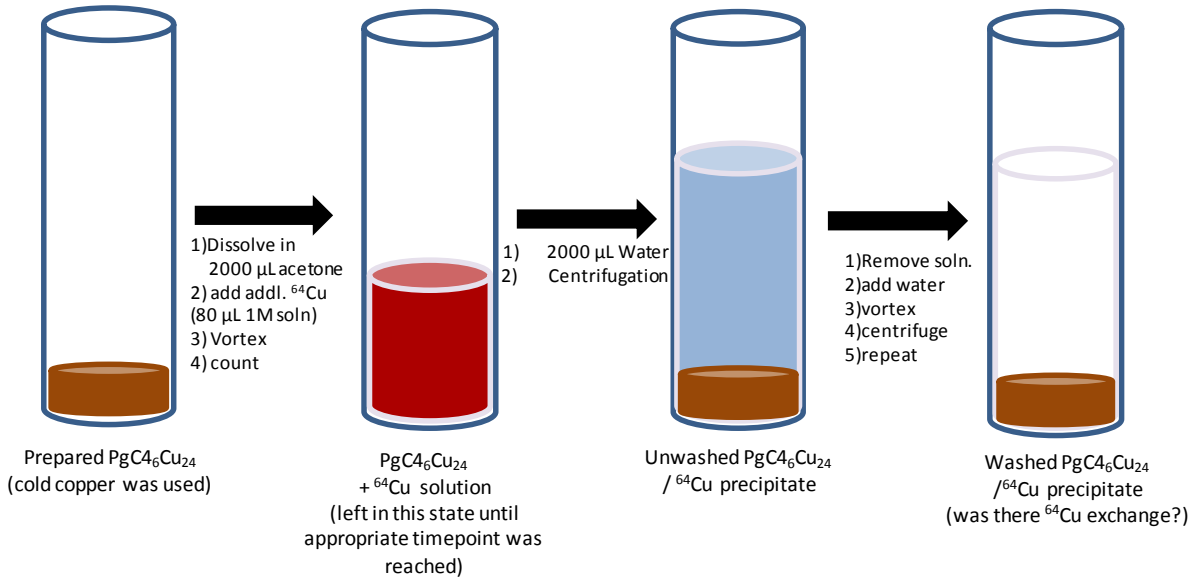

Figure 5.7: Scheme for experiments gauging the exchangeability of ^{64}Cu for coppers bound by $PgCx_6Cu_{24}$

As an initial test of exchange, an excess of carrier-added copper nitrate was added to $PgC3_6Cu_{24}$, so that it could definitively be determined whether or not exchange was occurring. 80 µL or 160 µL of 1 M carrier-added $^{64}Cu(NO_3)_2$ in water was added to each of two tubes containing purified $PgC3_6Cu_{24}$ dissolved in 2 mL of acetone. With both titers (80 and 160 µL), this was a large excess of copper with respect to the amount present in $PgC3_6Cu_{24}$: based on the previously calculated average yields of this MONC, this amounted to roughly 3.5 and 7 times more copper than what was present in the assembly. Two additional trials were also performed wherein "cold" (or non-radioactive) copper nitrate was added prior to the addition of 80 and 160 µL of hot (radioactive) copper solution. If exchange was, in fact occurring, the counts in this

case would be half of that in the first two trials, as the hot copper would compete with the cold copper for exchange. Precipitation with water was performed 15 minutes post-treatment, after which the material was centrifuged and washed with water several times to remove any free copper. It was then counted to determine if the previously non-radioactive material had incorporated any ^{64}Cu during this process.

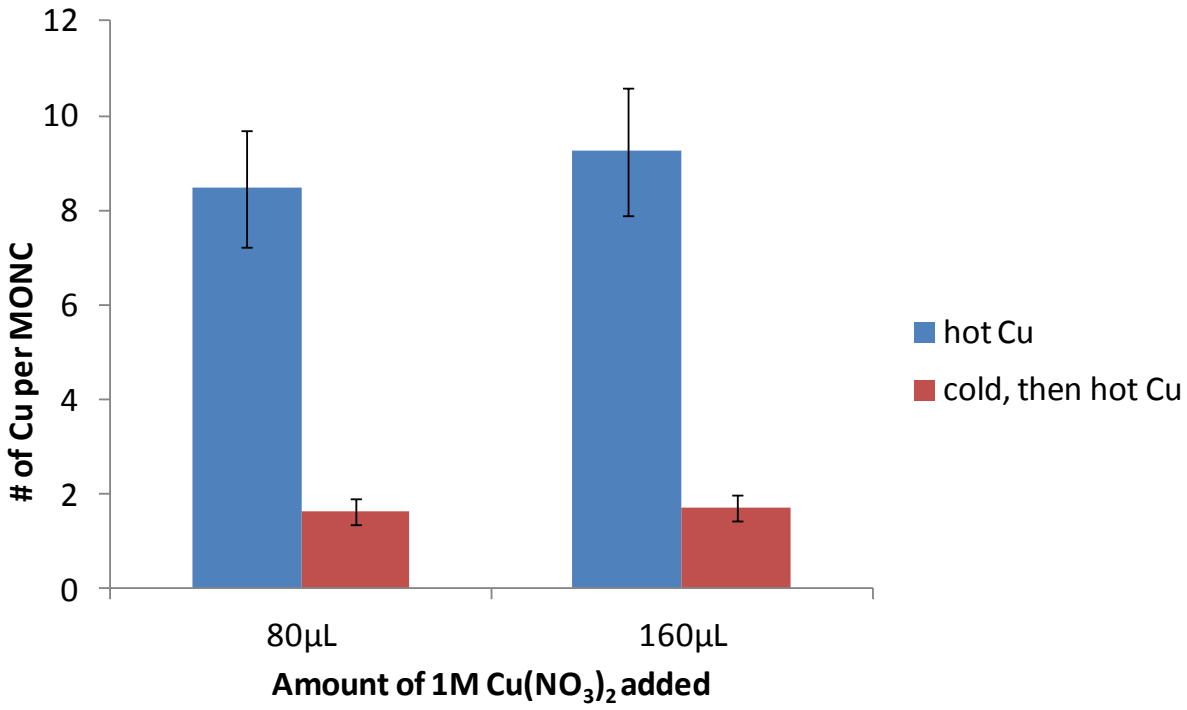

Graph 5.4: Results from the first "exchange experiment." ^{64}Cu can be found in $PgCx_6Cu_{24}$ nanocapsule, but pretreatment with "natural" copper prior to treatment with ^{64}Cu significantly diminishes the amount of ^{64}Cu that is retained. This result is suggestive of an unknown mode of copper incorporation.

The results of this experiment were rather unexpected (Graph 5.4). In the first two tubes, where only "hot" carrier-added $^{64}Cu^{2+}$ was added, the count rate, which signifies the amount of extra coppers that associated with the MONC, was essentially the same in both tubes, with only a slight increase after adding twice as much Cu^{2+}. The degree of exchange was surprising, as it was also significantly lower than expected, roughly amounting to 35% and 39% of the total

copper present in $PgC3_6Cu_{24}$, or approximately 9 coppers out of a total of 24 per capsule. This is not consistent with a fast exchange rate, as 3.5 and 7-fold excesses of carrier-added ^{64}Cu should have pushed out the majority of the originally existing framework coppers in $PgC3_6Cu_{24}$ and replaced them with the coppers in solution. Pretreatment of MONC with cold copper, prior to the addition of hot copper had an additional unexpected effect: the binding of hot copper was decreased to levels that were significantly lower. This was contrary to the expected result that should have been observed if exchange was truly occurring, namely that the count rate of the solid would be half of the 35% and 39% seen when only hot copper was used. This indicated that exchange was not occurring, but rather that additional coppers were binding in some unknown fashion to the already copper-laden MONC.

Although this experiment showed that some form of additional copper binding did occur, it was clear that a good deal of investigative work would still be required to fully understand this effect. One immediate factor of interest was the effect that free copper concentration played in copper binding. As the previous experiment only employed two volumes of added copper, both significantly more than what was apparently required, a new experiment was envisioned, wherein copper was added in a broad range of concentrations. The first of such experiments was unfortunately flawed in design, as $PgC3_6Cu_{24}$ precipitated immediately following the addition of free copper, rather than giving it time to react. However, it nevertheless showed several important results. $PgC3_6Cu_{24}$ (non-radioactive) was synthesized and purified in nine separate centrifuge tubes, then dissolved in 2000 μL of acetone. 1 M carrier-added $^{64}Cu(NO_3)_2$ in water was then added to separate tubes, in titers ranging from 5 μL to 240 μL. The tubes were initially counted using a NaI(Tl) well detector, vortexed, and water was added to each in order to form precipitate ($PgC3_6Cu_{24}$). The precipitate was washed several times with water to remove any

remaining free copper and the resulting precipitate was counted. An additional (inverse) experiment was carried out concomitantly, wherein MONCs formed with hot copper had cold copper added to them instead. As the previous experiment showed that peripheral exchange was not likely what was really going on, it was expected that a change in counts for these samples would not be observed, as cold copper binding would not be detected unless it actually displaced hot copper centers. This was, in effect, a null experiment.

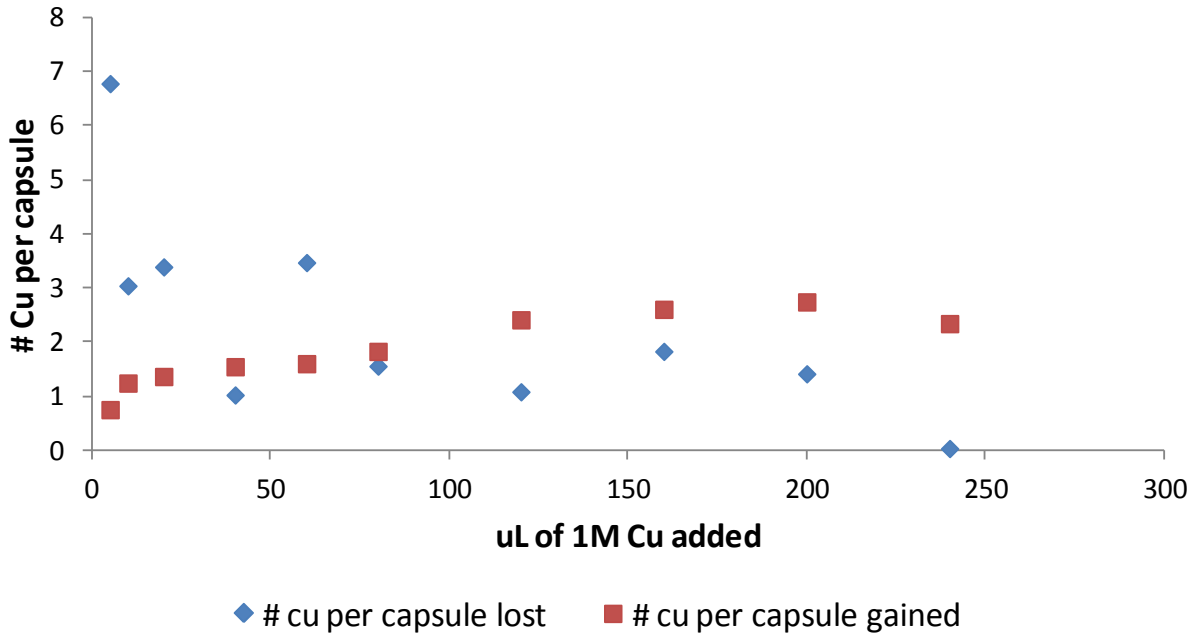

Graph 5.5: Results from the second "exchange experiment." Coppers gained does not track with coppers lost, suggesting that copper exchange does not occur. Instead, copper binds via an unknown modality.

The results of this experiment were, at first, a bit confusing, as the amount of retained copper was significantly lower when compared with the first experiment (Graph 5.5). Later experiments showed that this was due to the significantly shorter treatment duration as compared to that in the first experiment. However, the data nevertheless showed a direct correlation

between the amount of added copper and the count rate. The linearity of this seemed to vary, with the few initial data points seeing much more copper uptake than the latter points. The amount of retained counts then seemed to start to reach a maximum, and rose to approximately 2.7 coppers per capsule. It was unclear whether saturation was reached, as the highest point occurred immediately prior to the final data point. Although it was difficult to compare the two experiments, due to the shortened duration of treatment, this result was a good starting point for future experiments.

The inverse experiment, where hot $PgC3_6Cu_{24}$ was mixed with cold copper showed the predicted result, namely that no exchange was observed as evidenced by no real change in counts in any of the samples. The few points that did deviate from this trend, and did show a decrease in counts, were actually the first several data points. This loss, however, had an obvious reason and was the source of significant problems throughout the course of nearly all subsequent experiments; an emulsion formed, which led to unknown quantities of MONCs remaining suspended in solution even after precipitation and centrifugation . Indeed, several other experiments actually had to be discarded due to confounding data as a result of emulsion formation. However, it was discovered that as long as PgC_4 was used instead of other PgCs, and that, for the initial reaction, copper solution is added to PgC, and not *vice versa*, emulsions could (for the most part) be avoided.

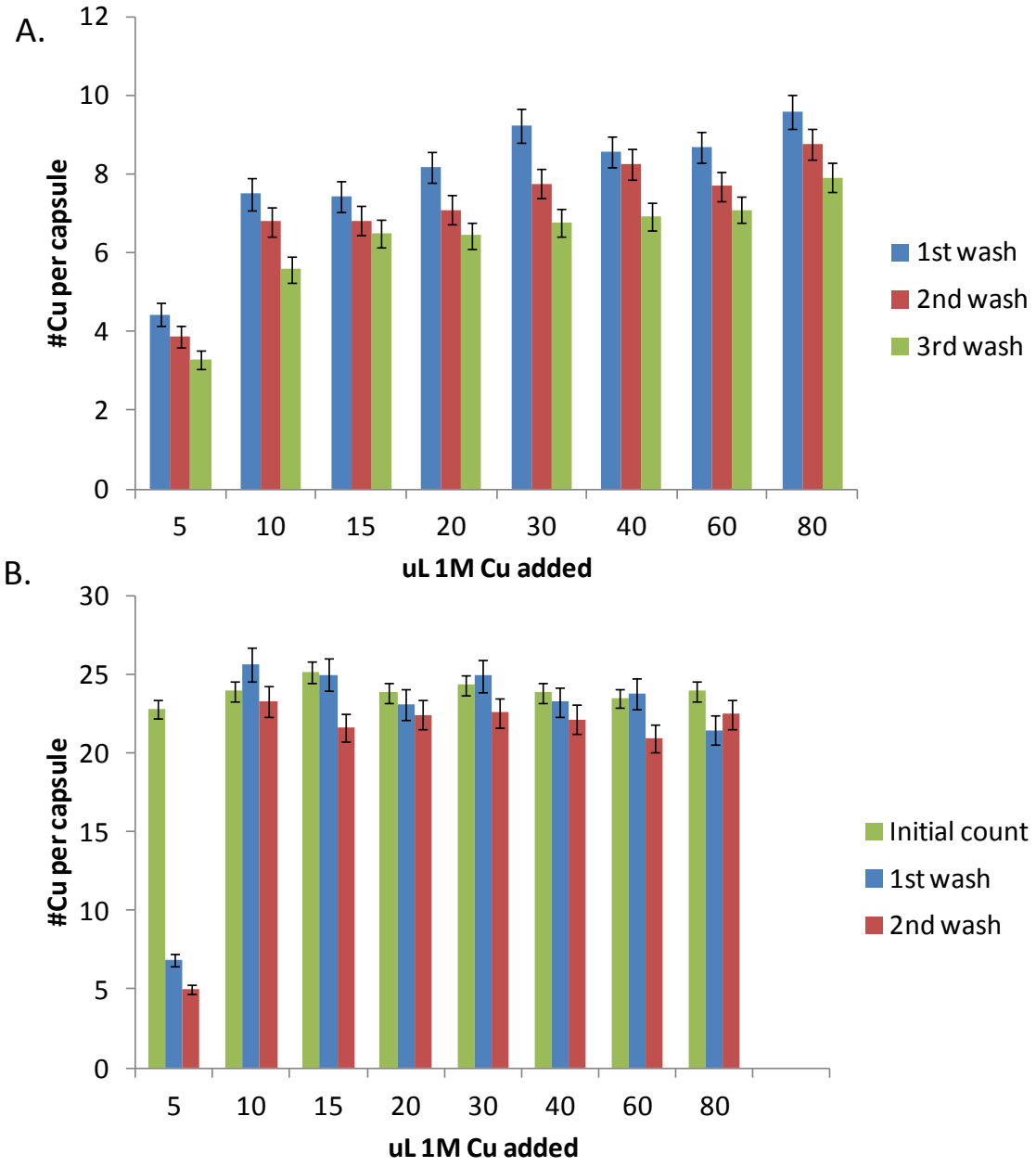

Graph 5.6: Graph A shows the results when "hot" copper is added to "cold" MONC: a concentration-dependent increase in counts is observed, which is significantly more pronounced in the earlier data points when compared to the later points. Graph B shows the results when "cold" copper is added to "hot" MONC: All originally present coppers stay in the MONC. The aberrant result in the first data point was due to the formation of an emulsion.

5.5.2 A comprehensive exchange experiment

Between the information gained in the two previous experiments, two new experiments were set up that sought to overcome the aforementioned problems and provide clearer data. The first of these experiments aimed to address the effect that concentration had on copper binding, albeit with a longer treatment duration. Eight titers of hot copper were added to acetone solutions of premade cold $PgC4_6Cu_{24}$, ranging from 5-80 µL of aqueous 1 M carrier-added $^{64}Cu(NO_3)_2$. The opposite was also done, with hot $PgC4_6Cu_{24}$ receiving cold copper in a separate set of eight centrifuge tubes. Instead of immediate precipitation, an hour-long incubation period was allowed to occur so that copper could fully occupy any of the (unknown) binding sites. Following precipitation with water, vials were centrifuged and washed three times with more water. The precipitated $PgC4_6Cu_{24}$ was counted prior to each wash so that any decrease in counts that occurred on washing would be detected.

Generally speaking, this experiment was successful in bridging the two previous experiments. The most notable effect was an overall increase in exchanged copper across the board, due to the longer incubation time (Graph 5.6). Copper retention increased from the previously seen ≈2.7 maximum with no incubation, to a maximum of approximately eight coppers, which mirrored the result in the first experiment with a 15 minute incubation time. This consistent result in both cases suggests that eight coppers is close to, or at the maximum of, available additional copper binding sites within the MONC using this set of conditions. As with both previous experiments, the amount of retained copper increased as more copper was added. However, the only large increase in counts was, again, in the lower range. In going from 5 to 10 µL, a 70% increase in counts was seen. Much smaller increases followed from there on out, with

an increase of 16% from 10 µL to 15 µL, and a less than 10% increase for all others. It is interesting to note that the 5 µL titer is the only one where the amount of added copper stayed below the theoretical 8 coppers per $PgC4_6Cu_{24}$, with a calculated value of 5.4 coppers per capsule. After this point, the copper titer, 10 µL, amounted to a theoretical 10.7 coppers per capsule, which exceeds the apparent eight copper maximum. This could be why a large jump in retained copper is seen at first, followed by relatively minor increases. Multiple water washes of the material had little effect on retained counts. A loss of approximately 10% of the retained copper per wash was seen with all titers. In addition, the "inverse" null experiment, where cold copper was added to a solution of hot $PgC4_6Cu_{24}$ showed the same result as before; no significant loss of counts was seen. The only instance where a real loss of counts occurred was at the lowest titer, 5 µL, and this was due to the formation of an emulsion after the first water wash. The only other losses were gradual losses with subsequent water washes, probably due to accidental loss of material during supernatant removal. While these were less than the previously seen 10% per wash, such loss of material was probably a contributing factor to count loss during water washes, in addition to the removal of free $^{64}Cu^{2+}$ that did not bind to the capsule. In summary, this experiment reiterated that free copper ions do bind to $PgC4_6Cu_{24}$ at a maximum of approximately 8 coppers per capsule, at least under the conditions employed in this experiment. The "inverse" experiment, meanwhile, showed that this was not due to exchange with the 24 framework coppers, as loss of these coppers was not observed.

5.5.3 The effect of anion on copper binding

To further understand this phenomenon, several other experiments were planned in which the conditions during exchange were varied. The first of these aimed to determine if the counterion affected copper binding. Previous work that sought to introduce cations into the

interior of the gallium-seamed MONC showed that anions often accompanied cations in the interior of the capsule. To this end, the "exchange" reaction was performed with several non-nitrate salts of copper. These included perchlorate, fluoroborate, chloride and sulfate. The sulfate salt was of particular interest, as it plays an important organizational role within the interior of gallium-seamed MONCs doped with Cs_2SO_4.[125] Unfortunately, it was found that copper sulfate quickly precipitated upon its addition to acetone, and thus could not be used. The others, however, stayed fully dissolved in acetone and were used for this experiment. The setup mirrored the previous study: "cold" $PgC4_6Cu_{24}$ was generated and dissolved in acetone. Carrier-added ^{64}Cu salts as 1 M aqueous solutions were then added at six titers to the acetone solution and were left undisturbed for three hours. A nitrate "control" was also prepared, so that copper binding could be compared without looking at past experiments. Since the 5 µL titer previously led to the formation of emulsions, it was not used in this experiment. Workup also followed the previous experiment: At the end of the three hour course of treatment, $PgC4_6Cu_{24}$ was counted, precipitated from solution with water, vortexed, centrifuged, and washed several more times with additional water. The material was then re-suspended in water and counted.

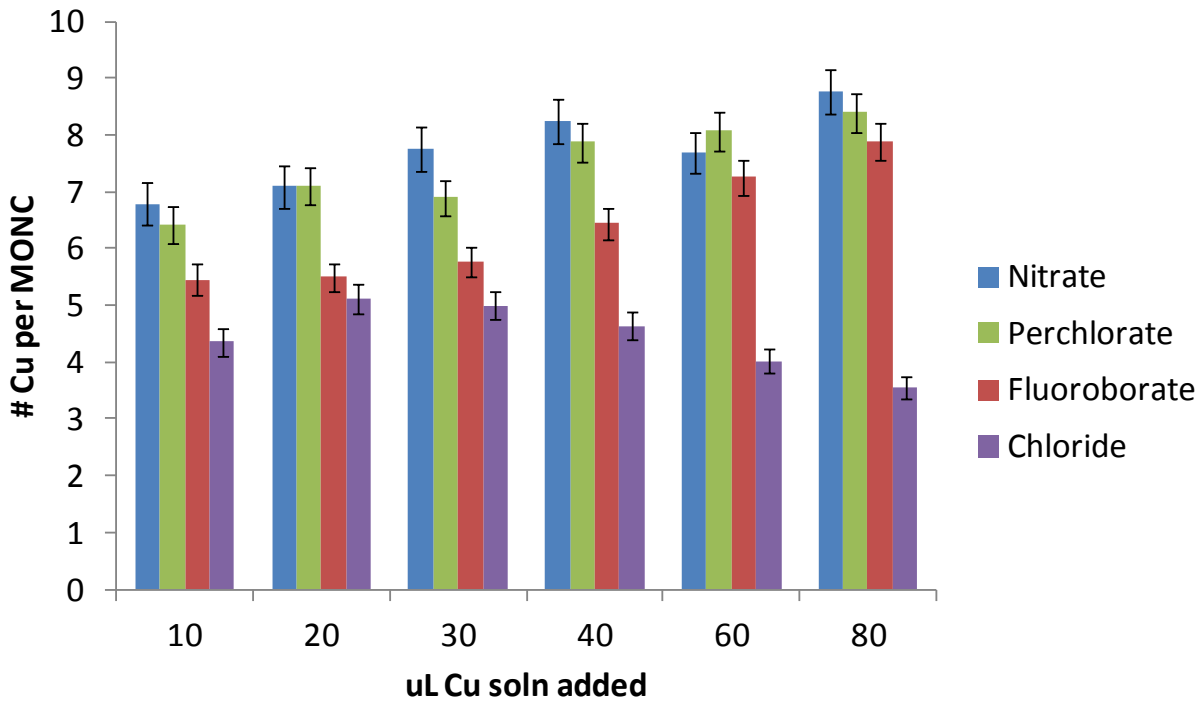

Graph 5.7: The effect of counterion on additional copper binding to MONCs

This experiment showed that the identity of the counterion did indeed have an effect on copper binding (Graph 5.7). The results with nitrate largely followed the same slow upward trend as in the previous experiment, with a maximum binding of approximately eight coppers per capsule at the highest titer. The other salts showed varying degrees of binding. Perchlorate was found to be the closest analog to nitrate, and bound to approximately the same degree throughout all of the titers. This was also the case with fluoroborate; it reached the eight-copper threshold but stayed somewhat lower than the other two. The chloride salt, however, differed significantly from the others. It bound to a lesser degree than the others throughout the course of the experiment, reaching a maximal binding of approximately 5 coppers per capsule at around the 30 µL titer and dropping afterwards to less than 4 coppers per capsule. This somewhat mirrors a

previous experiment, wherein a maximum of 240 µL of $Cu(NO_3)_2$ were added, with copper binding seemingly decreasing at the higher titers. The cause and chemistry of this discrepancy among the different copper salts cannot be currently determined, due to a lack of XRD data. However, if extra coppers are bound analogously to what is seen with the gallium-seamed MONC, namely, within the interior, it is likely that the counterion also associates with the MONC and thus may play some role in its retention. Following this stream of thought, it is likely that the chloride anion is simply not capable of being retained to the same degree as other salts, perhaps due to a different mode of binding to the capsular interior/exterior.

5.5.4 The effect of acid/base on copper binding

Another factor that was considered to potentially play a role in copper uptake by $PgC4_6Cu_{24}$ was the pH of the solution, or rather, the presence of additional acid or base in the acetonic solution. The thought process behind this was that since copper binds to $PgC4_6Cu_{24}$ in some way, the intact MONC is, in a sense, acting as a ligand. As the capacity of ligands to bind metals is typically affected by pH, it could likewise be reasonably assumed that the same would be true with $PgC4_6Cu_{24}$ as a "ligand" for additional copper. As such, an exchange experiment was undertaken where uptake occurred in the presence of 10^{-2} M HNO_3, or 1,8-Diazabicycloundec-7-ene (DBU), a non-coordinating base. To conduct this experiment, cold $PgC4_6Cu_{24}$ was prepared and dissolved in 2 mL of 10^{-2} M HNO_3 or DBU in acetone. Interestingly, while the acidic solution of $PgC4_6Cu_{24}$ remained the same red-orange color as usual, the DBU solution turned from a solution to a deep red-violet emulsion. Four different titers of carrier-added $^{64}Cu(NO_3)_2$ were then added; in this way both the effect of acid/base and concentration could be studied concomitantly. As before, an additional "inverse" experiment was also performed, where hot $PgC4_6Cu_{24}$ was mixed with four different titers of cold copper.

This "inverse" experiment was of additional importance in this case, as there was a chance that the MONC itself could be affected by the addition of acid/base. Concentrated acid, for example, typically leads to decomposition of PgC-based MONCs, including $PgC4_6Cu_{24}$. While the concentration in this case was by no means "concentrated," it was still important to determine if this was occurring. In all cases, the mixed solutions were incubated for one hour, and worked up as usual. The material was counted using a NaI(Tl) well-detector during all steps of the workup procedure.

The results of this experiment are as would be expected for a standard metal-ligand interaction, but they were rather unusual when one considers that the ligand in this case was the fully formed $PgC4_6Cu_{24}$ MONC (Graph 5.8). This was particularly the case with the DBU sample. Instead of the usual eight copper maximum that had been seen in all other experiments, the addition of base increased the copper content of $PgC4_6Cu_{24}$ to a maximum of 18 additional coppers per capsule. Initially, this large number seemed to immediately suggest that copper exchange with the periphery must have finally occurred and was responsible for the replacement of most framework coppers. However, once all the data was gathered from the inverse experiment, it was obvious that this was not the case, as there was no significant loss of framework coppers under acidic or basic conditions. There was also no blue precipitate observed in the sample, which would have suggested an increase in counts following the precipitation of insoluble copper salts (this is what had happened with $CuSO_4$ in the previous experiment). Thus, this result was real, albeit unexplainable.

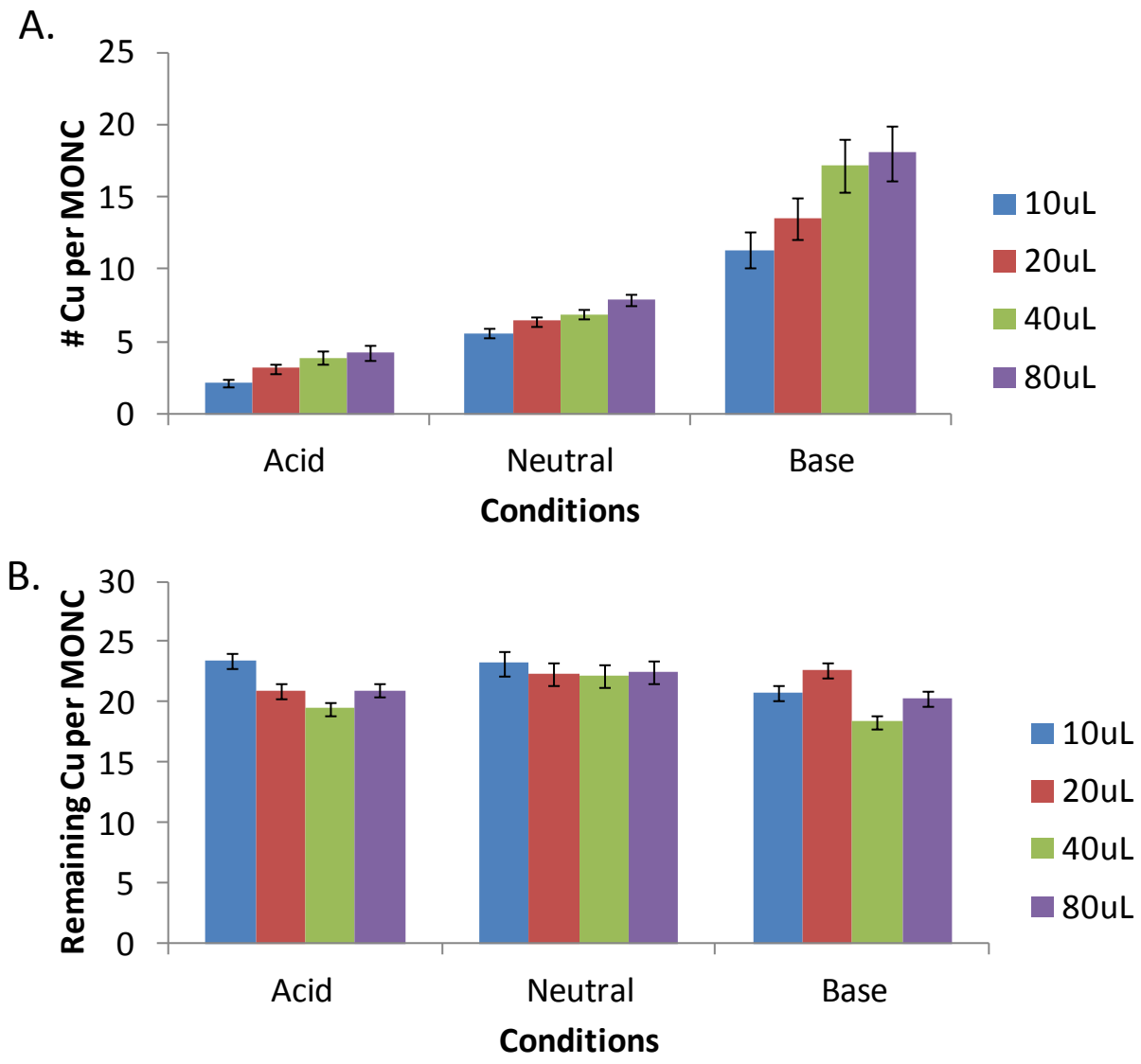

Graph 5.8: The effect of acid/base on the binding of additional copper to MONCs. Graph A shows the addition of "hot" copper to "cold" MONC: the extra copper binds in a manner that is dependent on the presence of acid/base. Graph B shows the addition of "cold" copper to "hot" MONC: as before, the extra copper that is added cannot abstract the original copper in the MONC.

From the increase seen with DBU, it was reasonable to expect that co-treatment with HNO_3 would instead lower the amount of retained coppers. This was, in fact, the case, with the number of retained coppers decreasing from eight under previously seen "neutral" conditions to a maximum of four under acidic conditions. As in other experiments, a gradual upward trend was seen with increasing copper titer.

Although it is difficult to explain these results without adequate XRD data, this behavior follows the MONC-as-a-ligand hypothesis quite nicely. The addition of acid to ligands tends to protonate sites that participate in coordinative metal bonding, lowering their ability to bind metal ions, while the addition of base does the opposite, deprotonating such sites and thereby enhancing their metal binding capability. Though the location of such sites within or outside the $PgC4_6Cu_{24}$ MONC is currently unknown, they must exist, as this ligand-like behavior is clearly apparent from this study. It can be conjectured that, as in zinc- and cobalt-seamed dimers, the nitrate anion may also play a role in copper sequestration by acting as a ligand. Likewise, the interior of the MONC is far from vacant, and, from calculations performed using MALDI-TOF mass spectrometry, can contain up to 24 water molecules. The protonation (or deprotonation) status of these guests may likewise play a part in this phenomenon. There is also some anecdotal evidence from scXRD studies for internal coordination of coppers, where electron density peaks seemingly "coordinate" to waters on the interior of the capsule (Fig. 5.8). Although the electron density at these peaks is very low, they may represent partial occupancy of copper, as the bond lengths to adjacent water molecules are of an appropriate length for copper coordination.

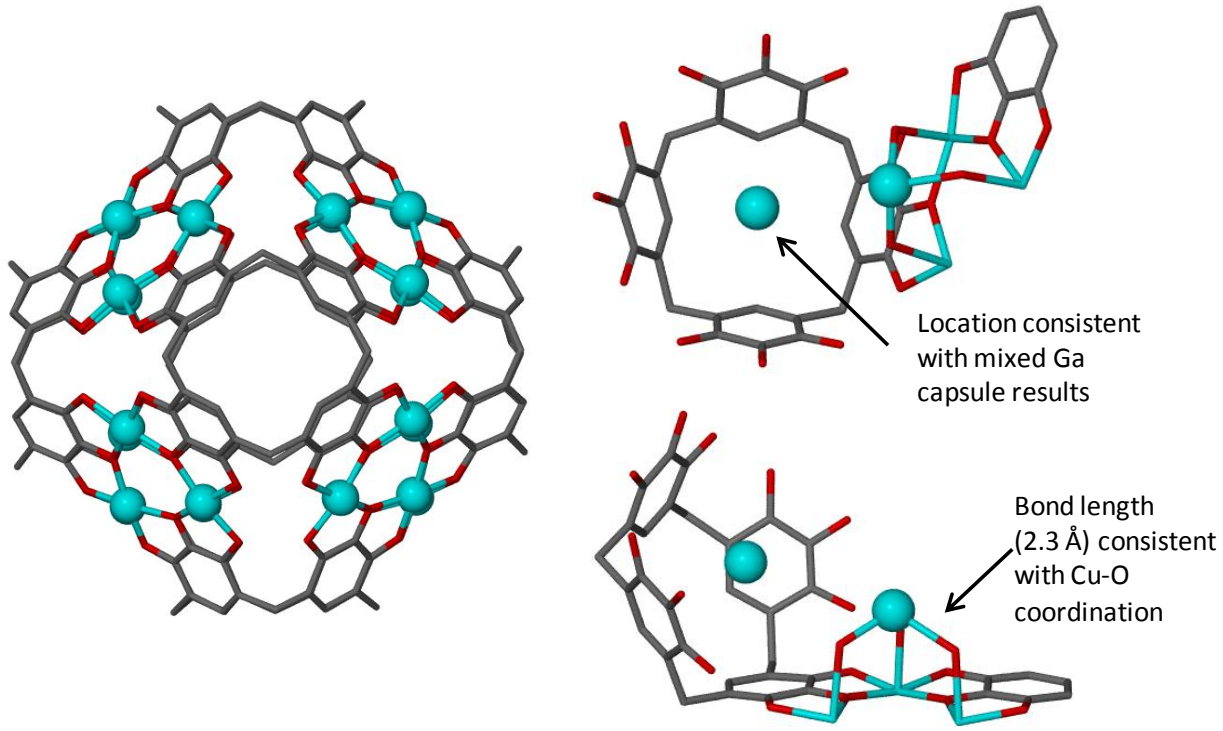

Figure 5.8: Two potential binding sites for additional coppers inside of the hexamer

5.5.5 The effect of pyridine on copper binding

Based on the unexpected results with DBU in the previous experiment, it was interesting to see whether other bases would likewise increase the binding propensity of copper to $PgC4_6Cu_{24}$. In particular, it was unknown whether coordinating bases would behave in a similar fashion to DBU, which itself is a non-coordinating base. Pyridine was an obvious choice for such experiments due to its role as a high-affinity ligand for PgC-based MONCs in previous research efforts. Pyridine and its analogs had been previously shown to coordinate to peripheral metals on the surface of the hexameric MONC. As such, using pyridine instead of DBU could help to determine if the exterior of the MONC, specifically the oxo-metallic "triads," play any

role in additional copper bonding, as these sites would effectively be blocked on the outside by pyridine ligands (Fig 5.9).

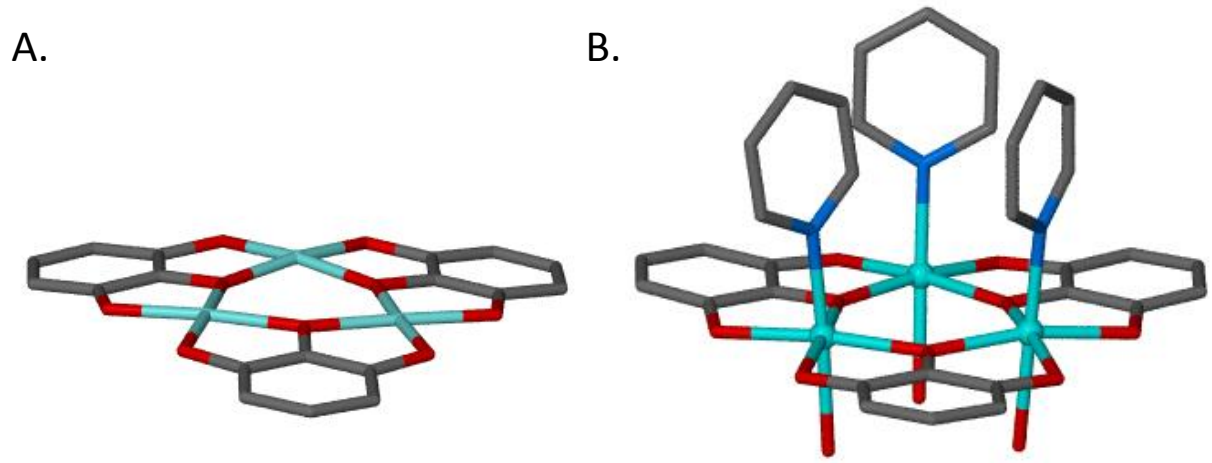

Figure 5.9: Representative images of "unblocked" (A) and "blocked" (B) oxometal triads.

Unlike the DBU experiment, where several different titers of copper were used, this experiment used one common titer of copper, 40 µL, and instead focused on investigating different concentrations of pyridine (and pyridinium nitrate, its conjugate acid) as a variable. Four centrifuge tubes of cold (nonradioactive) $PgC4_6Cu_{24}$ were prepared/purified as previously described and dissolved in 2 mL of acetone. Two of these tubes received pyridine as an aqueous 1 M solution, with either 8 or 16 equivalents with respect to (w.r.t.) PgC4. Another tube received equal equivalents (4) of pyridine and pyridinium nitrate, while the last received 8 equivalents of pyridinium nitrate. All samples were briefly vortexed, and 40 µL of 1 M aqueous carrier-added $^{64}Cu(NO_3)_2$ were then added to all tubes. The samples were then vortexed and allowed to react for 1 hr. They were then worked up and counted analogously to all previous experiments.

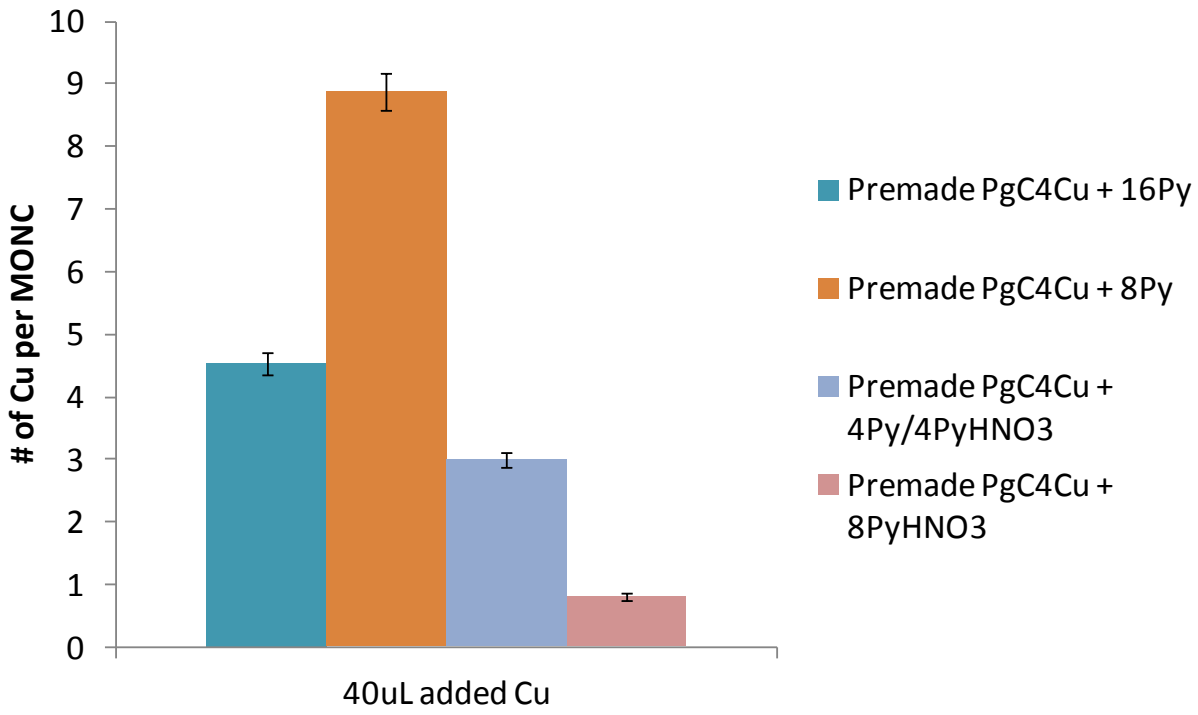

Graph 5.9: The effect of pyridine on copper binding. This effect is different than that with DBU, perhaps due to the coordinative behavior of pyridine.

This experiment showed that pyridine behaved quite differently from DBU as a base (Graph 5.9). In the case where pyridinium nitrate was used, the amount of retained copper mirrored the results of the acidic segment of the previous experiment (much less copper binding). This was not unexpected, as pyridinium nitrate is itself an acid and should behave accordingly. Interestingly, the tube containing a mixture of pyridinium nitrate and pyridine showed almost exactly the same results. Although the cause of this is unknown, perhaps it was due to coordinative bonding of free pyridine to framework coppers, leaving the rest as an acidic solution of pyridinium nitrate. Eight equivalents of pyridine led to an uptake of copper similar to, but slightly exceeding, the uptake seen when no base was used. At first glance, this result seems to indicate that the addition of pyridine does not affect copper uptake. However, copper

uptake actually decreased to slightly more than four coppers per capsule with sixteen equivalents of pyridine. This change indicates that pyridine does indeed affect copper retention, albeit through unclear means. One possible reason for this drop in bound copper following an increase in pyridine equivalents is, as previously stated, that its coordinative bonding to peripheral coppers may negatively affect copper bonding. A much more mundane explanation, however, is that free pyridine at high enough concentrations competes with $PgC4_6Cu_{24}$ as a ligand for copper. This fits well with the result of the previous experiment, where this decrease was not seen due to the non-coordinative nature of DBU.

5.5.6 The effect of pyridine on copper binding #2: addition of pyridine during synthesis

To further explore the role that bases have on copper binding, an additional experiment was conducted that was closely analogous to the previous one (**5.5.5**). The main difference, however was that pyridine was added during the synthesis of MONC rather than during the addition of extra copper, and after synthesis, any leftover pyridine was removed prior to the addition of extra copper. This experiment would help to determine if the reduction in copper binding was due to free copper interacting with free pyridine in solution, and thus forming a complex that competes with the MONC for Cu^{2+} binding. It was expected that in both cases (i.e., in the last experiment **5.5.5** and in this one), pyridine would also be bound as a peripheral ligand on framework copper centers, so this factor would be consistent between the experiments. However, as pyridine was added during synthesis, it was uncertain whether it would have an effect on the identity of the MONC that was formed. Due to this uncertainty, pyridine was added at two different times during synthesis, both before and after copper was added to PgC. It was expected that in the case where pyridine was added *after* copper was added, the MONC had

already formed, and all that the pyridine does at this point is bind to external coppers and neutralize any acid formed in the reaction. If the presence of pyridine before/during copper addition has any influence on the resultant product, it should readily be seen in the results further on down the line. An additional variable was also introduced, namely that synthesis was carried out in both methanol and acetonitrile. It is important to note that this experiment can only be used to analyze trends in data, as it is neither known what the yields of MONC were following this procedure, nor the identity (dimer or hexamer) of the MONC that was formed.

Four centrifuge tubes of cold (nonradioactive) $PgC4_6Cu_{24}$ were prepared using different procedures. In the first tube, 2 mL of 10^{-2} M PgC4 in 9:1 methanol:water was premixed with 8 equivalents of pyridine (160 µL of 1 M aqueous solution), after which 4 equivalents of Cu^{2+} (cold, 80 µL of 1 M aqueous solution) were added. A second tube received sixteen equivalents of pyridine (320 µL of 1 M aqueous solution), while in tubes three and four the PgC4 solution was first mixed with Cu^{2+} solution, followed by either eight or sixteen equivalents of pyridine. This procedure was also performed with 9:1 acetonitrile:water in an additional four tubes. The resultant product in all of the tubes was purified as previously described and dissolved in 2 mL of acetone. All samples were then briefly vortexed, and 40 µL of 1 M aqueous carrier-added $^{64}Cu(NO_3)_2$ were then added to all tubes. The samples were vortexed and allowed to react for 1 hr. They were then worked up and counted analogously to all previous experiments.

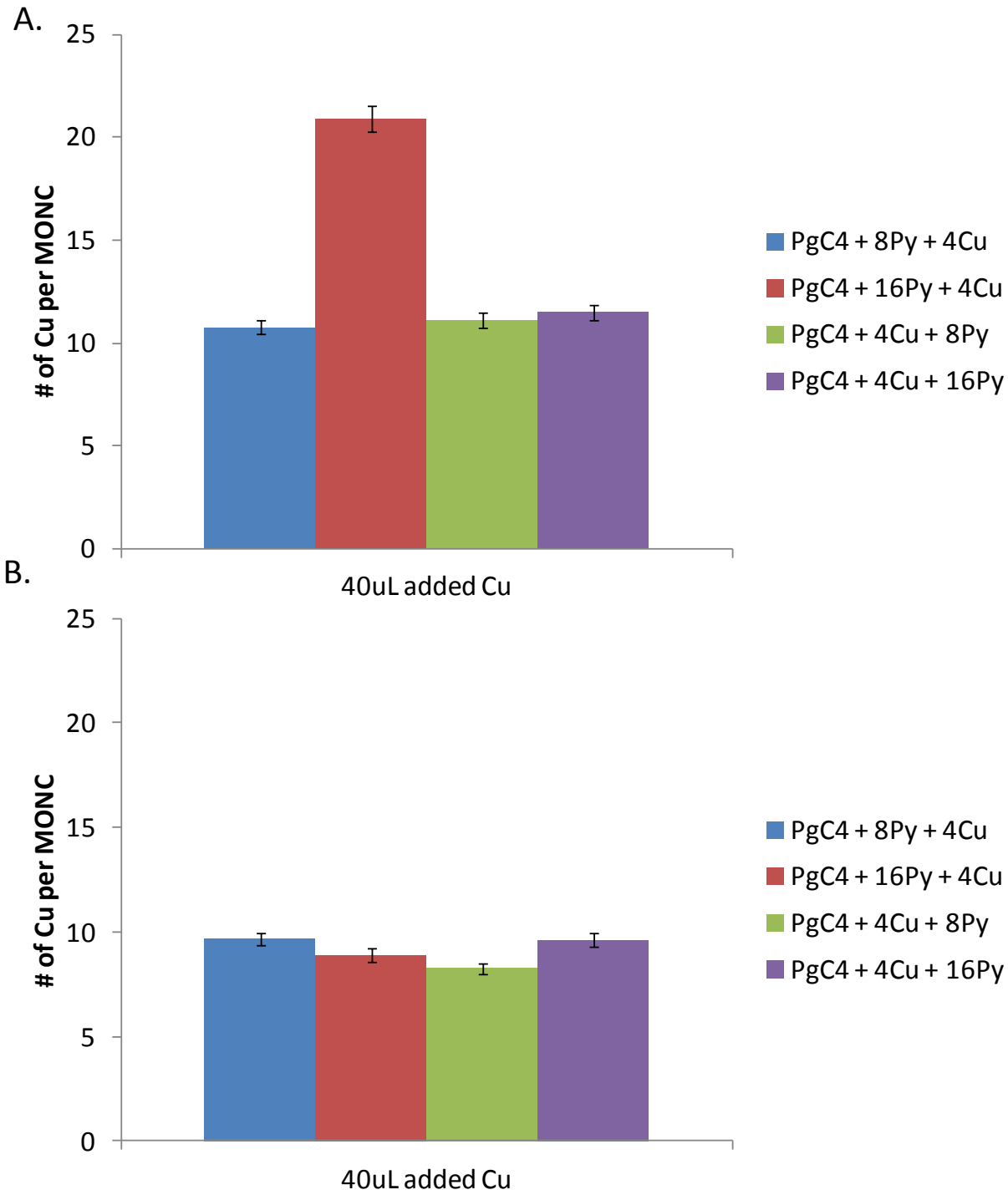

Graph 5.9: Results from the second experiment employing pyridine (A: synthesis in methanol; B:synthesis in acetonitrile). Copper binding is increased when compared to 5.5.5, theorized to be due to pyridine's role in coordinating to free Cu^{2+} and preventing it from binding to the MONC in 5.5.5.

The results of this experiment suggest that the position of its addition during the synthesis process is an important determinant of pyridine's behavior on copper uptake (Graph 5.9). A significant increase in copper uptake was seen in all of the materials made when compared to the previous experiment. Furthermore, the trend seen in the methanolic portion of this experiment is diametrically opposite to the one seen in the former; the sixteen equivalents of pyridine data point shows more uptake in this experiment, whereas it previously showed less uptake when compared to the eight pyridine data point. This suggests that free pyridine may in fact have prevented copper from interacting with the MONC in the previous experiment, possibly by forming a copper-pyridine complex, whereas in this experiment there is no free pyridine, as any free pyridine was washed away during the initial workup stages. It is not fully certain why more pyridine at the initial (methanolic) synthetic stage causes an increase in copper binding later on, but this may be due to a higher synthetic yield of MONC. Indeed, as previously stated, it is actually quite difficult to make any conclusive statements about this experiment as additional yield data was not collected, and thus the number of additional coppers that interact with the MONC can only be calculated on the basis of previous yield data. However, it must also be stated that the number of bound coppers is roughly the same as with a standard MONC at most of the data points, suggesting that (most likely) the yield is approximately the same.

5.5.7: Copper exchange: summary

This section explored the interaction of free Cu^{2+} and copper-seamed hexameric MONCs. One important result from this section is that Cu^{2+} does not freely exchange with coppers bound on the capsular periphery. This result may be of use in later studies as it gives credence to the

inherent stability of the hexameric MONC. It was also shown that Cu^{2+} does actually interact with the MONC in some way, and by treating the MONC with Cu^{2+}, a hybrid entity that bears additional metal centers is formed. This effect is modulated by a number of factors, including the identity of the Cu^{2+} counterion, the presence of acid or base, including whether the base is coordinating or not, as well as the concentration of Cu^{2+} that is added. Efforts to determine the structure of this hybrid identity using crystallography have not been successful so far. However, this is somewhat expected, as copper-seamed hexamers are very difficult to crystallize, especially if multiple species are present in solution, which may likely be the case in this system. MALDI-TOF mass spectrometry was also performed on several of the samples described in this chapter. The results, however, showed a typical bimodal distribution with a mass range indicative of an absolutely normal hexamer. This is also not a surprise, as these coppers are likely to be weakly bound, possibly even to the outside of the MONC (precedent from various gallium/alkali cation assemblies; see Fig. 5.8).[123] Exterior ligands and even interior guests are known to be removed during the mass spectrometric process, so it would stand to reason that these extra coppers could likewise be detached from the structure during analysis. Elemental analysis studies have not been performed so far, but will likely be of much assistance in verifying that extra coppers are truly bound to the MONC.

5.6.1 Investigating non-Cu metal exchange: intro

In addition to studying the effect that free Cu^{2+} has on copper-seamed MONCs, it was likewise pertinent to study the effect that other metal cations have on $PgC4_6Cu_{24}$. Namely, it was important to see whether other transition metal cations can displace copper from the periphery of the MONC. Previous work with gallium-seamed MONCs showed that such displacement is possible, and can lead to examples of "mixed metal" species. Hetero-metallic species break the inherent symmetry of singly metallated PgC-based MONCs, thereby making them interesting from a magnetic/electronic standpoint. Characterization of such entities, however, has proven challenging, partly due to the hexameric MONCs' poor propensity for crystallization. Even with structural data, it is still difficult, if not impossible, to determine the identity and ratio of individual metals in a mixed metal MONC, particularly if the metals are close to one another on the periodic table. As studies that evaluate hetero-metal exchange in non-gallium PgC-based MONCs via XRD have not been conducted, radiochemistry could instead be used to shed some light on this phenomenon.

5.6.2 $PgC4_6Cu_{24}$/$TM(NO_3)_2$ exchange experiment

Two studies were envisioned that aimed to study hetero-metal exchange with PgC-based MONCs. The first of these aimed to determine if the peripheral coppers of $PgC4_6Cu_{24}$ would exchange for other, non-copper, metal cations, particularly transition-metal (TM) cations. The metals used in this experiment were Ga^{3+}, Zn^{2+}, Ni^{2+}, Co^{2+} and Fe^{3+}. These were specifically chosen due to their use in other PgC-based MONCs, and thus were known to bind to this ligand. The setup of this experiment was essentially analogous to previous exchange experiments, wherein purified "hot" $PgC4_6Cu_{24}$ was treated with an aqueous solution of a metal nitrate salt and

precipitated with water (Fig. 5.10). The resultant precipitate was then washed and counted. A decrease in counts of the precipitate after treatment and purification would show that exchange had occurred and, therefore, a mixed-metal capsule had formed. As the rate of exchange (if it was occurring) was not known, exchange was monitored at three time points; after 1, 3, and 20 hours.

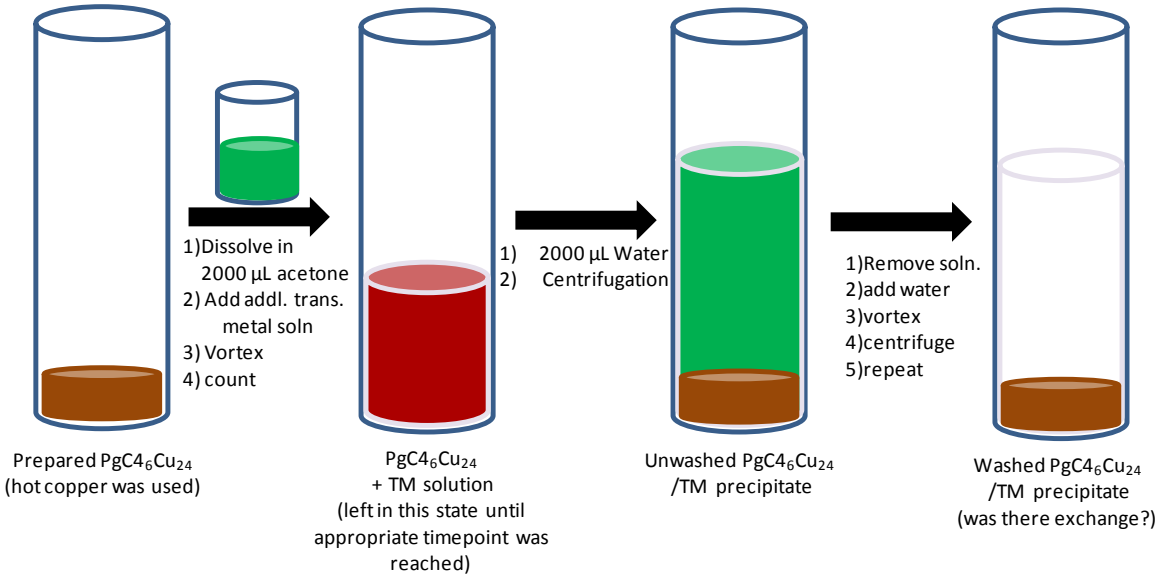

Figure 5.10: Scheme for metal exchange experiments, where $M(NO_3)_2$ is added to premade PgC4$_6$Cu$_{24}$ to determine if other metal cations can abstract copper from the MONC

As previously seen with Cu^{2+}exchange experiments, most of the metals used in this study did not abstract copper from the periphery of the capsule, at least in the short term (**Graph 5.10**). There was some evidence of copper loss at the twenty hour time point, but it was uncertain whether this was caused by loss due to metal exchange or, instead, due to the formation of an emulsion. In any case, copper loss amounted to no more than 3 coppers lost per capsule,

suggesting that if exchange was, in fact, occurring, it was rather unfavorable and would be of little experimental use, at least within the parameters of this experiment. Fe^{3+}, however, was completely different story, and its addition resulted in the loss of approximately 13 coppers per

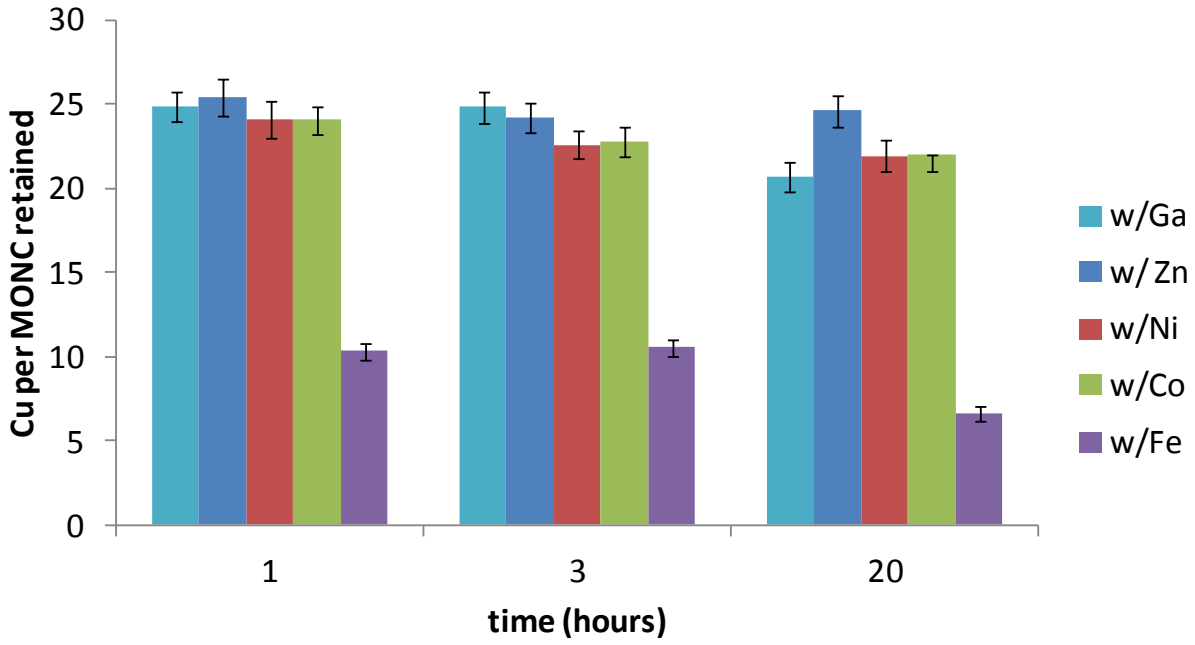

Graph 5.10: Results from $PgC4_6Cu_{24}/M(NO_3)_2$ exchange experiment. Aside from Fe^{3+}, Cu^{2+} is not abstracted by first series transition metal cations

capsule at the earlier time points, and 17 coppers at the 20 hour time point. That a reaction occurred between this metal cation and $PgC4_6Cu_{24}$ was also evident by a distinct change in coloration and behavior of the resultant light brown solid, which was significantly more soluble in acetone/water than the other samples. For this reason, it is uncertain whether copper losses for this sample were correctly quantified, as an unknown quantity of the bulk material itself was lost to dissolution during the initial precipitation step. Nevertheless, what was certain was that iron

had a distinct effect on copper retention in $PgC4_6Cu_{24}$. It is not surprising that such a profound effect was seen with this cation, as iron salts are, perhaps, the only other metal salts that will lead to an immediate reaction with PgCs, regardless of whether a base, such as pyridine, is added. This suggests that, like copper, iron has a higher affinity for the PgC ligand when compared to other transition metal cations. Overall, the results of this experiment are valuable, as they show that while copper-seamed MONCs are more resilient to metal exchange than those made with gallium, mixed metal entities are, in fact, possible given the appropriate metal cation.

5.6.3 PgC-TM complex exchange with Cu^{2+}

As the previous experiment showed that, with the exception of iron, copper-seamed MONCs are stable and resilient to exchange with other transition metal ions, it was likewise interesting to see whether MONCs formed with these transition metals would likewise be resilient to attack by Cu^{2+}. Previous evidence with gallium-seamed MONCs showed that copper can, in fact, incorporate into the framework of these entities by entering into unoccupied bonding sites that were left on the capsule's periphery after gallium coordination.[119,124,125] It was entirely uncertain, however, if this was the case with other MONCs. As such, we aimed to study whether late first-series transition metals could be abstracted using carrier-added $^{64}Cu^{2+}$.

Three sets of samples consisting of Ga^{3+}, Zn^{2+}, Ni^{2+}, Co^{2+}, and Fe^{3+} -seamed PgC4 complexes were synthesized by employing previously known synthetic techniques for these entities. For Zn^{2+}, Ni^{2+}, Co^{2+}, and Fe^{3+}, 80 µL (four equivalents) of 1 M aqueous metal nitrate solution were mixed with 2000 µL of 10^{-2} M PgC4 in 9:1 methanol:water. 320 µL (16 equivalents) of 1 M aqueous pyridine was then added, which led to immediate precipitation

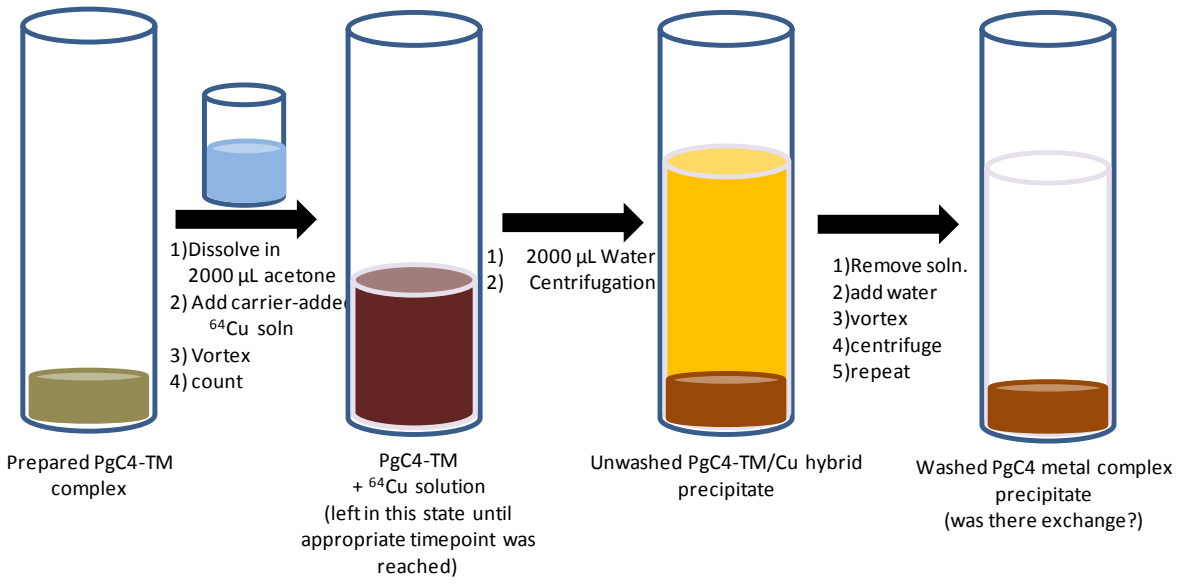

Figure 5.11: Scheme for metal exchange experiments, where $Cu(NO_3)_2$ is added to premade PgC4-TM complexes to determine if Cu^{2+} can abstract other TM cations from their respective PgC complexes

in the Zn, Co, and Fe centrifuge tubes. The identity of these entities is well known from previous experiments, with Zn and Co forming dimeric MONCs and Fe forming nanotubular (non-capsular) entities.[126,127,135,140] Addition of pyridine to the tube treated with Ni led to the formation of a black solution. This was known from past experience to consist of the hexameric Ni-seamed MONC. The corresponding Ni-seamed dimer typically precipitates as a yellow powder at these concentrations in other solvents, such as acetonitrile, but not in methanol. The hexameric product was precipitated from solution by adding 2 mL of water to the centrifuge tube, which led to the immediate formation of a black precipitate. With the exception of Ga^{3+}, all tubes were then centrifuged, had the mother liquor removed, and were washed twice with water akin to all prior experiments with copper-seamed MONCs. 2 mL of acetone was then added to all tubes and the mixtures were vortexed to dissolve all solids. The gallium-seamed MONC calls for a different synthetic protocol, and, as such, was synthesized in a different

manner from the others. The formation of the gallium-seamed MONC proceeds rather simply: 2000 µL of 10^{-2} M PgC4 in acetone was mixed with 80 µL of 1 M aqueous $Ga(NO_3)_3$ to form the MONC *in situ*. Thus, no purification was necessary for the gallium variant at this point. Each prepared tube then received 80 µL of 1 M carrier-added $^{64}Cu(NO_3)_2$ and was briefly vortexed to distribute the materials within the tube. The three sets of tubes were allowed to sit undisturbed for the same duration as in the previous experiment, for one, three, or twenty hours. After the appropriate amount of time, the tubes were counted and product MONC precipitated with water. This was followed by the typical workup procedure for MONCs, namely centrifugation, washing with water, and re-centrifugation (Fig. 5.11). Following this procedure, the resultant precipitate in the tubes was counted. Exchange was measured as a percent of total copper added, since the yields of the MONCs used in this experiment were not known. As in several previous studies, the results in this section are merely qualitative, as without knowing the net yield of these MONCs, it is difficult to tell exactly how many metal ions were removed and how many Cu^{2+} were added per MONC. However, this study can nevertheless tell us whether exchange occurs or not, and at least some idea as to the magnitude of exchange.

Unlike the previous experiment, where $PgC4_6Cu_{24}$ treatment with TM cations showed no loss of peripheral coppers, the data gathered from this experiment suggested that copper may have replaced peripheral metal centers in non-copper-seamed MONCs. This is evident by the retention of 40-70% of initial copper counts for all but the iron-seamed entity (Graph 5.11). Even the iron-seamed complex took up copper, albeit to a much lesser degree than the others. This seems to give credence to the hypothesis from the previous experiment that, as compared to Cu^{2+}, Fe^{3+} has a similar, if not greater, affinity for coordinative bonding to PgC. Thus, the overall result of this experiment was somewhat as expected; copper displaced cations that had a

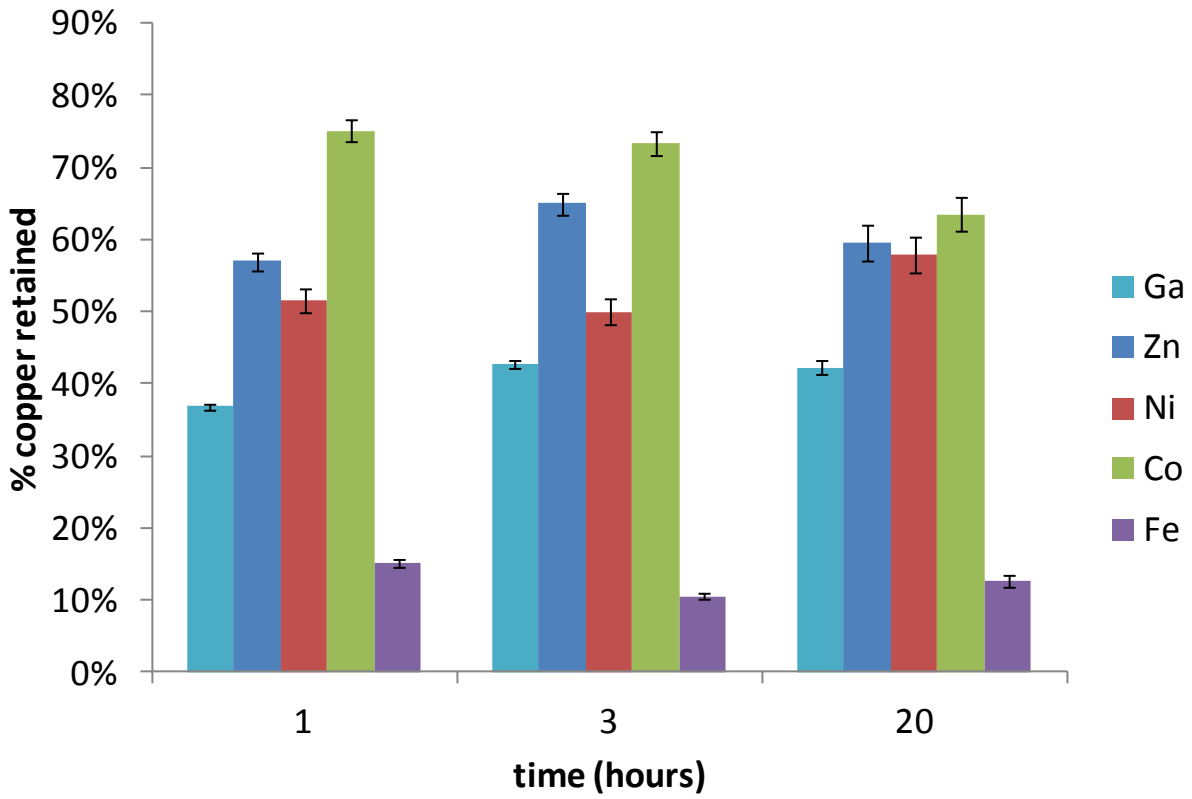

Graph 5.11: Results from PgC4-TM complex/$Cu(NO_3)_2$ exchange experiment. Copper is found in all of the complexes after exchange in significant amounts. Assuming 100% yield of the PgC4-TM complex, the amount of copper that is incorporated into the complex often exceeds the amount of TM cation. This is not the case with Fe^{3+}, which was also the outlier in the previous experiment **5.6.2**

lesser affinity for PgC, and did so to a much lesser degree for the one example of a cation with a higher affinity (Fe^{3+}). While the possibility that, like in $PgC4_6Cu_{24}$, some form of internal binding was occurring cannot be discounted, it is unlikely that this was the only cause of copper binding. This is because, assuming these MONCs behave similarly to $PgC4_6Cu_{24}$ in regards to non-peripheral bonding, the amount of retained copper is rather large compared to $PgC4_6Cu_{24}$, even if a stoichiometric yield (100%) for the MONCs used in this experiment is assumed.

Indeed, an additional piece of anecdotal evidence that strengthens the hypothesis that peripheral exchange had occurred comes from the color changes seen in the precipitates; most either turned brown (like $PgC4_6Cu_{24}$) or changed to a lighter or darker variant of the original color (the case with Ni and Fe).

Complex		Ratio (X:1) PGNAA	% Cu (PGNAA)	%Cu (Radiochem, 20 hrs)
PgC4Zn + Cu^{2+}	Cu/Zn	6.27 ± 0.55	86%	60%
PgC4Ni + Cu^{2+}	Cu/Ni	1.98 ± 0.06	66%	58%
PgC4Co + Cu^{2+}	Cu/Co	7.70 ± 0.35	89%	64%
PgC4Fe + Cu^{2+}	Fe/Cu	3.74 ± 0.22	21%	13%

Table 5.2: PGNAA analysis of several PgC-TM complexes where Cu^{2+} was used to replace the TM cations. Data gathered using ^{64}Cu is also presented so that a comparison can be made.

To determine if a more quantitative picture could be gathered in regard to these results, samples were sent to NIST for prompt gamma neutron activation analysis (PGNAA), which is a type of elemental analysis. In PGNAA, the analyte is placed into a neutron beam, which causes the elements in the analyte to absorb the neutrons and emit prompt gamma rays. As the gamma ray energies are element-specific, the count rate of gamma rays exhibiting a specific energy profile provides quantitative information about the element that produced it, and multiple elements can be analyzed simultaneously in this way. Thus, PGNAA is useful in determining element:element ratios, such as the metal:metal ratios in this system.

The results using this method mirror those gathered using ^{64}Cu, at least qualitatively (Table 5.2). The zinc, nickel and cobalt complexes all show a large degree of cation exchange for copper, while iron only shows marginal exchange. The ^{64}Cu results, however, show a consistently lower % of copper in the samples when compared with PGNAA. This is because

the yield of the PgC-TM complexes is less than the theoretical 100%. Assuming the accuracy of both of these methods, the yields of the PgC-TM complexes can actually be determined by dividing the ^{64}Cu % copper by the PGNAA % copper results. This gives yields of 70, 87, 72 and 62% yields for zinc, nickel, cobalt, and iron complexes, respectively.

5.7 Conclusion

This chapter focused on understanding the chemistry of metal-seamed MONCs using radiochemistry, with emphasis on the study of the hexameric copper-seamed assembly. The results gathered from this endeavor were both novel and unique, as there are few other methods that could have been used to gather the information found here. Data such as yields, solubility, and stability are of importance, as they are beneficial to have in almost any future research effort that involves these compounds. The finding that the $PgC4_6Cu_{24}$ MONC is inherently stable in aqueous and biologically relevant media, and even stable to exchange with free TM cations including free Cu^{2+}, is particularly valuable, as it lends well to any future studies of these assemblies where their stability is of importance.

While not entirely without precedence (gallium-seamed MONCs), the ability for the hexameric copper-seamed MONC to sequester additional transition metal cations was a particularly unexpected finding. This phenomenon was consistent over multiple experiments, and amounted to a generally constant 8-10 Cu^{2+} per capsule under neutral conditions. Copper binding was found to be influenced by several factors, with an increase seen under basic conditions and a decrease under acidic conditions as well as in the presence of the chloride counterion. The addition of pyridine, a coordinating base, had a significantly different effect than non-coordinating DBU, but this effect differed depending on when pyridine was added. Although it is not known why this occurred, it is theorized to be due to a competition between

the MONC and free pyridine as ligands for unbound Cu^{2+}. It is important to note that this result in particular gives credence to the use of radiochemistry to study PgC-based MONCs, as crystallographic and mass spectrometric techniques did not lead to a facile detection and analysis of this phenomenon.

Radiochemical methods were also used to study hetero-metal exchange. Introducing TM nitrates to a solution of $PgC4_6Cu_{24}$ MONC did not seem to lead to the loss of peripheral coppers in any case aside from Fe^{3+}. This cation did lead to the loss of peripheral coppers and seemed to lead to the formation of a unique new product. The converse study was also performed, wherein metal complexes formed from PgC and non-copper TM nitrates were treated with carrier-added $^{64}Cu^{2+}$. This treatment led to an increase in bound copper that was consistently higher than the results seen in $PgC4_6Cu_{24}/Cu^{2+}$ binding experiments, suggesting that copper displaced peripheral cations in these MONCs. Once again, the outlier was the complex formed from Fe^{3+}, which showed a much lower degree of copper binding and no visible color change, as was the case with the other TM/PgC complexes. The results of these experiments suggest that Cu^{2+} in particular has a high affinity for the PgC ligand, mirrored (or eclipsed) only by Fe^{3+}. This research serves as an important foundation for future mixed-metal MONC work, as it outlines a metal exchange hierarchy for copper-seamed MONCs, and for non-copper MONCs treated with copper.

5.8 Future Studies

Further investigation of MONCs with radiochemical methods can be envisioned to proceed from several different directions. Perhaps the most important direction is further bio-distribution studies. Although these studies have been unsuccessful so far, future efforts should nevertheless be directed toward figuring out appropriate conditions for ^{64}Cu labeling at low concentrations. Furthermore, existing methods should also be repeated on different PgC analogs,

particularly those with modifiable R-groups on the lower rim. This may allow for the functionalization of a MONC with a moiety that will target specific sites/organs *in vivo*, and could thus identify whether or not labeling had truly worked.

Future research efforts should also be directed towards a better understanding of the copper sequestration phenomenon. A particular emphasis should be placed on studying this phenomenon under varied pH (acidity and/or basicity), as basic/acidic conditions in particular seemed to have a pronounced effect on copper uptake. The presence of various anionic counterions also seemed to have an effect on copper sequestration. To this end, the effect of co-administration of several copper salts (or a copper salt plus a sodium salt with a different counterion) would be interesting to study and would be a great follow through that could help explain the role, if any, that the anion plays in helping to mediate copper uptake. The competition of copper for other transition metal cations, such as Ni^{2+}, or even other unrelated cations such as K^+ or NH_4^+ can also be investigated to determine if these cations also bond/coordinate to the same sites as Cu^{2+}.

The metal exchange studies in this section are also only a small fragment of what is possible, and there are many different parameters that can be studied for their effect on metal exchange. In addition, metal exchange (and copper sequestration for that matter) has not been studied with copper-seamed dimers. Such an investigation could further clarify the differences in chemistry between the dimeric and hexameric MONCs and would also be of significant importance. Lastly, radiochemical means can also help to clarify/reconfirm some of the results seen with SANS in chapter 3.

Appendix

Chapter A1: Structure and synthesis of various zinc-seamed dimers.

A1.1: Introduction and Rationale

This supplementary chapter contains several side projects that were conducted using the zinc-seamed MONCs. Unlike other metal cations, Zn^{2+} coordination to PgCs leads only to the dimeric product. The dimer formed in this way is air-stable and largely impervious to dissociation under most conditions. In addition, the zinc dimer is by far the easiest MONC to synthesize, purify and crystallize. Due to these benefits, the zinc dimer is a great test subject towards the study of dimeric MONCs under various conditions and was used for this purpose in this chapter.

A1.2: Synthesis of zinc-seamed dimers from PgC1 in the rctt (chair) conformation

Previous work in the Atwood lab has shown that even though PgCs in the rctt "chair" conformation do not have the appropriate bowl-shaped geometry to form a MONC, they nevertheless rearrange in the presence of Zn^{2+} and pyridine to form the dimeric product. This rearrangement is typically thought of as a "flip" where one of the pyrogallol rings passes through the center of the macrocycle, thereby leading to the formation of the typical "bowl". While the overall geometry of the macrocycle during this process changes from "chair" to "cone" , the stereochemistry at the prochiral centers remains the same, and as a result, two of the pendant R-groups are positioned perpendicular to the octametal belt, while the two others are positioned parallel. This is different from dimers formed from the rccc "cone" conformer, where all of the R-groups are perpendicular to the belt.

Typically, the only PgCs that can be synthesized in the rctt "chair" conformation to any great extent are those that are formed from aldehydes with phenyl R-groups at the alpha carbon. This leads to the formation of PgCs with phenyl R-groups at the bridging carbons between pyrogallol rings. The presence of an additional phenyl moiety so close to a methine hydrogen at this bridge has been hypothesized to increase the acidity of this proton and therefore destabilize this bond. This was thought to at least partially contribute to the "flipping" that occurred when a dimer is synthesized from PgCs in the chair conformation.

Aside from the phenyl PgCs, the only other PgC where the chair conformer is frequently encountered is PgC1. With this macrocycle, a typical synthesis leads to a 1:1 mixture of cone and chair, which are separated by the difference in their solubilities in hot methanol (cone dissolves, chair does not). Although the cone conformer is generally more useful than the chair, it was thought that the chair may find some use in the synthesis of dimeric MONCs, akin to the chair conformer phenyl analogs. However, as the C-methyl R-group does not increase the acidity of the bridging methine proton, it was uncertain whether the chair conformer would "flip" at all and could be used for this purpose. As such, an investigation into the metal binding capacity of the chair conformer could determine two different things: It could help to determine if a phenyl R-group was crucial to the ring flipping of chair conformers and it could help to find a purpose for the chair conformer of PgC1, which is usually discarded as a by-product.

A1.2.1: Synthesis

PgC1 was synthesized as described in previous chapters. In short, pyrogallol and acetaldehyde were mixed in a 1:1 molar ratio in ethanol/cat. HCl and refluxed for approximately 24 hours. The synthesis of this macrocycle is also discussed in supplementary chapters A2 and A3. Separation was also performed as previously described, but this process simply involved the boiling of crude PgC1 powder (produced *via* the standard acetonitrile purification technique) in 9:1 methanol:water, followed by filtration. The filtrate is rotovapped down to yield 85-95% cone conformer, while the solid is typically a mixture of cone and chair. The boiling process was repeated for a second time with the remaining solid, and the precipitate the second time around is typically 95+% pure chair conformer. Proton NMR was used to establish the composition of the resultant powders *via* peaks at δ = 6.695 ppm (rccc) and δ = 6.420 ppm and 5.762 ppm (rctt), corresponding to the aryl proton on the two conformers, respectively, in deuterated DMSO.

To make the PgC1(rctt) Zn dimer, 3.88g PgC1(chair) was weighed out into an Erlenmeyer flask along with 11.4g $Zn(NO_3)_2$ $6H_2O$ and 50mL methanol were added. The mixture was sonicated briefly to dissolve the Zn^{2+} and 9.1 mL pyridine was added. The flask was parafilmed shut and the contents were sonicated for approximately 30 minutes. During this time, the white PgC1(chair) suspension gradually turned yellow, indicating that zinc dimer had formed. The resultant mixture was allowed to cool for approximately 30 minutes and was filtered. The precipitate was washed with additional methanol, then placed in the dessicator to dry overnight. The material (approx. 1 g) was re-dissolved in minimal hot pyridine in a scintillation vial and removed from heat. Crystallization occurred after several days of standing uncapped. Structural analysis was then performed on the resultant yellow crystals. The

corresponding 4,4'-bipyridine-linked dimer was synthesized/crystallized as described in the zinc dimer section of chapter 4.

Crystal data for PgC$_1$chZn-Py in Py (A1.1): $C_{31.07}H_{24.53}Cl_{0.27}N_{2.80}O_{6.40}Zn_{2.13}$, M = 688.38, yellow plate, .1 × .15 × .5 mm^3, monoclinic, space group $P2_1/n$ (No. 14), a = 13.6150(14), b = 29.658(3), c = 31.246(3) Å, β = 98.0900(10)°, V = 12492(2) Å^3, Z = 15, D_c = 1.373 g/cm^3, F_{000} = 5254, Bruker SMART CCD area detector, MoKα radiation, λ = 0.71073 Å, T = 173(2)K, $2\theta_{max}$ = 46.6º, 87881 reflections collected, 17958 unique (R_{int} = 0.0503). Final *GooF* = 1.094, *R1* = 0.1086, *wR2* = 0.3036, *R* indices based on 12097 reflections with I >2sigma(I) (refinement on F^2), 1333 parameters, 270 restraints. Lp and absorption corrections applied, μ = 1.599 mm^{-1}.

Crystal data for PgC$_1$chairZn-4,4'bpy linking (A1.2): $C_{33.50}H_{30.50}N_{3.50}O_8S_2Zn_2$, M = 804.97, yellow rect. plate, 0.35 × 0.20 × 0.05 mm^3, orthorhombic, space group *Pban* (No. 50), a = 20.8415(3), b = 35.0876(6), c = 13.7027(3) Å, V = 10020.5(3) Å^3, Z = 8, D_c = 1.067 g/cm^3, F_{000} = 3296, Bruker SMART CCD area detector, MoKα radiation, λ = 0.71073 Å, T = 173(2)K, $2\theta_{max}$ = 55.0º, 50346 reflections collected, 11492 unique (R_{int} = 0.0753). Final *GooF* = 1.378, *R1* = 0.1219, *wR2* = 0.3994, *R* indices based on 4725 reflections with I >2sigma(I) (refinement on F^2), 476 parameters, 42 restraints. Lp and absorption corrections applied, μ = 1.079 mm^{-1}.

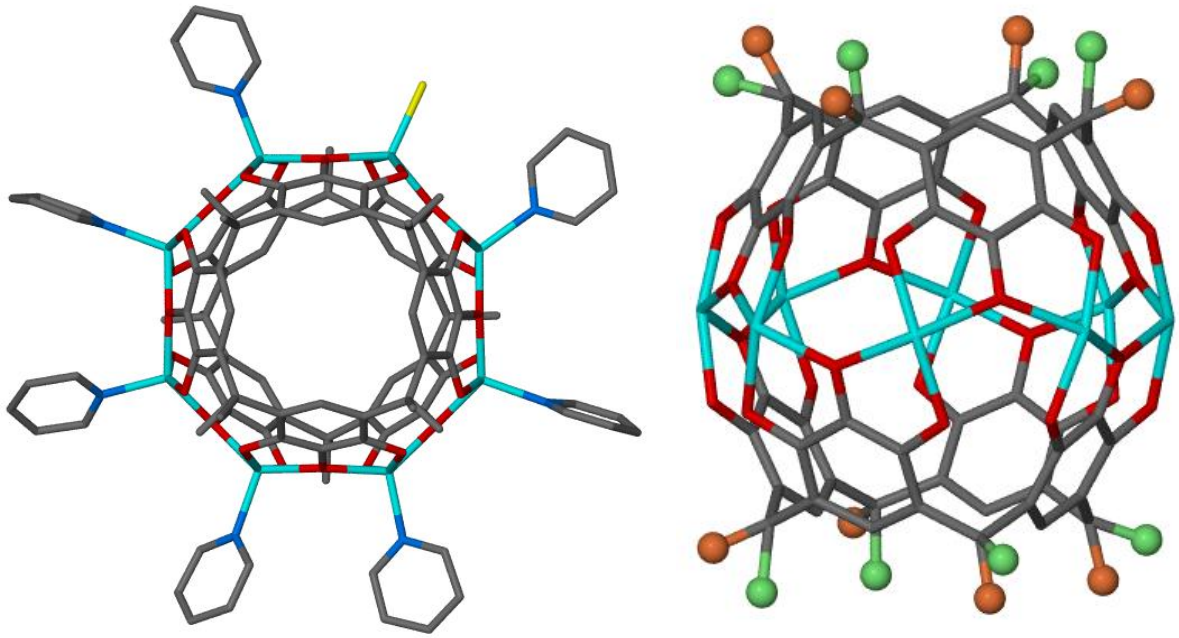

Figure A1.1: Structure of PgC1(rctt) Zn dimer A1.1. Alternate positions of *C*-methyl groups shown in orange and green. See section A1.4 for discussion of chloride anion

A1.2.2: Discussion

Compound **A1.1** was found to be a dimeric zinc MONC that closely resembled other such MONCs. Close inspection of the eight *C*-methyl R-groups in the dimer, however, suggested that they were each disordered over two positions; one that was parallel and one that was perpendicular to the octametal belt. The occupancies of these groups were allowed to refine to their optimal occupancy by entering "1.00" into the S.O.F (structural occupancy factor) box corresponding to these atoms in X-seed . It was found that the S.O.F.s of parallel R-groups reasonably matched with the perpendicular S.O.Fs on the diametrically opposite side of the macrocycle. This indicated that the rctt prochiral designations were retained during the process, akin to the result seen with phenyl analogs. This indicates that a phenyl group is not required for

ring flipping, and that it is likely that any PgC in the chair conformer can be used to synthesize dimeric MONCs.

An interesting feature of this structure was the relative disorder in the R-groups (i.e., the fact that both cis and trans positions at partial occupancy were present at all bridgehead carbons). This suggests that the dimer is rotationally disordered, as in the ideal structure, two cis and two trans R-groups should be found per macrocycle. This disorder is likely due to the small size of the C-methyl group, which has little effect on the packing of the MONCs in a crystal, therefore allowing the dimer to be oriented whichever way, without regard to these groups.

Further proof of this came in the use of **A1.1** to synthesize the corresponding bipyridine MOF (**A1.2**, synthetic information can be found in chapter 4). The unit cell and structure of this MOF is exactly the same as the zinc MOF in chapter 4, except that as in **A1.1**, the R-groups are disordered over multiple positions. This shows two things, namely that the smaller R-groups do not affect the packing of dimers in a structure, and also that the rctt dimer can be used analogously to the all-cis "rccc" dimer.

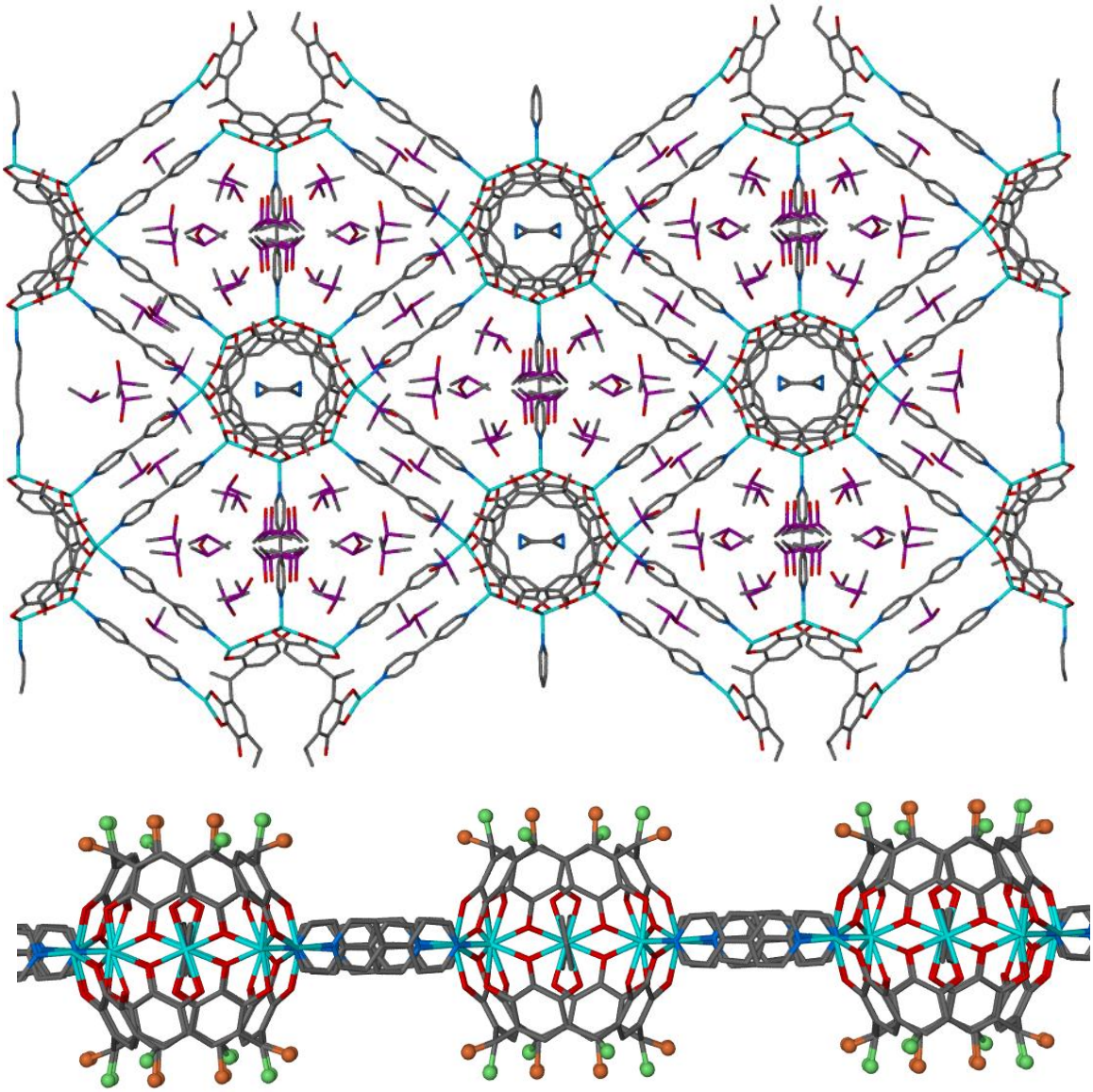

Figure A1.2: Structure of bipyridine-linked MOF **A1.2** that was synthesized from **A1.1**

A1.3: PgC1Zn dimers bearing t-butyl pyridine ligands: rationale

This experiment was performed to test the limits of encapsulation in zinc-seamed dimers. In typical zinc dimer syntheses involving a pyridine analog as the coordinating base, the pyridine analog is reproducibly found to inhabit the interior of the dimer as a guest. As such, it was of interest to determine how the zinc dimer would behave if a pyridine analog was used that is too large to fit into the capsular interior. 4-tert-butylpyridine was chosen as the analog, as it is readily available commercially and was calculated by the Deakyne group to warp the capsular interior if forced into the dimer.

A1.3.1: Synthesis

Two synthetic methodologies were envisioned that would allow us to test the behavior of this coordinating base. *In situ* crystallization in a solvent that typically does not enter the interior of the capsule would tell us if t-butylpyridine could be used at all for this reaction, as regardless of its affinity for the interior of the capsule, a suitably small guest (i.e, the solvent) would be present in the mixture to occupy the interior. A second "heavy-handed" approach would also be used. Here, the MONC would be synthesized in t-butylpyridine as the solvent, so that the MONC would have no choice but to use t-butylpyridine as the guest.

For the *in situ* approach (**A1.3**), several solvents were tested, but only acetone led to the growth of crystals. 15mL of 10^{-2} M PgC1 in 9:1 acetone:water were mixed with 600µL of aqueous 1M $Zn(NO_3)_2$ in a scintillation vial. 265µL of t-butylpyridine were then added, causing the mixture to darken. The scintillation vial was tightly capped and small green needle-like crystals of the product formed over the course of several days.

For the reaction where t-butylpyridine was used as a solvent (**A1.4**), 0.65g $Zn(NO_3)_2$ and 0.31g PgC1 were dissolved in 5.5mL tbuPy. The mixture was heated until near-boiling and was continually heated/stirred for an additional 10m. The color eventually changed from black to a pale yellow with the concomitant formation of precipitate. The solution was cooled, and the precipitate was removed by vacuum filtration and dried in a vacuum dessicator overnight. The dry material was then redissolved in minimal hot DMF and cooled, leading to crystal growth after several days.

Crystal data for PgC_1Zn-tbupy acetone *in situ* crystallization (A1.3):

$C_{28.08}H_{28.84}N_{1.68}O_{6.25}Zn_{1.68}$, M = 600.10, green plate, .01 × .05 × .6 mm^3, monoclinic, space group $P2_1/n$ (No. 14), a = 14.601(4), b = 55.093(17), c = 19.050(6) Å, β = 97.755(4)°, V = 15184(8) $Å^3$, Z = 19, D_c = 1.247 g/cm^3, F_{000} = 5884, Bruker SMART CCD area detector, MoKα radiation, λ = 0.71073 Å, T = 173(2)K, $2\theta_{max}$ = 55.0º, 173161 reflections collected, 34495 unique (R_{int} = 0.1477). Final *GooF* = 1.092, *R1* = 0.1660, *wR2* = 0.3806, *R* indices based on 19233 reflections with I >2sigma(I) (refinement on F^2), 1326 parameters, 76 restraints. Lp and absorption corrections applied, μ = 1.307 mm^{-1}.

Crystal data for PgC_1Zn-tbupy DMF (A1.4) : $C_{42.75}H_{35.75}N_{3.75}O_{8.25}Zn_2$, M = 864.74, yellow plate, .02 × .05 × .15 mm^3, monoclinic, space group $P2/n$ (No. 13), a = 19.569(3), b = 14.633(2), c = 31.385(5) Å, β = 93.540(2)°, V = 8970(2) $Å^3$, Z = 8, D_c = 1.281 g/cm^3, F_{000} = 3556, Bruker SMART CCD area detector, MoKα radiation, λ = 0.71073 Å, T = 173(2)K, $2\theta_{max}$ = 55.1º, 88509 reflections collected, 16697 unique (R_{int} = 0.0756). Final *GooF* = 1.018, *R1* = 0.0777, *wR2* = 0.2449, *R* indices based on 10755 reflections with I >2sigma(I) (refinement on F^2), 1002 parameters, 77 restraints. Lp and absorption corrections applied, μ = 1.122 mm^{-1}.

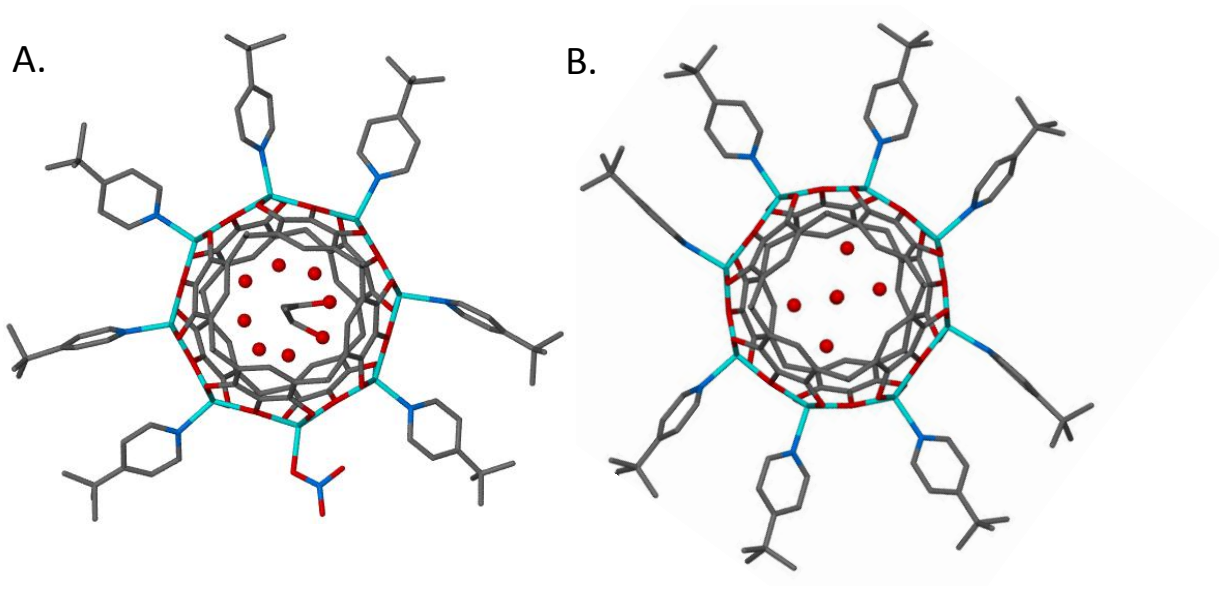

Figure A1.3: Zinc dimers A1.3 (A) and A1.4 (B).

A1.3.2: Discussion

As expected, both syntheses of **A1.3** and **A1.4** resulted in the formation of dimers. The structure of **A1.3** shows that t-butylpyridine was not encapsulated within the dimer, as the interior guest peaks do not even remotely resemble a pyridine molecule. Instead, the interior pattern of peaks, modeled as partial occupancy oxygens along with a pair of full occupancy carbons suggest that the internal guest is a single acetone molecule. This supports our hypothesis that, due to its large size, smaller guests must take the place of t-butyl pyridine inside the dimer.

This conclusion can also be reached by looking at structure **A1.4**. Although t-butyl pyridine was used as the solvent in an attempt to force it inside the capsule as a guest, the interior of the capsule is devoid of peaks that would suggest its presence. Instead, there are six symmetrically spaced peaks inside of the dimer. The distance between these peaks (2.7-3.0Å) is highly suggestive of hydrogen bonding and suggests that these peaks correspond to entrapped water molecules. These water molecules are present due to the zinc salt that was used, which is a

hexahydrate. Despite the small amount of water that was present in the sample (diminished even further by the heating of the sample during the reaction), the dimer nevertheless recruits water molecules into its interior to avoid a vacuum and/or the use of t-butyl pyridine as the guest. This result in **A1.4**, along with the same result in **A1.3** suggests a practical purpose for t-butyl pyridine as the base, namely that it forces guests that would normally not be encapsulated to occupy the interior of the capsule. Therefore, this effect can be used to study the effect that the dimer has on a variety of guest species, as it allows one to selectively encapsulate guest species as long as they are reasonably small. Several trivial attempts have been made to implement this effect with guests such as ferrocene and the benzoate anion, but they have unfortunately been fruitless so far. It may be that coordination to Zn^{2+} prior to the reaction is a requirement for a potential guest, and as such, appropriate coordinating guests should be selected.

A.1.4 Recrystallization of PgC1Zn dimers in the presence of acid

Although zinc-seamed dimers are impervious to many forms of chemical attack, most strong acids are capable of re-protonating the hydroxyl groups on the PgC upper-rim, thereby disrupting the coordinative bonds between the PgC and Zn^{2+} centers and leading to capsular decomposition. In fact, as is done for many other coordination complexes, strong acid is one of the few methods of cleaning labware that can remove stuck-on PgC MONC solid. Nevertheless, several prior cases (directly linked copper dimers, etc) have shown that dilute acid can be used to cause changes in the capsular periphery of the dimer, by removing protonatable ligands such as pyridine and causing their replacement with other functional groups. As such, acid treatment is one of the methods that can be used to post-synthetically modify PgC-based MONCs. Because

Zn^{2+} solely forms the easily crystallizable dimer, it was used to investigate the basic effects that acid treatment can have on MONCs

A1.4.1: Synthesis

To do this analysis, several *in situ* crystallization assays were set up, with acid concentration (HCl or HNO_3), base concentration (pyridine), and solvent as the variables. In a typical setup, 2 mL of 10^{-2}M PgC1 solution in 9:1 methanol/acetone/acetonitrile:water was mixed with 80 μL $Zn(NO_3)_2$ (or $ZnCl_2$). To prevent immediate precipitation of dimer, 8mL solvent was then added to the methanol and acetone vials, while 18mL solvent was added to the acetonitrile vials. Following this, the appropriate amount of pyridine was added, followed by the appropriate amount of HCl or HNO_3.

Crystal data for PgC_1ZnPy MeOH (A1.5): $C_{48.05}H_{33.50}N_3O_{14.50}Zn_4$, M = 1146.31, yellow plate, 0.45 × 0.30 × 0.05 mm^3, monoclinic, space group $C2/c$ (No. 15), a = 16.845(4), b = 27.528(6), c = 20.676(4) Å, β = 94.551(3)°, V = 9557(4) $Å^3$, Z = 8, D_c = 1.593 g/cm^3, F_{000} = 4630, Bruker SMART CCD area detector, MoKα radiation, λ = 0.71073 Å, T = 173(2)K, $2\theta_{max}$ = 55.2º, 54865 reflections collected, 10996 unique (R_{int} = 0.0983). Final *GooF* = 1.078, *R1* = 0.0708, *wR2* = 0.1932, *R* indices based on 5772 reflections with I >2sigma(I) (refinement on F^2), 629 parameters, 15 restraints. Lp and absorption corrections applied, μ = 2.054 mm^{-1}.

Crystal data for PgC_1ZnPy in acetone/py (A1.6): $C_{38.83}H_{29.17}Cl_0N_{3.83}O_{9.33}Zn_{2.67}$, M = 873.15, orange pyramidal, .25 × .25 × .3 mm^3, triclinic, space group P-1 (No. 2), a = 16.223(7), b = 16.234(7), c = 21.822(9) Å, α = 98.007(5), β = 92.229(5), γ = 96.679(5)°, V = 5644(4) $Å^3$, Z = 6,

D_c = 1.541 g/cm^3, F_{000} = 2662, Bruker SMART CCD area detector, MoKα radiation, λ = 0.71073 Å, T = 173(2)K, 2θ_{max} = 55.2º, 64093 reflections collected, 25385 unique (R_{int} = 0.0726). Final *GooF* = 1.654, *R1* = 0.1495, *wR2* = 0.4157, *R* indices based on 17527 reflections

Crystal data for PgC$_1$ZnPy/Cl (A1.7): $C_{38.33}H_{32.67}Cl_{0.33}N_{2.67}O_{9.67}Zn_{2.67}$, M = 871.48, yellow rod, 0.65 × 0.05 × 0.05 mm^3, monoclinic, space group $P2_1/n$ (No. 14), a = 14.464(6), b = 25.577(11), c = 31.138(14) Å, β = 99.009(6)°, V = 11377(9) Å^3, Z = 12, D_c = 1.526 g/cm^3, F_{000} = 5332, Bruker SMART CCD area detector, MoKα radiation, λ = 0.71073 Å, T = 173(2)K, 2θ_{max} = 55.3º, 133384 reflections collected, 26252 unique (R_{int} = 0.2008). Final *GooF* = 1.094, *R1* = 0.0938, *wR2* = 0.2256, *R* indices based on 12716 reflections with I >2sigma(I) (refinement on F^2), 1464 parameters, 36 restraints. Lp and absorption corrections applied, μ = 1.759 mm^{-1}.

with I >2sigma(I) (refinement on F^2), 1417 parameters, 60 restraints. Lp and absorption corrections applied, μ = 1.751 mm^{-1}.

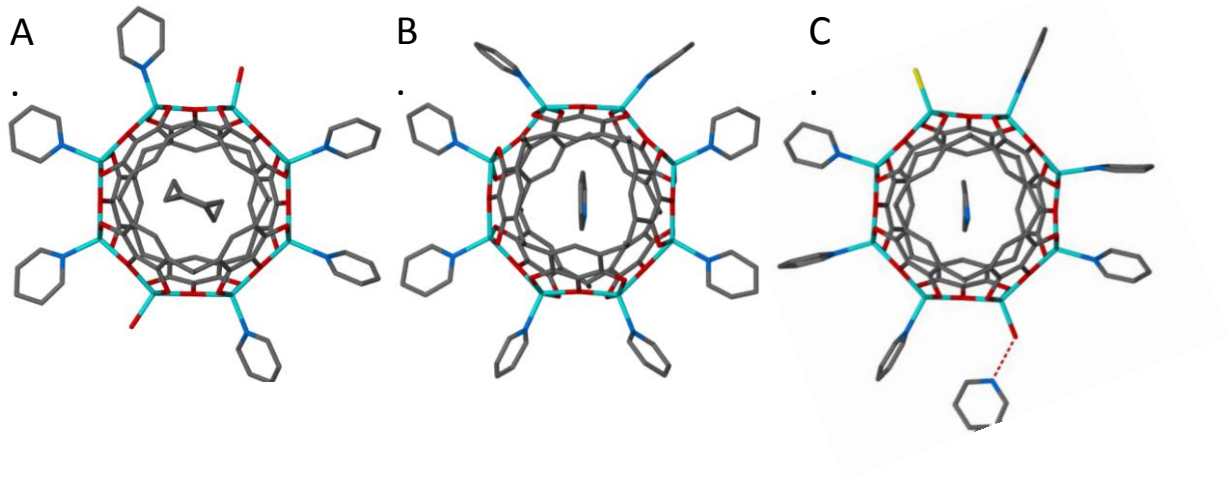

Figure A1.4: Structures of compounds A1.5-7

A1.4.2: Discussion

Hypothetically, it was expected that such a broad assay would lead to many different crystal structures, with the pyridines being replaced by solvent molecules at the higher acid (or lower base) titers. However, it was soon discovered that only three crystal types were formed. In the first part of the experiment, only the pyridine titer was varied. This was done to determine whether or not a lack or excess of pyridine would lead to unusual ligands. However, crystals only formed at the higher pyridine titers in methanol and acetone, leading to structures A1.5 (methanol) and A1.6 (acetone). The data was collected on the two samples where the largest pyridine titer was used, at a 1:4:20 PgC1:$Zn(NO_3)_2$:pyridine ratio. Both structures were rather normal in their appearance, with A1.5 containing two water/methanol molecules as ligands (along with a non-coordinating nitrate anion) and A1.6 containing solely pyridine ligands.

Because of the lack of a difference between these and "standard" zinc dimers synthesized using normal means, a second assay was conducted. Here, the ratio of reagents was kept constant at 1:4:20 PgC1:Zn^{2+}:pyridine (both the nitrate and the chloride zinc salts were used), but after mixing these reagents, and ostensibly forming the dimer, additional acid in the form of 5M aqueous HCl was added to remove the bound pyridines and hopefully replace them with solvent ligands. Instead, it was found that two crystal types formed once again, and largely at the lower titers of acid (1-10 equivalents w.r.t PgC1 concentration). When methanol was used as a solvent, the only crystals that could be found were, once again, crystals of **A1.5**. However, a different crystal type was found in the acetone and acetonitrile vials, which had a very similar unit cell regardless of what solvent was used. Structural analysis of these crystals showed that they indeed contained a dimer (**A1.7**) and that remarkably, the two diametrically opposite

coordinative positions on the exterior of the dimer that were devoid of pyridine ligands were not occupied by solvent molecules, but instead a water molecule on one side and a chloride ion on the other. The fact that a chloride ion was present was deduced by the high electron density at this site (modeling it as a water led to N.P.D due to low thermal parameter) and the longer bond distance to the zinc (2.25Å for Cl^-; approx. 2.00Å for water). Notably, this is the first example of a chloride *exo* ligand on any PgC-based MONC, and its presence among many different samples in this assay may indicate that it is also a versatile ligand for MONCs, albeit an overlooked one. It can be envisioned that other halide ions can likewise be used as ligands for MONCs, but this idea has yet to be explored. The water molecule on the diametrically opposite side of the Cl^- was also unique when compared to other instances of *exo* ligand waters. On initial inspection, the water ligand did not appear as anything special, but it was quickly discovered that a pyridine molecule was proximally positioned to it, at a distance (2.6Å) that was indicative of a hydrogen bond. This interaction was present in all data collections of **A1.7**, regardless of whether acetone or acetonitrile was used as a solvent, suggesting that it is a highly conserved and perhaps required motif in this structure. Although it is not possible to determine if the pyridine is neutrally charged or is instead in its positively-charged pyridinium form, it can be hypothesized that a positively-charged pyridinium would counterbalance the negative charge of the chloride ligand, therefore leading to a charge-neutral entity. Alternately, it can also be considered that the Cl- counterbalances the charge of the guest, which may also be a pyridinium cation. It is also unknown whether the water molecule is truly coordinated water, instead of another species such as a hydroxyl anion. Therefore, it is impossible to know what pyridine species it really is without NMR spectroscopy, which was unfortunately not done due to the low solubility of the crystals.

It is important to also add that multiple solvent molecules were observed in the interstitial space between dimers, and were relatively well-ordered at that. However, despite their different positions in the structure (acetone molecules assumed different positions than acetonitrile molecules) they did not seem to affect the overall structure of the material. This is unusual, as recrystallization of MONCs in different solvents typically has a significant effect on their crystalline packing. It was also observed, however, that the water ligand also forms a hydrogen bond to a hydroxyl on an adjacent dimer, which may stabilize the long range order in the crystal. Likewise, the dimers are located directly on top of one another, suggesting that VDW interactions between the tails (such as those seen in chapter 4) also contribute to long range order.

In summary, two assays were conducted that sought to produce dimers where pyridine ligands were replaced by solvent ligands. Unfortunately, it was found that under the conditions of these assays, this could not be readily accomplished. Several unique crystal structures were nevertheless obtained. It was found that only one structure could be produced from methanol, regardless of the conditions employed, which contained six pyridine exo ligands as well as two waters. Two structures could be obtained from acetonitrile and/or acetone. In the absence of Cl^-, the structure that was formed did not possess any special characteristics; it contained eight exo pyridines and a non-coordinating nitrate that is likely used to counterbalance the charge of the guest pyridinium cation. However, in the presence of Cl^-, it was found that this anion coordinates as an *exo* ligand. This presents the first case where a halide ion acts as a ligand for MONCs, although other anionic examples, such as nitrate anions, have been previously shown to do likewise. An interesting interaction between a water molecule and a pyridine/pyridinium was also found in the same structure.

A1.5 Zinc dimer with 2,4'-bipyridine ligands

Although this structure does not fit in well with the contents of chapter 4, it should nevertheless be included here. The purpose of using 2,4'-bipyridine as a ligand in zinc-seamed dimers was twofold. The initial purpose was to determine whether the statement made in chapter 4 was factually correct, notably that the bipyridine moiety does not lead to hexa-coordinate sites on zinc-seamed dimers, and that the presence of hexa-coordinate sites in the bipyridine-linked zinc MONC is merely a geometric coincidence. A 2,4'-bpy appended dimer would be useful in testing this theory, as it is unlikely to cause linking. Furthermore, as it was expected that the 4' end would coordinate to the Zn^{2+} centers, this synthesis would, in a sense lead to the formation of a functional material, as the 2' end would be free to coordinate to another (free) cation. Although this notion was not explored, a dimer was nonetheless synthesized with all zinc centers coordinating to the 4' end of this ligand.

The structure of the dimer (**A1.8**) resembles all other dimers, except that bipyridine ligands replace the pyridines that are typically present. Each Zn^{2+} center accommodates a single bipy ligand, and therefore all sites are penta-coordinate. This shows that the statement made in chapter 4 is factually correct; bipy ligands do not necessarily lead to hexa-coordinate sites on dimers. Additional research is required to determine whether or not this material has practical applications as a hybrid material. Perhaps these dimers can be linked by a cation with a low coordination number, such as Ag^{+}.

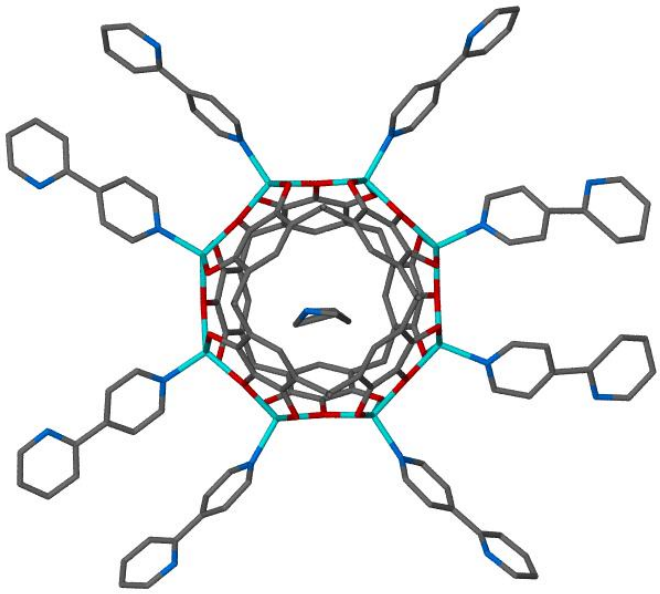

Figure A1.5: Structure of compound A1.8

A1.5.1 Synthesis:

1mL of 10^{-2}M PgC1in DMF was mixed with 40µL aqueous 1M $Zn(NO_3)_2$ and 80 µL aqueous 1M pyridine. The solution was briefly mixed and 40 µL 1M 2,4'-bipyridine in DMF was then added to this solution. The mixture was allowed to stand uncapped to crystallize. Crystallization occurred after several days.

Crystal data for PgC_1Zn 2,4'-bpy in DMF (A1.8): $C_{39.75}H_{30.25}N_{5.50}O_{7.25}S_0Zn_2$, M = 831.68, yellow plate, 0.35 × 0.15 × 0.02 mm^3, monoclinic, space group $P2_1/m$ (No. 11), a = 14.514(2), b = 25.822(4), c = 19.724(3) Å, β = 94.728(2)°, V = 7367.1(17) Å^3, Z = 8, D_c = 1.500 g/cm^3, F_{000} = 3402, Bruker SMART CCD area detector, MoKα radiation, λ = 0.71073 Å, T = 173(2)K, $2\theta_{max}$

= 55.0º, 84709 reflections collected, 17136 unique (R_{int} = 0.0678). Final *GooF* = 0.991, *R1* = 0.0637, *wR2* = 0.1813, *R* indices based on 10914 reflections with I >2sigma(I) (refinement on F^2), 984 parameters, 33 restraints. Lp and absorption corrections applied, μ = 1.362 mm^{-1}.

Chapter A2: Construction of tubular superstructures from PgC1 and various glycols

A2.1: Introduction

This chapter presents work that came about from an attempt to create a catalog of structures based on non-covalent interactions of PgC1 and various other molecules, including solvents. It was noted early on (from work focused on metal-seamed complexes) that a co-crystal of ethylene glycol (ethane diol) and PgC1 contains seemingly porous hydrophilic regions that appear nanotubular in their shape. As such, it was interesting to investigate this material and to determine if other glycols in combination with PgCs would likewise lead to similar architectures.

A2.2 Synthesis and crystallization:

PgC1 was prepared in a similar manner to that described in a previous report.[158] 30.07 g of pyrogallol (99%) was dissolved in 25 mL ethanol. The flask was fitted with a reflux adapter over an oil bath set at 200 °C and was kept under steady nitrogen flow. Through the top of the adapter, 20 mL of acetaldehyde (99.5%) were added along with 1 mL of concentrated hydrochloric acid solution. The mixture was then refluxed for 12 hours during which time the color of the solution changed from colorless to a deep red, accompanied by the precipitation of a white powder. The mixture was then cooled for approximately 30 minutes following reaction and

the solid was removed via filtration. The solid was washed with additional ethanol and dried in a desiccation oven for 24 hours. Proton NMR was used to determine the purity of the resultant powder and showed that both rccc (cone) and rctt (chair) conformers were present in the solid. To separate the two conformers, the powder was mixed into 100 mL of 9:1 methanol:water and heated until boiling. The mixture was then filtered and the filtrate was rotovapped down to a solid and dried separate from the undissolved precipitate in a desiccation oven (7.92g rccc; 4.62g rctt; total yield: 35.15%). Proton NMR was used to establish the composition of the resultant powders via peaks at δ = 6.695 ppm (rccc) and δ = 6.420 ppm and 5.762 ppm (rctt), corresponding to the aryl proton on the two conformers, respectively, in deuterated DMSO. 0.608g PgC1 was mixed with 5mL 1,2 ethane diol and the mixture was heated until all of the solid PgC1 was dissolved. Alternately, hot ethane diol could be added to a vial of solid PgC1 dropwise with stirring and heating until all of the PgC1 had dissolved. The solution was then allowed to cool, which led to rapid crystallization of very fine needle-like crystals that were largely unsuitable for single crystal x-ray diffraction. Dissolution of the crystalline material in a wide variety of solvents, such as methanol, acetonitrile and acetone (usually 10mL solvent per 250-500 mg crystalline material) led to the growth of larger, morphologically identical crystals. It should be noted that the ”first round” crystals were removed/purified by using vacuum filtration. However, this can take a significant amount of time as the needle/excess diol mixture is very thick. This second round of crystallization could be further improved by adding approximately 1mL of nitrobenzene to 10mL of the methanol (etc) solution. The larger crystals that were produced from a second round of crystallization were then analyzed *via* single crystal X-ray diffraction to reveal a unique tubular motif, wherein helices of PgC1 molecules formed a one dimensional hydrophilic cavity (cmpd. **A2.1**). This process was repeated with 1,3 propane

diol (**A2.2**), 1,4 butane diol (**A2.3**), and 1,5 pentane diol (**A2.4**) to yield similar crystalline morphologies (**Fig. A2.1 a-d**). Although the PgC1 molecules were crystallographically well-ordered, providing a good grasp of the structure of the assembly, the contents of this cavity (i.e solvent) could not be easily resolved in most cases.

Crystal data for PgC_1 1,2-ethane diol cocrystal (A2.1): $C_{34}H_{38}O_{14}$, M = 670.64, yellow rod, 1.00 × 0.15 × 0.15 mm^3, tetragonal, space group $I\text{-}4_2d$ (No. 122), $a = b$ = 33.1878(11), c = 17.8995(7) Å, V = 19715.0(12) $Å^3$, Z = 16, D_c = 0.904 g/cm^3, F_{000} = 5664, Bruker SMART CCD area detector, MoKα radiation, λ = 0.71073 Å, T = 173(2)K, $2\theta_{max}$ = 55.0º, 32650 reflections collected, 10043 unique (R_{int} = 0.0335). Final *GooF* = 1.763, *R1* = 0.1573, *wR2* = 0.4251, *R* indices based on 6990 reflections with I >2sigma(I) (refinement on F^2), 426 parameters, 0 restraints. Lp and absorption corrections applied, μ = 0.071 mm^{-1}. Absolute structure parameter = 0.00 (Flack, H. D. *Acta Cryst*. **1983**, *A39*, 876-881).

Crystal data for PgC_1 1,3-propane diol cocrystal (A2.2): $C_{48.67}H_{48}O_{20}$, M = 952.87, colorless rod, 0.18 × 0.06 × 0.06 mm^3, tetragonal, space group $I\text{-}4_2d$ (No. 122), $a = b$ = 32.253(5), c = 17.814(3) Å, V = 18531(5) $Å^3$, Z = 12, D_c = 1.025 g/cm^3, F_{000} = 6000, Bruker SMART CCD area detector, MoKα radiation, λ = 0.77490 Å, T = 100(2)K, $2\theta_{max}$ = 51.1º, 22741 reflections collected, 6679 unique (R_{int} = 0.0743). Final *GooF* = 1.625, *R1* = 0.1498, *wR2* = 0.3729, *R* indices based on 5576 reflections with I >2sigma(I) (refinement on F^2), 496 parameters, 0 restraints. Lp and absorption corrections applied, μ = 0.097 mm^{-1}. Absolute structure parameter = 0.00 (Flack, H. D. *Acta Cryst*. **1983**, *A39*, 876-881).

Crystal data for PgC_1 1,4-butane diol cocrystal (**A2.3**): $C_{21.33}H_{21.33}O_8$, M = 405.72, colorless rod, .1 × .2 × .75 mm^3, tetragonal, space group $I4_1cd$ (No. 110), $a = b$ = 33.094(11), c = 18.048(6) Å, V = 19766(11) $Å^3$, Z = 24, D_c = 0.818 g/cm^3, F_{000} = 5120, Bruker SMART CCD area detector, MoKα radiation, λ = 0.71073 Å, T = 173(2)K, $2\theta_{max}$ = 55.0º, 21695 reflections collected, 11287 unique (R_{int} = 0.0622). Final *GooF* = 2.044, *R1* = 0.2559, *wR2* = 0.5290, *R* indices based on 5481 reflections with I >2sigma(I) (refinement on F^2), 414 parameters, 1 restraint. Lp and absorption corrections applied, μ = 0.063 mm^{-1}. Absolute structure parameter = 0.00 (Flack, H. D. *Acta Cryst*. **1983**, *A39*, 876-881).

Crystal data for PgC_1 1,5-pentane diol cocrystal (A2.4): $C_{29.67}H_{26.67}O_{11.33}$, M = 564.51, colorless rod, 1.00 × 0.25 × 0.25 mm^3, tetragonal, space group $I4_1cd$ (No. 110), $a = b$ = 32.979(3), c = 18.2410(16) Å, V = 19839(3) $Å^3$, Z = 24, D_c = 1.134 g/cm^3, F_{000} = 7088, Bruker SMART CCD area detector, MoKα radiation, λ = 0.71073 Å, T = 173(2)K, $2\theta_{max}$ = 55.1º, 56651 reflections collected, 11249 unique (R_{int} = 0.0579). Final *GooF* = 1.116, *R1* = 0.1043, *wR2* = 0.2740, *R* indices based on 6881 reflections with I >2sigma(I) (refinement on F^2), 555 parameters, 1 restraint. Lp and absorption corrections applied, μ = 0.088 mm^{-1}. Absolute structure parameter = 0.00 (Flack, H. D. *Acta Cryst*. **1983**, *A39*, 876-881).

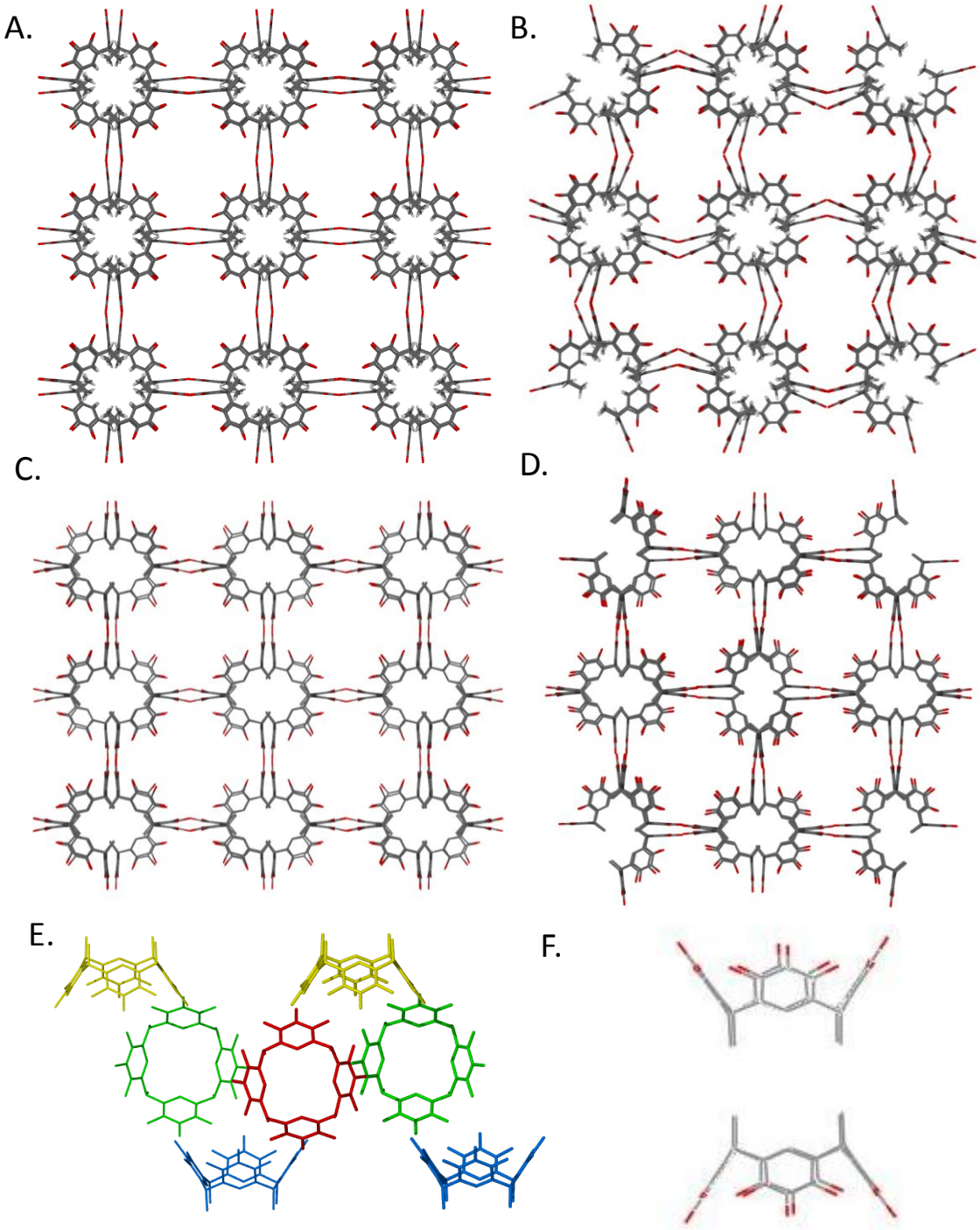

Figure A2.1: Comparison of tubular motifs constructed from 1,2 ethane diol (A) 1,3 propane diol (B) 1,4 butane diol (C) and 1,5 pentane diol (D). All four structures feature a hydrophilic helical region (E) as well as hydrophobic regions between the *C*-methyl groups of the PgC1 molecules (F)

A2.3 Structural Discussion of ethylene glycol/PgC1 cocrystal:

While the asymmetric unit of all four structures (**A2.1-4**) contains a single PgC1 macrocycle, symmetry expansion shows that the arrangement of the PgC1 macrocycles leads to the formation of two separate domains within the crystal structure: large hydrophilic channels and smaller hydrophobic voids. The channels are interlocked with one another and are a product of the helical arrangement of PgC1

Inspection of this helical motif shows that hydrogen bonding among the PgC1 upper rim hydroxyl protons is responsible for this packing arrangement. Each PgC1 is "connected" to an adjacent PgC1 through four hydrogen bonds, two shorter 2.725Å bonds along with two longer 3.079Å bonds. Individual tubular helices also contribute to the structural integrity of their neighbors. Adjacent helices are offset in such a way that the pyrogallol aromatic rings on one tube fill in some of the gaps along the edge of another tube, thereby also leading to additional hydrogen bonding interactions. As any given tube is surrounded by four others, overall this creates a completely gap-free outer surface for each tube. This unique cooperative helical arrangement of adjacent PgC1s also leads to another region within the structure; a series of hydrophobic cavities caused by tail-to-tail VDW interactions between *C*-methyl groups from the PgC1s. All of these structural features are co-dependent and are interlocked together to form a lattice-like superstructure. As such, discrete nanotubes do not exist in this structure as they are merely a product of the arrangement of PgCs. Further evidence for this comes from SANS, which shows that the only appropriate model for the dissolved material is a Schulz sphere with a radius of approx. 7Å (very bad statistics with cylindrical models: e.g 2.01951 ± 2915.57Å for a core-shell cylinder). This suggests that in solution, the PgCs are present as dimers, or more likely, in equilibrium between dimers that can be seen by SANS and individual monomeric

macrocycles that cannot. Therefore, the PgC1 macrocycles only organize into a porous lattice-like framework in the solid state.

A2.4: Structures of other PgC1-diol cocrystals

To determine if other diols would form similar assemblies, three common diols were also used as solvents for PgC1. An analogous procedure to that for the formation of **A2.1** was used, which led to similar results. Attempts with other PgCs also led to co-crystals of PgC and glycol, but most of these were rather uninteresting bilayer-type structures rather than nanotubes. The 1,3 propane diol analog was a bit tricky, as it required a significant quantity of PgC1 to be dissolved in a rather small volume of hot 1,3 propane diol prior to crystallization. In addition, this analog formed a crystalline layer during the first round of crystallization, rather than distinct crystals. Second round crystallization in methanol/nitrobenzene, however, led to the growth of better crystals. All of the materials formed needle-like crystals that were similar in morphology to the ethylene glycol analog. Interestingly, while the structures of the materials prepared in this way were similar to **A2.1**, they were nevertheless distinctly different in the way that the PgC macrocycles interlocked to form the hydrophobic and hydrophilic regions. This is likely due to slightly different hydrogen bonding between the glycols and the PgC1 molecule, which slightly alters the spacing between PgC1 macrocycles. This, in turn, causes the *C*-methyl chains to slide relative to those on an adjacent PgC1 and thereby occupy a slightly different position (**Fig. A2.2**). Therefore, a longer or shorter glycol chain affects both the hydrophilic and hydrophobic regions in these materials, although a distinct trend between glycol chain length and structure does not seem to be present.

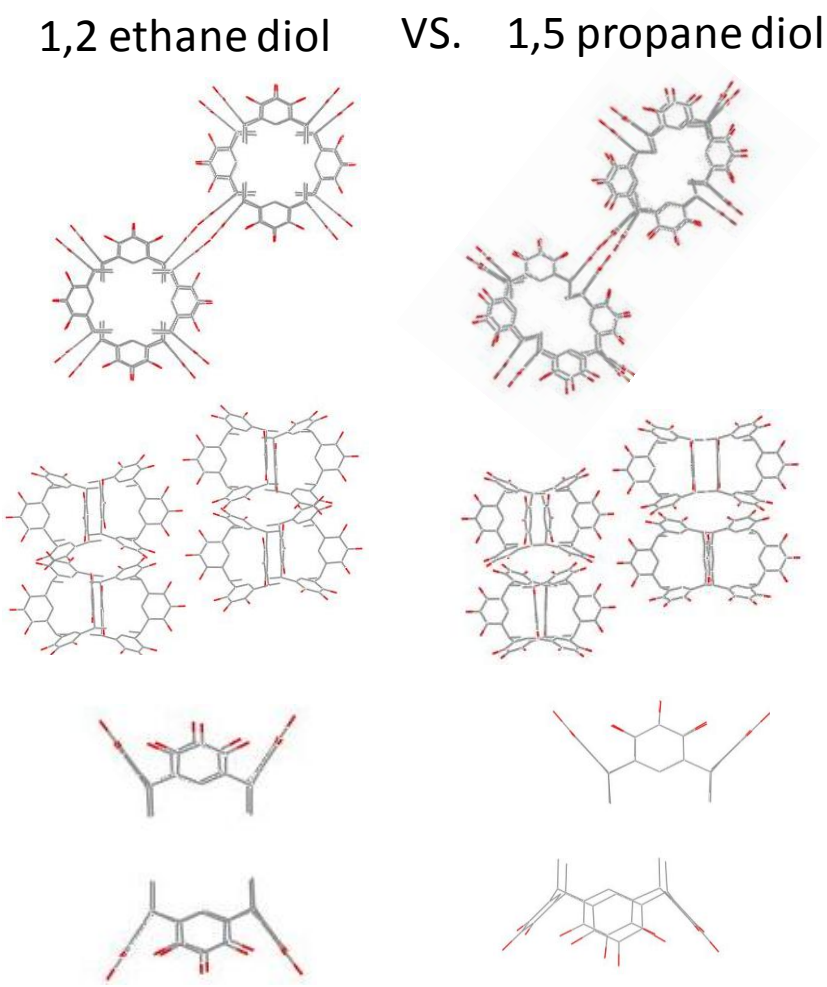

Figure A2.2: Differences in hydrogen bonding between PgC1 and different glycols leads changes in non-covalent stacking of PgC subunits

A2.5: PgC1-diol cocrystal as a starting reagent for another crystal form

The seemingly porous arrangement of macrocycles that make up the lattice of **A2.1-4** made this material a promising candidate for gas sorbtion studies. Several attempts, however, showed that this material is unsuitable for this purpose, as the high temperatures required to remove the glycols from the interior of the structures also leads to the decomposition of the

structure and gas sorbtion efforts with ethylene glycol in the framework lead to a null result. An important discovery was nevertheless made while investigating these materials, which may lead to a practical use for the glycol cocrystals of PgC1.

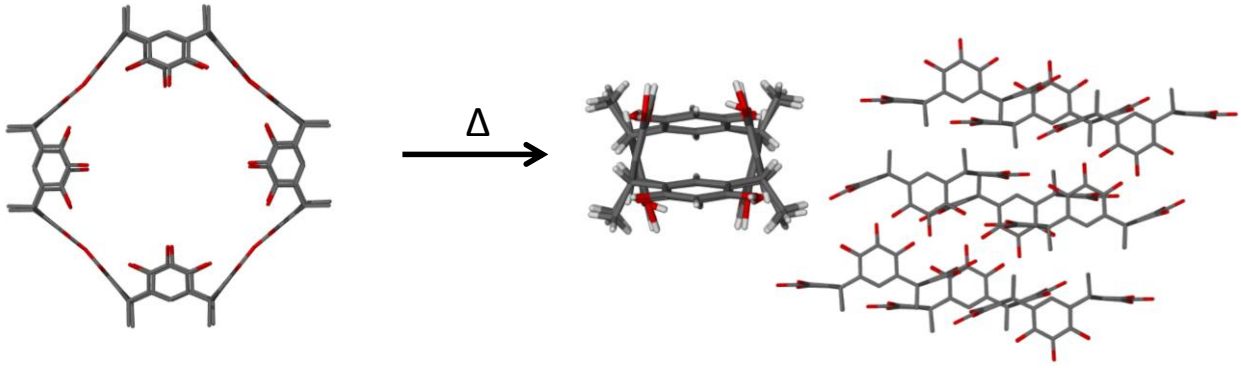

Figure A2.3: Heating PgC1-ethane diol under vacuum leads to decomposition and recrystallization into a guest-free form of PgC1

In order to remove glycol from the crystalline lattice at low(er) temperatures, a small amount of A2.1 was placed in a Schlenk flask under a vacuum. The contents were then heated over hot silicone oil on a heating mantle set at 200°C (in actuality, the temperature of the oil was likely lower c.a 140-150°C). It was observed that ethane diol in liquid form began to vacate the crystalline material and evaporate/run up the flask to the oil-air boundary. Some of this ethylene glycol dripped back down onto the crystalline material, seemingly dissolving it/causing it to melt. Further heating caused the remaining ethylene glycol to evaporate, solidifying this material as a pink, seemingly non-crystalline disc. The material was then cooled and removed from the schlenk flask. Unexpectedly, analysis of this material under a microscope revealed the presence of several large prism-like crystals that were significantly different from the needle-like crystals present earlier, suggesting that the needles decomposed into another crystalline form. Analysis of the unit cell *via* scXRD showed that this material also possessed an entirely different

crystal structure. Further structural analysis showed that this material was indeed different from any known PgC1 structure, in that it was a fully guest-free structure, only consisting of PgC1 macrocycles (**Fig. A2.3, cmpd. A2.5**). While a structure of the guest-free rctt chair has been previously reported, this is the first report of a guest-free form of PgC1 in the rccc boat/cone conformation. The structure of the material is unspectacular, other than the close packing between macrocycles, which is mediated by both hydrogen bonds as well as π-stacking interactions between the aryl rings. There is no indication that there are any void spaces within the structure, which is consistent with a closely-packed guest-free form of a molecule.

Crystal data for guest free PgC_1 (A2.5): $C_{32}H_{32}O_{12}$, M = 608.58, colorless prism, 0.25 × 0.15 × 0.10 mm^3, triclinic, space group P-1 (No. 2), a = 10.7723(19), b = 11.367(2), c = 12.051(2) Å, α = 104.401(2), β = 108.670(2), γ = 96.167(2)°, V = 1325.6(4) $Å^3$, Z = 2, D_c = 1.525 g/cm^3, F_{000} = 640, Bruker SMART CCD area detector, MoKα radiation, λ = 0.71073 Å, T = 173(2)K, $2\theta_{max}$ = 55.1º, 15676 reflections collected, 6024 unique (R_{int} = 0.0229). Final *GooF* = 1.048, *R1* = 0.0387, *wR2* = 0.0985, *R* indices based on 4859 reflections with I >2sigma(I) (refinement on F^2), 449 parameters, 0 restraints. Lp and absorption corrections applied, μ = 0.117 mm^{-1}.

Due to its lack of special features, it would seem as if the discovery of this material would be rather useless. However, there are nevertheless two potential applications for this material. Firstly, it should be noted that even with heat/vacuum, it is notoriously difficult to remove solvents from crystalline PgCs. As such, there is always a significant amount of residual water, methanol and acetonitrile present alongside the macrocycle when it is used for some purpose. As such, it is advantageous to have a method for producing the guest-free form of this

macrocycle so that any interference caused by these extra solvents is eliminated. The method described here is a relatively simple method to do so, as ethylene glycol is relatively inexpensive. A second application for this material is really more of a research focus. It has previously been determined that high pressure gas treatment of high-density TBC4 causes the crystalline material to undergo a crystalline transition into a low-density phase that is capable of sorbing gas to a greater extent. Although it is likely that the guest-free form of PgC1 cannot sorb gas on its own due to the close packing of the macrocycles, it can be envisioned that it can likewise be activated by appropriate means and can therefore be turned into a gas-sorbing material.

A2.6 Co-crystallization of RsC1 and ethane diol

RsC1 can likewise be cocrystallized with ethylene glycol to form a cocrystal (cmpd. A**2.6**). However, the structure that is produced is reminiscent of the structure formed when RsC1 is co-crystallized with methanol wherein two regions exist; one containing solvent and the other containing the macrocycle in the boat conformer (**Fig A2.4**). This structure is clearly not porous, but may nevertheless eventually serve some purpose, such as the production of a guest-free form of RsC1 analogously to the PgC1 result.

Crystal data for RsC$_1$ 1,2-ethane diol cocrystal (A2.6): $C_{30.67}H_{34.67}O_{14.67}$, M = 637.92, yellow hollow rod, 0.75 × 0.10 × 0.10 mm^3, monoclinic, space group $P2_1/n$ (No. 14), a = 14.804(6), b = 20.821(8), c = 16.136(6) Å, β = 90.731(5)°, V = 4973(3) Å^3, Z = 6, D_c = 1.278 g/cm^3, F_{000} = 2016, Bruker SMART CCD area detector, MoKα radiation, λ = 0.71073 Å, T = 173(2)K, $2\theta_{max}$ = 42.0º, 32136 reflections collected, 5271 unique (R_{int} = 0.0846). Final *GooF* = 2.075, *R1* = 0.1666, *wR2* = 0.4691, *R* indices based on 3779 reflections with I >2sigma(I) (refinement on F^2), 617 parameters, 2 restraints. Lp and absorption corrections applied, μ = 0.103 mm^{-1}.

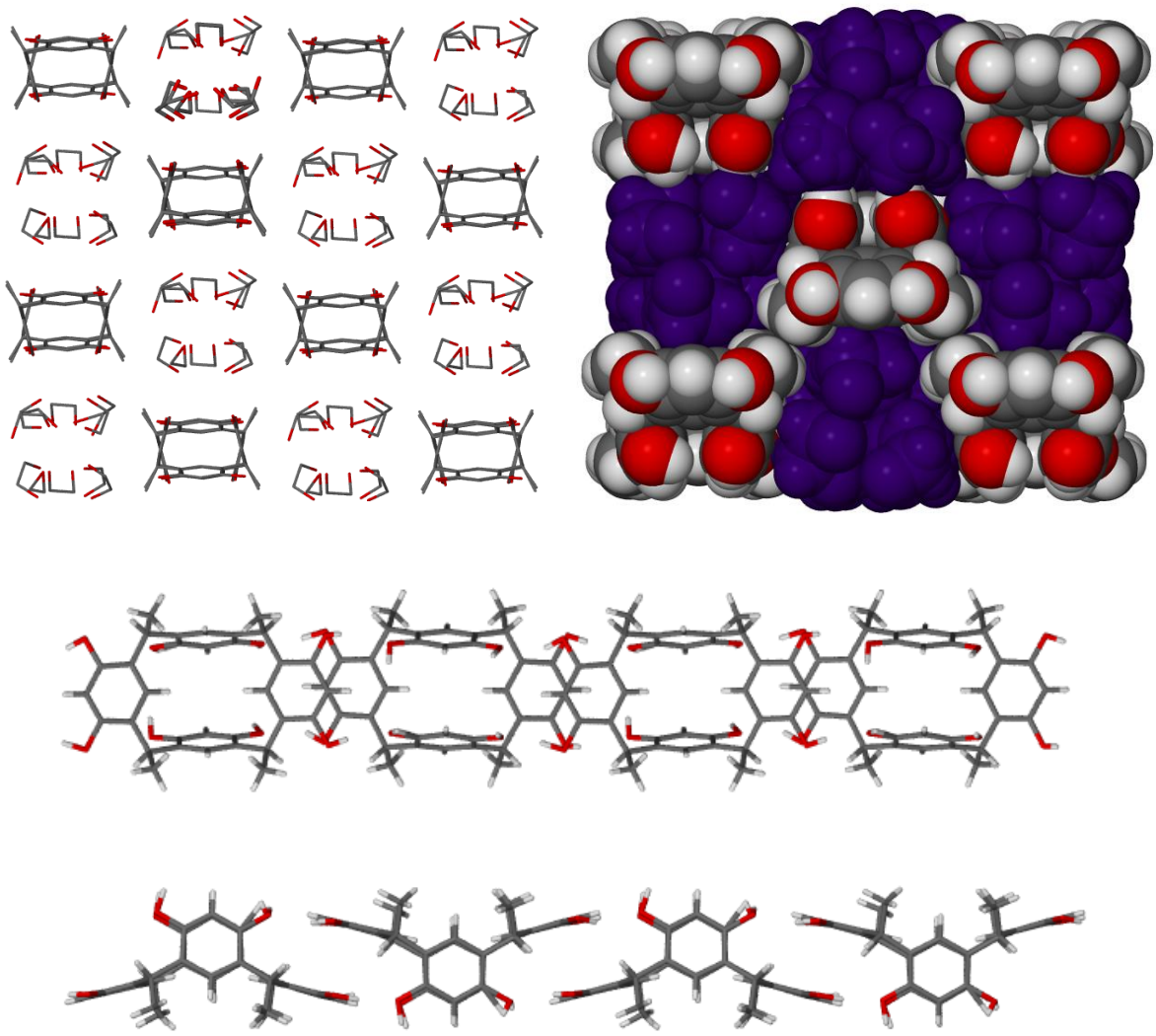

Figure A2.4: Crystallization of C-methylresorcin[4]arene in ethylene glycol leads to a completely different structure than with PgC1.

Chapter A3: Ferrocene as a hydrophobic templating agent with Pyrogallol[4]arenes[160]

A3.1 Introduction

Nanoscale materials based on the bowl-shaped members of the calixarene family continue to capture the imagination of the scientific community with potential applications in pharmaceuticals[161], catalysis[162,163], and as molecular magnets.[164,165] One particularly robust, yet less investigated member of this family is the *C*-alkylpyrogallol[4]arene (PgC).[94,166] Recent studies have shown that PgCs self-assemble into a wide range of superstructures based on both inter- and intramolecular hydrogen bonding,[167] as well as metal ion coordination.[168] The formation of these entities is largely dependent on interactions of the hydrophilic upper rim of the bowl with small, polar molecules. Larger molecules have also been shown to act as templating agents for more intricate superstructures. For example, PgCs with substituted pyrenes have been shown to form both tubular[103] and hexameric capsular solid-state structures.[169] We now show that ferrocene can likewise be used as a template towards the formation of a capsular motif.

Previous reports of ferrocene/calixarene (or resorcinarene) host-guest complexes cite electrostatic means of encapsulation, wherein oxidation to the ferrocenium cation is necessary for encapsulation.[170] Reports of encapsulating neutral ferrocene do exist, but all of these rely on a customized cavity based on upper rim modification or the addition of large structural elements.[171-173] To our knowledge, neither the complexation of ferrocene nor the ferrocenium cation has been reported with pyrogallol[4]arenes.

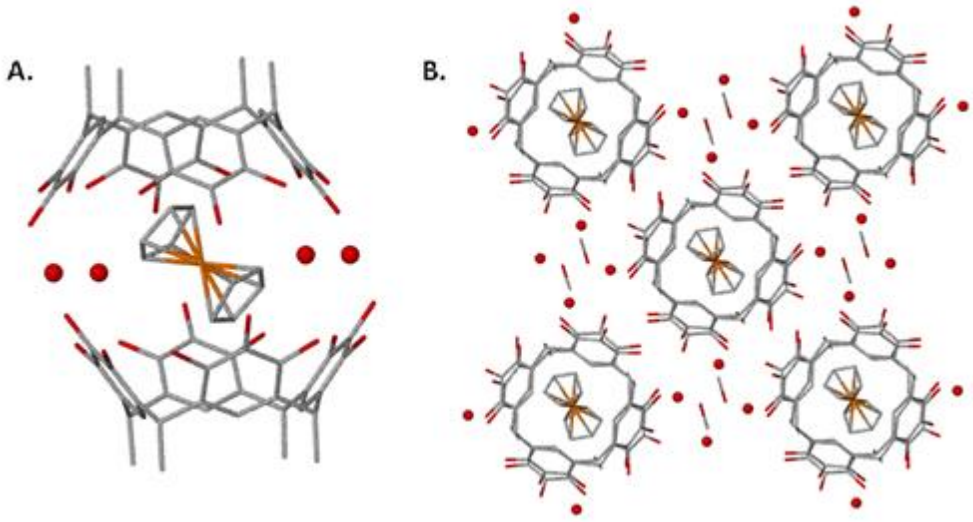

Figure A3.1: Image of an individual ferrocene containing dimer (A) and its corresponding packing arrangement within the crystal

A3.2: Methods and Discussion

Reagents. All reagents were purchased either from Sigma-Aldrich or ACROS Organics and were used without further purification. The purity of all reagents is included in the synthesis information below.

Proton NMR Analyses. All ^{1}H-NMR studies were conducted using the Bruker DRX 300MHz.

Crystal Structure Analyses. All single crystal X-ray data was collected using a Bruker

Apex II CCD detector. The samples are mounted on a fixed kappa three circle goniometer and cooled to a temperature of 173(2) K. The X-ray source is a MoKα sealed tube source with a wavelength of 0.71073A.

Synthesis of C-methylpyrogallol[4]arene (PgC1). PgC1 was prepared in a similar manner to that described in a previous report.[158] 30.07 g of pyrogallol (99%) were dissolved in 25mL ethanol. The flask was fitted with a reflux adapter over an oil bath set at 200 °C and was kept under steady nitrogen flow. Through the top of the adapter, 20 mL of acetaldehyde (99.5%) were added along with 1 mL of concentrated hydrochloric acid solution. The mixture was then refluxed for 12 hours during which time the color of the solution changed from colorless to a deep red, accompanied by the precipitation of a white powder. The mixture was then cooled for approximately 30 minutes following reaction and the solid was removed via filtration. The solid was washed with additional ethanol and dried in a dessication oven for 24 hours. Proton NMR was used to determine the purity of the resultant powder and showed that both rccc (cone) and rctt (chair) conformers were present in the solid. To separate the two conformers, the powder was mixed into 100 mL of 9:1 methanol:water and heated until boiling. The mixture was then filtered and the filtrate was rotovapped down to a solid and dried separate from the undissolved precipitate in a dessication oven (7.92g rccc; 4.62g rctt; total yield: 35.15%). Proton NMR was used to establish the composition of the resultant powders via peaks at δ = 6.695 ppm (rccc) and δ = 6.420 ppm and 5.762 ppm (rctt), corresponding to the aryl proton on the two conformers, respectively, in deuterated DMSO.

Synthesis of C-heptylpyrogallol[4]arene (PgC7). PgC7 was prepared in a similar manner to that described in a previous report.[119] 50.06 g of pyrogallol (99%) was dissolved in 50 mL of ethanol. The flask was fitted with a reflux adapter over an oil bath set at 200 °C and was kept under steady nitrogen flow. Through the top of the adapter, 65 mL of octylaldehyde (99%) was added along with 0.5 mL of concentrated hydrochloric acid solution. The mixture was then refluxed for 19 hours during which time the color of the solution changed from colorless to a deep red, accompanied by the precipitation of a white solid. The mixture was cooled for approximately 30 minutes following reaction and the solid was removed via filtration. The solid was washed with additional ethanol and dried in a dessication oven for 24 hours (35.58 g; 37.98% yield).

Synthesis of $(PgC1)_2 \subset Fe(Cp)_2 \cdot [(H_2O)_4\ (MeOH)_4]$. 1 mL of 10^{-1} M ferrocene in hot methanol was added to 9 mL of a 10^{-2} M solution of PgC1 in an 8:1 mixture of methanol to water. The mixture was allowed to evaporate under a slow air stream during the course of a week. The orange solution slowly turned green followed by the growth of blue prismatic crystals (labeled as **1** within the main text**).**

Synthesis of $(PgC1)_2 \subset Fe(Cp)_2 \cdot [(H_2O)_2\ (HCl)_1\ (MeOH)_1(MeCN)_2]$. 0.608 g of PgC1 was heated under vacuum at 150 °C for 24 hours to remove solvent of crystallization. This dried material was then dissolved in 100 mL 8:1 methanol: water mixture. To this, 10mL of 10^{-1} M ferrocene in hot acetonitrile and 10mL of 10^{-1} M HCl in water were added. The mixture was then left to evaporate, with blue prismatic crystals forming over several days.

Synthesis of $(PgC7)_2 \subset Fe(Cp)_2 \cdot [(H_2O)_3\ (HCl)_1\ (MeCN)_2]$. 0.5 mL of 10^{-1} M ferrocene in dichloromethane was added to 5 mL of a 10^{-2} M solution of PgC7 in dichloromethane. To this, 0.1 mL of concentrated hydrochloric acid was added. The mixture was allowed to evaporate, which it did to dryness within one day. To the dry dark solid, 15mL MeCN were then added, and the mixture was stirred to dissolve. The mixture was then left to evaporate, with blue prismatic crystals forming over several days.

Single Crystal X-ray Diffration Data:

Crystallographic Data for $(PgC1)_2 \subset Fe(Cp)_2 \cdot [(H_2O)_4\ (MeOH)_4]$:

C39H47Fe0.50O16, *M* = 799.69, blue plate, 0.45 × 0.15 × 0.05 mm3, triclinic, space group *P*-1 (No.2), *a* = 11.625(3), *b* = 12.010(2), *c* = 15.136(3) A, α = 105.893(2), β = 109.868(2), γ = 95.330(2)°, *V* = 1870.6(7) A3, *Z* = 2, *D*c = 1.420 g/cm3, *F*000 = 844, Bruker APEXII CCD area detector, MoKα radiation, λ = 0.71073 A, *T* = 173(2)K, 2θmax = 55.1o, 21861 reflections collected, 8467 unique (Rint = 0.0344). Final *GooF* = 1.158, *R1* = 0.0902, *wR2* = 0.2148, *R* indices based on 6706 reflections with I >2sigma(I) (refinement on *F*2), 552 parameters, 6 restraints. Lp and absorption corrections applied, μ = 0.293 mm-1.

Crystallographic Data for $(PgC1)_2 \subset Fe(Cp)_2 \cdot [(H_2O)_2\ (HCl)_1\ (MeOH)_1(MeCN)_2]$:

C148H148O48Fe2· Cl2, *M* = 3218.67, blue plate, 0.25 × 0.20 × 0.05 mm3, Monoclinic, *P*2/*c*, *a* =28.303 (3), *b* = 12.2325 (12), *c* = 22.597 (2) A, β = 102.652 (1)°, *V* = 7633.5 (13) A3, *Z* = 2, *D*c = 1.400 g/cm3, *F*000 = 3388, Bruker APEXII CCD area detector, MoKα radiation, λ = 0.71073 A,*T* = 173(2)K, 2θmax = 47.8o, 17433 unique (Rint = 0.0499). Final *GooF* = 1.035, *R1* = 0.074, *wR2*= 0. 234, *R* indices based on 11860 reflections with I >2sigma(I) (refinement on *F*2), 1047

parameters, 3 restraints. Lp and absorption corrections applied, μ = 0. 32 mm-1.

Crystallographic Data for $(PgC7)_2 \subset Fe(Cp)_2 \cdot [(H_2O)_3\,(HCl)_1\,(MeCN)_2]$:

Crystal data for C7ferrodimer: C126.80H182.40ClFeN2.40O26.60, *M* = 2254.03, Blue Prism, 0.45 ×0.25 × 0.15 mm3, triclinic, space group *P*-1 (No. 2), *a* = 12.1618(16), *b* = 23.123(3), *c* = 23.904(3) A, α = 113.9860(10), β = 91.738(2), γ = 91.407(2)°, *V* = 6133.8(14) A3, *Z* = 2, *D*c = 1.220 g/cm3, *F*000 = 2425, Bruker APEXII CCD area detector, MoKα radiation, λ = 0.71073 A, *T* = 173(2)K, 2θmax = 55.0o, 72543 reflections collected, 27784 unique (Rint = 0.0325). Final *GooF* = 1.030, *R1* = 0.0677, *wR2* = 0.1964, *R* indices based on 19467 reflections with I >2sigma(I) (refinement on *F*2), 1517 parameters, 20 restraints. Lp and absorption corrections applied, μ = 0.217 mm-1.

A 10^{-2} M solution of 1:1 PgC1:ferrocene in a 8:1 mixture of methanol to water was allowed to evaporate under a slow air stream during the course of a week. The orange solution, indicative of free ferrocene, slowly turned green, followed by the growth of blue prismatic crystals **A3.1** which were analyzed via single crystal XRD and found to be dimeric capsule. The crystal structure of **A3.1** (**Fig. A3.1**) shows an orderly hydrogen bonding architecture. The individual dimers are constructed primarily through intermolecular hydrogen bonding, and much like other PgC superstructures involve the upper-rim hydroxyl groups of each of the two PgC1s and water molecules as structural components. The iron is located on an inversion center, which implies that the asymmetric unit contains one cyclopentadienyl ring and one PgC1. The smaller volume of the dimeric capsule constrains the ferrocene such that the molecule is crystallographically well ordered. Three of the hydrogens on each cyclopentadienyl ring are positioned at the hydrophilic

periphery of the dimer while the other two are pointed directly at two aromatic rings in the macrocycle. The C-H···π centroid distances between the cyclopentadienyl hydrogen atoms and the adjacent PgC1 aromatic rings are 2.68 and 2.77 Å. The two PgC1s in the capsule are slightly offset from one another as can be seen in **Fig. A3.1a**. This differs from the more symmetrical dimeric structures as reported by Rissannen et. al. with quarternary ammonium cations, perhaps due to the larger size of the encapsulated ferrocene guest.[174]

Due to the similarity in bond lengths between ferrocene and the ferrocenium cation, it was difficult to crystallographically determine whether the guest was charged. Thus, ^{1}H NMR was used to determine the oxidation state of the encapsulated species. Broadening in the signal normally corresponding to ferrocene showed that this assembly likely consists of the paramagnetic ferrocenium cation. This is surprising, as no oxidizing agents were used during synthesis and no distinct counterions could be found in the crystal structure. However, this result does correlate well with the blue color of the crystalline material, which indeed suggests the presence of ferrocenium cation as opposed to neutral ferrocene.

In erratum to the described cocrystallization scheme, it was conveniently found that HCl added to the solution at a 10^{-2} M concentration greatly hastened the crystallization process, leading to crystallization in days rather than weeks. Interestingly, this modification also had a structural consequence, namely that HCl/Cl^- replaced a single water molecule in the hydrogen bonding network along the capsule's "equator." This modification leads to a slight deviation in hydrogen bond lengths from ~2.8 to ~3.0 Å, producing a slightly larger opening on one side of the inclusion complex, as compared to that of **A3.1** (see figure **A3.2**).

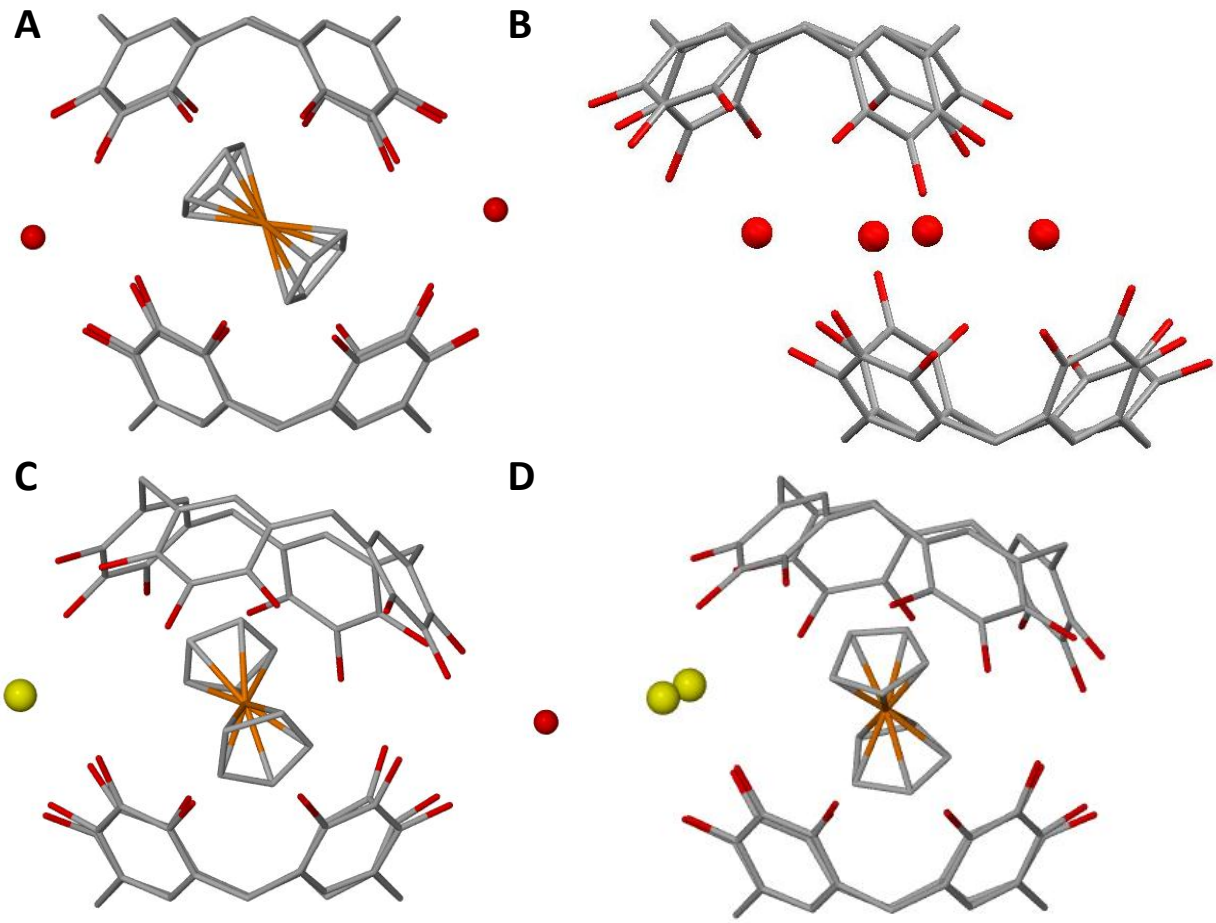

Figure A3.2: Comparison of A3.1 (A) to a typical PgC bilayer (B) and two ferrocene dimers that contain Cl- as structural units (C and D)

In contrast to the previously described dimer, wherein no counterion was apparent, the presence of HCl/Cl^- suggests a possible counterion to ferrocenium in the form of a chloride ion. Aside from this minor difference, the resultant PgC1/Ferrocene/HCl complexes are nearly isostructural with the non-HCl containing system. Thus, this speedier method was used to quickly determine whether other solvent systems and PgCs could lead to similar assemblies or if other host-guest complexes were preferred. In addition to the above mentioned host-guest complexes, both PgC1 and PgC7 formed analogs in acetonitrile. It is also of note that two ethyl acetate analogs with

PgC7 were also found, one of which was surprisingly doubly substituted with HCl/Cl^-, with both molecules at full occupancy (**Fig. A4.2c,d**). This suggests that at least one of the chlorides must necessarily exist as an HCl molecule, or contain a shared proton between two chloride centers. This is further corroborated by an intermolecular spacing of ~3.1 Å, which is too close for a Cl^-/Cl^- contact distance if both were present as chloride ions. As the overall structure of **A3.1** was conserved in all cases, even with major structural substitutions to the hydrogen-bonding framework and independent of PgC identity or solvent system, it can be surmised that this ferrocene inclusion complex is preferred over other possible capsular systems such as the previously reported hexameric containers with pyrogallol[4]arenes.

A3.3 Using SANS to describe this dimeric species in solution

In the discussion of any large supramolecular solid state structure, a question always arises: what does the solid state structure say about the species present in solution? The answer to this question is one typically based on NMR evidence or sheer speculation, neither of which were viable methods of analysis in this study. Small-Angle Neutron Scattering (SANS), however, is capable of providing geometric insight into the species present in solution, regardless of paramagnetism. SANS measurements were performed on the NG7 30m SANS instrument at the NIST Center for Neutron Research (NCNR-NIST). Pre-formed crystals of **A3.1** were dissolved in deuterated methanol and were measured at an optimized concentration of 3% by mass. Scattering from dimeric moiety **A3.1** fit[175] as a polydisperse sphere of mean radius (6.67 ± 0.02) Å with $\sqrt{(x^2/N)} = 1.34$. This radius corresponded rather closely to the experimental radius from our solid-state results (6.74Å, as measured from iron center to the centroid of methyl hydrogen atoms). This data provides evidence for at least the short-term stability of dimeric capsule **A3.1**

in protic media, a divergence from other PgC-based capsular entities which are typically only stable in aprotic solvents.[98]

A3.4: Conclusion

In conclusion, ferrocene served as an excellent guest for the study of templation with PgC macrocycles, exclusively producing dimeric nano-architectures in the solid state, regardless of conditions. SANS measurements also showed that this assembly was stable in methanolic solution, further demonstrating the robustness of this assembly under typically destructive conditions for PgC-based host-guest systems.

Chapter A4: Ferrocene species included within a pyrogallol[4]arene tube[176]

A4.1: Introduction

In addition to capsular motifs, the conical shape of the calixarenes[177], resorcinarenes[178], and pyrogallolarenes[104,179] can likewise lead to the formation of tubular solid-state structures. These often incorporate large non-solvent molecules as part of the tubular framework. An excellent example of this is a host-guest complex of *C*-hexylpyrogallol[4]arene (PgC6) with pyrene.[10] In this complex, tetramers of PgC6 associate with one another via hydrogen bonding, while the pyrene molecules intercalate between the *C*-hexyl pendant arms of the PgC. This leads to two distinct regions within the structure: a hydrophilic region that encloses guest solvents along with a hydrophobic region that accommodates the pyrene. Herein, we describe a second host-guest complex of *C*-methylpyrogallol[4]arene (PgC1) and ferrocene that conforms to a tubular structural motif. In contrast to the capsular motif, a tubular hydrophobic cavity, rather than a capsular cage, is responsible for incarceration of the guest, while the hydroxyls of the PgC1s along with polar solvent molecules form the long-range hydrogen-bonding superstructure.

A4.2: Synthesis and methods

Synthesis of *C*-methylpyrogallol[4]arene (PgC1): PgC1 was prepared in a similar manner to that described in a previous report.[94] 30.07 g of pyrogallol (99%) were dissolved in 25 mL ethanol. The flask was fitted with a reflux adapter over an oil bath set at 200 °C and was kept under steady nitrogen flow. Through the top of the adapter, 20 mL of acetaldehyde (99.5%) were added along with 1 mL of 12.1 mol/L hydrochloric acid solution. The mixture was then refluxed for 12 hours during which time the color of the solution changed from colorless to a

deep red, accompanied by the precipitation of a white powder. The mixture was then cooled for approximately 30 minutes following reaction and removed via filtration. The precipitate was washed with additional ethanol and dried in a dessication oven for 24 hours. Proton NMR was used to determine the purity of the resultant powder and showed that both rccc (cone) and rctt (chair) conformers were present in the solid. To separate the conformers, the powder was mixed into 100 mL of 9:1 methanol:water and heated until boiling. The mixture was then filtered and the filtrate was rotovapped down to a solid and dried along with the undissolved precipitate in a dessication oven (7.92 g rccc; 4.62 g rctt; total yield: 35.15%). Proton NMR was used to establish the composition of the resultant powders via peaks at δ = 6.695 ppm (rccc) and δ = 6.420 ppm and 5.762 ppm (rctt), corresponding to the aryl proton on the two conformers, respectively, in deuterated DMSO.

Synthesis of $(PgC1)_3(H_2O)_1(MeOH)_1\subset$Ferrocene. A 10^{-2} mol/L stock solution of PgC1 was made by dissolving 0.608 g of PgC1 (rccc) powder in 100 mL of 8:1 methanol:water. Likewise, a 10^{-1} mol/L stock solution of ferrocene was made by dissolving 0.372 g in 20 mL carrier solvent (benzene, chloroform, ethyl acetate, or acetone). 100 µL of ferrocene solution was mixed with various volumes of PgC1 solution, ranging from 1 to 10 mL in scintillation vials. 8:1 methanol:water mixture was then added to each to bring the total volume to 10 mL. The lids on the scintillation vials were partially unscrewed and crystallization occurred over a period of several weeks. A mixture of crystals often resulted at the higher PgC1: ferrocene concentrations and some manual sorting of crystals was necessary for SANS. Some evidence also suggests that use of a lower methanol:water ratio (4:1 or less) can lead to a greater proportion of crystals of the tubular motif.

Slow changes in concentration of a PgC1 and ferrocene solution *via* evaporation led to the crystallization of this unique architecture. Methanolic solutions containing various ratios of PgC1 to ferrocene (with the concentration of ferrocene set at 10^{-3} mol/L) were allowed to evaporate until crystallization was evident. At a 1:1 PgC1 to ferrocene ratio, crystals of the previously reported dimeric product were the sole product.[160] However, at ferrocene ratios of 6:1 or higher, two different crystal types were found to have formed, with green needle-like crystals accompanying the dark blue prisms of the ferrocene dimer. The dark green needles were shown by single crystal X-Ray diffraction to be a novel tubular motif **1** featuring ferrocene "beads" in a hydrophobic cylinder of repeating trimers of PgC1.

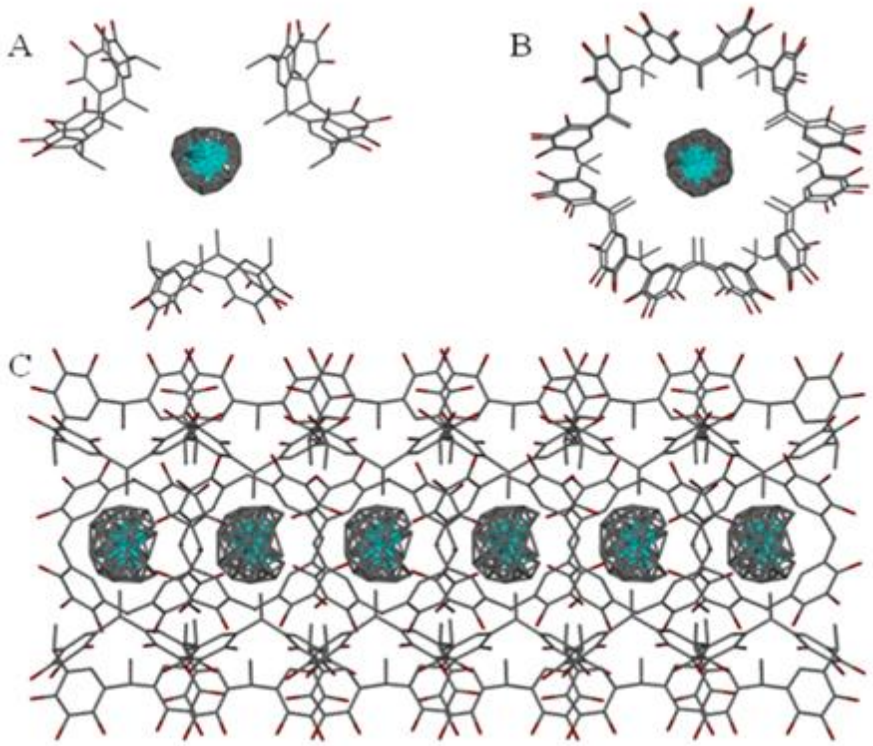

Figure A4.1: Structure of a single repeating unit of **A4.1** (A), two overlaid units (B), showing a 60° rotation, and a view showing the propagation of the tubular framework (C).

A4.3: Structural analysis

The tubular structure **A4.1** (Fig. A4.1) displays a complicated hydrogen-bonding arrangement of PgC1s. Each tube consists of alternating units of 3 PgC1s rotated by 60 degrees relative to one another along the crystallographic C-axis and a single ferrocene guest. The overall structure thus closely resembles a family of resorcinarene-based nanotubes described by Rissannen et. al. However, in contrast to both the resorcinarene tubes and our previously reported PgC/Ferrocene dimeric capsule, the guest is not located within the bowl-shaped cavity of the PgC1, but rather within the hydrophobic tubular environment spanned by the C-methyl pendant arms of the PgC1 (Fig. A4.1). A disordered methanol molecule instead occupies the space within the bowl. The location of the ferrocene within this environment does not lend well to C-H···π or other interactions with adjacent PgCs. Thus the Fe center is disordered over two positions and the cyclopentadiene rings are present as a highly disordered torus of electron density. This indicates a high degree of mobility of the ferrocenes within the tube. The three PgC1s located in each repeating layer (Fig. A4.1a) do not participate in hydrogen bonding with one another, but rather with four PgC1s in adjacent layers, two above and two below. Each PgC1 also participates in hydrogen bonding with four other PgC1s in adjacent tubes. A single water molecule located outside the cavity also participates in hydrogen bonding with each PgC1, helping to tie together three adjacent tubes. As an additional note, broadening in the peak corresponding to ferrocene in the ^{1}HNMR spectrum showed that the ferrocene guest was likely paramagnetic and thus present as the ferrocenium cation. The lack of a counterion suggests that a singly deprotonated PgC1 counterbalances the +1 charge of the ferrocenium ion.

A4.4: SANS studies

As with the previously described ferrocene dimer, small angle neutron scattering (SANS) was used to study this entity, **A4.1**, in solution. SANS measurements were performed on the NG7 30m SANS instrument at the NIST Center for Neutron Research, Gaithersburg, MD.[180] SANS provides structural details in solution that cannot be obtained with conventional techniques. Unlike light scattering techniques or diffusion NMR, SANS requires no assumption that dissolved species are spherical in solution.

The tubular assembly **A4.1** was dissolved in *d4*-methanol at a mass fraction of 2% to obtain sufficient scattering statistics with SANS. The sample was then left overnight to ensure saturation without precipitation. Three different sample to detector distances, 1.3 m, 4.5 m and 13 m, were used to cover the overall q range of 0.008 $Å^{-1} < q < 0.54$ $Å^{-1}$. It is important to note that unlike for capsular entities, scattering measurements for tubular entities were performed at much smaller angles. Scattering data was then analyzed on Igor Pro software provided by NIST.[138] To investigate host-guest interactions in solution, we first calculated scattering length densities (SLDs) of PgC1 trimers with and without ferrocene guest. These SLDs were then held fixed in data analyses and the measured data was fitted to various cylindrical, spherical and ellipsoidal models. Analysis of the data as a polydisperse sphere[139,181] both with and without ferrocene guest, however, led to a good fit of **A4.1** as spheres of radius 7.01 Å and 6.6 Å, respectively. A previous investigation has revealed the radius of 7 Å for a typical PgC_3 dimer while that of 10 Å for a PgC_3 hexamer.[182] Hence, even though all parameters and their error bars look reasonable for PgC1 with ferrocene, the size of the sphere reported is equal to that of PgC_3 dimer. On the other hand, the radius of 6.6 Å obtained for PgC1 without ferrocene guest is similar to that of our previous study of ferrocene enclosed hydrogen-bonded PgC1 dimer (r = 6.7

Å) in methanol.[183] Thus Schulz sphere fit for PgC1 without ferrocene guest represents the best fit and gives a true representation of the PgC1 - ferrocene structure in solution. The structural alteration of solid-state ferrocene enclosed PgC1 nanotubes to solution-phase hydrogen-bonded dimer indicates overall higher stability of dimers over tubes in solution. This study is intriguing since it demonstrates not only the effect of templation towards building molecular hosts with varying architectures but also unique structural variation and behavior of hosts in the two phases. In addition, the progression in size observed for pyrogallol[4]arene dimers is in agreement with solution-phase SANS studies of pyrogallol[4]arene hexamers with varying chain length.[184,185]

In conclusion, we have described a novel inclusion complex of PgC1 and ferrocene. Unlike the previously reported dimer, the tubular motif **A4.1** is not stable in methanolic solution and dissociates into a dimer. Its formation is thus likely due to a high PgC1 to ferrocene ratio coupled with shifting solvent conditions during evaporation. Future studies will focus on studying other hydrogen-bonded as well as metal-containing nanotubular frameworks in solution.

Chapter A5: Conservation of a unique non-covalent motif in a tetracyanoresorcin[4]arene silver complex.

This chapter was part of collaboration with Dr. Praput Thavornyutikarn in obtaining the crystal structures of several novel macrocyclic molecules that he had developed during the course of his graduate career. Several of these molecules had electron-pair donor atoms that seemed uniquely suited for coordination to metal cations. The structure presented here, a resorcin[4]arene with cyano groups at the 2-position, was thought to be an ideal candidate for coordination to Ag^{+} cations, and our investigation of its coordination to this tetracyanoresorcin[4]arene ligand is reported here. In addition to reporting the MOF-like structure that formed upon coordination, it was discovered that a novel non-covalent motif is present in this structure both before and after coordination, suggesting that like in the dimeric MONCs of chapter 4, non-covalent interactions decidedly influence the structure of the compound.

A5.1: Introduction:

Contrasting with their beginnings as hosts in host-guest systems, resorcin[4]arenes (RsCs) and pyrogallol[4]arenes (PgCs) are currently experiencing widespread use as ligands for metal ions. Examples of metal-bound systems involving RsCs and PgCs encompass a wide range of topologies including monomers[186-188], dimers[127,129,130,135,189,190], multi-component cages[125,191,192], and various networks[158,193,194]. Such metal-bound systems afford enhanced stability and rigidity over non-covalent systems. This property is specifically important in the construction of network solids used for gas sorption/separation, where a rigid scaffold helps maintain the integrity of the channels and voids inherent to such materials. To rationally direct the formation of such metal-organic frameworks (MOFs), rigid ligands with a pre-organized structure and

divergent coordination sites are often chosen.[195] This disfavors the formation of finite entities and, as an added benefit, may lead to porous materials without any additional templating agents. Based on these criteria, we investigated *C*-hexyl tetracyanoresorcin[4]arene (RsCNC6) as a ligand towards the construction of porous MOFs. The use of this ligand is topologically reasonable for this purpose, as the cyano groups on the RsC upper-rim are directionally divergent and the structure of this macrocycle is fixed in the rccc "cone" conformation. In this study, Ag^+ was chosen as a suitable metal centre due to its affinity toward cyano ligands, as well as its penchant for labile, or highly reversible, coordination chemistry. This allows for greater control over MOF growth, thereby improving crystallization and subsequent characterization *via* single crystal XRD[196]. Although cyanocalix[4]arenes were shown to form one-dimensional MOFs with Ag^+ on two previous instances, there are currently no reports of cyanoresorcin[4]arene silver complexes.[195,197]

A5.2: Synthesis

RsCNC6 was prepared following a previously reported protocol.[198] RsCNC6 was then recrystallised in a 8:1 methanol to water mixture to obtain **A5.1**. To prepare **A5.2**, 0.92 g (0.89 mmol) of crystalline **A5.1** was dissolved in 100 mL of 8:1 methanol to water mixture and 0.68 g (4.0 mmol) $AgNO_3$ in 20mL of methanol was added, changing the colour of the solution from a light yellow to a darker yellow. Precipitation of a tan solid occurred almost immediately, with a small amount of crystalline material forming after approximately 24 hours of standing. The pale yellow rodlike crystals were then analysed *via* single crystal XRD and found to consist of the MOF **A5.2**. For both **A5.1** and **A5.2**, data was collected on a Bruker SMART CCD diffractometer using Mo radiation. The structure was solved and refined using SHELX with X-

Seed[133] as the interface. The TWIN command was used during refinement as **A5.2** was found to be a racemic twin. Some atoms were refined isotropically due to the disorder in the structure.

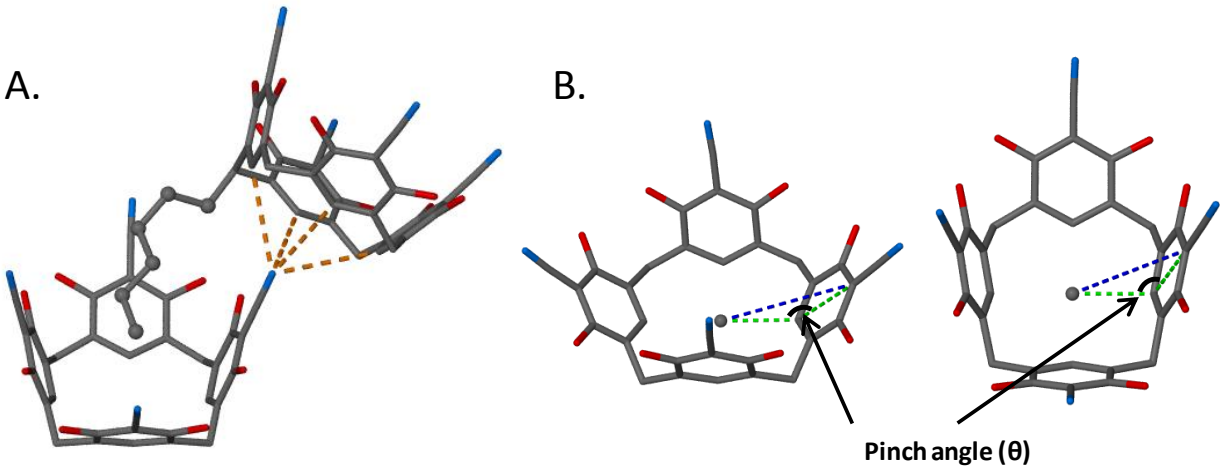

Figure A5.1: Head-to-tail noncovalent interaction found in 5.1 and 5.2 (A), and scheme for pinch angle measurements (B)

A5.3 Structural Discussion

The asymmetric unit of **A5.1** consists of a single RsCNC6 as well as one water molecule and three methanol molecules. The RsCNC6 adopts the rccc "pinched cone" conformation, with CCC angles of 112.12° and 110.63° for one pair of aryl rings and 136.34° and 140.54° for the other pair, as measured from the calculated centroid of the methine carbon atoms to carbon atoms adjacent and para to the cyano group on the aryl rings (Fig. A5.1b). The RsCNC6 subunits pack in an offset head-to-tail arrangement, with each "bowl" accommodating a single *C*-hexyl pendant arm of the RsCNC6 above it, and interacting with the cyano group from the RsCNC6 below *via* CH-N non-covalent bonding. (Fig. A5.1a). When viewed along the b-axis, symmetry expansion of the asymmetric unit results in the formation of RsCNC6 columns with solvent-occupied channels located between adjacent columns (Figure A5.2a). These channels

are occupied by two of the methanol molecules present in the asymmetric unit, which interact *via* hydrogen bonding interactions with one another (2.670(3) Å O-O distance), as well as with two

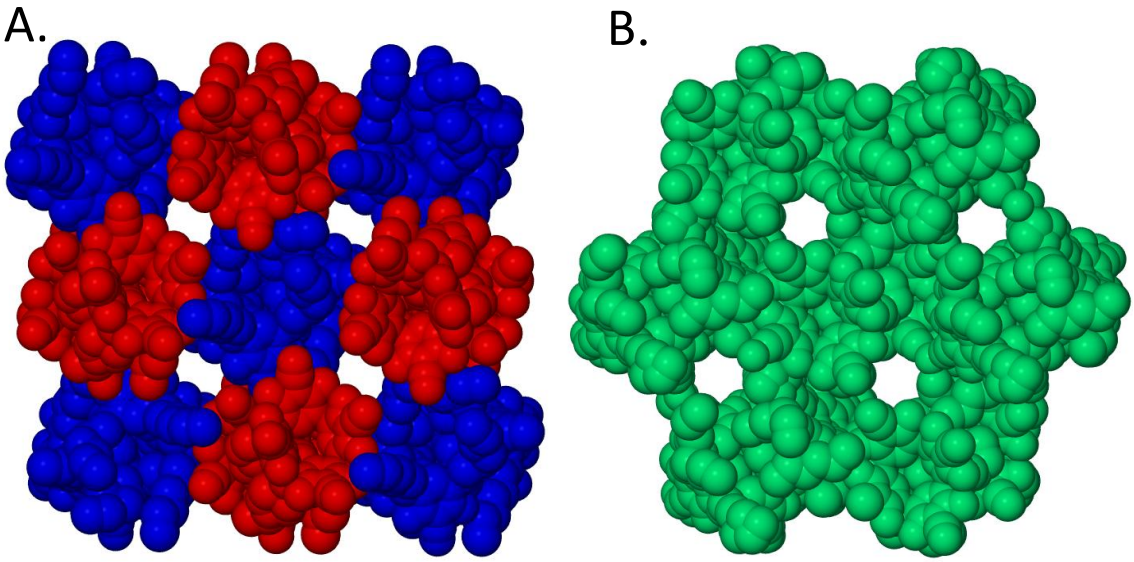

Figure A5.2: Space-filled illustration of channels within **A5.1** (A) and **A5.2** (B). Internal methanol molecules removed for clarity.

upper rim hydroxyl protons on the adjacent RsCNC6 molecules (2.916(3) Å , 2.583(2) Å O-O distances). The other molecules of crystallization, one methanol and one water, are located within hydrogen bonding distance of the upper-rim RsCNC6 hydroxyl and cyano groups (2.708(2) Å, 2.661(2) Å O-O and 2.856(2) Å O-N for water and 2.844(3) Å O-N for methanol), as well as within range of one another (2.677(2) Å O-O distance), but do not otherwise possess any interesting or distinguishing features that lend to the channel-like structure of **A5.1**.

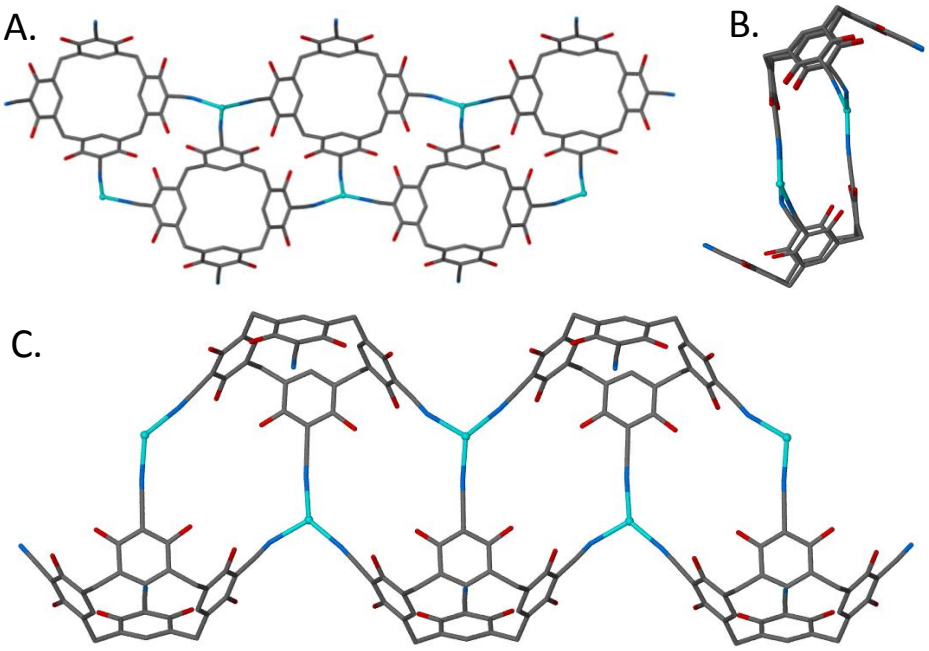

Figure A5.3: RsCNC6 Ag^+ MOF as viewed from a (A), b (B), and c (C) crystallographic axes. Solvent molecules and pendant *C*-hexyl groups removed for clarity.

As previously noted, the addition of Ag^+ to **1** resulted in the formation of a one dimensional MOF, with a RsCNC6:Ag stoichiometry of 1:1 (Fig A5.3). The asymmetric unit of **A5.2** consists of a single $ResCNC_6$, a single Ag^+ ion bound to three of the four upper-rim cyano groups on adjacent RsCNC6 molecules, as well as several disordered non-coordinating methanol molecules. As before, the RsCNC6 molecule adopts a "pinched cone" conformation. However, the pinch angles differ from that of **A5.1**, with angles of 120.57° and 118.10° for one pair of aryl rings and 135.25° and 136.01° for the other pair. This discrepancy can be attributed to the fluxional behavior of the resorcin[4]arene core as it undergoes a change in solvent and coordination environments. Each Ag center is tri-coordinate (2.181(6) Å, 2.186(9) Å, and 2.248(7) Å Ag-N distances) with N-Ag-N angles of 109.0(3)°, 117.2(3)°, and 131.0(3)°. This differs from both previously published reports of tetracyanocalixarene/Ag^+ complex, in which silver is tetra-coordinate.[195,197] Consistent with the previous report[197], however, **A5.2** packs as a

one-dimensional chain of RsCNC6 and Ag^+ cations, with adjacent Ag^+ slightly offset from one another in a 1·2·1·2 pattern (Fig. A5.3a,c). Interestingly, there is no evidence of a nitrate anion to balance the charge of the Ag^+ in this structure. This is likely due to a high degree of disorder of the nitrate anion. An alternate explanation is that deprotonation of one of the upper-rim hydroxyl protons on the RsCNC6 had occurred. Peaks in the difference map corresponding to hydrogen atoms were, however, located for all eight of the hydroxyl moieties. This suggests that if deprotonation of the aryl hydroxyl groups did occur, the deprotonation was random and thus not localized to any one specific hydroxyl.

Akin to the structure of **A5.1**, symmetry expansion of the asymmetric unit also reveals several solvent-occupied channels. When viewed along the crystallographic b-axis, the space between individual RsCNC6 and Ag^+ subunits forms a rectangular opening, referred to as a series of "windows" in the calixarene analogue report (**Fig. A5.3b**).[197] This channel is occupied by one of the methanol molecules and a *C*-hexyl pendant arm of an adjacent RsCNC6. An additional structural methanol located outside of the channel participates in hydrogen-bonding interactions between aryl hydroxyl protons and the methanol within the channel itself. Furthermore, an additional second channel containing several disordered methanol molecules is also evident when the structure is viewed along the a-axis (Fig. A5.2b). Interestingly, this channel is very similar to that in **A5.1**; when viewed from the b-axis, the channel is clearly the product of stacked columnar RsCNC6 subunits, with the same head-to-tail interactions as in **A5.1** (Fig. A5.1). This stacking motif coupled with Ag coordination leads to an offset interlocking of individual one-dimensional chains. The presence of this interaction in both structures points to a conserved motif among cyanoresorcinarenes, which can potentially be exploited to produce predictable long range order. Indeed, previous structural studies on RsC/MeCN clathrates have

also shown a similar interaction between the acetonitrile cyano group and the cavity of the RsC.[199]

A5.4 Conclusions

In conclusion, two novel crystal structures **A5.1** and **A5.2** have been reported. Although metal coordination strongly directs the long-range order of **A5.2**, there is a notable structural motif that is conserved when going from the free ligand to a metal-bound system, which largely influences the overall structure. The knowledge of such interactions can be used towards the rational design of other solid-state structures based on resorcinarenes and other calixarene-like macrocycles. Furthermore, the presence of channels within **A5.1** and **A5.2** suggests that they may be used as materials for gas sorption/separation experiments following activation/degassing to remove the encapsulated solvent.

Chapter A6: supplementary data for chapters 2-5

A6.1 Bond length, angle, and tau5 tables for chapters 2 and 4

The tables in this section coincide with the compounds described in chapters 2 and 4. Not all, but most of the compounds from these two chapters are represented here. Some of the tables also include only bond angle or only bond length data, but a good portion of them include both sets of data. Citations are included for any of the structures that have been published so far. In addition, data for several published compounds (not by the author) is also included. This includes data for a PgC3Cu hexamer and two sets of data from previously published zinc-seamed dimers. These data are located in tables A6.1.23-25.

Compound	2.1 published									
Metal #	**Ligand**	**θ_1**	**θ_2**	**τ5**	**Cu-O1**	**Cu-O2**	**Cu-O3**	**Cu-O4**	**Cu-ligand**	**Cu-ligand2**
Cu1	DMSO	171.75	151.76	0.333	1.957	1.961	1.971	1.988	2.177	n/a
Cu2	DMSO	173.05	154.59	0.308	1.954	1.959	1.982	1.985	2.163	n/a
Cu3	DMSO	173.16	152.79	0.340	1.951	1.962	1.981	1.987	2.169	n/a
Cu4	DMSO	171.81	152.23	0.326	1.961	1.965	1.973	1.99	2.189	n/a
Cu5	DMSO	171.09	151.05	0.334	1.954	1.961	1.967	2	2.167	n/a
Cu6	DMSO	171.08	151.37	0.329	1.942	1.943	1.973	1.988	2.187	n/a
Cu7	DMSO	172.25	151.66	0.343	1.958	1.961	1.987	1.988	2.194	n/a
Cu8	DMSO	171.53	151.3	0.337	1.957	1.963	1.986	1.99	2.203	n/a
Average		**172.0**	**152.1**	**0.33**	**1.954**	**1.959**	**1.978**	**1.990**	**2.18**	**#DIV/0!**
StD		**0.8**	**1.2**	**0.01**	**0.006**	**0.007**	**0.007**	**0.005**	**0.01**	**#DIV/0!**

Table A6.1.1: Bond angle and bond distance data for compound 2.1

Compound	2.2 published									
Metal #	**Ligand**	**θ_1**	**θ_2**	**τ5**	**Cu-O1**	**Cu-O2**	**Cu-O3**	**Cu-O4**	**Cu-ligand**	**Cu-ligand2**
Cu1	DMSO	173.19	153.38	0.330	1.955	1.96	1.985	1.986	2.213	n/a
Cu2	DMSO	171.46	151.82	0.327	1.957	1.967	1.968	1.978	2.207	n/a
Cu3	DMSO	171.53	150.53	0.350	1.956	1.964	1.976	1.99	2.203	n/a
Cu4	DMSO	172.96	152.55	0.340	1.951	1.964	1.976	1.978	2.193	n/a
Cu5	DMSO	172.87	153.35	0.325	1.951	1.958	1.981	1.986	2.222	n/a
Cu6	DMSO	172.12	151.63	0.342	1.958	1.97	1.983	1.985	2.182	n/a
Cu7	DMSO	171.67	151.33	0.339	1.954	1.964	1.969	1.972	2.199	n/a
Cu8	DMSO	173.45	153.64	0.330	1.961	1.964	1.983	1.986	2.184	n/a
Average		**172.4**	**152.3**	**0.34**	**1.955**	**1.964**	**1.978**	**1.983**	**2.20**	**#DIV/0!**
StD		**0.8**	**1.1**	**0.01**	**0.003**	**0.004**	**0.007**	**0.006**	**0.01**	**#DIV/0!**

Table A6.1.2: Bond angle and bond distance data for compound 2.2

Compound	2.3									
Metal #	**Ligand**	**θ_1**	**θ_2**	**τ5**	**Cu-O1**	**Cu-O2**	**Cu-O3**	**Cu-O4**	**Cu-ligand**	**Cu-ligand2**
Cu1	DMSO	172.08	151.92	0.336	1.96	1.968	1.982	1.987	2.185	n/a
Cu2	DMSO	169.74	150.1	0.327	1.973	1.976	1.981	2.002	2.141	n/a
Cu3	DMSO	170.16	148.52	0.361	1.976	1.979	1.985	1.97	2.172	n/a
Cu4	DMSO	171.28	150.21	0.351	1.972	1.98	1.985	1.993	2.152	n/a
Cu5	DMSO	171.92	151.45	0.341	1.962	1.969	1.983	1.988	2.199	n/a
Cu6	DMSO	170.56	149.34	0.354	1.971	1.976	1.98	1.985	2.16	n/a
Cu7	DMSO	169.89	148.73	0.353	1.979	1.981	1.986	1.99	2.179	n/a
Cu8	DMSO	172.27	151.53	0.346	1.966	1.975	1.976	1.983	2.167	n/a
Average		**171.0**	**150.2**	**0.35**	**1.970**	**1.976**	**1.982**	**1.987**	**2.17**	**#DIV/0!**
StD		**1.0**	**1.3**	**0.01**	**0.007**	**0.005**	**0.003**	**0.009**	**0.02**	**#DIV/0!**

Table A6.1.3: Bond angle and bond distance data for compound 2.3

Compound	2.4									
Metal #	**Ligand**	**θ_1**	**θ_2**	**τ5**	**Cu-O1**	**Cu-O2**	**Cu-O3**	**Cu-O4**	**Cu-ligand**	**Cu-ligand2**
Cu1	Acetone	173.51	153.07	0.341	1.958	1.964	1.967	1.97	2.258	n/a
Cu2	Acetone	173.02	152.15	0.348	1.959	1.961	1.979	1.98	2.28	n/a
Cu3	Acetone	172.44	151.85	0.343	1.951	1.955	1.971	1.99	2.267	n/a
Cu4	Acetone	172.93	152.06	0.348	1.948	1.956	1.966	1.966	2.22	n/a
Cu5	Acetone	173.19	152.19	0.350	1.954	1.973	1.976	1.975	2.233	n/a
Cu6	Acetone	172.06	151.59	0.341	1.946	1.958	1.97	1.987	2.235	n/a
Cu7	Acetone	172.74	151.43	0.355	1.948	1.957	1.969	1.994	2.276	n/a
Cu8	Acetone	173.39	152.95	0.341	1.956	1.96	1.964	1.979	2.265	n/a
Average		**172.9**	**152.2**	**0.35**	**1.953**	**1.961**	**1.970**	**1.980**	**2.25**	**#DIV/0!**
StD		**0.5**	**0.6**	**0.01**	**0.005**	**0.006**	**0.005**	**0.010**	**0.02**	**#DIV/0!**

Table A6.1.4: Bond angle and bond distance data for compound 2.4

Compound	2.5									
Metal #	**Ligand**	**θ_1**	**θ_2**	**τ5**	**Cu-O1**	**Cu-O2**	**Cu-O3**	**Cu-O4**	**Cu-ligand**	**Cu-ligand2**
Cu1	dmso	n/a	n/a	n/a	1.926	1.94	1.947	1.951	2.313	
Cu2	dmso	n/a	n/a	n/a	2	1.948	1.962	1.97	2.356	
Cu3	dmso	n/a	n/a	n/a	1.949	1.958	1.966	1.972	2.342	
Cu4	dmso, water	n/a	n/a	n/a	1.93	1.933	1.952	1.951	2.492	2.577
Cu5	dmso	n/a	n/a	n/a	1.954	1.944	1.955	1.967	2.29	
Cu6	dmso, water	n/a	n/a	n/a	1.93	1.936	1.958	1.963	2.469	2.649
Cu7		n/a	n/a	n/a						
Cu8		n/a	n/a	n/a						
Average		**#DIV/0!**	**#DIV/0!**	**#DIV/0!**	**1.938**	**1.943**	**1.957**	**1.962**	**2.38**	**2.61**
StD		**#DIV/0!**	**#DIV/0!**	**#DIV/0!**	**0.011**	**0.009**	**0.007**	**0.009**	**0.08**	**0.05**

Table A6.1.5: Bond distance data for compound 2.5

Compound	2.6									
Metal #	**Ligand**	**θ_1**	**θ_2**	**τ5**	**Cu-O1**	**Cu-O2**	**Cu-O3**	**Cu-O4**	**Cu-ligand**	**Cu-ligand2**
Cu1	water	n/a	n/a	n/a	1.945	1.946	1.947	1.948	2.369	
Cu2	water	n/a	n/a	n/a	2	1.949	1.954	1.964	2.41	
Cu3	water, water	n/a	n/a	n/a	1.935	1.943	1.954	1.957	2.496	2.466
Cu4	water, acetone	n/a	n/a	n/a	1.917	1.929	1.932	1.937	2.529	2.507
Cu5		n/a	n/a	n/a						
Cu6		n/a	n/a	n/a						
Cu7		n/a	n/a	n/a						
Cu8		n/a	n/a	n/a						
Average		**#DIV/0!**	**#DIV/0!**	**#DIV/0!**	**1.934**	**1.942**	**1.947**	**1.952**	**2.45**	**2.49**
StD		**#DIV/0!**	**#DIV/0!**	**#DIV/0!**	**0.012**	**0.009**	**0.010**	**0.012**	**0.07**	**0.03**

Table A6.1.6: Bond distance data for compound 2.6

Compound	2.7 published									
Metal #	**Ligand**	**θ_1**	**θ_2**	**τ5**	**Ni-O1**	**Ni-O2**	**Ni-O3**	**Ni-O4**	**Ni-ligand**	**Ni-ligand2**
Ni1	2x pyridine	159.27	110.45	0.813667	2.089	2.089	2.074	2.074	2.101	
Ni2	pyridine	170.34	144.59	0.429167	2.044	2.044	2.063	2.063	2.078	2.231
Ni3	pyridine	178.55	167.55	0.183333	2.009	2.009	2.039	2.039	2.018	
Ni4										
Ni5										
Ni6										
Ni7										
Ni8										
Average		**169.4**	**140.9**	**0.48**	**2.047**	**2.047**	**2.059**	**2.059**	**2.07**	**2.23**
StD		**9.7**	**28.7**	**0.32**	**0.040**	**0.040**	**0.018**	**0.018**	**0.04**	**#DIV/0!**

Table A6.1.7: Bond angle and bond distance data for compound 2.1.7

Compound	2.8a			
Metal #	**Ligand**	**θ_1**	**θ_2**	**τ5**
Ni1	pyridine	168.49	145.6	0.382
Ni2	pyridine	172.57	153.35	0.320
Ni3	pyridine	171.66	152.66	0.317
Ni4	pyridine	170.3	150.65	0.328
Ni5	pyridine	168.21	145.71	0.375
Ni6	pyridine	170.22	151.07	0.319
Ni7	pyridine	174.38	161.31	0.218
Ni8	pyridine	170.22	149.66	0.343
Average		**170.8**	**151.3**	**0.33**
StD		**2.1**	**5.0**	**0.05**

Compoun	2.8b			
Metal #	**Ligand**	**θ_1**	**θ_2**	**τ5**
Ni1	pyridine	169.75	146.86	0.382
Ni2	pyridine	169.32	151.24	0.301
Ni3	pyridine	174.11	154.11	0.333
Ni4	pyridine	170.78	151.95	0.314
Ni5	pyridine	170.76	151	0.329
Ni6	DMSO	167.39	147.57	0.330
Ni7	pyridine	171.82	155.27	0.276
Ni8	pyridine	172.39	153.8	0.310
Average		**170.8**	**151.5**	**0.32**
StD		**2.1**	**3.0**	**0.03**

Table A6.1.8: Bond angle and bond distance data for compound 2.1.8

Compound	2.9									
Metal #	**Ligand**	**θ_1**	**θ_2**	**τ5**	**Ni-O1**	**Ni-O2**	**Ni-O3**	**Ni-O4**	**Ni-ligand**	**Ni-ligand2**
Ni1	pyridine	169.1	147.66	0.357333						
Ni2	pyridine	169.91	151.7	0.3035						
Ni3	pyridine	175.66	157.89	0.296167						
Ni4	pyridine	170.15	148.78	0.356167						
Ni5	pyridine	173.01	148.74	0.4045						
Ni6	pyridine	173.34	150.74	0.376667						
Ni7	pyridine	171.41	149.93	0.358						
Ni8	pyridine	172.22	150.22	0.366667						
Average		**171.9**	**150.7**	**0.35**	**#DIV/0!**	**#DIV/0!**	**#DIV/0!**	**#DIV/0!**	**#DIV/0!**	**#DIV/0!**
StD		**2.2**	**3.2**	**0.04**	**#DIV/0!**	**#DIV/0!**	**#DIV/0!**	**#DIV/0!**	**#DIV/0!**	**#DIV/0!**

Table A6.1.9: Bond angle data for compound 2.1.9

Compound	2.10.									
Metal #	Ligand	θ_1	θ_2	τ5	Ni-O1	Ni-O2	Ni-O3	Ni-O4	Ni-ligand	Ni-ligand2
Ni1	pyridine	170.32	151.3	0.317	2.012	2.014	2.02	2.025	2.015	
Ni2	pyridine	170.68	151.61	0.317833	1.994	2.002	2.011	2.031	2.002	
Ni3	pyridine	170.49	150.1	0.339833	2.006	2.016	2.018	2.021	2.013	
Ni4	DMSO	169.6	147.59	0.366833	2.01	2.011	2.011	2.03	2.017	
Ni5	pyridine	169.61	149.7	0.331833	2.007	2.008	2.014	2.017	1.98	
Ni6	pyridine	168.07	147.67	0.34	2.005	2.022	2.027	2.029	2.007	
Ni7	pyridine	168.57	146.39	0.369667	1.999	2.004	2.024	2.037	2.012	
Ni8	pyridine	169.88	149.97	0.331833	2.014	2.015	2.021	2.023	1.993	
Average		**169.7**	**149.3**	**0.34**	**2.006**	**2.012**	**2.018**	**2.027**	**2.00**	**#DIV/0!**
StD		**0.9**	**1.9**	**0.02**	**0.007**	**0.007**	**0.006**	**0.006**	**0.01**	**#DIV/0!**

Table A6.1.10: Bond angle and bond distance data for compound 2.1.10

Compound	2.11a			
Metal #	Ligand	θ_1	θ_2	τ5
Ni1	pyridine	148.05	168.17	0.335333
Ni2	pyridine	150.53	170.66	0.3355
Ni3	pyridine	148.97	169.72	0.345833
Ni4	pyridine	156.71	175.15	0.307333
Ni5	pyridine	154.1	172.28	0.303
Ni6	pyridine	148.01	167.99	0.333
Ni7	pyridine	144.63	168.04	0.390167
Ni8	pyridine	143.74	167.11	0.3895
Average		**149.3**	**169.9**	**0.34**
StD		**4.4**	**2.7**	**0.03**

Compoun	2.11b			
Metal #	Ligand	θ_1	θ_2	τ5
Ni1	pyridine	151.26	170.26	0.316666667
Ni2	pyridine	146.5	168.56	0.367666667
Ni3	pyridine	146.38	168.49	0.3685
Ni4	pyridine	146.09	167.22	0.352166667
Ni5	pyridine	148.87	168.4	0.3255
Ni6	pyridine	150.06	171.01	0.349166667
Ni7	pyridine	151.49	170.22	0.312166667
Ni8	pyridine	159.04	175.17	0.268833333
Average		**150.0**	**169.9**	**0.33**
StD		**4.3**	**2.5**	**0.03**

Table A6.1.11: Bond angle data for compound 2.1.11

Compound	2.12									
Metal #	Ligand	θ_1	θ_2	τ5	Ni-O1	Ni-O2	Ni-O3	Ni-O4	Ni-ligand	Ni-ligand2
Ni1	2x pyridine	156.12	107.85	0.8045	2.008	2.005	2.022	2.021	2.044	
Ni2	pyridine	170.05	138.28	0.5295	1.989	1.995	2.021	2.038	2.013	
Ni3	pyridine	170.68	144.64	0.434	2.073	2.075	2.09	2.092	2.06	2.142
Ni4	pyridine	171.21	141.02	0.503167	1.959	1.999	2.015	2.055	2.022	
Ni5	2x pyridine	156.57	110.57	0.766667	1.985	1.994	2.036	2.043	1.962	
Ni6	pyridine	166.64	140.93	0.4285	2.002	1.996	2.002	2.017	2.043	
Ni7	pyridine	165.25	144.21	0.350667	2.09	2.1	2.122	2.126	2.03	2.125
Ni8	pyridine	169.84	133.54	0.605	1.964	1.983	1.996	2.007	2.041	
Average		**165.8**	**132.6**	**0.55**	**2.009**	**2.018**	**2.038**	**2.050**	**2.03**	**2.13**
StD		**6.2**	**14.9**	**0.16**	**0.048**	**0.044**	**0.045**	**0.041**	**0.03**	**0.01**

Table A6.1.12: Bond angle and bond distance data for compound 2.1.12

Compound	2.13									
Metal #	**Ligand**	**θ_1**	**θ_2**	**τ5**	**Ni-O1**	**Ni-O2**	**Ni-O3**	**Ni-O4**	**Ni-ligand**	**Ni-ligand2**
Ni1	2x pyridine	156.95	107.2	0.829167	2.018	2.018	2.023	2.023	1.994	
Ni2	pyridine	167.03	134.61	0.540333	2	2.009	2.015	2.044	2.007	
Ni3	pyridine	167.62	146.35	0.3545	1.998	2.011	2.02	2.032	1.986	
Ni4	pyridine	165.98	141.83	0.4025	1.994	2.008	2.025	2.025	2.032	
Ni5	pyridine	165.02	141.21	0.396833	2.081	2.081	2.091	2.091	2.051	2.051
Ni6										
Ni7										
Ni8										
Average		**164.5**	**134.2**	**0.50**	**2.018**	**2.025**	**2.035**	**2.043**	**2.01**	**2.05**
StD		**4.3**	**15.7**	**0.19**	**0.036**	**0.031**	**0.032**	**0.028**	**0.03**	**#DIV/0!**

Table A6.1.13: Bond angle and bond distance data for compound 2.1.13

Compound	2.14	published								
Metal #	**Ligand**	**θ_1**	**θ_2**	**τ5**	**Ni-O1**	**Ni-O2**	**Ni-O3**	**Ni-O4**	**Ni-ligand**	**Ni-ligand2**
Ni1	4-picoline, H2O				2.011	2.02	2.028	2.041	2.048	2.245
Ni2	4-picoline, H2O				2.007	2.02	2.023	2.051	2.118	2.278
Ni3	4-picoline, H2O				2.013	2.021	2.023	2.034	2.095	2.267
Ni4	4-picoline, H2O				1.995	2.024	2.026	2.032	2.066	2.29
Ni5	4-picoline, H2O				2.011	2.018	2.028	2.04	2.043	2.246
Ni6	4-picoline, H2O				2.016	2.019	2.03	2.038	2.1	2.359
Ni7	4-picoline, H2O				1.994	2.022	2.03	2.058	2.114	2.242
Ni8	4-picoline, H2O				2.023	2.025	2.03	2.05	2.163	2.22
Ni9	4-picoline, H2O				2.005	2.01	2.03	2.035	2.06	2.24
Ni10	4-picoline, H2O				1.987	2.001	2.02	2.033	2.085	2.27
Ni11	4-picoline, H2O				1.99	2	2.01	2.041	2.072	2.28
Ni12	4-picoline, H2O				2.013	2.016	2.02	2.048	2.112	2.294
Average		**#DIV/0!**	**#DIV/0!**	**#DIV/0!**	**2.005**	**2.016**	**2.025**	**2.042**	**2.090**	**2.269**
StD		**#DIV/0!**	**#DIV/0!**	**#DIV/0!**	**0.011**	**0.008**	**0.008**	**0.008**	**0.035**	**0.036**

Table A6.1.14: Bond distance data for compound 2.1.14

Compound	2.17 published									
Metal #	Ligand	θ_1	θ_2	τ5	Co-O1	Co-O2	Co-O3	Co-O4	Co-ligand	Co-ligand2
Co1	2x pyridine	156.69	120.33	0.606	2.098	2.098	2.102	2	2.187	2.187
Co2	pyridine	169.37	138.66	0.511833	2.08	2.08	2	2	2.038	
Co3	pyridine	173.2	149.24	0.399333	2.02	2.02	2.058	2.058	2.09	
Co4										
Co5										
Co6										
Co7										
Co8										
Average		**166.4**	**136.1**	**0.51**	**2.066**	**2.066**	**2.053**	**2.053**	**2.11**	**2.19**
StD		**8.6**	**14.6**	**0.10**	**0.041**	**0.041**	**0.051**	**0.051**	**0.08**	**#DIV/0!**

Table A6.1.17: Bond angle and bond distance data for compound 2.1.17

Compound	2.18a			
Metal #	Ligand	θ_1	θ_2	τ5
Ni1	DMSO	169.48	141.19	0.4715
Ni2	DMSO	167.35	135.77	0.526333
Ni3	DMSO	167.72	137.12	0.51
Ni4	DMSO	168.51	140.45	0.467667
Ni5	DMSO	169.41	140.54	0.481167
Ni6	DMSO	170.09	142.56	0.458833
Ni7	pyridine	169.07	143.04	0.433833
Ni8	DMSO	170.67	145.33	0.422333
Average		**169.0**	**140.8**	**0.47**
StD		**1.1**	**3.1**	**0.04**

Compoun	2.18b			
Metal #	Ligand	θ_1	θ_2	τ5
Ni1	DMSO	169.46	139.83	0.493833333
Ni2	DMSO	168.56	139.93	0.477166667
Ni3	DMSO	166.47	136.12	0.505833333
Ni4	DMSO	167.53	137.59	0.499
Ni5	DMSO	168.14	142.1	0.434
Ni6	Pyridine	168.52	144.26	0.404333333
Ni7	pyridine	172.13	147.15	0.416333333
Ni8	pyridine	167.75	141.44	0.4385
Average		**168.6**	**141.1**	**0.46**
StD		**1.7**	**3.5**	**0.04**

Table A6.1.18: Bond angle for compound 2.1.18

Compound	2.19									
Metal #	Ligand	θ_1	θ_2	τ5	Co-O1	Co-O2	Co-O3	Co-O4	Co-ligand	Co-ligand2
Co1	4-picoline	166.13	134.36	0.5295	2	2.02	2.079	2.105	2.039	
Co2	4-picoline	168.18	135.9	0.538	2.019	2.02	2.066	2.102	2.047	
Co3	4-picoline	166.64	136	0.510667	1.993	2.01	2.085	2.094	2.054	
Co4	DMSO	167.46	138.92	0.475667	2.088	2.004	2.028	2.069	1.994	
Co5	4-picoline	168.1	138	0.501667	1.996	2.013	2.091	2.089	2.031	
Co6	DMSO	167.43	137.72	0.495167	2.011	2.025	2.066	2.089	1.963	
Co7	DMSO	168.34	140.65	0.4615	2.004	2.013	2.08	2.103	1.931	
Co8	DMSO	168.18	140.21	0.466167	1.991	2.02	2.061	2.086	2.002	
Average		**167.6**	**137.7**	**0.50**	**2.013**	**2.016**	**2.070**	**2.092**	**2.01**	**#DIV/0!**
StD		**0.8**	**2.2**	**0.03**	**0.032**	**0.007**	**0.020**	**0.012**	**0.04**	**#DIV/0!**

Table A6.1.19: Bond angle and bond distance data for compound 2.1.19

Compound	2.20.									
Metal #	Ligand	θ_1	θ_2	τ5	Co-O1	Co-O2	Co-O3	Co-O4	Co-ligand	Co-ligand2
Co1	nitrate	161.52	126.95	0.576167	2.036	2.036	2.062	2	2.086	2.288
Co2	pyridine	166.98	136.04	0.515667	1.991	1.997	2.081	2.077	2.025	
Co3	nitrate	161.48	130.26	0.520333	2.056	2.075	2.09	2.094	2.186	2.221
Co4	pyridine	165.52	135.69	0.497167	1.992	1.993	2.08	2.088	2.045	
Co5	pyridine	166.72	140.2	0.442	2.026	2.037	2.087	2.027	2.048	
Co6	pyridine	166.68	133.82	0.547667	1.99	1.997	2.109	2.062	2.039	
Co7	pyridine x2	150.66	115.65	0.5835	2.075	2.09	2.131	2.218	2.146	2.17
Co8	pyridine	164.79	132.44	0.539167	1.99	2.032	2.057	2.064	2.032	
Average		**163.0**	**131.4**	**0.53**	**2.020**	**2.032**	**2.087**	**2.097**	**2.08**	**2.23**
StD		**5.5**	**7.5**	**0.05**	**0.034**	**0.036**	**0.024**	**0.059**	**0.06**	**0.06**

Table A6.1.20: Bond angle and bond distance data for compound 2.1.20

Compound	2.21.									
Metal #	Ligand	θ_1	θ_2	τ5	Mn-O1	Mn-O2	Mn-O3	Mn-O4	Mn-ligand	Mn-ligand2
Mn1	4-picoline, int. DMS(	169.94	152.85	0.284833	2.102	2.156	2.102	2.156	2.209	
Mn2	DMSO	162.1	143.46	0.310667	2.091	2.096	2.159	2.161	2.098	
Mn3	DMSO	159.25	137.92	0.3555	2.106	2.111	2.133	2.143	2.091	
Mn4	DMSO/H2O	157.92	136.14	0.363	2.099	2.117	2.13	2.146	2.102	2.082
Mn5	2xDMSO/DMSO, int	159.65	136.89	0.379333	2.11	2.11	2.158	2.158	2.022	2.354
Mn6										
Mn7										
Mn8										
Average		**161.8**	**141.5**	**0.34**	**2.102**	**2.118**	**2.136**	**2.153**	**2.10**	**2.22**
StD		**4.8**	**7.0**	**0.04**	**0.007**	**0.023**	**0.024**	**0.008**	**0.07**	**0.19**

Table A6.1.21: Bond angle and bond distance data for compound 2.1.21

Compound	2.22									
Metal #	Ligand	θ_1	θ_2	τ5	Mn-O1	Mn-O2	Mn-O3	Mn-O4	Mn-ligand	Mn-ligand2
Mn1	DMSO	160.88	140.76	0.335333	2.044	2.071	2.099	2.101	2.071	
Mn2	DMSO	161.54	142.01	0.3255	2.083	2.092	2.085	2.109	2.091	
Mn3	Benzoate	151.1	129.1	0.366667	2.131	2.148	2.161	2.204	2.189	2.28
Mn4	Benzoate	151.29	128.22	0.3845	2.132	2.138	2.155	2.188	2.2	2.23
Mn5	DMSO	160.62	140.21	0.340167	2.093	2.15	2.115	2.127	2.095	
Mn6	DMSO	163.42	145.78	0.294	2.024	2.04	2.057	2.068	2.121	
Mn7	DMSO/H2O	150.74	122.57	0.4695	2.14	2.187	2.223	2.219	2.45	2.44
Mn8	DMSO/H2O	149.48	122.82	0.444333	2.132	2.143	2.219	2.244	2.147	
Average		**156.1**	**133.9**	**0.37**	**2.097**	**2.121**	**2.139**	**2.158**	**2.17**	**2.32**
StD		**5.9**	**9.3**	**0.06**	**0.044**	**0.049**	**0.061**	**0.064**	**0.12**	**0.11**

Table A6.1.22: Bond angle and bond distance data for compound 2.1.22

Compound	PgC3ZnDMSO	published								
Metal #	Ligand	θ_1	θ_2	τ5	Zn-O1	Zn-O2	Zn-O3	Zn-O4	Zn-ligand	Zn-ligand
Zn1	DMSO	163.88	137.51	0.4395	2.033	2.061	2.005	2.064	1.987	
Zn2	DMSO	162.29	137.75	0.409	2.038	2.057	2.055	2.065	1.993	
Zn3	DMSO	162	137.75	0.404167	2.042	2.046	2.058	2.039	2.011	
Zn4	DMSO	163.19	136.25	0.449	2.043	2.059	2.041	2.049	2.011	
Zn5	DMSO	161.99	139.72	0.371167	2.036	2.061	2.04	2.038	1.999	
Zn6	DMSO	162.41	135.15	0.454333	2.041	2.078	2.039	2.052	1.962	
Zn7	DMSO	162.03	136.87	0.419333	2.042	2.046	2.03	2.063	1.997	
Zn8	DMSO	162.2	138.86	0.389	2.036	2.084	2.032	2.043	2	
Average		**162.5**	**137.5**	**0.42**	**2.039**	**2.062**	**2.038**	**2.052**	**2.00**	**#DIV/0!**
StD		**0.7**	**1.4**	**0.03**	**0.004**	**0.014**	**0.016**	**0.011**	**0.02**	**#DIV/0!**

Table A6.1.23: Bond angle and bond distance data for published PgC3Zn-DMSO dimer

Compound	PgC3ZnPyridine	published								
Metal #	Ligand	θ_1	θ_2	τ5	Zn-O1	Zn-O2	Zn-O3	Zn-O4	Zn-ligand	Zn-ligand
Zn1	Pyridine				2.046	2.053	2.049	2.052	2.056	
Zn2	Pyridine				2.065	2.037	2.061	2.039	2.052	
Zn3	Pyridine				2.071	2.042	2.059	2.04	2.026	
Zn4	Pyridine				2.045	2.054	2.055	2.044	2.022	
Zn5	Pyridine				2.034	2.05	2.045	2.062	2.05	
Zn6	Pyridine				2.042	2.057	2.041	2.053	2.039	
Zn7	Pyridine				2.053	2.061	2.039	2.063	2.05	
Zn8	Pyridine				2.049	2.063	2.062	2.045	2.036	
Average		**#DIV/0!**	**#DIV/0!**	**#DIV/0!**	**2.051**	**2.052**	**2.051**	**2.050**	**2.04**	**#DIV/0!**
StD		**#DIV/0!**	**#DIV/0!**	**#DIV/0!**	**0.012**	**0.009**	**0.009**	**0.009**	**0.01**	**#DIV/0!**

Table A6.1.24: Bond distance data for published PgC3Zn-pyridine dimer

Compound	Published PgC3Cu									
Metal #	Ligand	θ_1	θ_2	τ5	Cu-O1	Cu-O2	Cu-O3	Cu-O4	Cu-ligand	Cu-ligand2
Cu1	water				1.963	1.967	1.971	2.005	2.774	
Cu2	water				1.914	1.93	1.97	2.007		
Cu3	water				1.917	1.933	1.94	1.959	2.762	
Cu4	water				1.926	1.962	1.974	1.96	3.116	
Cu5	water				1.888	1.894	1.924	1.948	2.75	2.548
Cu6	water				1.972	1.978	1.988	1.924	2.679	
Cu7	water				1.921	1.93	1.954	1.958	2.945	3.016
Cu8	water				1.929	1.939	1.94	1.947	2.785	
Cu9	water				1.888	1.94	1.949	1.966	3.146	
Cu10	water				1.945	1.964	1.948	1.979	3.08	
Cu11	water				1.904	1.913	1.952	1.97	2.848	2.619
Cu12	water				1.952	1.973	1.886	1.972	2.866	
Average		**#DIV/0!**	**#DIV/0!**	**#DIV/0!**	**1.927**	**1.944**	**1.950**	**1.966**	**2.886**	**2.728**
StD		**#DIV/0!**	**#DIV/0!**	**#DIV/0!**	**0.027**	**0.026**	**0.027**	**0.023**	**0.162**	**0.252**

Table A6.1.25: Bond distance data for published PgC3Cu hexamer

Compound	4.1 published									
Metal #	Ligand	θ_1	θ_2	τ5	Cu-O1	Cu-O2	Cu-O3	Cu-O4	Cu-ligand	Cu-ligand2
Cu1	4,4'-bpy (l)	169.93	148.94	0.349833						n/a
Cu2	DMSO	170.18	151.12	0.317667						n/a
Cu3	DMSO	171.42	152.14	0.321333						n/a
Cu4	4,4'-bpy (l)	169.04	147.84	0.353333						n/a
Cu5	4,4'-bpy (l)	169.24	149.48	0.329333						n/a
Cu6	DMSO	172.55	153.32	0.3205						n/a
Cu7	4,4'-bpy (u)	172.82	152.53	0.338167						n/a
Cu8	4,4'-bpy (l)	171.19	151.45	0.329						n/a
Average		**170.8**	**150.9**	**0.33**	**#DIV/0!**	**#DIV/0!**	**#DIV/0!**	**#DIV/0!**	**#DIV/0!**	**#DIV/0!**
StD		**1.4**	**1.9**	**0.01**	**#DIV/0!**	**#DIV/0!**	**#DIV/0!**	**#DIV/0!**	**#DIV/0!**	**#DIV/0!**

Table A6.1.26: Bond angle data for compound 4.1

Compound	4.2									
Metal #	Ligand	θ_1	θ_2	τ5	Cu-O1	Cu-O2	Cu-O3	Cu-O4	Cu-ligand	Cu-ligand2
Cu1	4,4'-bpy	170.34	165.51	0.0805						n/a
Cu2	4,4'-bpy	169.6	149.81	0.329833						n/a
Cu3	4,4'-bpy	176.36	151.71	0.410833						n/a
Cu4	4,4'-bpy	156.74	138.08	0.311						n/a
Cu5										n/a
Cu6										n/a
Cu7										n/a
Cu8										n/a
Average		**168.3**	**151.3**	**0.28**	**#DIV/0!**	**#DIV/0!**	**#DIV/0!**	**#DIV/0!**	**#DIV/0!**	**#DIV/0!**
StD		**8.3**	**11.2**	**0.14**	**#DIV/0!**	**#DIV/0!**	**#DIV/0!**	**#DIV/0!**	**#DIV/0!**	**#DIV/0!**

Table A6.1.27: Bond angle data for compound 4.2

Compound	4.3 published									
Metal #	**Ligand**	**θ_1**	**θ_2**	**τ5**	**Zn-O1**	**Zn-O2**	**Zn-O3**	**Zn-O4**	**Zn-ligand**	**Zn-ligand**
Zn1	4,4'-bpy	170.15	148.21	0.365667	2.03	2.03				
Zn2	4,4'-bpy	165.76	138.77	0.449833	2.013	2				
Zn3	2x 4,4'-bpy	155.83	120.66	0.586167	2.109	2.109				
Zn4										
Zn5										
Zn6										
Zn7										
Zn8										
Average		**163.9**	**135.9**	**0.47**	**2.051**	**2.046**	**#DIV/0!**	**#DIV/0!**	**#DIV/0!**	**#DIV/0!**
StD		**7.3**	**14.0**	**0.11**	**0.051**	**0.056**	**#DIV/0!**	**#DIV/0!**	**#DIV/0!**	**#DIV/0!**

Table A6.1.27: Bond angle data for compound 4.3

Compound	4.4									
Metal #	**Ligand**	**θ_1**	**θ_2**	**τ5**	**Zn-O1**	**Zn-O2**	**Zn-O3**	**Zn-O4**	**Zn-ligand**	**Zn-ligand**
Zn1	bpy	165.6	141.34	0.404333						
Zn2	bpy	163.49	134.17	0.488667						
Zn3	2xbpy	152.48	116.72	0.596						
Zn4	bpy	163.73	135.08	0.4775						
Zn5	bpy	164.72	139.35	0.422833						
Zn6										
Zn7										
Zn8										
Average		**162.0**	**133.3**	**0.48**	**#DIV/0!**	**#DIV/0!**	**#DIV/0!**	**#DIV/0!**	**#DIV/0!**	**#DIV/0!**
StD		**5.4**	**9.7**	**0.08**	**#DIV/0!**	**#DIV/0!**	**#DIV/0!**	**#DIV/0!**	**#DIV/0!**	**#DIV/0!**

Table A6.1.28: Bond angle data for compound 4.4

Compound	4.7									
Metal #	**Ligand**	**θ_1**	**θ_2**	**τ5**	**Cu-O1**	**Cu-O2**	**Cu-O3**	**Cu-O4**	**Cu-ligand**	**Cu-ligand2**
Cu1	adj dimer	177.89	156.93	0.35						n/a
Cu2	water	173.91	153.81	0.34						n/a
Cu3	pyridine	170.96	150.26	0.35						n/a
Cu4	methanol	173.49	151.73	0.36						n/a
Cu5										n/a
Cu6										n/a
Cu7										n/a
Cu8										n/a
Average		**174.1**	**153.2**	**0.35**	**#DIV/0!**	**#DIV/0!**	**#DIV/0!**	**#DIV/0!**	**#DIV/0!**	**#DIV/0!**
StD		**2.9**	**2.9**	**0.01**	**#DIV/0!**	**#DIV/0!**	**#DIV/0!**	**#DIV/0!**	**#DIV/0!**	**#DIV/0!**

Table A6.1.29: Bond angle data for compound 4.7

Compound	4.8									
Metal #	**Ligand**	**θ_1**	**θ_2**	**τ5**	**Cu-O1**	**Cu-O2**	**Cu-O3**	**Cu-O4**	**Cu-ligand**	**Cu-ligand2**
Cu1	pyridine	168.81	147.1	0.36						n/a
Cu2	pyridine	168.48	147.13	0.36						n/a
Cu3	adj dimer	177.61	156.64	0.35						n/a
Cu4	n/a	169.88	169.38	0.01						n/a
Cu5	methanol	174.41	152.47	0.37						n/a
Cu6	methanol	172.45	151.07	0.36						n/a
Cu7	adj dimer	177.1	154.73	0.37						n/a
Cu8	water	169.3	145.02	0.40						n/a
Average		**172.3**	**152.9**	**0.32**	**#DIV/0!**	**#DIV/0!**	**#DIV/0!**	**#DIV/0!**	**#DIV/0!**	**#DIV/0!**
StD		**3.7**	**7.8**	**0.13**	**#DIV/0!**	**#DIV/0!**	**#DIV/0!**	**#DIV/0!**	**#DIV/0!**	**#DIV/0!**

Table A6.1.30: Bond angle data for compound 4.8

Compound	4.9									
Metal #	**Ligand**	**θ_1**	**θ_2**	**τ5**	**Cu-O1**	**Cu-O2**	**Cu-O3**	**Cu-O4**	**Cu-ligand**	**Cu-ligand2**
Cu1	n/a	171.88	168	0.06						n/a
Cu2	pyridine	171.55	151.72	0.33						n/a
Cu3	water	170.7	149.17	0.36						n/a
Cu4	adj dimer	176.03	155.94	0.33						n/a
Cu5	pyridine	167.65	145.26	0.37						n/a
Cu6	pyridine	166.87	144.25	0.38						n/a
Cu7	acetone	175.35	155.37	0.33						n/a
Cu8	adj dimer	176.91	156.27	0.34						n/a
Average		**172.1**	**153.2**	**0.31**	**#DIV/0!**	**#DIV/0!**	**#DIV/0!**	**#DIV/0!**	**#DIV/0!**	**#DIV/0!**
StD		**3.8**	**7.6**	**0.10**	**#DIV/0!**	**#DIV/0!**	**#DIV/0!**	**#DIV/0!**	**#DIV/0!**	**#DIV/0!**

Table A6.1.31: Bond angle data for compound 4.9

A6.2: Supplementary data for chapter 3

This data includes SANS values in various stages of processing that was required to create the graphs seen in chapter 3

S.No.	Method	Sample	Sqrt(χ^2/N)	Volume fraction Dimer	Volume fraction hexamer
	Pyridine to metal-Pg solution				
0 day	Synthesis at -40°C; Hold at RT; Measure at RT	PgC9 Ni: MeOH-d4	1.12	4.96E-04	3.18E-04
0 day	Synthesis at RT;Hold at RT;Measure at RT	PgC9 Ni: MeOH-d4	1.4	9.16E-04	3.16E-04
0 day	Synthesis at 50°C; Hold at RT; Measure at RT	PgC9 Ni: MeOH-d4	1.03	1.25E-03	7.64E-05
3 day	Synthesis at -40°C; Hold at RT; Measure at RT	PgC9 Ni: MeOH-d4	1.84	3.63E-03	0.00E+00
3 day	Synthesis at RT;Hold at RT;Measure at RT	PgC9 Ni: MeOH-d4	1.22	2.26E-03	1.84E-04
2 day	Synthesis at 50°C; Hold at RT; Measure at RT	PgC9 Ni: MeOH-d4	1.18	1.66E-03	4.15E-04
0 day	Synthesis at -40°C; Hold at RT; Measure at RT	PgC9 Ni: Ace-d6	1.49	1.15E-03	1.07E-03
0 day	Synthesis at RT;Hold at RT;Measure at RT	PgC9 Ni: Ace-d6	1.19	1.92E-03	7.08E-04
0 day	Synthesis at 50°C; Hold at RT; Measure at RT	PgC9 Ni: Ace-d6	1.46	2.00E-03	7.09E-04
3 day	Synthesis at -40°C; Hold at RT; Measure at RT	PgC9 Ni: Ace-d6	1.37	2.15E-03	4.40E-04
3 day	Synthesis at RT;Hold at RT;Measure at RT	PgC9 Ni: Ace-d6	1.29	2.00E-03	4.52E-04
3 day	Synthesis at 50°C; Hold at RT; Measure at RT	PgC9 Ni: Ace-d6	1.6	2.15E-03	8.51E-04
0 day	Synthesis at -40°C; Hold at RT; Measure at RT	PgC9 Cu: Ace-d6	1.39	4.49E-04	1.32E-03
0 day	Synthesis at RT;Hold at RT;Measure at RT	PgC9 Cu: Ace-d6	1.53	1.29E-03	6.66E-04
0 day	Synthesis at 50°C; Hold at RT; Measure at RT	PgC9 Cu: Ace-d6	1.2	1.81E-03	6.20E-04
3 day	Synthesis at -40°C; Hold at RT; Measure at RT	PgC9 Cu: Ace-d6	1.28	1.79E-03	4.50E-04
3 day	Synthesis at RT;Hold at RT;Measure at RT	PgC9 Cu: Ace-d6	1.53	1.80E-03	7.57E-04
3 day	Synthesis at 50°C; Hold at RT; Measure at RT	PgC9 Cu: Ace-d6	1.29	1.90E-03	7.44E-04
3 day	Synthesis at RT; Hold at RT; Measure at -20°C	PgC9 Ni: MeOH-d4	1.42	3.55E-03	0.00E+00
3 day	Synthesis at RT;Hold at RT;Measure at RT	PgC9 Ni: MeOH-d4	1.22	2.26E-03	1.84E-04
3 day	Synthesis at RT; Hold at RT; Measure at 50°C	PgC9 Ni: MeOH-d4	1.3	2.43E-03	2.90E-04
3 day	Synthesis at -40°C RT; Hold at -40°C ; Measure at -20 °C	PgC9 Ni: MeOH-d4	2.15	5.37E-03	0.00E+00
3 day	Synthesis at RT;Hold at RT;Measure at RT	PgC9 Ni: MeOH-d4	1.22	2.26E-03	1.84E-04
3 day	Synthesis at 50°C; Hold at 50°C ; Measure at 50°C	PgC9 Ni: MeOH-d4	1.29	2.38E-03	2.62E-04

Table A6.2.1: Raw volume fraction data provided by Dr. Harshita Kumari to the author (Andy Mossine)

MeasDay	Pyridine to metal-Pg solution	Di corr	Hex corr	PgC Di corr	PgC Hex corr
		1317.05	3942.34	2.00	6.00
0 day	Synthesis at -40°C; Hold at RT; Measure at RT	3.77E-07	8.07E-08	7.53E-07	4.84E-07
0 day	Synthesis at RT; Hold at RT; Measure at RT	6.95E-07	8.02E-08	1.39E-06	4.81E-07
0 day	Synthesis at 50°C; Hold at RT; Measure at RT	9.49E-07	1.94E-08	1.90E-06	1.16E-07
3 day	Synthesis at -40°C; Hold at RT; Measure at RT	2.76E-06	0.00E+00	5.51E-06	0.00E+00
3 day	Synthesis at RT; Hold at RT; Measure at RT	1.72E-06	4.67E-08	3.43E-06	2.80E-07
2 day	Synthesis at 50°C; Hold at RT; Measure at RT	1.26E-06	1.05E-07	2.52E-06	6.32E-07
0 day	Synthesis at -40°C; Hold at RT; Measure at RT	8.73E-07	2.71E-07	1.75E-06	1.63E-06
0 day	Synthesis at RT; Hold at RT; Measure at RT	1.46E-06	1.80E-07	2.92E-06	1.08E-06
0 day	Synthesis at 50°C; Hold at RT; Measure at RT	1.52E-06	1.80E-07	3.04E-06	1.08E-06
3 day	Synthesis at -40°C; Hold at RT; Measure at RT	1.63E-06	1.12E-07	3.26E-06	6.70E-07
3 day	Synthesis at RT; Hold at RT; Measure at RT	1.52E-06	1.15E-07	3.04E-06	6.88E-07
3 day	Synthesis at 50°C; Hold at RT; Measure at RT	1.63E-06	2.16E-07	3.26E-06	1.30E-06
0 day	Synthesis at -40°C; Hold at RT; Measure at RT	3.41E-07	3.35E-07	6.82E-07	2.01E-06
0 day	Synthesis at RT; Hold at RT; Measure at RT	9.79E-07	1.69E-07	1.96E-06	1.01E-06
0 day	Synthesis at 50°C; Hold at RT; Measure at RT	1.37E-06	1.57E-07	2.75E-06	9.44E-07
3 day	Synthesis at -40°C; Hold at RT; Measure at RT	1.36E-06	1.14E-07	2.72E-06	6.85E-07
3 day	Synthesis at RT; Hold at RT; Measure at RT	1.37E-06	1.92E-07	2.73E-06	1.15E-06
3 day	Synthesis at 50°C; Hold at RT; Measure at RT	1.44E-06	1.89E-07	2.89E-06	1.13E-06
3 day	Synthesis at RT; Hold at RT; Measure at -20°C	2.70E-06	0.00E+00	5.39E-06	0.00E+00
3 day	Synthesis at RT; Hold at RT; Measure at RT	1.72E-06	4.67E-08	3.43E-06	2.80E-07
3 day	Synthesis at RT; Hold at RT; Measure at 50°C	1.85E-06	7.36E-08	3.69E-06	4.41E-07
3 day	Synthesis at -40°C RT; Hold at -40°C ; Measure at -20 °C	4.08E-06	0.00E+00	8.15E-06	0.00E+00
3 day	Synthesis at RT; Hold at RT; Measure at RT	1.72E-06	4.67E-08	3.43E-06	2.80E-07
3 day	Synthesis at 50°C; Hold at 50°C ; Measure at 50°C	1.81E-06	6.65E-08	3.61E-06	3.99E-07

Table A6.2.2: Raw data corrected for the volume and PgC abundance for the dimer and hexamer

Temperature program:			**T, RT, RT**			
Metal	Solvent	Time (days)	Temperature (°C)	Dimer frac.	Hexamer frac.	MONC yield
Ni	MeOH	0	-40	0.54	0.35	0.89
Ni	MeOH	0	23	1	0.35	1.35
Ni	MeOH	0	50	1.36	0.08	1.44
Ni	MeOH	3	-40	3.96	0	3.96
Ni	MeOH	3	23	2.47	0.2	2.67
Ni	MeOH	2	50	1.81	0.45	2.26
Ni	Ace	0	-40	1.26	1.17	2.43
Ni	Ace	0	23	2.1	0.77	2.87
Ni	Ace	0	50	2.18	0.78	2.96
Ni	Ace	3	-40	2.35	0.48	2.83
Ni	Ace	3	23	2.18	0.49	2.67
Ni	Ace	3	50	2.35	0.93	3.28
Cu	Ace	0	-40	0.49	1.44	1.93
Cu	Ace	0	23	1.41	0.73	2.14
Cu	Ace	0	50	1.98	0.68	2.66
Cu	Ace	3	-40	1.95	0.49	2.44
Cu	Ace	3	23	1.97	0.83	2.8
Cu	Ace	3	50	2.07	0.81	2.88
Temperature program:			**RT, RT, T**			
Metal	Solvent	Time (days)	Temperature (°C)	Dimer frac.	Hexamer frac.	MONC yield
Ni	**MeOH**	**0**	**23**	**1**	**0.35**	**1.35**
Ni	MeOH	3	-40	3.88	0	3.88
Ni	**MeOH**	**3**	**23**	**2.47**	**0.2**	**2.67**
Ni	MeOH	3	50	2.65	0.32	2.97
Temperature program:			**T, T, T**			
Metal	Solvent	Time (days)	Temperature (°C)	Dimer frac.	Hexamer frac.	MONC yield
Ni	**MeOH**	**0**	**-40**	**0.54**	**0.35**	**0.89**
Ni	**MeOH**	**0**	**23**	**1**	**0.35**	**1.35**
Ni	**MeOH**	**0**	**50**	**1.36**	**0.08**	**1.44**
Ni	MeOH	3	-40	5.86	0	5.86
Ni	**MeOH**	**3**	**23**	**2.47**	**0.2**	**2.67**
Ni	MeOH	3	50	2.6	0.29	2.89

Table A6.2.3: Normalized results from experiment 3.3 that were used in the creation of the graphs in that section.

Yellow denotes the standard value for normalization.

A6.3 Supplementary data for chapter 5

The tables in this section include the raw data from the experiments that are discussed in chapter 5. Some of this data is decay-corrected; if this is the case, it is noted at the top of the table.

Solubility experiment									
H2O Uncorrected Counts			BKG: 24	Date: 12/14/2010	Time: 17:40				
	Initial (6sec)	Supernatant removal (6 sec)	wash 1 (60 sec)	final (6 sec)	sol. material (60 sec)	1000µL added, 500µL counted			StD
PgC1	4924	2590	1651	1115	84				9.165151
PgC2	3913	2051	2451	**1281**	**641**				25.31798
PgC3	4231	2363	3854	**1215**	**200**				14.14214
PgC4	3964	2118	7252	1057	216				14.69694
MeOH Uncorrected Counts			BKG: 24	Date: 12/14/2010	Time: 19:00				
	Initial (6sec)	Supernatant removal (6 sec)	wash 1 (60 sec)	final (6 sec)	sol. material (60 sec)	1000µL added, 500µL counted			StD
PgC1	4077	2684	1946	1114	85				9.219544
PgC2	4177	2295	5673	**974**	**384**				19.59592
PgC3	3919	2151	6701	956	119				10.90871
PgC4	3870	1997	7227	1061	115				10.72381
IsoOH Uncorrected Counts			BKG: 24	Date: 12/14/2010	Time: 20:00				
	Initial (6sec)	Supernatant removal (6 sec)	wash 1 (60 sec)	final (6 sec)	sol. material (12 sec)	1000µL added, 500µL counted			StD
PgC1	3907	2383	4415	892	598				24.45404
PgC2	3911	2264	4726	**1061**	**837**				28.93095
PgC3	3992	1781	10069	**1120**	**493**				22.2036
PgC4	4082	1918	8786	**1243**	**789**				28.08914
EtOH Uncorrected Counts			BKG: 24	Date: 12/14/2010	Time: 21:00				
	Initial (6sec)	Supernatant removal (6 sec)	wash 1 (60 sec)	final (6 sec)	sol. material (12 sec)	1000µL added, 500µL counted			StD
PgC1	3794	2485	1187	1595	21				4.582576
PgC2	3670	2478	768	**1134**	**760**				27.5681
PgC3	3776	2437	719	**1823**	**303**				17.4069
PgC4	3935	2491	732	**1649**	**428**				20.68816
Brine Uncorrected Counts			BKG: 23	Date: 12/15/2010	Time: 16:45	all were darker color than usual			
	Initial (6sec)	Supernatant removal (6 sec)	wash 1 (60 sec)	final (6 sec)	sol. material (60 sec)	1000µL added, 500µL counted			StD
PgC1	18934	13228	3658	**4133**	**1636**				40.4475
PgC2	17850	12221	3020	**4403**	**1030**				32.09361
PgC3	18323	12034	3129	4799	1593				39.9124
PgC4	21217	14265	3743	5097	1203				34.68429
Hexane Uncorrected Counts			BKG: 23	Date: 12/15/2010	Time: 17:45				
	Initial (6sec)	Supernatant removal (6 sec)	wash 1 (60 sec)	final (6 sec)	sol. material (6 sec)	1000µL added, 500µL counted			StD
PgC1	15557	11413	3025	4036	81				9
PgC2	14896	11188	2906	**2788**	**1706**				41.30375
PgC3	13681	10086	2906	4496	365				19.10497
PgC4	15674	11409	2991	4343	462				21.49419
MeCN Uncorrected Counts			BKG: 23	Date: 12/15/2010	Time: 18:30	all were darker color than usual			
	Initial (6sec)	Supernatant removal (6 sec)	wash 1 (60 sec)	final (6 sec)	sol. material (6 sec)	1000µL added, 500µL counted			StD
PgC1	15093	10980	2960	**3514**	**497**				22.2935
PgC2	15297	10760	2716	**3354**	**1146**				33.85262
PgC3	15382	10733	2878	2902	1682				41.01219
PgC4	16008	11265	2656	3734	985				31.38471
EtOAc Uncorrected Counts			BKG: 23	Date: 12/15/2010	Time: 19:15				
	Initial (6sec)	Supernatant removal (6 sec)	wash 1 (60 sec)	final (6 sec)	sol. material (6 sec)	1000µL added, 500µL counted			StD
PgC1	13078	9589	1995	1973	1626				40.32369
PgC2	14135	9952	2754	2231	1769				42.05948
PgC3	14382	9712	2726	2373	1955	**all dissolved**			44.21538
PgC4	15190	10277	2781	2453	1967	**all dissolved**			44.35087
Acetone Uncorrected Counts			BKG: 23	Date: 12/15/2010	Time: 20:00				
	Initial (6sec)	Supernatant removal (6 sec)	wash 1 (60 sec)	final (6 sec)	sol. material (6 sec)	250µL added, 125µL counted			StD
PgC1	13856	10203	2751	**2994**	**726**				26.94439
PgC2	14205	10168	2299	3553	586				24.20744
PgC3	14213	9999	2833	4058	227				15.06652
PgC4	14586	10232	2958	3789	288				16.97056

Table A6.3.1: Uncorrected counts from 5.3.1

	% of counts in 100µL soln								
	H2O	MeOH	IsoOH	EtOH	Brine	Hexane	MeCN	EtOAc	Acetone
PgC1	0.11%	0.11%	8.0%	0.20%	0.75%	0.38%	2.5%	9.0%	15.6%
PgC2	0.92%	0.71%	8.8%	8.0%	0.45%	7.6%	5.1%	8.8%	11.3%
PgC3	0.29%	0.20%	6.1%	2.8%	0.63%	1.49%	7.3%	9.0%	4.2%
PgC4	0.36%	0.17%	7.8%	4.09%	0.45%	1.92%	4.2%	8.9%	5.6%
	% of counts in 100µL soln (StD)								
	H2O	MeOH	IsoOH	EtOH	Brine	Hexane	MeCN	EtOAc	Acetone
PgC1	0.01%	0.01%	0.3%	0.04%	0.02%	0.04%	0.1%	0.2%	0.6%
PgC2	0.04%	0.04%	0.3%	0.3%	0.01%	0.2%	0.2%	0.2%	0.5%
PgC3	0.02%	0.02%	0.3%	0.2%	0.02%	0.08%	0.2%	0.2%	0.3%
PgC4	0.02%	0.02%	0.3%	0.20%	0.01%	0.09%	0.1%	0.2%	0.3%

Table A6.3.2: Data for experiment 5.3.1 (solubility as % of counts in 100µL of solution)

	Raw Data			
3/16-17/2012	PgC4		12s	
	80 (typical from 42H stab 1)	160 (6s) , 3/16	240 (12s), 3/17	320 (12s), 3/17
Initial	46330	9917	11357	14560
Final	13829	2642	2214	2403
Theoretical yield (4x)	46330	4959	3786	3640
% yield	29.85%	53.28%	58.48%	66.02%
	Background Correction, modeling			
3/16-17/2012	PgC4		12s	
	80 (typical from 42H stab 1)	160 (6s) , 3/16	240 (12s), 3/17	320 (12s), 3/17
Initial	46326.9	9913.8	11350.8	14553.8
Final	13827.1	2638.8	2207.8	2396.8
Theoretical yield (4x)	46326.9	4956.9	3783.6	3638.45
% yield	30%	53%	58%	66%
	Background Correction, modeling (±)			
3/16-17/2012	PgC4		12s	
	80 (typical from 42H stab 1)	160 (6s) , 3/16	240 (12s), 3/17	320 (12s), 3/17
Initial	215.2368463	99.56806717	106.5401333	120.6391313
Final	117.5886899	51.3692515	46.98723231	48.9571241
Theoretical yield (4x)	215.2368463	49.78403359	35.51337776	30.15978282
% yield	1%	2%	2%	2%

Table A6.3.3: PgC4-Cu yields from 5.2.1

	Raw Data			
17-Mar	RsC4	12s		
	80	160	240	320
Initial	3692	7069	10967	14091
Final	540	700	661	508
One more wash	522	533	439	342
Coppers per RsC	0.57	0.60	0.48	0.39
	Background Correction, modeling			
17-Mar	RsC4	12s		
	80	160	240	320
Initial	3685.8	7062.8	10960.8	14084.8
Final	533.8	693.8	654.8	501.8
One more wash	515.8	526.8	432.8	335.8
Coppers per RsC	0.56	0.60	0.47	0.38
	Background Correction, modeling (±)			
17-Mar	RsC4	12s		
	80	160	240	320
Initial	60.71078982	84.04046644	104.6938394	118.6794001
Final	23.10411219	26.34008352	25.58906016	22.40089284
One more wash	22.7112307	22.95212408	20.8038458	18.32484652
Coppers per RsC	0.03	0.03	0.02	0.02

Table A6.3.4: RsC data from 5.2.2

Yield Data For PgC1						
Initial (6sec)	First Removal (6 sec)	H2O rinse (60 sec)	Remaining (6 sec)	sol. material (60 sec)	% yield	As volume of Cu soln (uL)
49216	25876	1627	11126	60	0.227284	18.18270481
40746	26816	1922	11116	61	0.274309	21.94473077
39046	23806	4391	4436	2966	0.189571	15.16570199
37916	24826	1163	7951	81	0.211837	16.94693533
189317	132257	3635	41307	1613	0.22671	18.13677588
155547	114107	3002	40337	787	0.264383	21.150649
150907	10957	2937	35117	4947	0.265488	21.23904126
130757	95867	1972	19707	16237	0.274892	21.99132742
138537	102007	2728	29917	7237	0.268188	21.45506255
				Ave	0.24	20
				±	0.03	3
Yield Data For PgC2						
Initial (6sec)	First Removal (6 sec)	H2O rinse (60 sec)	Remaining (6 sec)	sol. material (60 sec)	% yield	As volume of Cu soln (uL)
39106	20486	2427	12786	617	0.342735	27.41881041
41746	22926	5649	9716	360	0.241364	19.30915537
39086	22616	4702	5281	4161	0.24157	19.32558973
36676	24756	744	5646	3776	0.256898	20.55185953
178477	122187	2997	44007	1007	0.252212	20.17694157
148937	111857	2883	27857	17037	0.301429	24.11435708
152947	10737	2693	33517	11437	0.293919	23.51350468
141327	99497	2731	22287	17667	0.282706	22.61648517
142027	101657	2276	35507	5837	0.2911	23.28796637
				Ave	0.28	22
				±	0.03	3
Yield Data For PgC3						
Initial (6sec)	First Removal (6 sec)	H2O rinse (60 sec)	Remaining (6 sec)	sol. material (60 sec)	% yield	As volume of Cu soln (uL)
42286	23606	3830	12126	176	0.290924	23.2738968
39166	21486	6677	9536	95	0.245902	19.67216463
39896	17786	10045	5576	2441	0.200947	16.07579707
37736	24346	695	9091	1491	0.280422	22.43375026
183207	120317	3106	47967	1570	0.270388	21.63105122
136787	100837	2883	44937	3627	0.355034	28.40269909
153797	10710	2855	28997	16797	0.297756	23.82049065
143797	97097	2703	23707	19527	0.30066	24.05279665
142107	99967	2810	40557	2247	0.30121	24.09677215
				Ave	0.28	23
				±	0.04	3
Yield Data For PgC4						
Initial (6sec)	First Removal (6 sec)	H2O rinse (60 sec)	Remaining (6 sec)	sol. material (60 sec)	% yield	As volume of Cu soln (uL)
39616	21156	7228	10546	192	0.271052	21.68416801
38676	19946	7203	10586	91	0.276063	22.08501396
40796	19156	8762	6191	3921	0.247867	19.82939504
39326	24886	708	8221	2116	0.262854	21.02832732
212147	142627	3720	50947	1180	0.245712	19.65693599
156717	114067	2968	43407	4597	0.30631	24.50480803
160057	11242	2633	37317	9827	0.294545	23.56360547
151877	102747	2758	24507	19647	0.290722	23.2577678
145837	102297	2935	37867	2857	0.279243	22.33946118
				Ave	0.27	22
				±	0.02	2

Table A6.3.5: Yield Data collected from 5.3.1

Background correction							Data Modeling			
	3 hour 6s counts	Synthesis	Final				3 hour 6s counts	Synthesis	Final	
	Stability	(3/13)	(3/13)				Stability	(3/13)	(3/13)	
	1	2	3	4			1	2	3	4
Initial (t=0)	6642	6946	6649	7196		Yield	3.73%	3.94%	-6.54%	0.78%
Pre Cu removal (t=0)	248	274	-435	56		Total precipitate	3065	3131	2729	3017
Initial (t=t)	3212	3046	2900	2946		Total supernatant	0	-12	268	56
rest of samp (t=t)	3065	3125	2863	3045		% counts lost	0.00%	-0.38%	9.82%	1.86%
1mL ali (t=t)	0	-6	134	28		SD	#DIV/0!	0.2%	0.8%	0.4%
SD	0	2	12	5						
	6 hour 6s counts	Synthesis	Final				6 hour 6s counts	Synthesis	Final	
	Stability	(3/14)	(3/14)				Stability	(3/14)	(3/14)	
	1	2	3	4			1	2	3	4
Initial (t=0)	17709	18903	18637	18474		Yield	32.33%	31.69%	25.38%	32.88%
Pre Cu removal (t=0)	5725	5990	4730	6074		Total precipitate	4451	4637	4216	4635
Initial (t=t)	4551	4598	4563	4727		Total supernatant	-20	-2	354	28
rest of samp (t=t)	4441	4636	4393	4649		% counts lost	-0.45%	-0.04%	8.40%	0.60%
1mL ali (t=t)	-10	-1	177	14		SD	0.1%	0.0%	0.6%	0.2%
SD	3	1	13	4						
	12 hour 6s counts	Synthesis	Final				12 hour 6s counts	Synthesis	Final	
	Stability	(3/14)	(3/14)				Stability	(3/14)	(3/14)	
	1	2	3	4			1	2	3	4
Initial (t=0)	19108	19095	19169	18568		Yield	31.67%	32.61%	26.15%	32.60%
Pre Cu removal (t=0)	6051	6226	5012	6054		Total precipitate	3634	3441	2921	3391
Initial (t=t)	3420	3575	3142	3424		Total supernatant	-16	18	542	32
rest of samp (t=t)	3626	3450	3192	3407		% counts lost	-0.44%	0.52%	18.56%	0.94%
1mL ali (t=t)	-8	9	271	16		SD	0.2%	0.2%	1.1%	0.2%
SD	3	3	16	4						
	18 hour 6s counts	Synthesis	Final				18 hour 6s counts	Synthesis	Final	
	Stability	(3/13)	(3/14)				Stability	(3/13)	(3/14)	
	1	2	3	4			1	2	3	4
Initial (t=0)	6947	6826	6842	7039		Yield	2.09%	3.44%	-10.08%	1.69%
Pre Cu removal (t=0)	145	235	-690	119		Total precipitate	1358	1368	1128	1216
Initial (t=t)	1330	1374	1339	1299		Total supernatant	-24	-24	220	0
rest of samp (t=t)	1346	1356	1238	1216		% counts lost	-1.77%	-1.75%	19.50%	0.00%
1mL ali (t=t)	-12	-12	110	0		SD	0.5%	0.5%	1.9%	0.0%
SD	3	3	10	0						
	24 hour 6s counts	Synthesis	Final				24 hour 6s counts	Synthesis	Final	
	Stability	(3/13)	(3/14)				Stability	(3/13)	(3/14)	
	1	2	3	4			1	2	3	4
Initial (t=0)	6196	5978	6010	5872		Yield	-1.40%	-0.25%	-7.62%	0.10%
Pre Cu removal (t=0)	-87	-15	-458	6		Total precipitate	1007	939	690	905
Initial (t=t)	844	909	878	876		Total supernatant	-22	-22	172	-16
rest of samp (t=t)	996	928	776	897		% counts lost	-2.18%	-2.34%	24.93%	-1.77%
1mL ali (t=t)	-11	-11	86	-8		SD	0.7%	0.7%	2.7%	0.6%
SD	3	3	9	3						
	30 hour 6s counts	Synthesis	Final				30 hour 6s counts	Synthesis	Final	
	Stability	(3/14)	(3/15)				Stability	(3/14)	(3/15)	
	1	2	3	4			1	2	3	4
Initial (t=0)	17552	17593	17048	17537		Yield	32.44%	34.21%	33.58%	32.43%
Pre Cu removal (t=0)	5694	6019	5725	5687		Total precipitate	1146	1192	968	1214
Initial (t=t)	1203	1274	1161	1201		Total supernatant	12	16	246	16
rest of samp (t=t)	1152	1200	1091	1222		% counts lost	1.05%	1.34%	25.41%	1.32%
1mL ali (t=t)	6	8	123	8		SD	0.4%	0.5%	2.3%	0.5%
SD	2	3	11	3						

Table A6.3.6: Part 1 of data collected in expt 5.4.1. Conditions are signified by 1-4: 1=water 2=PBS 3=1M EDTA 4=Mouse serum

	36 hour 6s counts	Synthesis	Final				36 hour 6s counts	Synthesis	Final	
	Stability	(3/13)	(3/15)				Stability	(3/13)	(3/15)	
	1	2	3	4			1	2	3	4
Initial (t=0)	30755	30960	31330	31159		Yield	27.13%	27.97%	19.27%	26.78%
Pre Cu removal (t=0)	8343	8658	6036	8344		Total precipitate	1744	1746	1369	1719
Initial (t=t)	1727	1767	1604	1789		Total supernatant	16	8	374	56
rest of samp (t=t)	1752	1750	1556	1747		% counts lost	0.92%	0.46%	27%	3.26%
1mL ali (t=t)	8	4	187	28		SD	0.3%	0.2%	2%	0.6%
SD	3	2	14	5						
	42 hour 6s counts	Synthesis	Final				42 hour 6s counts	Synthesis	Final	
	Stability	(3/13)	(3/15)				Stability	(3/13)	(3/15)	
	1	2	3	4			1	2	3	4
Initial (t=0)	43247	42903	42042	41687		Yield	24.85%	24.99%	24.68%	25.47%
Pre Cu removal (t=0)	10746	10722	10378	10617		Total precipitate	1642	1541	1185	1571
Initial (t=t)	1608	1621	1558	1554		Total supernatant	10	6	370	30
rest of samp (t=t)	1647	1544	1370	1586		% counts lost	0.6%	0.4%	31%	1.9%
1mL ali (t=t)	5	3	185	15		SD	0.3%	0.2%	2%	0.5%
SD	2	2	14	4						

Table A6.3.7: Part 2 of data collected in expt 5.4.1. Conditions are signified by 1-4: 1=water 2=PBS 3=1M EDTA 4=Mouse serum

	1: 80µL	2: 160µL	3: 80µL + 80µL cold	4: 160µL + 160µL cold
	Uncorrected Counts	BKG: 23	Date: 12/15/2010	Time: 21:00
	Initial (6sec)	First Supernatant (6 sec)	Second Supernatant (6 sec)	Remaining (6 sec)
1	11286	10426	773	1128
2	21192	20523	350	1232
3	10646	10803	325	220
4	20332	20569	556	229
	BKG corrected Counts	BKG: 23	Date: 12/15/2010	Time: 21:00
	Initial (6sec)	First Supernatant (6 sec)	Second Supernatant (6 sec)	Remaining (6 sec)
1	11283.7	10423.7	770.7	1125.7
2	21189.7	20520.7	347.7	1229.7
3	10643.7	10800.7	322.7	217.7
4	20329.7	20566.7	553.7	226.7
	BKG corrected Counts (±)	BKG: 23	Date: 12/15/2010	Time: 21:00
	Initial (6sec)	First Supernatant (6 sec)	Second Supernatant (6 sec)	Remaining (6 sec)
1	106.2247617	102.096523	27.76148411	33.55145302
2	145.5668231	143.2504799	18.64671553	35.06707858
3	103.1683091	103.9264163	17.96385259	14.75466028
4	142.582257	143.410948	23.53083084	15.05656003
	Ave yield (PgC3 MONC)	0.28	±	0.04
	# of Cu per capsule	±	% of total Cu	±
1	8.5	0.1	0.353	0.006
2	9.2	0.1	0.385	0.006
3	1.6	0.2	0.068	0.007
4	1.7	0.2	0.071	0.007

Table A6.3.8: Data from the exchange experiment in 5.5.1. Legend for experiment numbers is listed at the top of the table

Exchange Study #3					
Sample	Amt of Hot Cu (microL of 1M)	Initial Counts (60s-bkg)	First Removal (60s-bkg)	Second Removal (60s-bkg)	# of Cu per capsule gained
0	5	1099	262	157	0.8
1	10	2176	373	256	1.3
2	20	4772	673	308	1.4
3	40	9633	1027	352	1.6
4	60	15133	1615	382	1.6
5	80	21023	3258	454	1.9
6	120	26393	2093	501	2.4
7	160	34983	3338	538	2.6
8	200	44713	2553	579	2.8
9	240	54913	2463	506	2.4
	PgC3 yield	0.28	±	0.04	
Exchange Study #3 (±)					
Sample	Amt of Hot Cu (microL of 1M)	Initial Counts (60s-bkg)	First Removal (60s-bkg)	Second Removal (60s-bkg)	# of Cu per capsule gained
0	5	33.15116891	16.18641406	12.52996409	0.1
1	10	46.64761516	19.31320792	16	0.2
2	20	69.07966416	25.94224354	17.54992877	0.2
3	40	98.14784766	32.04684072	18.76166304	0.2
4	60	123.0162591	40.18706259	19.54482029	0.2
5	80	144.9931033	57.07889277	21.30727575	0.3
6	120	162.4592257	45.74931693	22.38302929	0.4
7	160	187.0374294	57.7754273	23.19482701	0.4
8	200	211.4544868	50.52722039	24.06241883	0.4
9	240	234.33523	49.62862077	22.49444376	0.4

	Exchange Study #3 (Inverse)				
	Synthesis Portion	background corrected after counts were multiplied by 10			
Sample	Amt of Cold Cu (microL of 1M	2nd rem/ initial	Cold Cu + Removal	2nd Removal	# of Cu per capsule lost
0	5	28133	**19413**	18943	**7.84**
1	10	28373	**24723**	**23523**	**4.10**
2	20	28463	28403	**23183**	**4.45**
3	40	29583	28733	27013	2.08
4	60	29813	27423	**24183**	**4.53**
5	80	28413	28353	25313	2.62
6	120	29443	29113	26813	2.14
7	160	30553	27173	26873	2.89
8	200	30633	29593	27473	2.48
9	240	30023	29553	28653	1.10
	Exchange Study #3 (Inverse, ±)				
	Synthesis Portion	background corrected after counts were multiplied by 10			
Sample	Amt of Cold Cu (microL of 1M	2nd rem/ initial	Cold Cu + Removal	2nd Removal	# of Cu per capsule lost
0	5	167.728948	139.3305422	137.6335715	0.07
1	10	168.4428687	157.2354922	153.3720965	0.04
2	20	168.70981	168.5318961	152.2596467	0.04
3	40	171.997093	169.5081119	164.3563202	0.02
4	60	172.6644144	165.598913	155.5088422	0.04
5	80	168.5615615	168.3834909	159.1005971	0.02
6	120	171.5896267	170.6253205	163.7467557	0.02
7	160	174.7941647	164.8423489	163.9298631	0.02
8	200	175.0228557	172.0261608	165.7498115	0.02
9	240	173.2714633	171.9098601	169.2719705	0.01

Table A6.3.9: Data from the second exchange study in 5.5.1. Bold numbers denote the formation of an emulsion

Data	Exchange Expt 6							
BCG corr								
	1 hour 24s counts	Synthesis	Final					
	cold MONC hot exch	10/10/2012	10/10/2012					
uL 1M Cu(NO3)2	5	10	15	20	30	40	60	80
Initial (t=0)								
Pre Cu removal (t=0)								
Initial (t=t)	1393.5	2623.5	3786	5043.5	7378.5	9753.5	14916	19461
After ppt/rem (t=t)	1186	1883.5	1801	1976	2178.5	2003.5	2066	2233.5
wash w/ solvent/rem (t=t)	1038.5	1708.5	1648.5	1713.5	1828.5	1928.5	1833.5	2043.5
2nd wash w/ solvent/rem (t=t)	876	1403.5	1568.5	1556	1596	1616	1691	1843.5
	hot MONC cold exch							
uL 1M Cu(NO3)2	5	10	15	20	30	40	60	80
Initial (t=0)	16841	16886	17286	17846	17636	17741	18131	17671
Pre Cu removal (t=0)	4601	4841	5203.5	5091	5133.5	5063.5	5101	5066
Initial (t=t)	4868.5	4528.5	5033.5	4841	4783.5	4846	4861	4783.5
After ppt/rem (t=t)	1461	4841	4996	4691	4903.5	4723.5	4926	4286
wash w/ solvent/rem (t=t)	1073.5	4398.5	4323.5	4553.5	4438.5	4503.5	4336	4486
Data								
#Cu per capsule								
	1 hour 24s counts	Synthesis	Final					
	cold MONC hot exch	10/10/2012	10/10/2012					
uL 1M Cu(NO3)2	5	10	15	20	30	40	60	80
Initial (t=0)								
Pre Cu removal (t=0)								
Initial (t=t)	5.215873089	10.43174618	15.64761927	20.86349	31.29524	41.72698	62.59048	83.45397
After ppt/rem (t=t)	4.439200204	7.489305861	7.443571659	8.174137	9.23991	8.571284	8.669343	9.577845
wash w/ solvent/rem (t=t)	3.88710743	6.793458489	6.813285886	7.088251	7.755417	8.250422	7.693728	8.763074
2nd wash w/ solvent/rem (t=t)	3.278869628	5.580695926	6.482644168	6.436719	6.769289	6.913498	7.095769	7.905421
	hot MONC cold exch							
uL 1M Cu(NO3)2	5	10	15	20	30	40	60	80
Initial (t=0)								
Pre Cu removal (t=0)								
Initial (t=t)	**22.79981672**	23.92518453	25.12164352	23.80725	24.29184	23.81879	23.47905	23.92495
After ppt/rem (t=t)	**6.842052424**	25.57619925	24.93448516	23.06957	24.90123	23.21669	23.79301	21.43668
wash w/ solvent/rem (t=t)	**5.027339683**	23.23836241	21.5781118	22.39337	22.53984	22.13535	20.94326	22.43699

Table A6.3.10: cold + hot data from 5.5.2 (comprehensive exchange experiment)

Data	Cu salt Experiment					
BCG corrected						
Cu(BF4)2	3 hour 24s counts	Synthesis	Final			
	hot MONC cold exch	10/10/2012	10/10/2012			
uL 1M Cu2+	10	20	30	40	60	80
Initial (t=t)	3756	7678.5	11221	15151	21783.5	30131
After ppt/rem (t=t)	2248.5	2181	2316	2498.5	2573.5	3016
wash w/ solvent/rem (t=t)	1961	2021	2071	2338.5	2523.5	2848.5
Cu(ClO4)2	3 hour 24s counts	Synthesis	Final			
	hot MONC cold exch	10/10/2012	10/10/2012			
uL 1M Cu2+	10	20	30	40	60	80
Initial (t=t)	3831	7378.5	10921	14106	21551	29051
After ppt/rem (t=t)	2608.5	2686	2696	2866	3123.5	3088.5
wash w/ solvent/rem (t=t)	2356	2513.5	2408.5	2661	2778.5	2923.5
CuCl2	3 hour 24s counts	Synthesis	Final			
	hot MONC cold exch	10/10/2012	10/10/2012			
uL 1M Cu2+	10	20	30	40	60	80
Initial (t=t)	3556	6838.5	10188.5	13121	20303.5	26941
After ppt/rem (t=t)	2041	1971	1916	1601	1521	1313.5
wash w/ solvent/rem (t=t)	1486	1676	1626	1458.5	1303.5	1143.5
Cu(NO3)2	3 hour 24s counts	Synthesis	Final			
	hot MONC cold exch	10/10/2012	10/10/2012			
uL 1M Cu2+	10	20	30	40	60	80
Initial (t=t)	2623.5	5043.5	7378.5	9753.5	14916	19461
After ppt/rem (t=t)	1883.5	1976	2178.5	2003.5	2066	2233.5
wash w/ solvent/rem (t=t)	1708.5	1713.5	1828.5	1928.5	1833.5	2043.5

Table A6.3.11: Data from copper salt experiment 5.5.3

Data	Cu salt Experiment					
# Cu per capsule						
40 uL 1M Cu(BF4)2	3 hour 24s counts	Synthesis	Final			
	hot MONC cold exch	10/10/2012	10/10/2012			
	10	20	30	40	60	80
Initial (t=t)	10.43174618	20.86349236	31.29523854	41.72698	62.59048	83.45397
After ppt/rem (t=t)	6.244883196	5.926063272	6.459297072	6.881055	7.394431	8.353429
wash w/ solvent/rem (t=t)	5.446393572	5.49132227	5.775994921	6.440404	7.250766	7.889504
40 uL 1M Cu(ClO4)2	3 hour 24s counts	Synthesis	Final			
	hot MONC cold exch	10/10/2012	10/10/2012			
	10	20	30	40	60	80
Initial (t=t)	10.43174618	20.86349236	31.29523854	41.72698	62.59048	83.45397
After ppt/rem (t=t)	7.102900002	7.594950257	7.725662768	8.47792	9.071568	8.872245
wash w/ solvent/rem (t=t)	6.415346906	7.107188187	6.901802217	7.871509	8.069586	8.398254
40 uL 1M CuCl2	3 hour 24s counts	Synthesis	Final			
	hot MONC cold exch	10/10/2012	10/10/2012			
	10	20	30	40	60	80
Initial (t=t)	10.43174618	20.86349236	31.29523854	41.72698	62.59048	83.45397
After ppt/rem (t=t)	5.987399874	6.01329874	5.885231097	5.091449	4.688852	4.068772
wash w/ solvent/rem (t=t)	4.359273009	5.113287006	4.994460211	4.638275	4.018356	3.54217
Cu(NO3)2	3 hour 24s counts	Synthesis	Final			
	hot MONC cold exch	10/10/2012	10/10/2012			
uL 1M Cu2+	10	20	30	40	60	80
Initial (t=t)	10.43174618	20.86349236	31.29523854	41.72698	62.59048	83.45397
After ppt/rem (t=t)	7.489305861	8.174137186	9.239910165	8.571284	8.669343	9.577845
wash w/ solvent/rem (t=t)	6.793458489	7.088251047	7.755416909	8.250422	7.693728	8.763074
Yields	Average	StD				
Yield (%)	0.287583684	0.007429324				
mMol Cu	23.00669475	0.594345915				

Table A6.3.12: Modeled data from copper salt experiment 5.5.3

BCG correction		Standard Dev							
3hr			**hot+cold**	bcg 31	12s counts				
			Initial	removal 1	removal 2	Exch Init	removal 1	removal 2	removal 3
	Acid	10uL	105.7582	57.6090271	56.371979	51.20352	53.812638	47.6948635	50.574697
		20uL	114.9991	62.2559234	52.257057	52.73329	49.394332	53.7847562	49.252411
		40uL	109.1549	61.8368822	53.598507	52.22834	54.669919	53.1770627	47.061662
		80uL	112.1151	58.8115635	52.752251	50.4361	54.044426	47.4742035	47.167786
			hot+cold						
			Initial	removal 1	removal 2	Exch Init	removal 1	removal 2	removal 3
	Base	10uL	110.2851	55.2792909	52.988678	50.19761	48.018746	47.7786563	46.699036
		20uL	111.0126	58.4705054	53.092372	46.76323	48.94691	46.602575	45.429066
		40uL	111.9455	56.3897154	52.142113	48.63949	49.130439	49.2828571	42.553496
		80uL	113.0124	60.8177606	56.716841	50.90972	49.847768	44.9866647	46.784613
		Net yields							
				Initial	Final	Net yield	±		
		Acid	10uL	11184.8	3177.8	0.284118	0.005308		
			20uL	13224.8	2730.8	0.206491	0.0043731		
			40uL	11914.8	2872.8	0.241112	0.0049086		
			80uL	12569.8	2782.8	0.221388	0.0044721		
		Base	10uL	12162.8	2807.8	0.230851	0.0046276		
			20uL	12323.8	2818.8	0.228728	0.0043178		
			40uL	12531.8	2718.8	0.216952	0.0043382		
			80uL	12771.8	3216.8	0.251867	0.0045668		
		Average				0.235188			
		StD				0.024244			

Table A6.3.13: Data from acid/base (DBU) experiment 5.5.4

#Cu per capsule									
3hr			hot+cold	bcg 31	12s counts				
			Initial	removal 1	removal 2	Exch Init	removal 1	removal 2	removal 3
	Acid	10uL				24	26.5082	20.8235563	23.414143
		20uL				24	21.056962	24.9666283	20.936133
		40uL				24	26.296356	24.8798299	19.486473
		80uL				24	27.556883	21.2639358	20.990329
			hot+cold						
			Initial	removal 1	removal 2	Exch Init	removal 1	removal 2	removal 3
	Base	10uL				24	21.961743	21.742678	20.771172
		20uL				24	26.293763	23.8353759	22.650082
		40uL				24	24.486939	24.6391073	18.369769
		80uL				24	23.009183	18.7403349	20.268231
			cold+hot	bcg 31	12s counts				
			Initial	removal 1	removal 2	Exch Init	removal 1	removal 2	removal 3
		10uL				12.75573	3.2404058	2.78821141	2.1724573
		20uL				25.51146	3.2670619	2.94376827	3.150317
		40uL				51.02292	4.283242	4.91909328	3.896202
		80uL				102.0458	6.7657348	5.5963713	4.2612712
			cold+hot						
			Initial	removal 1	removal 2	Exch Init	removal 1	removal 2	removal 3
		10uL				12.75573	11.699331	10.8634989	11.339459
		20uL				25.51146	12.963242	14.3643856	13.513058
		40uL				51.02292	14.979103	15.9123805	17.191614
		80uL				102.0458	18.706252	18.3921255	18.069273
	Neutral (from Exch 6		cold+hot						
			Initial	removal 1	removal 2	Exch Init	removal 1	removal 2	removal 3
		10uL				10.43175	7.4893059	6.79345849	5.5806959
		20uL				20.86349	8.1741372	7.08825105	6.4367194
		40uL				41.72698	8.5712835	8.2504219	6.9134985
		80uL				83.45397	9.577845	8.76307418	7.9054207
			hot+cold						
			Initial	removal 1	removal 2	Exch Init	removal 1	removal 2	removal 3
		10uL				24	23.925185	25.5761993	23.238362
		20uL				24	23.807249	23.0695731	22.39337
		40uL				24	23.818791	23.2166859	22.135354
		80uL				24	23.924951	21.4366761	22.436988

Table A6.3.14: Modeled data from acid/base (DBU) experiment 5.5.4

Pyrdine as Base Experiment												
				then dissolve in Ace, add 40uL 1M Cu(NO3)2								
	3 hour 24s counts	Synthesis	Final									
	cold MONC hot exch	10/10/2012	10/10/2012									
Sample #	1	2	3	4	5	6	7	8	9	10	11	12
Initial (t=t)	4944	4839	4746	5004	4930	4835	5007	4966	**5019**	4882	4948	4971
After ppt/rem (t=t)	1320	2629	1398	1583	735	1147	458	125	**1206**	1107	1010	1100
wash w/ solvent/rem (t=t)	1284	2427	1273	1382	545	1036	368	106	**1169**	1048	986	1154
Data												
BCG correction												
	3 hour 24s counts	Synthesis	Final									
	cold MONC hot exch	10/10/2012	10/10/2012									
Sample #	1	2	3	4	5	6	7	8	9	10	11	12
Initial (t=t)	12336	12073.5	11841	12486	12301	12063.5	12493.5	12391	12523.5	12181	12346	12403.5
After ppt/rem (t=t)	3276	6548.5	3471	3933.5	1813.5	2843.5	1121	288.5	2991	2743.5	2501	2726
wash w/ solvent/rem (t=t)	3186	6043.5	3158.5	3431	1338.5	2566	896	241	2898.5	2596	2441	2861
Data												
#Cu per capsule												
	3 hour 24s counts	Synthesis	Final									
	cold MONC hot exch	10/10/2012	10/10/2012									
Sample #	1	2	3	4	5	6	7	8	9	10	11	12
Initial (t=t)	41.72698471	41.72698471	41.72698471	41.72698	41.72698	41.72698	41.72698	41.72698	41.72698	41.72698	41.72698	41.72698
After ppt/rem (t=t)	11.08119341	22.63214142	12.23159902	13.14537	6.151686	9.835511	3.744023	0.971531	9.965697	9.398078	8.452875	9.170618
wash w/ solvent/rem (t=t)	10.77676502	20.8868209	11.13036747	11.46606	4.540409	8.875653	2.992546	0.811573	9.657497	8.892805	8.250087	9.624776
Yields	Average	StD										
Yield (%)	0.287583684	0.007429324										
mMol Cu	23.00669475	0.594345915										

Table A6.3.15: Data from 5.5.5 and 5.5.6

Metal Exchange Expts	**Background Correction**									
	1 hour 6s counts	Synthesis	Final							
	hot Cu MONC cold exch	(3/16)	(3/16)			cold metal MONC hot Cu exch				
1	1	2	3	4	5	1	2	3	4	5
Initial	1035.8	948.8	1646.8	1602.8	1625.8	5261.8	5136.8	5056.8	4938.8	23289.8
Final (after 2x washes)	1096.8	953.8	1648.8	689.8	1682.8	2996.8	2647.8	3797.8	744.8	8582.8
% cu remaining	106%	101%	100%	43%	104%	57%	52%	75%	15%	37%
#Cu per capsule remaini	25.41340027	24.12648	24.02915	10.32892	24.84143	13.66893	12.37097	18.02468	3.619341	8.844524
±	5%	5%	3%	2%	4%	1%	1%	2%	1%	0.5%
	1.1	1.1	0.8	0.5	0.9	0.3	0.3	0.4	0.1	0.1
3	3 hour 6s counts	Synthesis	Final							
	hot Cu MONC cold exch	(3/16)	(3/16)			cold metal MONC hot Cu exch				
	1	2	3	4	5	1	2	3	4	5
Initial	1036.8	1478.8	1461.8	1411.8	1372.8	4416.8	4428.8	4458.8	4398.8	19609.8
Final (after 2x washes)	1044.8	1391.8	1386.8	619.8	1419.8	2868.8	2214.8	3273.8	463.8	8356.8
% cu remaining	101%	94%	95%	44%	103%	65%	50%	73%	11%	43%
#Cu per capsule remaini	24.18518519	22.58804	22.76864	10.53634	24.82168	15.58848	12.00217	17.6216	2.530508	10.2277
± % cu rem	4%	4%	4%	2%	4%	2%	1%	2%	1%	1%
± Cu per capsule	1.1	0.8	0.9	0.5	0.9	0.4	0.3	0.4	0.1	0.1
20	20 hour 12s, 6s counts	Synthesis	Final							
	hot Cu MONC cold exch	(3/16)	(3/17)			cold metal MONC hot Cu exch				
	1	2	3	4	5	1	2	3	4	5
Initial	700.8	1140.8	1199.8	1057.8	1162.8	1612.8	1788.8	1860.8	1687.8	7852.8
Final (after 2x washes)	718.8	1042.8	1097.8	291.8	1003.8	959.9	1035.9	1181.9	212.9	3318.9
% cu remaining	103%	91%	91%	28%	86%	60%	58%	64%	13%	42%
#Cu per capsule remaini	24.61643836	21.93829	21.95966	6.620533	20.71827	14.28423	13.89848	15.24377	3.027373	10.14334
± % cu rem	5%	4%	4%	2%	4%	2%	2%	2%	1%	1%
± Cu per capsule	1.3	0.9	0.9	0.4	0.9	0.6	0.5	0.6	0.2	0.2

Table A6.3.16: Data from 4.6.2 and 4.6.3

REFERENCES

(1) Farha, O. K.; Hupp, J. T. *Accounts of Chemical Research* **2010**, *43*, 1166.

(2) Gong, H.-Y.; Rambo, B. M.; Cho, W.; Lynch, V. M.; Oh, M.; Sessler, J. L. *Chemical Communications (Cambridge, United Kingdom)* **2011**, *47*, 5973.

(3) Li, Q.; Zhang, W.; Miljanic, O. S.; Sue, C.-H.; Zhao, Y.-L.; Liu, L.; Knobler, C. B.; Stoddart, J. F.; Yaghi, O. M. *Science (Washington, DC, United States)* **2009**, *325*, 855.

(4) Zhu, X.-D.; Lin, Z.-J.; Liu, T.-F.; Xu, B.; Cao, R. *Crystal Growth & Design* **2012**, *12*, 4708.

(5) Isaeva, V. I.; Tkachenko, O. P.; Brueva, T. R.; Kapustin, G. I.; Afonina, E. V.; Mishin, I. V.; Gryunert, V.; Kustov, L. M.; Solov'eva, S. E.; Antipin, I. S. *Russian Journal of Physical Chemistry A* **2011**, *85*, 293.

(6) Gao, W.-Y.; Niu, Y.; Chen, Y.; Wojtas, L.; Cai, J.; Chen, Y.-S.; Ma, S. *CrystEngComm* **2012**, *14*, 6115.

(7) Keskin, S.; van Heest, T. M.; Sholl, D. S. *ChemSusChem* **2010**, *3*, 879.

(8) Cragg, P. J. *Supramolecular Chemistry : From Biological Inspiration to Biomedical Applications*; Springer: Dordrecht, NLD, 2010.

(9) Schottel, B. L.; Chifotides, H. T.; Dunbar, K. R. *Chem. Soc. Rev.* **2008**, *37*, 68.

(10) Desiraju, G. R. *Chemical Communications (Cambridge, United Kingdom)* **2005**, 2995.

(11) Nishio, M. *CrystEngComm* **2004**, *6*, 130.

(12) Rambo, B. M.; Gong, H.-Y.; Oh, M.; Sessler, J. L. *Accounts of Chemical Research* **2012**, *45*, 1390.

(13) Davis, J. J.; Orlowski, G. A.; Rahman, H.; Beer, P. D. *Chemical Communications (Cambridge, United Kingdom)* **2010**, *46*, 54.

(14) Kim, K. *Chem. Soc. Rev.* **2002**, *31*, 96.

(15) Aakeroy, C. B.; Sinha, A. S.; Epa, K. N.; Chopade, P. D.; Smith, M. M.; Desper, J. *Crystal Growth & Design* **2013**, *13*, 2687.

(16) Li, W.-L.; Wu, A.-K.; Lee, K.-M. *CrystEngComm* **2012**, *14*, 6072.

(17) Kuduva, S. S.; Craig, D. C.; Nangia, A.; Desiraju, G. R. *Journal of the American Chemical Society* **1999**, *121*, 1936.

(18) Yamato, K.; Kline, M.; Gong, B. *Chemical Communications (Cambridge, United Kingdom)* **2012**, *48*, 12142.

(19) Goodman, C. M.; Choi, S.; Shandler, S.; DeGrado, W. F. *Nature Chemical Biology* **2007**, *3*, 252.

(20) Huc, I. *European Journal of Organic Chemistry* **2004**, 17.

(21) Gellman, S. H. *Accounts of Chemical Research* **1998**, *31*, 173.

(22) Friscic, T. *Chem. Soc. Rev.* **2012**, *41*, 3493.

(23) Videnova-Adrabinska, V. *Coordination Chemistry Reviews* **2007**, *251*, 1987.

(24) Pedersen, C. J. *J. Amer. Chem. Soc.* **1967**, *89*, 7017.

(25) Kotlyar, S. A.; Zubatyuk, R. I.; Shishkin, O. V.; Chuprin, G. N.; Kiriyak, A. V.; Kamalov, G. L. *Acta Crystallographica, Section E: Structure Reports Online* **2005**, *61*, m2163.

(26) Ravikumar, I.; Suresh, E.; Ghosh, P. *Inorganic Chemistry* **2006**, *45*, 10046.

(27) Mateus, P.; Lima, L. M. P.; Delgado, R. *Polyhedron* **2013**, *52*, 25.

(28) Du, J.; Huang, Z.; Yu, X.-Q.; Pu, L. *Chemical Communications (Cambridge, United Kingdom)* **2013**, *49*, 5399.

(29) Pederson, C. J.; Lehn, J. M.; Cram, D. J. *Resonance* **2001**, *6*, 71.

(30) Kang, S.-O.; Llinares, J. M.; Day, V. W.; Bowman-James, K. *Chem. Soc. Rev.* **2010**, *39*, 3980.

(31) Pasloske, K. S.; Lau, K.; Richardson, S. J.; Willis, A. E.; (Jurox Pty. Ltd., Australia). Application: WO
WO, 2013, p 62pp.

(32) Mangia, A.; Grisenti, P.; Monti, R.; Reza Elahi, S.; Verza, E.; (Euticals S.p.A., Italy). Application: EP
EP, 2012, p 41pp.

(33) Klaveness, J.; Rongved, P.; (OmegaTri AS, Norway; Campbell, Neil). Application: WO
WO, 2009, p 38pp.

(34) Futo, T.; Nakai, S.; De Jong, R. L.; Lee, B.; Christopher, R. J.; (Takeda Pharmaceutical Co., Ltd., Japan). Application: WO
WO, 2009, p 122pp.

(35) Millan, R. D. S.; Demichele, C. P.; Frezard, F. J. G.; Demelo, A. L.; Ferreira, L. A. M.; Bejarano, R. O.; (Universidade Federal de Minas Gerais - UFMG, Brazil). Application: WO
WO, 2006, p 36 pp.

(36) Lyons, R. T.; Chang, J.; Chang, C.-M.; (Allergan, Inc., USA). Application: US
US, 2004, p 7 pp

(37) Tarre Perez, M. T.; Font Faus, X.; Trullols Casas, M.; (Laboratorio de Aplicaciones Farmacodinamicas, S.A., Spain). Application: EP
EP, 2001, p 4 pp.

(38) Bellia, F.; La Mendola, D.; Pedone, C.; Rizzarelli, E.; Saviano, M.; Vecchio, G. *Chem. Soc. Rev.* **2009**, *38*, 2756.

(39) Enright, G. D.; Udachin, K. A.; Ripmeester, J. A. *CrystEngComm* **2010**, *12*, 1450.

(40) Breslow, R.; Dong, S. D. *Chemical Reviews (Washington, D. C.)* **1998**, *98*, 1997.

(41) Baek, K.; Kim, Y.; Kim, H.; Yoon, M.; Hwang, I.; Ko, Y. H.; Kim, K. *Chemical Communications (Cambridge, United Kingdom)* **2010**, *46*, 4091.

(42) Liang, L.-L.; Ni, X.-L.; Zhao, Y.; Chen, K.; Xiao, X.; Zhang, Y.-Q.; Redshaw, C.; Zhu, Q.-J.; Xue, S.-F.; Tao, Z. *Inorganic Chemistry* **2013**, *52*, 1909.

(43) Lagona, J.; Mukhopadhyay, P.; Chakrabarti, S.; Isaacs, L. *Angewandte Chemie, International Edition* **2005**, *44*, 4844.

(44) Isaacs, L. *Chemical Communications (Cambridge, United Kingdom)* **2009**, 619.

(45) Gerasko, O. A.; Fedin, V. P. *Russian Journal of Inorganic Chemistry* **2011**, *56*, 2025.

(46) Boehmer, V. *Angewandte Chemie, International Edition in English* **1995**, *34*, 713.

(47) Gutsche, C. D.; Rogers, J. S.; Stewart, D.; See, K. A. *Pure and Applied Chemistry* **1990**, *62*, 485.

(48) Casnati, A.; Sansone, F.; Ungaro, R. *Accounts of Chemical Research* **2003**, *36*, 246.

(49) Atwood Jerry, L.; Barbour Leonard, J.; Heaven Michael, W.; Raston Colin, L. *Chemical communications (Cambridge, England)* **2003**, 2270.

(50) Atwood, J. L.; Barbour, L. J.; Dalgarno, S.; Raston, C. L.; Webb, H. R. *Journal of the Chemical Society, Dalton Transactions: Inorganic Chemistry (1972-1999)* **2002**, 4351.

(51) Gutsche, C. D.; Muthukrishnan, R. *Journal of Organic Chemistry* **1978**, *43*, 4905.

(52) Gutsche, C. D.; Iqbal, M.; Nam, K. S.; See, K.; Alam, I. *Pure and Applied Chemistry* **1988**, *60*, 483.

(53) Haino, T.; Yanase, M.; Fukunaga, C.; Fukazawa, Y. *Tetrahedron* **2006**, *62*, 2025.

(54) Kunsagi-Mate, S.; Szabo, K.; Bitter, I.; Nagy, G.; Kollar, L. *Tetrahedron Letters* **2004**, *45*, 1387.

(55) Raston, C. L.; Atwood, J. L.; Nichols, P. J.; Sudria, I. B. N. *Chemical Communications (Cambridge)* **1996**, 2615.
(56) Mokhtari, B.; Pourabdollah, K. *Drug and Chemical Toxicology (1977)* **2013**, *36*, 119.
(57) Tabakci, B.; Yilmaz, M.; Beduk, A. D. *Journal of Applied Polymer Science* **2012**, *125*, 1012.
(58) Dong, Z.; Luo, Q.; Liu, J. *Chem. Soc. Rev.* **2012**, *41*, 7890.
(59) Chini, M. G.; Terracciano, S.; Riccio, R.; Bifulco, G.; Ciao, R.; Gaeta, C.; Troisi, F.; Neri, P. *Organic Letters* **2010**, *12*, 5382.
(60) Nimse, S. B.; Kim, T. *Chem. Soc. Rev.* **2013**, *42*, 366.
(61) Baghbanian, S. M.; Babajani, Y.; Tashakorian, H.; Khaksar, S.; Farhang, M. *Comptes Rendus Chimie* **2013**, *16*, 129.
(62) Fernandes, S. A.; Natalino, R.; Gazolla, P. A. R.; da Silva, M. J.; Jham, G. N. *Tetrahedron Letters* **2012**, *53*, 1630.
(63) da Silva, D. L.; Fernandes, S. A.; Sabino, A. A.; de Fatima, A. *Tetrahedron Letters* **2011**, *52*, 6328.
(64) Shimizu, S.; Shimada, N.; Sasaki, Y. *Green Chemistry* **2006**, *8*, 608.
(65) Atwood, J. L.; Barbour, L. J.; Hardie, M. J.; Raston, C. L. *Coordination Chemistry Reviews* **2001**, *222*, 3.
(66) Orr, G. W.; Barbour, L. J.; Atwood, J. L. *Science (Washington, D. C.)* **1999**, *285*, 1049.
(67) MacGillivray, L. R.; Atwood, J. L. *Journal of the American Chemical Society* **1997**, *119*, 6931.
(68) MacGillivray, L. R.; Atwood, J. L. *Nature (London)* **1997**, *389*, 469.
(69) Shivanyuk, A.; Rebek, J., Jr. *Chemical Communications (Cambridge, United Kingdom)* **2001**, 2424.
(70) Adriaenssens, L.; Escribano-Cuesta, A.; Homs, A.; Echavarren, A. M.; Ballester, P. *European Journal of Organic Chemistry* **2013**, *2013*, 1494.
(71) Shimizu, S.; Usui, A.; Sugai, M.; Suematsu, Y.; Shirakawa, S.; Ichikawa, H. *European Journal of Organic Chemistry* **2013**, *2013*, 4734.
(72) Bianchini, G.; La Sorella, G.; Canever, N.; Scarso, A.; Strukul, G. *Chemical Communications (Cambridge, United Kingdom)* **2013**, *49*, 5322.
(73) Bianchini, G.; Scarso, A.; Sorella, G. L.; Strukul, G. *Chemical Communications (Cambridge, United Kingdom)* **2012**, *48*, 12082.
(74) Beyeh, N. K.; Rissanen, K. *Israel Journal of Chemistry* **2011**, *51*, 769.
(75) Avram, L.; Cohen, Y. *Organic Letters* **2008**, *10*, 1505.
(76) Lepakshaiah, M.; Guru Row, T. N. *Journal of Molecular Structure* **2009**, *918*, 10.
(77) Mansikkamaki, H.; Busi, S.; Nissinen, M.; Ahman, A.; Rissanen, K. *Chemistry - A European Journal* **2006**, *12*, 4289.
(78) Ma, B.-Q.; Ferreira, L. F. V.; Coppens, P. *Organic Letters* **2004**, *6*, 1087.
(79) Ma, B.-Q.; Coppens, P. *Crystal Growth & Design* **2004**, *4*, 211.
(80) Friscic, T.; MacGillivray, L. R. *Journal of Organometallic Chemistry* **2003**, *666*, 43.
(81) MacGillivray, L. R.; Papaefstathiou, G. S.; Reid, J. L.; Ripmeester, J. A. *Crystal Growth & Design* **2001**, *1*, 373.
(82) MacGillivray, L. R.; Diamente, P. R.; Reid, J. L.; Ripmeester, J. A. *Chemical Communications (Cambridge)* **2000**, 359.
(83) Zambrano, C. H.; Kass, J. P.; Dueno, E. E.; Ke, Y.; Zhou, H.-C. *Journal of Chemical Crystallography* **2006**, *36*, 67.
(84) Dalgarno, S. J.; Power, N. P.; Antesberger, J.; McKinlay, R. M.; Atwood, J. L. *Chemical Communications (Cambridge, United Kingdom)* **2006**, 3803.

(85) Han, J.; Song, X.; Liu, L.; Yan, C. *Journal of Inclusion Phenomena and Macrocyclic Chemistry* **2007**, *59*, 257.

(86) Chen, J.; Chen, W.; Yan, C. *Chinese Journal of Chemistry* **2009**, *27*, 1703.

(87) Mendrek, B.; Trzebicka, B. *European Polymer Journal* **2009**, *45*, 1979.

(88) Iwanek, W.; Urbaniak, M.; Bochenska, M. *Tetrahedron* **2002**, *58*, 2239.

(89) Atwood, J. L.; Barbour, L. J.; Jerga, A. *Proceedings of the National Academy of Sciences of the United States of America* **2002**, *99*, 4837.

(90) Avram, L.; Cohen, Y. *Journal of the American Chemical Society* **2004**, *126*, 11556.

(91) Antesberger, J.; Cave, G. W. V.; Ferrarelli, M. C.; Heaven, M. W.; Raston, C. L.; Atwood, J. L. *Chemical Communications (Cambridge, United Kingdom)* **2005**, 892.

(92) Funck, M.; Guest, D. P.; Cave, G. W. V. *Tetrahedron Letters* **2010**, *51*, 6399.

(93) Yan, C.; Chen, W.; Chen, J.; Jiang, T.; Yao, Y. *Tetrahedron* **2007**, *63*, 9614.

(94) Gerkensmeier, T.; Iwanek, W.; Agena, C.; Frohlich, R.; Kotila, S.; Nather, C.; Mattay, J. *European Journal of Organic Chemistry* **1999**, 2257.

(95) Atwood, J. L.; Barbour, L. J.; Jerga, A. *Journal of Supramolecular Chemistry* **2002**, *1*, 131.

(96) Cave, G. W. V.; Antesberger, J.; Barbour, L. J.; McKinlay, R. M.; Atwood, J. L. *Angewandte Chemie, International Edition* **2004**, *43*, 5263.

(97) Avram, L.; Cohen, Y. *Journal of the American Chemical Society* **2003**, *125*, 16180.

(98) Barrett, E. S.; Dale, T. J.; Rebek, J., Jr. *Journal of the American Chemical Society* **2008**, *130*, 2344.

(99) Palmer, L. C.; Rebek, J., Jr. *Organic Letters* **2005**, *7*, 787.

(100) Chapin, J. C.; Kvasnica, M.; Purse, B. W. *Journal of the American Chemical Society* **2012**, *134*, 15000.

(101) Dalgarno, S. J.; Antesberger, J.; McKinlay, R. M.; Atwood, J. L. *Chemistry--A European Journal* **2007**, *13*, 8248.

(102) Kline, K. K.; Fowler, D. A.; Tucker, S. A.; Atwood, J. L. *Chemistry--A European Journal* **2011**, *17*, 10848.

(103) Dalgarno, S. J.; Cave, G. W. V.; Atwood, J. L. *Angewandte Chemie, International Edition* **2006**, *45*, 570.

(104) Kulikov, O. V.; Daschbach, M. M.; Yamnitz, C. R.; Rath, N.; Gokel, G. W. *Chemical Communications (Cambridge, United Kingdom)* **2009**, 7497.

(105) Negin, S.; Daschbach, M. M.; Kulikov, O. V.; Rath, N.; Gokel, G. W. *Journal of the American Chemical Society* **2011**, *133*, 3234.

(106) Schnatwinkel, B.; Rekharsky, M. V.; Brodbeck, R.; Borovkov, V. V.; Inoue, Y.; Mattay, J. *Tetrahedron* **2009**, *65*, 2711.

(107) Schnatwinkel, B.; Rekharsky, M. V.; Borovkov, V. V.; Inoue, Y.; Mattay, J. *Tetrahedron Letters* **2009**, *50*, 1374.

(108) Fujisawa, I.; Takeuchi, D.; Kitamura, Y.; Okamoto, R.; Aoki, K. *Journal of Physics: Conference Series* **2012**, *352*, 012043/1.

(109) Fujisawa, I.; Kitamura, Y.; Okamoto, R.; Murayama, K.; Kato, R.; Aoki, K. *Journal of Molecular Structure* **2013**, *1038*, 188.

(110) Fowler, D. A.; Teat, S. J.; Baker, G. A.; Atwood, J. L. *Chemical Communications (Cambridge, United Kingdom)* **2012**, *48*, 5262.

(111) Fowler, D. A.; Atwood, J. L.; Baker, G. A. *Chemical Communications (Cambridge, United Kingdom)* **2013**, *49*, 1802.

(112) Fowler, D. A.; Tian, J.; Barnes, C.; Teat, S. J.; Atwood, J. L. *CrystEngComm* **2011**, *13*, 1446.

(113) Daschbach, M. M.; Kulikov, O. V.; Long, E. F.; Gokel, G. W. *Chemistry--A European Journal* **2011**, *17*, 8913.

(114) Li, R.; Kulikov, O. V.; Gokel, G. W. *Chemical Communications (Cambridge, United Kingdom)* **2009**, 6092.
(115) Nakazono, M.; Ohba, Y.; Zaitsu, K. *Chemical & Pharmaceutical Bulletin* **1999**, *47*, 569.
(116) Ziaja, P.; Jodko-Piorecka, K.; Kuzmicz, R.; Litwinienko, G. *Polymer Chemistry* **2012**, *3*, 93.
(117) Kersting, B.; Lehmann, U. *Advances in Inorganic Chemistry* **2009**, *61*, 407.
(118) McKinlay, R. M.; Cave, G. W. V.; Atwood, J. L. *Proceedings of the National Academy of Sciences of the United States of America* **2005**, *102*, 5944.
(119) Dalgarno, S. J.; Power, N. P.; Warren, J. E.; Atwood, J. L. *Chemical Communications (Cambridge, United Kingdom)* **2008**, 1539.
(120) Kulikov, O. V.; Li, R.; Gokel, G. W. *Angewandte Chemie, International Edition* **2009**, *48*, 375.
(121) Kumari, H.; Kline Steven, R.; Schuster Nathaniel, J.; Barnes Charles, L.; Atwood Jerry, L. *J Am Chem Soc* **2011**, *133*, 18102.
(122) McKinlay, R. M.; Thallapally, P. K.; Cave, G. W. V.; Atwood, J. L. *Angewandte Chemie, International Edition* **2005**, *44*, 5733.
(123) Jin, P.; Dalgarno, S. J.; Barnes, C.; Teat, S. J.; Atwood, J. L. *Journal of the American Chemical Society* **2008**, *130*, 17262.
(124) Jin, P.; Dalgarno, S. J.; Warren, J. E.; Teat, S. J.; Atwood, J. L. *Chemical Communications (Cambridge, United Kingdom)* **2009**, 3348.
(125) Jin, P.; Dalgarno, S. J.; Atwood, J. L. *Coordination Chemistry Reviews* **2010**, *254*, 1760.
(126) Power, N. P.; Dalgarno, S. J.; Atwood, J. L. *New Journal of Chemistry* **2007**, *31*, 17.
(127) Power, N.; Dalgarno, S. J.; Atwood, J. L. *Angewandte Chemie, International Edition* **2007**, *46*, 8601.
(128) Maerz Andrew, K.; Thomas Haunani, M.; Power Nicholas, P.; Deakyne Carol, A.; Atwood Jerry, L. *Chemical communications (Cambridge, England)* **2010**, *46*, 1235.
(129) Ahman, A.; Nissinen, M. *Chemical Communications (Cambridge, United Kingdom)* **2006**, 1209.
(130) Dalgarno, S. J.; Power, N. P.; Atwood, J. L. *Chemical Communications (Cambridge, United Kingdom)* **2007**, 3447.
(131) Addison, A. W.; Rao, T. N.; Reedijk, J.; Van Rijn, J.; Verschoor, G. C. *Journal of the Chemical Society, Dalton Transactions: Inorganic Chemistry (1972-1999)* **1984**, 1349.
(132) Sheldrick, G. M. *Acta Crystallographica, Section A: Foundations of Crystallography* **2008**, *64*, 112.
(133) Barbour, L. J. *Journal of Supramolecular Chemistry* **2003**, *1*, 189.
(134) Connolly, M. L. *Journal of Molecular Graphics* **1993**, *11*, 139.
(135) Atwood, J. L.; Brechin, E. K.; Dalgarno, S. J.; Inglis, R.; Jones, L. F.; Mossine, A.; Paterson, M. J.; Power, N. P.; Teat, S. J. *Chemical Communications (Cambridge, United Kingdom)* **2010**, *46*, 3484.
(136) Kumari, H.; Mossine, A. V.; Kline, S. R.; Dennis, C. L.; Fowler, D. A.; Teat, S. J.; Barnes, C. L.; Deakyne, C. A.; Atwood, J. L. *Angewandte Chemie, International Edition* **2012**, *51*, 1452.
(137) Hollamby, M. J. *Physical Chemistry Chemical Physics* **2013**, *15*, 10566.
(138) Kline, S. R. *Journal of Applied Crystallography* **2006**, *39*, 895.
(139) Schulz, G. V. *Z. physik. Chem.* **1939**, *B43*, 25.
(140) Kumari, H.; Kline, S. R.; Dennis, C. L.; Mossine, A. V.; Paul, R. L.; Deakyne, C. A.; Atwood, J. L. *Angewandte Chemie, International Edition* **2012**, *51*, 9263.
(141) Davis, M. E. *Nature (London, United Kingdom)* **2002**, *417*, 813.
(142) Rosseinsky, M. J. *Microporous and Mesoporous Materials* **2004**, *73*, 15.
(143) Ferey, G. *Chem. Soc. Rev.* **2008**, *37*, 191.
(144) Phuengphai, P.; Youngme, S.; Gamez, P.; Reedijk, J. *Dalton Transactions* **2010**, *39*, 7936.

(145) Lee, J. Y.; Farha, O. K.; Roberts, J.; Scheidt, K. A.; Nguyen, S. B. T.; Hupp, J. T. *Chem. Soc. Rev.* **2009**, *38*, 1450.

(146) Natarajan, S.; Mahata, P. *Chem. Soc. Rev.* **2009**, *38*, 2304.

(147) Liu, B.; Wong-Foy, A. G.; Matzger, A. J. *Chemical Communications (Cambridge, United Kingdom)* **2013**, *49*, 1419.

(148) Kolotilov, S. V.; Pavlishchuk, V. V. *Theoretical and Experimental Chemistry* **2009**, *45*, 277.

(149) Khan Nazmul, A.; Hasan, Z.; Jhung Sung, H. *Journal of hazardous materials* **2013**, *244-245*, 444.

(150) Mittermueller, M.; Volmer, D. A. *Analyst (Cambridge, United Kingdom)* **2012**, *137*, 3195.

(151) Wang, J.-L.; Wang, C.; Lin, W. *ACS Catalysis* **2012**, *2*, 2630.

(152) Gu, Z.-Y.; Yang, C.-X.; Chang, N.; Yan, X.-P. *Accounts of Chemical Research* **2012**, *45*, 734.

(153) Li, H.; Eddaoudi, M.; O'Keeffe, M.; Yaghi, M. *Nature (London)* **1999**, *402*, 276.

(154) Eddaoudi, M.; Kim, J.; Rosi, N.; Vodak, D.; Wachter, J.; O'Keeffe, M.; Yaghi, O. M. *Science (Washington, DC, United States)* **2002**, *295*, 469.

(155) Chorazy, S.; Podgajny, R.; Nitek, W.; Rams, M.; Ohkoshi, S.-i.; Sieklucka, B. *Crystal Growth & Design* **2013**, *13*, 3036.

(156) Li, F.; Xu, L. *Dalton Transactions* **2011**, *40*, 4024.

(157) Li, N.; Jiang, F.; Chen, L.; Li, X.; Chen, Q.; Hong, M. *Chemical Communications (Cambridge, United Kingdom)* **2011**, *47*, 2327.

(158) Fowler, D. A.; Mossine, A. V.; Beavers, C. M.; Teat, S. J.; Dalgarno, S. J.; Atwood, J. L. *Journal of the American Chemical Society* **2011**, *133*, 11069.

(159) Ehmann, W. D.; Vance, D. E. *Chemical Analysis, Vol. 116: Radiochemistry and Nuclear Methods of Analysis*, 1991.

(160) Mossine, A. V.; Kumari, H.; Fowler, D. A.; Maerz, A. K.; Kline, S. R.; Barnes, C. L.; Atwood, J. L. *Israel Journal of Chemistry* **2011**, *51*, 840.

(161) Steed, J. W.; Atwood, J. L.; Editors *Supramolecular Chemistry, Second Edition*, 2009.

(162) Asfari, Z.; Bohmer, V.; Harrowfield, J.; Vicens, J.; Editors *Calixarenes 2001*, 2001.

(163) Timmerman, P.; Verboom, W.; Reinhoudt, D. N. *Tetrahedron* **1996**, *52*, 2663.

(164) Atwood Jerry, L.; Brechin Euan, K.; Dalgarno Scott, J.; Inglis, R.; Jones Leigh, F.; Mossine, A.; Paterson Martin, J.; Power Nicholas, P.; Teat Simon, J. *Chemical communications (Cambridge, England)*, *46*, 3484.

(165) Karotsis, G.; Evangelisti, M.; Dalgarno, S. J.; Brechin, E. K. *Angewandte Chemie, International Edition* **2009**, *48*, 9928.

(166) Atwood, J. L.; Barbour, L. J.; Jerga, A. *Chemical Communications (Cambridge, United Kingdom)* **2001**, 2376.

(167) Atwood, J. L.; Steed, J. W.; Editors *Organic Nanostructures*, 2008.

(168) Dalgarno, S. J.; Power, N. P.; Atwood, J. L. *Coordination Chemistry Reviews* **2008**, *252*, 825.

(169) Dalgarno, S. J.; Tucker, S. A.; Bassil, D. B.; Atwood, J. L. *Science (Washington, DC, United States)* **2005**, *309*, 2037.

(170) Philip, I. E.; Kaifer, A. E. *Journal of the American Chemical Society* **2002**, *124*, 12678.

(171) MacGillivray, L. R.; Spinney, H. A.; Reid, J. L.; Ripmeester, J. A. *Chemical Communications (Cambridge)* **2000**, 517.

(172) Moon, K.; Kaifer, A. E. *Journal of the American Chemical Society* **2004**, *126*, 15016.

(173) Moon, K.; Philip, I.; Sun, H.; Kaifer, A. E. *Journal of Solid State Electrochemistry* **2007**, *11*, 1635.

(174) Ahman, A.; Luostarinen, M.; Rissanen, K.; Nissinen, M. *New Journal of Chemistry* **2007**, *31*, 169.

(175) Kline, S. *Journal of Applied Crystallography* **2006**, *39*, 895.

(176) Mossine, A. V.; Kumari, H.; Fowler, D. A.; Shih, A.; Kline, S. R.; Barnes, C. L.; Atwood, J. L. *Chemistry--A European Journal* **2012**, *18*, 10258.

(177) Kennedy, S.; Beavers, C. M.; Teat, S. J.; Dalgarno, S. J. *New Journal of Chemistry* **2011**, *35*, 28.

(178) Mansikkamaeki, H.; Nissinen, M.; Rissanen, K. *Angewandte Chemie, International Edition* **2004**, *43*, 1243.

(179) Dalgarno Scott, J.; Cave Gareth, W. V.; Atwood Jerry, L. *Angewandte Chemie (International ed. in English)* **2006**, *45*, 570.

(180) Glinka, C. J.; Barker, J. G.; Hammouda, B.; Krueger, S.; Moyer, J. J.; Orts, W. J. *J. Appl. Crystallogr.* **1998**, *31*, 430.

(181) Schulz, G. V. *Z. physik. Chem.* **1935**, *B30*, 379.

(182) Kumari, H.; Mossine, A. V.; Kline, S. R.; Dennis, C. L.; Fowler, D. A.; Barnes, C. L.; Teat, S. J.; Deakyne, C. A.; Atwood, J. L. *Angew. Chem.* **2011**, In press. DOI: anie.201107182.

(183) Mossine, A. V.; Kumari, H.; Fowler, D. A.; Maerz, A. K.; Kline, S. R.; Barnes, C. L.; Atwood, J. L. *Isr. J. of Chem.* **2011**, *51*, 840.

(184) Kumari, H.; Kline, S. R.; Schuster, N. J.; Atwood, J. L. *Chem. Commun.* **2011**, *47*, 12298.

(185) Kumari, H.; Kline, S. R.; Schuster, N. J.; Barnes, C. L.; Atwood, J. L. *J. of Am. Chem. Soc.* **2011**, *133*, 18102.

(186) Solari, E.; Lesueur, W.; Klose, A.; Schenk, K.; Floriani, C.; Chiesi-Villa, A.; Rizzoli, C. *Chemical Communications (Cambridge)* **1996**, 807.

(187) McQuillan, F. S.; Berridge, T. E.; Chen, H.; Hamor, T. A.; Jones, C. J. *Inorganic Chemistry* **1998**, *37*, 4959.

(188) Eisler, D. J.; Puddephatt, R. J. *Inorganic Chemistry* **2006**, *45*, 7295.

(189) Harrison, R. G.; Fox, O. D.; Meng, M. O.; Dalley, N. K.; Barbour, L. J. *Inorganic Chemistry* **2002**, *41*, 838.

(190) Botta, B.; Delle Monache, G.; Zappia, G.; Misiti, D.; Baratto Maria, C.; Pogni, R.; Gacs-Baitz, E.; Botta, M.; Corelli, F.; Manetti, F.; Tafi, A. *The Journal of organic chemistry* **2002**, *67*, 1178.

(191) Ugono, O.; Moran, J. P.; Holman, K. T. *Chemical Communications (Cambridge, United Kingdom)* **2008**, 1404.

(192) Fox, O. D.; Cookson, J.; Wilkinson, E. J. S.; Drew, M. G. B.; MacLean, E. J.; Teat, S. J.; Beer, P. D. *Journal of the American Chemical Society* **2006**, *128*, 6990.

(193) Kantar, C.; Agar, E.; Sasmaz, S. *Polyhedron* **2009**, *28*, 3485.

(194) Martin, A. D.; Sobolev, A. N.; Spackman, M. A.; Raston, C. L. *Crystal Growth & Design* **2009**, *9*, 3759.

(195) Mislin, G.; Graf, E.; Hosseini, M. W.; De Cian, A.; Kyritsakas, N.; Fischer, J. *Chemical Communications (Cambridge)* **1998**, 2545.

(196) Khlobystov, A. N.; Blake, A. J.; Champness, N. R.; Lemenovskii, D. A.; Majouga, A. G.; Zyk, N. V.; Schroder, M. *Coordination Chemistry Reviews* **2001**, *222*, 155.

(197) Elisabeth, E.; Barbour, L. J.; Orr, G. W.; Holman, K. T.; Atwood, J. L. *Supramolecular Chemistry* **2000**, *12*, 317.

(198) Chen, W.-H.; Nishikawa, M.; Tan, S.-D.; Yamamura, M.; Satake, A.; Kobuke, Y. *Chemical Communications (Cambridge, United Kingdom)* **2004**, 872.

(199) Kuzmicz, R.; Kowalska, V.; Domagala, S.; Stachowicz, M.; Wozniak, K.; Kolodziejski, W. *Journal of Physical Chemistry B* **2010**, *114*, 10311.

VITA

Andrew V. Mossine was born in Kiev, Ukraine on January 7, 1987. His family moved to Columbia, Missouri in 1993, where he attended primary and secondary school. In 2005, he was accepted into the Arts & Science program at the University of Missouri-Columbia, where he pursued a degree in chemistry. While working towards his degree, Andy worked in the lab of Prof. Anand Chandrasekhar and later, the lab of Prof. Jerry Atwood. Andy graduated in 2009 with a BS in chemistry with honors and a minor in mathematics. He continued on with his education at MU and is currently finishing his doctoral work in chemistry with Prof. Jerry Atwood. His thesis is entitled Understanding the self-assembly process and behavior of metal-seamed pyrogallol[4]arene nanocapsules.